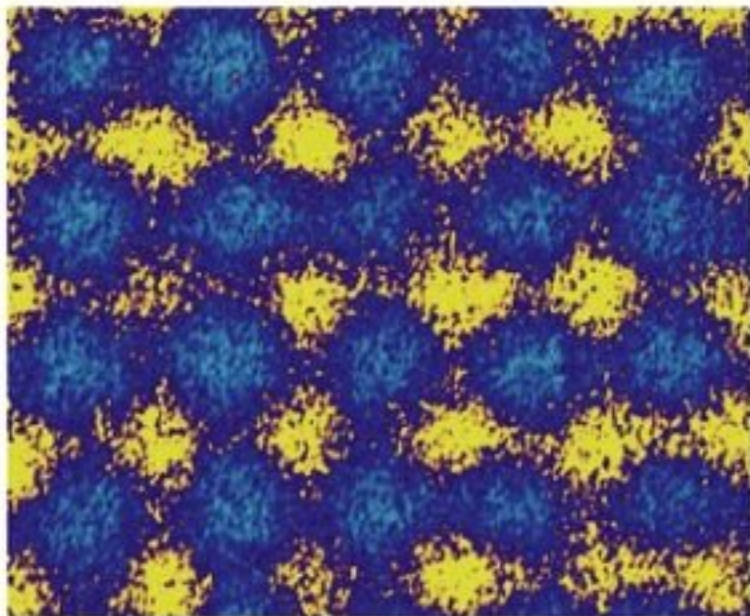


Edited by  
Günter Schmid

WILEY-VCH

# Nanoparticles

From Theory to Application



## **Nanoparticles**

*Edited by Günter Schmid*

## *Further Titles of Interest*

M. Köhler, W. Fritzsche

### **Nanotechnology**

2004, ISBN 3-527-30750-8

C. N. R. Rao, A. Müller, A. K. Cheetham (Eds.)

### **The Chemistry of Nanomaterials**

**Synthesis, Properties and Applications**

2003, ISBN 3-527-30686-2

P. M. Ajayan, L. S. Schadler, P. V. Braun

### **Nanocomposite Science and Technology**

2003, ISBN 3-527-30359-6

F. Caruso (Ed.)

### **Colloids and Colloid Assemblies**

2003, ISBN 3-527-30660-9

Z. L. Wang (Ed.)

### **Characterization of Nanophase Materials**

1999, ISBN 3-527-29837-1

J. H. Fendler (Ed.)

### **Nanoparticles and Nanostructured Films**

**Preparation, Characterization and Applications**

1998, ISBN 3-527-29443-0

# Nanoparticles

From Theory to Application

*Edited by Günter Schmid*



WILEY-VCH Verlag GmbH & Co. KGaA



**Prof. Dr. Günter Schmid**  
Institute of Inorganic Chemistry  
University Duisburg-Essen  
Universitätsstr. 5-7  
45117 Essen  
Germany



This book was carefully produced. Nevertheless, authors, editor and publisher do not warrant the information contained therein to be free of errors. Readers are advised to keep in mind that statements, data, illustrations, procedural details or other items may inadvertently be inaccurate.

**Library of Congress Card No.: applied for**

A catalogue record for this book is available from the British Library.

Bibliographic information published by Die Deutsche Bibliothek

Die Deutsche Bibliothek lists this

publication in the Deutsche

Nationalbibliografie; detailed bibliographic

data is available in the Internet at <http://dnb.ddb.de>

© 2004 WILEY-VCH Verlag GmbH & Co. KGaA, Weinheim

All rights reserved (including those of translation in other languages). No part of this book may be reproduced in any form – by photoprinting, microfilm, or any other means – nor transmitted or translated into machine language without written permission from the publishers. Registered names, trademarks, etc. used in this book, even when not specifically marked as such, are not to be considered unprotected by law.

Printed in the Federal Republic of Germany.

Printed on acid-free paper.

**Typesetting** Asco Typesetters, Hong Kong

**Printing** betz-druck gmbh, Darmstadt

**Bookbinding** Litges & Dopf Buchbinderei GmbH, Heppenheim

**ISBN** 3-527-30507-6

## Contents

<b>1</b>	<b>General Introduction</b>	<b>1</b>
	<i>Günter Schmid</i>	
<b>2</b>	<b>Quantum Dots</b>	<b>4</b>
	<i>Wolfgang Johann Parak, Liberato Manna, Friedrich Christian Simmel, Daniele Gerion, and Paul Alivisatos</i>	
2.1	Introduction and Outline	4
2.2	Nanoscale Materials and Quantum Mechanics	6
2.2.1	Nanoscale Materials as Intermediate between Atomic and Bulk Matter	6
2.2.2	Quantum Mechanics	7
2.3	From Atoms to Molecules and Quantum Dots	8
2.4	Shrinking Bulk Material to a Quantum Dot	10
2.4.1	Three-Dimensional Systems (Bulk Material)	10
2.4.2	Two-Dimensional Systems	14
2.4.3	One-Dimensional Systems (Quantum Wires)	18
2.4.4	Zero-Dimensional Systems (Quantum Dots)	20
2.5	Energy Levels of a (Semiconductor) Quantum Dot	21
2.6	Varieties of Quantum Dots	24
2.6.1	Lithographically Defined Quantum Dots	25
2.6.2	Epitaxially Self-Assembled Quantum Dots	27
2.6.3	Colloidal Quantum Dots	28
2.7	Optical Properties of Quantum Dots	29
2.7.1	Absorption and Emission Spectra	29
2.7.2	Spectral Diffusion and Blinking	31
2.7.3	Metal Nanoparticles	33
2.7.4	Overview of Some Selected Applications	33
2.8	Some (Electrical) Transport Properties of Quantum Dots	34
2.8.1	Coulomb Blockade: Basic Theory and Historical Sketch	35
2.8.2	Single-Electron Tunneling	37
2.8.3	Tunneling Transport – Line Shape of Conductance Peaks	41
2.8.4	Some Applications	42
	References	44

<b>3</b>	<b>Syntheses and Characterizations</b>	<b>50</b>
3.1	Semiconductor Nanoparticles	50
3.1.1	Synthesis and Characterization of II–VI Nanoparticles	50
	<i>Alexander Eychmüller</i>	
3.1.1.1	Historical Review	50
3.1.1.2	Thiol-Stabilized Nanoparticles	57
3.1.1.3	The “TOP/TOPO” Synthesis	61
3.1.1.4	Core-Shell Nanocrystals	63
3.1.1.5	Quantum Dot Quantum Wells	65
	References	71
3.1.2	Synthesis and Characterization of III–V Semiconductor Nanoparticles	79
	<i>Uri Banin</i>	
3.1.2.1	Introduction	79
3.1.2.2	Synthetic Strategy	81
3.1.2.3	InAs and InP Nanocrystals	84
3.1.2.4	III–V Core/Shell Nanocrystals – Synthesis and Characterization	89
	Acknowledgement	105
	References	105
3.1.3	Synthesis and Characterization of Ib–VI Nanoclusters	107
	<i>Stefanie Dehnen, Andreas Eichhöfer, John F. Corrigan, and Dieter Fenske</i>	
3.1.3.1	Introduction	107
3.1.3.2	Chalcogen-Bridged Copper Clusters	108
3.1.3.3	Chalcogen-Bridged Silver Clusters	158
3.1.3.4	Selenium-Bridged Gold Clusters	181
	References	183
3.2	Synthesis of Metal Nanoparticles	185
3.2.1	Noble Metal Nanoparticles	186
	<i>John S. Bradley and Günter Schmid</i>	
3.2.1.1	Introduction	186
3.2.1.2	History and Background	186
3.2.1.3	Generation of Metal Particles	187
3.2.1.4	Stabilization of Colloidal Metal Particles in Liquids	189
3.2.1.5	Synthetic Methods for the Preparation of Colloidal Transition Metals	191
3.2.2	Synthesis and Characterization of Magnetic Nanoparticles	199
	<i>Dmitri V. Talapin, Elena V. Shevchenko, Horst Weller</i>	
3.2.2.1	Introduction	199
3.2.2.2	Organometallic Synthesis of Magnetic Nanoparticles	202
3.2.2.3	Size- and Shape-Dependent Magnetic Properties of Ferromagnetic Metal Nanoparticles	220
	References	230
<b>4</b>	<b>Organization of Nanoparticles</b>	<b>239</b>
4.1	Semiconductor Nanoparticles	239
	<i>Alexander Eychmüller</i>	

4.1.1	Molecular Crystals	239
4.1.2	Superlattices of Semiconductor Nanoparticles	242
4.1.3	Layers of Semiconductor Nanocrystals	244
4.1.4	Coupling of Semiconductor Nanocrystals	249
4.2	Metal Nanoparticles	251
	<i>Günter Schmid, Dmitri V. Talapin, and Elena V. Shevchenko</i>	
4.2.1	Three-dimensional Organization of Metal Nanoparticles	251
4.2.2	Ordered Monolayers of Metal Nanoparticles	260
4.2.2.1	Self-Assembly	261
4.2.2.2	Guided Self-Assembly	268
4.2.2.3	Aimed Structures	277
4.2.3	One-dimensional Arrangements	280
	References	298
<b>5</b>	<b>Properties</b>	<b>305</b>
5.1	Semiconductor Nanoparticles	305
5.1.1	Optical and Electronic Properties of III–V and II–VI Nanoparticles	305
	<i>Uri Banin and Oded Millo</i>	
5.1.1.1	Introduction	305
5.1.1.2	Semiconductor Nanocrystals as Artificial Atoms	306
5.1.1.3	Theoretical Descriptions of the Electronic Structure	313
5.1.1.4	Atomic-like States in Core/Shell Nanocrystals – Spectroscopy and Imaging	314
5.1.1.5	Level Structure of CdSe Quantum Rods	319
5.1.1.6	Optical Gain and Lasing in Semiconductor Nanocrystals	320
	Acknowledgements	322
5.1.2	Optical and Thermal Properties of Ib–VI Nanoparticles	322
	<i>Stefanie Dehnen, Andreas Eichhöfer, John F. Corrigan, and Dieter Fenske</i>	
5.1.2.1	Optical Spectra and Thermal Behavior	322
5.1.2.2	Optical Spectra in the Solid State	326
5.2	Electrical Properties of Metal Nanoparticles	328
	<i>Ulrich Simon</i>	
5.2.1	Introduction	328
5.2.2	Physical Background and Quantum Size Effect	329
5.2.3	Single-Electron Tunneling	331
5.2.3.1	Working Principles of Metal-Based Single-Electron Tunneling Devices	333
5.2.4	Single-Electron Tunneling in Nanoparticles	338
5.2.4.1	Thin Film Structures and STM Single-Electron Systems	340
5.2.4.2	SET on Single Chemically Tailored Nanoparticles	342
5.2.4.3	Metal Nanoparticles in Single-Electron Devices	345
5.2.4.4	Mesoscopic Arrays with Nanoelectrodes	347
5.2.4.5	Chemical Switching and Gating of Current through Nanoparticles	352
5.2.5	From Single-Particle Properties to Collective Charge Transport	353
5.2.5.1	One-Dimensional Arrangements	356
5.2.5.2	Two-Dimensional Arrangements	358

5.2.5.3	Three-Dimensional Arrangements	359
	References	362
<b>6</b>	<b>Biomaterial-Nanoparticle Hybrid Systems: Synthesis, Properties, and Applications</b>	<b>368</b>
	<i>Eugenii Katz, Andrew N. Shipway, and Itamar Willner</i>	
6.1	Introduction	368
6.2	The Synthesis and Properties of Biomaterial-Functionalized Nanoparticles	371
6.2.1	Functionalization by Electrostatic Adsorption	371
6.2.2	Functionalization by Chemisorption of Thiol-Derivatized Biomaterials	372
6.2.3	Functionalization by Specific Interactions	373
6.2.4	Properties of Nanoparticle-Biomaterial Composites	374
6.3	Biomaterial-Functionalized Nanoparticles for Controlled Chemical Reactivity	376
6.3.1	Controlling DNA Reactivity	376
6.3.2	Reporting on DNA Reactivity	377
6.4	The Aggregation of Biomaterial-Functionalized Nanoparticles	377
6.4.1	Receptor-Induced Aggregation of Guest-Functionalized Nanoparticles	379
6.4.2	Nucleic Acid-Functionalized Nanoparticles for Controlled Aggregation	382
6.4.3	Composite Assemblies of Nucleic Acids, Proteins, and Nanoparticles	385
6.5	Assembly of Biomaterial-Nanoparticle Architectures on Surfaces	390
6.5.1	Assembly of Layered Nanoparticle-Protein Assemblies	391
6.5.2	Nucleic Acid – Nanoparticle Architectures on Surfaces	392
6.6	Functional Biomaterial-Nanoparticle Structures on Surfaces for Sensoric and Electronic Applications	397
6.6.1	Nanoparticle-Biomaterial Conjugates for Optical Sensing and Analysis	398
6.6.2	Electronic Transduction of Biosensing Events by Nanoparticle-Biomaterial-Functionalized Arrays	400
6.6.3	Biomaterial-Nanoparticle Arrays for Electronic Circuitry	407
6.7	Biomaterial-Functionalized Magnetic Particles	409
	Acknowledgment	415
	References	415
<b>7</b>	<b>Conclusions and Perspectives</b>	<b>422</b>
	<i>All Authors</i>	

## Contributors

### **Prof. Paul Alivisatos**

University of California, Berkeley  
Department of Chemistry  
Berkeley, CA 94720-1460  
USA

### **Dr. Uri Banin**

Department of Physical Chemistry  
The Hebrew University  
Jerusalem 91904  
Israel

### **Prof. John S. Bradley**

Dept. of Inorganic and Materials Chemistry  
School of Physical Sciences  
University of Hull  
Cottingham Road  
Hull HU6 7RX  
UK

### **Prof. John F. Corrigan**

Department of Chemistry  
The University of Western Ontario  
Chemistry Building  
London, Ontario, N6A 5B7  
Canada

### **Dr. Stefanie Dehnen**

Institut für Anorganische Chemie  
Universität Karlsruhe  
Kaiserstraße 12  
76131 Karlsruhe  
Germany

### **Dr. Andreas Eichhöfer**

Forschungszentrum Karlsruhe  
Institut für Nanotechnologie  
Postfach 3640  
76021 Karlsruhe  
Germany

### **Dr. Alexander Eychmüller**

Institut für Physikalische Chemie  
Universität Hamburg  
Bundesstraße 45  
20146 Hamburg  
Germany

### **Prof. Dr. D. Fenske**

Universität Karlsruhe  
Institut für Anorganische Chemie  
Engesserstraße  
76128 Karlsruhe  
Germany

### **Daniele Gerion**

University of California, Berkeley  
Department of Chemistry  
Berkeley, CA 94720-1460  
USA

### **Prof. Eugenii Katz**

Department of Chemistry  
The Hebrew University of Jerusalem Givat  
Ram  
91904 Jerusalem  
Israel

### **Dr. Liberato Manna**

National Nanotechnology Lab of INFN  
Via Arnesano  
73100 Lecce  
Italy

### **Dr. W. J. Parak**

Universität München  
Lehrstuhl für Angewandte Physik  
Amalienstr. 54  
80799 München  
Germany

**Prof. Dr. Günter Schmid**

Institut für Anorganische Chemie  
Universitätsstraße 5-7  
Universität Duisburg-Essen  
45117 Essen  
Germany

**Dr. Elena V. Shevchenko**

Institute of Physical Chemistry  
University of Hamburg  
Bundesstraße 45  
20146 Hamburg  
Germany

**Dr. Andrew N. Shipway**

Department of Chemistry  
The Hebrew University of Jerusalem Givat  
Ram  
91904 Jerusalem  
Israel

**Dr. Friedrich C. Simmel**

Sektion Physik der LMU  
Geschwister-Scholl-Platz 1  
80539 München  
Germany

**Prof. Dr. Ulrich Simon**

RWTH Aachen  
Anorganische Chemie  
Professor Pirlet Straße 1  
52054 Aachen  
Germany

**Dr. Dmitri V. Talapin**

Institute of Physical Chemistry  
University of Hamburg  
Bundesstraße 45  
20146 Hamburg  
Germany

**Prof. Horst Weller**

Institute of Physical Chemistry  
University of Hamburg  
Bundesstraße 45  
20146 Hamburg  
Germany

**Prof. Itamar Willner**

The Institute of Chemistry  
The Hebrew University of Jerusalem  
91904 Jerusalem  
Israel

## 1

**General Introduction***Günter Schmid*

In 1994 the book entitled “Clusters and Colloids – from Theory to Applications” was published with the goal of summarizing the state of the art in the field of metal clusters and colloids. Nine years ago, interest was mainly focused on synthetic and structural aspects. Theoretical considerations were limited to small molecule-like organometallic clusters. The very first hints of important novel electronic properties of nanosized particles stimulated further activity. Practical applications could be foreseen – at least if the will was there.

Nine years of worldwide revolutionary developments in nanoscience, combining physics, chemistry, material science, theory and even biosciences, have brought us to another level of understanding. “Nanotechnology” became a key word of public interest, since even politicians and economists realized the social power of nanotechnological developments. Nanotechnology is called the technology of the next century, coming after microtechnology. Nanotechnology unfortunately also became a catchword for people with ambitions in science fiction. Such people threaten us with visions of horror, as when self-replicating machines will destroy mankind. Nevertheless, nanoscience, and consequently nanotechnology, is going to initiate a technological impact that can probably not be compared with any other technical development up to the present time, since it will concern all aspects of human life, ranging from novel building materials to medicine. Of course, it is sometimes difficult to distinguish between vision and reality. However, nanotechnology has already become part of our daily lives, even if we do not recognize this. The most revolutionary consequences can be expected if the most valuable properties of nanoparticles, their electronic properties, are exploited. These are of a fascinating nature and will bring about a real technological revolution. Meanwhile, we know the most important basic facts about nanoparticles and so can predict future applications based on their novel properties.

This book does not, of course, deal with any kind of unsubstantiated visions, in either a positive or a negative sense. It reports strictly on the present state of scientific development, which is impressive enough for any kind of science fiction to be quite unnecessary.



Semiconductor and metal nanoparticles occupy the center of scientific interest because of their unique electronic nature: they follow quantum mechanical rules instead of the laws of classical physics which govern bulk materials. Therefore, small molecular clusters, mainly of the organometallic type, are not considered further. It is also no longer helpful to strictly distinguish clusters from colloids. In general, we call compounds of interest nanoparticles, which implies that predominantly they do not exhibit classical bulk properties, while, on the other hand, differing from molecules in so far as they in some way represent pieces of matter related to the bulk material they originate from.

Consequently the first chapter of this book is called “Quantum Dots”, as it deals with those very special properties of matter in the nanosize regime. The understanding of quantum-confined electrons in very small particles is the basis for the understanding of properties which will be described in following chapters.

Although the principal synthetic routes to nanoparticles of semiconductor or metallic nature have been well known for some decades, some novel developments seem worth reporting here, and for reasons of completeness classical procedures will at least briefly be reconsidered. Syntheses of semiconductor nanoparticles of II–VI, III–V and Ib–VI types will be followed by routes to metal nanoparticles.

The science of nanoparticles during the last decade is characterized by, among other things, the enormous efforts which have been made to organize nanoparticles in three and two dimensions, and to some extent one dimension. Three-dimensional organization of atoms, ions, or molecules is a well-known natural process, called crystallization. Three-dimensional organization of nanoparticles is, however, not always a simple matter, since, with some exceptions, particles of a few up to some dozens of nanometers in size usually do not possess exactly the same number of atoms or, consequently, the same shape. Classically, only identical species were believed to form crystals. Then we learned that particles of similar but not identical size and shape may be able to organize three-, even two-dimensionally. These aspects become important, as we shall see, in applications of nanoparticles in future nanoelectronic or magnetic devices, for instance in relation to storage problems. This is why the organization of semiconductor and metal nanoparticles will be discussed in detail.

The chapter on the various properties of nanoparticles is of central importance in this book. With the parallel development of analytical tools, highly sophisticated intrinsic properties of all kinds of nanoparticles became visible. Optical, electronic, and magnetic properties of nanoparticles open up a novel world with immense implications for future developments.

As already mentioned, biomaterials became part of nanoscience after we learned to use biomolecules as tools to combine inorganic nanoparticles. DNA and proteins developed into valuable materials of manifold excellent utility. The combination of inorganic and biochemical building blocks led to a wide variety of novel hybrid systems with unexpected properties. This field of nanoscience is still at the very beginning and is expected to develop very fast in the near future.

Just like its predecessor, “Clusters and Colloids”, this book will need a successor in a couple of years, because of the extremely rapid development of nanoscience.

Therefore, it should be stated that this book simply gives an insight into our current, short-lived knowledge of important aspects of nanoscience.

This brings us to those parts of nanoscience that will not be considered here, because they would overstep the limits of this book too much. Thus, we will not consider the rapidly growing field of nanorods and nanowires. Also, nanosized biological and supramolecular aspects will not be discussed, except in some special cases relating to quantum dots. Nanostructured surfaces will also not be explicitly treated, except those resulting from decoration with nanoparticles. Indeed, these are considerable restrictions. However, it is not the purpose of this work to serve as an encyclopedia. Rather it is an attempt to describe one important part of nanoscience that may play a decisive role in future nanotechnology.

## 2

**Quantum Dots**

*Wolfgang Johann Parak, Liberato Manna, Friedrich Christian Simmel, Daniele Gerion, and Paul Alivisatos*

## 2.1

**Introduction and Outline**

In the last decade, new directions of modern research, broadly defined as “nano-scale science and technology”, have emerged [1, 2]. These new trends involve the ability to fabricate, characterize, and manipulate artificial structures, whose features are controlled at the nanometer level. They embrace areas of research as diverse as engineering, physics, chemistry, materials science, and molecular biology. Research in this direction has been triggered by the recent availability of revolutionary instruments and approaches that allow the investigation of material properties with a resolution close to the atomic level. Strongly connected to such technological advances are the pioneering studies that have revealed new physical properties of matter at a level intermediate between atomic/molecular and bulk.

Materials science and technology is a field that is evolving at a very fast pace and is currently giving the most significant contributions to nanoscale research. It is driven by the desire to fabricate materials with novel or improved properties. Such properties can be, for instance, strength, electrical and thermal conductivity, optical response, elasticity, or wear resistance. Research is also evolving toward materials that are designed to perform more complex and efficient tasks. Examples include materials that bring about a higher rate of decomposition of pollutants, a selective and sensitive response toward a given biomolecule, an improved conversion of light into current, or more efficient energy storage. For such and more complex tasks to be realized, novel materials have to be based on several components whose spatial organization is engineered at the molecular level. This class of materials can be defined as “nano-composites”. They are made of assembled nanosized objects or molecules. Their macroscopic behavior arises from the combination of the novel properties of the individual building blocks and their mutual interaction.

In electronics, the design and the assembly of functional materials and devices based on nanoscale building blocks can be seen as the natural, inevitable evolution of the trend toward miniaturization. The microelectronics industry, for instance, is fabricating integrated circuits and storage media whose basic units are approach-

ing the size of few tens of nanometers. For computers, “smaller” means higher computational power at lower cost and with higher portability. However, this race toward higher performance is driving current silicon-based electronics to the limits of its capability [3–6]. The design of each new generation of smaller and faster devices involves more sophisticated and expensive processing steps, and requires the solution of new sets of problems, such as heat dissipation and device failure. If the trend toward further miniaturization persists, silicon technology will soon reach limits at which these problems become insurmountable. In addition to this, scientists have found that device characteristics in very small components are strongly altered by quantum mechanical effects. In many cases, these effects will undermine the classical principles on which most of today’s electronic components are based. For these reasons, alternative materials and approaches are currently being explored for novel electronic components in which the laws of quantum mechanics regulate their functioning in a predictable way. Perhaps in the near future a new generation of computers will rely on fundamental processing units that are made only of a few atoms.

Fortunately, the advent of new methods for the controlled production of nanoscale materials has provided new tools that can be adapted for this purpose. New terms such as nanotubes, nanowires, and quantum dots are now common jargon of scientific publications. These objects are among the smallest man-made units that display physical and chemical properties which make them promising candidates as fundamental building blocks for novel transistors. The advantages envisaged here are higher device versatility, faster switching speed, lower power dissipation, and the possibility of packing many more transistors on a single chip. Prototypes of these new single nano-transistors are nowadays fabricated and studied in research laboratories and are far from commercialization. How millions of such components could be arranged and interconnected in complex architectures and at low cost still remains a formidable problem to be solved.

With a completely different objective, the pharmaceutical and biomedical industries try to synthesize large supramolecular assemblies and artificial devices that mimic the complex mechanisms of nature or that can be potentially used for more efficient diagnoses and better cures for diseases. Examples in this direction are nanocapsules such as liposomes, embodying drugs that can be selectively released in living organs, or bioconjugate assemblies of biomolecules and magnetic (or fluorescent) nanoparticles that may provide faster and more selective analysis of biotissues. These prototype systems may one day evolve into more complex nanomachines with highly sophisticated functional features able to carry out complicated tasks at the cellular level in a living body.

This chapter is not meant as a survey of the present state and future developments of nanoscale science and technology, and the list of examples mentioned above is far from being complete. Nanoscience and nanotechnology will definitely have a strong impact on our lives in many disparate areas. We can mention, as the most significant examples, information technology and the telecommunications industry, materials science and engineering, medicine. In this introductory chapter, we want to stress the point that any development in nanoscience necessarily

requires an understanding of the physical laws that govern matter at the nanoscale and of how the interplay of the various physical properties of a nanoscopic system translates into some novel behavior or into a new physical property. In this sense, the chapter will serve as an overview of basic physical rules governing nanoscale materials, with a particular emphasis on quantum dots, including their various physical realizations and their possible applications. Quantum dots are the ultimate example of a solid in which all dimensions shrink down to a few nanometers. Moreover, semiconductor quantum dots are probably the most studied nanoscale systems.

The outline of this chapter is as follows. In Section 2.2 we try to explain with a few examples why the behavior of nanoscale materials can be remarkably different from that of bulk materials and from their atomic counterparts, and how quantum mechanics can help us in rationalizing this. Following this discussion, we give a definition of a “quantum dot”. In Section 2.3 we follow a bottom-up approach and give the simplified picture of a solid as being a very large molecule, where the energy levels of the individual atomic components have merged into bands. The electronic structure of a quantum dot, being intermediate between that of the two extreme cases of single atoms and bulk material, will then be an easier concept to grasp. In Section 2.4 we use the model of a free-electron gas and the concept of quantum confinement to explain what happens to a solid when its dimensions shrink one by one. This leads us to a more accurate definition of quantum well, quantum wire, and quantum dot. In Section 2.5 we examine in more detail the electronic structure of quantum dots, although we try to keep the discussion at a simple level. Section 2.6 is a brief overview of the most popular methods used to fabricate quantum dots. Different methods lead to different varieties of quantum dots, which can be suited for specific applications. In Section 2.7 we discuss the optical properties of quantum dots. As they are quite unique for this class of materials, the optical properties are probably the most important reason why the research on quantum dots has exploded in the last decade. The discussion here will be focused more on colloidal nanocrystal quantum dots. Electrical and transport properties are nonetheless extremely relevant, as is described in Section 2.8, since, for instance, the addition or subtraction of a charge from a quantum dot leads to dramatic modification of its electronic structure and of the way the dot will handle a further addition or subtraction of a charge. This can be of fundamental importance for future applications in electronics.

## 2.2

### Nanoscale Materials and Quantum Mechanics

#### 2.2.1

##### Nanoscale Materials as Intermediate between Atomic and Bulk Matter

Nanoscale materials frequently show behavior which is intermediate between that of a macroscopic solid and that of an atomic or molecular system. Consider, for

instance, the case of an inorganic crystal composed of few atoms. Its properties will be different from those of a single atom, but we cannot imagine that they will be the same as those of a bulk solid. The number of atoms on the crystal's surface, for instance, is a significant fraction of the total number of atoms, and therefore will have a large influence on the overall properties of the crystal. We can easily imagine that this crystal might have a higher chemical reactivity than the corresponding bulk solid and that it will probably melt at lower temperatures. Consider now the example of a carbon nanotube, which can be thought of as a sheet of graphite wrapped in such a way that the carbon atoms on one edge of the sheet are covalently bound to the atoms on the opposite edge of the sheet. Unlike its individual components, a carbon nanotube is chemically extremely stable because the valences of all its carbon atoms are saturated. Moreover, we would guess that carbon nanotubes can be good conductors because electrons can freely move along these tiny, wire-like structures. Once again, we see that such nanoscopic objects can have properties which do not belong to the realm of their larger (bulk) or smaller (atoms) counterparts. However, there are many additional properties specific to such systems which cannot easily be grasped by simple reasoning. These properties are related to the sometimes counterintuitive behavior that charge carriers (electrons and holes) can exhibit when they are forced to dwell in such structures. These properties can only be explained by the laws of quantum mechanics.

### 2.2.2

#### **Quantum Mechanics**

A fundamental aspect of quantum mechanics is the particle-wave duality, introduced by De Broglie, according to which any particle can be associated with a matter wave whose wavelength is inversely proportional to the particle's linear momentum. Whenever the size of a physical system becomes comparable to the wavelength of the particles that interact with such a system, the behavior of the particles is best described by the rules of quantum mechanics [7]. All the information we need about the particle is obtained by solving its Schrödinger equation. The solutions of this equation represent the possible physical states in which the system can be found. Fortunately, quantum mechanics is not required to describe the movement of objects in the macroscopic world. The wavelength associated with a macroscopic object is in fact much smaller than the object's size, and therefore the trajectory of such an object can be excellently derived using the principles of classical mechanics. Things change, for instance, in the case of electrons orbiting around a nucleus, since their associated wavelength is of the same order of magnitude as the electron-nucleus distance.

We can use the concept of particle-wave duality to give a simple explanation of the behavior of carriers in a semiconductor nanocrystal. In a bulk inorganic semiconductor, conduction band electrons (and valence band holes) are free to move throughout the crystal, and their motion can be described satisfactorily by a linear combination of plane waves whose wavelength is generally of the order of nanometers. This means that, whenever the size of a semiconductor solid becomes

comparable to these wavelengths, a free carrier confined in this structure will behave as a particle in a potential box [8]. The solutions of the Schrödinger equation in such case are standing waves confined in the potential well, and the energies associated with two distinct wavefunctions are, in general, different and discontinuous. This means that the particle energies cannot take on any arbitrary value, and the system exhibits a discrete energy level spectrum. Transitions between any two levels are seen as discrete peaks in the optical spectra, for instance. The system is then also referred to as “quantum confined”. If all the dimensions of a semiconductor crystal shrink down to a few nanometers, the resulting system is called a “quantum dot” and will be the subject of our discussion throughout this chapter. The main point here is that in order to rationalize (or predict) the physical properties of nanoscale materials, such as their electrical and thermal conductivity or their absorption and emission spectra, we need first to determine their energy level structure.

For quantum-confined systems such as quantum dots, the calculation of the energy structure is traditionally carried out using two alternative approaches. One approach has just been outlined above. We take a bulk solid and we study the evolution of its band structure as its dimensions shrink down to a few nanometers. This method will be described in more detail later (Section 2.4). Alternatively, we can start from the individual electronic states of single isolated atoms as shown in Section 2.3 and then study how the energy levels evolve as atoms come closer and start interacting with each other.

## 2.3

### From Atoms to Molecules and Quantum Dots

From the point of view of a chemist, the basic building blocks of matter are atomic nuclei and electrons. In an atom, electrons orbit around the single nucleus, and the number of electrons depends on the element. In the simplest case of the hydrogen atom, one electron orbits around one proton. The electronic states of the hydrogen atom can be calculated analytically [9, 10]. As soon as more than one electron is involved, however, the calculation of the energy levels becomes more complicated, since, in addition to the interaction between the nucleus and the electron, now also electron-electron interactions have to be taken into account. Although the energy states of many-electron atoms can no longer be derived analytically, approximations such as the Hartree-Fock method exist [10]. Each electron can be ascribed to an individual orbit, called an atomic orbital (AO), with an associated discrete energy level. Depending on the angular moment of the orbit, AOs can have spherical (*s*-orbital), club-like (*p*-orbital) or a more complicated (*d*-, *f*-orbitals) shape. The eight valence electrons of a neon atom, for example, occupy one *s*- and three *p*-orbitals around the nucleus, one spin up and one spin down per orbit [10], where the energy level of the *s*-orbital is lower than that of the *p*-orbitals. In accordance with the rules of quantum mechanics, the energy levels are discrete.

The next bigger structure, obtained from the combination of several atoms, is

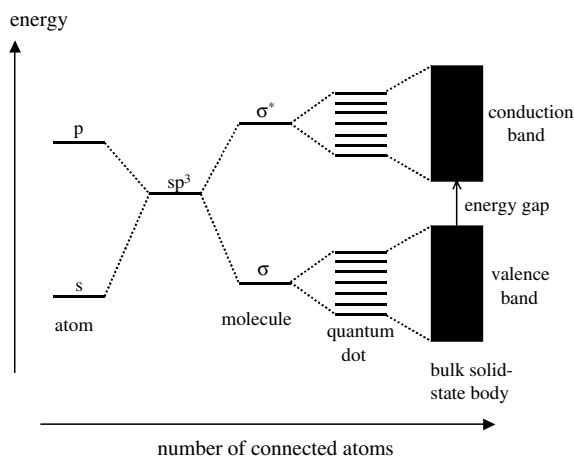


**Fig. 2-1** Electronic energy levels depending on the number of bound atoms. By binding more and more atoms together, the discrete energy levels of the atomic orbitals merge into energy bands (here shown for a semiconducting material) [16]. Therefore semiconducting nanocrystals (quantum dots) can be regarded as a hybrid between small molecules and bulk material.

the molecule. Now electrons orbit collectively around more than one nucleus. In a molecule, electrons that are responsible for the covalent bonds between individual atoms can no longer be ascribed to one individual atom, but they are “shared”. In methane ( $\text{CH}_4$ ), for instance, each of the four  $sp^3$  atomic orbitals of the central carbon atom is linearly combined with the  $s$  orbital of a hydrogen atom to form a bonding ( $\sigma$ ) and an anti-bonding ( $\sigma^*$ ) orbital, respectively [9]. Since these orbitals are “shared” between the atoms, they are called molecular orbitals (MO, see Figure 2-1). Only the lowest energy (bonding) orbitals are occupied, and this explains the relative stability of methane [10]. Using the same principle, it is possible to derive the electronic structure of more complex systems such as large molecules or atomic clusters. When combining atoms to form a molecule, we start from discrete energy levels of the atomic orbitals and we still end up obtaining discrete levels for the molecular orbitals [9].

When the size of a polyatomic system becomes progressively larger, the calculation of its electronic structure in terms of combinations of atomic orbitals becomes unfeasible [11–13]. However, simplifications arise if the system under study is a periodic, infinite crystal. The electronic structure of crystalline solids can be in fact described in terms of periodic combinations of atomic orbitals (Bloch functions) [14, 15]. In this model, perfect translational symmetry of the crystal structure is assumed, and contributions from the surface of the crystal are neglected by assuming an infinite solid (periodic boundary conditions). Electrons are described as a superposition of plane waves extended throughout the solid. As opposed to the case of atoms and molecules, the energy structure of a solid no longer consists of discrete energy levels, but rather of broad energy bands [14, 15], as sketched in Figure 2-1. Every band can be filled only with a limited amount of charge carriers.



In very small crystals of nanometer dimensions, so called nanocrystals, the assumptions of translational symmetry and infinite size of the crystal are no longer valid, and thus these systems cannot be described with the same model used for a bulk solid. We can imagine indeed that the electronic structure of a nanocrystal should be something intermediate between the discrete levels of an atomic system and the band structure of a bulk solid. This can be evidenced from Figure 2-1: the energy levels of a nanocrystal are discrete, their density is much larger, and their spacing is smaller than for the corresponding levels of one atom or a small atomic cluster. Because of their discrete energy levels, such structures are called also quantum dots. The concept of energy bands and band gap can still be used. Highest occupied atomic levels of the atomic (or ionic) species interact with each other to form the valence band of the nanocrystal. Similarly, lowest unoccupied levels combine to form the conduction band of the nanocrystal. The energy gap between the valence and conduction bands results in the band gap of the nanocrystal. As an example, consider a metallic quantum dot. Its level spacing at the Fermi level is roughly proportional to  $\sim E_F/N$ , where  $N$  is the number of electrons in the quantum dot. Given that  $E_F$  is a few eV and that  $N$  is close to 1 per atom, the band gap of a metallic quantum dot becomes observable only at very low temperatures. Conversely, in the case of semiconductor quantum dots, the band gap is larger and its effects can be observed at room temperature. The size-tunable fluorescence emission of CdSe quantum dots in the visible region of the spectrum is for instance a very explanatory illustration of the presence of a size-dependent band gap.

## 2.4

### Shrinking Bulk Material to a Quantum Dot

In this chapter we will use the concept of quantum confinement of carriers in a solid to derive a more detailed description of the electronic band structure in a low-dimensional solid. This description, although more elaborate than the one just given above, is indeed more powerful and will underline the general physics of a solid when its dimensions shrink one by one down to few nanometers. We will start first with an elementary model of the behavior of electrons in a bulk solid. This model will then be adapted to the case of confined carriers.

#### 2.4.1

##### Three-Dimensional Systems (Bulk Material)

We now consider the case of a three-dimensional solid of size  $d_x, d_y, d_z$ , containing  $N$  free electrons. “Free” means that these electrons are delocalized and thus not bound to individual atoms. Furthermore, we will make the assumption that the interactions between the electrons, as well as the interactions between the electrons and the crystal potential, can be neglected as a first approximation. Such a model system is called “free-electron gas” [14, 15].

Astonishingly, this oversimplified model still captures many of the physical aspects of real systems. From more complicated theories it has been learnt that many of the expressions and conclusions from the free-electron model remain valid as a first approximation even when one takes electron-crystal and electron-electron interactions into account. In many cases it is sufficient to replace the free-electron mass  $m$  by an “effective” mass  $m^*$ , which implicitly contains the corrections for the interactions. To keep the story simple, we proceed with the free-electron picture. In the free-electron model, each electron in the solid moves with a velocity  $\vec{v} = (v_x, v_y, v_z)$ . The energy of an individual electron is then just its kinetic energy:

$$E = \frac{1}{2} m \vec{v}^2 = \frac{1}{2} m (v_x^2 + v_y^2 + v_z^2) \quad (1)$$

According to Pauli’s exclusion principle, each electron must be in a unique quantum state. Since electrons can have two spin orientations ( $m_s = +\frac{1}{2}$  and  $m_s = -\frac{1}{2}$ ), only two electrons with opposite spins can have the same velocity  $\vec{v}$ . This case is analogous to the Bohr model of atoms, in which each orbital can be occupied by two electrons at maximum. In solid-state physics, the wavevector  $\vec{k} = (k_x, k_y, k_z)$  of a particle is more frequently used instead of its velocity to describe the particle’s state. Its absolute value  $k = |\vec{k}|$  is the wavenumber. The wavevector  $\vec{k}$  is directly proportional to the linear momentum  $\vec{p}$  and thus also to the velocity  $\vec{v}$  of the electron:

$$\vec{p} = m\vec{v} = \frac{h}{2\pi} \vec{k} \quad (2)$$

The scaling constant is the Planck constant  $h$ , and the wavenumber is related to the wavelength  $\lambda$  associated with the electron through the De Broglie relation [14, 15]:

$$\pm k = |\vec{k}| = \pm \frac{2\pi}{\lambda} \quad (3)$$

The wavelengths  $\lambda$  associated with the electrons traveling in a solid are typically of the order of nanometers<sup>1)</sup>, much smaller than the dimensions of an ordinary solid.

The calculation of the energy states for a bulk crystal is based on the assumption of periodic boundary conditions. Periodic boundary conditions are a mathematical trick to “simulate” an infinite ( $d \rightarrow \infty$ ) solid. This assumption implies that the conditions at opposite borders of the solid are identical. In this way, an electron that is close to the border does not really “feel” the border. In other words, the electrons at the borders “behave” exactly as if they were in the bulk. This con-

1) In fact, the wavelength depends on the electron density. The wavelength for electrons in metals is typically around 10 nm; in

semiconductors it may vary between 10 nm and 1  $\mu\text{m}$ .

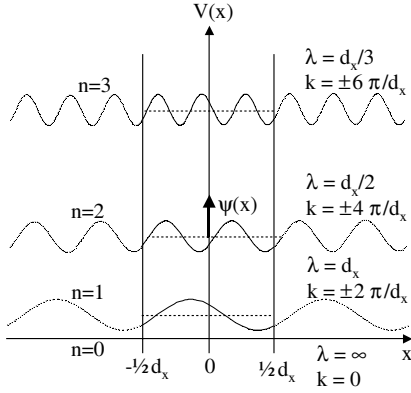


**Fig. 2-2** Periodic boundary conditions (only drawn for the  $x$ -dimension) for a free-electron gas in a solid with thickness  $d$ . The idea of periodic boundary conditions is to mathematically “simulate” an infinite solid. Infinite extension is similar to an object without any borders. This means that a particle close to the “border” must not be affected by the border, but “behaves” exactly as it were in the bulk. This can be realized by using a wavefunction  $\psi(x)$  that is periodic within the thickness  $d$  of the solid. Any electron that leaves the solid from its right boundary would reenter under

exactly the same conditions on its left side. For the electron the borders are quasi-nonexistent. The probability density  $|\psi(x)|^2$  is the probability that an electron is at the position  $x$  in the solid. Different states for the electrons ( $n = 0, 1, 2, \dots$ ) have different wavefunctions.  $\lambda$  is the De Broglie wavelength of the electrons and  $k$  is their corresponding wavenumber. A “real” bulk solid can be approximated by an infinite solid ( $d \rightarrow \infty$ ) and its electronic states in  $k$ -space are quasi-continuously distributed:  $\Delta k = 2\pi/d_x \rightarrow 0$ .

dition can be realized mathematically by imposing the following condition to the electron wavefunctions:  $\psi(x, y, z) = \psi(x + d_x, y, z)$ ,  $\psi(x, y, z) = \psi(x, y + d_y, z)$ , and  $\psi(x, y, z) = \psi(x, y, z + d_z)$ . In other words, the wavefunctions must be periodic with a period equal to the whole extension of the solid [15, 17]. The solution of the stationary Schrödinger equation under such boundary conditions can be factorized into the product of three independent functions  $\psi(x, y, z) = \psi(x)\psi(y)\psi(z) = A \exp(ik_x x) \exp(ik_y y) \exp(ik_z z)$ . Each function describes a free electron moving along one Cartesian coordinate. In the argument of the functions,  $k_{x,y,z}$  is equal to  $\pm n\Delta k = \pm n2\pi/d_{x,y,z}$  and  $n$  is an integer [14, 15, 17]. These solutions are waves that propagate along the negative and the positive direction, for  $k_{x,y,z} > 0$  and  $k_{x,y,z} < 0$ , respectively. An important consequence of the periodic boundary conditions is that all the possible electronic states in the  $\vec{k}$  space are equally distributed. There is an easy way of visualizing this distribution in the ideal case of a one-dimensional free-electron gas: there are two electrons ( $m_s = \pm \frac{1}{2}$ ) in the state  $k_x = 0$  ( $v_x = 0$ ), two electrons in the state  $k_x = +\Delta k$  ( $v_x = +\Delta v$ ), two electrons in the state  $k_x = -\Delta k$  ( $v_x = \Delta v$ ), two electrons in the state  $k_x = +2\Delta k$  ( $v_x = +2\Delta v$ ), and so on.

For a three-dimensional bulk material we can follow an analogous scheme. Two electrons ( $m_s = \pm \frac{1}{2}$ ) can occupy each of the states  $(k_x, k_y, k_z) = (\pm n_x \Delta k, \pm n_y \Delta k,$

$\pm n_z \Delta k$ ), again with  $n_{x,y,z}$  being an integer. A sketch of this distribution is shown in Figure 2-3. We can easily visualize the occupied states in  $\vec{k}$ -space because all these states are included into a sphere whose radius is the wavenumber associated with the highest energy electrons. At the ground state, at 0 K, the radius of the sphere is the Fermi wavenumber  $k_F$  (Fermi velocity  $v_F$ ). The Fermi energy  $E_F \propto k_F^2$  is the energy of the last occupied electronic state. All electronic states with an energy  $E \leq E_F$  are occupied, whereas all electronic states with higher energy  $E > E_F$  are empty. In a solid, the allowed wave numbers are separated by  $\Delta k = \pm n 2\pi/d_{x,y,z}$ . In a bulk material  $d_{x,y,z}$  is large, and so  $\Delta k$  is very small. Then the sphere of states is filled quasi-continuously [15].

We need now to introduce the useful concept of the density of states  $D_{3d}(k)$ , which is the number of states per unit interval of wavenumbers. From this definition,  $D_{3d}(k)\Delta k$  is the number of electrons in the solid with a wavenumber between  $k$  and  $k + \Delta k$ . If we know the density of states in a solid we can calculate, for instance, the total number of electrons having wavenumbers less than a given  $k_{\max}$ , which we will call  $N(k_{\max})$ . Obviously,  $N(k_{\max})$  is equal to  $\int_0^{k_{\max}} D_{3d}(k) dk$ . In the ground state of the solid, all electrons have wavenumbers  $k \leq k_F$ , where  $k_F$  is the Fermi wavenumber. Since in a bulk solid the states are homogeneously distributed in  $\vec{k}$ -space, we know that the number of states between  $k$  and  $k + \Delta k$  is proportional to  $k^2 \Delta k$  (Figure 2-3). This can be visualized in the following way. The volume in three-dimensional  $\vec{k}$ -space varies with  $k^3$ . If we only want to count the number of states with a wavenumber between  $k$  and  $k + \Delta k$ , we need to determine the volume of a spherical shell with radius  $k$  and thickness  $\Delta k$ . This volume is proportional to product of the surface of the sphere (which varies as  $k^2$ ) with the thickness of the shell (which is  $\Delta k$ ).  $D_{3d}(k)\Delta k$  is thus proportional to  $k^2 \Delta k$ , and in the limit when  $\Delta k$  approaches zero, we can write:

$$D_{3d}(k) = \frac{dN(k)}{dk} \propto k^2 \quad (4)$$

Instead of knowing the density of states in a given interval of wavenumbers it is more useful to know the number of electrons that have energies between  $E$  and  $E + \Delta E$ . From Eqs. (1) and (2) we know that  $E(k)$  is proportional to  $k^2$ , and thus  $k \propto \sqrt{E}$ . Consequently,  $dk/dE \propto 1/\sqrt{E}$ . By using Eq. (4), we obtain for the density of states for a three-dimensional electron gas [17]:

$$D_{3d}(E) = \frac{dN(E)}{dE} = \frac{dN(k)}{dk} \frac{dk}{dE} \propto E \cdot 1/\sqrt{E} \propto \sqrt{E} \quad (5)$$

This can be seen schematically in Figure 2-3. With Eq. (5) we conclude our simple description of a bulk solid. The possible states in which an electron can be found are quasi-continuous. The density of states varies with the square root of the energy. More details about the free-electron gas model and more refined descriptions of electrons in solids can be found in any solid state physics textbook [14].

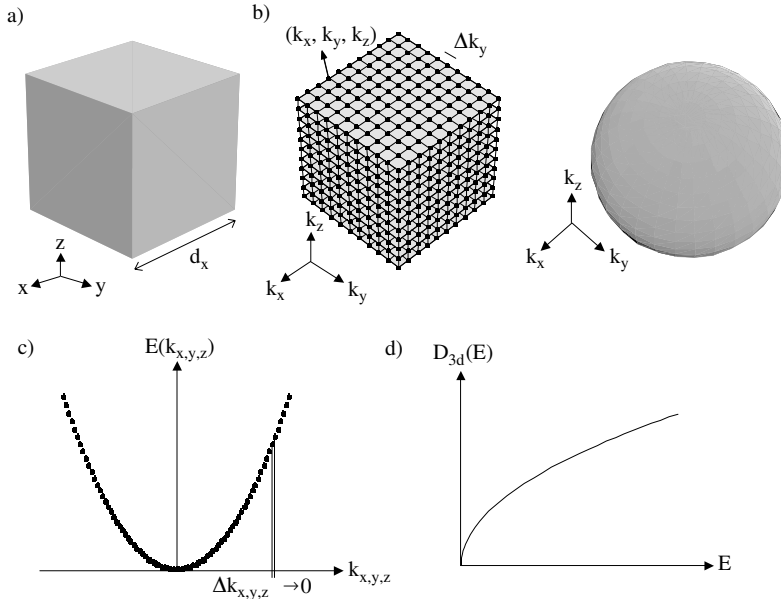


**Fig. 2-3** Electrons in a three-dimensional bulk solid [15]. (a) Such a solid can be modeled as an infinite crystal along all three dimensions  $x, y, z$ . (b) The assumption of periodic boundary conditions yields standing waves as solutions for the Schrödinger equation for free electrons. The associated wavenumbers  $(k_x, k_y, k_z)$  are periodically distributed in the reciprocal  $k$ -space [17]. Each of the dots shown in the figure represents a possible electronic state  $(k_x, k_y, k_z)$ . Each state in  $k$ -space can be only occupied by two electrons. In a large solid the spacing  $\Delta k_{x,y,z}$  between individual electron states is very small, and therefore the  $k$ -space is quasi-continuously filled with states. A sphere with radius  $k_F$  includes all states with  $k = (k_x^2 + k_y^2 + k_z^2)^{1/2} < k_F$ . In the ground

state, at 0 K, all states with  $k < k_F$  are occupied by two electrons, and the other states are empty. Since the  $k$ -space is homogeneously filled with states, the number of states within a certain volume varies with  $k^3$ . (c) Dispersion relation for free electrons in a three-dimensional solid. The energy of free electrons varies with the square of the wavenumber, and its dependence on  $k$  is described by a parabola. For a bulk solid the allowed states are quasi-continuously distributed and the distance between two adjacent states (here shown as points) in  $k$ -space is very small. (d) Density of states  $D_{3d}$  for free electrons in a three-dimensional system. The allowed energies are quasi-continuous and their density varies with the square root of the energy  $E^{1/2}$ .

## 2.4.2

### Two-Dimensional Systems

We now consider a solid that is fully extended along the  $x$ - and  $y$ -directions, but whose thickness along the  $z$ -direction ( $d_z$ ) is only a few nm (see Figure 2-5). Free electrons can still move freely in the  $x$ - $y$  plane. However, movement in the  $z$ -direction is now restricted. Such a system is called a 2-dimensional electron gas (2DEG) [18]. As mentioned in Section 2.2, when one or more dimensions of a solid become smaller than the De Broglie wavelength associated with the free charge carriers, an additional contribution of energy is required to confine the

component of the motion of the carriers along this dimension. In addition, the movement of electrons along such a direction becomes quantized. This situation is shown in Figure 2-4. No electron can leave the solid, and electrons that move in the  $z$ -direction are trapped in a “box”. Mathematically this is described by infinitely high potential wells at the border  $z = \pm \frac{1}{2}d_z$ .

The solutions for the particle-in-a-box situation can be obtained by solving the one-dimensional Schrödinger equation for an electron in a potential  $V(z)$ , which is zero within the box but infinite at the borders. As can be seen in Figure 2-4, the solutions are stationary waves with energies<sup>2)</sup>  $E_{nz} = \hbar^2 k_z^2 / 2m = \hbar^2 k_z^2 / 8\pi^2 m = \hbar^2 n_z^2 / 8md_z^2$ ,  $n_z = 1, 2, \dots$  [9, 17]. This is similar to states  $k_z = n_z \Delta k_z$  with  $\Delta k_z = \pi/d_z$ . Again, each of these states can be occupied at maximum by two electrons.

Let us compare the states in the  $k$ -space for three- and two dimensional materials (Figures 2-3 and 2-5). For a two-dimensional solid that is extended in the  $x$ - $y$ -plane only discrete values are allowed for  $k_z$ . The thinner the solid in the  $z$ -direction, the larger is the spacing  $\Delta k_z$  between these allowed states. On the other hand, the distribution of states in the  $k_x$ - $k_y$  plane remains quasi-continuous. Therefore one can describe the possible states in the  $k$ -space as planes parallel to the  $k_x$ - and  $k_y$ -axes, with a separation  $\Delta k_z$  between the planes in the  $k_z$ -direction. We can number the

- 2) The particle-in-a-box approach (Figure 2-4) looks similar to the case of the periodic boundary conditions (Figure 2-2). There are indeed important differences between the two cases. Periodic boundary conditions “emulate” an infinite solid. A quantum mechanical treatment of this problem yields propagating waves that are periodic within the solid. Such waves can be seen as the superposition of plane waves. For an idealized one-dimensional solid, with boundaries fixed at  $x = \pm d/2$ , a combination of plane waves can be, for instance,  $\psi(x) = A \cdot \exp(ikx) + B \cdot \exp(-ikx)$  with  $k = n2\pi/d$ . Written in another way, the solutions are of the type  $\exp(ikx)$ , with  $k = \pm n2\pi/d$ . The solutions for  $k = +n2\pi/d$  and  $k = -n2\pi/d$  are linearly independent. The waves  $\exp(+in2\pi x/d)$  propagate to the right, the waves  $\exp(-in2\pi x/d)$  to the left side of the solid. Neither wave feels the boundaries. Since  $\exp(ikx) = \cos(kx) + i \sin(kx)$  and  $\exp(-ikx) = \cos(kx) - i \sin(kx)$ , we also can write  $\psi(x) = C \cdot \sin(kx) + D \cdot \cos(kx)$  with  $k = n2\pi/d$  as solutions. The only constraint here is that the wavefunction must be periodic throughout the solid. The state with wavenumber  $k = 0$  is a solution, since  $C \cdot \sin(0) + D \cdot \cos(0) = D \neq 0$ . Therefore the state with the lowest kinetic energy is  $E \propto k^2 = 0$  for  $k = 0$ . The individual states in  $k$ -space are very close to each other because  $\Delta k = 2\pi/d$  tends to 0 when  $d$  increases. On

the other hand, the particle-in-a-box model describes the case in which the motion of the electrons is confined along one or more directions. Outside the box the probability of finding an electron is zero. For a one-dimensional problem the solutions are standing waves of the type  $\psi(x) = A \cdot \sin(kx)$  with  $k = n\pi/d$ . There is only one solution of this type. The function  $\psi(x) = B \cdot \sin(-kx)$  can be written as  $\psi(x) = -B \cdot \sin(kx)$  and therefore is still of the type  $\psi(x) = A \cdot \sin(kx)$ . Because of the boundary conditions  $\psi(x = \pm d/2) = 0$  there is no solution of the type  $\psi(x) = B \cdot \cos(kx)$ . Since the standing wave is confined to the box, there is only the solution  $k = +n\pi/d > 0$ . For a small box the energy states are far apart from each other in  $k$ -space, and the distribution of states and energies is discrete. An important difference with respect to the extended solid is the occurrence of a finite zero-point energy [9]. There is no solution for  $k = 0$ , since  $\psi(0) = A \cdot \sin(0) = 0$ . Therefore the energy of the lowest possible state ( $n = 1$ ) is equal to  $E = \hbar^2 / 8md^2$ , i.e.  $k = \pi/d$ . This energy is called zero-point energy and is a purely quantum mechanical effect. It can be understood as the energy that is required to “confine” the electron inside the box. For a large box the zero-point energy tends to zero. However, for small boxes this energy becomes significant as it varies with the square of the reciprocal of the box size  $d^2$ .

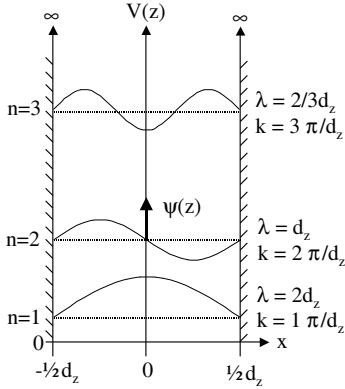


**Fig. 2-4** Particle-in-a-box model for a free electron moving along in the  $z$ -axis. The movement of electrons in the  $z$ -direction is limited to a “box” with thickness  $d$ : since electrons cannot “leave” the solid (the box), their potential energy  $V(x)$  is zero within the

solid, but is infinite at its borders. The probability density  $|\psi(z)|^2$  is the probability that an electron is located at position  $x$  in the solid. Different states for the electrons ( $n = 1, 2, \dots$ ) differ in their wavefunction.

individual planes with  $n_z$ . Since within one plane the number of states is quasi-continuous, the number of states is proportional to the area of the plane. This means that the number of states is proportional to  $k^2 = k_x^2 + k_y^2$ . The number of states in a ring with radius  $k$  and thickness  $\Delta k$  is therefore proportional to  $k \cdot \Delta k$ . Integration over all rings yields the total area of the plane in  $k$ -space. Here, in contrast to the case of a three-dimensional solid, the density of states varies linearly with  $k$ :

$$D_{2d}(k) = \frac{dN(k)}{dk} \propto k \quad (6)$$

In the ground state, all states with  $k \leq k_F$  are occupied by two electrons. We now want to know how many states exist for electrons that have energies between  $E$  and  $E + \Delta E$ . From Eqs. (1) and (2) we know the relation between  $k$  and  $E$ :  $E(k) \propto k^2$  and thus  $k \propto \sqrt{E}$  and  $dk/dE \propto 1/\sqrt{E}$ . By using Eq. (6) we obtain the density of states for a 2-dimensional electron gas, see also Figure 2-5 [17].

$$D_{2d}(E) = \frac{dN(E)}{dE} = \frac{dN(k)}{dk} \frac{dk}{dE} \propto \sqrt{E} \cdot 1/\sqrt{E} \propto 1 \quad (7)$$

The density of electronic states in a two-dimensional solid is therefore remarkably different from the three-dimensional case. The spacing between the allowed energy levels in the bands increases, because fewer levels are now present. As soon as one dimension is reduced to nanometer size, dramatic changes due to quantum confinement occur, as, for example, the non-negligible zero-point energy. In two-

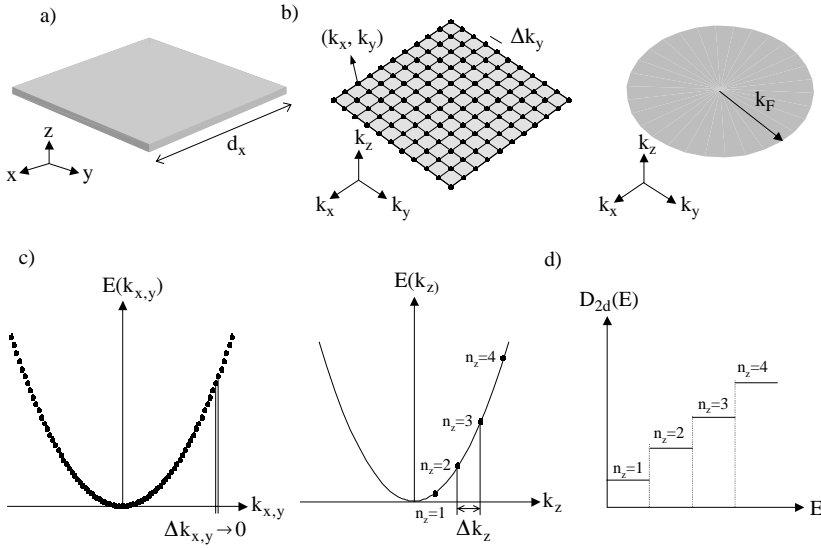


**Fig. 2-5** Electrons in a two-dimensional system. (a) A two-dimensional solid is (almost) infinitely extended in two dimensions (here  $x, y$ ), but is very thin along the third dimension (here denoted as  $z$ ), which is comparable to the De Broglie wavelength of a free electron ( $d_z \rightarrow \lambda$ ). (b) Electrons can still move freely along the  $x$ - and  $y$ -directions. The wavefunctions along such directions can be found again by assuming periodic boundary conditions.  $k_x$  and  $k_y$  states are quasi-continuously distributed in  $k$ -space. The movement of electrons in the  $z$ -direction is restricted and electrons are confined to a “box”. Only certain quantized states are allowed along this direction. For a discrete  $k_z$ -state, the distribution of states in three-dimensional  $k$ -space can be described as a series of planes parallel to the  $k_x$ - and  $k_y$ -axes. For each discrete  $k_z$ -state, there is a separate plane parallel to the  $k_x$  and to the  $k_y$ -axes. Here only one of those planes is shown. The  $k_x$ - and  $k_y$ -states within one plane are quasi-continuous, since  $\Delta k_{x,y} = 2\pi/d_{x,y} \rightarrow 0$ . The distance between two planes for two separate  $k_z$ -states is large, since  $\Delta k_z = \pi/d_z \gg 0$ . For each  $k_z$ -value the  $k_x$ - and  $k_y$  states are homogeneously distributed on the  $k_x$ - $k_y$ -plane

[17]. The number of states within this plane is therefore proportional to the area of a disk around  $k_x = k_y = 0$ . This means that the number of states for a certain wavenumber varies with  $k^2$ . In the ground state all states with  $k \leq k_F$  are occupied with two electrons, while the remaining states are empty. (c) Free electrons have a parabolic dispersion relation ( $E(k) \propto k^2$ ). The energy levels  $E(k_x)$  and  $E(k_y)$  for the electron motion along the  $x$ - and the  $y$ -directions are quasi-continuous (they are shown here as circles). The wavefunction  $\psi(z)$  at the border of a small “box” must be zero, leading to standing waves inside the box. This constraint causes discrete energy levels  $E(k_z)$  for the motion along the  $z$ -direction. Electrons can only occupy such discrete states ( $n_{z1}, n_{z2}, \dots$ , shown here as circles). The position of the energy levels now changes with the thickness of the solid in the  $z$ -direction, or in other words with the size of the “box”. (d) Density of states for a two-dimensional electron gas. If electrons are confined in one direction ( $z$ ) but can move freely in the other two directions ( $x, y$ ), the density of states for a given  $k_z$ -state ( $n_z = 1, 2, \dots$ ) does not depend on the energy  $E$ .



dimensional materials the energy spectrum is still quasi-continuous, but the density of states now is a step function [17, 19].

The quantum-mechanical behavior of electrons in a two-dimensional solid is the origin of many important physical effects. With recent progress in nanoscience and technology, the fabrication of two-dimensional structures has become routine. 2D systems are usually formed at interfaces between different materials or in layered systems in which some of the layers may be only a few nanometers thick. Structures like this can be grown, for example, by successive deposition of the individual layers by molecular beam epitaxy. In such geometry, charge carriers (electrons and holes) can move freely parallel to the semiconductor layer, but their movement perpendicular to the interface is restricted. The study of these nanostructures led to the discovery of remarkable 2-dimensional quantized effects, such as the Integer and the Fractional Quantum Hall Effect [20–23].

### 2.4.3

#### One-Dimensional Systems (Quantum Wires)

Let us now consider the case in which the solid also shrinks along a second ( $y$ ) dimension. Now electrons can only move freely in the  $x$ -direction, and their motion along the  $y$ - and  $z$ -axes is restricted by the borders of the solid (see Figure 2-6). Such a system is called a quantum wire or – when electrons are the charge carriers – a one-dimensional electron system (1DES). The charge carriers and the

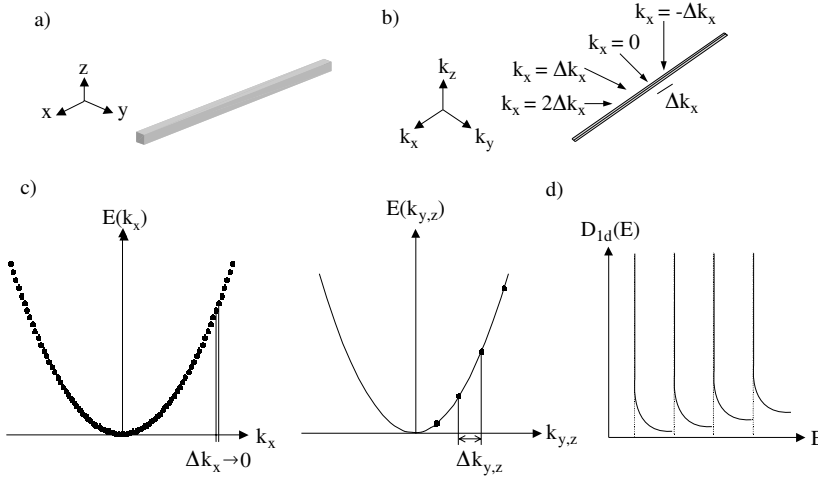


**Fig. 2-6** (a) One-dimensional solid. (b) The allowed  $(k_x, k_y, k_z)$ -states can be visualized as lines parallel to the  $k_x$ -axes in the three-dimensional  $k$ -space. In this figure only one line is shown as an example. Within each line, the distribution of states is quasi-continuous, since  $\Delta k_x \rightarrow 0$ . The arrangement of the individual lines is discrete, since only certain discrete  $k_y$ - and  $k_z$ -states are allowed. (c) This

can also be seen in the dispersion relations. Along the  $k_x$ -axes the energy band  $E(k_x, k_y, k_z)$  is quasi-continuous, but along the  $k_y$ - and  $k_z$ -axes only certain energies exist. (d) The density of states within one line along the  $k_x$ -axes is proportional to  $E^{-1/2}$ . Each of the hyperbolas shown in the  $D_{1d}$ -diagram corresponds to an individual  $(k_y, k_z)$ -state.

excitations now can move only in one dimension and occupy quantized states in the other two dimensions.

The states of a one-dimensional solid now can be obtained by methods analogous to those described for the three- and two-dimensional materials. In the  $x$ -direction electrons can move freely, and again we can apply the concept of periodic boundary conditions. This yields a quasi-continuous distribution of states parallel to the  $k_x$ -axis as well as a quasi-continuous distribution of the corresponding energy levels. Electrons are confined along the remaining directions and their states can be derived from the Schrödinger equation for a particle-in-a-box potential. Again, this yields discrete  $k_y$  and  $k_z$ -states. We can now visualize all possible states as lines parallel to the  $k_x$ -axis. The lines are separated by discrete intervals along  $k_y$  and  $k_z$ , but within each line the distribution of  $k_x$  states is quasi-continuous (Figure 2-6). We can count the number of states along one line by measuring the length of the line. The number of states is therefore proportional to  $k = k_x$ . Hence, the number of states with wavenumbers in the interval between  $k$  and  $k + \Delta k$  is proportional to  $\Delta k$ :

$$D_{1d}(k) = \frac{dN(k)}{dk} \propto 1 \quad (8)$$

In the ground state, all states with  $k \leq k_F$  are occupied by two electrons. From Eqs. (1) and (2) we know that the relation between  $k$  and  $E$  for free electron is:  $E(k) \propto k^2$  and thus  $k \propto \sqrt{E}$  and  $dk/dE \propto 1/\sqrt{E}$ . By using Eq. (8) we obtain the density of states for a 1-dimensional electron gas:

$$D_{1d}(E) = \frac{dN(E)}{dE} = \frac{dN(k)}{dk} \frac{dk}{dE} \propto 1 \cdot 1/\sqrt{E} \propto 1/\sqrt{E} \quad (9)$$

The density of states is depicted in Figure 2-6. In one-dimensional systems the density of states has a  $E^{-1/2}$ -dependence and thus exhibits singularities near the band edges [17]. Each of the hyperbolas contains a continuous distribution of  $k_x$  states but only one discrete  $k_y$ - and  $k_z$ -state.

The quantization of states in two dimensions has important consequences for the transport of charges. Electrons can only flow freely along the  $x$ -axes but are limited to discrete states in the  $y$ - and  $z$ -directions. Therefore they are only transported in discrete “conductivity channels”. This may be of considerable importance for the microelectronics industry. If the size of electronic circuits is reduced more and more, at one point the diameter of wires will become comparable to the De Broglie wavelength of the electrons. The wire will then exhibit the behavior of a quantum wire. Quantum aspects of 1D transport were first observed in so-called quantum point contacts, which were lithographically defined in semiconductor heterostructures [24, 25]. More recent examples of such 1D wires include short organic semiconducting molecules [26–31], inorganic semiconductor and metallic nanowires [32–37] or break junctions [38–40]. A particular role is played by carbon nanotubes [27, 41–47]. Carbon nanotubes have been extensively studied both as model systems for one-dimensional confinement and for potential applications, such as electron emitters [48].

## 2.4.4

**Zero-Dimensional Systems (Quantum Dots)**

When charge carriers and excitations are confined in all three dimensions, the system is called a “quantum dot”. The division is somewhat arbitrary, since, for instance, clusters made of very few atoms are not necessarily considered as quantum dots. Although clusters are smaller than the De Broglie wavelength, their properties depend critically on their exact number of atoms. Large clusters have a well-defined lattice and their properties no longer depend critically on their exact number of atoms. We will therefore use the term “quantum dots” to refer to such systems [49–59].

In a quantum dot, the movement of electrons is confined in all three dimensions and there are only discrete  $(k_x, k_y, k_z)$ -states in the  $k$ -space. Each individual state in  $k$ -space can be represented by a point. The final consequence is that only discrete energy levels are allowed, and they can be seen as delta-peaks in the distribution  $D_{0d}(E)$ . As we can see, the energy bands converge to atom-like energy states, with the oscillator strength compressed into a few transitions. This change is most dramatic at the edges of the bands and so influences semiconductors more than metals. In semiconductors the electronic properties are in fact strongly related to the transitions between the edges of the valence band and the conduction band, respectively. In addition to the discreteness of the energy levels, we want to stress again the occurrence of a finite zero-point energy. In a dot, even in the ground state, electrons have energies larger than bulk electrons at the conduction band edge. These points will be discussed in more detail in the next section.

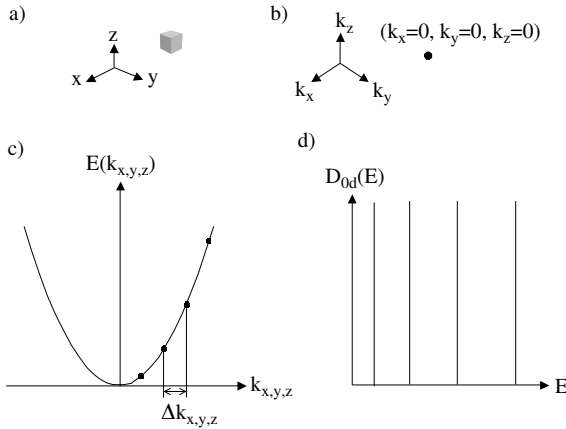


**Fig. 2-7** A zero-dimensional solid. (a) The solid is shrunk in all three dimensions to a thickness that is comparable to the De Broglie wavelength of its charge carriers. (b) Because of such confinement, all states  $(k_x, k_y, k_z)$  are discrete points in the three-dimensional  $k$ -

space. (c) Only discrete energy levels are allowed. (d) The one-dimensional density of states  $D_{0d}(E)$  contains delta peaks, which correspond to the individual states. Electrons can occupy only states with these discrete energies.

## 2.5

### Energy Levels of a (Semiconductor) Quantum Dot

In this section we will describe in more detail a zero-dimensional solid. Since many quantum effects are more pronounced in semiconductors compared to metals, we will focus on the case of a semiconducting material. In Section 2.4 we have described how the properties of a free-electron gas change when the dimensions of the solid are reduced. The model of the free-electron gas does not include the “nature” of the solid. However, from a macroscopic point of view we distinguish between metals, semiconductors and insulators [14]. The model of a free-electron gas describes relatively well the case of electrons in the conduction band of metals. On the other hand, electrons in an insulating material are only poorly described by the free-electron model. In order to extend the model of free electrons for semiconducting materials the concept of a new charge carrier, the hole, was introduced [15]. If one electron from the valence band is excited to the conduction band, the “empty” electronic state in the valence band is called a hole. Some basic properties of semiconducting materials can be described by the model of free electrons and free holes. The energy bands for electrons and holes are separated by a band gap [14, 15]. The dispersion relations for the energy of electrons and holes in a semiconductor are parabolic at first approximation. This approximation holds true only for electrons (holes) occupying the levels that lie at the bottom (top) of the conduction (valence) band. Each parabola represents a quasi-continuous set of electron (hole) states along a given direction in  $k$ -space. The lowest unoccupied energy band and the highest occupied energy band are separated by an energy gap  $E_g(\text{bulk})$ , as shown in Figure 2-8. The band gap for a bulk semiconductor can range from a fraction of an eV up to a few eV.

We might expect that the energy dispersion relations are still parabolic in a quantum dot. However, since only discrete energy levels can exist in a dot, each of the original parabolic bands of the bulk case is now fragmented into an ensemble of points. The energy levels of a quantum dot can be estimated with the particle-in-a-box model. As described in the previous paragraph (Figure 2-4), the lowest energy for an electron in a one-dimensional potential well is

$$E_{\text{well}, 1d} = 1/8 \, h^2 / m d^2 \quad (10)$$

Here,  $d$  is the width of the well. In a quantum dot, the charge carriers are confined in all three dimensions, and this system can be described as an infinite 3-dimensional potential well. The potential energy is zero everywhere inside the well but is infinite on its walls. We can also call this well a “box”. The simplest shapes of a three-dimensional box can be, for instance, a sphere or a cube. If the shape is cubic, the Schrödinger equation can be solved independently for each of the three translational degrees of freedom, and the overall zero-point energy is simply the sum of the individual zero point energies for each degree of freedom [9, 60]:

$$E_{\text{well}, 3d(\text{cube})} = 3 \, E_{\text{well}, 1d} = 3/8 \, h^2 / m d^2 \quad (11)$$

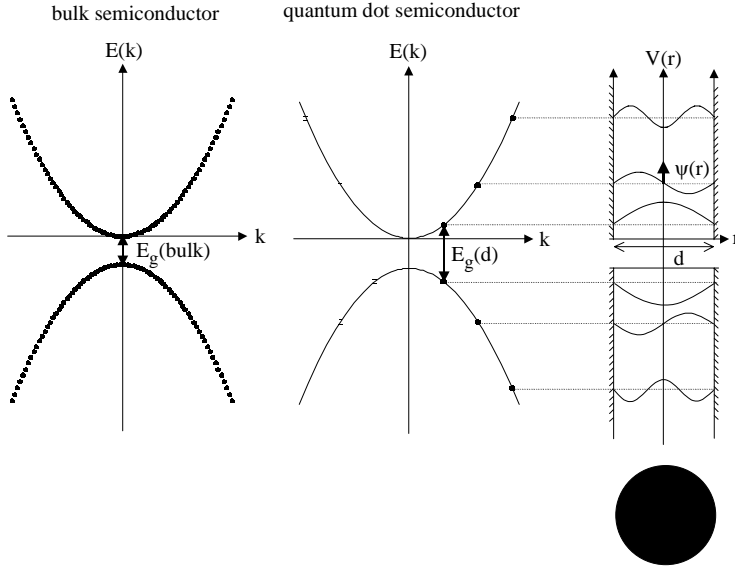


**Fig. 2-8** Free charge carriers in a solid have a parabolic dispersion relation ( $E(k) \propto k^2$ ). In a semiconductor the energy bands for free electrons and holes are separated by an energy gap  $E_g$ . In a bulk semiconductor, the states are quasi-continuous, and each point in the energy bands represents an individual state. In a quantum dot the charges are confined to a small volume. This situation can be described as a charge carrier confined in an infinite

potential well of width  $d$ . Here, the width  $d$  of the potential well corresponds to the diameter of the quantum dot. The only allowed states are those whose wavefunctions vanish at the borders of the well [7]. This leads to discrete energy levels [7, 10]. The energy gap between the lowest possible energy levels for electrons and holes  $E_g(d)$  is larger than that of a bulk material  $E_g(\text{bulk})$ .

If the box is a sphere of diameter  $d$ , the Schrödinger equation can be solved by introducing spherical coordinates and by separating the equation into a radial part and a part that contains the angular momentum [61, 62]. The lowest energy level (with angular momentum = 0) is then

$$E_{\text{well, 3d(sphere)}} = 1/2 \, h^2 / m d^2 \quad (12)$$

The effect of quantum confinement is again remarkable. More confined charge carriers lead to a larger separation between the individual energy levels, as well as to a greater zero-point energy. If carriers are confined to a sphere of diameter  $d$ , the zero-point energy is higher than that for charges that are confined to a cube whose edge length is equal to  $d$  ( $E_{\text{well, 3d(sphere)}} > E_{\text{well, 3d(cube)}}$ ). This is because such a sphere simply has a smaller volume ( $\pi/6 \, d^3$ ) than the cube ( $d^3$ ).

An electron-hole pair can be generated in the quantum dot, for instance, by a photoinduced process, or by charge injection. The minimum energy  $E_g$  required for creating an electron-hole pair in a quantum dot is made up of several contributions. One contribution is the bulk band gap energy,  $E_g(\text{bulk})$ . Another

important contribution is the confinement energy for the carriers, which we call  $E_{\text{well}} = E_{\text{well}}(e^-) + E_{\text{well}}(h^+)$ . For large particles (bulk:  $d \rightarrow \infty$ )  $E_{\text{well}}$  tends to zero. We can estimate the overall confinement energy for an electron-hole pair in a spherical quantum dot. It is the zero point energy of the potential well, or in other words, the energy of the state of a potential box with the lowest energy. This can be written as

$$E_{\text{well}} = \hbar^2 / 2m^* d^2 \quad (13)$$

where  $m^*$  is the reduced mass of the exciton and is given by [63]

$$1/m^* = 1/m_e + 1/m_h. \quad (14)$$

Here  $m_e$  and  $m_h$  are the effective masses for electrons and holes, respectively. In order to calculate the energy required to create an electron-hole pair, another term ( $E_{\text{Coul}}$ ) has to be considered. The Coulomb interaction  $E_{\text{Coul}}$  takes into account the mutual attraction between the electron and the hole, multiplied by a coefficient that describes the screening of the carriers by the crystal. In contrast to  $E_{\text{well}}$ , the physical meaning of this term can be understood within the framework of classical electrodynamics. However, an estimate of such a term is only possible if the wave-functions for the electron and the hole are known. The strength of the screening coefficient depends on the dielectric constant  $\epsilon$  of the semiconductor. An estimate of the coulomb term yields

$$E_{\text{Coul}} = -1.8 \, e^2 / 2\pi\epsilon\epsilon_0 d \quad (15)$$

This term can be quite significant, because the average distance between an electron and a hole in a quantum dot can be small [50, 64–67]. We can now estimate the size-dependent energy gap of a spherical semiconductor quantum dot, which is [50, 63–67]:

$$E_g(\text{dot}) = E_g(\text{bulk}) + E_{\text{well}} + E_{\text{Coul}} \quad (16)$$

Then, by inserting Eqs. (13) and (15) into (16) we get:

$$E_g(d) = E_g(\text{bulk}) + \hbar^2 / 2m^* d^2 - 1.8 \, e^2 / 2\pi\epsilon\epsilon_0 d \quad (17)$$

Here we have emphasized the size dependence in each term. Equation (17) is only a first approximation. Many effects, such as the crystal anisotropy and the spin-orbit coupling, have to be considered in a more sophisticated calculation. The basic approximation for the band gap of a quantum dot comprises two size-dependent terms: the confinement energy, which varies as  $1/d^2$ , and the Coulomb attraction, which varies as  $1/d$ . The confinement energy is always a positive term, and thus the energy of the lowest possible state is always raised with respect to the bulk situation. On the other hand, the Coulomb interaction is always attractive for

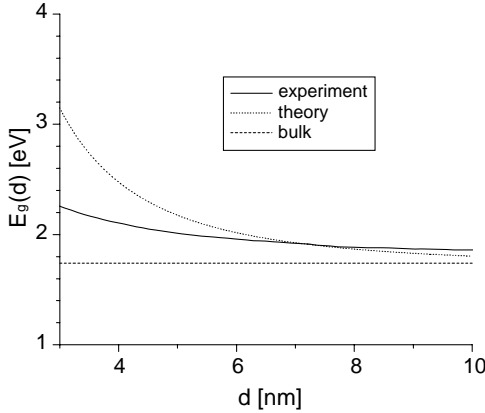


**Fig. 2-9** Size dependence of the energy gap  $E_g(d)$  for colloidal CdSe quantum dots with diameter  $d$ . The bulk value for the energy gap is  $E_g(\text{bulk}) = 1.74$  eV [63]. The theoretical curve was obtained using Eq. (17) with the following parameters: effective mass of electrons/holes  $m_e = 0.13m_0$ ,  $m_h = 0.4m_0$ ,  $m_0$  = mass of free electrons ( $m = 9.1095 \cdot 10^{-31}$  kg)  $\Rightarrow m^* = 0.098$  m [63];

dielectric constant  $\epsilon_{\text{CdSe}} = 5.8$  [176], permittivity constant  $\epsilon_0 = 8.854 \cdot 10^{-12} \text{ C}^2 \text{ N}^{-1} \text{ m}^{-2}$ , Planck's constant  $h = 6.63 \cdot 10^{-34}$  Js,  $1 \text{ eV} = 1.602 \cdot 10^{-19}$  J. The experimental values were obtained in the Alivisatos group by recording the absorption spectra of CdSe quantum dots of different sizes and determining the size of the quantum dots by transmission electron microscopy (TEM).

an electron-hole pair system and therefore lowers the energy of its formation. Because of the  $1/d^2$  dependence, the quantum confinement effect becomes the predominant term for very small quantum dot sizes.

The size-dependent energy gap can be a useful tool for designing materials with well-controlled optical properties. A much more detailed analysis on this topic can be found, for example, in an article by Efros and Rosen [56]. Before we start describing the physical consequences of the size-dependent band gap on the optical and electronic properties, we will first give a short overview of how quantum dots can be fabricated in practice.

## 2.6

### Varieties of Quantum Dots

The ultimate technique for the fabrication of quantum dots should be able to produce significant amounts of sample, with such a high control of quantum dot size, shape and monodispersity that single-particle properties are not averaged by sample inhomogeneity. So far, ensembles of quantum dots produced by the best available techniques still show behavior deriving from a distribution of sizes, but this field is evolving very rapidly. In this Section we give a short survey of the most popular fabrication approaches. Different techniques lead to different typologies of quantum dots. The confinement can be obtained in several different ways, and in addition the quantum dot itself can have a peculiar arrangement with respect to its

surrounding: it can be embedded into a matrix or grown onto a substrate, or it can be a “free” nanoparticle. Each of these cases is strictly related to the preparative approach chosen.

### 2.6.1

#### Lithographically Defined Quantum Dots

Lithographically defined quantum dots are formed by isolating a small region of a two-dimensional electron system (see Section 2.4b) via tunneling barriers from its environment. Such two-dimensional electron systems (2DES) or 2D electron gases (2DEGs) can be found in metal-oxide-semiconductor field effect transistors (MOSFETs) or in the so-called semiconductor heterostructures [17, 18]. Heterostructures are composed of several thin layers of different semiconductor materials grown on top of each other, using a technique called molecular beam epitaxy (MBE). The layer sequence can be chosen in such a way that all free charge carriers are confined to a thin slice of the crystal, forming essentially a two-dimensional electron system. A superstructure derived from the periodic repetition of this sequence of layers is also called a “multiple quantum well”. One of the most widely investigated systems is, for instance, the aluminum gallium arsenide/gallium arsenide (AlGaAs/GaAs) quantum well. AlGaAs has the same lattice constant as GaAs but a wider band gap, whose exact value depends on the aluminum content of the layer. Therefore electrons in the GaAs layer are confined to this layer and form a two-dimensional electron gas.

Quantum dot systems can be generated in a lateral or a vertical arrangement, as shown in Figure 2-10a. In the lateral geometry, the 2DEG is locally electrostatically depleted by applying negative voltages to electrodes deposited on top of the crystal. We can understand this effect from the following argument. Let us assume that we apply a negative voltage to the metal electrodes above the two-dimensional electron gas. Because of electrostatic repulsions, electrons will be repelled by the electric field of the electrodes, and the region of the 2DEG below the electrodes will be depleted of electrons. A charge-depleted region behaves like an insulator. Therefore, by applying an electric field with metal electrodes of an appropriate shape it is possible to create an island of charges insulated from the rest of the 2DEG. If the island within the 2DEG is small enough, it behaves as a quantum dot. In the vertical geometry, a small pillar of the 2DEG is isolated by etching away the heterostructure around it. In such arrangement charge carriers are again confined in all three dimensions.

Most of the electron transport measurements on quantum dots that have been performed to date have used the two types of quantum dots as samples that we have just described. The lateral arrangement offers a relatively high degree of freedom for the design of the structure, as this is determined by the choice of the electrode geometry. In addition, it is possible to fabricate and study “artificial molecules” [68–70, 71, 72–74] composed of several quantum dots linked together. With the vertical arrangement, structures with very few electrons can be fabricated [75]. At the present time, several research efforts are focused on the investigation of



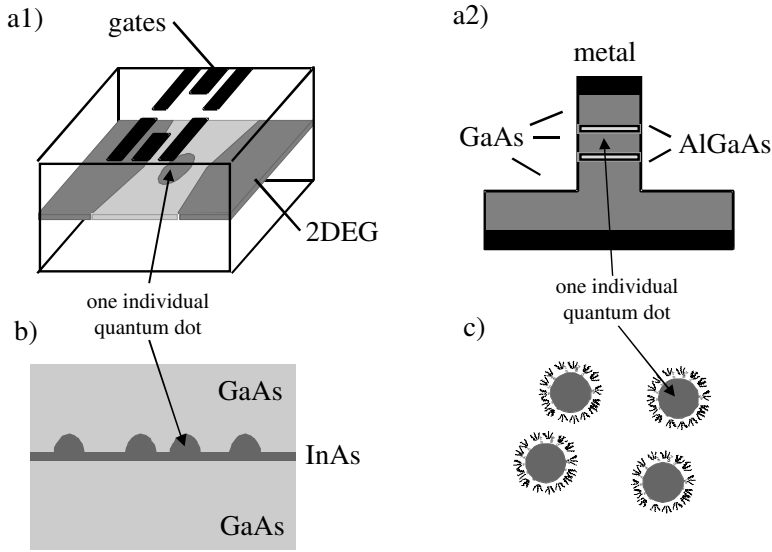


**Fig. 2-10** Three different types of quantum dots. (a1) A lithographically defined quantum dot in lateral arrangement can be formed by electrostatic depletion of a two-dimensional electron gas (2DEG, shown in dark gray) via gate electrodes. The 2DEG is formed typically 20–100 nm below the surface of a semiconductor heterostructure (usually GaAs/AlGaAs). Application of negative voltages to metal gates on top of the heterostructure depletes the 2DEG below the gates (shown in light gray) and cuts out a small electron island from the 2DEG. Electrons can still tunnel onto and from the island. Electrical contact to the 2DEG is realized through ohmic contacts (not shown in this picture). (a2) A vertical quantum dot can be formed in a double barrier heterostructure. A narrow pillar is etched out of a GaAs/AlGaAs/GaAs/AlGaAs/GaAs heterostructure. The AlGaAs layers (light gray) form tunnel barriers that isolate the central GaAs region

from the contact region. This central GaAs region behaves now as a quantum dot (shown in dark gray). Electrical contact is made via metal contacts (depicted in black) on top of the pillar and below the heterostructure. (b) Self-assembled quantum dots: molecular beam epitaxy (MBE) growth of InAs (dark gray) on GaAs (light gray) first leads to the formation of an extended layer of InAs (the wetting layer) and then to the formation of small InAs islands. Single electrons or electron-hole pairs (excitons) can be confined into these InAs quantum dots, either electrically or optically. (c) Colloidal quantum dots: these colloidal particles, having a diameter of only a few nanometers, are formed using wet chemistry and can be produced for most of the II–VI, III–V, IV–VI and some type IV semiconductors. The surface of colloidal quantum dots is coated with a layer of surfactant molecules that prevents aggregation of the particles.

many-body phenomena in these quantum dot systems. Relevant examples are, for instance, the study of the Kondo effect [76–79] and the design and the control of coherent quantum states with the ultimate goal of quantum information processing (for references see Section 2.8).

A remarkable advantage of lithographically defined quantum dots is that their electrical connection to the “macro-world” is straightforward. The manufacturing processes are similar to those used in chip fabrication, and in principle such structures could be embedded within conventional electronic circuits. However, as

the geometry of these quantum dots is determined lithographically, it is limited to the usual size and resolution limits of lithographic techniques. Even by using electron beam lithography for the fabrication of the quantum dots, it is not possible to tailor their size with nanometer precision. Lithographically fabricated quantum dots are typically larger than 10 nm, and therefore only relatively low lateral confining energies can be achieved.

### 2.6.2

#### **Epitaxially Self-Assembled Quantum Dots**

A breakthrough in the field of epitaxially grown nanostructures was the discovery of epitaxial growth regimes that favored the formation of nanometer size islands of semiconductor materials on suitable substrates. These islands, exhibiting quantum dot behavior, are naturally obtained by epitaxially growing a thin layer of a low band gap material over a higher band gap material, using MBE or MOCVD techniques [59, 80–82]. The respective crystal faces in contact must have a significant lattice mismatch (1–8%), as in the case of InAs on GaAs [83, 84] and Ge on Si [85, 86]. During the growth, a strained film, called the “wetting layer”, initially forms. The maximum thickness of this layer is related to the difference between the lattice constants of the two materials. Past this critical thickness, a  $2D \rightarrow 3D$  transition in the growth regime is observed, with the spontaneous formation of an array of nanometer-sized islands (Stranski-Krastanov regime), leading to a partial release of the strain. If the growth is not interrupted at this step, misfit dislocations form because the energy of formation of these defects becomes smaller than the elastic energy accumulated in the strained film. The formation of dislocations in highly strained epilayers (when the lattice mismatch is of the order of 10% or more) before the formation of islands limits the range of possible island-substrate materials. The shape of the islands can be controlled by the growth conditions. Usually, the islands have a truncated pyramidal shape, but it is also possible to form, e.g., ring-shaped quantum dots [87]. The final step consists in the growth, on the top of the islands, of several layers of the substrate material, so that the dots are completely buried and interfaces are passivated. The relative alignment of the band gaps creates a confining potential for charge carriers that accumulate inside the quantum dots. In addition, strain fields in the proximity of the island-substrate interface, because of the lattice mismatch between the two materials, create potentials that modify the band gap of the quantum dots at the bottom of the island. Holes are more likely to be localized in this region, as they are heavier than electrons.

Self-assembled quantum dots can have a diameter as small as a few nanometers, and so very pronounced quantum size effects can be observed in these systems. Self-assembled quantum dots have predominantly been characterized using optical or capacitance spectroscopy in a regime where they contain only a small number of charge carriers. Measurements on ensembles still suffer from inhomogeneous broadening of the spectroscopic features. However, in recent years it has been possible to look only at a few self-assembled quantum dots at a time, or even at single dots, by reducing the number of quantum dots by mesa-etching [88] or by

using confocal microscopy techniques [89]. Photoluminescence from single self-assembled quantum dots is a highly efficient process, characterized by several, narrow emission lines related to different exciton states in the dots, and is reminiscent of the emission from atoms. As mentioned already for the case of lithographically defined quantum dots, many parallels can be drawn between atoms and quantum dots [88, 90–92]. For these reasons, quantum dots have gained the nickname of artificial atoms. Current research efforts are devoted to the ordering and positioning of quantum dots and also to the reduction of their size distribution. In contrast to the case of lithographically defined quantum dots, it is a challenge to make electrical contact to self-assembled quantum dots, and therefore most of the possible applications can be found in optics. One of the major goals of research on self-assembled quantum dots is the fabrication of non-classical light sources from single dots. Another possible application is to use them as light-addressable storage devices (see Section 2.7).

### 2.6.3

#### **Colloidal Quantum Dots**

Colloidal quantum dots are remarkably different from quantum dots formed by the systems mentioned above, as they are chemically synthesized using wet chemistry and are free-standing nanoparticles or nanocrystals grown in solution [51]. Colloidal quantum dots are just a subgroup of a broader class of materials that can be synthesized at the nanoscale level using wet chemical methods. In the fabrication of colloidal nanocrystals, the reaction chamber is a reactor containing a liquid mixture of compounds that control the nucleation and the growth. In a general synthesis of quantum dots in solution, each of the atomic species that will be part of the nanocrystals is introduced into the reactor in the form of a precursor. A precursor is a molecule or a complex containing one or more atomic species required for growing the nanocrystals. Once the precursors are introduced into the reaction flask they decompose, forming new reactive species (the monomers) that will cause the nucleation and growth of the nanocrystals. The energy required to decompose the precursors is provided by the liquid in the reactor, either by thermal collisions or by a chemical reaction between the liquid medium and the precursors, or by a combination of these two mechanisms [93].

The key parameter in the controlled growth of colloidal nanocrystals is the presence of one or more molecular species in the reactor, here broadly termed “surfactants”. A surfactant is a molecule that is dynamically adsorbed to the surface of the growing quantum dot under the reaction conditions. It must be mobile enough to provide access for the addition of monomer units, while stable enough to prevent the aggregation of nanocrystals. The choice of surfactants varies from case to case: a molecule that binds too strongly to the surface of the quantum dot is not suitable, as it would not allow the nanocrystal to grow. On the other hand, a weakly coordinating molecule would yield large particles, or aggregates [94]. Some examples of a suitable surfactant include, for instance, alkyl thiols, phosphines, phosphine oxides, phosphates, phosphonates, amides or amines, carboxylic acids, and

nitrogen-containing aromatics. If the growth of nanocrystals is carried out at high temperatures (for instance at 200–400 °C), then the surfactant molecules must be stable under such conditions in order to be a suitable candidate for controlling the growth.

At low temperatures or, more generally, when the growth is stopped, the surfactants are more strongly bound to the surface of the nanocrystals and provide their solubility in a wide range of solvents. This coating allows for great synthetic flexibility in that it can be exchanged with another coating of organic molecules having different functional groups or polarity. In addition, the surfactants can be temporarily removed and an epitaxial layer of another material with different electronic, optical, or magnetic properties can be grown on the initial nanocrystal [95, 96].

By controlling the mixture of surfactant molecules that are present during the generation and the time of growth of the quantum dots, excellent control of their size and shape is possible [93, 97, 98].

Since colloidal nanocrystals are dispersed in solution, they are not bound to any solid support as is the case for the other two quantum dots systems described above. Therefore, they can be produced in large quantities in a reaction flask and can later be transferred to any desired substrate or object. It is, for example, possible to coat their surface with biological molecules such as proteins or oligonucleotides. Many biological molecules perform tasks of molecular recognition with an extremely high efficiency. This means that ligand molecules bind with very high specificity to certain receptor molecules, similarly to a key-lock system. If a colloidal quantum dot is tagged with ligand molecules, it specifically binds to all the positions where a receptor molecule is present. In this way it has, for example, been possible to make small groupings of colloidal quantum dots mediated by molecular recognition [99–101] and to label specific compartments of a cell with different types of quantum dots [102–104].

Although colloidal quantum dots are rather hard to connect electrically, a few electron transport experiments have been reported. In these experiments, nanocrystals were used as the active material in devices that behave as single-electron transistors [105, 106] (see also Section 2.8).

## 2.7

### Optical Properties of Quantum Dots

#### 2.7.1

##### Absorption and Emission Spectra

In chemistry, size-dependent optical properties of colloidal semiconductor particles have been observed since the beginning of the last century, for instance in CdS colloids [107], although it was only toward its end [65] that this fact was rationalized in terms of “size quantization”. As we have discussed in Section 2.5, the most striking effect in semiconductor nanoparticles is the widening of the gap  $E_g$  between the highest occupied electronic states (the top of the original valence

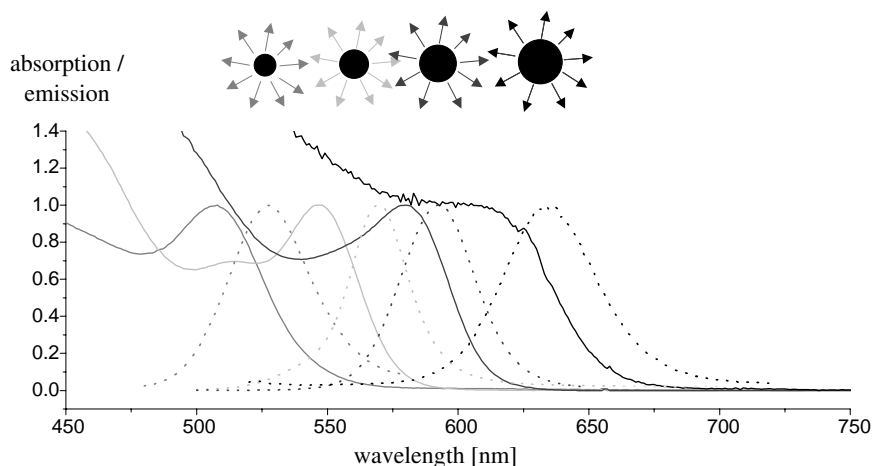


**Fig. 2-11** Absorption (plain lines) and emission spectra (dotted lines) of colloidal CdSe quantum dots of different sizes. The absorption peaks of green/yellow/orange/red fluorescent nanocrystals of 2.3/4.0/3.8/4.6 nm diameter are at 507/547/580/605 nm. The fluorescence peaks are at 528/57/592/637 nm.

band) and the lowest unoccupied states (the bottom of the original conduction band) [108]. This directly affects the optical properties of quantum dots as compared to the corresponding bulk material. The minimum energy needed to create an electron-hole pair in a quantum dot (an “exciton”) is defined by its band gap ( $E_g$ ). Light with energy lower than  $E_g$  cannot be absorbed by the quantum dot. Since the band gap depends on the size of a quantum dot, the onset of absorption is also size dependent [50, 93]. In Figure 2-11 we show that smaller quantum dots have an absorption spectrum that is shifted to shorter wavelengths with respect to larger quantum dots and to the bulk material.

Excitons in semiconductors have a finite lifetime because of the recombination of the photo-excited electron-hole pair. In quantum dots, the energy released upon exciton annihilation is too large to be dissipated by vibrational modes. Instead it is released in the form of emitted photons. Radiative decay through emission of photons, in other words fluorescence, is a highly probable decay channel in quantum dots [109].

As is the case of organic fluorophores, the range of energies emitted from a colloidal dot sample after excitation is centered at a value that is smaller than the one required to excite the sample (and which must be at least as large as its band gap). In other words, the wavelength of the fluorescence is longer than that of the absorbed light. The shift between the lowest energy peak in the absorption spectrum of a quantum dots and the corresponding emission peak is called the “Stokes shift” (Figure 2-11) [9]. In order to explain the Stokes shift, a more advanced model than that presented in Figure 2-8 is necessary.

In quantum dots, the Stokes shift is explained by examining their complex exciton structure [110–113]. More complex theoretical models and calculations show that the ground state of an exciton in a dot has a total angular momentum equal to

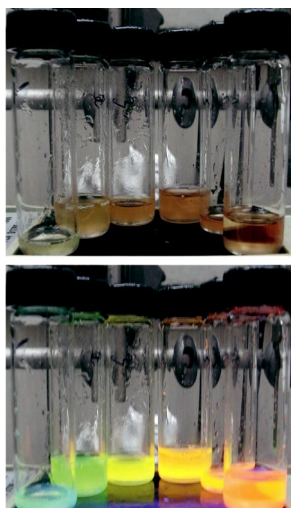


**Fig. 2-12** Colloidal CdSe quantum dots of different size dissolved in chloroform. The size of the quantum dots increases from the left to the right vial. (a) Photograph of the solutions. (b) Photograph of the solutions upon UV-illumination from below. The different colors of fluorescence can be seen.

zero. In the dipole approximation, the creation of an exciton through absorption of a photon leads to an exciton state having angular momentum equal to  $\pm 1$ . The energy needed for this excitation is the absorption energy. In quantum dots, this excited state now relaxes very fast to a state with an angular momentum of 2. This relaxation is non-radiative. In first order, this state cannot relax to the ground state with angular momentum 0 by emitting a photon, because only transitions that change the angular momentum by  $\pm 1$  are allowed. Since no photon can be emitted in first order, this state is called “dark exciton”. However, slight perturbations of the crystal lattice and even a weak coupling with phonons allow this state to relax under emission of a photon. As a result, the decay time of the fluorescence is long, and the fluorescence energy is red-shifted with respect to the absorption band edge energy [114]. The dark exciton model is supported by many experimental data, in particular by magnetic field-dependent lifetime measurements. The position of the luminescence peak is also dependent on the average quantum dot size, and its width is correlated to the nanocrystals size distribution (Figures 2-11 and 2-12). Consequently, the maximum of the emission spectrum and its width can be used to estimate the mean size and the size distribution during nanocrystal growth.

### 2.7.2

#### Spectral Diffusion and Blinking

Several crucial differences appear between self-assembled and colloidal quantum dots. For instance, stable, ultra-narrow fluorescence peaks have been observed in

the emission spectra of single, self-assembled quantum dots. Colloidal semiconductor quantum dots can have a very narrow size distribution, as observed under a transmission electron microscope. Nevertheless, in ensemble measurements their emission spectra still have a full width at half maximum of several meV [115, 116]. Although this broad range of emission energies was initially ascribed to the residual size distribution, it is now ascribed to an intrinsic property of colloidal quantum dots. Although the emission peak from a single colloidal quantum dot can be less than 0.1 meV wide, but its emission energy shifts randomly over time. This behavior is referred to as “spectral jumps” or “spectral diffusion” [116]. First observed by Empedocles et al. at cryogenic temperatures, spectral diffusion now can also be observed at room temperature [117, 118]. Spectral diffusion is likely related to the local environment of the quantum dots, which creates rapidly fluctuating electric fields that may perturb the energy levels of the system. Similarly, spectral diffusion can also be observed in single organic fluorophores [119]. Conversely, self-assembled quantum dots embedded in a matrix do not exhibit spectral jumps, because their local environment does not change with time.

In self-assembled quantum dots, multiexciton states can be observed and studied at high pumping power, but they have never been observed in colloidal quantum dots. The absence of multiexcitons in single colloidal quantum dots is believed to be correlated with the fluorescence intermittence observed in these systems [120]. The fluorescence emission from a single quantum dot exhibits a dramatic on/off behavior, referred to as “blinking” and is another spectroscopic feature that distinguishes colloidal from self-assembled quantum dots [121, 122]. This behavior is similar to that of single organic fluorophores [123]. Blinking in CdSe quantum dots can readily be observed in a standard epifluorescence microscope. In a nanocrystal, off time periods may vary from milliseconds to several minutes. The mechanism responsible for the blinking is believed to involve an Auger photoionization of the colloidal quantum dots. In this model, if two electron-hole pairs are present simultaneously inside the quantum dots, the energy released by the annihilation of one electron-hole pair is transferred to the other pair. This excess of energy may eject one of the carriers into the environment of the quantum dot, leaving the quantum dot charged. If an electron-hole pair is created during this time, the energy released by its recombination is transferred to the third remaining carrier via a non-radiative process. This is why ionized quantum dots do not emit. If the ejected carrier returns inside the quantum dot or if the quantum dot is neutralized, radiative emission is restored. The probability of occurrence of Auger processes in nanocrystals is higher than in the bulk because of the breakdown of translational symmetry. The probability is also related to the spatial overlap of the carrier wavefunctions, and for this reason is higher in colloidal than in self-assembled quantum dots, the former being usually much smaller than the latter. The probability of Auger processes increases further in the case of finite and defective barriers, which offer a wide range of electronic states where the excited carriers can be localized. Again, this is the case with colloidal quantum dots, but not with self-assembled quantum dots, which are buried in an inorganic, defect-free, thick matrix. A more detailed description of the Auger effect in colloidal quantum dots can be found in the literature [116, 124, 125].

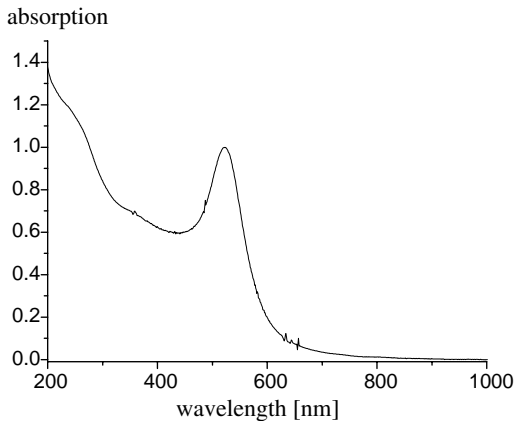


**Fig. 2-13** Absorption spectrum of colloidal gold nanocrystals of 10 nm diameter.

### 2.7.3

#### **Metal Nanoparticles**

Colloidal metal nanoparticles can have optical absorption spectra with an absorption peak that looks similar to the absorption peak of colloidal semiconductor particles (compare, for instance, Figures 2-11 and 2-13). However, this absorption does not derive from transitions between quantized energy states. Instead, in metal particles, collective modes of motion of the electron gas can be excited. They are referred to as surface plasmons [126, 127]. The peak in the absorption spectrum is the resonance frequency for the generation of surface plasmons. The size dependence of the plasmon frequency is negligible. For instance, the absorption maximum for colloidal gold nanocrystals hardly shifts for nanoparticles in the size range between 5 and 30 nm. This contrasts with the dramatic size effect in the absorption of colloidal semiconductor nanocrystals when the diameter is changed by only fractions of a nanometer (see Figure 2-11).

### 2.7.4

#### **Overview of Some Selected Applications**

Many applications of the quantum-mechanical aspects of quantum dots can be found in optics. As in the more general case of atoms or molecules, quantum dots can be excited either optically or electrically. Regardless of the nature of the excitation, quantum dots may emit photons when they relax from an excited state to the ground state. Based on these properties, quantum dots may be used as lasing media, as single photon sources, as optically addressable charge storage devices, or as fluorescent labels.

Self-assembled quantum dots incorporated into the active layer of a quantum well laser significantly improve the operation characteristics of the laser. This is because of the zero-dimensional density of states of quantum dots. In quantum dot lasers, the threshold current density is reduced, its temperature stability is improved, and the differential gain is increased. A first demonstration of the lasing



operation of a quantum dot laser structure was given as early as 1994 [128, 129]. Since then, the lasing characteristics have been improved by better control of the growth of the self-organized quantum dot layers. Today, quantum dot lasers are on the road toward commercialization [130]. Optical gain and stimulated emission have been observed also from CdSe and CdS colloidal nanocrystal quantum dots [131]. On the basis of this result, it is conceivable that optical devices could also be built using self-assembly of colloidal quantum dots.

Quantum dots have been used not only as conventional laser sources but also as “non-classical” light sources. Photons emitted from thermal light sources have characteristic statistical correlations: in arrival time measurements it is found that they tend to “bunch” together (super-poissonian counting statistics). For applications in quantum information processing, however, it would be desirable to emit single photons one at a time (sub-poissonian counting statistics, or anti-bunching). In the last few years it has been possible to demonstrate first prototypes of such single-photon sources based on single quantum dots [132–136].

Self-assembled quantum dots have also been discussed as the basis of an all-optical storage device. In such a device, excitons are optically generated and electrons and holes are stored separately in coupled quantum dot pairs [137]. Applying an electric field, electron and hole can be forced to recombine and generate a photon which provides an optical read-out.

Colloidal quantum dots have also been used for the development of light-emitting diodes [138, 139]. In these devices, colloidal quantum dots are incorporated into a thin film of conducting polymer. Furthermore, colloidal quantum dots have been used for the fabrication of photovoltaic devices [140, 141].

Chemically synthesized quantum dots fluoresce in the visible range with a wavelength tunable by the size of the colloids. The possibility of controlling the onset of absorption and the color of fluorescence by tailoring the size of colloidal quantum dots makes them interesting objects for the labeling of biological structures [102, 103] as a new class of fluorescent markers. The tunability combined with extremely reduced photobleaching makes colloidal quantum dots an interesting alternative to conventional fluorescent molecules [51]. Possible biological applications of fluorescent colloidal quantum dots will be discussed in detail in the other chapters of this book.

## 2.8

### Some (Electrical) Transport Properties of Quantum Dots

Electron transport through ultrasmall structures such as quantum dots is governed by charge and energy quantization effects. Charge quantization comes into play for structures with an extremely small capacitance. The capacitance of a nanostructure – which, roughly speaking, is proportional to its typical linear dimension – may become so small that the energy required to charge the structure with one additional charge carrier (electron, hole, cooper pair) exceeds the thermal energy available. In this case, charge transport through the structure is blocked – an effect

which has appropriately been termed the “Coulomb blockade” (CB) effect. As will be shown below, this effect can be exploited to manipulate single electrons within nanostructures. Also because of the smallness of the structures, energy quantization may become considerable. In contrast to bulk structures, charge carriers within a quantum dot are only allowed to occupy discrete energy levels, as in the case of electrons within an atom. In a manner resembling scattering effects known from atomic and nuclear physics, the occurrence of these discrete energy levels can modify the charge transport characteristics of ultrasmall devices. In metallic nanostructures, Coulomb blockade can also occur without “quantum aspects”, as the energy level spacing in these structures is usually too small to be observable. In fact, energy quantization is the reason for the name “quantum dot” and differentiates this from most of the metallic nanostructures. However, in extremely small metallic nanoparticles and clusters, quantum effects can also be considerable. In this section we give a short introduction of the history and fundamentals of the Coulomb blockade effect. We will discuss single-electron tunneling transport through quantum dots and we will also give an overview of the possible applications of these effects.

### 2.8.1

#### Coulomb Blockade: Basic Theory and Historical Sketch

The Coulomb blockade effect was originally observed in experiments on small metallic or superconducting particles [142–145]. In these experiments, nanometer-sized metallic grains were embedded within a metal-oxide-metal tunnel junction. Electronic measurements performed on these systems at low temperatures ( $T \approx 1$  K) revealed anomalous behavior of the resistance (or differential capacitance) at zero bias. It was realized that this behavior was caused by the extremely small capacitance of the metallic particles. In a simple model, a spherical particle of diameter  $d$  embedded in a dielectric with permittivity  $\varepsilon$  has a capacitance

$$C = 2\pi\varepsilon\varepsilon_0 d \quad (18)$$

and therefore at low enough temperatures the charging energy<sup>3)</sup>

$$E_C = \frac{e^2}{2C} = \frac{e^2}{4\pi\varepsilon\varepsilon_0 d} \quad (19)$$

required for the addition of a single electron to the particle may well exceed the thermal energy  $k_B T$ . As an example, a metallic particle of radius 10 nm embedded

3) Although the charging energy  $E_C = e^2/4\pi\varepsilon\varepsilon_0 d$  (Eq. (19)) looks very similar to the Coulomb energy  $E_{\text{Coul}} = -1.8 \cdot e^2/2\pi\varepsilon\varepsilon_0 d$  (Eq. (1)), the two terms describe different situations. The charging energy describes the energy that is needed to add an additional electron to an

already negatively charged system (a sphere with capacity  $C$ ), and therefore it is repulsive ( $E > 0$ ). The Coulomb energy describes the attraction ( $E < 0$ ) between an electron and a hole within a sphere.

in a dielectric with  $\varepsilon = 4$  has a charging energy of  $E_C = 18$  meV, which corresponds to a temperature of about 200 K. Below this temperature (as a rule of thumb,  $E_C > 10k_B T$  should be satisfied), it is impossible to add or remove a single charge to the particle at zero bias, and therefore electronic transport is blocked. This explains the highly increased resistance of the tunnel junctions at low temperatures observed in the early experiments. However, the Coulomb blockade can be lifted if enough energy is supplied by applying a bias over the structure. It is found that for  $|V_{\text{bias}}| > e/2C$  the conductance starts to rise from its suppressed value. The voltage interval  $[-e/2C, +e/2C]$  over which conduction is suppressed is often referred to as the “Coulomb gap”. Apart from the smallness of the conductive island, the other essential requirement for Coulomb blockade to be observed is that the metallic island or particle be isolated from the contacts via tunnel barriers. This ensures that the charge on the island is “sufficiently well quantized”. If the island were coupled more strongly to the contacts, charge could “leak out” and thus destroy the effect. To be more precise, the energy uncertainty of the electrons due to the finite lifetime  $\tau$  of its energy state (given roughly by the  $RC$  time of the island, where  $R$  is resistance) should be less than the charging energy, i.e.

$$\Delta E \approx \frac{\hbar}{\tau} = \frac{\hbar}{RC} < \frac{e^2}{C} \quad (20)$$

Solving for  $R$  yields as a condition for the resistance  $R > \hbar/e^2$  which just means that  $R$  should be of the order of the resistance quantum<sup>4)</sup>.

Many years after the initial experiments, the Coulomb blockade effect was observed for the first time in a lithographically defined metallic structure [146]. In contrast to the earlier experiments, the effect could now be observed for a single metallic island rather than averaged over a large population of nanoparticles. Shortly after, Coulomb blockade was also observed in a semiconductor microstructure [147]. The use of lithographic techniques facilitates the fabrication of well-defined three-terminal geometries. In such a geometry, in addition to the source and drain contacts, a gate electrode is placed near the electron island. With this gate the electrostatic energy of the island can be tuned, and therefore the number of electrons on the island can be changed one by one. Variation of the gate voltage therefore leads to almost periodic conductance oscillations, which indicate the charging of the island with single electrons (see discussion below).

In most cases, for a metallic nanostructure, Coulomb blockade is a purely classical (electrostatic) phenomenon in the sense that the energy level spacing  $\Delta E$  in the structure is much smaller than the thermal energy<sup>5)</sup>  $k_B T$  which is due to the metal's high density of states at the Fermi level. This is strikingly different from the case of semiconductor nanostructures, for which the level spacing can become comparable to or even larger than the charging energy. Hence, in semiconductor nanostructures the energy required to add or remove single electrons is strongly modified by the quantum-mechanical energy levels. For this reason, the

4)  $\hbar/e^2$  is the “resistance quantum”. It is equal to the resistance of a single non-degenerate conduction mode of a one-dimensional

conducting channel connecting two large reservoirs.

5)  $k_B$  is the Boltzmann constant

term “quantum dots” is usually used for such ultrasmall semiconductor structures. Following the initial experiments mentioned above, a huge body of work has been published on transport properties of metallic islands and semiconductor quantum dots in the Coulomb blockade regime.

### 2.8.2

#### Single-Electron Tunneling

A number of excellent reviews of the theoretical and experimental aspects of Coulomb blockade and single-electron tunneling have been given in the last decade. An early review on single-electron tunneling in metallic islands has been given by Averin and Likharev [148]. An updated treatment by G. Schön emphasizing other aspects can be found in [149]. Theoretical aspects of Coulomb blockade in semiconductor nanostructures are surveyed in [150]. A good review of transport experiments on semiconductor quantum dots is in [53]. We also recommend the shorter reviews in [151] and [152]. In this Section we give a brief introduction to a simple model of a single-electron transistor which already captures many of the relevant aspects. For detailed discussions we refer to the more specialized reviews and references therein.

A schematic representation of a single-electron transistor is given in Figure 2-14. It consists of a small conducting island connected to its surroundings via two tunneling barriers and a gate electrode. The capacitances of the barriers and the gate are denoted  $C_S$ ,  $C_D$  and  $C_G$ , and the drain-source and gate voltages  $V = V_D - V_S$  and  $V_G$ . The total capacitance of the island is given by  $C = C_S + C_D + C_G$ . The electrostatic energy of the island in this model is given by

$$E(N, Q_G) = \frac{(Ne - Q_G)^2}{2C} \quad (21)$$

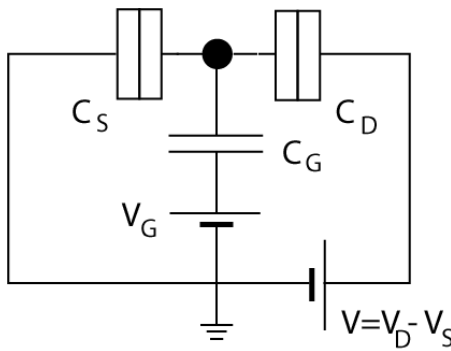


**Fig. 2-14** Schematic circuit diagram for a single-electron transistor. The electron island is indicated by the black dot. It is connected to source and drain contacts via tunneling barriers having capacitances  $C_S$  and  $C_D$ . Additionally, the electrostatic energy of the

island can be tuned with a capacitively coupled gate (capacitance  $C_G$ ). In this circuit, the source contact has been set to ground and the gate voltage is applied with respect to the ground potential.

where the integer  $N$  is the number of electrons on the island,  $-e$  is the electronic charge and the gate charge  $Q_G = C_D V_D + C_G V_G + C_S V_S$  (in our circuit diagram we set  $V_S = 0$  as the reference potential). Terms independent of  $N$  have been omitted in this expression.  $E(N, Q_G)$  defines a set of parabolas with minima at  $Ne = Q_G$ . Whereas the gate charge  $Q_G$  can be varied continuously by the external voltage sources, in the Coulomb blockade regime the charge on the island can only vary in integer numbers. For different gate charges (gate voltages) the island may therefore be occupied by a different number of electrons. In other words, the gate voltage can be used to tune the number of electrons on the island. The charge can fluctuate, however, if the energies for two successive occupation numbers are degenerate, i.e., if  $E(N+1, Q_G) = E(N, Q_G)$ . At these points the Coulomb blockade is lifted and charges can be added to or removed from the dot, i.e., the conductance of the dot becomes finite. Solving for the gate charge leads to the condition for charge fluctuation<sup>6)</sup>  $Q_G^{(N)} = (N + \frac{1}{2})e$ . The distance between two adjacent degeneracy points is therefore  $Q_G^{(N+1)} - Q_G^{(N)} = e$ . Let us consider the special case  $V_{DS} = 0$  (zero bias). Then,  $Q_G = C_G V_G$  and  $\Delta V_G = V_G^{(N+1)} - V_G^{(N)} = e/C_G$ . This shows that the gate voltages at which a finite conductance can be measured are equally spaced – leading to the periodic conductance oscillations of a single-electron transistor in the Coulomb blockade regime.

In a thermodynamic description of the system, the charge on the island can fluctuate if the probability to find  $N$  electrons on the island equals that to find  $N+1$  electrons, or  $P(N) = P(N+1)$ , where the equilibrium probability  $P$  is given by

$$P(N) = \frac{1}{Z} \exp(-(E(N) - \mu N)/k_B T) \quad (22)$$

$Z$  is the partition function (Zustandssumme) [153] and  $\mu$  is the chemical potential of the contacts. The condition for fluctuation thus becomes  $E(N+1) - E(N) = \mu$ . The left side of this equation is called the addition energy for the  $(N+1)$ -th electron. If a finite bias  $V$  is applied over the system, the electrochemical potentials of the two reservoirs differ by  $eV$ . In this case a “conductance window” opens, and Coulomb blockade is lifted for

$$\mu - e\chi V < E(N+1) - E(N) < \mu + e(1-\chi)V \quad (23)$$

where  $\chi$  ( $0 \leq \chi \leq 1$ ) is the fractional voltage drop over the drain barrier.

6) by using Eq. (19) the condition for charge fluctuation  $E(N+1, Q_G) = E(N, Q_G)$  becomes

$$\begin{aligned} ((N+1)E - Q_G)^2/2C &= (NE - Q_G)^2/2C \\ \Leftrightarrow (N+1)^2 E^2 - 2(N+1)EQ_G & \\ + Q_G^2 &= N^2 E^2 - 2NEQ_G + Q_G^2 \end{aligned}$$

$$\begin{aligned} \Leftrightarrow N^2 E^2 + 2NE^2 + E^2 - 2NEQ_G & \\ - 2EQ_G + Q_G^2 & \\ = N^2 E^2 - 2NEQ_G + Q_G^2 & \\ \Leftrightarrow 2NE^2 + E^2 - 2EQ_G = 0 & \\ \Leftrightarrow 2EQ_G = (2N+1)E^2 & \\ \Leftrightarrow Q_G = (N + \frac{1}{2})E & \end{aligned}$$

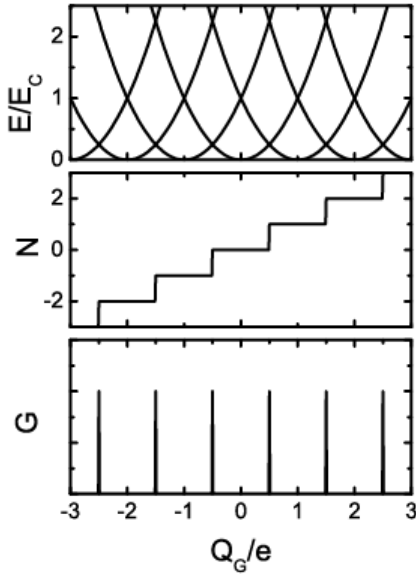


**Fig. 2-15** Schematic depiction of electrostatic energy  $E/E_C$ , occupation number  $N$  and conductance  $G$  of the single-electron transistor (SET) shown in Figure 2-14 as a function of the gate charge  $Q_G$ . The occupation of the SET changes when the energy for  $N$  electrons

equals that of  $N + 1$ . At the points where the charge can fluctuate, the conductance becomes finite and the Coulomb blockade is lifted. In real systems, the line shape of the conductance peaks is determined by temperature and/or lifetime broadening.

I–V curves can be calculated from a master equation for the occupation probability of the Coulomb blockade island. For the single-electron transistor with two tunneling barriers and one island, the master equation is [148, 149]

$$\begin{aligned}
 \frac{d}{dt} p(N, t) = & [\Gamma_{L \rightarrow I}(N - 1) + \Gamma_{R \rightarrow I}(N - 1)] p(N - 1, t) \\
 & + [\Gamma_{I \rightarrow L}(N + 1) + \Gamma_{I \rightarrow R}(N + 1)] p(N + 1, t) \\
 & - [\Gamma_{L \rightarrow I}(N) + \Gamma_{I \rightarrow R}(N) + \Gamma_{R \rightarrow I}(N) + \Gamma_{I \rightarrow R}(N)] p(N, t)
 \end{aligned} \quad (24)$$

where  $p(N, t)$  is the nonequilibrium probability of finding  $N$  electrons on the island at time  $t$ . The  $\Gamma_{X \rightarrow Y}(N)$  are tunneling rates for transitions from  $X$  to  $Y$ , where  $X$  and  $Y$  can be  $L$  (left contact),  $R$  (right contact) or  $I$  (island). An example of a typical IV curve obtained from the master equation is shown in Figure 2-16. In the Coulomb blockade regime (when the gate charge is  $Q_G = Ne$ ), the current in the Coulomb gap around  $V = 0$  is zero. For  $Q_G = (N + \frac{1}{2})E$ , the Coulomb blockade is lifted and the IV curve is linear with finite slope at  $V = 0$ .

For a quantum dot, one also has to account for the energy quantization of the electrons on the island. In the simplest model, sometimes referred to as “constant interaction (CI) model”, one assumes that the electrons successively occupy single-

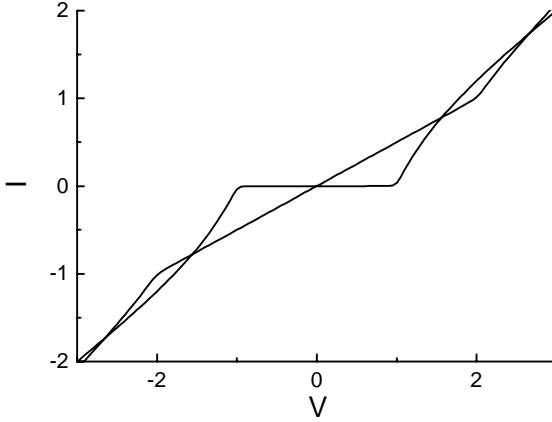


**Fig. 2-16** Calculated I–V-curves for a single electron transistor for two different values of the gate charge. The source and drain tunnel resistances and capacitances are assumed equal, the charging energy is  $100 k_B T$ . For gate charge  $Q_G = 0$  the SET is in the Coulomb blockade regime. The I–V curve exhibits the “Coulomb gap”. For a gate charge  $Q_G = 0.5$

the Coulomb blockade is lifted (cf. Fig. 2-15), and the I–V curve is linear around  $V = 0$ . The calculation was performed using the program SETTRANS [SETTRANS by Alexander N. Korotkov<sup>7)</sup> is available for noncommercial use under <http://hana.physics.sunysb.edu/set/software/index.html>].

particle energy levels  $\varepsilon_i$  (see Figure 2-4<sup>8)</sup>), and the mutual electrostatic repulsion of the electrons is accounted for by a classical capacitance. Thus the energy for  $N$  electrons on the quantum dot is

$$E(N) \approx \frac{(Ne)^2}{2C} + \sum_{i=1}^N \varepsilon_i \quad (25)$$

The addition energy therefore becomes

$$E(N+1) - E(N) = \frac{(2N+1)e^2}{2C} + \varepsilon_{N+1} \quad (26)$$

and the distance between two adjacent conductance resonances follows as

$$\Delta\mu_N = E(N+1) - 2E(N) + E(N-1) = \frac{e^2}{C} + \Delta\varepsilon_N \quad (27)$$

7) The program SETTRANS by Alexander N. Korotkov is available for noncommercial use under <http://hana.physics.sunysb.edu/set/software/index.html>

8) In order to avoid confusion, we here denote the discrete energy levels of electrons in a

potential well by  $\varepsilon_i$ . These energy levels are identical to those shown in Figure 2-4. For a three-dimensional potential box we obtain  $\varepsilon_i = i^2 h^2 / 2md^2$ ,  $i = 1, 2, 3, \dots$  (cf. Eq. (12)). The lowest possible energy ( $i = 1$ ) is  $h^2 / 2md^2$ .

where  $\Delta\epsilon_N = \epsilon_{N+1} - \epsilon_N$  is the  $N$ th level spacing. In the CI model, the distance between adjacent conductance maxima is given by a classical charging term and the spacing between single particle energy levels. This shows how the quantum nature of quantum dots directly enters its electrical properties.

In systems where the CI model can be applied, the spectrum of the quantum dot can, in principle, be deduced from transport or capacitance measurements, experimental techniques which therefore have been termed transport or capacitance spectroscopy. The CI model is quite reasonable for systems with very few electrons, but in many situations many-body effects lead to strong deviations from this simple behavior. The relative importance of energy quantization versus charging energy can be judged from the magnitude of the terms  $e^2/C$  and  $\Delta\epsilon$  in the expression above. Typically, the capacitance  $C$  varies with the diameter  $d$  of a system like  $C \approx 2\pi\epsilon\epsilon_0 d$  (cf. Eq. (18)), and thus  $E_C \propto e^2/\epsilon\epsilon_0 d$  (cf. Eq. (19)), whereas the quantization energies are of the order of  $\Delta\epsilon \approx \hbar^2/2m^*d^2$  (cf. Eq. (13)). Most trivially, for smaller systems quantum effects become stronger.

### 2.8.3

#### Tunneling Transport – Line Shape of Conductance Peaks

A slightly different approach to treating electron transport through quantum dots considers conduction as a transmission problem through an electron island. In this formulation, single-electron tunneling through quantum dots bears similarities to the well-known description of resonant tunneling transport. Resonant tunneling occurs when a system with discrete energy levels is connected to two reservoirs via tunneling barriers. In the case of quantum dots, the discreteness of the energies naturally comes in because of either Coulomb blockade or quantum confinement, or both. In Figure 2-17, such a system is depicted schematically. The

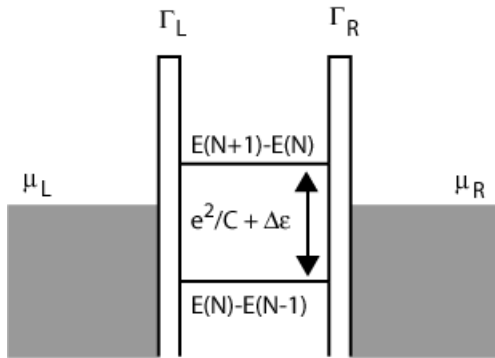


**Fig. 2-17** Electron transport through a quantum dot viewed as double barrier tunneling. The “resonant energies” of the quantum dot are given by the addition energies discussed in the text. In the constant interaction model the difference between

adjacent resonances is approximated by a charging term and the single particle energy level spacing. The chemical potentials of the reservoirs are denoted  $\mu_L$  and  $\mu_R$ , the tunneling rates through the barriers are  $\Gamma_L$  and  $\Gamma_R$ .



tunneling rates through the left and right tunnel barriers are denoted by  $\Gamma_L$  and  $\Gamma_R$ ; the quantum level in the dot has energy  $\varepsilon_1$ . One can show that the transmission at energy  $E$  through such a system is approximately given by

$$T(E) = \frac{\Gamma_L \Gamma_R}{(E - \varepsilon_1)^2 + \left(\frac{\Gamma_L + \Gamma_R}{2}\right)^2} \quad (28)$$

where the tunneling rates have been assumed to be energy independent. The current is then given by

$$I = \frac{2e}{h} \int [f(E) - f(E - eV_{ds})] T(E) dE \quad (29)$$

Here,  $f(E)$  denotes the Fermi function, and the factor of two accounts for spin degeneracy. From this expression, the conductance of the system can be determined and hence the shape of the conductance oscillations in the Coulomb blockade regime. Depending on the relative size of the coupling energies  $\hbar\Gamma_L$ ,  $\hbar\Gamma_R$  and the thermal energy  $k_B T$ , the line shape is dominated by lifetime broadening of the energy state on the island or by temperature broadening. In the low bias regime ( $eV_{DS} \approx 0$ ), the Fermi function in the above expression can be expanded, which yields for the conductance

$$G = -\frac{2e^2}{h} \int f'(E) T(E) dE \quad (30)$$

Thus, if temperature broadening dominates, the conductance oscillations have the shape of the derivative of the Fermi function ( $\propto \cosh^{-2}(E/2k_B T)$ ). If lifetime broadening dominates, the conductance peaks are of Lorentzian shape.

#### 2.8.4

##### Some Applications

The peculiar properties of quantum dots described in the previous sections may be used in a variety of device applications. The most important of these features are the discrete energy spectrum, the smallness of the capacitance, and (which is related) the possibility of manipulating single charges. The survey of device applications given in the following sections is by no means complete. It is intended to demonstrate the wealth of work done in the field and the many directions pursued.

The possibility of manipulating single charges in single-electron tunneling devices led to early proposals for metrological applications of the Coulomb blockade effect. Devices called “electron turnstiles” can be used to count single electrons and could form the basis of accurate current standards based on the definition of the second. Electron turnstiles basically consist of a number of electron islands

connected together via tunneling barriers. The potentials of the islands can be controlled individually using gates. If the gate voltages are changed in a particular operation cycle, the potentials of the islands can be changed in such a manner that single electrons are “pumped” through the system. If the operation cycle is repeated at a frequency  $f$ , the resulting current is  $I = ef$ . Thus, the current is directly linked to the definition of the second via frequency [154–156]. The same principles can be used to construct capacitance standards [157].

Single-electron transistors were also discussed as the basis of logic circuits. Some concepts try to implement conventional CMOS (complementary metal-oxide-semiconductor) logic using single-electron transistors as replacements for  $n$ -MOS and  $p$ -MOS transistors (depending on whether the SET is in the CB region or whether CB is lifted) [158, 159]. In other concepts, the logical states are essentially represented by single electrons, e.g., in quantum dot cellular automata [160]. All of these proposals face strong conceptual and technical challenges. So far, it does seem unlikely that single electronics offers a competitive alternative to traditional CMOS-based logic. Among the problems are the required smallness of the quantum dots for reliable room temperature operation, the sensitivity to background charges, the need for strategies for reproducible placing and interconnecting of quantum dots to build VLSI structures, and the lack of gain of single-electron transistors [161].

Because of their low capacitance, nanometer-sized metallic islands or quantum dots are extremely sensitive to neighboring charges. Whereas in some situations this is unfavorable, e.g., if fluctuating background charges disturb the operation of an SET, this effect can also be exploited for device applications. A promising application of the charge sensitivity of quantum dots is the fabrication of single-electron memories. In one approach, the floating gate memory technique which is already used in CMOS memories is adapted to utilize single-electron effects. A single-electron transistor is used as an electrometer which senses the charging or discharging of a floating gate [162]. The charge state of the floating node can thus be used as a memory whose state is read out by an SET.

Some of the most promising applications of single-electron devices lie in the area of sensorics. An obvious sensor application is charge sensing and electrometry: SETs are the most sensitive charge detectors to date with an equivalent charge noise of the order of  $10^{-3}$  to  $10^{-5} e/\sqrt{\text{Hz}}$  at 10 Hz operation frequency (see, for example, [163, 164]). A charge noise of about  $2 \cdot 10^{-5} e/\sqrt{\text{Hz}}$  could be achieved at a higher operation frequency of 4 kHz [165] and even  $1.2 \cdot 10^{-5} e/\sqrt{\text{Hz}}$  at 1.1 MHz (with an “RF-SET”) [166]. SET-based electrometers were employed to characterize other physical systems, e.g., for the characterization of quantum Hall edge states [167] or for capacitance spectroscopy of vertical quantum dots [168]. SET electrometers were even employed as charge sensors for scanning probe microscopy (SPM) [169]. An interesting application not explicitly based on charge sensitivity is the utilization of quantum dots for the detection of single photons in the far-infrared range [170]. More generally, single-electron transistors are expected to prove useful in many low-noise analog applications, in particular in the amplification of quantum signals [171].

Most of the device proposals mentioned above do not rely on the quantum nature of quantum dots, but simply make use of the Coulomb blockade effect based on the ultrasmall capacitance of small electron islands. The majority of applications of energy quantization within quantum dots are naturally found in optics (see Section 2.7). But also in electronics, the possible utilization of quantum dot energy levels for quantum information processing has recently attracted considerable attention. To build a quantum computer, techniques have to be developed to produce and manipulate “qubits” (quantum bits) – the information unit in quantum information processing and quantum computing. Qubits can be realized in any physical system with two quantum states which can be identified as logical “0” or “1” (in Dirac notation  $|0\rangle$  and  $|1\rangle$ ). The difference between classical and quantum logical states is that a quantum system can also be in a superposition of  $|0\rangle$  and  $|1\rangle$  [172]. Certain classes of computational problems – e.g. factorization of large numbers – are expected to be solved more efficiently on quantum computers. Possible realizations of qubits are the spin states of particles (spin up – spin down), the polarization of photons (vertical – horizontal) or other physical systems which can be approximately described as two-level quantum systems. Implementations of quantum computers in quantum dots make use of the quasi-molecular states formed in two coupled quantum dots [173]. The  $|0\rangle$  and  $|1\rangle$  states correspond to an electron localized on one or other of the two dots. Superpositions can be formed by strongly coupling the two dots together. First experimental realizations of such artificial molecular states in quantum dots have already been reported [174, 175]. Compared to other proposals for quantum computers, quantum dot-based schemes have the important advantage of being compatible with conventional solid state electronics. A severe problem, however, is posed by the relatively short decoherence times, which corrupt the desired evolution of the system states.

## References

- 1 LANE, N. *Journal of Nanoparticle Research* **2001**, 3, 95–103.
- 2 SERVICE, R. F. *Science* **2000**, 290, 1526–1527.
- 3 KINGON, A. I.; MARIA, J.-P.; STREIFFER, S. K. *Nature* **2000**, 406, 1032–1038.
- 4 LLOYD, S. *Nature* **2000**, 406, 1047–1054.
- 5 ITO, T.; OKAZAKI, S. *Nature* **2000**, 406, 1027–1031.
- 6 PEERCEY, P. S. *Nature* **2000**, 406, 1023–1026.
- 7 COHEN-TANNOUDJI, C.; DIU, B.; LAIOE, F. *Quantum Mechanics*; 1st edn.; John Wiley & Sons: New York, 1997.
- 8 YOFFE, A. D. *Adv. Physics* **2001**, 50, 1–208.
- 9 ATKINS, P. W. *Physical Chemistry*; 3rd edn.; Oxford University Press: Oxford, 1986.
- 10 KARPLUS, M.; PORTER, R. N. *Atoms and Molecules*; 1st edn.; W. A. Benjamin, Inc.: New York, 1970.
- 11 HARRISON, W. A. *Electronic Structure and the Properties of Solids: The Physics of the Chemical Bond*; Dover Publications: Dover, 1989.
- 12 KOBAYASHI, A.; SANKEY, O. F.; VOLZ, S. M.; DOW, J. D. *Phys. Rev. B* **1983**, 28, 935–945.
- 13 BURDETT, J. K. *Progress in Solid State Chemistry* **1984**, 15, 173–255.

- 14 KITTEL, C. *Einführung in die Festkörperphysik*; 8th edn.; R. Oldenbourg Verlag: München, Wien, 1989.
- 15 ASHCROFT, N. W.; MERMIN, N. D. *Solid State Physics*; Saunders College: Philadelphia, 1976.
- 16 ALIVISATOS, A. P. *Endeavour* **1997**, 21, 56–60.
- 17 DAVIES, J. H. *The Physics of Low-Dimensional Semiconductors*; Cambridge University Press: Cambridge, 1998.
- 18 ANDO, T.; FOWLER, A. B.; STERN, F. *Rev. Mod. Phys.* **1982**, 54, 437–672.
- 19 MORIARTY, P. *Reports on Progress in Physics* **2001**, 64, 297–381.
- 20 ZHITENEV, N. B.; FULTON, T. A.; YACOBY, A.; HESS, H. F.; PFEIFFER, L. N.; WEST, K. W. *Nature* **2000**, 404, 473–476.
- 21 SUEN, Y. W.; ENGEL, L. W.; SANTOS, M. B.; SHAYEGAN, M.; TSUI, D. C. *Phys. Rev. Lett* **1992**, 68, 1379–1382.
- 22 STORMER, H. L. *Solid State Commun.* **1998**, 107, 617–622.
- 23 STORMER, H. L.; DU, R. R.; KANG, W.; TSUI, D. C.; PFEIFFER, L. N.; BALDWIN, K. W.; WEST, K. W. *Semicond. Sci. Technol.* **1994**, 9, 1853–1858.
- 24 WHARAM, D. A.; THORNTON, T. J.; NEWBURY, R.; PEPPER, M.; AHMED, H.; FROST, J. E. F.; HASKO, D. G.; PEACOCK, D. C.; RITCHIE, D. A.; JONES, G. A. C. *J. Phys. C* **1988**, 21, L209.
- 25 VAN\_WEES, B. J.; HOUTEN, H. v.; BEENAKKER, C. W. J.; WILLIAMS, J. G.; KOUWENHOVEN, L. P.; MAREL, D. v. d.; FOXON, C. T. *Phys. Rev. Lett.* **1988**, 60, 848.
- 26 BUMM, L. A.; ARNOLD, J. J.; CYGAN, M. T.; DUNBAR, T. D.; BURGIN, T. P.; II, L. J.; ALLARA, D. L.; TOUR, J. M.; WEISS, P. S. *Science* **1996**, 271, 1705–1707.
- 27 ANANTRAM, M. P.; DATTA, S.; XUE, Y. Q. *Phys. Rev. B* **2000**, 61, 14219–14224.
- 28 COBDEN, D. H. *Nature* **2001**, 409, 32–33.
- 29 FREEMANTLE, M. *C&EN* **2001**, March 5, 2001, 38.
- 30 CUI, X. D.; PRIMAK, A.; ZARATE, X.; TOMFOHR, J.; SANKEY, O. F.; MOORE, A. L.; MOORE, T. A.; GUST, D.; HARRIS, G.; LINDSAY, S. M. *Science* **2001**, 294, 571–574.
- 31 REED, M. A. *MRS Bulletin* **2001**, February 2001, 113–120.
- 32 HU, J. T.; ODOM, T. W.; LIEBER, C. M. *Accounts Chem. Res.* **1999**, 32, 435–445.
- 33 CUI, Y.; DUAN, X.; HU, J.; LIEBER, C. M. *J. Phys. Chem. B* **2000**, 104, 5213–5216.
- 34 RODRIGUES, V.; FUHRER, T.; UGARTE, D. *Phys. Rev. Lett.* **2000**, 85, 4124–4127.
- 35 RAO, C. N. R.; KULKARNI, G. U.; GOVINDARAJ, A.; SATISHKUMAR, B. C.; THOMAS, P. J. *Pure. Appl. Chem.* **2000**, 72, 21–33.
- 36 HÄKKINEN, H.; BARNETT, R. N.; SCHERBAKOV, A. G.; LANDMAN, U. *J. Phys. Chem. B* **2000**, 104, 9063–9066.
- 37 CUI, Y.; LIEBER, C. M. *Science* **2001**, 291, 851–853.
- 38 REED, M. A.; ZHOU, C.; MULLER, C. J.; BURGIN, T. P.; TOUR, J. M. *Science* **1997**, 278, 252–254.
- 39 VAN DEN BROM, H. E.; YANSON, A. I.; RUITENBEEK, J. M. *Physica B* **1998**, 252, 69–75.
- 40 XE, H. X.; LI, C. Z.; TAO, N. J. *Appl. Phys. Lett.* **2001**, 78, 811–813.
- 41 TANS, S. J.; DEVORET, M. H.; DAI, H.; THESS, A.; SMALLEY, R. E.; GEERLIGS, L. J.; DEKKER, C. *Nature* **1997**, 386, 474–477.
- 42 SAITO, S. *Science* **1997**, 278, 77–78.
- 43 MCEUEN, P. L.; BOCKRATH, M.; COBDEN, D. H.; LU, J. G. *Microelectronic Engineering* **1999**, 47, 417–420.
- 44 YAO, Z.; POSTMA, H. W. C.; BALENTS, L.; DEKKER, C. *Nature* **1999**, 402, 273–276.
- 45 ODOM, T. W.; HUANG, J.-L.; KIM, P.; LIEBER, C. M. *J. Phys. Chem. B* **2000**, 104, 2794–2809.
- 46 MCEUEN, P. L. *Physics World* **2000**, June 2000, 31–36.
- 47 JACOBY, M. *C&EN* **2001**, April 30, 2001, 13.
- 48 DE HEER, W. A.; AL, E. *Science* **1995**, 270, 1179–1180.
- 49 BASTARD, G.; BRUM, J. A. *IEEE J. Quantum Electron.* **1986**, QE 22, 1625–1644.

- 50 BAWENDI, M. G.; STEIGERWALD, M. L.; BRUS, L. E. *Annu. Rev. Phys. Chem.* **1990**, 41, 477–496.
- 51 ALIVISATOS, A. P. *Science* **1996**, 271, 933–937.
- 52 ALIVISATOS, A. P. *MRS Bulletin* **1998**, 23, 18–23.
- 53 KOUWENHOVEN, L. P.; MARCUS, C. M.; McEUEEN, P. L.; TARUCHA, S.; WESTERVELT, R. M.; WINGREEN, N. S. In *Mesoscopic Electron Transport (NATO ASI Series E)*; L. L. SOHN, L. P. K. (Ed.) Kluwer: Dordrecht, 1997.
- 54 WARBURTON, R. J.; MILLER, B. T.; DÜRR, C. S.; BÖRDEFELD, C.; KOTTHAUS, J. P.; MEDEIROS-RIBEIRO, G.; PETROFF, P. M.; HUANT, S. *Phys. Rev. B* **1998**, 58, 16221–16231.
- 55 ALIVISATOS, P. *Pure. Appl. Chem.* **2000**, 72, 3–9.
- 56 EFROS, A. L.; ROSEN, M. *Annu. Rev. Mater. Sci.* **2000**, 30, 475–521.
- 57 SOLOVIEV, V. N.; EICHHOFFER, A.; FENSKE, D.; BANIN, U. *J. Am. Chem. Soc.* **2000**, 122, 2673–2674.
- 58 ZRENNER, A. J. *Chem. Phys.* **2000**, 112, 7790–7798.
- 59 PETROFF, P. M.; LORKE, A.; IMAMOGLU, A. *Physics Today* **2001**, May 2001, 46–52.
- 60 LANDAU, L. D.; LIFSCHITZ, E. M. *Quantenmechanik*; 9th edn.; Akademie-Verlag: Berlin, 1979; Vol. 3.
- 61 SCHWABL, F. *Quantenmechanik*; 2nd edn.; Springer Verlag: Berlin, 1990.
- 62 MESSIAH, A. *Quantenmechanik (Band 1)*; Walter de Gruyter: Berlin, 1976.
- 63 TRINDADE, T.; O'BRIEN, P.; PICKETT, N. L. *Chem. Mat.* **2001**, 13, 3843–3858.
- 64 BRUS, L. E. *J. Chem. Phys.* **1983**, 79, 5566–5571.
- 65 BRUS, L. E. *J. Chem. Phys.* **1984**, 80, 4403–4409.
- 66 BRUS, L. *J. Phys. Chem* **1986**, 90, 2555–2560.
- 67 STEIGERWALD, M. L.; BRUS, L. E. *Acc. Chem. Res.* **1990**, 23, 183–188.
- 68 FÜHRER, A.; LÜSCHER, S.; IHN, T.; HEINZEL, T.; ENSSLIN, K.; WEGSCHEIDER, W.; BICHLER, M. *Nature* **2001**, 413, 822–825.
- 69 BLICK, R. H.; WEIDE, D. W. v. d.; HAUG, R. J.; EBERL, K. *Phys. Rev. Lett* **1998**, 81, 689–692.
- 70 KEMERINK, M.; MOLENKAMP, L. W. *Appl. Phys. Lett.* **1994**, 65, 1012.
- 71 WAUGH, F. R.; BERRY, M. J.; MAR, D. J.; WESTERVELT, R. M.; CAMPMAN, K. L.; GOSSARD, A. C. *Phys. Rev. Lett.* **1995**, 75, 705.
- 72 HOFMANN, F.; WHARAM, D. A. *Advances in Solid State Physics* **1995**, 35, 197.
- 73 BLICK, R. H.; HAUG, R. J.; WEIS, J.; PFANNKUCHE, D.; KLITZING, K. v.; EBERL, K. *Phys. Rev. B* **1996**, 53, 7899–7902.
- 74 BAYER, M.; GUTBROD, T.; REITHMAIER, J. P.; FORCHEL, A.; REINECKE, T. L.; KNIPP, P. A.; DREMIN, A. A.; KULAKOVSKII, V. D. *Phys. Rev. Lett* **1998**, 81, 2582–2585.
- 75 TARUCHA, S.; AUSTING, D. G.; HONDA, T.; HAGE, R. J. v. d.; KOUWENHOVEN, L. P. *Phys. Rev. Lett.* **1996**, 77, 3613.
- 76 GOLDBABER-GORDON, D.; SHTRIKMAN, H.; MAHALU, D.; ABUSCH-MAGDER, D.; MEIRAV, U.; KASTNER, M. A. *Nature* **1998**, 391, 156.
- 77 CRONENWETT, S. M.; OOSTERKAMP, T. H.; KOUWENHOVEN, L. P. *Science* **1998**, 281, 540.
- 78 SIMMEL, F.; BLICK, R. H.; KOTTHAUS, J. P.; WEGSCHEIDER, W.; BICHLER, M. *Phys. Rev. Lett.* **1999**, 83, 804.
- 79 SCHMID, J.; WEIS, J.; EBERL, K.; KLITZING, K. v. *Phys. Rev. Lett.* **2000**, 84, 5824.
- 80 CHO, A. Y. *Journal of Crystals Growth* **1999**, 202, 1–7.
- 81 FAFARD, S.; LEON, R.; LEONARD, D.; MERZ, J. L.; PETROFF, P. M. *Superlattices and Microstructures* **1994**, 16, 303–309.
- 82 PETROFF, P. M.; DENBAARS, S. P. *Superlattices and Microstructures* **1994**, 15, 15–21.
- 83 LEON, R.; PETROFF, P. M.; LEONARD, D.; FAFARD, S. *Science* **1995**, 267, 1966–1968.
- 84 LUYKEN, R. J.; LORKE, A.; GOVOROV, A. O.; KOTTHAUS, J. P.; MEDEIROS-RIBEIRO, G.; PETROFF, P. M. *Appl. Phys. Lett* **1999**, 74, 2486–2488.
- 85 LIU, Z. F.; SHEN, Z. Y.; ZHU, T.; HOU, S. F.; YING, L. Z.; SHI, Z. J.; GU, Z. N. *Langmuir* **2000**, 16, 3569–3573.
- 86 PAUL, D. J. *Adv. Mater.* **1999**, 11, 191–204.

- 87 GARCIA, J. M.; MEDEIROS-RIBEIRO, G.; SCHMIDT, K.; NGO, T.; FENG, J. L.; LORKE, A.; KOTTHAUS, J.; PETROFF, P. M. *Appl. Phys. Lett.* **1997**, 71, 2014–2016.
- 88 BAYER, M.; STERN, O.; HAWRYLAK, P.; FAFARD, S.; FORCHEL, A. *Nature* **2000**, 405, 923–926.
- 89 Warburton, R. J.; Schäflein, C.; Haft, D.; Bickel, F.; Lorke, A.; Karrai, K.; Garcia, J. M.; Schoenfeld, W.; Petroff, M. P. *Nature* **2000**, 405, 926–929.
- 90 TARUCHA, S. *MRS Bulletin* **1998**, 23, 49–53.
- 91 LORKE, A.; LUYKEN, R. J. *Physica B: Condensed Matter* **1998**, 256–258, 424–430.
- 92 GAMMON, D. *Nature* **2000**, 405, 899–900.
- 93 MURRAY, C. B.; NORRIS, D. J.; BAWENDI, M. G. *J. Am. Chem. Soc.* **1993**, 115, 8706–8715.
- 94 PENG, X.; WICKHAM, J.; ALIVISATOS, A. P. *J. Am. Chem. Soc.* **1998**, 120, 5343–5344.
- 95 DABBOUSI, B. O.; RODRIGUEZ-VIEJO, J.; MIKULEC, F. V.; HEINE, J. R.; MATTOUSSI, H.; OBER, R.; JENSEN, K. F.; BAWENDI, M. G. *J. Phys. Chem. B* **1997**, 101, 9463–9475.
- 96 PENG, X.; SCHLAMP, M. C.; KADAVANICH, A. V.; ALIVISATOS, A. P. *J. Am. Chem. Soc.* **1997**, 119, 7019–7029.
- 97 PENG, X.; MANNA, L.; YANG, W.; WICKHAM, J.; SCHER, E.; KADAVANICH, A.; ALIVISATOS, A. P. *Nature* **2000**, 404, 59–61.
- 98 PUNTES, V. F.; KRISHNAN, K.; ALIVISATOS, A. P. *Topics in Catalysis* **2002**, 19, 145–148.
- 99 MIRKIN, C. A.; LETSINGER, R. L.; MUCIC, R. C.; STORHOFF, J. J. *Nature* **1996**, 382, 607–609.
- 100 LOWETH, C. J.; CALDWELL, W. B.; PENG, X. G.; ALIVISATOS, A. P.; SCHULTZ, P. G. *Angew. Chem. Int. Ed.* **1999**, 38, 1808–1812.
- 101 ZANCHET, D.; MICHEEL, C. M.; PARAK, W. J.; GERION, D.; WILLIAMS, S. C.; ALIVISATOS, A. P. *J. Phys. Chem. B* **2002**, 106, 11758–11763.
- 102 BRUCHEZ, M. J.; MORONNE, M.; GIN, P.; WEISS, S.; ALIVISATOS, A. P. *Science* **1998**, 281, 2013–2016.
- 103 CHAN, W. C. W.; NIE, S. *Science* **1998**, 281, 2016–2018.
- 104 DUBERTRET, B.; SKOURIDES, P.; NORRIS, D. J.; NOIREAUX, V.; BRIVANLOU, A. H.; LIBCHABER, A. *Science* **2002**, 298, 1759–1762.
- 105 KLEIN, D. L.; McEuen, P. L.; BOWEN-KATARI, J. E.; ROTH, R.; ALIVISATOS, A. P. *Appl. Phys. Lett* **1996**, 68, 2574–2576.
- 106 KLEIN, D. L.; ROTH, R.; LIM, A. K. L.; ALIVISATOS, A. P.; McEuen, P. L. *Nature* **1997**, 389, 699–701.
- 107 JAECKEL, G. Z. *Tech. Phys.* **1926**, 6, 301–304.
- 108 GAPONENKO, S. V. *Optical Properties of Semiconductor Nanocrystals*; Cambridge University Press: Cambridge, 1998.
- 109 KLIMOV, V. I.; McBRANCH, D. W.; LEATHERDALE, C. A.; BAWENDI, M. G. *Phys. Rev. B* **1999**, 60, 13740–13749.
- 110 NIRMAL, M.; NORRIS, D. J.; KUNO, M.; BAWENDI, M. G.; EFROS, A. L.; ROSEN, M. *Phys. Rev.* **1995**, 75, 3728–3731.
- 111 EFROS, A. L.; ROSEN, M.; KUNO, M.; NIRMAL, M.; NORRIS, D. J.; BAWENDI, M. *Phys. Rev. B* **1996**, 54, 4843–4856.
- 112 REBOREDO, F. A.; FRANCESCHETTI, A.; ZUNGER, A. *Phys. Rev. B* **2000**, 61, 13073–13087.
- 113 JOHNSTON-HALPERIN, E.; AWSCHALOM, D. D.; CROOKER, S. A.; EFROS, A. L.; ROSEN, M.; PENG, X.; ALIVISATOS, A. P. *Phys. Rev. B* **2001**, 63, 205309–205323.
- 114 DAHAN, M.; LAURENCE, T.; PINAUD, F.; CHEMLA, D. S.; ALIVISATOS, A. P.; SAUER, M.; WEISS, S. *Opt. Lett.* **2001**, 26, 825–827.
- 115 EMPEDOCLES, S. A.; NORRIS, D. J.; BAWENDI, M. G. *Phys. Rev. Lett* **1996**, 77, 3873–3876.
- 116 EMPEDOCLES, S.; BAWENDI, M. *Accounts Chem. Res.* **1999**, 32, 389–396.
- 117 EMPEDOCLES, S. A.; BAWENDI, M. G. *J. Phys. Chem. B* **1999**, 103, 1826–1830.
- 118 NEUHAUSER, R. G.; SHIMIZU, K. T.; WOO, W. K.; EMPEDOCLES, S. A.; BAWENDI, M. G. *Phys. Rev. Lett* **2000**, 85, 3301–3304.
- 119 BASCHE, T. J. *Luminescence* **1998**, 76–7, 263–269.

- 120 NIRMAL, M.; DABBOUSI, B. O.; BAWENDI, M. G.; MACKLIN, J. J.; TRAUTMAN, J. K.; HARRIS, T. D.; BRUS, L. E. *Nature* **1996**, *383*, 802–804.
- 121 EFROS, A. L.; ROSEN, M. *Phys. Rev. Lett* **1997**, *78*, 1110–1113.
- 122 KUNO, M.; FROMM, D. P.; HAMANN, H. F.; GALLAGHER, A.; NESBITT, D. J. *J. Chem. Phys.* **2000**, *112*, 3117–3120.
- 123 DICKSON, R. M.; CUBITT, A. B.; TSIEN, R. Y.; MOERNER, W. E. *Nature* **1997**, *388*, 355–358.
- 124 NIRMAL, M.; BRUS, L. *Accounts Chem. Res.* **1999**, *32*, 407–414.
- 125 EMPEDOCLES, S. A.; NEUHAUSER, R.; SHIMIZU, K.; BAWENDI, M. G. *Adv. Mater.* **1999**, *11*, 1243–1256.
- 126 HODAK, J. H.; HENGLEIN, A.; HARTLAND, G. V. *Pure. Appl. Chem.* **2000**, *72*, 189–197.
- 127 MULVANEY, P. *Langmuir* **1996**, *12*, 788–800.
- 128 LEDENTSOV, N. N.; USTINOV, V. M.; EGOROV, A. Y.; ZHUKOV, A. E.; MAKSIMOV, M. V.; TABATADZE, I. G.; KOP'EV, P. S. *Semiconductors* **1994**, *28*, 832.
- 129 KIRSTAEDTER, N.; LEDENTSOV, N. N.; GRUNDMANN, M.; BIMBERG, D.; USTINOV, V. M.; RUVIMOV, S. S.; MAXIMOV, M. V.; KOP'EV, P. S.; ALFEROV, Z. I.; RICHTER, U.; WERNER, P.; GÖSELE, U.; HEYDENREICH, J. *Electron. Lett.* **1994**, *30*, 1416.
- 130 BIMBERG, D.; GRUNDMANN, M.; HEINRICHSORFF, F.; LEDENTSOV, N. N.; USTINOV, V. M.; ZHUKOV, A. E.; KOVSH, A. R.; MAXIMOV, M. V.; SHERNYAKOV, Y. M.; VOLOVİK, B. V.; TSATSUL'NIKOV, A. F.; KOP'EV, P. S.; ALFEROV, Z. I. *Thin Solid Films* **2000**, *367*, 235.
- 131 KLIMOV, V. I.; MIKHAILOVSKY, A. A.; XU, S.; MALKO, A.; HOLLINGSWORTH, J. A.; LEATHERDALE, C. A.; EISLER, H.-J.; BAWENDI, M. G. *Science* **2000**, *290*, 314–317.
- 132 MICHLER, P.; IMAMOGLU, A.; MASON, M. D.; CARSON, P. J.; STROUSE, G. F.; BURATTO, S. K. *Nature* **2000**, *406*, 968–970.
- 133 MICHLER, P.; KIRAZ, A.; BECHER, C.; SCHOENFELD, W. V.; PETROFF, P. M.; ZHANG, L.; HU, E.; IMAMOGLU, A. *Science* **2000**, *290*, 2282.
- 134 MICHLER, P.; IMAMOGLU, A.; KIRAZ, A.; BECHER, C.; MASON, M. D.; CARSON, P. J.; STROUSE, G. F.; BURATTO, S. K.; SCHOENFELD, W. V.; PETROFF, P. M. *Phys. Status Solidi B-Basic Res.* **2002**, *229*, 399–405.
- 135 ZWILLER, V.; BLUM, H.; JONSSON, P.; PANEV, N.; JEPPESEN, S.; TSEGAYE, T.; GOOBAR, E.; PISTOL, M.-E.; SAMUELSON, L.; BJÖRK, G. *Appl. Phys. Lett.* **2001**, *78*, 2476.
- 136 SANTORI, C.; FATTAL, D.; VUCKOVIC, J.; SOLOMON, G. S.; YAMAMOTO, Y. *Nature* **2002**, *419*, 594.
- 137 LUNDSTROM, T.; SCHOENFELD, W.; LEE, H.; PETROFF, P. M. *Science* **1999**, *286*, 2312.
- 138 COLVIN, V. L.; SCHLAMP, M. C.; ALIVISATOS, A. P. *Nature* **1994**, *370*, 354–357.
- 139 DABBOUSI, B. O.; BAWENDI, M. G.; ONOTSUKA, O.; RUBNER, M. F. *Appl. Phys. Lett.* **1995**, *66*, 1316.
- 140 HUYNH, W. U.; DITTMER, J. J.; ALIVISATOS, A. P. *Science* **2002**, *295*, 2425–2427.
- 141 HUYNH, W. U.; PENG, X.; ALIVISATOS, A. P. *Adv. Mater.* **1999**, *11*, 923–927.
- 142 GORTER, C. J. *Physica* **1951**, *17*, 777.
- 143 GIAEVER, I.; ZELLER, H. R. *Phys. Rev. Lett.* **1968**, *20*, 1504.
- 144 ZELLER, H. R.; GIAEVER, I. *Phys. Rev.* **1969**, *181*, 791.
- 145 LAMBE, J.; JAKLEVIC, R. C. *Phys. Rev. Lett.* **1969**, *22*, 1371.
- 146 FULTON, T. A.; DOLAN, G. J. *Phys. Rev. Lett.* **1987**, *59*, 109–112.
- 147 SCOTT-THOMAS, J. H. F.; FIELD, S. B.; KASTNER, M. A.; SMITH, H. I.; ANTONIADIS, D. A. *Phys. Rev. Lett.* **1989**, *62*, 583.
- 148 AVERIN, D. V.; LIKHAREV, K. K. In *Mesoscopic Phenomena in Solids*; ALTSHULER, B. L., LEE, P. A., WEBB, R. A., Eds.; Elsevier: Amsterdam, 1991.
- 149 SCHÖN, G. In *Quantum Transport and Dissipation*; DITTRICH, T., HÄNGGI, P., INGOLD, G.-L., KRAMER, B., SCHÖN, G., ZWIRGER, W., Eds.; Wiley-VCH: Weinheim, 1998.

- 150 VAN\_HOUTEN, H.; BEENAKKER, C. W. J.; STARING, A. A. M. In *Single Charge Tunneling (NATO ASI Series B)*; GRABERT, H., DEVORET, M. H., Eds.; Plenum: New York, 1991.
- 151 KASTNER, M. A. *Physics Today* **1993**, January 1993, 24–31.
- 152 ASHOORI, R. C. *Nature* **1996**, 379, 413–419.
- 153 REICHL, L. E. *A modern course in statistical physics*; 2nd edn.; John Wiley: New York, 1998.
- 154 GEERLIGS, L. J.; ANDEREGG, V. F.; HOLWEG, P. A. M.; MOOIJ, J. E.; POTHIER, H.; ESTEVE, D.; URBINA, C.; M. H. DEVORET *Phys. Rev. Lett.* **1990**, 64, 2691.
- 155 KELLER, M. W.; MARTINIS, J. M.; ZIMMERMAN, N. M.; STEINBACH, A. H. *Appl. Phys. Lett.* **1996**, 69, 1804.
- 156 KELLER, M. W.; MARTINIS, J. M.; KAUTZ, R. L. *Phys. Rev. Lett.* **1998**, 80, 4313.
- 157 KELLER, M. W.; EICHENBERGER, A. L.; MARTINIS, J. M.; ZIMMERMAN, N. M. *Science* **1999**, 285, 1706.
- 158 TUCKER, J. R. *J. Appl. Phys.* **1992**, 72, 4399.
- 159 CHEN, R. H.; KOROTKOV, A. N.; LIKHAREV, K. K. *Appl. Phys. Lett.* **1996**, 68, 1954.
- 160 AMLANI, I.; ORLOV, A. O.; TOTH, G.; BERNSTEIN, G. H.; LENT, C. S.; G. L. SNIDER *Science* **1999**, 284, 289.
- 161 LIKHAREV, K. K. *Proc. IEEE* **1999**, 87, 606.
- 162 CHEN, C. D.; NAKAMURA, Y.; TSAI, J. S. *Appl. Phys. Lett.* **1997**, 71, 2038.
- 163 VISSCHER, E. H.; LINDEMAN, J.; VERBRUGH, S. M.; HADLEY, P.; MOOIJ, J. E. *Appl. Phys. Lett.* **1996**, 68, 2014.
- 164 KRUPENIN, V. A.; PRESNOV, D. E.; SCHERER, H.; ZORIN, A. B.; NIEMEYER, J. *J. Appl. Phys.* **1998**, 84, 3212.
- 165 STARMARK, B.; HENNING, T.; CLAESON, T.; DELSING, P.; KOROTKOV, A. N. *J. Appl. Phys.* **1999**, 86, 2132.
- 166 SCHOELKOPF, R. P.; WAHLGREN, P.; KOZHEVNIKOV, A. A.; DELSING, P.; PROBER, D. E. *Science* **1998**, 280, 1238–1242.
- 167 WEI, Y. Y.; WEIS, J.; KLITZING, K. v.; EBERL, K. *Phys. Rev. Lett.* **1998**, 77, 1674.
- 168 KOLTONYUK, M.; BERMAN, D.; ZHITENEV, N. B.; ASHOORI, R. C.; PFEIFFER, L. N.; WEST, K. W. *Appl. Phys. Lett.* **1999**, 74, 555.
- 169 YOO, M. J.; FULTON, T. A.; HESS, H. F.; WILLETT, R. L.; DUNKLEBERGER, L. N.; CHICHESTER, R. J.; PFEIFFER, L. N.; WEST, K. W. *Science* **1997**, 276, 579–582.
- 170 KOMIYAMA, S.; ASTAFIEV, O.; ANTONOV, V.; KUTSUWA, T.; HIRAI, H. *Nature* **2000**, 403, 405.
- 171 DEVORET, M. H.; SCHOELKOPF, R. J. *Nature* **2000**, 406, 1039–1046.
- 172 NIELSEN, M. A.; CHUANG, I. L. *Quantum Computation and Quantum Information*; Cambridge University Press: Cambridge, 2000.
- 173 LOSS, D.; DI\_VINCENZO, D. P. *Phys. Rev. A* **1998**, 57, 120.
- 174 BAYER, M.; HAWRYLAK, P.; HINZER, K.; FAFARD, S.; KORKUSINSKI, M.; WASILEWSKI, Z. R.; STERN, O.; FORCHEL, A. *Science* **2001**, 291, 451–453.
- 175 HOLLEITNER, A. W.; BLICK, R. H.; HÜTTEL, A. K.; EBERL, K.; KOTTHAUS, J. P. *Science* **2002**, 297, 70.
- 176 GORSUA, M.; NAZAREWICZ, W. *Phys. Stat. Sol. A* **1974**, 65, 193–202.



## 3

**Syntheses and Characterizations**

## 3.1

**Semiconductor Nanoparticles**

## 3.1.1

**Synthesis and Characterization of II–VI Nanoparticles**

*Alexander Eychmüller*

The field of “synthesis” or “preparation” of II–VI semiconductor nanoparticles has experienced an enormous development in the past two decades. The literature dealing with this topic is virtually unmanageable. Nevertheless, the present chapter attempts to give a chronological overview of some of the major historical lines in this area, starting with the earliest work on CdS nanocrystals prepared in aqueous solution. At several points in the story, mostly when successful preparations are reported for the first time, the chapter branches into these evolving sub-fields and leads to Sections 3.1.1.2 “Thiol-Stabilized Nanoparticles” and 3.1.1.3 “The “TOP/TOPO” Synthesis”. The remainder of this historical review then deals with matters distinct from these preparational approaches. Sections 3.1.1.4 “Core-Shell Nanoparticles” and 3.1.1.5 “Quantum Dot Quantum Wells” deal with more complicated nanoheterostructures in which two compounds are involved in the build-up of spherically layered particles.

Naturally, in all chapters, the view of the author is indicated concerning the importance of work reviewed for the evolution of the subject as a whole. Besides this necessarily subjective viewpoint, it is not impossible that other important work may be overlooked. Thus, even if a particular chapter provides little more than a list of literature references, only questions like “What has been done in this field” may be answered but never those like “What has not been done yet”!

3.1.1.1 **Historical Review**

Even the shortest history of the preparation of II–VI semiconductor nanoparticles has to start with the work published by A. Henglein in 1982 [1]. Like others [2–7], this paper deals with surface chemistry, photodegradation, and catalytic processes in colloidal semiconductor particles. But it is this very work which reveals the first absorption spectrum of a colloidal solution of size-quantized CdS nanocrystals.

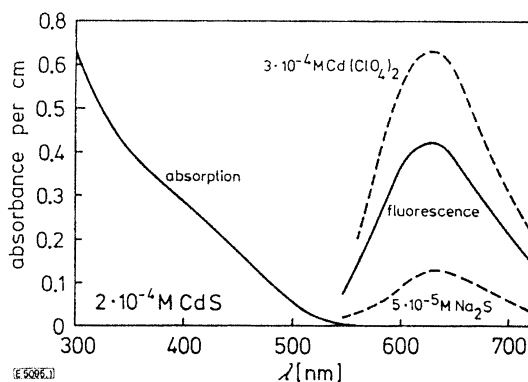
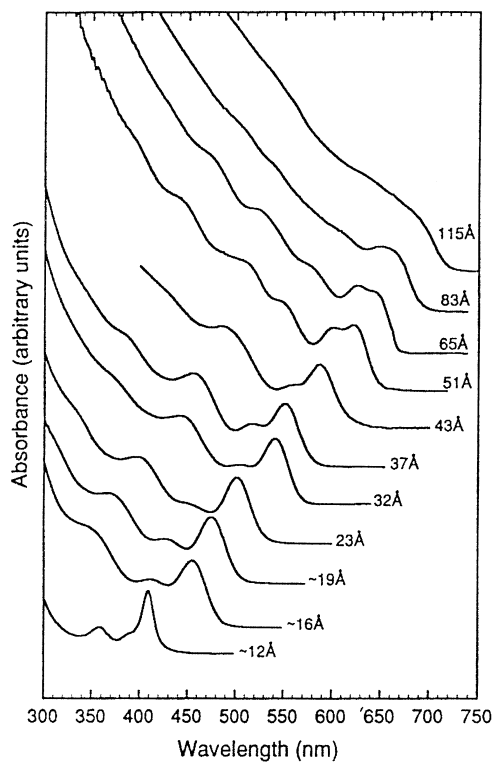


Fig. 3-1 Absorption and emission spectra of a colloidal CdS solution [1].

These were prepared from  $\text{Cd}(\text{ClO}_4)_2$  and  $\text{Na}_2\text{S}$  on the surface of commercial silica particles. As seen from Figure 3-1, the absorption onset is shifted considerably to higher energies with respect to the bulk bandgap of CdS (515 nm). In addition, the sol emits light upon excitation at 390 nm, which is also a matter of investigation in this paper. The first correct interpretation of the observed blue shift of the absorption as a quantum mechanical effect is due to L. Brus [8]. In the framework of the effective mass approximation, the shift in the kinetic energy of the charge carriers due to their spatial restriction to the volume of the nanometer-sized semiconductors is calculated. (It is noted that comparable experimental [9] and theoretical work [10] was carried out at almost the same time on the I–VII compound  $\text{CuCl}$  in the Soviet Union.)

Another milestone in the preparation of II–VI semiconductor nanocrystals is the work by Murray, Norris and Bawendi from 1993 [11]. Their synthesis is based on the pyrolysis of organometallic reagents like dimethyl cadmium and trioctylphosphine selenide after injection into a hot coordinating solvent. This approach provides temporally discrete nucleation and permits a controlled growth of the nanocrystals. Figure 3-2 shows the evolution of the absorption spectra of a series of CdSe crystallites ranging in size from about 1.2 to 11.5 nm. This series spans a range of sizes from more or less molecular species to fragments of the bulk lattice containing tens of thousands of atoms. The remarkable quality of these particles is clearly seen in several features of the absorption spectra, e.g., the steepness of the absorption onset, the narrow absorption bands, and the occurrence of higher energy transitions.

By comparison of Figure 3-1 with Figure 3-2, it is evident that within about a decade tremendous progress was made in the preparation of such systems. To illustrate what happened during this period of time, a few endeavors in both preparation and characterization from a number of different laboratories will be mentioned. Rossetti et al. reported on quantum size effects in the redox potentials and electronic spectra of CdS nanocrystals [12]. Resonance Raman spectra were taken from freshly prepared samples and from larger, “aged” particles. The size distributions were studied with transmission electron microscopy (TEM), and the crys-



**Fig. 3-2** 1993 state-of-the-art absorption spectra of CdSe colloidal solutions ("TOP-TOPO synthesis") [11].

tallinity and crystal structure were determined. In a series of publications, Henlein and coworkers placed stress on the dissolution of CdS particles [13], enlarged the field by the preparation of ZnS and ZnS/CdS co-colloids (including TEM characterization) [14, 15], gave insight into photophysical properties like time-resolved fluorescence decays [16], and introduced the term "magic agglomeration numbers" [17]. Ramsden and Grätzel presented the synthesis of CdS particles formed in aqueous solution from  $\text{Cd}(\text{NO}_3)_2$  and  $\text{H}_2\text{S}$  or  $\text{Na}_2\text{S}$  [18]. In combination with luminescence data, transmission electron microscopic images were reported, and the particles obtained were assigned to the cubic phase. In 1985, A. J. Nozik appeared on the scene with a paper on phosphate-stabilized CdS and small PbS colloids [19]. After yet another theoretical paper [20], it was again L. Brus who published in 1986 a review-like article [21] summarizing the then current status in the field of semiconductor clusters, from both an experimental and a theoretical viewpoint. Also in 1986, attempts at a fractional separation by exclusion chromatography of an as-prepared sol of hexametaphosphate (HMP) (more correctly: Grahams salt)-stabilized CdS particles were presented, together with stopped-flow experiments on extremely small clusters [22]. The binding of simple amines to the sur-

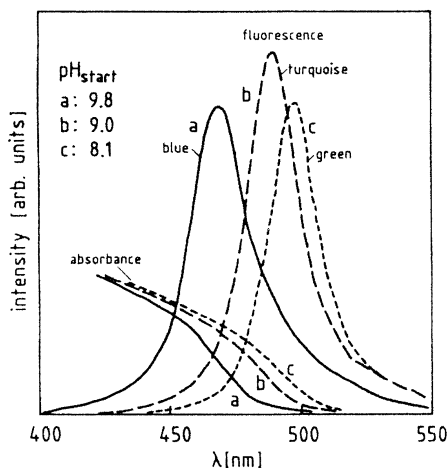


Fig. 3-3 Absorption and luminescence spectra of CdS sols ("polyphosphate preparation") with varying starting pH [27].

face of CdS particles of various sizes prepared by conventional routes as well as in AOT/H<sub>2</sub>O/heptane reverse micelles enhances their luminescence quantum yield dramatically [23]. This effect is interpreted as a modification of mid-gap states which may play an important role in the non-radiative recombination processes of electron and hole in the materials under investigation. New preparative approaches were presented, e.g., the preparation of CdS particles in dihexadecyl phosphate (DHP) surfactant vesicles [24] and the synthesis of colloidal CdSe [25], which has now become the most important model system for the investigation of the properties of nanocrystalline matter. As determined in pulse radiolysis experiments, an excess electron on the surface of CdS colloids causes a bleaching of the optical absorption at wavelengths close to the onset of absorption [26]. One year later, a study was published, likewise from the Henglein group, which since then has been cited frequently [27]. CdS sols with particles ranging in size between 4 and 6 nm (as seen from TEM-based particle size histograms) were prepared by first precipitating Cd<sup>2+</sup> ions with the stoichiometric amount of injected H<sub>2</sub>S followed by an "activation" of the colloid by addition of NaOH and excess Cd<sup>2+</sup> ions, resulting in a strong emission band close to the energy of the band edge. Figure 3-3 reflects the influence of the "starting pH" on the color of the emitted light after the "activation" process as well as on the particle size. The "activation" is interpreted in terms of a precipitation of cadmium hydroxide onto the surface of the CdS particles. By this procedure, the photostability of the sols is strongly increased approaching that of organic dyes like Rhodamine 6G.

The reported fluorescence quantum yields, >50% in this publication and 80% in earlier publications of other authors [23], seem over-optimistic. From our modern viewpoint, the "activation" should rather be interpreted as being the result of the creation of a shell of the large bandgap material Cd(OH)<sub>2</sub> on the surface of the CdS

particles (cf. also Section 3.1.1.4). This results in the formation of an electronic barrier at the surface of the particles, preventing the charge carriers from escaping from the particles' core. This preparation operated as the basis for some novel core-shell structures and multilayered nanotopologies, described in more detail in Sections 3.1.1.4 and 3.1.1.5.

An enormous step forward (especially in terms of the characterization involving, among others, infrared and NMR spectroscopy, high-resolution electron microscopy (HRTEM), and X-ray diffraction (XRD)) was achieved by the work of the AT&T group of Steigerwald and Brus from 1988 [28]. Organometallic compounds were used to synthesize nanometer-sized clusters of CdSe in inverse micellar solutions. Chemical modification of the surface of these clusters was performed, the cluster molecules could be removed and isolated from the reaction mixture, and this was followed by a detailed powder XRD investigation. Later in the year, reports on microheterogeneous systems appeared involving CdS,  $\text{Zn}_x\text{Cd}_{1-x}\text{S}$ , and CdS coated with ZnS, which were formed in and stabilized by, again, DHP vesicles [29]. Additionally, layers of CdS particles (5 nm in size) were prepared by the Langmuir-Blodgett technique [30]. These and many more results on small particle research both on metal and on semiconductor particles are summarized in review articles by Henglein [31, 32] and by Steigerwald and Brus [33]. Furthermore, considerable progress has been made in the radiolytic production of CdS particles [34], in the preparation of CdTe and ZnTe [35], and in the application of tunneling microscopy to quantum-sized CdS [36]. The use of thiophenol as the stabilizing agent for CdS clusters is reported by Herron et al. [37]. Competitive reaction chemistry between CdS core cluster growth and surface capping by thiophenolate is assumed to be responsible for the evolution of clusters whose core consists of essentially cubic CdS and whose reactive surface has been passivated by covalently attached thiophenyl groups. The synthesis of porous quantum-size CdS membranes is achieved in three subsequent steps: initial colloid preparation following standard procedures [27], concentration of the suspension and dialysis, and finally the controlled evaporation of the residual solvent [38]. In a study of photoreductive reactions on small ZnS particles, an elaborate HRTEM analysis was presented enabling the determination of the actual particle size by simply counting the lattice planes [39]. Post-preparative size separation of colloidal CdS by gel electrophoresis was demonstrated [40], and an ion-dilution technique was utilized in order to form ultrasmall particles of CdS and CdSe in Nafion membranes [41]. After initial investigations of the recombination processes of electron-hole pairs in clusters [16, 42–44], two reports appeared on this topic, both of which proposed a mechanism of delayed emission for the radiative “band-to-band” recombination [45, 46]. During this time, several reports dealt with quenching and “anti-quenching”, i.e., the enhancement of the luminescence of nanosized CdS, all contributing in a qualitative manner to a deeper understanding of optical properties of suspended nanocrystals [47–52]. CdS nanoparticles were synthesized in several non-aqueous solvents, and their catalytic efficiency in the photoinitiation of polymerization of various vinylic monomers were examined in detail [53].

Early in 1993, a special issue of *The Israel Journal of Chemistry* was devoted to

quantum-size particles and thus contained several articles which are concerned predominantly with the synthesis and characterization of II–VI-semiconductor nanoparticles [54–60]. Later in the year, two frequently cited articles summarized the achievements in the field [61, 62]. The characterization of wet-chemically synthesized CdTe and HgTe as well as of ternary HgCdTe compounds (including XRD, TEM and photoluminescence) were the focus of work by Müllenborn et al. [63]. The nature of the stabilizer plays an important role in the efficiency of luminescence quenching as demonstrated by the comparison of inverse micelle/HMP- and thiophenol-capped CdS [64]. Thiol capping is also the clue to synthesizing differently-sized CdTe particles prepared in aqueous solution [65]. In this interesting paper, the bandgaps of 2.0 nm, 2.5 nm, 3.5 nm, and 4.0 nm crystallites were estimated from pulse radiolysis experiments, and their dependence on the size of the particles was found to be in better agreement with pseudopotential [66] and tight-binding models [67, 68] than with the effective mass approximation [20]. An important result of the work of Rajh et al. is the observation that the extinction coefficient per particle is independent of the size as predicted by theory [69–71]. This again brings us to the time of the work by Murray et al. [11]. Yet another aspect of its superior quality should now be mentioned, namely the thoroughness of the characterization of the particles prepared. Among other findings, HRTEM images revealed the presence of stacking faults in certain crystallographic directions, and showed that the particles are prolate and that the crystallites arrange themselves freely into secondary structures. The investigations probing only a limited number of particles were supplemented by a carefully conducted X-ray diffraction study including structural simulations. This work forms the basis of the “organometallic preparative route”. Their most recent accomplishments are outlined in Section 3.1.1.3, and some of the work on core-shell nanoparticles is described in Section 3.1.1.4.

Like this approach, thiol stabilization proved to offer a very successful route toward monosized nanoparticles of various compounds. Since this preparative approach has also gained widespread interest, it will be outlined separately in the next chapter.

From this point onwards in this “historical review” we will focus only on some recent developments which differ from the “organometallic route” and from the thiol technique.

Narrowing of the size distribution of a quite polydisperse CdS colloid by size-selective photocorrosion was demonstrated by Matsumoto et al. [72]. In order to replace the hazardous metal alkyls in the organometallic synthesis, a single-source approach to the synthesis of II–VI nanocrystallites was presented by Trindade and O’Brian [73]. CdSe particles were formed from methyldiethyldiselenocarbamate cadmium (II), a compound which was synthesized beforehand from dimethyl cadmium and bisdiethyldiselenocarbamate cadmium (II). Vesicles were again used as reaction compartments [74], and nanophase reactors were generated by binary liquids at the surface of colloidal silica particles also acting as reaction compartments for small CdS and ZnS particles [75]. The fabrication of composites from CdSe nanoclusters and phosphine-functionalized block copolymers was the aim of

Fogg et al. [76]. CdS particles formed from  $\text{Na}_2\text{S}$  and  $\text{CdSO}_4$  have been studied extensively by  $^{113}\text{Cd}$  and  $^1\text{H}$  NMR [77]. From a careful analysis of the temperature-dependent NMR spectra, three different  $\text{Cd}^{2+}$  species (located in the core, at the surface, and in solution) are distinguished, and a considerable amount of water has been found to be present in the dry samples. Several procedures are reported to achieve a protection of the surface (by e.g.  $\text{SiO}_2$  [78]) or an encapsulation [79, 80]. However, it is a complex interplay between the nature of the solvent, the anions of the cadmium salt, the ratio of salt to thiurea, and the temperature which controls the morphology and sizes of nanocrystalline CdS products. As shown by XRD and TEM, spheres of various sizes, rods and even nanowires of up to 900 nm in length were generated by a solvothermal process [81]. The luminescence properties of CdS particles prepared either in the presence of a poly(aminoamine) dendrimer or polyphosphate were revisited with special emphasis on the polarization of the emitted light [82] and on the luminescence lifetimes [83]. In another report, the charging of individual CdSe particles was studied [84]. Further synthetical efforts yielded HgE ( $\text{E} = \text{S}, \text{Se}, \text{Te}$ ) nanoparticles [85], PbS sols with various capping agents like poly(vinyl-alcohol), poly(vinyl-pyrrolidone), gelatin, DNA, polystyrene, and poly(methyl-methacrylate) [86], and ZnS nanoparticles in a silica matrix [87]. Small CdTe particles are accessible by a preparation in reverse micelles [88], and “peanut-like” nanostructures of CdS and ZnS were obtained by reactions at a static organic/aqueous biphasic boundary [89]. In 2001, the group of M. Lahav reported on the organization of CdS and PbS nanoparticles in hybrid organic/inorganic Langmuir-Blodgett films and the characterization of the layers by XRD- and TEM-techniques [90]. The zeolite MCM-41 is suitable as a host for CdS nanocrystals which are formed via an ion-exchange reaction as shown by Zhang and coworkers [91]. A completely new approach to the synthesis of Cd-chalcogenide nanoparticles is demonstrated by Peng and Peng using CdO as the cadmium precursor and strong ligands such as hexylphosphonic acid or tetradecylphosphonic acid [92]. Very fine (“high-quality”) nanocrystals are gained by this method, and even shape control (i.e. spheres or rods) is demonstrated. Four types of binding sites at the surface of CdS particles prepared by precipitation from a solution of cadmium carboxylate in dimethyl sulfoxide (DMSO) were identified by means of IR and NMR spectroscopy, namely oxidized sulfur, adsorbed acetate, oxygen-bound DMSO, and hydroxyl ions [93]. Micelles of various compositions are involved in preparations of CdS (block-copolymer (compound) micelles [94, 95]) and triangularly shaped CdS nanocrystals ( $\text{Cd}(\text{AOT})_2$ /isooctane/water reverse micelles [96]). The protection of CdS particles by capping with a shell of silica was reported by Farmer and Patten [97]. Furthermore, organic dendrons have been used for the stabilization of CdSe quantum dots [98]. The optical properties of CdS quantum dots in Nafion are the focus of a study by Nandakumar et al. [99], namely the two-photon absorption and the photon-number squeezing with CdSe particles in PMMA [100]. Molecular species like  $(\text{Li})_4\text{[Cd}_{10}\text{Se}_4(\text{SPh})_{16}]$  as fragments of the bulk structure act as templates for the growth of nanocrystalline CdSe in hexadecylamine as the solvent [101]. This approach may also be applied to the synthesis of ZnSe and CdSe/ZnS core-shell nanocrystals.

Many of these efforts have also been included in review-like articles [102–108]. Empiricism, chemical imagination, and intuition largely form the basis for the preparation of nanosized objects in solution. In the opinion of the author, this will continue for a number of years despite attempts to successfully predict superior preparative routes by means of combinatorial and computer scientific approaches [109].

### 3.1.1.2 Thiol-Stabilized Nanoparticles

The use of thiols as capping agents in the synthesis of II–VI semiconductor nanocrystals has been mentioned several times in the preceding section. After some preliminary work [110, 111, 54] based on earlier work by Dance et al. [112–114] and others [115, 116], this approach came to full fruition for the first time in a paper by Herron et al. [117]. This reported on the synthesis and optical properties of a cluster with a 1.5 nm CdS core having the total formula  $[\text{Cd}_{32}\text{S}_{14}(\text{SPh})_{36}] \cdot 4 \text{ DMF}$  (SPh = thiophenol, DMF = *N,N*-dimethylformamide). Its structure, being a piece of the cubic lattice as determined by single crystal XRD, will be discussed in more detail in Section 4.2.1. In 1994 a paper was published on the synthesis, the characterization, and several optical properties of thiol- and polyphosphate-stabilized CdS particles ranging in size from 1.3 nm to about 10 nm as determined from small- and wide-angle XRD as well as from TEM [118]. Furthermore, this paper yields chemical and thermogravimetric analysis data, explains (also for CdS small particles) the independence of the extinction coefficient per particle on the particle size, plots the temperature dependence of the first electronic transition for the differently sized particles, and reports the observation of a “reversible absorbance shift”. This shift is detected as the difference between the transition energy recorded in solution and that of a film formed from the particles on a quartz slide.

Initially, this was taken as an indication of a cluster-cluster interaction operative in the films. One year later, Nosaka et al. reported on the formation process of “ultrasmall particles” from cadmium complexes of 2-mercaptoethanol [119]. In this very thorough study, the stopped-flow technique was utilized to gain insight into the very first steps of the particle evolution, and NMR yielded information as to the presence of several different cluster species in solution amongst which the  $[\text{Cd}_{17}\text{S}_4(\text{SR})_{24}]^{2+}$  (RS = 2-mercaptoethanol) exhibits the same tetrahedral core structure as the crystallized  $[\text{Cd}_{17}\text{S}_4(\text{SR})_{26}]$  cluster of Vossmeier et al. [120]. (cf. Section 4.2.1).

The same preparative approach, i.e. the dissolution of a metal salt in water in the presence of a stabilizing thiol, yields nanocrystals of CdSe [121], CdTe [122–124], HgTe [125], and CdHgTe [126–128]. The thiols used were 1-thioglycerol, 2-mercaptoethanol, 1-mercapto-2-propanol, 1,2-dimercapto-3-propanol, thioglycolic acid, thiolactic acid, and cysteamine [129]. Subsequent to the first steps in the preparation, heating of the reaction solution may be applied in order to initiate particle growth. Thus, this preparative approach relies on the separation of nucleation and growth in a way very similar to the organometallic TOP/TOPO (tri-octyl phosphine/tri-octyl phosphine oxide) preparation outlined in more detail in the following chapter [11]. Yet another similarity between the two strategies is the post-



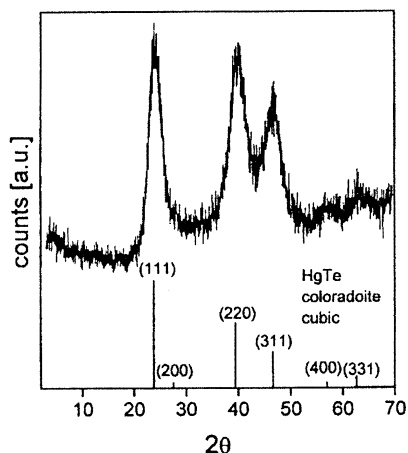


**Fig. 3-4** Powder X-ray diffractogram of HgTe nanocrystals ("thiol synthesis") with corresponding bulk values given as a line spectrum [125].

preparative treatment by applying size-selective precipitation to the crude cluster solutions [130]. The sizes of the evolving nanocrystals depend mainly on the concentration ratios of the chemicals involved and on the duration of the heat treatment.

As examples of standard characterizations, some findings of studies on nano-sized HgTe particles are shown [125]. Figure 3-4 shows the powder X-ray diffraction pattern (P-XRD) of a fraction of HgTe nanoparticles. The crystalline structure derived from the positions of the wide-angle diffraction peaks is clearly the cubic (coloradoite) HgTe phase. The wide-angle diffraction peaks are broadened because of the small particle size. The mean cluster sizes estimated from the full width at half-maximum intensity of the (111) reflection according to the Scherrer equation gives a value of about 3.5 nm. The weakly resolved small-angle X-ray diffraction peak indicates a rather broad size distribution of the HgTe nanocrystals in the aqueous colloidal solution. In order to determine the size, shape, and crystal structure of the particles, HRTEM images are taken. Figure 3-5 shows a typical overview image of the sample together with a micrograph of an individual HgTe particle with the corresponding Fast Fourier Transform (FFT). Like the X-ray diffraction data, the HRTEM images indicate a rather broad size distribution of the HgTe nanoparticles, with sizes ranging from 3 to 6 nm. The existence of the lattice planes on the HRTEM images of the particles indicates a high sample crystallinity. The images of single particles exhibit an interplanar distance of 3.73 Å, belonging to the (111) lattice plane of the coloradoite HgTe phase, which again is consistent with the X-ray diffraction data. The photophysical properties of such thiol-stabilized particles, such as photoluminescence [131] and optically detected magnetic resonance (ODMR) [132], their dispersion in polymer films in order to fabricate light-emitting devices [133–135], their possible use in telecommunication

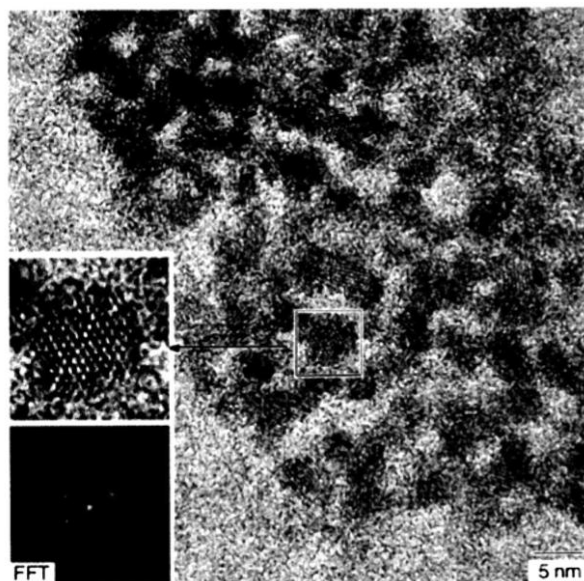


**Fig. 3-5** High-resolution transmission electron microscopy of thiol-stabilized HgTe nanocrystals; single particle in the inset with 1st fast Fourier transform [125].

devices [136], further structural properties unraveled by EXAFS (extended X-ray absorption fine structure) [137–141], and their incorporation into photonic crystals [142–144] and silica spheres [145] have been reported and have been in part already reviewed in several survey papers [146–149].

As an example of the capabilities of EXAFS spectroscopy, in Figure 3-6 the mean Cd–S distances as a function of the diameters of a series of CdS nanocrystals is depicted [139]. These data are gained from a thorough temperature-dependent study of the size dependence of various structural and dynamic properties of CdS nanoparticles ranging in size from 1.3 to 12.0 nm. The properties studied include the static and the dynamic mean-square relative displacement, the asymmetry of the interatomic Cd–S pair potential, with conclusions drawn as to the crystal structure of the nanoparticles, the Debye temperatures, and the Cd–S bond lengths. As seen from Figure 3-6, the thiol-stabilized particles (samples 1–7) show an expansion of the mean Cd–S distance, whereas the phosphate-stabilized particles (samples 8–10) are slightly contracted with respect to the CdS bulk values. The difference between the two series of nanocrystals consists in the type of interaction between the ligands and the Cd atoms at the surfaces. The thiols are covalently bound, and through this they have an influence on the structure of the particles as a whole (most probably including steric requirements of the ligands at the surfaces), whereas the phosphates are only loosely bound, which allows the particles to contract slightly like a liquid droplet which tries to minimize its surface.

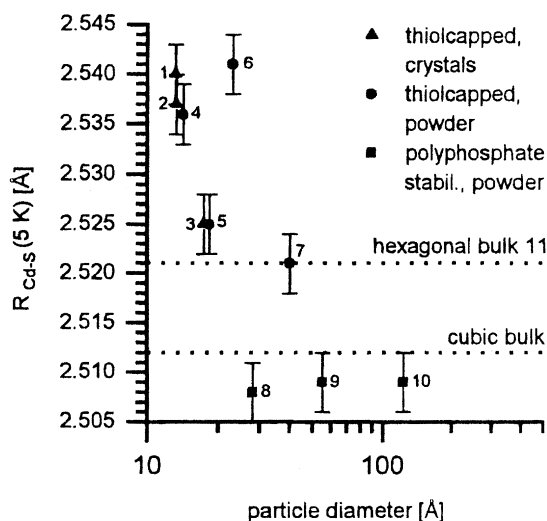


**Fig. 3-6** Mean Cd–S distances of thiol- and phosphate-stabilized CdS nanocrystals determined by EXAFS at 5 K as a function of the particle diameter [137–139].

A large percentage of the atoms of particles in the nanometer size regime are located at their surface, which makes investigations into the surface structure highly desirable. The surface structure of thiophenol-stabilized CdS nanocrystals is the subject of two articles (1997 and 1998) [150, 151]. Both research groups use NMR techniques in order to study the functionalization, structure and dynamics of the terminating ligands. Also, PbS [152] and ZnS [153, 154] nanocrystals may be prepared with thiols as capping agents, showing again the versatility of this approach. The interaction of  $\gamma$ -radiation with  $\text{Cd}^{2+}$ - and thiol-containing sols yields small CdS particles, with the dose of the radiation determining the size of the evolving particles [155]. The reverse process, i.e. the size-selective dissolution of preformed CdS nanocrystals by photoetching, is demonstrated in a recent paper by Torimoto et al. [156]. In an impressive study, Aldana, Wang and Peng give detailed insight into the photochemical degradation of thiol-stabilized CdSe particles [157]. At least three steps are involved in this process, namely photocatalytic oxidation of the thiol ligands on the surface, photooxidation of the nanocrystals, and finally precipitation of the nanocrystals. A bichromophoric nanoparticle system consisting of thioglycolic acid-stabilized CdTe particles and layer-by-layer assembled films of an anionic polyelectrolyte is presented by Westenhoff and Kotov [158]. The first investigation into the electronic structure of a nanoparticle dimer was reported by Nosaka and Tanaka [159]. The semiempirical molecular orbital calculations first investigated the influence of phenyl-capping of polynuclear cadmium complexes and subsequently yielded negligible influence on the excited state by dimer formation.

In a recent report, Gaponik et al. stress the advantages of thiol-capping of CdTe as an alternative to organometallic preparation routes [160]. This article reports on

the aqueous synthesis, the structure, some optical properties, and the processability of thiol-capped CdTe nanocrystals, with an emphasis on the procedures, leading to highly luminescent particles having room temperature quantum efficiencies of up to 40%. The advantages and disadvantages of different thiols used as capping agents of CdTe QDs which are relevant for the further design of surface properties of the nanocrystals are discussed. Summarizing the experimental data available today, thiol-capped CdTe nanocrystals synthesized in aqueous solution represent a kind of highly luminescent core-shell QD system with a naturally sulfur-capped surface (CdS shell) created by mercapto-groups covalently attached to the surface cadmium atoms. In yet another article, the stability of thiol-stabilized semiconductor particles is investigated [161]. Various analytical methods like Analytical Ultracentrifugation, UV-vis absorption spectroscopy, NMR spectroscopy, and powder X-ray diffraction are applied. Reduced particle sizes are found in solution at low particle concentrations. Most probably, the assumed covalently bound thiols desorb from the surface of the particles, leaving behind vulnerable unstabilized particles that might even undergo continuous decay over time. Additionally, breaking of the intra-ligand S–C bond is observed, resulting in a cadmium sulfide particle synthesis introducing sulfur only by the ligands, without any additional sulfide ions.

Finally, it may be noted that the nanocrystals prepared in aqueous solutions may be transferred into different nonpolar organic solvents [162]. This is accomplished by a partial ligand exchange, with acetone playing an important role in the efficient phase transfer. Since the nanocrystals retain their luminescence properties after being transferred, this procedure provides a new source of easily processable luminescent materials for possible applications.

### 3.1.1.3 The “TOP/TOPO” Synthesis

The term “TOP/TOPO” synthesis refers to an organometallic approach to synthesizing CdE (E = S, Se, Te) nanocrystals first introduced in 1993 by Murray et al. [11]. The preparative route is based on the pyrolysis of organometallic reagents (like dimethylcadmium and bis(trimethylsilyl)selenium) by injection into hot coordinating solvents (like tri-*n*-octylphosphine oxide (TOPO) and tri-*n*-octylphosphine (TOP)). This provides temporally discrete nucleation and permits the controlled growth of nanocrystals. Subsequent size-selective precipitation isolates samples with very narrow size distributions. The widespread success of this preparation is largely due to its versatility, its reproducibility and, last but not least, the high quality of the particles in terms of crystallinity and uniformity. The versatility is seen, e.g., in the successful transformation of the preparation principles beyond the II–VI materials to the classes of the III–V and IV–VI semiconductor nanocrystals [163–172]. It is probably not an exaggeration to identify the first reports on the organometallic synthesis also as the trigger for elaborate theoretical work on size-dependent properties of semiconductor clusters like, e.g., the electronic structure (see, e.g., [173–183]). The years immediately after the “invention” of the TOP/TOPO preparation are characterized by investigations into the optical properties of CdSe particles of a wide range of sizes and the surface properties of the evolving

nanocrystals [184–195]. Most of this beautiful work has been presented in a very readable review by the founders of the field [196], including the outstanding work on Förster energy transfer taking place in close packed assemblies of CdSe quantum dot solids [197, 198]. The photostability and the high luminescence quantum yield made the particles ideal candidates for single-particle emission studies [199–212].

Also, some of the early work on “high-tech” applications of semiconductor nanoparticles is based on the above-mentioned preparative route, namely the construction of a light-emitting diode made from CdSe nanocrystals and a semiconducting polymer [213–215], and even a single electron transistor is made by the use of CdSe nanocrystals [216].

The charge-tunable optical properties of CdSe particles derived by the TOP/TOPO method are studied [217], and these are used as precursors for the generation of thin films of CdTe [218]. Other effects like the photoionization in CdTe particles embedded in TOPO are investigated, elucidating some of the photo-physical observations made in single-particle studies [219]. *N*-type colloidal semiconductor particles of CdSe are made via an electron transfer process [220], and the synthesis of ZnSe nanocrystals [221] and their doping with manganese is reported [222]. The fate of the photogenerated charge carriers is the topic of several studies of particles derived by the organometallic procedure (see, e.g., the review [223] and references therein and [224–231, 100]), including the size-dependent photoconductivity of CdSe nanoparticles [232]. Spin spectroscopy of “dark excitons” (see also the contribution of U. Banin in this book) in CdSe particles of various sizes is performed as a function of temperature and magnetic field strength [233]. The influence on the sizes, size distributions, and luminescence quantum yields of various amines on addition to the reaction mixtures is studied by Talapin and coworkers [234–236]. Alternative routes toward high quality CdSe nanocrystals are discovered by Qu, Peng and Peng by varying the solvents/ligands and the precursors like CdO and Cd(Ac)<sub>2</sub> instead of Cd(CH<sub>3</sub>)<sub>2</sub> [92, 237].

Organometallically synthesized CdSe (and InAs) nanocrystals act as experimental examples in a very interesting study concerning the kinetics of nanocrystal growth [238]. It is demonstrated that diffusion-limited growth can lead to narrowing of size distributions with time and that, under certain conditions, the kinetics of nanocrystal growth may also be influenced by the variation of the surface energy with size. (The matter of kinetic-dependent crystal growth is also considered for size-tunable CdS particles prepared by other routes [239] and for nanometer sized crystalline particles in glassy media [240].) In a theoretical study, the ideas of Alivisatos [238] are reconsidered, giving even more detailed insight into the evolution of ensembles of nanoparticles in colloidal solutions [241]. An outline is given of how the growth of nanoparticles in the diffusion-controlled regime may result in better final size distributions than those found for nanoparticles grown in the reaction-controlled regime. Additionally, possible ways of controlling the particle size distributions in colloidal solutions are discussed. These include, for example, the increase in the surface tension at the solvent-nanoparticle interface and the decrease in the diffusion or mass transfer coefficient. A related experimental study

is published by Qu and Peng in 2002 [242] in which the photoluminescence quantum yield (PL QY) of organometallically prepared CdSe nanocrystals is studied *during* their growth. A “bright point” is observed which denotes the fact that under a given set of initial conditions of the colloidal solution the PL QY increases to a maximum value before decreasing again. Very similar results are reported in an even more thorough investigation by Talapin et al. [243]. Results concerning the dynamic distribution of growth rates within ensembles of CdSe and InAs nanoparticles prepared organometallically and CdTe prepared in aqueous solutions are presented indicating that the observed phenomenon of fraction-dependent PL QY is of more general character. Relating the results to the above-mentioned theoretical work, it is proposed that the nanocrystal fractions with the best surface quality (in terms of a minimum of defects) correspond to particles with the smallest net growth rate within the ensemble because annealing of surface defects is most effective at this “zero growth rate”. In a further study stretching beyond the topic of this chapter, X. Peng et al. report even on shape control over CdSe nanoobjects by proper adjustment of the initial experimental conditions [244] (see also [245, 246]).

In two recent studies, the absorption cross section (or extinction coefficient) of CdSe nanocrystals has been under investigation [247, 248]. Striolo et al. [247] report (among other results) that the oscillator strength of the first exciton transition per CdSe unit is more or less independent of particle size, in accord with Schmelz et al. [249]. In contrast, Bawendi and coworkers clearly show that as the quantum dot radius decreases, the oscillator strength per CdSe unit of the lowest-energy transition increases (as reported by others for CdS [118] and CdTe [65] prepared differently), whereas the spectra converge for higher energies. Thus, this issue remains to be elucidated further.

#### 3.1.1.4 Core-Shell Nanocrystals

Coating a given ensemble of nanoparticles by another material yields “core-shell” nanocrystals. In these structures, the cores may be any kind of colloidal particles, i.e. metals, insulators, and all classes of semiconductors. Likewise, the shells may consist of any sort of materials including organic ones. This survey concentrates on semiconductor cores and inorganic shells mainly of semiconductor materials.

In the majority of cases, the electronic structure of the core shell particles is as follows. The core material having a certain bandgap is capped by a material with a larger bandgap, the conduction band energy of the capping material being higher (more negative in an electrochemical sense) than that of the core material and the valence band energy of the capping material being lower (more positive on the electrochemical energy scale) than that of the core material. This energetic situation is frequently called a type-I structure. The main consequence of this capping is that the exciton photogenerated in the core is prevented from spreading over the entire particle, and by this it is forced to recombine while spatially confined to the core. In most cases this is accompanied by enhanced luminescence.

Early reports on the formation of coated nanoparticles include the aqueous polyphosphate-stabilized CdS/Cd(OH)<sub>2</sub> system [27]. The preparative procedure is to add to a given sol of CdS particles a large excess of Cd ions, while increasing the

pH to achieve strongly basic conditions. The obtained increase in luminescence quantum yield in comparison with the uncoated CdS particles is explained by saturation of free valences at the particle surface, and this is taken as an indication of the formation of the proposed structure. The report is speculative in a sense that a structural characterization is not performed. This is not very surprising, since obtaining clear-cut evidence for shell formation of a few monolayers of material on nanoobjects is a characterizational challenge. This challenge has been accepted more or less since then in a wealth of reports on systems like Ag<sub>2</sub>S on CdS [250], ZnS on CdS [29], Ag<sub>2</sub>S on AgI [251], CdSe on ZnS [252], CdSe on ZnSe [253], HgS on CdS [254], PbS on CdS [255], CdS on HgS [256], ZnSe on CdSe [257], ZnS on CdSe [258–261], CdS on CdSe [262] and vice versa [263]. Many of these endeavors have already been reviewed [32, 62, 61, 103, 102, 147, 264–267] and will therefore not be mentioned in detail. A very fine example of the most careful characterization of the overgrowth of CdSe nanocrystals with ZnS is reported in the paper of Dabbousi et al. (1997) [259]. For the shell growth on the preformed CdSe nanocrystals, diethylzinc and hexamethyldisilathiane are used as Zn and S precursors. Dissolution of equimolar amounts of the precursors in suitable solvents is followed by dropwise addition to vigorously stirred CdSe colloidal solutions held at temperatures between 140 and 220 °C, depending on the core sizes. Besides optical spectroscopy, the authors managed to perform wavelength dispersive X-ray spectroscopy, X-ray photoelectron spectroscopy, small- and wide-angle X-ray scattering, and (high-resolution) electron microscopy. As an example of the thorough characterization, Figure 3-7 is taken from this work. It demonstrates the X-ray scattering in the small-angle region of bare 4.2 nm CdSe dots (curve *a*) and the increase of the dot diameters with the increase in the ZnS shell thickness from 0.65 monolayers (curve *b*) to 5.3 monolayers (curve *c*). The gradual shift of the ringing pattern to smaller angles indicates that ZnS is in fact growing onto the CdSe dots instead of nucleating separate ZnS nanocrystals. This is also deduced from the size histograms gained from electron microscopy of the same series of particles. In Figure 3-8, the uniform growth of the particles is clearly demonstrated, together with a broadening of the size distribution. The aspect ratio histograms (right hand side of Figure 3-8) of the slightly elongated particles are monitored as well and are used to generate accurate fits to the small angle X-ray data shown above. In an effort to relate the structural to the optical properties, the growth of the ZnS shell on the CdSe cores is described as locally epitaxial. The ZnS shell tends to create defects at coverages of more than 1.3 monolayers, accompanied by a decrease in luminescence quantum yield.

Based on this work, progress has been made with similar particles, e.g., in understanding the photo- and electrodarkening effects [260, 268] and in the assembly of luminescing semiconductor nanocrystals with biological objects in order to create fluorescent probes in sensing, imaging or other diagnostic applications [269–271]. Just to name a few, in other reports using the described synthesis of CdSe/ZnS core-shell particles, high-resolution spectral hole burning is performed [272] or effects like photooxidation and photobleaching are investigated on the single particle level [273]. Likewise, the emission properties of single ZnS or CdS

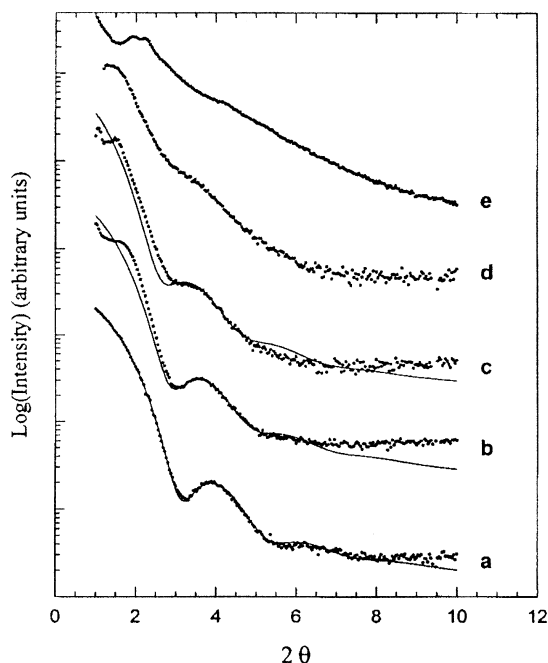


**Fig. 3-7** Small-angle X-ray scattering data from bare 4.2 nm CdSe particles (a) overgrown by 0.65 (b) to 5.3 (e) monolayers of ZnS [259].

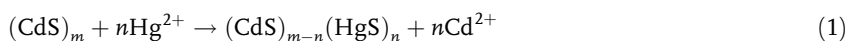
overcoated CdSe particles are investigated by several groups [200, 202–204, 206, 207, 209–211] (summaries in e.g. [212, 147]).

Other reports include structures in which either the core or the shell is a II–VI semiconductor material such as CdS capped by sulfur or polysulfide [274, 275], InAs capped by CdSe [276], ZnSe and ZnS [277, 278], or InP capped by ZnCdSe<sub>2</sub> [279] or ZnS (see, e.g., [280]).

New synthetic approaches include the formation of core-shell type particles from CdTe and CdS [281], ZnSe on CdSe [282, 283], and CdS on HgTe [284]. In the latter report, a synthetic route to strongly IR-emitting nanocrystals is outlined whereby in this case capping enhances the robustness of the particles rather than the (already high) luminescence quantum yield.

#### 3.1.1.5 Quantum Dot Quantum Wells

As an extension of the work of precipitating HgS on polyphosphate-stabilized CdS and CdS on HgS [254, 256], a wet chemical synthesis has been developed which yields a nanoheterostructure consisting of three domains, viz., the system CdS/HgS/CdS. The basic preparative idea involves the substitution reaction





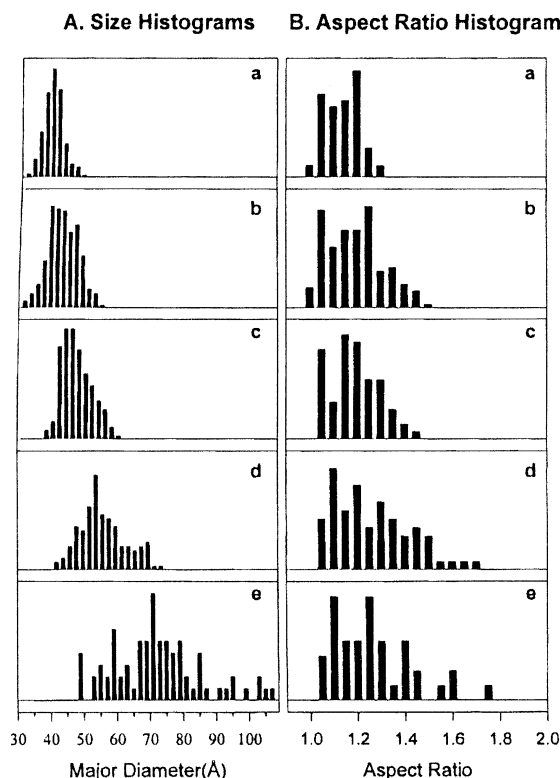


**Fig. 3-8** Size histograms of a series of CdSe nanocrystals overgrown with 0.65 (b) to 5.3 (e) monolayers of ZnS (A) and corresponding aspect ratios (B) [259].

taking place at the surface of the preformed CdS particles. This reaction proceeds because of the at least 22 orders of magnitude smaller solubility product of HgS compared to that of CdS. The art consists in managing the reaction to take place only at the surface, which is largely achieved by strictly controlling the experimental conditions regarding pH, concentrations, duration of the addition, stirring, etc. After a monolayer of HgS is built on the CdS cores, this structure is capped by more CdS via the addition of  $\text{H}_2\text{S}$  and further Cd ions. The first reports deal with structures having a CdS core of about 5 nm surrounded by a shell of 1–3 monolayers of HgS, which again is coated by up to five monolayers of CdS [285, 286].  $\beta$ -HgS with a bulk band gap of 0.5 eV forms a quantum well inside the cubic CdS (bulk band gap 2.5 eV), which forced the authors to describe these new structures as “quantum dot quantum wells” or briefly QDQWs. Probably, an even better term would be “quantum well in a quantum dot”. Colloquially, the term “nano-onions” has been established meanwhile. The first four papers on these particles were published in 1993 and 1994 and describe the synthesis, the characterization [285, 286], transient bleaching after laser excitation [287], and a widely applied theory

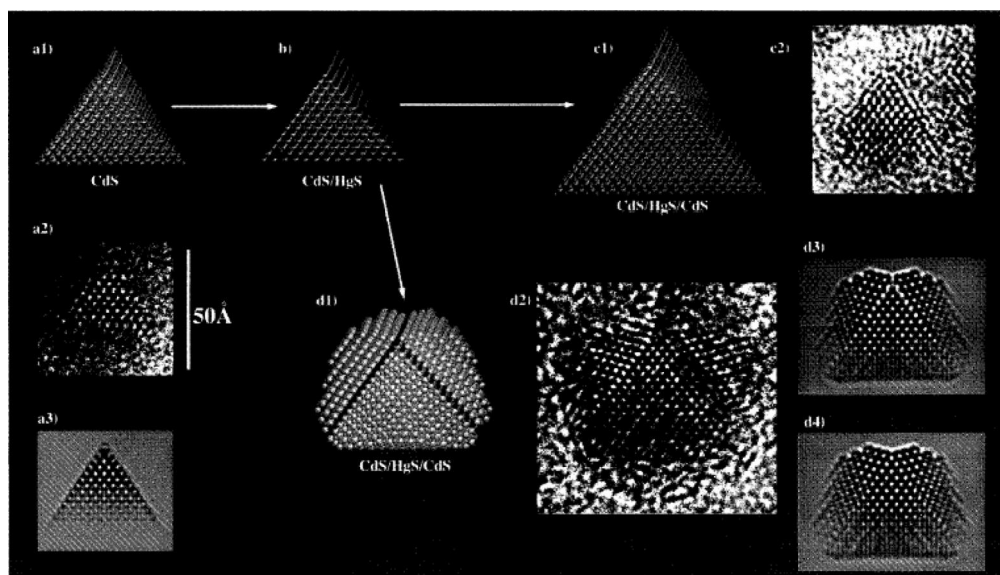


**Fig. 3-9** Models (a1, b, c1, and d1), HRTEM micrographs (a2, c2, d2) and simulations (a3, d3, and d4) of CdS and CdS/HgS nano-heterostructures in the course of preparation.

The CdS surface is replaced by HgS (a1 to b). Covering this structure with CdS leads to epitaxial growth (b to c1) or to twinned epitaxial growth (b to d1) [289].

based on the “effective mass approximation” [288]. As with the other findings, also the bleaching experiments on the nanoheterostructures, make them to seem to be homogeneous electronic systems, and the results are not explainable by the superposition of the properties of the segments. Together, these efforts are summarized in review articles [103, 289, 290]. Reference [289] also contains the results of Mews and Alivisatos [291, 292], including an impressive HRTEM investigation (see also [105]) with accompanying simulations presenting information about the shape and the crystallinity of the particles (cf. Figure 3-9). Hole burning and fluorescence line narrowing experiments provide evidence on the degree of charge carrier localization in the HgS layer. Theoretical papers [293, 294] (likewise described in [289]) refer to these experiments and deduce that a “dark exciton” represents the lowest excitation state in these nanoheterostructures, too. A recent tight-binding study by Perez-Conde and Bhattacharjee also detects bright and dark states together with the strong localization of electron and hole states within the HgS well [295]. The tight-binding approach is also found by Bryant and Jaskolski to provide a good description for nanosystems with monolayer variations in composition [296]. It is pointed out that trap states cannot be described solely as states in the quantum well. Instead, depending on the shell thickness and band offset, trap states can have a large interface character.

Two articles by El-Sayed and coworkers [297, 298] published in 1996 and 1998 prove experimentally that the electronic structure is more complicated and can be

observed by advanced spectroscopic techniques. The authors carry out experiments analogous to the transient bleaching at CdS and CdS/HgS/CdS particles, but with femtosecond time resolution. By this means it is possible to observe the kinetics of the charge carrier capture in traps and in the HgS quantum well, respectively. Obviously, the spectral diffusion of the bleaching (of the “optical hole”, as it is called by the authors) takes place over an intermediate state to which the authors assign an energetically relatively high “dark exciton” state predicted by theory [294]. In this state, the electron is situated in the HgS well, whereas the hole is in the CdS cladding layer of the particle and the “well” has a rather barrier-like effect on the hole. In a subsequent study, similar experiments were carried out on particles with a two-monolayer-thick well of HgS, giving good agreement with theoretical predictions regarding the exciton energies [299]. The dynamics of the localization of the exciton in CdS/HgS QDQWs is also the topic of an investigation published by Yeh et al. [300]. By comparing the results from nanosecond hole-burning experiments with those having femtosecond time resolution, the authors conclude that the primary optical interaction excites electrons from a delocalized QDQW ground state and not from a localized HgS well state. Only after longer times, of the order of 400 fs, will the exciton finally be localized in the HgS well. ODMR (optically detected magnetic resonance) is applied to QDQW samples with varying layer thickness of HgS as well as of the outer CdS by Lifshitz and coworkers [301]. Because of its sufficient longevity, it is possible to study by this technique especially the trap luminescence, which, compared to the near band edge fluorescence, occurs red-shifted by about 400–700 meV. The change in luminescence which is induced by magnetic resonance in the excited state is detected. From measurements carried out in dependence on the intensity of the luminescence excitation and on the frequency of the coupled microwaves, with subsequent simulations of the spectra, it may be concluded that there are at least two different recombination channels via traps in the particles. These traps are localized in the CdS–HgS interfaces and could possibly be twin grain boundaries and edge dislocations. In a photoluminescence experiment, an enhancement of the band edge emission was observed upon excitation with two differently colored beams instead of one in an ordinary experiment [302]. This result is explained as being the consequence of a partial quenching of the defect emission, suggesting a mutual interaction of the two luminescence events.

A strong reduction in the spectral and intensity fluctuations is observed when QDQWs of CdS and HgS are compared with pure CdS particles in single-particle emission studies [303]. This is, again, explained by charge carrier localization in the HgS region of the nanocrystals.

A QDQW with a large lattice mismatch, namely ZnS/CdS/ZnS, was prepared by the El-Sayed group [304]. Established techniques were combined to synthesize small seeds of CdS and ZnS, and afterwards nanoepitaxy was applied to grow ZnS/CdS nanoheterostructures. The evolving absorption spectra of the particles are presented together with a theoretical treatment.

Very recently, the same group has published first results on a QDQW system that contains two wells of HgS separated by a wall of CdS. The two-well system is

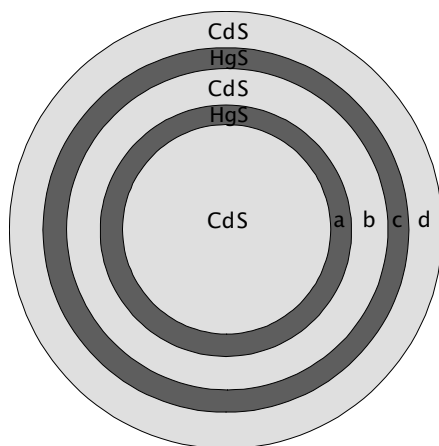


**Fig. 3-10** Schematic drawing of the double-well nano-heterostructures described in the text. The wells (a and c) consist of the small bandgap material  $\beta$ -HgS. The core, the barrier between the wells (b) and the cladding layer (d) are made from CdS.

characterized by absorption and emission spectroscopy, clearly revealing the formation of a two-well system rather than a single double-layer structure [305].

In an article in the same year, Dorfs outlined efforts aimed in the same direction, namely the preparation and characterization of a series of QDQWs containing two wells [306]. The preparative route firstly follows the established procedures which yield single-well particles consisting of a CdS core of diameter 4.7 nm surrounded by one or two monolayers of HgS capped by two, three or four layers of CdS. Following the same concept as that for the single-well particles, i.e. repetition of the replacement of the surface CdS by HgS, addition of a second monolayer of HgS and capping of the whole structure by three monolayers of CdS yields a whole new family of particles. As a nomenclature, the authors suggest for these nanoheterostructures the following (cf. Figure 3-10): CdS/HgS is represented by “*abcd*”, where, starting with the CdS core, “*a*” is the number of HgS monolayers, “*b*” is the number of monolayers of CdS as the barrier between the wells, “*c*” is the number of monolayers of the second HgS well, and “*d*” is the number of cladding layers.

In Figure 3-11 are summarized the absorption spectra of a total of eight different double-well QDQWs prepared according to the above outlined procedures. All eight samples have in common the core size 4.7 nm and the outer cladding of three monolayers of CdS. They differ in the three inner compartments: the inner well consists of either one or two monolayers of HgS, the barrier between the wells are either two or three monolayers wide, and the outer well again consists of one or two monolayers of HgS. Thus, the structures CdS/HgS 1213, 1223, 1313, 1323, 2213, 2223, 2313, and 2323 are generated. The most remarkable findings gained from the absorption spectra and the accompanying TEM study are as follows:

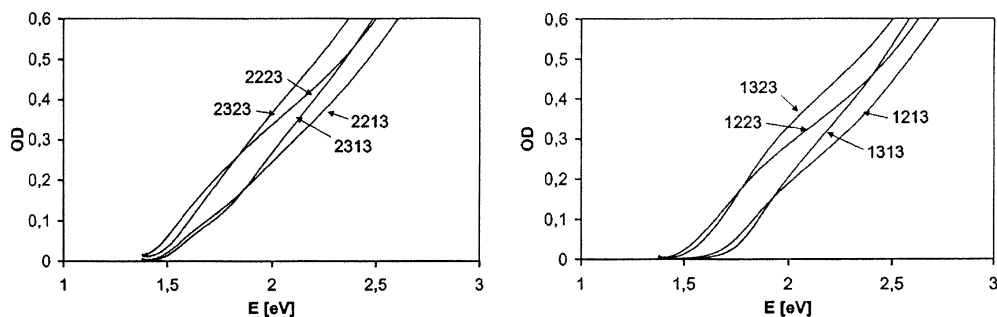


**Fig. 3-11** Absorption spectra of eight different double-well nanoheterostructures. In CdS nanocrystals two wells of HgS are embedded. Well thickness and well separations vary. For nomenclature see text [306].

1. Judging from the particle size histograms, there is no indication of separately formed CdS or HgS. Exclusively homogeneous particle growth is observed.
2. The position of the first electronic transition is further into the red spectral region the more HgS is present in the structures.
3. Comparing the four pairs of samples having the same well composition, the transition is located further into the red when the wells are separated by only two monolayers of CdS instead of three, which is explained by an enhanced electronic coupling on decreasing the well separation.
4. The onset of absorption of the particles exhibiting an asymmetric inner potential (e.g. CdS/HgS 2313 and 1323) takes place at the same energy.
5. The high-energy absorption depends on the total amount of material present in solution.

Some of these findings have already been treated theoretically, giving insight into very interesting electronic properties and charge separation features [307].

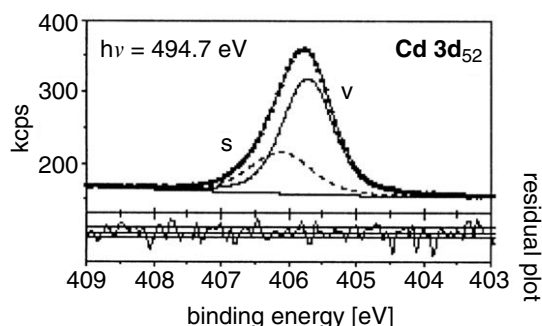


**Fig. 3-12** High-resolution XPS spectrum of the Cd 3d<sub>5/2</sub> core level in the CdS/HgS/CdS/HgS/CdS double-quantum-well nanocrystals at a surface-sensitive energy [308].

In an investigation by photoelectron spectroscopy (XPS) with tunable synchrotron radiation, a member of this family of particles was compared to single-well CdS/HgS/CdS QDQWs [308]. As is to be expected, the photoemission spectra of the CdS/HgS/CdS/HgS/CdS double-quantum-well nanocrystals look quite similar to those of the single-well species. As seen in Figure 3-12, in addition to a bulk species, high-resolution spectra also reveal a surface environment for Cd, while different S species could not be resolved. To some extent the XPS experiments allow the characterization and verification of the onion-like structure of the quantum dot quantum well nanocrystals, which is shown also by an extension of a previously developed model for core-shell nanocrystals [309].

## References

- 1 A. HENGLEIN, *Ber. Bunsenges. Phys. Chem.* **1982**, 86, 301.
- 2 K. KALYANASUNDARAM, E. BORGARELLO, D. DUONGHONG, M. GRÄTZEL, *Angew. Chem., Int. Ed. Engl.* **1981**, 20, 987.
- 3 J. R. DARWENT, G. PORTER, *J. Chem. Soc., Chem. Commun.* **1981**, 145.
- 4 R. ROSSETTI, L. BRUS, *J. Phys. Chem.* **1982**, 86, 4470.
- 5 D. DUONGHONG, J. RAMSDEN, M. GRÄTZEL, *J. Am. Chem. Soc.* **1982**, 104, 2977.
- 6 J. KUCZYNSKI, J. K. THOMAS, *Chem. Phys. Lett.* **1982**, 88, 445.
- 7 M. A. FOX, B. LINDIG, C. C. CHEM, *J. Am. Chem. Soc.* **1982**, 104, 5828.
- 8 L. E. BRUS, *J. Chem. Phys.* **1983**, 79, 5566.
- 9 A. I. EKIMOV, A. A. ONUSHCHENKO, *Sov. Phys.-Semiconductors* **1982**, 16, 775.
- 10 A. L. EFROS, A. L. EFROS, *Sov. Phys.-Semiconductors* **1982**, 16, 772.
- 11 C. B. MURRAY, D. J. NORRIS, M. G. BAWENDI, *J. Am. Chem. Soc.* **1993**, 115, 8706.
- 12 R. ROSSETTI, S. NAKAHARA, L. E. BRUS, *J. Chem. Phys.* **1983**, 79, 1086.
- 13 M. GUTIERREZ, A. HENGLEIN, *Ber. Bunsenges. Phys. Chem.* **1983**, 87, 474.
- 14 A. HENGLEIN, M. GUTIERREZ, *Ber. Bunsenges. Phys. Chem.* **1983**, 87, 852.
- 15 A. HENGLEIN, M. GUTIERREZ, C. FISCHER, *Ber. Bunsenges. Phys. Chem.* **1984**, 88, 170.
- 16 H. WELLER, U. KOCH, M. GUTIERREZ, A. HENGLEIN, *Ber. Bunsenges. Phys. Chem.* **1984**, 88, 649.
- 17 A. FOJTIK, H. WELLER, U. KOCH, A. HENGLEIN, *Ber. Bunsenges. Phys. Chem.* **1984**, 88, 969.
- 18 J. J. RAMSDEN, M. GRÄTZEL, *J. Chem. Soc., Farad. Trans. 1* **1984**, 80, 919.
- 19 A. J. NOZIK, F. WILLIAMS, M. T. NENADOVIC, T. RAJH, O. I. MICIC, *J. Phys. Chem.* **1985**, 89, 397.
- 20 L. E. BRUS, *J. Chem. Phys.* **1984**, 80, 4403.
- 21 L. E. BRUS, *J. Phys. Chem.* **1986**, 90, 2555.
- 22 C.-H. FISCHER, H. WELLER, A. FOJTIK, C. LUME-PEREIRA, E. JANATA, A. HENGLEIN, *Ber. Bunsenges. Phys. Chem.* **1986**, 90, 46.
- 23 T. DANNHAUSER, M. O'NEIL, K. JOHANSSON, D. WHITTEN, G. MCLENDON, *J. Phys. Chem.* **1986**, 90, 6074.
- 24 Y.-M. TRICOT, J. H. FENDLER, *J. Phys. Chem.* **1986**, 90, 3369.
- 25 J. M. NEMELJOKVIC, M. T. NENADOVIC, O. I. MICIC, A. J. NOZIK, *J. Phys. Chem.* **1986**, 90, 12.
- 26 A. HENGLEIN, A. KUMAR, E. JANATA, H. WELLER, *Chem. Phys. Letters* **1986**, 132, 133.
- 27 L. SPANHEL, M. HAASE, H. WELLER, A. HENGLEIN, *J. Am. Chem. Soc.* **1987**, 109, 5649.
- 28 M. L. STEIGERWALD, A. P. ALIVISATOS, J. M. GIBSON, T. D. HARRIS, R. KORTAN, A. J. MULLER, A. M. THAYER, T. M. DUNCAN, D. C. DOUGLASS, L. E. BRUS, *J. Am. Chem. Soc.* **1988**, 110, 3046.
- 29 H.-C. YOUN, S. BARAL, J. H. FENDLER, *J. Phys. Chem.* **1988**, 92, 6320.

- 30 E. S. SMOTKIN, C. LEE, A. J. BARD, A. CAMPION, M. A. FOX, T. E. MALLOUK, S. E. WEBBER, J. M. WHITE, *Chem. Phys. Lett.* **1988**, 152, 265.
- 31 A. HENGLEIN, *Top. Curr. Chem.* **1988**, 143, 113.
- 32 A. HENGLEIN, *Chem. Rev.* **1989**, 89, 1861.
- 33 M. L. STEIGERWALD, L. E. BRUS, *Acc. Chem. Res.* **1990**, 23, 183.
- 34 D. HAYES, O. I. MICIC, M. T. NENADOVIC, V. SWAYAMBUNATHAN, D. MEISEL, *J. Phys. Chem.* **1989**, 93, 4603.
- 35 U. RESCH, H. WELLER, A. HENGLEIN, *Langmuir* **1989**, 5, 1015.
- 36 J.-M. ZEN, F.-R. F. FAN, G. CHEN, A. J. BARD, *Langmuir* **1989**, 5, 1355.
- 37 N. HERRON, Y. WANG, H. ECKERT, *J. Am. Chem. Soc.* **1990**, 112, 1322.
- 38 L. SPANHEL, M. A. ANDERSON, *J. Am. Chem. Soc.* **1990**, 112, 2278.
- 39 S. YANAGIDA, M. YOSHIYA, T. SHIRAGAMI, C. J. PAC, H. MORI, H. FUJITA, *J. Phys. Chem.* **1990**, 94, 3104.
- 40 A. EYCHMÜLLER, L. KATSIKAS, H. WELLER, *Langmuir* **1990**, 6, 1605.
- 41 E. S. SMOTKIN, R. M. BROWN, L. K. RABENBERG, K. SALOMON, A. J. BARD, A. CAMPION, M. A. FOX, T. E. MALLOUK, S. E. WEBBER, J. M. WHITE, *J. Phys. Chem.* **1990**, 94, 7543.
- 42 N. CHESTNOY, T. D. HARRIS, R. HULL, L. E. BRUS, *J. Phys. Chem.* **1986**, 90, 3393.
- 43 Y. WANG, N. HERRON, *J. Phys. Chem.* **1987**, 91, 257.
- 44 Y. WANG, N. HERRON, *J. Phys. Chem.* **1988**, 92, 4988.
- 45 M. O'NEIL, J. MAROHN, G. MCLENDON, *J. Phys. Chem.* **1990**, 94, 4356.
- 46 A. EYCHMÜLLER, A. HÄSSELBARTH, L. KATSIKAS, H. WELLER, *Ber. Bunsenges. Phys. Chem.* **1991**, 95, 79.
- 47 R. R. CHANDLER, J. L. COFFER, *J. Phys. Chem.* **1991**, 95, 4.
- 48 M. HIRAMOTO, K. HASHIMOTO, T. SAKATA, *Chem. Phys. Lett.* **1991**, 139.
- 49 T. UCHIHARA, T. NAKAMURA, A. KINJO, *J. Photochem. Photobiol. A: Chem.* **1992**, 66, 379.
- 50 U. RESCH, A. EYCHMÜLLER, M. HAASE, H. WELLER, *Langmuir* **1992**, 8, 2215.
- 51 A. KUMAR, S. KUMAR, *J. Photochem. Photobiol. A: Chem.* **1992**, 69, 91.
- 52 S. R. BIGHAM, J. COFFER, *J. Phys. Chem.* **1992**, 96, 10581.
- 53 A. J. HOFFMAN, G. MILLS, H. YEE, M. R. HOFFMANN, *J. Phys. Chem.* **1992**, 96, 5546.
- 54 Y. WANG, M. HARMER, N. HERRON, *Isr. J. Chem.* **1993**, 33, 31.
- 55 J. H. FENDLER, *Isr. J. Chem.* **1993**, 33, 41.
- 56 P. V. KAMAT, M. D. VANWIJNGAARDEN, S. HOTCHANDANI, *Isr. J. Chem.* **1993**, 33, 47.
- 57 C. LUANGDILOK, D. MEISEL, *Isr. J. Chem.* **1993**, 33, 53.
- 58 O. I. MICIC, T. RAJH, J. M. NEDELJKOVIC, M. I. COMOR, *Isr. J. Chem.* **1993**, 33, 59.
- 59 K. JOHANSSON, R. COWDERY, M. ONEIL, J. REHM, G. MCLENDON, A. MARCHETTI, D. G. WHITTEN, *Isr. J. Chem.* **1993**, 33, 67.
- 60 H. WELLER, A. EYCHMÜLLER, R. VOGEL, L. KATSIKAS, A. HÄSSELBARTH, M. GIERSIG, *Isr. J. Chem.* **1993**, 33, 107.
- 61 H. WELLER, *Angew. Chem. Int. Ed. Engl.* **1993**, 32, 41.
- 62 H. WELLER, *Adv. Mater.* **1993**, 5, 88.
- 63 M. MÜLLENBORN, R. F. JARVIS, B. G. YACOBI, R. B. KANER, C. C. COLEMAN, N. M. HAEGEL, *Appl. Phys. A* **1993**, 56, 317.
- 64 R. R. CHANDLER, J. L. COFFER, *J. Phys. Chem.* **1993**, 97, 9767.
- 65 T. RAJH, O. I. MICIC, A. J. NOZIK, *J. Phys. Chem.* **1993**, 97, 11999.
- 66 M. V. RAMA KRISHNA, R. A. FRIESNER, *J. Chem. Phys.* **1991**, 95, 8309.
- 67 P. E. LIPPENS, M. LANNOO, *Phys. Rev. B* **1989**, 39, 10935.
- 68 P. E. LIPPENS, M. LANNOO, *Phys. Rev. B* **1990**, 41, 6079.
- 69 S. SCHMITT-RINK, D. A. B. MILLER, D. S. CHEMLA, *Phys. Rev. B* **1987**, 35, 8113.
- 70 E. HANAMURA, *Phys. Rev. B* **1988**, 37, 1273.
- 71 Y. KAYANUMA, *Phys. Rev. B* **1988**, 38, 9797.
- 72 H. MATSUMOTO, T. SAKATA, H. MORI, H. YONEYAMA, *J. Phys. Chem.* **1996**, 100, 13781.
- 73 T. TRINDADE, P. O'BRIAN, *Adv. Mater.* **1996**, 8, 161.

- 74 B. A. KORGEL, H. G. MONBOUQUETTE, *J. Phys. Chem.* **1996**, *100*, 346.
- 75 I. DEKANY, L. NAGY, L. TURI, Z. KIRALY, N. A. KOTOV, J. H. FENDLER, *Langmuir* **1996**, *12*, 3709.
- 76 D. E. FOGG, L. H. RADZIŁOWSKI, R. BLANSKI, R. R. SCHROCK, E. L. THOMAS, *Macromolecules* **1997**, *30*, 417.
- 77 V. LADIZHANSKY, G. HODES, S. VEGA, *J. Phys. Chem.* **1998**, *102*, 8505.
- 78 M. A. CORREA-DUARTE, M. GIERSIG, L. M. LIZ-MARZAN, *Chem. Phys. Lett.* **1998**, *286*, 497.
- 79 D. G. KURTH, P. LEHMANN, C. LESSER, *Chem. Commun.* 949.
- 80 B. I. LEMON, R. M. CROOKS, *J. Am. Chem. Soc.* **2000**, *122*, 12886.
- 81 S.-H. YU, J. YANG, Z.-H. HAN, Y. ZHOU, R.-Y. YANG, Y.-T. QIAN, Y.-H. ZHANG, *J. Mater. Chem.* **1999**, *9*, 1283.
- 82 J. R. LAKOWICZ, I. GRYCZINSKI, Z. GRYCZINSKI, C. J. MURPHY, *J. Phys. Chem. B* **1999**, *103*, 7613.
- 83 F. WU, J. Z. ZHANG, R. KHO, R. K. MEHRA, *Chem. Phys. Lett.* **2000**, 237.
- 84 B. ALPERSON, I. RUBINSTEIN, G. HODES, D. PORATH, O. MILLO, *Appl. Phys. Lett.* **1999**, 1751.
- 85 Y. LI, Y. DING, H. LIAO, Y. QIAN, *J. Phys. Chem. Sol.* **1999**, *60*, 965.
- 86 A. A. PATEL, F. WU, J. Z. ZHANG, C. L. TORRES-MARTINEZ, R. K. MEHRA, Y. YANG, S. H. RISBUD, *J. Phys. Chem.* **2000**, *104*, 11598.
- 87 N. HEBALKAR, A. LOBO, S. R. SAINKAR, S. D. PRADHAN, W. VOGEL, J. URBAN, S. K. KULKARNI, *J. Mater. Sci.* **2001**, *36*, 4377.
- 88 D. INGERT, N. FELTIN, L. LEVRY, P. GOUZERH, M. P. PILENI, *Adv. Mater.* **1999**, *11*, 220.
- 89 Y. XIE, J. HUANG, B. LI, Y. LIU, Y. QIAN, *Adv. Mater.* **2000**, *12*, 1523.
- 90 L. KONOPNY, M. BERFELD, R. POPOVITZ-BIRO, I. WEISSBUCH, L. LEISEROWITZ, M. LAHAV, *Adv. Mater.* **2001**, 580.
- 91 Z. ZHANG, S. DAI, X. FAN, D. A. BLUM, S. J. PENNYCOOK, Y. WEI, *J. Phys. Chem. B* **2001**, *105*, 6755.
- 92 Z. A. PENG, X. PENG, *J. Am. Chem. Soc.* **2001**, *123*, 183.
- 93 R. ELBAUM, S. VEGA, G. HODES, *Chem. Mater.* **2001**, *13*, 2272.
- 94 H. ZHAO, E. P. DOUGLAS, B. S. HARRISON, K. S. SCHANZE, *Langmuir* **2001**, *17*, 8428.
- 95 H. ZHAO, E. P. DOUGLAS, *Chem. Mater.* **2002**, *14*, 1418.
- 96 N. PINNA, K. WEISS, H. SACK-KONGEHL, W. VOGEL, J. URBAN, M. P. PILENI, *Langmuir* **2001**, *17*, 7982.
- 97 S. C. FARMER, T. E. PATTEN, *Chem. Mater.* **2001**, *13*, 3920.
- 98 Y. A. WANG, J. J. LI, H. CHEN, X. PENG, *J. Am. Chem. Soc.* **2002**, *124*, 2293.
- 99 P. NANDAKUMAR, C. VIJAYAN, Y. V. G. S. MURTI, *J. Appl. Phys.* **2002**, *91*, 1509.
- 100 R. G. ISPASOIU, Y. JIN, J. LEE, F. PAPADIMITRAKOPOULOS, T. GOODSON III, *Nano Lett.* **2002**, *2*, 127.
- 101 S. L. CUMBERLAND, K. M. HANIF, A. JAVIER, G. A. KHITROV, G. F. STROUSE, S. M. WOESSNER, C. S. YUN, *Chem. Mater.* **2002**, *14*, 1576.
- 102 A. HENGLEIN, *Ber. Bunsenges. Phys. Chem.* **1995**, *99*, 903.
- 103 H. WELLER, A. EYCHMÜLLER, *Adv. Photochem.* **1995**, *20*, 165.
- 104 A. P. ALIVISATOS, *Science* **1996**, *271*, 933.
- 105 A. P. ALIVISATOS, *J. Phys. Chem.* **1996**, *100*, 13226.
- 106 H. WELLER, A. EYCHMÜLLER. Preparation and Characterization of Semiconductor Nanoparticles. In *Semiconductor Nanoclusters*; V. KAMAT, P., MEISEL, D., Eds.; Elsevier Science B. V.: Amsterdam, **1996**, *103*, 5.
- 107 P. A. ALIVISATOS, P. F. BARBARA, A. W. CASTLEMAN, J. CHANG, D. A. DIXON, M. L. KLEIN, G. L. MCLENDON, J. S. MILLER, M. A. RATNER, P. J. ROSSKY, S. I. STUPP, M. E. THOMPSON, *Adv. Mater.* **1998**, *10*, 1297.
- 108 T. TRINDADE, P. O'BRIAN, N. L. PICKETT, *J. Mater. Chem.* **2001**, *13*, 3843.
- 109 J. M. WHITLING, G. SPREITZER, D. W. WRIGHT, *Adv. Mater.* **2000**, *12*, 1377.
- 110 W. E. FARNETH, N. HERRON, Y. WANG, *Chem. Mater.* **1992**, *4*, 916.
- 111 N. HERRON, A. SUNA, Y. WANG, *J. Chem. Soc., Dalton Trans.* **1992**, 2329.
- 112 I. G. DANCE, A. CHOY, M. L. SCUDDER, *J. Am. Chem. Soc.* **1984**, *106*, 6285.



- 113 G. S. H. LEE, D. C. CRAIG, I. MA, M. L. SCUDDER, T. D. BAILEY, I. G. DANCE, *J. Am. Chem. Soc.* **1988**, *110*, 4863.
- 114 G. S. H. LEE, K. J. FISHER, D. C. CRAIG, M. L. SCUDDER, I. G. DANCE, *J. Am. Chem. Soc.* **1990**, *112*, 6435.
- 115 P. STRICKLER, *J. Chem. Soc., Chem. Commun.* **1969**, 655.
- 116 G. SCHWARZENBACH, K. GAUTSCHI, J. PETER, K. TUNABOYLU, *Trans. R. Inst. Technol. Stockholm* **1972**, 271, 295.
- 117 N. HERRON, J. C. CALABRESE, W. E. FARNETH, Y. WANG, *Science* **1993**, *259*, 1426.
- 118 T. VOSSMEYER, L. KATSIKAS, M. GIERSIG, I. G. POPOVIC, K. DIESNER, A. CHEMSEDDINE, A. EYCHMÜLLER, H. WELLER, *J. Phys. Chem.* **1994**, *98*, 7665.
- 119 Y. NOSAKA, H. SHIGENO, T. IKEUCHI, *J. Phys. Chem.* **1995**, *99*, 8317.
- 120 T. VOSSMEYER, G. RECK, L. KATSIKAS, E. T. K. HAUPT, B. SCHULZ, H. WELLER, *Inorg. Chem.* **1995**, *34*, 4926.
- 121 A. L. ROGACH, A. KORNOWSKI, M. GAO, A. EYCHMÜLLER, H. WELLER, *J. Phys. Chem. B* **1999**, *103*, 3065.
- 122 A. L. ROGACH, L. KATSIKAS, A. KORNOWSKI, D. S. SU, A. EYCHMÜLLER, H. WELLER, *Ber. Bunsenges. Phys. Chem.* **1996**, *100*, 1772.
- 123 A. L. ROGACH, L. KATSIKAS, A. KORNOWSKI, D. SU, A. EYCHMÜLLER, H. WELLER, *Ber. Bunsenges. Phys. Chem.* **1997**, *101*, 1668.
- 124 M. GAO, S. KIRSTEIN, H. MÖHWALD, A. L. ROGACH, A. KORNOWSKI, A. EYCHMÜLLER, H. WELLER, *J. Phys. Chem. B* **1998**, *102*, 8360.
- 125 A. L. ROGACH, S. V. KERSHAW, M. BURT, M. HARRISON, A. KORNOWSKI, A. EYCHMÜLLER, H. WELLER, *Adv. Mater.* **1999**, *11*, 552.
- 126 S. V. KERSHAW, M. BURT, M. HARRISON, A. L. ROGACH, H. WELLER, A. EYCHMÜLLER, *Appl. Phys. Lett.* **1999**, *75*, 1694.
- 127 M. T. HARRISON, S. V. KERSHAW, M. G. BURT, A. EYCHMÜLLER, H. WELLER, A. L. ROGACH, *Mater. Sci. Eng. B* **2000**, *69*, 355.
- 128 A. L. ROGACH, M. T. HARRISON, S. V. KERSHAW, A. KORNOWSKI, M. G. BURT, A. EYCHMÜLLER, H. WELLER, *phys. stat. sol. (b)* **2001**, *224*, 153.
- 129 K. HOPPE, E. GEIDEL, H. WELLER, A. EYCHMÜLLER, *Phys. Chem. Chem. Phys.* **2002**, *4*, 1704.
- 130 A. CHEMSEDDINE, H. WELLER, *Ber. Bunsenges. Phys. Chem.* **1993**, *97*, 636.
- 131 A. M. KAPITONOV, A. P. STUPAK, S. V. GAPONENKO, E. P. PETROV, A. L. ROGACH, A. EYCHMÜLLER, *J. Phys. Chem. B* **1999**, *103*, 10109.
- 132 A. GLOZMAN, E. LIFSHITZ, K. HOPPE, A. L. ROGACH, H. WELLER, A. EYCHMÜLLER, *Isr. J. Chem.* **2001**, in Druck.
- 133 M. GAO, C. LESSER, S. KIRSTEIN, H. MÖHWALD, A. L. ROGACH, H. WELLER, *J. Appl. Phys.* **2000**, *87*, 2297.
- 134 N. P. GAPONIK, D. V. TALAPIN, A. L. ROGACH, A. EYCHMÜLLER, *J. Mater. Chem.* **2000**, *10*, 2163.
- 135 D. V. TALAPIN, S. K. POZNYAK, N. P. GAPONIK, A. L. ROGACH, A. EYCHMÜLLER, *Physica E* **2002**, *14*, 237.
- 136 M. T. HARRISON, S. V. KERSHAW, M. G. BURT, A. L. ROGACH, A. KORNOWSKI, A. EYCHMÜLLER, H. WELLER, *Pure Appl. Chem.* **2000**, *72*, 295.
- 137 J. ROCKENBERGER, L. TRÖGER, A. KORNOWSKI, A. EYCHMÜLLER, J. FELDHAUS, H. WELLER, *J. Phys. IV France* **1997**, *7*, 1213.
- 138 J. ROCKENBERGER, L. TRÖGER, A. KORNOWSKI, T. VOSSMEYER, A. EYCHMÜLLER, J. FELDHAUS, H. WELLER, *Ber. Bunsenges. Phys. Chem.* **1997**, *101*, 1613.
- 139 J. ROCKENBERGER, L. TRÖGER, A. KORNOWSKI, T. VOSSMEYER, A. EYCHMÜLLER, J. FELDHAUS, H. WELLER, *J. Phys. Chem. B* **1997**, *101*, 2691.
- 140 J. ROCKENBERGER, L. TRÖGER, A. L. ROGACH, M. TISCHER, M. GRUNDMANN, H. WELLER, A. EYCHMÜLLER, *Ber. Bunsenges. Phys. Chem.* **1998**, *102*, 1561.
- 141 J. ROCKENBERGER, L. TRÖGER, A. L. ROGACH, M. TISCHER, M. GRUNDMANN, A. EYCHMÜLLER, H. WELLER, *J. Chem. Phys.* **1998**, *108*, 7807.
- 142 S. V. GAPONENKO, A. M. KAPITONOV, V. N. BOGOMOLOV, A. V. PROKOFIEV, A. EYCHMÜLLER, A. L. ROGACH, *JETP Lett.* **1998**, *68*, 142.
- 143 S. V. GAPONENKO, *Optical Properties of Semiconductor Nanocrystals*; Cambridge University Press: Cambridge, 1998.

- 144 S. V. GAPONENKO, V. N. BOGOMOLOV, E. P. PETROV, A. M. KAPITONOV, A. EYCHMÜLLER, A. L. ROGACH, I. I. KALOSHA, F. GINDELE, U. WOGGON, *J. Lumin.* **2000**, 87–89, 152.
- 145 A. L. ROGACH, D. NAGESHA, J. W. OSTRANDER, M. GIERSIG, N. A. KOTOV, *Chem. Mater.* **2000**, 12, 2676.
- 146 A. EYCHMÜLLER, A. L. ROGACH, *Pure Appl. Chem.* **2000**, 72, 179.
- 147 A. EYCHMÜLLER, *J. Phys. Chem. B* **2000**, 104, 6514.
- 148 A. L. ROGACH, *Mater. Sci. Eng. B* **2000**, 69–70, 435.
- 149 A. L. ROGACH. Optical Properties of Colloidally Synthesised II–VI Semiconductor Nanocrystals. In *Optical Properties of Semiconductor Nanostructures*; SADOWSKI, M. L., Ed.; Kluwer Academic Publishers, 2000; pp 379.
- 150 J. G. C. VEINOT, M. GINZBURG, W. J. PIETRO, *Chem. Mater.* **1997**, 9, 2117.
- 151 J. R. SACHLEBEN, V. COLVIN, L. EMSLEY, E. W. WOOTEN, A. P. ALIVISATOS, *J. Phys. Chem. B* **1998**, 102, 10117.
- 152 S. CHEN, L. A. TRUAX, J. M. SOMMERS, *Chem. Mater.* **2000**, 12, 3864.
- 153 N. KUMBHOJKAR, V. V. NIKESH, A. KSHIRSAGAR, S. MAHAMUNI, *J. Appl. Phys.* **2000**, 88, 6260.
- 154 J. NANDA, S. SAPRA, D. D. SARMA, N. CHANDRASEKHARAN, G. HODES, *Chem. Mater.* **2000**, 12, 1018.
- 155 M. MOSTAFAVI, Y. LIU, P. PERNOT, J. BELLONI, *Rad. Phys. Chem.* **2000**, 59, 49.
- 156 T. TORIMOTO, H. KONTANI, Y. SHIBUTANI, S. KUWABATA, T. SAKATA, H. MORI, H. YONEYAMA, *J. Phys. Chem. B* **2001**, 105, 6838.
- 157 J. ALDANA, Y. A. WANG, X. PENG, *J. Am. Chem. Soc.* **2001**, 123, 8844.
- 158 S. WESTENHOFF, N. A. KOTOV, *J. Am. Chem. Soc.* **2002**, 124, 2448.
- 159 Y. NOSAKA, H. TANAKA, *J. Phys. Chem. B* **2002**, 106, 3389.
- 160 N. P. GAPONIK, D. V. TALAPIN, A. L. ROGACH, K. HOPPE, E. V. SHEVCHENKO, A. KORNOWSKI, A. EYCHMÜLLER, H. WELLER, *J. Phys. Chem. B* **2002**, 106, 7177.
- 161 H. DÖLLEFELD, K. HOPPE, J. KOLNY, K. SCHILLING, H. WELLER, A. EYCHMÜLLER, *Phys. Chem. Chem. Phys.* **2002**, 4, 4747.
- 162 N. GAPONIK, D. V. TALAPIN, A. L. ROGACH, A. EYCHMÜLLER, H. WELLER, *Nano Lett.* **2002**, 2, 803.
- 163 O. I. MICIC, C. J. CURTIS, K. M. JONES, J. R. SPRAGUE, A. J. NOZIK, *J. Phys. Chem.* **1994**, 98, 4966.
- 164 O. I. MICIC, J. R. SPRAGUE, C. J. CURTIS, K. M. JONES, J. L. MACHOL, A. J. NOZIK, H. GIESSEN, B. FLUEGEL, G. MOHS, N. PEYGHAMBARIAN, *J. Phys. Chem.* **1995**, 99, 7754.
- 165 O. I. MICIC, J. SPRAGUE, Z. H. LU, A. J. NOZIK, *Appl. Phys. Lett.* **1996**, 68, 3150.
- 166 O. I. MICIC, A. J. NOZIK, *J. Lumin.* **1996**, 70, 95.
- 167 A. A. GUZELIAN, U. BANIN, A. V. KADAVANICH, X. PENG, A. P. ALIVISATOS, *Appl. Phys. Lett.* **1996**, 69, 1432.
- 168 A. A. GUZELIAN, J. E. B. KATARI, A. V. KADAVANICH, U. BANIN, K. HAMAD, E. JUBAN, A. P. ALIVISATOS, R. H. WOLTERS, C. C. ARNOLD, J. R. HEATH, *J. Phys. Chem.* **1996**, 100, 7212.
- 169 O. I. MICIC, H. M. CHEONG, H. FU, A. ZUNGER, J. R. SPRAGUE, A. MASCARENHAS, A. J. NOZIK, *J. Phys. Chem. B* **1997**, 101, 4904.
- 170 D. BERTRAM, O. I. MICIC, A. J. NOZIK, *Phys. Rev. B* **1998**, 57, R4265.
- 171 U. BANIN, C. J. LEE, A. A. GUZELIAN, A. V. KADAVANICH, A. P. ALIVISATOS, W. JASKOLSKI, G. W. BRYANT, A. L. EFROS, M. ROSEN, *J. Chem. Phys.* **1998**, 109, 2306.
- 172 B. L. WEHRENBURG, C. WANG, P. GUYOT-SIONNEST, *J. Phys. Chem. B* **2002**, 106, 10634.
- 173 N. A. HILL, K. B. WHALEY, *J. Chem. Phys.* **1993**, 99, 3707.
- 174 N. A. HILL, K. B. WHALEY, *J. Chem. Phys.* **1994**, 100, 2831.
- 175 B. ZORMAN, M. V. RAMAKRISHNA, R. A. FRIESNER, *J. Phys. Chem.* **1995**, 99, 7649.
- 176 L. W. WANG, A. ZUNGER, *Phys. Rev. B* **1996**, 53, 9579.
- 177 A. L. EFROS, M. ROSEN, M. KUNO, M. N. NIRMAL, D. J., M. G. BAWENDI, *Phys. Rev. B* **1996**, 54, 4843.

- 178 M. CHAMARRO, C. GOURDON, P. LAVALLARD, O. LUBLINSKAYA, A. I. EKIMOV, *Phys. Rev. B* **1996**, 53, 1336.
- 179 K. EICKHORN, R. AHLRICHS, *Chem. Phys. Lett.* **1998**, 288, 235.
- 180 S. H. WEI, S. B. ZHANG, A. ZUNGER, *J. Appl. Phys.* **2000**, 87, 1304.
- 181 A. FRANCESCETTI, A. ZUNGER, *Phys. Rev. B* **2000**, 62, R16287.
- 182 J. LI, J. B. XIA, *Phys. Rev. B* **2000**, 61, 15880.
- 183 J. PEREZ-CONDE, A. K. BHATTACHARJEE, *Phys. Rev. B* **2001**, 63, 245318.
- 184 D. J. NORRIS, M. NIRMAL, C. B. MURRAY, A. SACRA, M. B. BAWENDI, *Z. Phys. D* **1993**, 26, 355.
- 185 M. NIRMAL, C. B. MURRAY, D. J. NORRIS, M. G. BAWENDI, *Z. Phys. D* **1993**, 26, 361.
- 186 D. J. NORRIS, A. SACRA, C. B. MURRAY, M. G. BAWENDI, *Phys. Rev. Lett.* **1994**, 72, 2612.
- 187 M. NIRMAL, C. B. MURRAY, M. G. BAWENDI, *Phys. Rev. B* **1994**, 50, 2293.
- 188 D. J. NORRIS, M. G. BAWENDI, *J. Chem. Phys.* **1995**, 103, 5260.
- 189 A. SACRA, D. J. NORRIS, C. B. MURRAY, M. G. BAWENDI, *J. Chem. Phys.* **1995**, 103, 5236.
- 190 M. NIRMAL, D. J. NORRIS, M. KUNO, M. G. BAWENDI, A. L. EFROS, M. ROSEN, *Phys. Rev. Lett.* **1995**, 75, 3728.
- 191 D. J. NORRIS, M. G. BAWENDI, *Phys. Rev. B* **1996**, 53, 16338.
- 192 D. J. NORRIS, A. L. EFROS, M. ROSEN, M. G. BAWENDI, *Phys. Rev. B* **1996**, 53, 16347.
- 193 C. BURDA, S. LINK, T. C. GREEN, M. A. EL-SAYED, *J. Phys. Chem. B* **1999**, 103, 10775.
- 194 P. GUYOT-SIONNEST, M. SHIM, C. MATRANGA, M. HINES, *Phys. Rev. B* **1999**, 60, R2181.
- 195 D. S. GINGER, A. S. DHOOT, C. E. FINLAYSON, N. C. GREENHAM, *Appl. Phys. Lett.* **2000**, 77, 2816.
- 196 C. B. MURRAY, C. R. KAGAN, M. G. BAWENDI, *Annu. Rev. Mater. Sci.* **2000**, 30, 545.
- 197 C. R. KAGAN, C. B. MURRAY, M. NIRMAL, M. G. BAWENDI, *Phys. Rev. Lett.* **1996**, 76, 3043.
- 198 C. R. KAGAN, C. B. MURRAY, M. G. BAWENDI, *Phys. Rev. B* **1996**, 54, 8633.
- 199 M. NIRMAL, B. O. DABBOUSI, M. G. BAWENDI, J. J. MACKLIN, J. K. TRAUTMAN, T. D. HARRIS, L. E. BRUS, *Nature* **1996**, 383, 802.
- 200 S. A. EMPEDOCLES, D. J. NORRIS, M. G. BAWENDI, *Phys. Rev. Lett.* **1996**, 77, 3873.
- 201 S. A. BLANTON, M. A. HINES, P. GUYOT-SIONNEST, *Appl. Phys. Lett.* **1996**, 69, 3905.
- 202 S. A. EMPEDOCLES, M. G. BAWENDI, *Science* **1997**, 278, 2114.
- 203 S. A. EMPEDOCLES, M. G. BAWENDI, *J. Phys. Chem. B* **1999**, 103, 1826.
- 204 U. BANIN, M. BRUCHEZ, A. P. ALIVISATOS, T. HA, S. WEISS, D. S. CHEMLA, *J. Chem. Phys.* **1999**, 110, 1195.
- 205 T. D. KRAUSS, L. E. BRUS, *Phys. Rev. Lett.* **1999**, 83, 4840.
- 206 R. G. NEUHAUSER, K. T. SHIMIZU, W. K. WOO, S. A. EMPEDOCLES, M. G. BAWENDI, *Phys. Rev. Lett.* **2000**, 85, 3301.
- 207 M. KUNO, D. P. FROMM, H. F. HAMANN, A. GALLAGHER, D. J. NESBITT, *J. Chem. Phys.* **2000**, 112, 3117.
- 208 T. D. KRAUSS, S. O'BRIEN, L. E. BRUS, *J. Phys. Chem. B* **2001**, 105, 1725.
- 209 K. T. SHIMIZU, R. G. NEUHAUSER, C. A. LEATHERDALE, S. A. EMPEDOCLES, W. K. WOO, M. G. BAWENDI, *Phys. Rev. B* **2001**, 63, 205316.
- 210 F. KOBERLING, A. MEWS, T. BASCHÉ, *Adv. Mater.* **2001**, 13, 672.
- 211 G. SCHLEGEL, J. BOHNENBERGER, I. POTAPOVA, A. MEWS, *Phys. Rev. Lett.* **2002**, 88, 137401.
- 212 S. A. EMPEDOCLES, R. NEUHAUSER, K. SHIMIZU, M. G. BAWENDI, *Adv. Mater.* **1999**, 11, 1243.
- 213 V. L. COLVIN, M. C. SCHLAMP, A. P. ALIVISATOS, *Nature* **1994**, 370, 354.
- 214 B. O. DABBOUSI, M. G. BAWENDI, O. ONITSUKA, M. F. RUBNER, *Appl. Phys. Lett.* **1995**, 66, 1316.
- 215 H. MATTOUSSI, L. H. RADZIŁOWSKI, B. O. DABBOUSI, E. L. THOMAS, M. G. BAWENDI, M. F. RUBNER, *J. Appl. Phys.* **1998**, 83, 7965.
- 216 D. L. KLEIN, R. ROTH, A. K. L. LIM, A. P. ALIVISATOS, P. L. MCEUEN, *Nature* **1997**, 389, 699.

- 217 M. SHIM, C. WANG, P. GUYOT-SIONNEST, *J. Phys. Chem. B* **2001**, 105, 2369.
- 218 M. PEHNT, D. L. SCHULZ, C. J. CURTIS, K. M. JONES, D. S. GINLEY, *Appl. Phys. Lett.* **1995**, 67, 2176.
- 219 M. Y. SHEN, M. ODA, T. GOTO, *Phys. Rev. Lett.* **1999**, 82, 3915.
- 220 M. SHIM, P. GUYOT-SIONNEST, *Nature* **2000**, 407, 981.
- 221 M. A. HINES, P. GUYOT-SIONNEST, *J. Phys. Chem. B* **1998**, 102, 3655.
- 222 D. J. NORRIS, N. YAO, F. T. CHARNOCK, T. A. KENNEDY, *Nano Lett.* **2001**, 1, 3.
- 223 V. I. KLIMOV, *J. Phys. Chem. B* **2000**, 6112.
- 224 V. I. KLIMOV, D. W. McBRANCH, C. A. LEATHERDALE, M. G. BAWENDI, *Phys. Rev. B* **1999**, 60, 13740.
- 225 V. I. KLIMOV, C. J. SCHWARZ, D. W. McBRANCH, C. A. LEATHERDALE, M. G. BAWENDI, *Phys. Rev. B* **1999**, 60, R2177.
- 226 C. BURDA, T. C. GREEN, S. LINK, M. A. EL-SAYED, *J. Phys. Chem. B* **1999**, 103, 1783.
- 227 J. Z. ZHANG, *J. Phys. Chem. B* **2000**, 104, 7239.
- 228 V. I. KLIMOV, A. A. MIKHAILOVSKY, D. W. McBRANCH, C. A. LEATHERDALE, M. G. BAWENDI, *Phys. Rev. B* **2000**, 61, R13349.
- 229 V. I. KLIMOV, A. A. MIKHAILOVSKY, D. W. McBRANCH, C. A. LEATHERDALE, M. G. BAWENDI, *Science* **2000**, 287, 1011.
- 230 V. I. KLIMOV, A. A. MIKHAILOVSKY, S. XU, A. MALKO, J. A. HOLLINGSWORTH, C. A. LEATHERDALE, H. J. EISLER, M. G. BAWENDI, *Science* **2000**, 290, 314.
- 231 R. G. ISPASOIU, J. LEE, F. PAPADIMITRAKOPOULOS, T. GOODSON III, *Chem. Phys. Lett.* **2001**, 340, 7.
- 232 M. C. BEARD, G. M. TURNER, C. A. SCHMUTTENMAER, *Nano Lett.* **2002**, 2, 983.
- 233 E. JOHNSTON-HALPERIN, D. D. AWSCHALOM, S. A. CROOKER, A. L. EFROS, M. ROSEN, X. PENG, A. P. ALIVISATOS, *Phys. Rev. B* **2001**, 63, 205309.
- 234 D. V. TALAPIN, S. HAUBOLD, A. L. ROGACH, A. KORNOWSKI, M. HAASE, H. WELLER, *J. Phys. Chem. B* **2001**, 105, 2260.
- 235 D. V. TALAPIN, A. L. ROGACH, A. KORNOWSKI, M. HAASE, H. WELLER, *Nano Lett.* **2001**, 1, 207.
- 236 D. V. TALAPIN, A. L. ROGACH, I. MEKIS, S. HAUBOLD, A. KORNOWSKI, M. HAASE, H. WELLER, *Coll. Surf. A* **2002**, 202, 145.
- 237 L. QU, A. PENG, X. PENG, *Nano Lett.* **2001**, 1, 333.
- 238 X. PENG, J. WICKHAM, A. P. ALIVISATOS, *J. Am. Chem. Soc.* **1998**, 120, 5343.
- 239 C.-S. YANG, D. D. AWSCHALOM, G. D. STUCKY, *Chem. Mater.* **2001**, 13, 594.
- 240 L. GRANASY, P. F. JAMES, *J. Chem. Phys.* **2000**, 113, 9810.
- 241 D. V. TALAPIN, A. L. ROGACH, M. HAASE, H. WELLER, *J. Phys. Chem. B* **2001**, 105, 12278.
- 242 L. QU, X. PENG, *J. Am. Chem. Soc.* **2002**, 124, 2049.
- 243 D. V. TALAPIN, A. L. ROGACH, E. V. SHEVCHENKO, A. KORNOWSKI, M. HAASE, H. WELLER, *J. Am. Chem. Soc.* **2002**, 124, 5782.
- 244 X. PENG, L. MANNA, W. YANG, J. WICKHAM, E. SCHER, A. KADAVANICH, A. P. ALIVISATOS, *Nature* **2000**, 404, 59.
- 245 Z. A. PENG, X. PENG, *J. Am. Chem. Soc.* **2001**, 123, 1389.
- 246 Z. A. PENG, X. PENG, *J. Am. Chem. Soc.* **2002**, 124, 3343.
- 247 A. STRIOLO, J. WARD, J. M. PRAUSNITZ, W. J. PARAK, D. ZANCHET, D. GERION, D. MILLIRON, A. P. ALIVISATOS, *J. Phys. Chem. B* **2002**, 106, 5500.
- 248 C. A. LEATHERDALE, W. WOO, F. V. MIKULEC, M. G. BAWENDI, *J. Phys. Chem. B* **2002**, 106, 7619.
- 249 O. SCHMELZ, A. MEWS, T. BASCHE, A. HERRMANN, K. MÜLLEN, *Langmuir* **2001**, 17, 2861.
- 250 L. SPANHEL, H. WELLER, A. FOJTIK, A. HENGLEIN, *Ber. Bunsenges. Phys. Chem.* **1987**, 91, 88.
- 251 A. HENGLEIN, M. GUTIERREZ, H. WELLER, A. FOJTIK, J. JIRKOVSKY, *Ber. Bunsenges. Phys. Chem.* **1989**, 93, 593.
- 252 A. R. KORTAN, R. HULL, R. L. OPILA, M. G. BAWENDI, M. L. STEIGERWALD, P. J. CARROL, L. E. BRUS, *J. Am. Chem. Soc.* **1990**, 112, 1327.

- 253 C. F. HOENER, K. A. ALLAN, A. J. BARD, A. CAMPION, M. A. FOX, T. E. MALLOUK, S. E. WEBBER, J. M. WHITE, *J. Phys. Chem.* **1992**, 96, 3812.
- 254 A. EYCHMÜLLER, A. HÄSSELBARTH, H. WELLER, *J. Lumin.* **1992**, 53, 113.
- 255 H. S. ZHOU, I. HONMA, H. KOMIYAMA, J. W. HAUS, *J. Phys. Chem.* **1993**, 97, 895.
- 256 A. HÄSSELBARTH, A. EYCHMÜLLER, R. EICHBERGER, M. GERSIG, A. MEWS, H. WELLER, *J. Phys. Chem.* **1993**, 97, 5333.
- 257 M. DANEK, K. F. JENSEN, C. B. MURRAY, M. G. BAWENDI, *Chem. Mater.* **1996**, 8, 173.
- 258 M. A. HINES, P. GUYOT-SIONNEST, *J. Phys. Chem.* **1996**, 100, 468.
- 259 B. O. DABBOUSI, J. RODRIGUEZ-VIEJO, F. V. MIKULEC, J. R. HEINE, H. MATTOUSSI, R. OBER, K. F. JENSEN, M. B. BAWENDI, *J. Phys. Chem. B* **1997**, 101, 9436.
- 260 J. RODRIGUEZVIEJO, K. F. JENSEN, H. MATTOUSSI, J. MICHEL, B. O. DABBOUSI, M. G. BAWENDI, *Appl. Phys. Lett.* **1997**, 70, 2132.
- 261 M. KUNO, J. K. LEE, B. O. DABBOUSI, F. V. MIKULEC, M. G. BAWENDI, *J. Chem. Phys.* **1997**, 106, 9869.
- 262 X. PENG, M. C. SCHLAMP, A. V. KADAVANICH, A. P. ALIVISATOS, *J. Am. Chem. Soc.* **1997**, 119, 7019.
- 263 Y. TIAN, T. NEWTON, N. A. KOTOV, D. M. GULDI, J. H. FENDLER, *J. Phys. Chem.* **1996**, 100, 8927.
- 264 H. WELLER, A. EYCHMÜLLER. Preparation and Characterization of Semiconductor Nanoparticles. In *Studies in Surface Science and Catalysis*; KAMAT, P. V., MEISEL, D., DELMON, B., YATES, J. T., Eds.; Elsevier Science B. V.: Amsterdam, Lausanne, New York, Oxford, Shannon, Tokyo, **1997**, 103, 5.
- 265 D. MEISEL. Charge transfer in nanoparticles. In *Semiconductor Nanoclusters*; KAMAT, P. V., MEISEL, D., Eds.; Elsevier Science B. V.: Amsterdam, **1997**, 103, 79.
- 266 P. V. KAMAT. Composite semiconductor nanoclusters. In *Semiconductor Nanoclusters*; V. KAMAT, P., MEISEL, D., Eds.; Elsevier Science B. V.: Amsterdam, **1997**, 103, 237.
- 267 P. V. KAMAT, K. VINODGOPAL. Environmental Photochemistry with Semiconductor Nanoparticles. In *Organic and Inorganic Photochemistry*; RAMAMURTHY, V., SCHANZE, K. S., Eds.; Marcel Dekker, Inc.: New York, **1998**, 2, 307.
- 268 J. RODRIGUEZVIEJO, H. MATTOUSSI, J. R. HEINE, M. K. KUNO, J. MICHEL, M. G. BAWENDI, K. F. JENSEN, *J. Appl. Phys.* **2000**, 87, 8526.
- 269 H. MATTOUSSI, J. M. MAURO, E. R. GOLDMAN, G. P. ANDERSON, V. C. SUNDAR, F. V. MIKULEC, M. G. BAWENDI, *J. Am. Chem. Soc.* **2000**, 122, 12142.
- 270 D. M. WILLARD, L. L. CARILLO, J. JUNG, A. VAN ORDEN, *Nano Lett.* **2001**, 1, 469.
- 271 D. GERION, F. PINAUD, S. C. WILLIAMS, W. J. PARAK, D. ZANCHET, S. WEISS, A. P. ALIVISATOS, *J. Phys. Chem. B* **2001**, 105, 8861.
- 272 P. PALINGINIS, H. WANG, *Appl. Phys. Lett.* **2001**, 78, 1541.
- 273 W. G. J. H. M. VAN SARK, P. L. T. M. FREDERIX, D. J. VAN DEN HEUVEL, H. C. GERRITSEN, A. A. BOL, J. N. J. VAN LINGEN, C. DE MELLO DONEGA, A. MEIJERINK, *J. Phys. Chem. B* **2001**, 105, 8281.
- 274 S. GORER, J. A. GANSKE, J. C. HEMMINGER, R. M. PENNER, *J. Am. Chem. Soc.* **1998**, 120, 9584.
- 275 S. GORER, R. M. PENNER, *J. Phys. Chem. B* **1999**, 103, 5750.
- 276 Y.-W. CAO, U. BANIN, *Angew. Chem. Int. Ed.* **1999**, 38, 3692.
- 277 Y. W. CAO, U. BANIN, *J. Am. Chem. Soc.* **2000**, 122, 9692.
- 278 O. MILLO, D. KATZ, Y. W. CAO, U. BANIN, *Phys. Rev. Lett.* **2001**, 86, 5751.
- 279 O. I. MICIC, B. B. SMITH, A. J. NOZIK, *J. Phys. Chem. B* **2000**, 104, 12149.
- 280 H. BORCHERT, S. HAUBOLD, M. HAASE, H. WELLER, C. MCGINLEY, M. RIEDLER, T. MÖLLER, *Nano Lett.* **2002**, 2, 151.
- 281 B. SCHREDER, T. SCHMIDT, V. PTATSCHEK, U. WINKLER, A. MATERNY, E. UMBACH, M. LERCH, G. MÜLLER, W. KIEFER, L. SPANHEL, *J. Phys. Chem. B* **2000**, 104, 1677.
- 282 P. REISS, J. BLEUSE, A. PRON, *Nano Lett.* **2002**, 2, 781.

- 283 M. A. MALIK, P. O'BRIAN, N. REVAPRASADU, *Chem. Mater.* **2002**, *14*, 2004.
- 284 M. T. HARRISON, S. V. KERSHAW, A. L. ROGACH, A. KORNOWSKI, A. EYCHMÜLLER, H. WELLER, *Adv. Mater.* **2000**, *12*, 123.
- 285 A. EYCHMÜLLER, A. MEWS, H. WELLER, *Chem. Phys. Lett.* **1993**, *208*, 59.
- 286 A. MEWS, A. EYCHMÜLLER, M. GIERSIG, D. SCHOOSS, H. WELLER, *J. Phys. Chem.* **1994**, *98*, 934.
- 287 A. EYCHMÜLLER, T. VOSSMEYER, A. MEWS, H. WELLER, *J. Luminescence* **1994**, *58*, 223.
- 288 D. SCHOOSS, A. MEWS, A. EYCHMÜLLER, H. WELLER, *Phys. Rev. B* **1994**, *49*, 17072.
- 289 A. MEWS, A. EYCHMÜLLER, *Ber. Bunsenges. Phys. Chem.* **1998**, *102*, 1343.
- 290 A. MEWS, A. EYCHMÜLLER, CdS/HgS/CdS nanoheterostructures: quantum wells within quantum dots. In *Physics, Chemistry and Application of Nanostructures*, 1999.
- 291 A. MEWS, A. V. KADAVANICH, U. BANIN, A. P. ALIVISATOS, *Phys. Rev. B* **1996**, *53*, 13242.
- 292 A. MEWS, U. BANIN, A. V. KADAVANICH, A. P. ALIVISATOS, *Ber. Bunsenges. Phys. Chem.* **1997**, *101*, 1621.
- 293 G. W. BRYANT, *Phys. Rev. B* **1995**, *52*, R16997.
- 294 W. JASKOLSKI, G. W. BRYANT, *Phys. Rev. B* **1998**, *57*, R4237.
- 295 J. PEREZ-CONDE, A. K. BHATTACHARJEE, *Phys. Stat. Sol. (b)* **2002**, *229*, 485.
- 296 G. BRYANT, W. JASKOLSKI, *phys. stat. sol. (b)* **2001**, *224*, 751.
- 297 V. F. KAMALOV, R. LITTLE, S. L. LOGUNOV, M. A. EL-SAYED, *J. Phys. Chem.* **1996**, *100*, 6381.
- 298 R. B. LITTLE, C. BURDA, S. LINK, S. LOGUNOV, M. A. EL-SAYED, *J. Phys. Chem. A* **1998**, *102*, 6581.
- 299 M. BRAUN, C. BURDA, M. MOHAMED, M. EL-SAYED, *Phys. Rev. B* **2001**, *64*, 035317.
- 300 A. T. YEH, G. CERULLO, U. BANIN, A. MEWS, A. P. ALIVISATOS, C. V. SHANK, *Phys. Rev. B* **1999**, *59*, 4973.
- 301 E. LIFSHITZ, H. PORTEANU, A. GLOZMAN, H. WELLER, M. PFLUGHOEFFT, A. EYCHMÜLLER, *J. Phys. Chem. B* **1999**, *103*, 6875.
- 302 H. PORTEANU, E. LIFSHITZ, M. PFLUGHOEFFT, A. EYCHMÜLLER, H. WELLER, *phys. stat. sol. (b)* **2001**, *226*, 219.
- 303 F. KOBERLING, A. MEWS, T. BASCHÉ, *Phys. Rev. B* **1999**, *60*, 1921.
- 304 R. B. LITTLE, M. A. EL-SAYED, G. BRYANT, S. BURKE, *J. Chem. Phys.* **2001**, *114*, 1813.
- 305 M. BRAUN, C. BURDA, M. A. EL-SAYED, *J. Phys. Chem. A* **2001**, *105*, 5548.
- 306 D. DORFS, A. EYCHMÜLLER, *Nano Lett.* **2001**, *1*, 663.
- 307 K. CHANG, J.-B. XIA, *Phys. Rev. B* **1998**, *57*, 9780.
- 308 H. BORCHERT, D. DORFS, C. MCGINLEY, S. ADAM, T. MÖLLER, H. WELLER, A. EYCHMÜLLER, *J. Phys. Chem. B* **2003**, *107*, 7481.
- 309 H. BORCHERT, S. HAUBOLD, M. HAASE, H. WELLER, C. MCGINLEY, M. RIEDLER, T. MÖLLER, *Nano Lett.* **2002**, *2*, 151.

### 3.1.2

## Synthesis and Characterization of III–V Semiconductor Nanoparticles

Uri Banin

### 3.1.2.1 Introduction

The preparation of nanocrystals of III–V semiconductors presented a significant and important challenge to researchers in the field for over a decade [1–7]. Many of the III–V semiconductors are direct gap semiconductors, unlike silicon. This has led to their widespread implementation as the central building blocks of present day optoelectronic devices such as diode lasers, ubiquitous in telecommunication

applications, providing obvious technological motivation for development of wet chemical synthesis approaches for preparing nanocrystals of these materials. Furthermore, the opportunity to develop such routes for preparing III–V semiconductor nanocrystals presents a challenge for synthetic chemistry. While II–VI semiconductors can be prepared directly in aqueous media using ionic precursors, no equivalent synthetic procedures could be developed for the III–V semiconductor compounds. This results from the more covalent bonding typical of III–V compounds and the high energetic barriers in the formation of the semiconductor from suitable precursors.

The availability of high quality III–V semiconductor nanocrystals has contributed significantly to fundamental studies of the size-dependent electronic, optical, electrical, and structural properties of nanocrystals [8–10]. An interesting case is that of InAs, a narrow-band semiconductor (bulk band gap  $E_g = 0.42$  eV). Under the conditions of quantum confinement, the band gap of InAs nanocrystals can be tuned over a broad range in the near infra-red, where the selection of traditional organic dyes is poor and their stability is low. This points toward potential applications of such nanocrystals in optoelectronic devices relevant for telecommunications [11] and as biological fluorescent markers in the near IR spectral region [12].

As III–V semiconductor QDs (for example, InAs) can also be prepared via a strain-induced growth mechanism using molecular beam epitaxy (MBE) [13, 14], there is an opportunity for direct comparison of the properties of two QD systems – colloidal grown nanocrystals versus MBE-grown dots [15].

Early attempts to prepare III–V semiconductor nanocrystals include the synthesis of GaAs nanocrystals in 1990 by Olshavsky et al. [16] using a dehalosilylation reaction of  $\text{GaCl}_3$  and  $\text{As}(\text{Si}(\text{CH}_3)_3)_3$  developed by Wells [17], where quinoline was used as both the solvent and as the surface passivating ligand. These reactions produced nanocrystals about 3–4 nm in diameter, but the optical absorption of the particles showed some interference due to suspected Ga-quinoline complexes or quinoline oligomeric species [18]. To date, most work on the preparation of III–V nanocrystalline materials has been based on similar dehalosilylation reactions, with variation of reactants, reaction conditions, and solvents.

An additional route for the preparation of GaAs, was reported by Nozik et al. [19], who used  $\text{Ga}(\text{acac})_3$  and  $\text{As}(\text{Si}(\text{CH}_3)_3)_3$  with triglyme as the solvent to produce GaAs nanocrystals. However, the absorption spectra did not show a well-defined feature that shifts with particle diameter, indicating a poor size distribution or other problems with nanocrystal quality. Wells et al. [20, 21] have also prepared nanocrystalline GaAs as well as GaP using the metathetical reaction of  $\text{GaCl}_3$  and  $(\text{Na/K})_3\text{E}$  ( $\text{E} = \text{P, As}$ ) in glymes. These reactions produced nanocrystalline material, but there is no separation of sizes, and the optical spectra do not exhibit the characteristic well-defined absorption feature.

InP nanocrystals were prepared by Nozik et al. using the dehalosilylation reaction of an uncharacterized  $\text{InCl}_3$ -oxalate complex and  $\text{P}(\text{Si}(\text{CH}_3)_3)_3$  with trioctylphosphine oxide (TOPO) serving as the solvent and surface-passivating group [4]. This synthesis procedure provides high quality nanocrystals, and a size-dependent feature is observed in the absorption spectra. Nozik also reports the synthesis of

nanocrystals of the indirect gap semiconductor GaP and the ternary material GaInP<sub>2</sub> using analogous reactions. Additionally, Guzelian et al. reported the successful synthesis of size-controlled InP nanocrystals [3]. Here, InCl<sub>3</sub> dissolved in TOP reacts with P(Si(CH<sub>3</sub>)<sub>3</sub>)<sub>3</sub> in TOPO. The preparation of InAs nanocrystals is an example of a synthesis procedure where a very high level of control on particle size and monodispersity has been demonstrated [5]. We therefore choose to focus on this particular system to obtain a more detailed view of the reaction procedure. Recently, Nozik and coworkers also reported the synthesis of colloidal GaN nanocrystals. They used a polymeric gallium imide precursor  $\{\text{Ga}(\text{NH})_{3/2}\}_n$ , reacted in trioctylamine at 360 °C to produce GaN nanocrystals [22].

Following the improvements in the synthesis of InAs and InP nanocrystals, workers in the field have implemented several strategies to improve the fluorescence and stability of the functional particles. The optical and electronic properties of the particles can be further controlled by fabricating advanced core/shell nanocrystal structures, where a shell of a higher band gap semiconductor is grown on the core, yielding superior surface passivation, as demonstrated first for II–VI semiconductor nanocrystals [23–26] and more recently for III–V nanocrystals. Synthesis of core/shell nanocrystals with InAs cores was recently developed and will be outlined here [24–26]. The preparation of InP/ZnS core/shells with improved luminescence properties was reported by Weller and coworkers [27], while Nozik and coworkers reported the synthesis of lattice-matched shells of ZnCdSe<sub>2</sub> on InP cores [28]. Another approach to improving the luminescence of InP nanocrystals was reported by Nozik and coworkers using etching with HF [29].

The chapter begins with a general discussion of the synthetic strategy employed for III–V semiconductor nanocrystals. This is followed by a description of the synthesis of InAs nanocrystals as a prototypical example, and the characterization of the particles by various methods is briefly reviewed. We then detail the synthesis of core/shell nanocrystals with III–V semiconductor cores, focusing particularly on InAs cores.

### 3.1.2.2 Synthetic Strategy

The first step in the synthesis of a nanocrystal is the nucleation of the particles. Successful nucleation is an indication of whether the reaction in question is appropriate for the formation of nanocrystals. For a monodisperse sample, the nucleation event must be well separated in time from the growth step, which generally means that nucleation must occur on a short time scale, of the order of a fraction of a second. In contrast, if nucleation is spread out in time such that nucleation and growth overlap, different nucleation sites will undergo growth of different durations, resulting in a broad size distribution.

An effective way to achieve separation of nucleation from growth is the use of a method of injecting suitable precursors into the solvent at high temperature such that nucleation occurs immediately on contact with the hot solvent. This method has been perfected in the preparation of CdSe nanocrystals [30, 31] and was also implemented for InP and InAs nanocrystals [3–5]. Difficulties in fully realizing the benefits of the injection method in the case of III–V semiconductor nanocrystals



include the need for prolonged reaction times to overcome the high reaction barriers and the need for annealing at high temperature to achieve better crystallinity of the nanocrystals.

The next stage in the nanocrystal synthesis is the growth of the particles. As with nucleation, intermediate species and the growing particle must stay in solution throughout the process. Growth is completed when the reagents are consumed, although additional high-temperature annealing time may be needed to obtain good crystallinity. Under prolonged high-temperature annealing, the possibility of Ostwald ripening arises – an undesired mechanism that will broaden the size distribution [32]. Growth can also be effectively quenched by cooling the reaction mixture. A typical behavior during the growth stage was found by Alivisatos and coworkers, who studied the growth of both CdSe and InAs nanocrystals and introduced the important concept of size focusing [31]. This concept is based on the existence of a critical size that depends on the reaction conditions (concentration of reactants, temperature, solvent etc.). Above the critical size, growth rate decreases with increased size, leading to a narrowing or focusing of the size distribution, while below the critical size, defocusing results because the growth rate of smaller particles is slower than that of the bigger particles. To achieve a narrow distribution, conditions should be optimized so that during growth the reaction remains within size focusing conditions.

An additional critical issue for high quality nanocrystals is the passivation of the surface. During the synthesis, surface passivation helps to control the growth of the nanocrystal, prevents agglomeration and fusing of particles, and provides for the solubility of the nanocrystals in common solvents. Solvation is important not only for the nanocrystals, but also for the reactants and intermediates. Surface passivation is achieved by using an organic molecule to coordinate or bond to the nanocrystal surface. Most commonly, this organic molecule is the solvent for the reaction. This strategy benefits from having the capping molecule in huge excess and from having a common solvation medium for the reactants, intermediates, and nanocrystals.

Capping groups typically contain an electron-rich donating group such as phosphine oxides, phosphines, amines, or thiols and behave as a Lewis base, which coordinates to the electron-poor Lewis acid-like metal of the semiconductor such as cadmium or indium. This coordination passivates the dangling orbitals at the nanocrystal surface, preventing further growth or agglomeration. The other end of the ligand imparts solubility to the nanocrystal by giving the particle a hydrophilic or hydrophobic surface. For example, the alkyl groups of TOPO or TOP result in nanocrystals that are soluble in relatively nonpolar solvents, while using ligands such as mercaptobenzoic acid renders the particles soluble in polar solvents like methanol [33].

Surface passivation plays an important role not only during the synthesis. It can also be used to further derivatize the surface of the particles, providing additional chemical control to attach nanocrystals to a surface [34], to electrodes [35], to other nanocrystals, and to biomolecules [36]. Because of the relatively weak coordination bonds of most surface-capping groups, these molecules can easily be exchanged

after the initial synthesis. Many of the properties of nanocrystals, notably photoluminescence, are sensitive to the surface passivation, and manipulation of the surface-capping groups can be used to tune these properties [37, 38]. The core/shell approach discussed in a later section proves to be a powerful method for enhancing the fluorescence quantum yield and the stability of the particles toward oxidation and photodegradation.

Improvement of the size distribution after the synthesis is also a widely used strategy for achieving monodisperse samples. Size-selective precipitation is commonly applied to obtain fractions of nanocrystals with improved size distribution from a given reaction [5, 30]. The method is based on the size-dependent solubility of the nanocrystals, which can be used to destabilize the dispersion of the large particles first. This is achieved by adding controlled amounts of a non-solvent to the solution of particles, thereby leading to precipitation of the large nanocrystals, which can be then separated by either filtration or centrifugation. Such steps can be carried out consecutively to obtain a sequence of nanocrystal fractions with smaller and smaller diameters. A similar procedure may in principle be applied yet again to each fraction to further narrow the size distribution.

While the precise chemical mechanisms of nanocrystal syntheses have not been investigated, several general comments can be made regarding the effect of the reaction mechanism on the nanocrystal product. To accomplish the ideal nucleation event discussed above, the reaction needs to be rapid and complete. These requirements suggest simple mechanisms using reagents with low barriers to reaction. For example, at one extreme is the aqueous or micelle synthesis of CdS or CdSe, where cadmium salts such as  $\text{CdCl}_2$  are the cadmium source and  $\text{H}_2\text{S}$  or  $\text{H}_2\text{Se}$  is the group VI source. In these types of reactions, the metal ion is available for reaction with a very simple group VI source. These reactions are rapid and can even occur at room temperature. On the down side, the reactions are so facile that it is difficult to control and isolate nucleation.

The chemistry of group III–V materials has proven to be more difficult as far as designing a system with the attributes of both rapid and complete reaction yet controlled nucleation. In contrast to cadmium, the group III metals are too reactive to be used as ionic sources, as they would react too strongly with the solvent medium. Attempts to develop reactions involving group III alkyls analogous to  $(\text{CH}_3)_2\text{Cd}$  (a reagent commonly used in the synthesis of CdSe nanocrystals) were unsuccessful, as these compounds also appear to be too reactive, tending to proceed uncontrollably to the bulk phase regardless of capping group.

A general strategy to reduce the reactivity of these materials would be to attach ligands to the group III and group V centers and then react these molecules, presumably in a more controlled fashion. Over the past several years, there has been much interest in novel routes to bulk III–V materials [39–42], particularly GaAs, because of the difficult and hazardous nature of traditional reactions involving  $\text{Ga}(\text{CH}_3)_3$  and  $\text{AsH}_3$ . Substituted gallium and arsenic compounds were developed in the hope of reducing reactant toxicity, eliminating gaseous reagents, and lowering reaction temperatures. As mentioned, Wells and coworkers [17] developed a dehalosilylation reaction using  $\text{GaCl}_3 + \text{As}(\text{Si}(\text{CH}_3)_3)_3$ , which produced GaAs with

the elimination of  $(\text{CH}_3)_3\text{SiCl}$ . Barron et al. [43] used an analogous reaction to produce bulk InP. These reactions are driven by the formation of the  $\text{CH}_3\text{SiCl}$  bond in combination with the good lability of the  $\text{Si}(\text{CH}_3)_3$  ligand. They are reactions widely utilized in the synthesis of III–V semiconductor nanocrystals.

### 3.1.2.3 InAs and InP Nanocrystals

#### Synthesis of InAs and InP Nanocrystals

The synthesis of InP and InAs are analogous, and InAs will be treated in detail. All steps of the reaction and the manipulation of the reagents are carried out under argon or in a dry box. The setup for performing the synthesis is schematically shown in Figure 3-13. The nanocrystals produced are crystalline and highly soluble in a variety of organic solvents including hexanes, toluene, and pyridine. Particles with diameters ranging from ca. 2–10 nm, with narrow size distributions, can be prepared. The surface of the nanocrystals can be further derivatized with a variety of ligands including amines, thiols, and phosphines.

The reaction can be written as



Details of this synthesis are reported elsewhere [5, 7, 31], and here we can discuss a typical preparation: TOP (3 g) was heated in a three-necked flask on a Schlenk line under an Ar atmosphere to a temperature of 300 °C with vigorous stirring. Stock solution (1 mL, see below) was rapidly injected and the solution was cooled to 260 °C for further growth. The growth was monitored by taking the absorption spectra of aliquots extracted from the reaction solution. Additional injections were used to grow larger diameter cores. Upon reaching the desired size, the reaction mixture was allowed to cool down to room temperature and was transferred to a glove box. Anhydrous toluene was added to the reaction solution, and the nanocrystals were precipitated by adding anhydrous methanol. The size distribution of the nanocrystals in a typical reaction was of the order of  $\pm 15\%$ . This was improved using size-selective precipitation with toluene and methanol as the solvent and non-solvent respectively.

**Stock solution of InAs core:** Under an Ar atmosphere,  $\text{InCl}_3$  (9 g) was dissolved in TOP (30 mL) at 260 °C with stirring. Then the solution was cooled, and taken into the glove box. The stock solution was prepared by mixing a desired amount of  $(\text{TMS})_3\text{As}$  and  $\text{InCl}_3$ -TOP solution with the As:In molar ratios at 1:2 to 1:1.5.

In the stock solution,  $\text{InCl}_3$  forms a complex with TOP. While this complex has not been isolated, several examples of  $\text{InCl}_3$ -phosphine oxide complexes have been discussed [44], and an interaction between the Lewis acid-like  $\text{InCl}_3$  and the strongly donating phosphine or phosphine oxide ligand would be expected. This complex is necessary for the success of the reaction, as it helps to maintain the solubility of the reaction intermediates and establishes the interaction that ultimately passivates the surface of the nanocrystals.

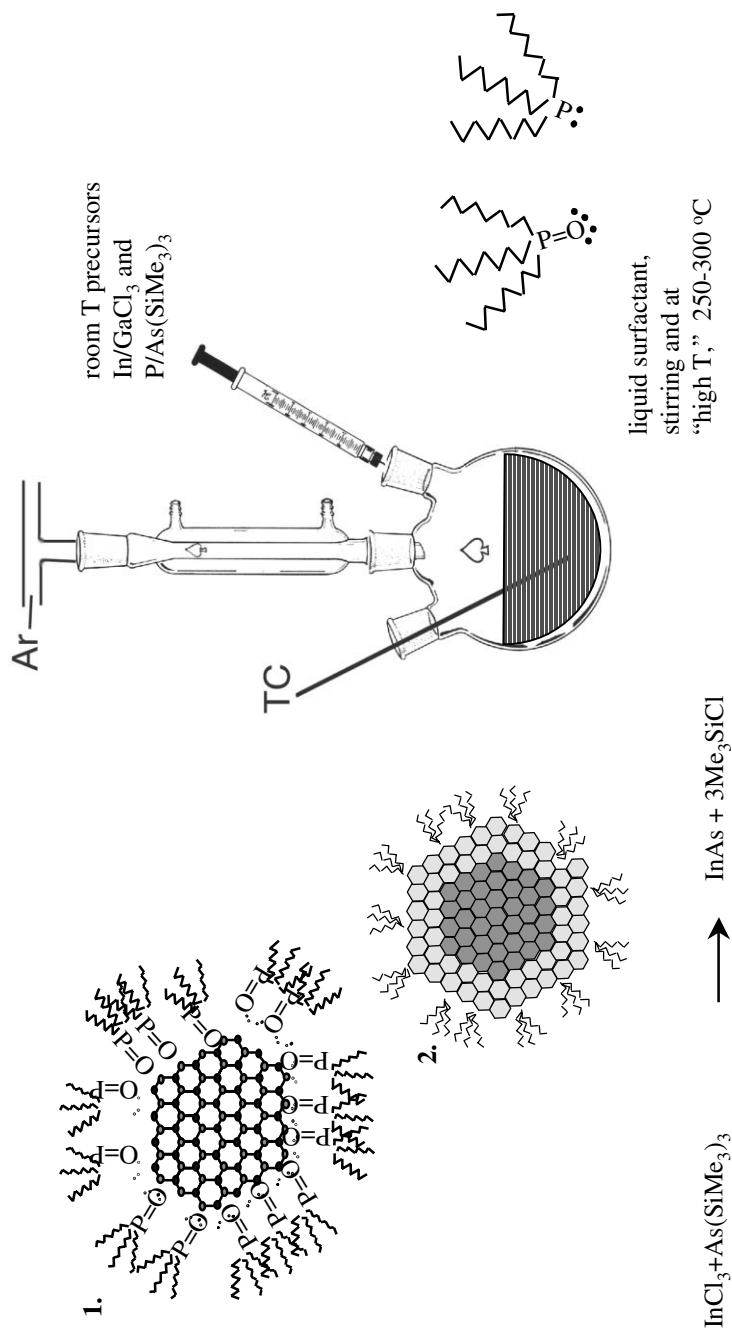


**Fig. 3-13** Schematic reaction setup and reaction scheme for III–V semiconductor nanocrystals consisting of either cores coated by organic ligands (1) or core/shell nanocrystals (2).

It is valuable to examine this nanocrystal synthesis using the methodology of nucleation, growth, and termination described earlier. While the details of the reaction's initial stages have not been worked out, we can look to the work of Barron [43] and Wells [45] to provide insight into the structure of these initial reaction intermediates in the case of InP. Both groups have used the  $\text{InCl}_3 + \text{P}(\text{Si}(\text{CH}_3)_3)_3$  reaction to synthesize bulk InP at temperatures above 400 °C while investigating intermediate products at lower temperatures. They report a stepwise elimination of the three equivalents of  $(\text{CH}_3)_3\text{SiCl}$ , beginning with the formation of  $[\text{Cl}_2\text{InP}(\text{SiCH}_3)_2]_x$  at room temperature or below. The exact intermediate product in the reaction discussed here probably has a slightly different structure due to the action of the coordinating solvent and evidenced by the increased solubility of the product, but the important element is the formation of the In–P bond. Wells further establishes this In–P interaction by providing a crystal structure for the related 1:1 adduct  $\text{I}_3\text{In}\cdot\text{P}(\text{Si}(\text{CH}_3)_3)_3$ . Barron sees evidence of the elimination of additional  $(\text{CH}_3)_3\text{SiCl}$  at temperatures as low as 150 °C along with the appearance of peaks in the XPS spectrum characteristic of indium in an InP environment. However, to eliminate the final equivalent of  $(\text{CH}_3)_3\text{SiCl}$  and obtain crystalline material, higher temperatures are required, with reactions producing InP or InAs nanocrystals at a minimum of about 240 °C.

The termination of the particle is accomplished by the coordinating solvent medium. Both TOPO and TOP are effective in passivating the particle surface. TOP is known as a strong donor ligand, with both high polarity and polarizability contributing to its donor strength [44, 46, 47]. Based on analogy to CdSe and standard donor-acceptor analysis, TOP would coordinate to acceptor indium surface sites providing a passivating shell to terminate growth, prevent agglomeration among particles, and through its alkyl groups provide for excellent solubility in organic solvents such as toluene and hexanes.

In order to study size-dependent phenomena, a variety of different sizes, each with a narrow size distribution, need to be isolated. By taking advantage of the differential solubility of various sizes of nanocrystals, narrow size distributions can be obtained using size-selective precipitation techniques. The solubility of a specific nanocrystal is determined by several factors, most notably the size of the particle, its shape, and the nature of the particle surface. Because of the alkyl groups of the TOP cap, the particles are soluble in relatively nonpolar solvents. If a more polar solvent is added to a solution of nanocrystals, the ability of the combined solvent system to solvate the nanocrystals will be reduced. The mechanism of agglomeration is dominated by attractive Van der Waals forces between particles [48–51], and at some composition of solvents the solvation ability of the system will no longer overcome these attractive forces and the particles will begin to agglomerate and precipitate. The key to size-selective precipitation is the fact that different sizes, shapes, and surface coverages will have different solubilities and thus can be separated. Assuming that the dominant difference in the nanocrystals is that of particle size, the ensemble of nanocrystals will be separated by size, while the degree of resolution among sizes will be determined by the smaller differences in the sample such as shape or surface structure. The largest particles will precip-

itate first because of their stronger attraction. One primary solvent system employed is toluene/methanol. The nanocrystals are soluble in toluene, but are insoluble in highly polar methanol. Starting with the initial reaction mixture diluted in toluene, the incremental addition of methanol results in the size-selective precipitation of the nanocrystals and the isolation of nanocrystals with individual size distributions.

### Structural and Basic Optical Characterization of InAs and InP Nanocrystals

The evaluation of nanocrystal structure encompasses several important areas including the identity and crystallinity of the core, the morphology of the particles, and the composition of the nanocrystal surface. The crystallinity of the core can be studied using powder XRD, electron diffraction, and the morphology of the particles, including their shape and size distributions, determined by transmission electron microscopy (TEM). X-ray photoelectron spectroscopy (XPS) can be used to examine the nanocrystal composition, with particular attention to the surface capping groups and will be discussed in a later section concerning the core/shell nanocrystals. InAs and InP nanocrystals will be treated together, with representative data shown from one or both systems.

Powder X-ray diffraction spectra of a series of InAs nanocrystal sizes are shown in Figure 3-14. The peak positions index well with the bulk InAs lattice reflections. Information on the domain size of the sample can be obtained from the width of the lattice reflections using the Debye-Scherrer formula for spherical particles [52]:

$$D = \frac{1.2\lambda}{[(\Delta 2\theta)(\cos \theta)]}$$

In this equation,  $\lambda$  is 1.5418 Å for CuK $\alpha$  radiation,  $\Delta 2\theta$  is the measured linewidth in radians,  $\theta$  is 1/2 of the measured diffraction angle, and  $D$  is the estimated particle size in Angstroms. An average domain size for a given sample was obtained by averaging  $D$  for the (111), (220), and (311) peaks and is shown in the figure.

TEM is crucial for investigating the structure of the nanocrystals as it allows a direct evaluation of both the size and shape of the particles. A high-resolution TEM image of InAs nanocrystals, 2 and 6 nm in diameter, is shown in Figure 3-15. Cross fringes are observed, indicating a high degree of crystallinity, with the lattice spacings indexing to those of InAs. The nanocrystals are almost spherical.

TEM is also essential for calculating the size and size distribution of a nanocrystal sample. For the wide variety of size-dependent properties exhibited by the nanocrystals, this is clearly a crucial measurement. Size distributions can be obtained by the direct measurement of images of large numbers of nanocrystals, typically a few hundred. The results of these measurements for InP show size distributions with standard deviations of about 20%, while for InAs the distributions are substantially narrower than 10%.

The quality of the size distribution is most clearly borne out in Figure 3-16, showing ordered self-assembled solids of InAs nanocrystals, with diameter of 5.8

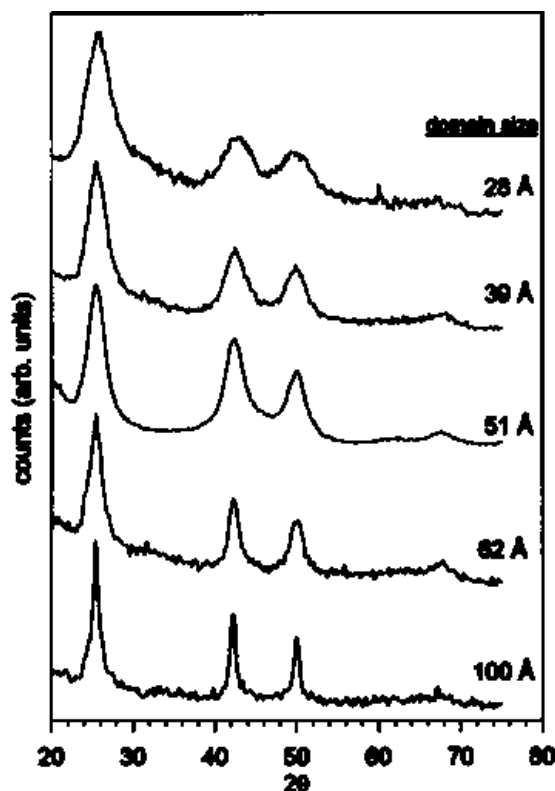
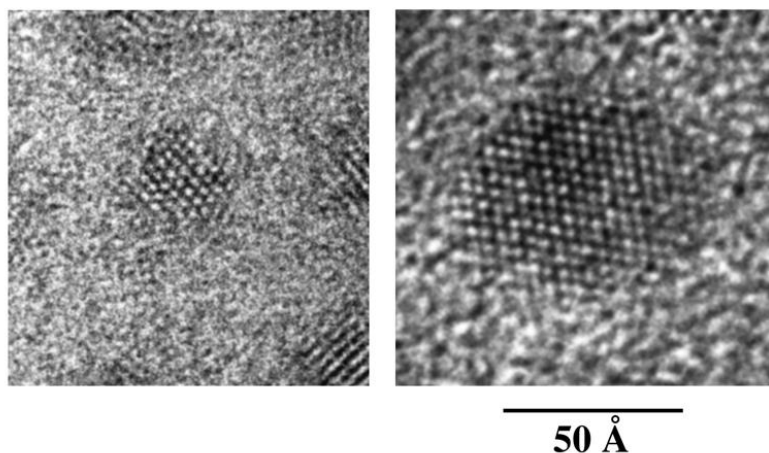


Fig. 3-14 Powder X-ray diffraction spectra of InAs nanocrystals of different sizes. The domain size was calculated from the width of the reflections as detailed in the text. Reproduced from *Appl. Phys. Lett.* **69**, 1432 (1996).

nm, dissolved in toluene, and deposited onto the TEM grid. Figures 3-16A–C exhibit the real space images for three different superlattice (SL) faces detected on the grid, while Figures 3-16D–F represent the optical diffraction patterns measured for the corresponding TEM negatives. Ordered domains extending over regions of lengths measured in microns were observed. Both the real space images and the diffraction patterns, which in effect correspond to a two-dimensional Fourier transform of the image, allow the assignment of the three different faces to different views along three zone axes of the close-packed face centered cubic (FCC) structure. Figure 3-16A and its corresponding diffraction pattern Figure 3-16D represent the superlattice when viewed along the  $(111)_{\text{SL}}$  zone axis, Figure 3-16B (diffraction Figure 3-16E) represent the  $(110)_{\text{SL}}$  zone axis, and Figure 3-16C (diffraction Figure 3-16F) represent the  $(100)_{\text{SL}}$  zone axis. Figure 3-16G–I show images of ordered monolayers with three different packings corresponding to three different superlattice faces resolved in Figures 3-16A–C respectively.



**Fig. 3-15** HRTEM images of two InAs nanocrystals, 2.2 and 5 nm in diameter. Reproduced from *Appl. Phys. Lett.* **69**, 1432 (1996).

Quantum confinement effects of nanocrystals are evidenced most clearly in the optical properties of the system as the electronic energy levels of the clusters become a function of size. A detailed account of this aspect will be provided in Chapter 5. Basic optical characterization of semiconductor nanocrystals provides important information on particle size, from the position of the band gap energy, and on the size distribution, from the sharpness of peaks in absorption and luminescence. Figure 3-17 shows room temperature absorption spectra for a series of InAs nanocrystal sizes along with the photoluminescence spectra. The quantum confinement effects are clearly evident from the size-dependent nature of the spectra. The band gap in all samples is shifted substantially from the bulk InAs gap of 0.42 eV. In all samples, the onset of absorption is characterized by a distinct feature at the absorption edge corresponding to the first excitonic transition. Additional features are resolved at higher energy, corresponding to higher excited states. All states shift with nanocrystal size. The width of the features is primarily due to inhomogeneous broadening resulting from size variations of the particles within a specific sample. The size distribution as obtained from TEM is shown in the right-hand frame of Figure 3-17. The absorption of InP nanocrystals shows similar effects, the absorption onset shifting to the blue with decreasing cluster diameter as discussed in [4].

#### 3.1.2.4 III–V Core/Shell Nanocrystals – Synthesis and Characterization

The emission color from semiconductor nanocrystal quantum dots is tunable by the size as a result of the quantum-confinement effect [53, 54]. Harnessing this emission for real-world applications such as biological fluorescence marking [55, 56] and optoelectronic devices [11, 57–60] is an important challenge, which imposes stringent requirements for a high fluorescence quantum yield (QY) and stability against photo-degradation. These characteristics are difficult to achieve in



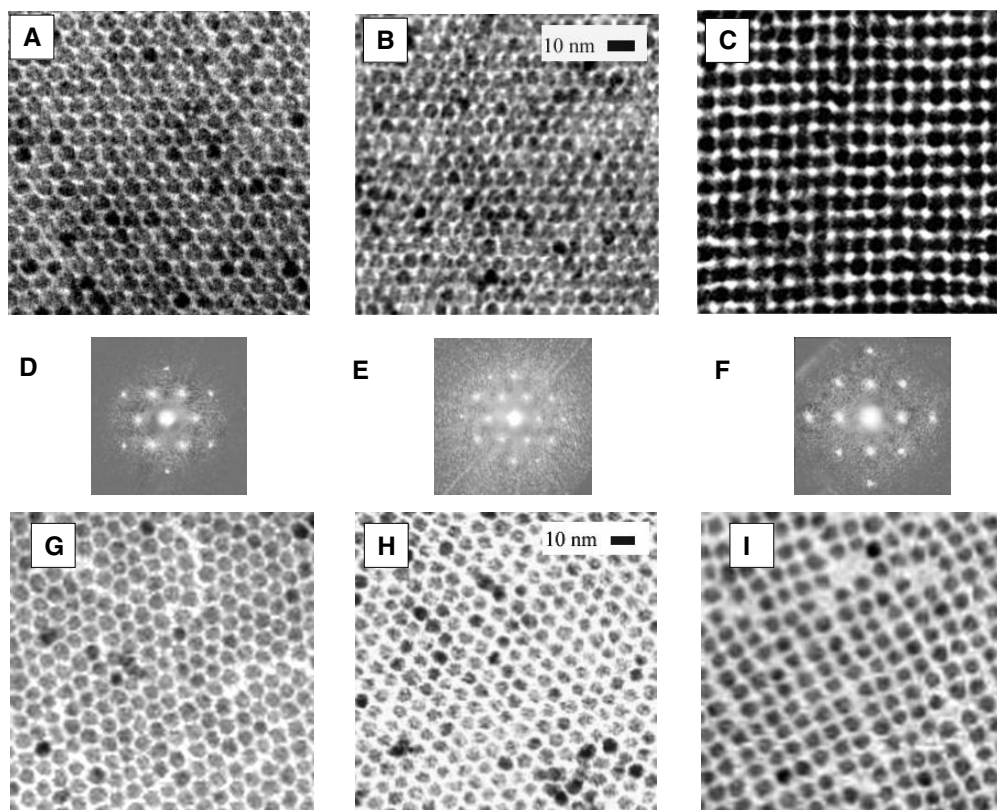


**Fig. 3-16** TEM images of arrays and superlattices prepared from InAs nanocrystals, 5.8 nm in diameter. Frames A–C show ordered superlattices prepared from InAs nanocrystals,

while frames D–F show the optical diffraction pattern from the micrographs. Frames G–I show TEM images of monolayers. See text for details.

semiconductor nanocrystals coated with organic ligands because of imperfect surface passivation. In addition, the organic ligands are labile in exchange reactions because of their weak bonding to the nanocrystal surface atoms [37]. As discussed previously, a proven strategy for increasing both the fluorescence QY and the stability is to grow a shell of a higher band gap semiconductor on the core nanocrystal [23–27, 61]. In such composite core/shell structures, the shell type and shell thickness provide further control for tailoring the optical, electronic, electrical and chemical properties of semiconductor nanocrystals. Several reports of III–V core/shell nanocrystals have already been mentioned, and here we shall focus on our own detailed study of core/shell nanocrystals with InAs cores [6–7]. The band gap energy of these core/shell nanocrystals is tunable in the near IR (NIR) spectral range, covering the wavelengths that are important for telecommunication applications. Recently, they were successfully incorporated with semiconducting polymers to form an LED structure that provides efficient electroluminescence at

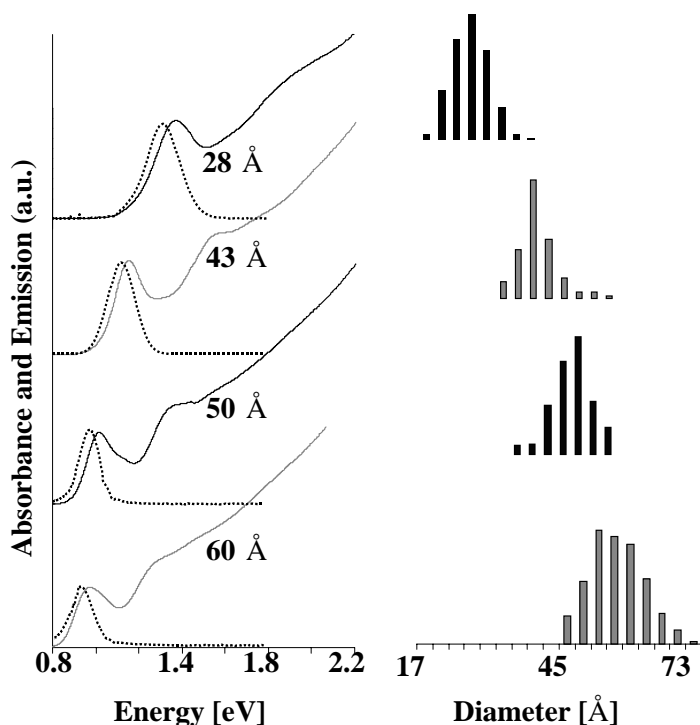


**Fig. 3-17** The right-hand panel shows the distribution of diameters for 4 InAs nanocrystal samples obtained from HRTEM measurements. The left-hand panel displays the room temperature absorption (solid lines), and emission spectra (dashed lines) for the corresponding samples. The mean diameter of each sample is noted. Reproduced from *Superlatt. Microstruct.* **22**, 559 (1996).

1.3  $\mu\text{m}$  [11]. These core/shell nanocrystals may be further developed to serve as efficient fluorescent labels for biological applications in the NIR range.

The core/shell approach is conceptually closely related to the approach used in two-dimensional quantum wells [62]. In a quantum well, a thin layer, of nanometric dimensions, of a low band gap semiconductor is sandwiched between thick layers of a high band gap semiconductor, forming a square potential well for the electron and hole wavefunctions. The determining factor for growth of quantum wells is the lattice mismatch between the two semiconductors. The electronic properties of the quantum well are determined primarily by the energetic offsets between the conduction and valence band edges of the two semiconductors. Therefore, the influence of the lattice mismatch and the band offsets on the growth and electronic properties of core/shell nanocrystals with InAs cores was investigated. Figure 3-18 shows schematically the values of both parameters for InAs and a variety of shell materials [63]. The lattice mismatch ranges from nearly zero for CdSe shells to as high as 10.7% for ZnS shells. The band offsets cover a broad range of values as well. Note that the shell materials include both II–VI and III–V

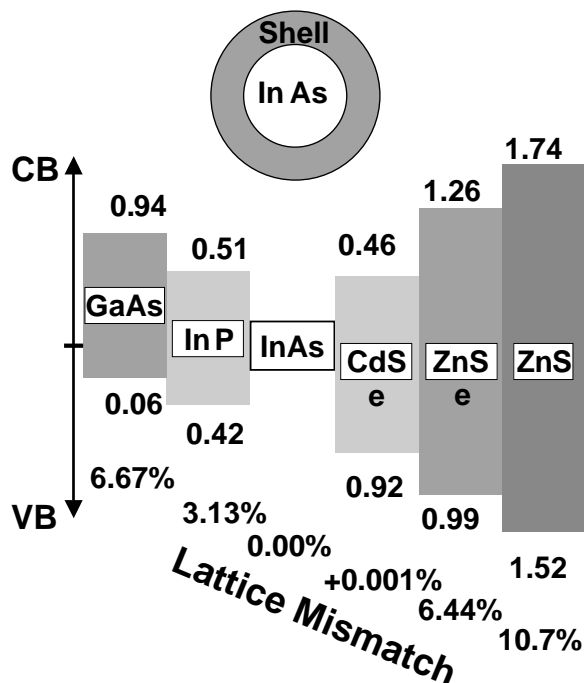


**Fig. 3-18** Summary of the band offsets (in eV) (right side) grown in this work. CB = conduction band; VB = valence band. Reproduced from *J. Am. Chem. Soc.* **122**, 9692–9702 (2000).

semiconductors, a selection that provides substantial tunability for the properties of the composite core/shell nanocrystals.

### Synthesis of Core/Shell Nanocrystals with InAs Cores

The preparation of the InAs core/shell nanocrystals is carried out in a two-step process. In the first step the InAs cores are prepared using the injection method with TOP as solvent, which has enabled us to obtain hundreds of mg of nanocrystals per synthesis, as detailed earlier. We used size-selective precipitation to improve the size distribution of cores to  $\sigma \sim 10\%$ . In the second step, the shells of the various materials were grown on these cores. This two-step approach follows the methods developed for synthesis of the II–VI core/shell nanocrystals.

The details of the synthesis of the core/shell nanocrystals can be found elsewhere [6, 7]. Briefly, TOP-capped InAs cores (5–20 mg) were dissolved in TOP (3–6 g, or a mixture with TOPO) in a three-necked flask. Under Ar flow on a Schlenk line, the nanocrystal solution was heated to 260 °C, and the shell precursor solution was introduced into the hot solution by drop-wise addition. The growth of core/shells was monitored by UV-VIS spectroscopy of aliquots taken from the reaction flask. After the desired shell thickness had grown, the reaction

mixture was cooled to room temperature. Core/shell nanocrystals passivated by TOP were obtained by precipitation using a mixture of methanol and toluene.

Attempts to carry out the growth of III–V semiconductor shells, InP and GaAs, at a temperature of 160 °C in TOP were not successful. Low temperature reduces the rate of nucleation of nanocrystals of the shell material, which is an undesired process competing with shell growth. In addition, the alloying process of core and shell materials is less likely at low temperatures. However, growth could not be achieved at this low temperature. These shells could be grown only at higher temperatures:  $T > 240$  °C. This minimal temperature is required to overcome the reaction barrier for the precursors, similarly to the conditions required for growth of III–V semiconductor nanocrystal cores. Above this limit, controlled growth of InP shells of varying thickness was achieved.

Thin GaAs shells could also be grown, but, in contrast to InP shells, growth was limited to a thickness of less than two monolayers. This difference may be related to strong bonding of Ga to TOP, consistent with the observation that it is difficult to synthesize GaAs nanocrystals in this way [64]. An additional difference between the GaAs and the InP shells is in the solubility of the core/shell nanocrystals of each kind. InAs/InP core/shells are readily soluble in organic solvents after precipitation of the nanocrystals from the growth solution. Special conditions were required to obtain good solubility of the InAs/GaAs core/shells [1].

In contrast to the III–V semiconductor shells, the growth of the II–VI semiconductor shells, CdSe, ZnSe and ZnS, was observed even at much lower temperatures (above 150 °C). For CdSe shells, it was found that to limit the nucleation and achieve controlled shell growth TOP could be used instead of TOPO as the growth medium. This is consistent with stronger bonding of Cd to TOP versus TOPO.

For InAs/ZnSe and InAs/ZnS core/shells grown in TOP, solubility after separation from the growth solution is poor as the TOP ligands can easily be removed by methanol. Additionally, upon growth of thick ZnS shells, substantial nucleation of ZnS nanocrystals was observed by XRD measurements. To overcome these difficulties, a TOP-TOPO mixture can be used as the growth solution instead of TOP. In this case, nucleation could be minimized, and soluble nanocrystals were obtained. The growth rate of ZnSe and ZnS shells was substantially lower for the TOP-TOPO mixture compared with TOP. These features are consistent with stronger bonding of Zn to TOPO versus TOP, as was reported in the synthesis of ZnSe nanocrystals [65]. Cd is a softer Lewis acid than Zn and binds strongly to TOP, a softer Lewis base than TOPO, while Zn, the harder Lewis acid, binds more strongly to TOPO the harder Lewis base. This follows the general hard-soft concept for interaction strength between Lewis acids and bases [66].

### Optical Characterization of the Core/Shell Nanocrystals

The most direct and immediate probes for shell growth are the absorption and fluorescence spectra. Figure 3-19 shows the sequence of absorption spectra measured for aliquots taken from the reaction solution during the growth of InP shells on InAs cores with an initial radius of 1.3 nm. The first absorption peak shifts to

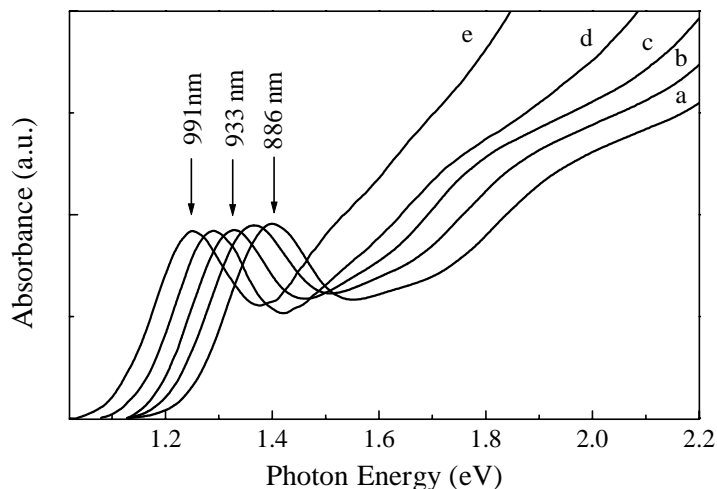


**Fig. 3-19** Evolution of the absorption spectra during the growth of InP shells on InAs cores with an initial radius of 1.3 nm (a). The InP shell thickness in number of monolayers is: (b) 0.5, (c) 1.1, (d) 1.7, (e) 2.5. Reproduced from *J. Am. Chem. Soc.* **122**, 9692–9702 (2000).

the red upon shell growth. The red shift occurs because the conduction band offset between InAs and InP is smaller than the confinement energy of the electron, and, as the shell grows, the electron wavefunction extends to a larger box and its confinement energy is lowered. As the electron effective mass,  $m_e^*$ , in InAs is extremely small ( $m_e^* = 0.024m_e$ ,  $m_e$  is the mass of the free electron [67]), it is highly delocalized, and a large potential step is required to confine it to the core. The spectral features remain sharp during the reaction, indicating that the growth is controlled and the size distribution is maintained. However, the fluorescence of the InAs/InP core/shells is quenched substantially as compared to the original cores.

For CdSe, which has a conduction band offset similar to that of InP, shell growth also leads to a red shift of the absorption onset. Figure 3-20A,B shows the evolution of the absorption and the emission spectra during growth of InAs/CdSe core/shells with two different initial core radii, 1.2 nm (Figure 3-20A), and 2.5 nm (Figure 3-20B). As in the case of InP shells, this red shift results from the lower confinement energy of the electron, whose wavefunction extends to the shell region. In this case, the sharpness of the spectral features is partially washed out during the growth. In contrast to InAs/InP core/shells, the band gap fluorescence QY for InAs/CdSe core/shells is substantially enhanced, up to a maximum value of 21%, nearly 20 times larger than the QY of the cores. These values of the QY compete favorably with QY values for organic NIR laser dyes [12]. This pronounced difference in emission of InP versus CdSe shells was ascribed to the different in the quality of the outer surface of the nanocrystals. In both cases, the similar and relatively small conduction band offset leads to a substantial probability of the presence of the electron wavefunction at the nanocrystal surface. As a result, for

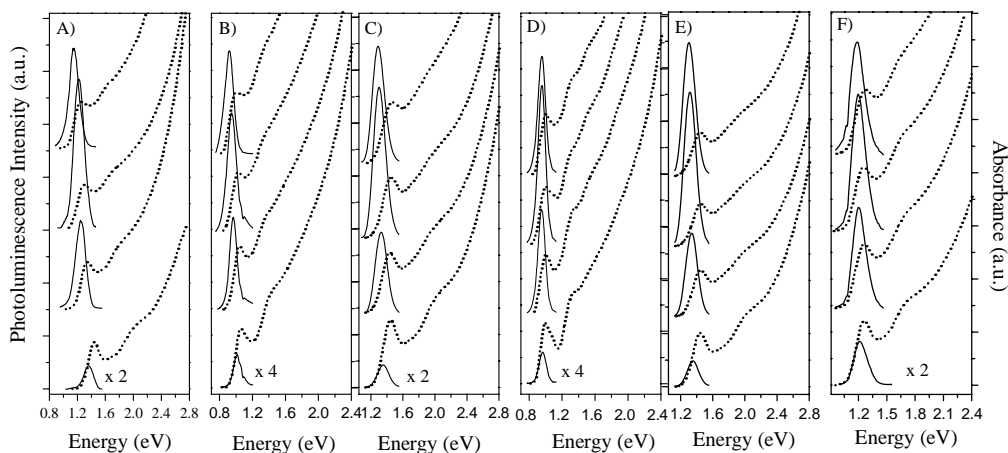


**Fig. 3-20** Evolution of absorption (dashed lines), and photoluminescence (solid lines) for growth of core/shells. The PL spectra are given on a relative scale for comparison of the enhancement of QY with shell growth. Reproduced from *J. Am. Chem. Soc.* **122**, 9692–9702 (2000). A. InAs/CdSe with initial core radius of 1.2 nm. The shell thickness (in number of monolayers) and QY for the traces from bottom to top are respectively: 0, 1.2%; 0.6, 13%; 1.2, 21%; 1.8, 18%. B. InAs/CdSe with initial core radius of 2.5 nm. The shell thickness (in number of monolayers) and QY for the traces from bottom to top are respectively: 0, 0.9%; 0.7, 11%; 1.2, 17%; 1.6, 14%. C. InAs/ZnSe with initial core radius of 1.2 nm. The shell thickness (in number of

monolayers) and QY for the traces from bottom to top are respectively: 0, 1.2%; 0.6, 9%; 1.5, 18%; 2.5, 14%. D. InAs/ZnSe with initial core radius of 2.8 nm. The shell thickness (in number of monolayers) and QY for the traces from bottom to top are respectively: 0, 0.9%; 0.7, 13%; 1.3, 20%; 2.2, 15%. E. InAs/ZnS with initial core radius of 1.2 nm. The shell thickness (in number of monolayers) and QY for the traces from bottom to top are respectively: 0, 1.2%; 0.7, 4%; 1.3, 8%; 1.8, 7%. F. InAs/ZnS with initial core radius of 1.7 nm. The shell thickness (in number of monolayers) and QY for the traces from bottom to top are respectively: 0, 1.1%; 0.6, 5%; 1.3, 7.1%; 2.2, 6.3%.

both cases the emission is sensitive to the outer surface and susceptible to trapping in unpassivated surface sites. Indeed, this problem is known for InP nanocrystals prepared in TOP/TOPO, which have a very low fluorescence QY that could be enhanced by surface treatments such as oxidation and etching [22]. CdSe TOP/TOPO-coated nanocrystals, on the other hand, display band gap emission with a room temperature QY of a few percent.

ZnSe and ZnS are shell materials with much larger band offsets relative to that of InAs. The evolution of the absorption and emission spectra for ZnSe and ZnS shell growth on cores with various radii is presented in Figures 3-20C,D and 3-20E,F respectively. For both core/shells, the absorption onset is nearly the same as in the original core. This can be explained by the large conduction and valence band offsets of ZnSe and ZnS relative to InAs, which create a substantial potential barrier for the electron and hole wavefunctions at the core/shell interface. Unlike the CdSe and InP shells, here the electron and hole wavefunctions are both confined primarily to the core region, and thus the band gap does not shift from the value of

the core. As shown in Figures 3-20C–F, the fluorescence QY is enhanced for both shells. For ZnSe the maximum QY values are 20%, while in ZnS the maximum QY is 8%, achieved for a shell thickness of 1.2–1.8 monolayers. With further shell growth, the QY decreases. This reduction may be ascribed to trapping of the charge carriers at the core/shell interface. The lattice mismatch between InAs and both ZnSe and ZnS is large. In thin shells the strain can still be sustained, and epitaxial growth of the shell on the core can occur. With further shell growth, defects may form at the core/shell interface, and these could trap the carriers, leading to the gradual reduction of QY in the thicker shells. A similar observation was reported for the II–VI semiconductor core/shells CdSe/ZnS and CdSe/CdS [25, 26].

The selection of core/shells extends the control afforded over the electronic properties of the composite nanocrystals. As an example of the flexible control, two types of core/shells are demonstrated, InAs/ZnSe and InAs/CdSe, which emit strongly at 1.3  $\mu\text{m}$ , a wavelength with significant technological importance in fiber-optic communications. Figure 3-20B presents the absorption and emission for a CdSe shell overgrown on a core with a radius of 2.5 nm. The core band gap emission is at 1220 nm, and with the growth of the shell the emission shifts to the red. This is accompanied by substantial enhancement of the QY, up to a value of 17% achieved at 1306 nm. For ZnSe shells the band gap hardly shifts. Figure 3-15D shows that using a bigger core, with radius of 2.8 nm, we could achieve a high QY of 20% at 1298 nm by growing the ZnSe shell. Such core/shell nanocrystals were recently used as the optically active chromophores in efficient light-emitting diodes covering the near IR spectral range [11]. The LED was based on a nanocrystal-semiconductor polymer composite.

### Chemical and Structural Characterization

**X-ray photoelectron spectroscopy (XPS):** XPS can be used effectively to examine the chemical composition of the core/shells [68]. Figure 3-21 shows the XPS survey spectra for InAs cores of radius 1.7 nm and for InAs/CdSe core/shells prepared with the same core and with shell thickness of 3 monolayers. Indium and arsenic peaks are clearly resolved for the core (lower spectrum). Additional peaks belonging to Cd and Se, the shell materials, can be identified in the core/shells (top spectrum). The ratio of the core atom XPS peak heights for cores to core atom XPS peak heights for core/shells is energy dependent. The relative intensity of the peaks at high binding energies (e.g.,  $\text{In}_{\text{MNN}}$ ), which have a small kinetic energy and thus a small escape depth, is quenched more upon shell growth, compared with the peaks at small binding energy and large escape depth (e.g.,  $\text{As}_{\text{LMN}}$ ).

High-resolution XPS provides quantitative evidence for shell growth based on the finite escape depth,  $\lambda$ , of photoelectrons from the core atoms [26]. The typical escape depths are of the order of the shell thickness, and the photoelectron signal from core atoms should decrease accordingly in the core/shell structure [68].

The application of XPS to the study of shell growth is demonstrated in Figure 3-22, showing the XPS data for InAs/ZnSe core/shells with an initial core radius of 1.7 nm. We performed high-resolution XPS measurements on a sequence of core/

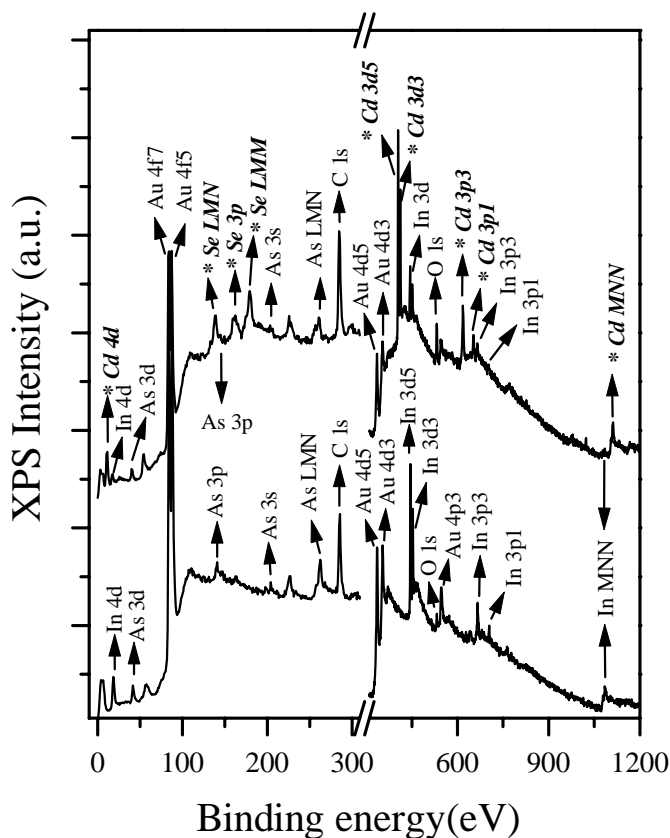


**Fig. 3-21** XPS survey spectrum for InAs cores with radius of 1.7 nm (lower trace), and for InAs/CdSe core/shells with shell thickness of 3 monolayers (top trace). The assignment of the peaks is indicated. The new peaks in the XPS spectrum for the core/shells associated with Cd and Se are emphasized in bold italic type. Reproduced from *J. Am. Chem. Soc.* **122**, 9692–9702 (2000).

shell samples of varying thickness. The figure shows the experimental results (squares) for the log of the ratio of the  $\text{In}_{3d5}$  to the  $\text{In}_{\text{MNN}}$  Auger peak, normalized by the ratio in the core. The ratio increases upon ZnSe shell growth. The number of atoms for the two peaks is identical, and the increase in the ratios is due to the difference in the escape depths, which is lower for the Auger peak. As a result, the shell growth leads to larger reduction in the relative intensity of the Auger peak. To check these effects, the expected ratio for a spherical geometry was simulated assuming a core/shell configuration (solid line), or alloy formation (dashed line). Clearly, only the calculated ratio for the core/shell structure is in agreement with experimental data.

**Transmission electron microscopy:** Figure 3-23 presents HRTEM images of core and core/shell nanocrystals. Frame B shows a micrograph of an InAs core with a



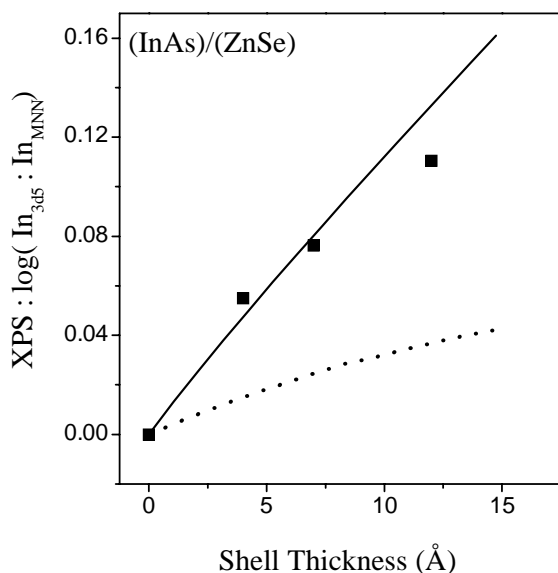


**Fig. 3-22** Summary of high-resolution XPS data for InAs/ZnSe. The log of the ratio of the intensity of the In<sub>3d5</sub> to that of the In<sub>MNN</sub> is plotted against the shell thickness. The ratio is normalized to the ratio in the cores. Squares:

experimental data. Solid line: calculated ratio for core/shell structure. Dotted line: calculated ratio for alloy formation. Reproduced from *J. Am. Chem. Soc.* **122**, 9692–9702 (2000).

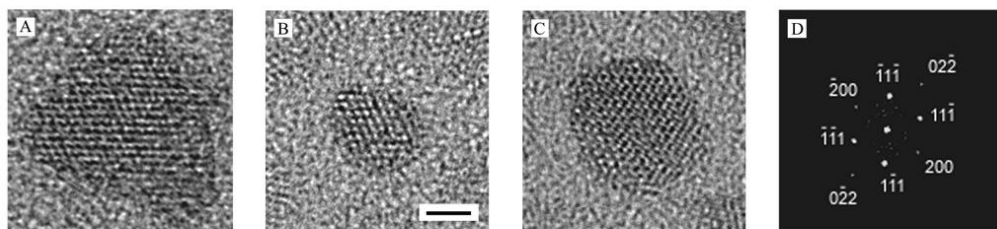


**Fig. 3-23** HRTEM images of InAs/InP core/shell (frame A, core radius 1.7 nm, shell thickness 2.5 nm), InAs core (frame B, core radius 1.7 nm), and InAs/CdSe core/shell (frame C, core radius 1.7 nm, shell thickness 1.5 nm). The scale bar is 2 nm. The

nanocrystals are viewed along the [011] zone axis. Frame D shows the Fourier transform of image C, and the pattern corresponds to the diffraction pattern from the 011 zone of the cubic crystal structure. Reproduced from *J. Am. Chem. Soc.* **122**, 9692–9702 (2000).

radius of 1.7 nm, and frames A and C respectively show InAs/InP and InAs/CdSe core/shell nanocrystals with thick shells grown on similar cores. The crystalline interior is viewed along the [011] zone axis of the cubic lattice. The cubic lattice is resolved for the InAs/CdSe core/shell as well, as clearly revealed also by the Fourier transform of the image presented in Figure 3-23D. CdSe nanocrystals grown in such conditions form the wurtzite structure, but here they adopt the cubic structure on the InAs core. For all three cases, the fringes are visible across the entire nanocrystals in accordance with epitaxial shell growth in these particles.

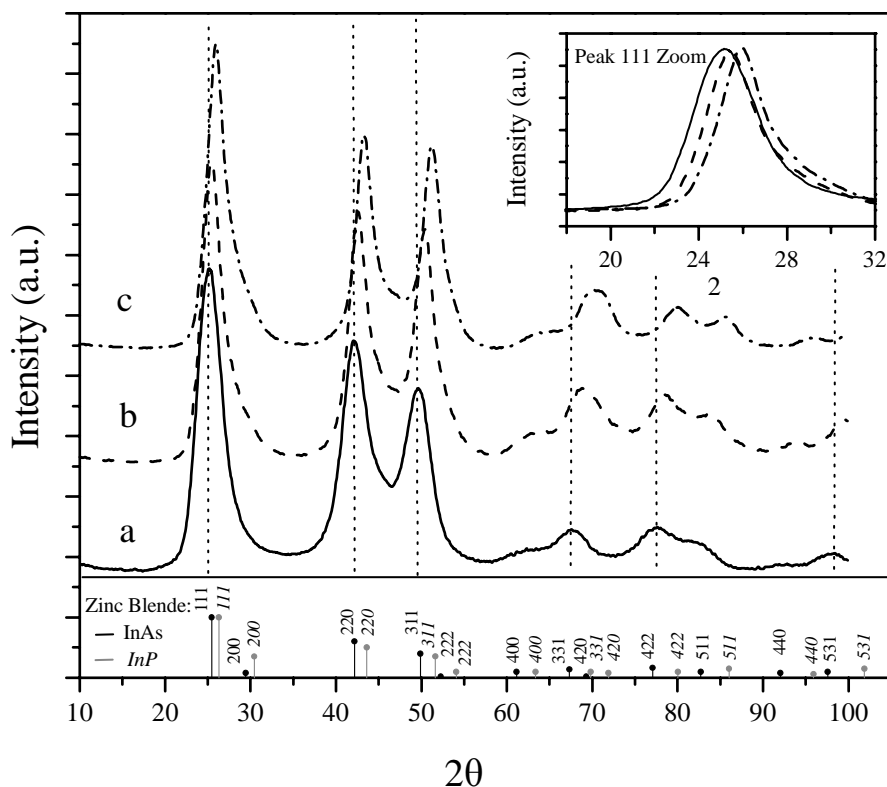


**Fig. 3-24** XRD patterns for InAs cores with radius of 1.7 nm (trace *a*, solid line), and InAs/InP core/shells with shell thickness of 2.4 monolayers (trace *b*, dashed line), and 6.2 monolayers (trace *c*, dot-dashed line). The

inset shows a zoom of the 111 peak. The diffraction peak positions of bulk cubic InAs (dark) and InP (light, italic) are indicated. Reproduced from *J. Am. Chem. Soc.* **122**, 9692–9702 (2000).

**X-ray diffraction:** Powder XRD patterns for the InAs core, radius 1.7 nm, and for InAs/InP core/shells with increasing thickness are presented in Figure 3-24. The InAs XRD pattern consists of the characteristic peaks of cubic InAs, which are broadened because of the finite crystalline domain. With InP shell growth, the diffraction peaks shift to larger angles consistent with the smaller lattice constant for InP compared with InAs. The shift is most clearly resolved for the high angle peaks. In addition, the diffraction peaks narrow. This is demonstrated for the (111) peak shown in the inset of Figure 3-24. This narrowing indicates that the crystalline domain is larger for the core/shells, providing direct evidence for epitaxial growth mode of the shell. The relatively simple diffraction pattern for cubic InAs allows a clear observation of the narrowing as the shell is grown. In contrast, in the case of cores/shells with CdSe cores, the narrowing is masked by the complex diffraction pattern of the wurtzite structure [15].

The XRD patterns for a series of core/shells with different shell materials and varying thickness are displayed in Figure 3-25 (filled circles). The general pattern

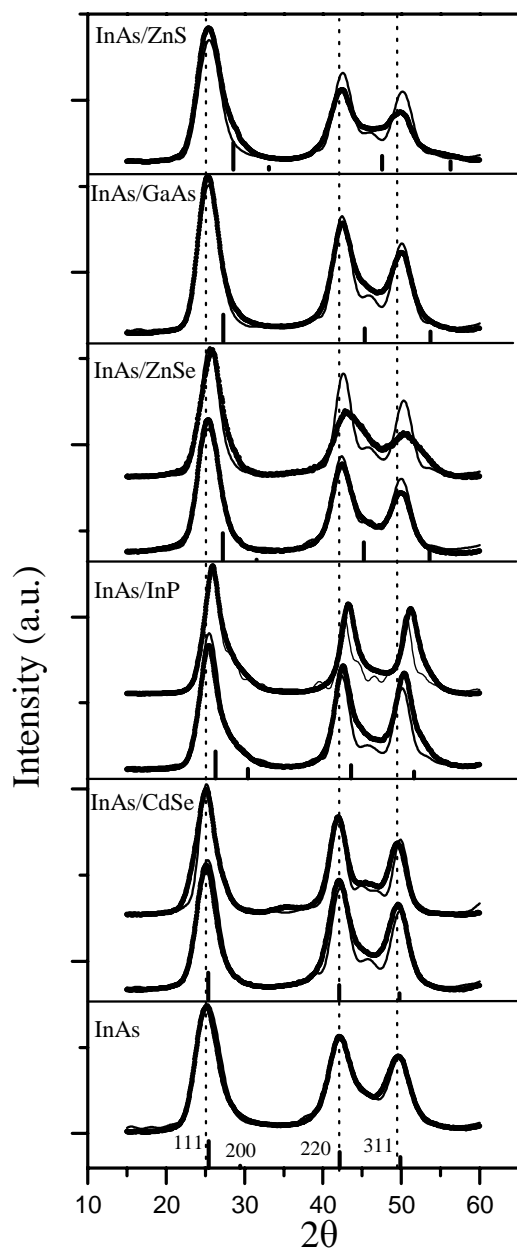


**Fig. 3-25** X-ray diffraction patterns for InAs cores and various core shells. The experimental curves (filled circles) are compared with the simulated curves (thin solid lines). See text and Table 1 for the details of the simulated structures. The markers on the bottom of each frame indicate the diffraction peak positions

and the relative intensities for the InAs core material (lower frame) and the various shell materials (other traces). The vertical dashed lines indicate the positions of the InAs core nanocrystal diffraction peaks. Reproduced from *J. Am. Chem. Soc.* **122**, 9692–9702 (2000).

of the cubic lattice is maintained for all materials. The diffraction peaks narrow with shell growth in the case of CdSe, ZnSe, and GaAs shells for the reasons discussed above. But this is not the case for ZnS, probably because of the very large lattice mismatch of ZnS and InAs (10.7%). In this case, the large strain may lead to cracking at the InAs/ZnS interface already at early growth stages. Moreover, ZnS nanocrystals in these growth conditions preferentially form the wurtzite structure, which may create additional defects upon shell growth. Both effects may explain the relatively small enhancement of the PL QY for the ZnS shells.

To further prove the interpretation of the XRD data and to obtain more quantitative information about the core/shell structures, the powder diffraction patterns were simulated [7, 69]. Nanocrystals are built by stacking planes along the (111) axis of the cubic lattice. The sum of the specified core radius,  $r_c$ , and shell thickness,  $r_s$ , was used to carve out the nanocrystal assuming a spherical shape.

The experimental data (filled circles) and the simulation results (thin lines) for the core and a series of core/shells are displayed in Figure 3-25. The simulation of the cores fits the experimental data very well. The fit was obtained using the simulated XRD pattern for an equally weighted combination of two kinds of core nanocrystal structures with the same radii, differing in the (111) plane stacking sequence. Both nanocrystal structures have three stacking faults. The experimental diffraction intensity between the (220) and the (311) peaks does not go to zero, while in the simulated pattern for nanocrystals without stacking faults the value is close to zero. Thus, three stacking faults along the (111) direction are required to quantitatively reproduce the experimental pattern. Introduction of surface disorder has little effect on the simulated patterns.

For InAs/CdSe core/shells, the lattice mismatch is zero. The experimental peak positions do not shift with shell growth. This is well reproduced in the simulation. An additional stacking fault was added in the shell region for the thicker shell of three monolayers, to better reproduce the experimental pattern.

For the other core/shells there is a lattice mismatch, which ranges from 3.13% for InP to 10.7% for ZnS. A gradual shift of the diffraction peaks with shell growth towards larger angles is observed for these core/shells (Figures 12 and 13). This means that the lattice spacing is modified in the shell region. In order to achieve epitaxial growth mode, atoms in both core and shell regions at the core/shell interface must have identical lattice spacings. To simulate the smooth switching of the lattice spacing from the core to the shell, a Fermi-like switching function was used. This switching provides a physical model for understanding the epitaxial growth mode, while reproducing the observed change in the peak positions upon shell growth.

The simulated patterns reproduce the two main effects observed upon shell growth in InAs/InP, InAs/ZnSe, and InAs/GaAs core/shells, namely the shifting of all the diffraction peaks to larger angles and the narrowing of the peaks (Figure 3-25). This provides further evidence for the epitaxial shell growth mode. For InAs/ZnS, no narrowing was observed in the experimental diffraction pattern, indicating that in InAs/ZnS core/shells the interface region is not fully epitaxial, as explained above. Similarly to the case of InAs/CdSe core/shells, for the thick InP shells (6.2

monolayers), stacking faults had to be added in the shell region to better reproduce the experimental pattern. On average, a stacking fault exists for every four to five layers in InAs core/shell nanocrystals. In these stacking faults the bonds of atoms remain fully saturated, and charge carrier traps do not necessarily form. Therefore, it is likely that these planar stacking faults do not reduce the fluorescence QY substantially.

### Model Calculations for the Band Gap

The core/shell band offsets provide control for modifying the electronic and optical properties of these composite nanocrystals. To examine the effect of the band offsets of various shells on the band gap of the composite nanocrystals, calculations using a particle-in-a-spherical-box model were performed [16, 70]. Briefly, in this model the electron and hole wavefunctions are treated separately, and the coulomb interaction is then added within first order perturbation theory [71]. Three radial potential regions should be considered in the core/shell nanocrystals: core, shell and the surrounding organic layer. Continuity is required for the radial part of the wavefunctions for both electron and hole at the interfaces. In addition, the probability current,  $(1/m_i^*)(d/dr)R_i(k_i r)$ , where  $m_i^*$  is the effective mass in region  $i$ ,  $R_i$  is the radial part of the lowest energy  $1S_{e/h}$  electron or hole wavefunction, and  $k_i$  is the wave vector in region  $i$ , has to be continuous. The effective masses and dielectric constants of the bulk semiconductors were used in the calculations [67]. The band offsets were taken from [63]. First, for InAs cores of radius 1.7 nm, a barrier height of 4.5 eV was used for the surrounding organic layer for both carriers. The confinement energy for the electron is sensitive to the barrier height because of the small electron effective mass, while the heavier hole is much less sensitive. The experimental value is in reasonable agreement with the calculated band gap, although there is a deviation, which is understandable in this simplistic model [72]. The calculated versus measured relative change of the band gap upon growth of the different shells is plotted for various core/shells in Figure 3-26. The error in the band gap shifts should be small compared with that in the absolute band gap energies. The agreement for the band gap shifts is good. For the ZnS shells (dot-dashed line), hardly any shift is observed either in the experiment or in the calculations. This is consistent with the large band offsets between InAs and ZnS. For both InP (dashed line) and CdSe (solid line) shells, the experimental and calculated band gaps shift to the red upon shell growth. This is mainly because of the reduction in the electron confinement energy in these core/shells. The lowest  $1S_e$  level of the electron is above the core/shell barrier for both InP and CdSe shells, leading to a high probability of the presence of the electron in the shells.

### Stability of Core/Shell Nanocrystals

Core/shell passivation with a shell of a semiconductor material that has large band offsets compared with the core also provides increased protection and stability compared with the organically passivated core nanocrystals. The photostability of the core/shells was compared to IR140, a typical near IR organic laser dye [73]. Solutions of nanocrystals and of the dye saturated with oxygen were irradiated at

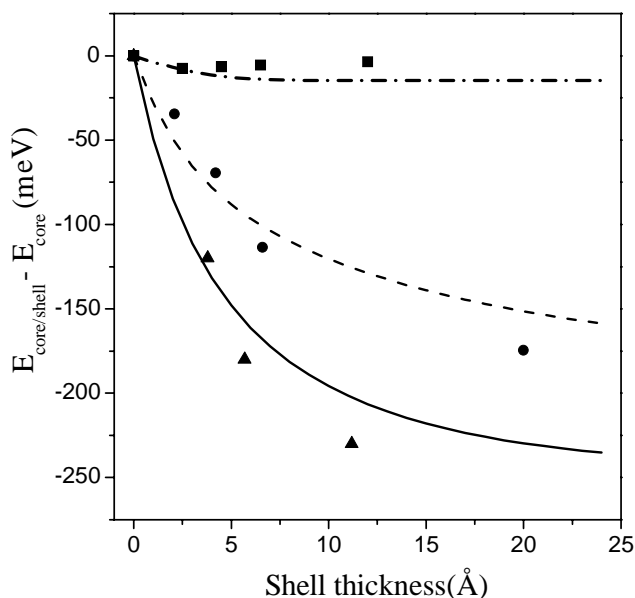


**Fig. 3-26** Experimental and calculated shifts of the band gap energy in various core/shells versus the shell thickness. InAs/ZnS core/shells: experimental data – squares, calculated shift of gap – dot-dashed line. InAs/CdSe core/shells: experimental data – circles, calculated shift of gap – dashed line. InAs/InP core/shells: experimental data – triangles, calculated shift of gap – solid line. Reproduced from *J. Am. Chem. Soc.* **122**, 9692–9702 (2000).

810 nm with a Ti-sapphire laser for 30 min. An intensity of 250 mW was used, and the optical density of the irradiated solutions was 0.2 at 810 nm. Under these conditions, each nanocrystal and dye molecule absorbs a total of approximately  $0.5 \times 10^6$  photons. For the dye, following the irradiation, the main absorption peak at 830 nm vanished, indicating that the dye had completely degraded. For InAs cores (radius 1.7 nm), the absorption maximum shifted to the blue by 10 nm and the optical density slightly decreased. The PL intensity decreased by a factor of 2.1. For InAs/ZnSe core/shells (core radius 1.7 nm, shell thickness  $\sim 2$  monolayers), the absorption did not change upon the irradiation, and the PL intensity decreased by a factor of 1.7 to a value still eight times stronger than that for the fresh core. Finally, for InAs/CdSe core/shells (core radius 1.7 nm, shell thickness  $\sim 1.8$  monolayers), the absorption shifted to the blue by 5 nm, and the PL intensity decreased by only 10%. This experiment demonstrates the improved photostability of the core/shells compared with a typical near-IR laser dye.

These core/shells also display greatly increased stability toward oxidation compared with the cores. The stability of the bare (TOP-coated) InAs cores and that of the two core/shell samples similar to the ones examined above were studied. Absorption and emission spectra of the fresh samples and of samples that were kept for ten months in a solution saturated with oxygen under daylight conditions were compared, as summarized in Figure 3-27. The InAs cores under these conditions

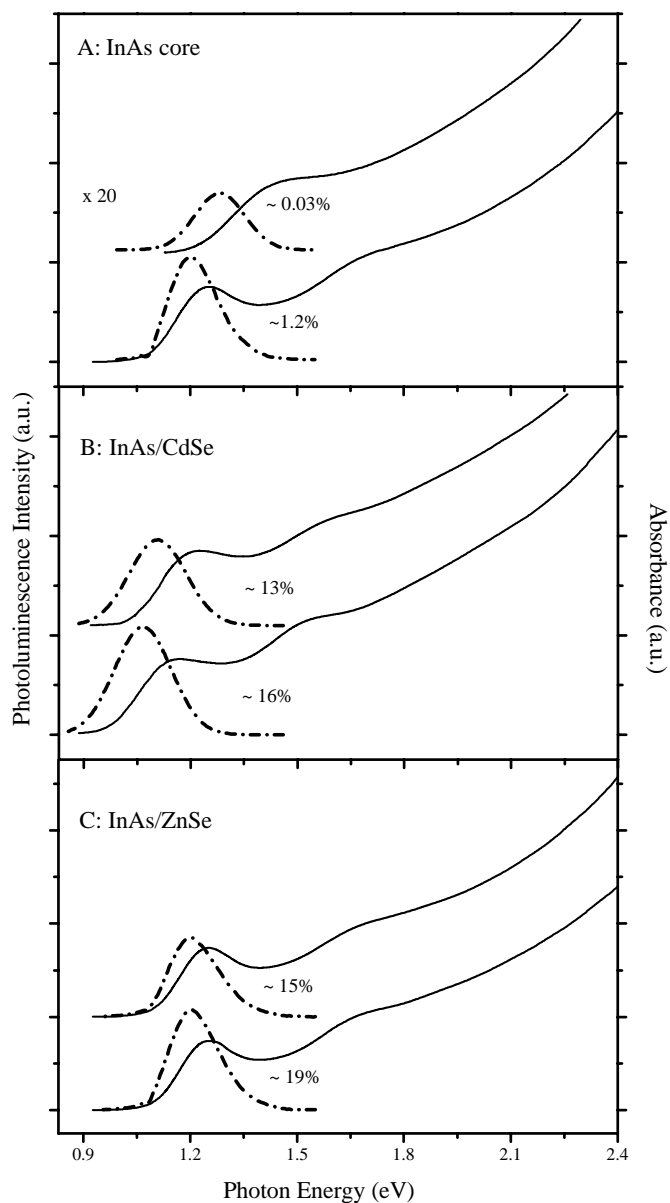


**Fig. 3-27** Comparison of stability of cores (frame A), InAs/CdSe core/shells (frame B), and InAs/ZnSe core/shells (frame C). Absorption spectra (solid lines) and PL spectra (dashed lines) are shown on the same energy scale for fresh nanocrystals (bottom traces in

each frame) and for nanocrystals kept in an oxygen-saturated solution for 10 months (top traces in each frame). The photoluminescence QY (%) is also indicated in each case. Reproduced from *J. Am. Chem. Soc.* **122**, 9692–9702 (2000).

exhibited a considerable blue shift of the absorption accompanied by washing out of the spectral features. The emission was quenched by a factor of 40 compared with the fresh cores (Figure 3-27A). These phenomena indicate substantial oxidation of the bare cores. The core/shells under similar conditions show a very different behavior. For InAs/CdSe core/shells the absorption shifted slightly to the blue and the QY decreased from 16% to 13% (Figure 3-27B). Finally, for the InAs/ZnSe core/shells, the absorption hardly shifted and the emission QY was reduced from 19% to 15% (Figure 3-27C).

### Acknowledgement

I wish to thank my coworkers and colleagues who have contributed immensely to the work reviewed in this chapter. Special thanks to A. Paul Alivisatos, Andrew Guzelian and Yunwei Cao. [This work was supported by the ISF, BSF and the DIP programs.]

### References

- 1 ALIVISATOS, A. P. *Science* **1996**, 271, 933.
- 2 NOZIK, A. J., MICIC, O. I. *MRS Bull.* **1998**, 23, 24.
- 3 GUZELIAN, A. A., KATARI, J. E. B., KADAVANICH, A. V., BANIN, U., HAMAD, K., JUBAN, E., ALIVISATOS, A. P., WOLTERS, R. H., ARNOLD, C. C., HEATH, J. R. *J. Phys. Chem.* **1996**, 100, 7212.
- 4 MICIC, O. I., CURTIS, C. J., JONES, K. M., SPRAGUE, J. R., NOZIK, A. J. *J. Phys. Chem.* **1994**, 98, 4966.
- 5 GUZELIAN, A. A., BANIN, U., KADAVANICH, A. V., PENG, X., ALIVISATOS, A. P. *Appl. Phys. Lett.* **1996**, 69, 1462.
- 6 CAO, Y. W., BANIN, U. *Angew. Chem. Int. Ed. Engl.* **1999**, 38, 3692.
- 7 CAO, Y. W., BANIN, U. *J. Am. Chem. Soc.* **2000**, 122, 9692.
- 8 BANIN, U., CAO, Y. W., KATZ, D., MILLO, O. *Nature* **1999**, 400, 542.
- 9 MICIC, O. I., CHEONG, H. M., FU, H., ZUNGER, A., SPRAGUE, J. R., MASCARENHAS, A., NOZIK, A. J. *J. Phys. Chem. B* **1997**, 101, 4904.
- 10 BANIN, U., LEE, J. C., GUZELIAN, A. A., KADAVANICH, A. V., ALIVISATOS, A. P., JASKOLSKI, W., BRYANT, G. W., EFROS, A. L., ROSEN, M. *J. Chem. Phys.* **1998**, 109, 2306.
- 11 TESSLER, N., MEDVEDEV, V., KAZES, M., KAN, S., BANIN, U. *Science* **2002**, 295, 1506.
- 12 DAEHNE, S., RESCH-GENDER, U., WOLFBEIS, O. S. (Eds.) *Near-Infrared Dyes for High Technology Applications*; Kluwer Academic Publishers: Dordrecht, 1997.
- 13 GRUNDMANN, M., CHRISTEN, J., LEDENTSOV, N. N. et al. *Phys. Rev. Lett.* **1995**, 74, 4043.
- 14 LEON, R., PETROFF, P. M., LEONARD, D., FAFARD, S. *Science* **1995**, 267, 1966.
- 15 BANIN, U., LEE, J. C., GUZELIAN, A. A., KADAVANICH, A. V., ALIVISATOS, A. P. *Superlattices and Microstructures* **1997**, 22, 559–568.
- 16 OLSHAVSKY, M. A., GOLDSTEIN, A. N., ALIVISATOS, A. P. *J. Am. Chem. Soc.* **1990**, 112, 9438.
- 17 WELLS, R. L., PITT, C. G., MCPHAIL, A. T., PURDY, A. P., SHAFIEEZAD, S., HALLOCK, R. B. *Chem. Mater.* **1989**, 1, 4.
- 18 UCHIDA, H., CURTIS, C. J., NOZIK, A. J. *J. Phys. Chem.* **1991**, 95, 5382.
- 19 UCHIDA, H., CURTIS, C. J., KAMAT, P. V., JONES, K. M., NOZIK, A. J. *J. Phys. Chem.* **1992**, 96, 1156.
- 20 KHER, S. S., WELLS, R. L. *Chem. Mater.* **1994**, 6, 2056–2062.
- 21 KHER, S. S., WELLS, R. L. *Nanostructured Materials* **1996**, 7, 591.



- 22 MICIC, O. I., AHRENKIEL, S. P., BERTRAM, D., NOZIK, A. J. *Appl. Phys. Lett.* **1999**, *75*, 478.
- 23 MEWS, A., EYCHMÜLLER, A., GIERSIG, M., SCHOOS, D., WELLER, H. *J. Phys. Chem.* **1994**, *98*, 934.
- 24 HINES, M. A., GUYOT-SIONNEST, P. J. *J. Phys. Chem.* **1996**, *100*, 468.
- 25 PENG, X., SCHLAMP, M. C., KADAVANICH, A. V., ALIVISATOS, A. P. *J. Am. Chem. Soc.* **1997**, *119*, 7019.
- 26 DABBOUSI, B. O., RODRIGUEZ-VIEJO, J., MIKULEC, F. V., HEINE, J. R., MATTOUSSI, H., OBER, R., JENSEN, K. F., BAWENDI, M. G. *J. Phys. Chem. B* **1997**, *101*, 9463.
- 27 TALAPIN, D. V., ROGACH, A. L., KORNOWSKI, A., HAASE, M., WELLER, H. *Nano Lett.* **2001**, *1*, 207.
- 28 MICIC, O. I., SMITH, B. B., NOZIK, A. J. *J. Phys. Chem. B* **2000**, *104*, 12149.
- 29 MICIC, O. I., SPRAGUE, J., LU, Z. H., NOZIK, A. J. *Appl. Phys. Lett.* **1996**, *68*, 3150.
- 30 MURRAY, C. B., NORRIS, D. J., BAWENDI, M. G. *J. Am. Chem. Soc.* **1993**, *115*, 8706.
- 31 PENG, X., WICKHAM, J., ALIVISATOS, A. P. *J. Am. Chem. Soc.* **1998**, *120*, 5343.
- 32 SMITH, A. L. *Particle Growth in Suspensions*; Academic Press: London, 1983.
- 33 CHAN, W. C. W., NIE, S. *Science* **1998**, *281*, 2016.
- 34 KATARI, J. E. B., COLVIN, V. L., AILIVISATOS, A. P. *J. Phys. Chem.* **1994**, *98*, 4109.
- 35 (a) KLEIN, D. L., ROTH, R., LIM, A. K. L., ALIVISATOS, A. P., MCEUEN, P. L. *Nature* **1997**, *389*, 699; (b) KLEIN, D. L. et al. *Appl. Phys. Lett.* **1996**, *68*, 2574.
- 36 LOWETH, C. J., CALDWELL, W. B., PENG, X. G., ALIVISATOS, A. P., SCHULTZ, P. G. *Angew. Chem. Int. Ed. Engl.* **1999**, *38*, 1812.
- 37 KUNO, M., LEE, J. K., DABBOUSI, B. O., MIKULEC, F. V., BAWENDI, M. G. *J. Chem. Phys.* **1997**, *106*, 9869.
- 38 JACOBSON-HILSON, M., MOKARI, T., BANIN, U. *J. Phys. Chem. B* **2001**, *105*, 12726–12731.
- 39 COWLEY, A. H., JONES, R. A. *Angew. Chem. Int. Ed. Engl.* **1989**, *28*, 1208.
- 40 WELLS, R. L. *Coord. Chem. Rev.* **1992**, *112*, 273.
- 41 COWLEY, A. H., HARRIS, P. R., JONES, R. A., NUNN, C. M. *Organometallics* **1991**, *10*, 652.
- 42 MILLER, J. E., KIDD, K. B., COWLEY, A. H., JONES, R. A., EKERDT, J. G., GYSLING, H. J., WERNBERG, A. A., BLANTON, T. N. *Chem. Mater.* **1990**, *2*, 589.
- 43 HEALY, M. D., LAIBINIS, P. E., STUPIK, P. D., BARRON, A. R. *J. Chem. Soc. Chem. Commun.* **1989**, 359.
- 44 ROBINSON, W. T., WILKINS, C. J., ZEING, Z. *J. Chem. Soc. Dalton Trans.* **1990**, 219.
- 45 WELLS, R. L., AUBUCHON, S. R., SHER, S. S., LUBE, M. S., WHITE, P. S. *Chem. Mater.* **1995**, *7*, 737.
- 46 JIN, S., MCKEE, V., NIEUWENHUYZEN, M., ROBINSON, W. T., WILKENS, C. J. *J. Chem. Soc. Dalton Trans.* **1993**, 3111.
- 47 INOUE, K., YOSHIZUKA, K., YAMAGUCHI, S. *J. Chem. Eng. Japan* **1994**, *27*, 737.
- 48 SATO, T., RUCH, R. *Stabilization of Colloidal Dispersions by Polymer Adsorption*, Marcel Dekker: New York 1980, pp 46–51.
- 49 KIMURA, K. *J. Phys. Chem.* **1994**, *98*, 11997.
- 50 HAMAKER, H. C. *Recl. Trav. Chim.* **1937**, *56*, 3.
- 51 VERWEY, E. J., OVERBEEK, J. Th. G. *Theory of Stability of Lyophobic Colloid*, Elsevier: Amsterdam 1948, p 160.
- 52 GUINIER, A. *X-Ray Diffraction*, Freeman: San Francisco 1963.
- 53 NIRMAL, M., BRUS, L. *Acc. Chem. Res.* **1999**, *32*, 407.
- 54 WELLER, H. *Angew. Chem. Int. Ed. Engl.* **1993**, *32*, 41.
- 55 BRUCHEZ, M., MORONNE, M., GIN, P., WEISS, S., ALIVISATOS, A. P. *Science* **1998**, *281*, 2013.
- 56 MITCHELL, G. P., MIRKIN, C. A., LETSINGER, R. L. *J. Am. Chem. Soc.* **1999**, *121*, 8122.
- 57 COLVIN, V. L., SCHLAMP, M. C., ALIVISATOS, A. P. *Nature* **1994**, *370*, 354.
- 58 DABBOUSI, B. O., BAWENDI, M. G., ONITSUKA, O., AND RUBNER, M. F. *Appl. Phys. Lett.* **1995**, *66*, 1316.
- 59 SCHLAMP, M. C., PENG, X. G., ALIVISATOS, A. P. *J. Appl. Phys.* **1997**, *82*, 5837.
- 60 MATTOUSSI, H., RADZIŁOWSKI, L. H., DABBOUSI, B. O., THOMAS, E. L.,

- BAWENDI, M. G., RUBNER, M. F. *J. Appl. Phys.* **1998**, 83, 7965.
- 61 HARRISON, M. T., KERSHAW, S. V., ROGACH, A. L., KORNOWSKI, A., EYCHMÜLLER, A., WELLER, H. *Adv. Mater.* **2000**, 12, 123.
- 62 ALLAN, G., BASTARD, G., BOCARA, N., LANOO, M., VOOS, M. (Eds.) *Heterojunctions and Semiconductor Superlattices*, Springer: Berlin Heidelberg 1986.
- 63 WEI, S., ZUNGER, A. *Appl. Phys. Lett.* **1998**, 72, 2011.
- 64 GUZELIAN, A. A. *Synthesis and Characterization of III–V Semiconductor Nanocrystals* Ph.D. Thesis, University of California: Berkeley 1996.
- 65 HINES, M. A., GUYOT-SIONNEST, P. *J. Phys. Chem. B* **1998**, 102, 3655.
- 66 LAGOWSKI, J. J. *Modern Inorganic Chemistry*, Marcel Dekker: NY 1973, pp. 320–322.
- 67 MADELUNG, O., SCHULZ, M., HEISS, H. (Eds.) *Landolt-Bornstein: Numerical Data and Functional Relationships in Science and Technology*, New Series Vol. 17, Springer-Verlag: New York 1982.
- 68 HOENER, C. F., ALLAN, K. A., BARD, A. J., CAMPION, A., FOX, M. A., MALLOUK, T. E., WEBBER, S. E., WHITE, J. M. *J. Phys. Chem.* **1992**, 96, 3812.
- 69 WICKHAM, J. N., HERHOLD, A. B., ALIVISATOS, A. P. *Phys. Rev. Lett.* **2000**, 84, 923.
- 70 SCHOOS, D., MEWS, A., EYCHMÜLLER, A., WELLER, H. *Phys. Rev. B* **1994**, 49, 17072.
- 71 BRUS, L. E. *J. Chem. Phys.* **1984**, 80, 4403.
- 72 WILLIAMSON, A. J., ZUNGER, A. *Phys. Rev. B* **1999**, 59, 15819.
- 73 LEDUC, M., WEISBUCH, C. *Optics Commun.* **1978**, 26, 78.

## 3.1.3

**Synthesis and Characterization of Ib-VI Nanoclusters**

*Stefanie Dehnen, Andreas Eichhöfer, John F. Corrigan, and Dieter Fenske*

**3.1.3.1 Introduction**

The synthesis of chalcogen-bridged molecular clusters of the coinage metal elements, copper, silver, and gold, represents an area of increasing activity in recent chemical and materials science research. This can be attributed in large part to two facts. Firstly, binary coinage metal chalcogenides feature relatively high ionic [1] and even higher electric [2] conductivity in the solid state, leading to properties that are positioned between those of *semi*-conducting and metallic phases. Secondly, an enormous general interest exists in the size dependency of the chemical, physical, and structural properties of substances when going from small molecules to bulk materials [3]. Therefore, numerous research groups are concentrating on the syntheses and properties of colloidal *nano* particles with narrow size distributions [4]. An alternative approach is the formation and isolation of crystalline cluster compounds that are suitable for single-crystal X-ray diffraction. In both cases, the molecules have to be kinetically protected from further condensation reactions to form the thermodynamically favored binary phases. Therefore, a ligand sphere coordinating to either surface metal centers or chalcogen atoms is necessary, and this in most cases consists uniquely of tertiary phosphine molecules or phosphines in combination with other organic groups. Herein we focus on ligand-stabilized chalcogen-bridged metal nanoclusters.

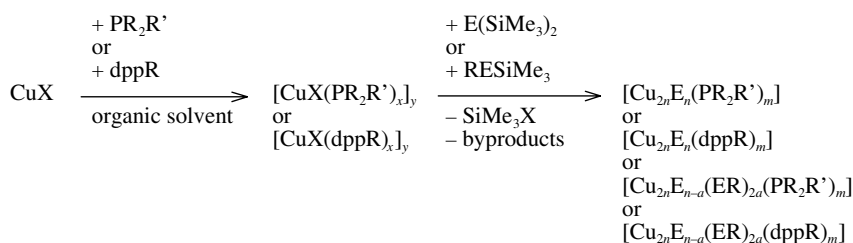
Experimental [5–33] and quantum chemical [34–37] investigations have been undertaken during the last decade in order to study the transition from the obviously *non-metal* Cu<sub>2</sub>E monomer (E = S, Se, Te) to bulk Cu<sub>2</sub>E [38–40]. From the synthetic point of view, the merit of the endeavors was the perception of the close relationship of the chosen reaction conditions with the formation of the desired products, as well as the use of the acquired knowledge for the synthesis of different cluster types. Furthermore, the great number of isolated and structurally characterized cluster compounds and comprehensive computational work on this subject allowed the development and explanation of size-dependent structure principles observed in the molecules. Lastly, various calculations and measurements have been carried out in order to get an insight into the physical properties of the cluster materials [10b–12].

### 3.1.3.2 Chalcogen-Bridged Copper Clusters

#### Synthesis Routes

The compounds are – with some exceptions – highly air and moisture sensitive. Therefore, all reaction steps have to be carried out with rigorous exclusion of air and moisture in a high purity inert atmosphere by employing standard Schlenk-line techniques. All solvents are dried and freshly distilled prior to use. Most chalcogen-bridged copper compounds have been synthesized according to the following general reaction pathway and possess one of the formulas given in Scheme 3-1.

From Scheme 3-1 one recognizes the importance of the CuX to phosphine ratio, the counterion X of the copper salt, and especially the nature of the phosphine used. In the first step, the latter complexes to the copper center to result in a coordination complex whose reactivity can be subtly modified by the choice of X and PR<sub>2</sub>R'. Furthermore, the driving force of the reactions is the formation of thermodynamically stable SiMe<sub>3</sub>X and is thus determined by the choice of X via the bond



X = Cl, OAc (Ac = OCCH<sub>3</sub>)

R, R' = organic group

dppR = bis-(diphenylphosphino)-alkane, -alkene, alkyne or -aryl

E = S, Se, Te

main byproducts are Cu<sub>2</sub>E, E=PR<sub>2</sub>R', (Me<sub>3</sub>Si)<sub>2</sub>, (RE)<sub>2</sub>

**Scheme 3-1** General synthesis route for the formation of phosphine-ligated, chalcogen-bridged copper clusters.

strength of the Si–X bond [41]. Finally, the steric demand of the  $\text{PR}_2\text{R}'$  molecules coating the cluster surface – as measured by Tolman's cone angle  $\theta$  [42] – is, though not linearly, closely related to the final size and shape of the copper chalcogenide core.

In addition to these variables, other reaction conditions, such as the chosen solvent and the reaction temperature or temperature program, strongly influence the course of the synthesis. It has been shown that under similar reaction conditions the use of derivatives  $\text{RE}(\text{SiMe}_3)$  ( $\text{R}$  = organic group) leads to the formation of completely different structures compared to reactions employing  $\text{Se}(\text{SiMe}_3)_2$ . The reason for this is the different reactivities of the compared substances as well as a partly incomplete Se–C bond cleavage. Thus, some  $\text{RE}^-$  fragments are bonded at the periphery of the cluster framework and also act as surface ligands in conjunction with the phosphines.

The copper atoms in the vast majority of the clusters can be assigned a formal charge of +1, while the chalcogen ligands are formally viewed as  $\text{E}^{2-}$  or  $\text{RE}^-$  groups. Some of the selenium-bridged species, however, and nearly all copper telluride clusters form *non*-stoichiometric compounds that display mixed valence metal centers in the formal oxidation states 0 and +I or +I and +II. These observations correlate with those made for the binary phases  $\text{Cu}_2\text{S}$ ,  $\text{Cu}_{2-x}\text{Se}$ , and  $\text{Cu}_{2-x}\text{Te}$  [38–40].

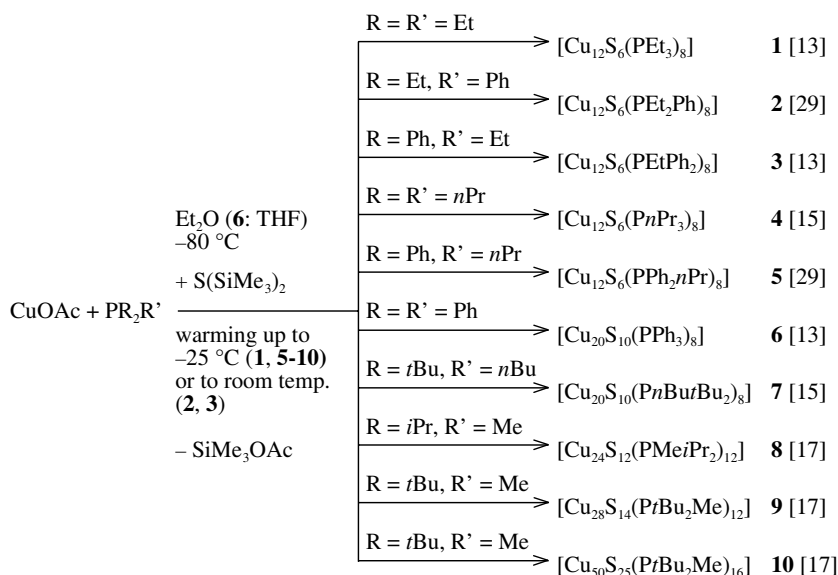
Even though most ligand-covered copper chalcogenide clusters were prepared using the above described methods, other approaches for the generation of ligated or naked  $[\text{Cu}_{2n}\text{E}_n]$  cluster compounds have been reported previously. In addition to syntheses in solvent environments [5–31] that led to the formation of, e.g.,  $[\text{PhMe}_3\text{As}]_4[\text{Cu}_8\{\text{S}_2\text{C}_2(\text{CN})_2\}_6]$  [5],  $(\text{Me}_4\text{N})_2[\text{Cu}_5(\text{SPh})_7]$  [6],  $(\text{Ph}_4\text{P})_4[\text{Cu}_{12}\text{S}_8]$  [7], or  $[\text{Cu}_6\{\text{Se}(2,4,6\text{-iPr}_3\text{C}_6\text{H}_2)\}_6]$  [8], ligand-free particles have been generated and characterized by means of laser ablation techniques in combination with mass spectroscopy.

### Sulfur-Bridged Copper Cluster

The reactions yielding the phosphine-coated sulfur-bridged copper clusters that have been isolated and structurally characterized to date are summarized in Scheme 3-2 in order of increasing cluster size.

Sulfur-bridged clusters could not be obtained by reactions starting from copper halides. The reason is the lower reactivity of a primary copper acetate-phosphine complex when compared to analogous halide complexes due to chelating acetate ligands that leave in a double-step substitution of sulfur ligands for oxygen [43]. Reactants of higher reactivity lead directly to the formation and precipitation of  $\text{Cu}_2\text{S}$  even at low temperatures. The kinetic restrictions at the beginning of the synthesis combine with those at the end of the cluster growth. The phosphine molecules have to display a certain minimum steric demand, as it has not yet proved possible to generate sulfur-bridged copper clusters stabilized with  $\text{PMe}_3$  ligands using this strategy.

Half the number of known copper sulfide clusters adhere to the general formula  $[\text{Cu}_{12}\text{S}_6(\text{PR}_2\text{R}')_8]$ , which represents the smallest known copper chalcogenide



**Scheme 3-2** Survey of the synthesis of sulfur-bridged copper clusters protected by terminal phosphine ligands.

$[\text{Cu}_{2n}\text{E}_n]$  cluster core (1–5) [13, 15, 18]. The respective molecular structure corresponds to one of two possible isomers that can both be derived from two highly symmetric polyhedra of metal or chalcogen atoms. The highly symmetric conformation is the reason for the strong preference for “ $\text{Cu}_{12}$ ” species, where an  $\text{S}_6$  octahedron is penetrated by a  $\text{Cu}_{12}$  cubooctahedron. The latter is distorted, however, because of the coordination of the metal centers to phosphine ligands, as there is only enough space for eight instead of twelve phosphine molecules at the cluster surface within reasonable Cu–P bond distances. Different distributions of the terminal ligands to the cubooctahedron atoms lead to the formation of isomers I or II, respectively. Both cluster structures as well as a computed hypothetical “naked”, undistorted  $[\text{Cu}_{12}\text{S}_6]$  [35] core are shown in Figure 3-28.

In the “ $\text{Cu}_{12}$ ” clusters, two coordination modes for copper atoms can be observed. The copper atoms that do not bind to phosphine ligands are nearly linearly coordinated by sulfur neighbors and are positioned either in the equatorial  $\text{Cu}_4$  ring of the cubooctahedron (I) or two each in the top and bottom of the  $\text{Cu}_4$  planes (II). Copper atoms that are attached to  $\text{PR}_2\text{R}'$  groups are surrounded in a nearly trigonal planar manner by two sulfur neighbors and one phosphorus atom. The phosphine molecules formally “pull” the respective metal atoms out of the based  $\text{Cu}_{12}$  polyhedron, whereas the “naked” copper atoms are slightly pushed towards the cluster center. All sulfur ligands act as  $\mu_4$  bridges between copper atoms. In molecules of type I, the eight phosphorus atoms are arranged around the cluster surface in a cubic manner, whereas one finds a  $\text{P}_8$  delta-dodecahedron in the other isomer. Both arrangements are counted among the most stable polyhedra of eight points on a spherical surface.

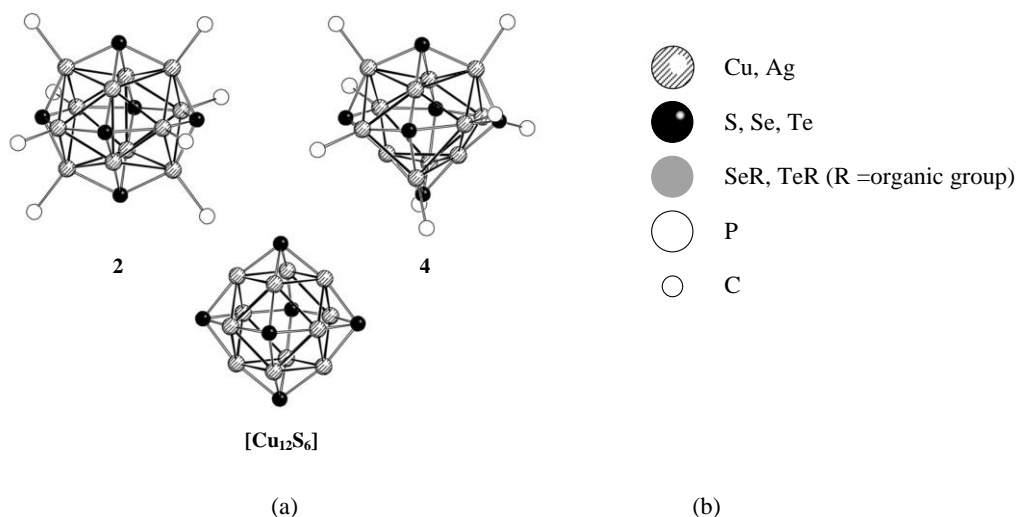


**Fig. 3-28** Molecular structures of  $[\text{Cu}_{12}\text{S}_6(\text{PEt}_2\text{Ph})_8]$  (**2**) and  $[\text{Cu}_{12}\text{S}_6(\text{P}n\text{Pr}_3)_8]$  (**4**) (without organic groups) and of a calculated “naked”  $[\text{Cu}_{12}\text{S}_6]$  core. (a) General labelling of the molecular structures in chapter 3.1.3.1.

Quantum chemical investigations with the program system TURBOMOLE [44, 45], employing MP2 [46] and DFT [47, 48] methods, were carried out assigning the highest possible symmetry in order to explain the obvious experimentally observed preference for type I clusters in comparison to those of type II [36]. For model ligands  $\text{PH}_3$  (MP2 and DFT, highest possible symmetry:  $D_{4h}$  for type I or  $S_4$  for type II), both structures that represent local minima on the energy hyperface were iso-energetic within the limits of the methods used. On calculating the clusters  $[\text{Cu}_{12}\text{S}_6(\text{PR}_3)_8]$  with  $\text{R} = \text{Et}$  or  $\text{R} = \text{Pr}$  according to both structural isomers (DFT, highest possible symmetry:  $C_{4h}$  or  $S_4$ ), i.e. one real (**1**, **4**) and one hypothetical species each, one does not find a direct correlation of a certain type of substituent at the phosphorus atoms with purely thermodynamic stabilization. Thus, further kinetic effects such as solubility and mobility of the hydrocarbyl groups at the experimental temperatures ( $\gg 0 \text{ K}$ ) were found to play key roles in the discrimination of isomers. The same cone angle values of  $\text{PEt}_3$  and  $\text{P}n\text{Pr}_3$  also serve to underline this conclusion.

A second pair of isomers is formed in the presence of sterically more demanding phosphines,  $\text{PPh}_3$  or  $\text{P}n\text{Bu}t\text{Bu}_2$ , that contain 20 copper atoms in the cluster framework [13, 15]. The positions of eight Cu–P groups again determine the shape of the entire cluster, whose undistorted base can be viewed as a formal condensation product of the two  $[\text{Cu}_{12}\text{S}_6]$  units given in Figure 3-28.

A continuation of cluster growth also takes place with  $\text{PMeiPr}_2$ . Being too bulky for an arrangement of eight molecules around a  $[\text{Cu}_{12}\text{S}_6]$  core and not generating a suitable ligand sphere with six terminal ligands, the phosphine groups force a for-

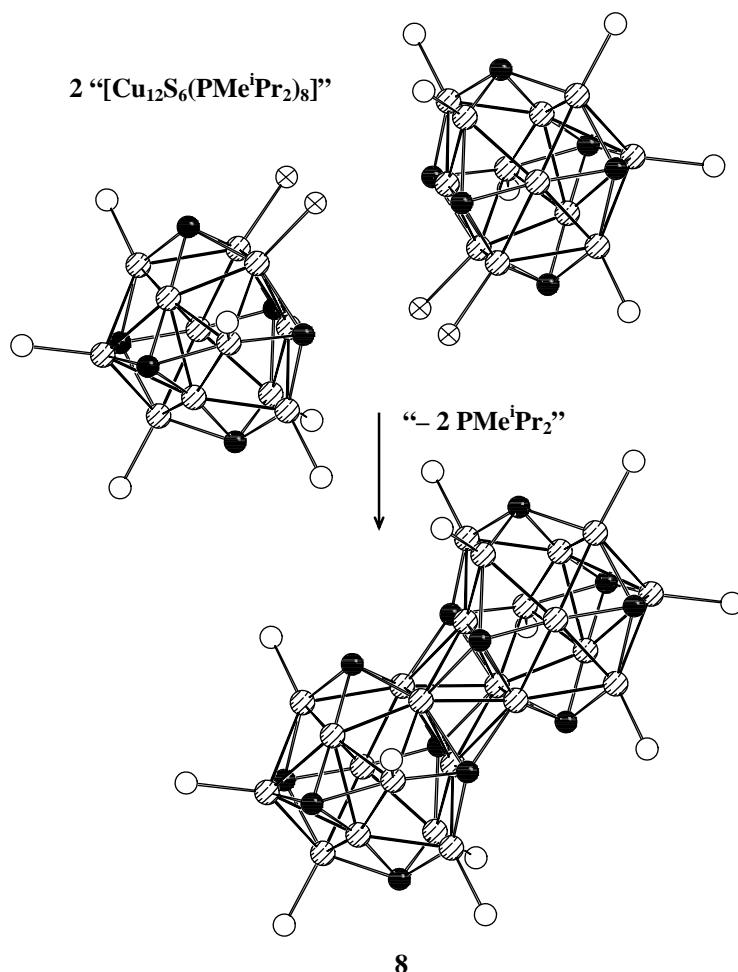


**Fig. 3-29** Formal dimerization/condensation reaction of two hypothetical clusters  $[\text{Cu}_{12}\text{S}_6(\text{PMe}^i\text{Pr}_2)_8]$ , resulting in the molecular structure of  $[\text{Cu}_{24}\text{S}_{12}(\text{PMe}^i\text{Pr}_2)_{12}]$  (**8**) (without organic groups). Phosphine ligands that are formally lost during the dimerization/condensation are marked with a cross.

mal dimerization of  $[\text{Cu}_{12}]$  clusters to the  $[\text{Cu}_{24}\text{S}_{12}]$  core in **8** [17]. Figure 3-29 shows the formal dimerization of two  $[\text{Cu}_{12}\text{S}_6(\text{PR}_2\text{R}')_8]$  clusters of type II, which results in the molecular structure of **8** after the loss of two phosphine groups.

In contrast to the formal condensation,  $2 \times [\text{Cu}_{12}] \rightarrow [\text{Cu}_{20}] - 4 \text{ Cu}$ , that leads to the sharing of a  $\text{Cu}_4$  rectangular face in **6**, one observes a conjunction via two  $\text{Cu}_3$  triangular faces of the two based cubooctahedra. Thus a  $\text{Cu}_6$  octahedron is formed around the inversion center of the cluster. These six copper atoms show a novel coordination pattern: they are surrounded in a trigonal planar manner exclusively by sulfur neighbors. The four sulfur atoms in the cluster center are found

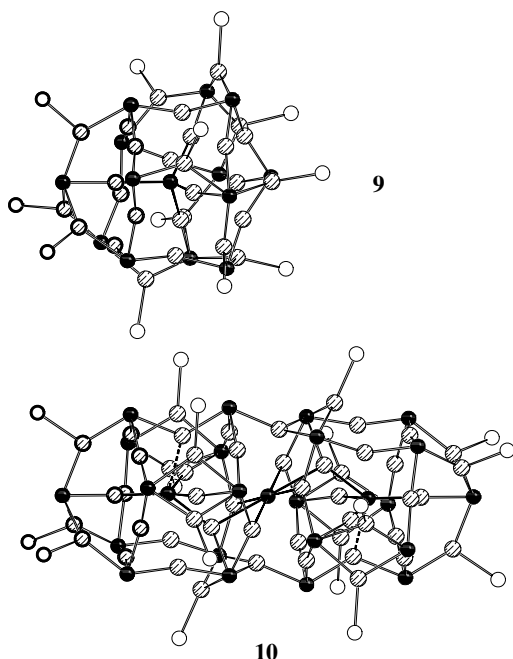


**Fig. 3-30** Molecular structures of  $[\text{Cu}_{28}\text{S}_{14}(\text{PtBu}_2\text{Me})_{12}]$  (**9**) and  $[\text{Cu}_{50}\text{S}_{25}(\text{PtBu}_2\text{Me})_{16}]$  (**10**) (without organic groups). The atoms of topologically equal zones are stressed with bold drawing.

to act as  $\mu_5$  bridges, whereas all sulfur ligands in the previously described clusters and all other additional sulfur ligands in **8** are  $\mu_4$  bridging. Naturally, the  $\mu_5$  bridges exhibit longer average Cu–S bond distances when compared to  $\mu_4$  bridging sulfur ligands by binding to four copper neighbors within normal distances (2.159(3)–2.378(3) Å) and possessing one significantly longer Cu–S bond each to copper atoms of the opposite asymmetric unit (2.485(3), 2.509(3) Å).

In the molecular structure of **8**, one observes the beginning of the transition from the so-called “small” copper sulfide clusters to the “middle-sized” species. Both cluster sizes possess spherical Cu–S–P frameworks with copper centers near the  $\text{S}_n$  polyhedral edges, but the “middle-sized” examples show some new structural features: coordination numbers other than four for sulfur atoms and copper centers that bind to more than two sulfur neighbors.

The same observations are made for clusters **9** and **10**, and to a greater extent for the latter [17]. Unlike the clusters described above, clusters **9** and **10** are topologically independent from smaller complexes. They are however themselves structurally related and are indeed produced side by side from the same reaction. The molecular structures of **9** and **10** are given in Figure 3-30 emphasizing their structural relationship. In Figure 3-31, the based  $\text{S}_{14}$  or  $\text{S}_{25}$  polyhedra are contrasted.

Besides various bridging modes of the sulfur atoms ( $\mu_3$ – $\mu_5$  in **9**,  $\mu_4$ – $\mu_6$  in **10**) and the higher numbers of three sulfur ligands around several copper atoms in **10**,



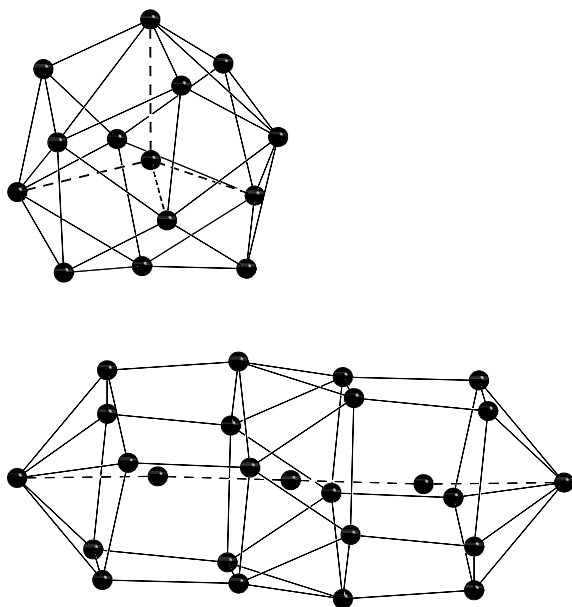


**Fig. 3-31**  $S_{14}$  (top) and  $S_{25}$  (bottom) polyhedra in **9** and **10**, respectively. The drawn S–S contacts do not represent binding interactions, but only serve to explain the geometries of the polyhedra.

both clusters show another new structural feature characterizing “middle-sized” Cu–S clusters. Only for these two largest examples of copper sulfide clusters does one observe sulfur atoms inside an outer Cu–S shell, generating inner Cu–S units. In **9**, one sulfur ligand centers a distorted  $S_{13}$  deltahedron with four copper atoms bonded to the central sulfur atom to yield an inner  $[SCu_4]$  unit. The remaining Cu centers are positioned either slightly below the edges of the  $S_{13}$  polyhedron if they show no Cu–P bonds or slightly above if bonded to phosphine ligands. Near  $C_3$  symmetry of the Cu–S core is distorted by an “irregular” position of a single copper atom that also promotes the  $\mu_3$  or  $\mu_5$  bridging modes of two sulfur ligands. The spherical cluster core is enclosed by a distorted icosahedron of the twelve phosphorus atoms. The sulfur substructure of **10** represents a cylinder-shaped polyhedron of near  $D_{5d}$  symmetry with a length of 17.14 Å. Underlining the supposition that **10** is formed from **9** through rough dimerization-condensation, three inner sulfur atoms are present. Two of them – formally arising from the central sulfur atom in **9** – are also  $\mu_4$  bridging, resulting in an  $[SCu_4]$  fragment. One of the corresponding copper centers in each of these units, however, belongs to the cluster surface rather than remaining an inner metal atom because of structural differences between **9** and **10** when approaching the center in **10**. Here one observes the most unusual feature of any of the copper sulfide clusters reported: the central sulfur ligand binds to six copper atoms in a slightly corrugated chair type

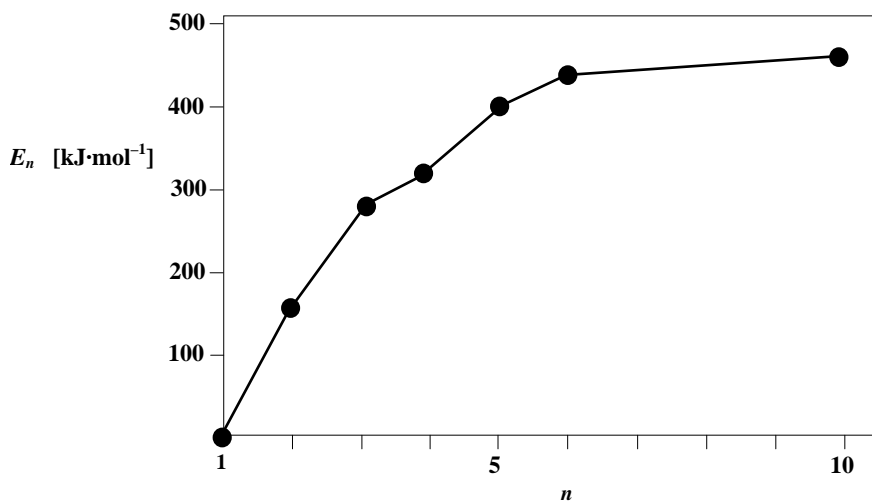
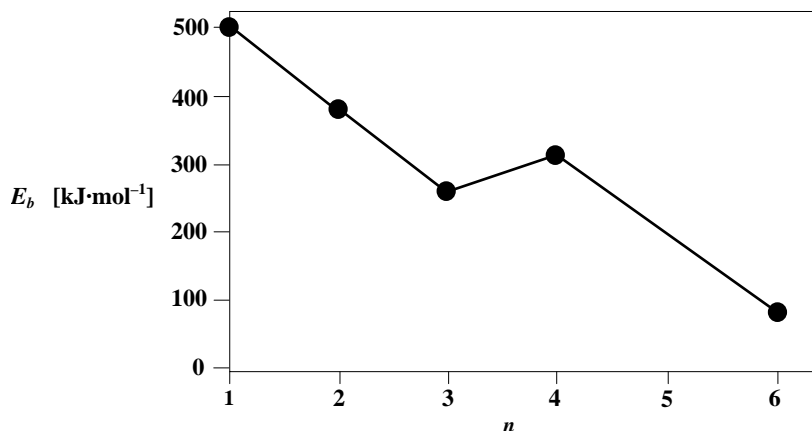


Fig. 3-32 Course of the stabilization energies per monomer unit  $E_n$  in “naked” clusters  $[\text{Cu}_{2n}\text{S}_n]$  ( $n = 1-4, 6, 10$ ). The given values consider the total energies of the most stable structural isomers computed on MP2 level.

manner. This arrangement, which is unknown for all other copper sulfide compounds, displays large Cu–S distances in the range 2.633(4)–2.673(5) Å, which are about 0.3–0.5 Å longer than usual Cu–S bonds. Considering the next ten copper atoms at distances of within 2.896(5)–3.814(5) Å around the sulfur center, a spherical  $[\text{SCu}_{16}]$  arrangement results in the cluster hub. The structural observations give evidence for an interstitial  $\text{S}^{2-}$  anion rather than a more covalently bonded sulfur ligand.

By a comprehensive *ab initio* study of clusters  $[\text{Cu}_{2n}\text{S}_n(\text{PH}_3)_m]$  ( $n = 1-4, 6, 10$ ;  $m = 0, 2, 4, 6, 8$ ) with an MP2 level (program system TURBOMOLE), stabilization energies for the sequential attachment of one  $\text{Cu}_2\text{S}$  unit to a given “naked” cluster ( $m = 0$ , Figure 3-32) as well as the course of the phosphine binding energies for clusters containing up to twelve copper atoms ( $m > 0$ , Figure 3-33) were developed [35]. For “naked” clusters, the stabilization energies increase continuously with the cluster size, which proves the investigated molecules to be thermodynamically unstable species *in vacuo*, and thus have to be stabilized by ligands. Moreover, the increment of the stabilization energy per monomer unit decreases with increasing cluster size as expected, since it should theoretically converge with infinite cluster size, i.e. solid  $\text{Cu}_2\text{S}$ .

As a third result, one gathers from the calculations that the Cu–P binding energy per Cu–P bond decreases rapidly from a value of ca. 140  $\text{kJ}\cdot\text{mol}^{-1}$  for  $[\text{Cu}_2\text{S}(\text{PH}_3)_2]$  – with a short relaxation when the Cu:P ratio is decreased (1 for  $n = 1-3$ ,  $>1$  for  $n = 4, 6$ ) – to a value of ca. 56  $\text{kJ}\cdot\text{mol}^{-1}$  for the “ $\text{Cu}_{12}$ ” species. Even if one assigns a higher Cu–P binding energy to the “real” tertiary phosphines with organic side chains, it is evident that the phosphine ligands are bonded very



**Fig. 3-33** Course of the Cu–P binding energies per Cu–P bond  $E_b$  in phosphine-ligated clusters  $[\text{Cu}_{2n}\text{S}_n(\text{PH}_3)_m]$  ( $n = 1\text{--}4, 6$ ;  $m = 2, 4, 6, 8$ ). The given values consider the total energies of the most stable structural isomers computed on MP2 level with respect to the total energy of  $\text{PH}_3$  calculated by the same method.

weakly to the copper sulfide core. Therefore, an additional stabilization by solvents or a crystal lattice is required.

### Selenium-Bridged Copper Clusters

Scheme 3-3 summarizes the reactions yielding all  $\text{PR}_2\text{R}'$ -coated selenium-bridged copper clusters that have been isolated and structurally characterized to date, in order of increasing cluster size.

In contrast to the sulfur-bridged compounds, the synthesis of selenium-bridged clusters can start from either copper acetate or copper chloride. This can be ascribed to the lower reactivity of  $\text{Se}(\text{SiMe}_3)_2$  when compared to the sulfur analog [49, 50]. Thus, the formation of  $\text{Cu}_2\text{Se}$  does not occur as rapidly as the formation of  $\text{Cu}_2\text{S}$ , and the cluster growth and ligand protection can often be observed even at room temperatures. However, by reacting copper acetate and by choosing low temperatures, one obtains smaller clusters that can be characterized as being intermediates during the course of the formation of larger molecules. In addition to a great number of “stoichiometric” compounds that formally contain  $\text{Cu}^+$  and  $\text{Se}^{2-}$ , some clusters were characterized that exhibit a Cu:Se ratio less than two, indicating mixed valence metal centers. All selenium ligands feature the formal charge  $-2$ , as one does not find any Se–Se binding interactions and one can therefore assign  $\text{Cu}^{\text{I}}$  and  $\text{Cu}^{\text{II}}$  within the same cluster core in **14**, **17**, **27**, and **33**. The phosphine ligands again play a key role in the determination of the observed cluster size and shape; however, the number of known compositions is approximately four times that of the copper sulfide system and the cluster growth pro-

$\text{CuX} + \text{PR}_2\text{R}'$ $(\text{X} = \text{Cl, OAc})$	$\xrightarrow[\text{- SiMe}_3\text{X}]{\text{Et}_2\text{O or THF} + \text{Se}(\text{SiMe}_3)_2}$	$\text{R} = \text{Ph, R}' = \text{Et} \rightarrow$	$[\text{Cu}_{12}\text{Se}_6(\text{PEtPh}_2)_8]$	<b>11</b> [13]
		$\text{R} = \text{R}' = n\text{Pr} \rightarrow$	$[\text{Cu}_{12}\text{Se}_6(\text{P}n\text{Pr}_3)_8]$	<b>12</b> [29]
		$\text{R} = \text{R}' = n\text{Pr} \rightarrow$	$[\text{Cu}_{12}\text{Se}_6(\text{PCy}_3)_6]$	<b>13</b> [18]
		$\text{R} = \text{R}' = \text{Et} \rightarrow$	$[\text{Cu}_{20}\text{Se}_{13}(\text{PEt}_3)_{12}]$	<b>14</b> [10b]
		$\text{R} = \text{Et, R}' = \text{Ph} \rightarrow$	$[\text{Cu}_{26}\text{Se}_{13}(\text{PEt}_2\text{Ph})_{14}]$	<b>15</b> [18]
		$\text{R} = \text{R}' = \text{Cy} \rightarrow$	$[\text{Cu}_{26}\text{Se}_{13}(\text{PCy}_3)_{10}]$	<b>16</b> [18]
		$\text{R} = \text{R}' = i\text{Pr} \rightarrow$	$[\text{Cu}_{29}\text{Se}_{15}(\text{P}i\text{Pr})_{12}]$	<b>17</b> [10a]
		$\text{R} = \text{R}' = i\text{Pr} \rightarrow$	$[\text{Cu}_{30}\text{Se}_{15}(\text{PR}_2\text{R}')_{12}]$	<b>18</b> [10a]
		$\text{R} = \text{R}' = i\text{Pr} \rightarrow$	$[\text{Cu}_{30}\text{Se}_{15}(\text{PR}_2\text{R}')_{12}]$	<b>19</b> [17]
		$\text{R} = \text{R}' = \text{Ph} \rightarrow$	$[\text{Cu}_{31}\text{Se}_{15}(\text{SeSiMe}_3)(\text{PrBu}_2\text{Me})_{12}]$	<b>20</b> [17]
		$\text{R} = \text{R}' = \text{Ph} \rightarrow$	$[\text{Cu}_{32}\text{Se}_{16}(\text{PPh}_3)_{12}]$	<b>21</b> [21]
		$\text{R} = \text{R}' = t\text{Bu} \rightarrow$	$[\text{Cu}_{36}\text{Se}_{18}(\text{PrBu}_3)_{12}]$	<b>22</b> [10a]
		$\text{R} = \text{Et, R}' = \text{Ph} \rightarrow$	$[\text{Cu}_{44}\text{Se}_{22}(\text{PEt}_2\text{Ph})_{18}]$	<b>23</b> [14]
		$\text{R} = t\text{Bu, R}' = n\text{Bu} \rightarrow$	$[\text{Cu}_{44}\text{Se}_{22}(\text{P}n\text{Bu}t\text{Bu}_2)_{12}]$	<b>24</b> [14]
		$\text{R} = \text{Me, R}' = \text{Ph} \rightarrow$	$[\text{Cu}_{48}\text{Se}_{24}(\text{PMe}_2\text{Ph})_{20}]$	<b>25</b> [17]
		$\text{R} = \text{R}' = \text{Ph} \rightarrow$	$[\text{Cu}_{52}\text{Se}_{26}(\text{PPh}_3)_{16}]$	<b>26</b> [21]
		$\text{R} = \text{R}' = \text{Ph} \rightarrow$	$[\text{Cu}_{59}\text{Se}_{30}(\text{PCy}_3)_{15}]$	<b>27</b> [18]
		$\text{R} = i\text{Pr, R}' = \text{Me} \rightarrow$	$[\text{Cu}_{70}\text{Se}_{35}(\text{PR}_2\text{R}')_{21}]$	<b>28</b> [29]
		$\text{R} = t\text{Bu, R}' = \text{Me} \rightarrow$		<b>29</b> [17]
		$\text{R} = \text{R}' = \text{Et} \rightarrow$	$[\text{Cu}_{70}\text{Se}_{35}(\text{PEt}_3)_{22}]$	<b>30</b> [10b]
		$\text{R} = \text{Et, R}' = \text{Ph} \rightarrow$	$[\text{Cu}_{70}\text{Se}_{35}(\text{PEt}_2\text{Ph})_n] (n = 23, 24)$	<b>31</b> [26]
		$\text{R} = \text{R}' = \text{Ph} \rightarrow$	$[\text{Cu}_{72}\text{Se}_{36}(\text{PPh}_3)_{20}]$	<b>32</b> [21]
		$\text{R} = \text{R}' = \text{Cy} \rightarrow$	$[\text{Cu}_{74}\text{Se}_{38}(\text{PCy}_3)_{18}]$	<b>33</b> [31]
		$\text{R} = \text{R}' = \text{Et} \rightarrow$	$[\text{Cu}_{140}\text{Se}_{70}(\text{PR}_2\text{R}')_{34}]$	<b>34</b> [23]
		$\text{R} = \text{Et, R}' = \text{Ph} \rightarrow$		<b>35</b> [31]
		$\text{R} = \text{R}' = \text{Et} \rightarrow$	$[\text{Cu}_{140}\text{Se}_{70}(\text{PEt}_3)_{36}]$	<b>36</b> [23]
		$\text{R} = \text{R}' = \text{Ph} \rightarrow$	$[\text{Cu}_{146}\text{Se}_{73}(\text{PPh}_3)_{30}]$	<b>37</b> [12]

**Scheme 3-3** Survey of the synthesis of selenium-bridged copper clusters protected by terminal phosphine ligands.

ceeds to a much higher extent. Again, the lower tendency to precipitate the binary phase can be held responsible for this observation.

Another route into selenium-bridged copper polynuclear complexes or clusters is their synthesis using  $\text{RSeSiMe}_3$  ( $\text{R}$  = organic group) in the presence of either tertiary phosphines or chelating ligands such as 1,2-bipyridyl, diphenylphosphino acid or bidentate phosphines  $\text{dppR}$  ( $\text{R}$  = organic spacer). The compounds thus prepared are listed in Scheme 3-4 and ordered according to their core size.

Again, one finds clusters containing exclusively  $\text{Cu}^{\text{I}}$ , as well as compounds with mixed-valence metal centers. In contrast to the compounds presented in Schemes 2 and 3, one example of a selenido/selenolato-bridged cluster exists apparently containing  $\text{Cu}^{\text{I}}$  and  $\text{Cu}^0$ . Apart from this peculiarity, the cluster size and conformation of the  $\text{Se}^{2-}/\text{SeR}^-$ -bridged compounds is now not only influenced by the nature and steric demand of the phosphine used, but it is also dependent on the spatial properties of the organic substituent at the selenium reactant. This determines both the  $\text{Se}^{2-}:\text{SeR}^-$  ratio and the ensuing arrangement of  $\text{Se}^{2-}$  ligands positioned inside the cluster core and  $\text{SeR}^-$  ligands at the periphery of the molecules.

The delicate, *non*-linear structural influence of the phosphine ligands allows for the formation of different clusters of often significantly varying size and shape in the presence of the same phosphine. The isolation of various cluster compounds is then enabled only by the judicious choice of reaction conditions. In contrast, the use of different  $\text{PR}_2\text{R}'$  ligands can lead to clusters of the same  $[\text{Cu}_{2n}\text{Se}_n]$  cores that possibly display differing numbers of terminal ligands and/or structural isomerism. These observations have already been illustrated and explained for the sulfur-bridged copper clusters, but they are more pronounced for the Cu–Se species, and a much higher structural variety is found. As for the copper sulfide compounds, one can discriminate between “small” (11–13) and “middle-sized” (14–27) clusters with respect to their shape and the coordination properties of the atoms concerned. However a novel group of “large” clusters (28–37) exists for the Cu–Se system. Whereas the transition from the first to the second type of molecular size occurs almost seamlessly, a clear break occurs when the number of copper atoms exceeds 59.

The only composition and structure that is identical for both the copper sulfide and selenide clusters is that for  $[\text{Cu}_{12}\text{E}_6(\text{PR}_2\text{R}')_8]$  ( $\text{E} = \text{S}, \text{Se}$ ;  $\text{PR}_2\text{R}' = \text{PEtPh}_2, \text{PnPr}_3$ ; respective cone angles: 141, 132°). Compounds 11 [13] and 12 [29] are topologically identical to their sulfur analogs. The use of a much larger phosphine ligand  $\text{PCy}_3$  does not lead to a condensation or dimerization of cluster cores as observed for 6–8 with  $\text{PR}_2\text{R}'$  groups of medium or large size around. Unlike the copper sulfide system, in the presence of  $\text{PPh}_3$ ,  $\text{PnBu}t\text{Bu}_2$ , or  $\text{PMeiPr}_2$  a reduction in the number of terminal ligands to six is acceptable in the case of 13 [18], and the resulting ligand shell is suitable for the cluster core. The clearly larger cone angle of  $\text{PCy}_3$  when compared to  $\text{PPh}_3$ ,  $\text{PnBu}t\text{Bu}_2$ , or  $\text{PMeiPr}_2$  (170° vs 145, 146, and 165°) allows a distorted  $\text{P}_6$  octahedron to sufficiently protect the copper selenide framework, although a third variation of a distortion of the  $[\text{Cu}_{12}\text{E}_6]$  core is observed.



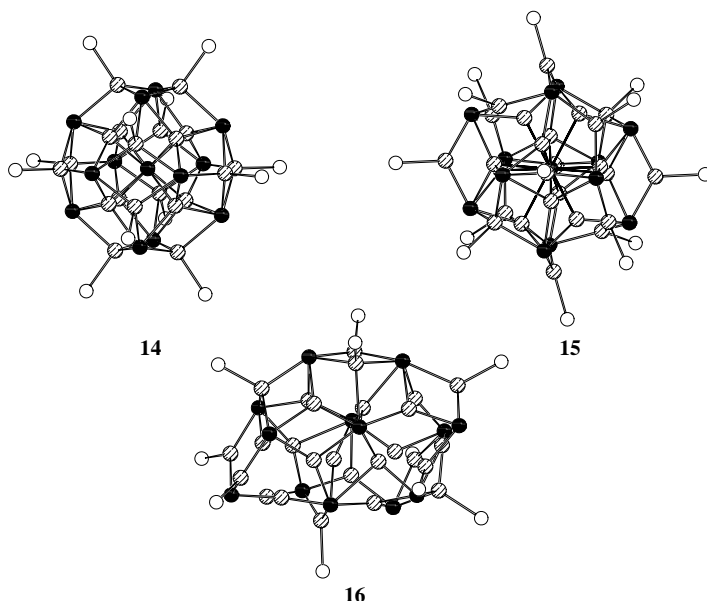


**Fig. 3-34** Molecular structures of  $[\text{Cu}_{20}\text{Se}_{13}(\text{PEt}_3)_{12}]$  (**14**),  $[\text{Cu}_{26}\text{Se}_{13}(\text{PEt}_2\text{Ph})_{14}]$  (**15**), and  $[\text{Cu}_{26}\text{Se}_{13}(\text{PCy}_3)_{10}]$  (**16**) (without organic groups).

With the clusters discussed, one perceives the strong preference for highly symmetric substructures of all components involved in the heavy atom framework. Capped or uncapped, sometimes condensed octahedral, prismatic, cubic, dodecahedral, cubooctahedral, or icosahedral arrangements of either metal, chalcogen or phosphorus atoms penetrate or enclose each other in all structures. Among the discussed compounds, the “ $\text{Cu}_{12}$ ” molecules possess the most symmetric substructures. Selenium ligands, however, evidently prefer higher bridging modes. Therefore the formation of “small” clusters with a strong  $\mu_4$  bridging restriction is disadvantaged and thus rarer than the formation of larger ones. For the Cu–Se clusters, three additional “middle-sized” compounds are interesting with respect to their symmetry properties as well as being an additional illustration of the phosphines’ structural influence. The cluster frameworks of **14**, [10b] and the Cu–Se isomers **15** [18], and **16** [18] can again be described as an alternating packing of copper, selenium and phosphorus polyhedra, respectively. Regular polyhedra are, however, only observed in the structures of **14** and **15**, whereas the  $[\text{Cu}_{26}\text{Se}_{13}]$  isomeric core of **16**, being surrounded by only ten  $\text{PCy}_3$  (versus 14  $\text{PEt}_2\text{Ph}$  groups), does not follow a known polyhedral pattern. The molecular structures of **14–16** are shown in Figure 3-34.

Clusters **14** and **15** are topologically related, as both contain a centered icosahedron of selenium atoms, although the penetrating polyhedra of copper atoms are arranged in different manners according to the different number of copper atoms and Cu– $\text{PR}_2\text{R}'$  fragments (**14**:  $\text{R} = \text{R}' = \text{Et}$ , **15**:  $\text{R} = \text{Et}$ ,  $\text{R}' = \text{Ph}$ ) in both clusters (Figure 3-35).

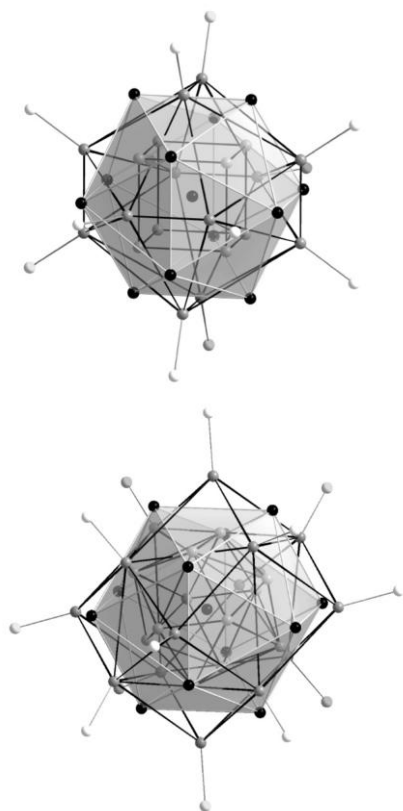


**Fig. 3-35** Comparison of the penetrative polyhedra in **14** (top) and **15** (bottom) that form the heavy atom cluster cores. The drawn lines only represent polyhedral edges and do not specify binding interactions.

In **14**, a  $\text{Cu}_8$  cube surrounds the inner selenium atom below the  $\text{Se}_3$  faces of the  $\text{Se}_{12}$  icosahedron. An outer  $\text{Cu}_{12}$  icosahedron follows, which is positioned above and perpendicular to the  $\text{Se}_{12}$  shell. The eight copper centers inside the cluster thus form tetrahedral  $[\text{CuSe}_4]$  groups, and the twelve outer ones display a  $[\text{Se}_3\text{CuP}]$  environment by binding to the equally orientated  $\text{P}_{12}$  icosahedron of the  $\text{PEt}_3$  ligands. In **15**, the inner selenium atom has twelve copper next nearest neighbors that form an icosahedron, each edge being positioned below an  $\text{Se}-\text{Se}$  edge of the enclosing  $\text{Se}_{12}$  polyhedron and perpendicular to it, resulting in a coordinative occupation of one copper atom per  $\text{Se}_3$  face. Slightly above the  $\text{Se}_{12}$  icosahedral surface, an arrangement of 14  $\text{Cu}-\text{PEt}_2\text{Ph}$  units can be described as a sixfold capped cube. The twelve inner copper atoms and the eight metal centers of the capped cube that are all placed near  $\text{Se}_3$  faces are approximately tetrahedrally coordinated by either four selenium ligands or three selenium atoms and one phosphorus ligand – characteristic of clusters being larger than “small” ones. The six remaining  $\text{Cu}-\text{PCy}_3$  fragments are situated above six  $\text{Se}-\text{Se}$  edges and therefore represent three-coordinated  $[\text{Se}_2\text{CuP}]$  units, common for both “small” and



“middle-sized” clusters. When comparing the Cu:Se ratio for **14** and **15**, one notices the fundamental difference that may be responsible for the structural differences. Cluster **14** represents a mixed-valence compound featuring formally six  $\text{Cu}^{\text{II}}$  and fourteen  $\text{Cu}^{\text{I}}$  centers to balance the  $26^-$  charge of the  $\text{Se}_{13}$  substructure. The intermetallic distances in **14** however (Cu(1)–Cu(1): 2.821(4), Cu(1)–Cu(2): 2.678(4) Å) do not suggest significant interatomic interactions despite the partial deficiency of electrons. The only structural hint of different valence situations in **14** or **15** is that, apart from equal average Cu–P bond lengths (2.247 Å in **14** and **15**) and similar average intermetallic distances Cu–Cu (2.707 Å in **14**, 2.682 Å in **15**), one measures significantly shorter average Cu–Se bonds in the mixed-valence compound **14** (2.365 Å) versus **15** (2.457 Å).

The molecular structure of **16** differs from those of **14** and **15**, since a very irregular  $\text{Se}_{13}$  deltahedron forms the selenium substructure. Twelve of the copper centers and ten Cu–PCy<sub>3</sub> fragments are bonded to the  $\text{Se}_{13}$  polyhedron in such a way that they are again three- or four-coordinate. Unlike the situation in **14** or **15**, one also observes four copper atoms that show a nearly linear coordination to two selenium neighbors. This pattern is typical of “small” Cu–E clusters and again underlines the partial propagation of these properties in the “middle-sized” compounds.

Similar to the “Cu<sub>12</sub>”–“Cu<sub>20</sub>”, “Cu<sub>12</sub>”–“Cu<sub>24</sub>” and “Cu<sub>28</sub>”–“Cu<sub>50</sub>” relationships discussed for copper sulfide clusters, the molecular structures of **14** and **15** prove to be closely related, even though the numbers and ratios of heavy atoms are very different. In contrast, a similar number of copper and selenium atoms *can*, but need not necessarily lead to a topological relationship. Compounds **17**–**21** [**10a**, **17**, **21**] contain 29, 30, 31 and 32 copper atoms, respectively, in addition to 15 or 16 selenium ligands. Nevertheless, three completely different molecular frameworks are observed. The first structural type is adopted by **17** [**10a**], **18** [**10a**], and **19** [**17**]. As an example, the molecular structure of **17** is given in Figure 3-36.

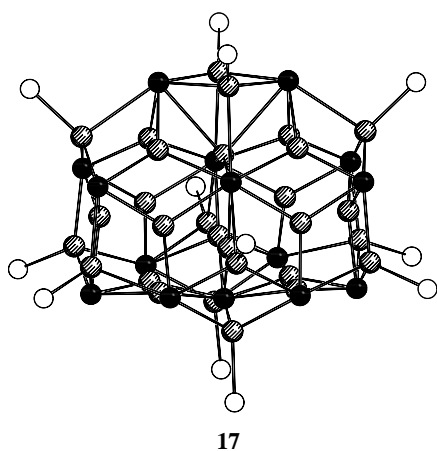


**Fig. 3-36** Molecular structure of  $[\text{Cu}_{29}\text{Se}_{15}(\text{PiPr})_{12}]$  (**17**) (without organic groups).

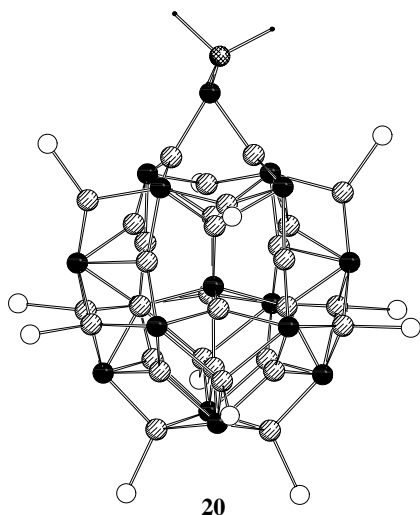
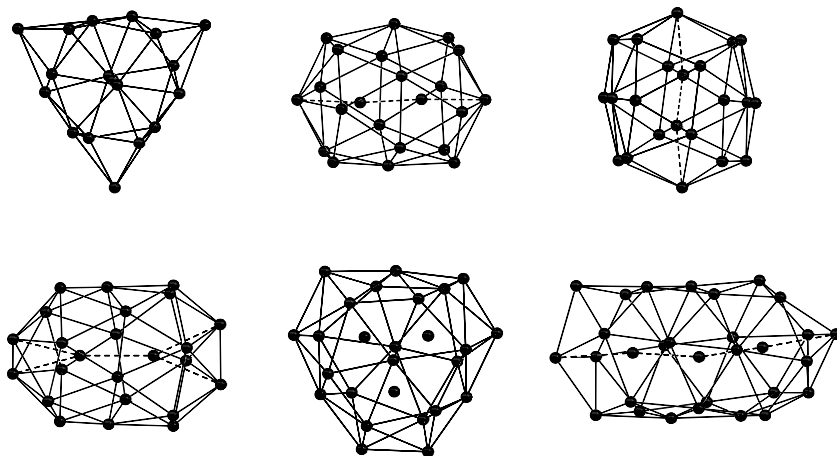


Fig. 3-37 Molecular structure of  $[\text{Cu}_{31}\text{Se}_{15}(\text{SeSiMe}_3)(\text{PtBu}_2\text{Me})_{12}]$  (**20**) (without organic groups).

Although the number of copper atoms is reduced by one in **17** in comparison to **18** or **19**, indicating a mixed valence situation, all clusters show identical Cu–Se–P cores. The additional copper atom present in **18** and **19** is positioned in the cluster center. A reaction employing the same reactants and temperatures as for the synthesis of **19**, but using a 40% higher  $\text{PtBu}_2\text{Me}:\text{CuOAc}$  ratio, yields compound **20** [17]. Analogous atomic arrangements or corresponding polyhedra are not found in **19** and **20**, even though the cluster core of **20** (Figure 3-37) can equally be described as consisting of five parallel planes of copper and selenium atoms that are surrounded by twelve phosphine ligands.

The  $\text{SeSiMe}_3$  group in **20**, whose occurrence is unique for copper chalcogenide clusters, not only influences the molecular structure of **20** but it also clears up the obvious reason for the structural differences for this series. Cluster **20** can be viewed as a “frozen” intermediate on the way to the formation of a larger cluster such as the “ $\text{Cu}_{70}$ ” cluster **29** [17] (see below), as a leaving group is still present. The latter uniquely acts as a protecting unit with the phosphine ligands, and therefore further cluster growth is slowed down to such an extent that the compound crystallizes preferentially. Its formation is thus naturally independent of the cluster growth yielding **19**. A third structural type for similar cluster sizes is found in **21** [21], in which the selenium atoms form a flattened polyhedron consisting of *non*-bonded  $\text{Se}_3$  triangles. The copper atoms show *quasi*-linear, distorted trigonal planar or tetrahedral coordination geometries. These coordination patterns and  $\mu_5$  and  $\mu_6$  bridging modes of the selenium ligands are common for “middle-sized” Cu–E clusters. Complexes **17** and **21** represent exceptions for their cluster size in another way, as they do not contain copper or selenium atoms inside a spherically tolerable Cu–Se shell. All other “middle-sized” clusters with 20 copper atoms and



**Fig. 3-38** Selenium substructures in **22–27** (from top left to bottom right). The drawn Se–Se contacts do not represent bonding interactions, but rather illustrate the geometries of the polyhedra.

upwards (beginning with **14**) have either central copper atoms (**18**, **19**) or central selenium ligands (**14–16**, **20**).

The larger molecules **22–27** [10a, 14, 17, 21, 18] also enclose selenium atoms within a  $\text{Se}_n$  polyhedron ( $n = 18, 22, 24, 26$ , or  $30$ ). The number of inner selenium ligands consequently increases with increasing cluster size from one central atom (**22**) [10a] to two inner ones (**23–25**) [14, 17] to three selenium centers inside the cluster core (**26**, **27**) [21, 18]. The respective underlying selenium substructures are summarized and contrasted in Figure 3-38.

Although these six compounds are all classified as being spherical “middle-sized” clusters, and all have central units within a Cu–Se surface, one can distinguish two different shapes. Clusters **22** and **26** (Figure 3-39) adopt a triangular topology, whereas **23–25** and **27** form ellipsoid-type cluster surfaces (Figures 13 and 14).

The molecular structures of both **22** and **26** display idealized  $C_3$  symmetry that is not realized in the crystal (**22**:  $C_1$  symmetry, **26**:  $C_2$  symmetry). Along the idealized threefold axis one finds a selenium ligand at the top and at the bottom of the flattened trigonal prism, as roughly formed by the cluster atoms. In **22**, a third selenium ligand is positioned between the latter two in the cluster center, whereas in **26**, three inner selenium atoms are grouped around the center of the Cu–Se core and two copper atoms are arranged along the pseudo  $C_3$  axis between the two above-mentioned selenium ligands. Beginning with the central unit, the cluster is formed by the usual alternating bonds from copper to selenium atoms. For **22**,  $[\text{Se}_2\text{Cu}]$ ,  $[\text{Se}_3\text{Cu}]$ , or  $[\text{Se}_2\text{CuP}]$  coordination environments around copper centers and  $\mu_3$ – $\mu_6$  bridging selenium ligands result, with Cu–Se distances of between 2.347(4) and 2.875(5) Å. The larger cluster core of **26** features consequently higher

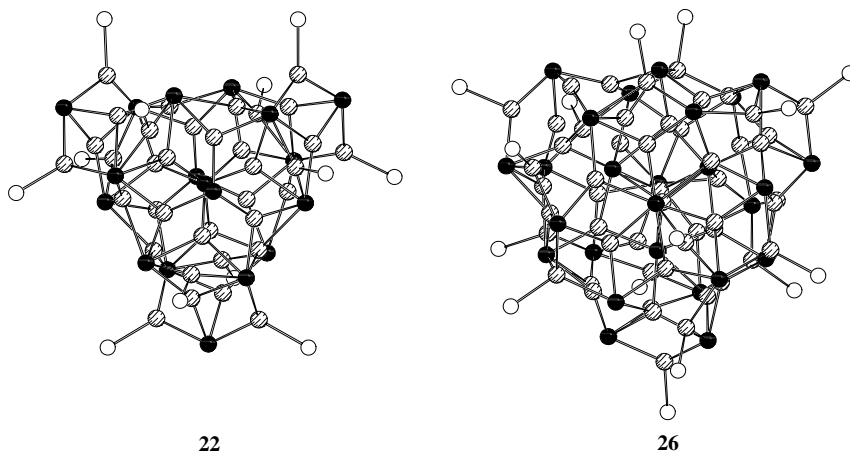


Fig. 3-39 Molecular structures of  $[\text{Cu}_{36}\text{Se}_{18}(\text{PtBu}_3)_{12}]$  (**22**) and  $[\text{Cu}_{52}\text{Se}_{26}(\text{PPh}_3)_{16}]$  (**26**) (without organic groups).

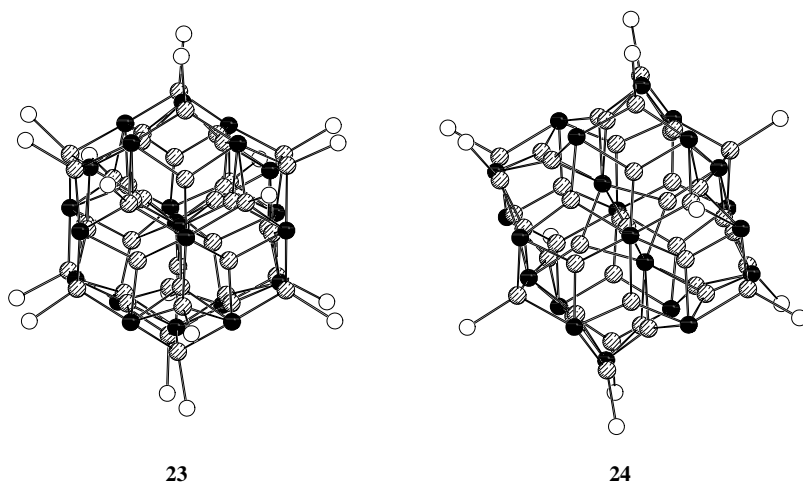
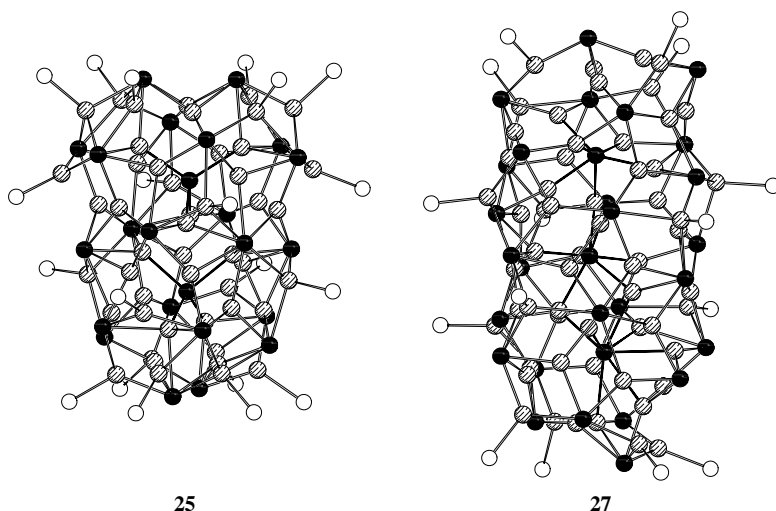


Fig. 3-40 Molecular structures of  $[\text{Cu}_{44}\text{Se}_{22}(\text{PEt}_2\text{Ph})_{18}]$  (**23**) and  $[\text{Cu}_{44}\text{Se}_{22}(\text{PnBu}_4\text{Bu}_2)_{12}]$  (**24**) (without organic groups).

coordination numbers that show near-tetrahedral  $[\text{Se}_3\text{CuP}]$  arrangements in addition to two- and three-coordinated copper atoms as in **22**, and the selenium atoms act as  $\mu_4-\mu_8$  bridges within a wide Cu–Se range of distances ranging from 2.19 to 2.91 Å. Twelve  $\text{PtBu}_3$  ligands enclose the copper selenide core of **22**, and sixteen  $\text{PPh}_3$  ligands are bonded to the Cu–Se core of **26**.

The structural isomers **23** and **24** are obtained via completely different reaction conditions including the use of phosphine ligands, different molar ratios of  $\text{CuOAc}:\text{PR}_2\text{R}'$ , and the exposure of the reaction mixtures to different final reaction temperatures.



**Fig. 3-41** Molecular structures of  $[\text{Cu}_{48}\text{Se}_{24}(\text{PMe}_2\text{Ph})_{20}]$  (**25**) and  $[\text{Cu}_{59}\text{Se}_{30}(\text{PCy}_3)_{15}]$  (**27**) (without organic groups).

The spatial demands of the phosphine ligands allowed ligand shells of either eighteen  $\text{PEt}_2\text{Ph}$  or twelve  $\text{PnBu}_t\text{Bu}_2$  groups to sufficiently stabilize a  $[\text{Cu}_{44}\text{Se}_{22}]$  core. In **23**, the phosphorus atoms form a regular deltahedron of alternating, eclipsed rings  $\text{P}_3$ ,  $\text{P}_6$ ,  $\text{P}_6$ , and  $\text{P}_3$  along the long axis of the cluster. The twelve phosphorus atoms at the periphery of the cluster core in **24** define a highly distorted icosahedron. As a result of the different number and thus arrangement of  $\text{PR}_2\text{R}'$  ligands that expectedly affect the core geometry by “pulling” the attached copper atoms somewhat out of the Cu–Se core, some differences are observed on examining the copper selenide frameworks in detail. This is clearly seen when the respective  $\text{Se}_{22}$  substructures are compared with each other (Figure 3-38). Apart from different distortions of the described peripheral  $\text{Se}_{20}$  polyhedron (total lengths or widths of the  $\text{Se}_{22}$  substructures according to the orientations in Figure 3-41:  $11.43 \times 8.64 \text{ \AA}$  in **23**,  $8.34 \times 10.60 \text{ \AA}$  in **24**), the relative positions of the inner  $\text{Se}_2$  “dumbbells” are perpendicular to each other. One can therefore assign a fragment of twelve copper and two selenium atoms in both cluster cores that are positioned completely differently, which is initiated by the significantly different situations on the cluster surface mentioned above. The isomerism observed with the “ $\text{Cu}_{44}$ ” clusters again shows that certain  $[\text{Cu}_{2n}\text{E}_n]$  compositions represent “isles of stability” – within given limits of structural isomers – that are experimentally obtained whenever a suitable ligand shell can be realized by means of the selected phosphine molecules.

Two further ellipsoid-like arrangements are found for clusters **25** and **27** (Figure 3-4). Apparently, it is not possible to create a phosphine shell for surrounding a  $[\text{Cu}_{44}\text{Se}_{22}]$  cluster by a suitable number and arrangement of  $\text{PMe}_2\text{Ph}$  groups (cone angle:  $127^\circ$ ). Instead, the smallest compound to be stable and insoluble enough for isolation is the slightly larger cluster **25**, which is however structurally related to

the somewhat smaller species **23**. The ellipsoid-like  $\text{Se}_{24}$  substructure of **25** (Figure 3-38) can be derived from the  $\text{Se}_{22}$  arrangement in **23** via substitution of two selenium ligands capping the outer  $\text{Se}_6$  rings for the single Se center in the smaller polyhedron. Again, one finds all coordination features typical of “middle-sized” Cu–Se clusters, with four copper atoms that show a nearly tetrahedral environment of four selenium ligands. Unlike all smaller clusters that contain selenium atoms inside the cluster core, **25** displays two tetrahedral  $[\text{SeCu}_4]$  units – linked by a *trans*-edge junction via a compressed  $\text{Cu}_4$  tetrahedron – with a uniquely small bridging number of four at the two inner selenium ligands (cf. bridging modes of the inner selenium ligands in **14–16**, **20**, **22–24**:  $\mu_5$ – $\mu_8$ ,  $\mu_{12}$ ). Together with **14** and **17**, **27** is the third copper selenide cluster that displays a number of metal centers that is too small for an overall +I oxidation state at the copper atoms. A single  $\text{Cu}^{2+}$  center cannot however be assigned and the “lack” of one electron is likely to be delocalized over the cluster framework. As in **23–25**, the molecule is oblong in shape and represents the largest spherical copper selenide cluster known. It concludes the series of “middle-sized” Cu–Se clusters. The selenium atoms form a highly irregular  $\text{Se}_{27}$  polyhedron around three inner chalcogen centers (Figure 3-38) that can alternatively be viewed as a rough arrangement of selenium ligands in three layers. The molecular structure of **27** includes all possible coordination environments around copper atoms,  $[\text{Se}_2\text{Cu}]$ ,  $[\text{Se}_3\text{Cu}]$ ,  $[\text{Se}_4\text{Cu}]$ ,  $[\text{Se}_2\text{CuP}]$ , and  $[\text{Se}_3\text{CuP}]$ . Selenium ligands are observed to act as  $\mu_4$ ,  $\mu_5$ ,  $\mu_6$ , or  $\mu_7$  bridges.

Summarizing the structural properties of the “small” Cu–Se clusters **11–13** and the “middle-sized” ones **14–27**, one perceives the spherical shape and the absence of any topological relationship with that of the bulk material  $\text{Cu}_2\text{Se}$  as a central feature. Only the tendency toward higher coordination numbers three and four at the copper centers with increasing cluster size approaches the situation in the binary phase. The principal difference between “small” and “middle-sized” clusters is the occurrence of inner atoms that appears firstly with a copper selenide core of 33 atoms (**14**). Typical of the coordination patterns in the “middle-sized” molecules is a mixture of higher and lower coordination numbers or bridging modes, the lower being observed in “small” clusters without variation.

Although only eleven additional copper atoms are observed in compounds **28–31** [**17**, **10b**, **29**, **26**], they represent the smallest examples of a new type of copper selenide clusters. The so-called “large” Cu–Se clusters are characterized by significantly different cluster shapes, structural principles and relationships to the bulk material when compared to the smaller species. Clusters **28–37** display A-B-A-type packed layers of selenium atoms that form large triangular frameworks. A weak image of the molecular structures of **22** or **26** arises; however, a closer examination clearly enables the latter series to be distinguished from the layer-type structures. Clusters **28–37** are all based on three such selenium layers, of which the middle one possesses the most chalcogen atoms. Figure 3-42 shows the selenium networks of the “large” clusters **28** [**29**] (as an example of the  $\text{Cu}_{70}\text{Se}_{35}$  cores), **32** [**21**] ( $\text{Cu}_{72}\text{Se}_{36}$  core), **33** [**31**] ( $\text{Cu}_{74}\text{Se}_{38}$  core), **34** [**23**] (as an example of the  $\text{Cu}_{140}\text{Se}_{70}$  cores), and **37** [**12**] ( $\text{Cu}_{146}\text{Se}_{73}$  core). It is worth mentioning that this structural pattern seems to be exceptionally advantaged for large copper selenide

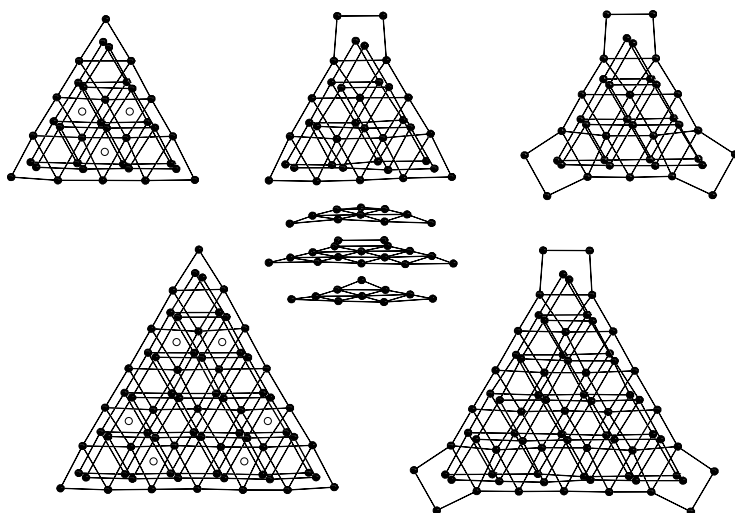


**Fig. 3-42** Selenium substructures in **28**, **32**, **33**, **34**, and **37** (from top left to bottom right), which contain 35, 36, 38, 70, or 73 selenium atoms. The drawn Se–Se contacts do not represent binding interactions, but only serve to visualize the A–B–A packing of selenium

atoms in three layers, which is additionally demonstrated by the supplementary view of the  $\text{Se}_{36}$  substructure of **32** (top mid). Open circles represent the positions of disordered copper atoms (see text and following figures).

clusters, as it is observed equally for a size range from “ $\text{Cu}_{70}$ ” to “ $\text{Cu}_{146}$ ”, i.e. even with a doubling of the molecular mass.

Clusters **28**–**31** contain  $\text{Se}_{10}$ ,  $\text{Se}_{15}$  and  $\text{Se}_{10}$  layers that represent perfect triangles. The next larger selenium substructure should be formed by an arrangement of  $\text{Se}_{15}$ ,  $\text{Se}_{21}$ , and  $\text{Se}_{15}$  triangular layers, each displaying one more row of selenium atoms. A corresponding “[ $\text{Cu}_{102}\text{Se}_{51}$ ]” cluster core is as yet unknown, and one observes instead the formation of smaller clusters in between this range that show selenium layers with the middle one deviating from a perfect triangular shape. In **32**, one corner of the middle layer is modified with respect to the corresponding one in the “ $\text{Cu}_{70}$ ” clusters in such a way that two selenium atoms replace one. All three corners are similarly changed, to result in the  $\text{Se}_{10}$ – $\text{Se}_{18}$ – $\text{Se}_{10}$  selenium framework of **33**, and this compound is another cluster featuring fewer copper centers than  $\text{Cu}_{2n}$  with respect to  $\text{Se}_n$ . The third “idealized” cluster composition is actually realized with **34**, **35** and **36**. The underlying selenium layers contain 21, 28, and 21 atoms. By replacing all corner selenium centers of the middle triangle by two chalcogen atoms, one obtains the  $\text{Se}_{73}$  substructure that is observed in **37**. For this third possible size, a successive substitution of triangle corners in the middle layer could not as yet be experimentally proven, whereas for the first, smaller size (35 selenium atoms), a modification of one or three corners was observed.

The reason for the missing “ $\text{Cu}_{102}$ ” cluster might be related to the primary steps of the cluster growth mechanism. Selenium networks consisting of three triangle

hexagonal layers based on  $0.5[n(n+1)]$  selenium atoms ( $n$  = number of straight rows in the triangle network) in *A-B-A* order offer three possible situations for the center of the triangle: one either finds a hole (representing the unoccupied *C* position), one selenium atom in the middle layer (located on a *B* position), or two selenium atoms belonging to the two outer layers (located on *A* positions).<sup>1)</sup> Since one observed only such “large” Cu–Se cluster that follow the last two possibilities, the presence of a central  $\text{Cu}_x\text{Se}_y$  axis ( $\text{Se}_A\text{--Cu--Cu--Se}_A$  in **28–33**,  $\text{Cu--Se}_B\text{--Cu}$  in **34–37**) seems to be necessary for the formation of a stable cluster core. Assuming that the cluster growth begins in the center of the molecule, the presupposition of such a  $[\text{Cu}_2\text{Se}]$  or a  $[\text{Cu}_2\text{Se}_2]$  fragment being situated at this place appears feasible for a *non*-spherical cluster. Therefore, only those molecules that contain either one (middle; cf. **34–37**) or two (outer; cf. **28–33**) selenium layers with a central selenium atom instead of a central triangular hole are formed and experimentally observed. Indeed, neither  $\text{Se}_{15}$  nor  $\text{Se}_{21}$  layers that would be exclusively underlying a “ $\text{Cu}_{102}$ ” molecule contain central selenium atoms and should therefore be only found together with other triangles.

In Figure 3-43, the cores of the clusters containing 70 (**28–31**), 72 (**32**) and 74 (**33**) copper atoms are compared.

The “ $\text{Cu}_{70}$ ” core is quite tolerant with regard to its ligand shell. An increase in the spatial demand of the  $\text{PR}_2\text{R}'$  molecules is not strictly coupled with a decreased number of terminal ligands. However, one still finds a rough correlation, since twenty-one groups of the bulkier phosphines  $\text{PMeiPr}_2$  (cone angle:  $146^\circ$ ) and  $\text{PtBu}_2\text{Me}$  (cone angle:  $161^\circ$ ) are arranged around the Cu–Se core, whereas twenty-two and twenty-three terminal ligands are observed for the smaller phosphines  $\text{PET}_3$  or  $\text{PET}_2\text{Ph}$  (cone angles:  $132$  or  $136^\circ$  respectively). The clusters **28**, **29** [17], and **31** [26] differ marginally with respect to their molecular structures. In **28** and **29**, the only observable difference is a slightly less complete ligand shell achieved by the less demanding  $\text{PMeiPr}_2$  groups. Cluster **31** displays a disorder problem with the  $\text{PET}_2\text{Ph}$  groups, such that it cannot be determined with certainty whether the total number of phosphine ligands sums to twenty-three or twenty-four. Accordingly, for the formation of the cluster, another two (or three) additional phosphine molecules – versus **28** or **29** – are formally arranged in the triangle corners in such a way that two (or three) corners possess four instead of three Cu– $\text{PET}_2\text{Ph}$  groups and one corner (or none) retains three of them. An intermediate number of phosphine ligands, twenty-two, is observed with a more distinct structural modification, but it is again the corner region that is affected. In contrast to all of the corner arrangements of copper and selenium atoms in the other “ $\text{Cu}_{70}$ ” clusters that cannot be described by means of regular patterns, in **30** [10b] only two corners follow this pattern. The third shows a highly ordered  $[\text{Cu}_9\text{Se}_3(\text{PET}_3)_4]$  configuration featuring a centered cube of copper atoms that is capped at three faces by  $\mu_4$ -selenium ligands and carries four phosphine groups at the bottom atoms. This

1) Respective layers are potentially one of every third number  $0.5[n(n+1)]$ , i.e.  $\text{Se}_1$ ,  $\text{Se}_{10}$ ,  $\text{Se}_{28}$ , etc., whereas the layers that feature a central hole show selenium numbers in between, i.e.  $\text{Se}_3$ ,  $\text{Se}_6$ ,  $\text{Se}_{15}$ , etc.



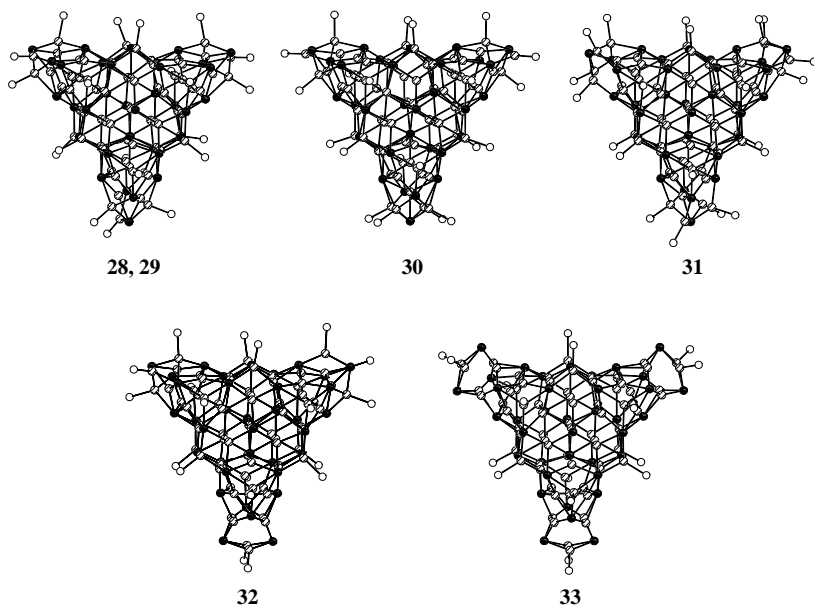


**Fig. 3-43** Molecular structures of  $[\text{Cu}_{70}\text{Se}_{35}(\text{PR}_2\text{R}')_{21}]$  ( $\text{R} = i\text{Pr}, t\text{Bu}$ ;  $\text{R}' = \text{Me}$ ) (**28, 29**),  $[\text{Cu}_{70}\text{Se}_{35}(\text{PEt}_3)_{22}]$  (**30**),  $[\text{Cu}_{70}\text{Se}_{35}(\text{PEt}_2\text{Ph})_n]$  ( $n = 23, 24$ ) (**31**),  $[\text{Cu}_{72}\text{Se}_{36}(\text{PPh}_3)_{20}]$  (**32**), and  $[\text{Cu}_{74}\text{Se}_{38}(\text{PCy}_3)_{18}]$

(**33**) (without organic groups). Two copper atoms that are positioned around the central Se–Cu–Cu–Se axis are statistically distributed with a 0.67 occupation over three positions in **28, 29** or **31**.

peculiarity of one cluster corner in **30** is one of two reasons for the missing pseudo-threefold molecular symmetry. A  $\text{C}_3$  symmetry of the  $[\text{Cu}_{70}\text{Se}_{35}]$  core of **28, 29** or **31** is additionally approached – apart from one “wrong” Cu– $\text{PR}_2\text{R}'$  position in **28** or **29** – by the statistical disorder of two copper atoms. The latter are distributed over three positions – with an accordant 0.67 occupancy – around the Cu–Se–Se–Cu pseudo-threefold axis running through the center of the molecule. The mentioned disorder situation of  $\text{PEt}_2\text{Ph}$  ligands in **31** also leads to a pseudo- $\text{C}_3$  axis as far as 24 phosphine groups are assigned to the ligand shell. In contrast, a close look to the cluster center in **30** shows an open copper atom position. The two other metal atom sites are fully occupied, leading to a lower – but crystallographically realized –  $\text{C}_2$  symmetry.

The molecular structure of **32** can be derived from that of **28** or **29** in a simple manner if one firstly fully occupies all three positions of copper atoms around the Cu–Se–Se–Cu axis mentioned before, and, secondly, one formally substitutes one  $[\text{Se}_2\text{CuPPh}_3]$  unit for one corner selenium atom. In this way, the modification of the central selenium layer occurs. The number of phosphine groups that enclose the respective corner is additionally reduced to two, since two of the three copper atoms that bind  $\text{PR}_2\text{R}'$  ligands in the analogous corners in **28** or **29** remain “naked” in **32**. Such (formal) alteration of the cluster corner, and full occupation of the  $\text{Cu}_3$  group around the cluster center, cause the formation of the mixed-valence

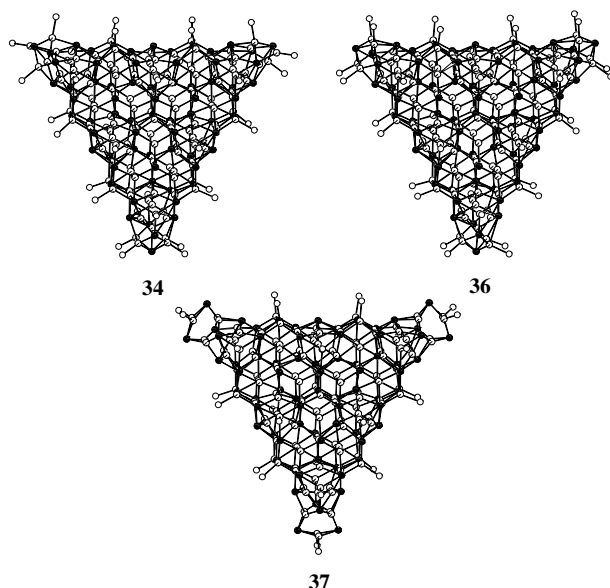


**Fig. 3-44** Molecular structures of  $[\text{Cu}_{140}\text{Se}_{70}(\text{PET}_3)_{34}]$  (**34**),  $[\text{Cu}_{140}\text{Se}_{70}(\text{PET}_3)_{36}]$  (**36**), and  $[\text{Cu}_{146}\text{Se}_{73}(\text{PPh}_3)_{30}]$  (**37**) (without organic groups). In **34** and **36**, the two central copper atoms are each half occupied to result

in one atom in the sum, being statistically distributed over two sites. Six further copper atoms are assigned a 0.67 occupation, resulting in four instead of six metal atoms in the sum.

cluster framework in **33**. With pseudo- $C_{3h}$  symmetry, the point group symmetry of the molecule does not exceed  $C_2$  in the crystal because of slight distortions and the positions of the organic groups bonded to phosphorus atoms.

The largest copper selenide clusters isolated to date possess 140 or 146 copper atoms with 70 or 73 selenium ligands, respectively. The molecular structures of **34**, **36** [23], and **37** are shown in Figure 3-44.

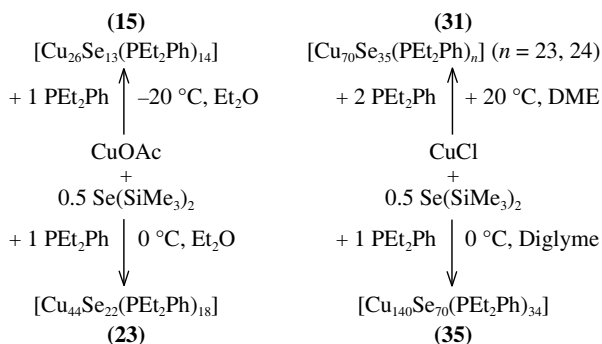
The different number of  $\text{PR}_2\text{R}'$  groups observed in **34** or **35** on the one hand and **36** on the other, affects the corresponding molecular structures in a manner similar to that for the “ $\text{Cu}_{70}$ ” species. Having a look at the corners again, **34**, containing thirty-four terminal  $\text{PET}_3$  ligands, reveals an enlarged analog of **30**. As in the smaller compound, two corners are arranged irregularly, whereas the third one shows the regular, centered cubic fragment. Increasing the number of  $\text{PET}_3$  groups to thirty-six in **36**, all three corners show an ordered arrangement of copper, selenium and phosphorus atoms. This structural unit, which is only found for the  $\text{PET}_3$ -ligated “large” Cu–Se clusters, underlines the structural relationship of **30**, **34**, and **36** and demonstrates another steric influence of certain types of  $\text{PR}_2\text{R}'$  molecules. All other phosphine ligands that surround “large” copper selenide clusters feature larger cone angles, which could be the reason for a forced modification to a more staggered arrangement if four corner Cu– $\text{PR}_2\text{R}'$  units are present. Consequently, in **35**, all three corners show arrangements like that in the smaller

analog 31. Disordered copper atoms that increase the molecular pseudo-symmetry are again present in the “Cu<sub>140</sub>” clusters. Additionally, there is a twofold disorder of one central copper atom on two positions to result in an actual “Cu<sub>0.5</sub>”–Se–“Cu<sub>0.5</sub>” axis. Such metal atoms are again affected by a two-thirds occupancy factor and lie in the plane spanned by the middle selenium layer. In addition, the six next-but-one metal atoms viewed from the cluster center are disordered statistically to amount to four atoms in the sum.

Three formal replacements [Se<sub>2</sub>Cu(PR<sub>2</sub>R'<sub>2</sub>)] of three corner selenium atoms removal of six PR<sub>2</sub>R' molecules in 36, and full occupation of all split positions present in the “Cu<sub>140</sub>” clusters yield the composition and *D*<sub>3d</sub> symmetric molecular structure of 37. Thus the structural transitions of the “Cu<sub>70</sub>” compounds to slightly larger species and the transition occurring with the largest known copper selenide clusters are related.

All of the “large” Cu–Se clusters show an A-B-A packing of selenium hexagonal layers, the metal centers occupying either trigonal or tetrahedral holes or being situated outside the selenium layers in a likewise trigonal or tetrahedral coordination environment. Thus, the layer-type clusters clearly show a closer relationship to solid-state structures than do the spherical ones. For the Cu<sub>2–x</sub>Se phases, however, only cubic and not hexagonal modifications are known. Interestingly, for the Cu<sub>2</sub>S (chalcosine) high temperature phase [38], a hexagonal lattice with mainly trigonally surrounded copper atoms in addition to tetrahedrally and linearly coordinated ones does exist. In contrast, the cubic Cu<sub>2–x</sub>Se crystal structures [39] can be derived from an anti-fluorite lattice [51] by positioning the selenium atoms on defined lattice places. Six to eight copper atoms per unit cell – according to the phase composition – are localized in trigonal, tetrahedral or octahedral holes. In α-Cu<sub>2</sub>Se, the metal centers are placed in an ordered manner within the selenium lattice, whereas in β-Cu<sub>2</sub>Se they are statistically distributed. Even though the reported structural properties of copper selenide binary phases are not uniform, there is clear agreement regarding the dominating coordination number of four for the copper atoms and the absence of any linearly coordinated metal centers. Because of the hexagonal modification and the preferred coordination number of three for the copper atoms, the layer-type Cu–Se clusters approach the bulk material situation only in principle.

For the copper selenide clusters presented herein, one perceives that it is not possible to assign a special range of cluster sizes to one given phosphine ligand, being followed by another PR<sub>2</sub>R' type to protect the next larger clusters and so on. It can rather be recognized that even very different types of phosphines – perhaps varying in size – are in the position to provoke the formation and crystallization of similar, isomeric or even identical Cu–Se cores if the ligand shells comply with certain requirements of regular geometry and thus protective properties. In contrast, an examination of Scheme 3-3 rationalizes the formation of several clusters that may vary significantly in size, in the presence of the same phosphine, where different reaction conditions permit various suitable ligand shells to be realized. In order to illustrate dependence of the size of the cluster core on the use of different copper salts, stoichiometries, solvents, and reaction temperatures, the cluster for-



**Scheme 3-5** Synthesis of various copper selenide clusters in the presence of  $\text{PEt}_2\text{Ph}$  under different reaction conditions.

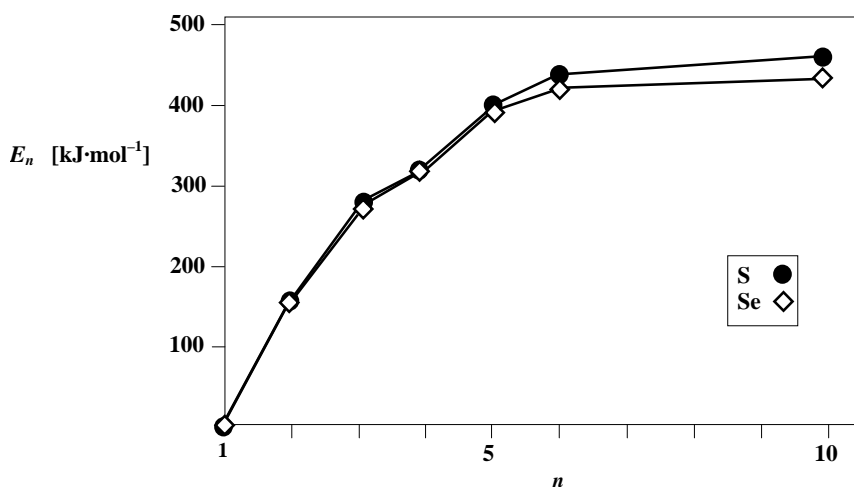


**Fig. 3-45** Course of the stabilization energies per monomer unit  $E_n$  in “naked” clusters  $[\text{Cu}_{2n}\text{E}_n]$  ( $\text{E} = \text{S, Se}$ ;  $n = 1-4, 6, 10$ ). The given values consider the total energies of the most stable structural isomers computed on MP2 level.

mation reactions in the presence of  $\text{PEt}_2\text{Ph}$  as phosphine ligand are shown in Scheme 3-5, with thorough description of the respective conditions.

As for the copper sulfide clusters, comprehensive theoretical investigations within the MP2 approximation (program system TURBOMOLE) were carried out for the  $[\text{Cu}_{2n}\text{Se}_n]$  clusters [34]. Again, stabilization energies per monomeric unit for a “naked” cluster growth from  $n = 1$  to  $n = 6$  and  $n = 10$  were calculated, as were the phosphine binding energies for mono-, di-, tri-, tetra- and hexameric species. The results are given in Figures 18 and 19 respectively. The corresponding graphs for the Cu–S clusters (see Figures 5 and 6) are reproduced once more for comparison.

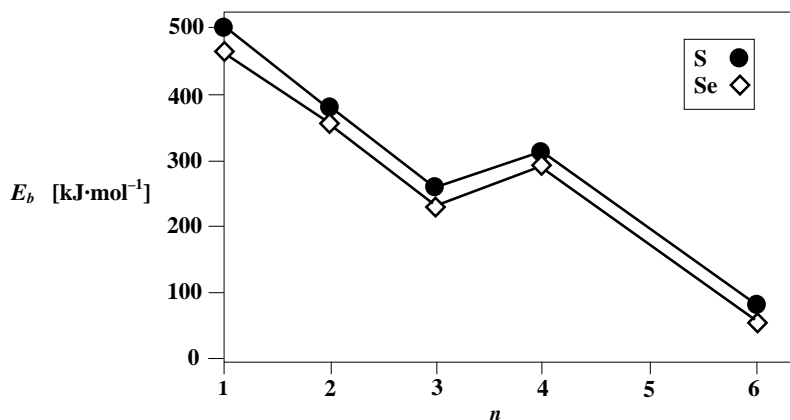


**Fig. 3-46** Course of the Cu–P binding energies per Cu–P bond  $E_b$  in phosphine-ligated clusters  $[\text{Cu}_{2n}\text{E}_m(\text{PH}_3)_m]$  ( $\text{E} = \text{S}, \text{Se}; n = 1\text{--}4, 6; m = 2, 4, 6, 8$ ). The given values consider the total energies of the most stable structural isomers computed on MP2 level with respect to the total energy of  $\text{PH}_3$  calculated by the same method.

The course of both energies is equivalent for the quantum chemically investigated sulfur- or selenium-bridged copper clusters. Thus the statement describing the kinetic stability of the species and the very low Cu–P binding energy is the same as that for the Cu–S compounds. Additionally, a comparison of the energetic properties of sulfur- vs selenium-bridged copper clusters produces two results. Firstly, with nearly identical courses of the stabilization energy (maximum differences:  $\pm 5 \text{ kJ}\cdot\text{mol}^{-1}$ ,  $<2\%$ ) up to  $n = 4$ , one notices a stabilization gain for the Cu–S species from  $n = 6$  onwards. This correlates with a larger absolute value for the formation enthalpy of solid  $\text{Cu}_2\text{S}$  ( $\Delta H_f^\circ: -83.4 \text{ kJ}\cdot\text{mol}^{-1}$ ) [49] when compared to solid  $\text{Cu}_2\text{Se}$  ( $\Delta H_f^\circ: -59.3 \text{ kJ}\cdot\text{mol}^{-1}$ ) [50]. The stabilization energies per monomeric unit for the calculated, rather small, clusters however do not exceed differences of 5%. Thus it is comprehensible why laser ablation spectra of copper chalcogenides do not vary much for different chalcogen types. Secondly, the phosphine molecules are generally bonded by  $4\text{--}7 \text{ kJ}\cdot\text{mol}^{-1}$  (4–9%) higher values of the Cu–P binding energy for the sulfur-bridged compounds. This correlates with the discrepancy between the experiments reported by Dance et al. [32] that show similar behavior for different chalcogens – in agreement with the calculations of “naked” species – and the experimental observations of significant differences in the syntheses and structures of phosphine-clad sulfur or selenium-bridged copper clusters, respectively. The larger Cu–P binding energies computed for Cu–S clusters, when compared to the Cu–P binding energies of their Cu–Se analogs help to explain the different synthetic product spectra. Assuming that the activation energy  $E_a$  for Cu–P bond cleavage increases by a value comparable to the Cu–P binding energy itself when going from the Cu–Se to the Cu–S systems, one calculates a decrease in the respective reaction rate constant  $k$  by means of the Arrhenius equation (Eq. 1) [52].

$$k = A \cdot e^{-E_a/(R \cdot T)}$$

For a typical cluster formation temperature  $T$ , e.g. 250 K, an increase in the activation energy  $E_a$  of about  $5 \text{ kJ} \cdot \text{mol}^{-1}$  causes a reduction in the rate constant  $k$  by one order of magnitude. Thus, the cluster growth that is initiated by the descent of a primary terminal phosphine ligand shell will occur less intensely for sulfur-bridged clusters. Consequently, unlike the selenium-bridged copper clusters, the Cu–S species show a much lower tendency to exceed the aggregation beyond “Cu<sub>12</sub>”.

The use of alkylated or arylated derivatives RSeSiMe<sub>3</sub> (R = organic group) provokes syntheses according to another mechanism that leads to the formation of selenido-/selenolato-bridged copper clusters. The given synthesis route (Schemes 3-1 and 3-4) in no case produces selenolato-free species. This differs from similar reactions with tellurolato reactants RTeSiMe<sub>3</sub> (see below). The experimentally isolated and characterized compounds that are listed in Scheme 3-4 display significantly different structures with regard to the purely E<sup>2-</sup>-bridged molecules (E = S, Se). This applies even for reactions in the presence of tertiary phosphines PPh<sub>3</sub> or PiPr<sub>3</sub> that were likewise used for the syntheses of copper selenide clusters. The expanded ligand properties of SeR<sup>-</sup>, which can act as both a bridging and a terminal ligand, leads to the crystallization of low nuclearity complexes with two, three, six or nine metal centers respectively (38–42) [20, 22, 30] if Se–C bond cleavage is suppressed. Larger cluster compounds can be isolated whenever Se<sup>2-</sup> particles are produced during the reaction to make inner selenium bridges available. However, these molecules containing selenide and selenolato ligands show structural patterns that are also common for Cu–Se clusters as far as the inner core is concerned. In Figure 3-47, the compounds illustrated (38–42) contain only SeR<sup>-</sup> and no Se<sup>2-</sup> ligands.

Binuclear complexes 38 [30] and 39 [20] formally show analogous compositions, but structurally differ according to the restrictions of the different types of ligating components present. These restrictions have structural relevancy for all Se<sup>2-</sup>/SeR<sup>-</sup>-bridged copper clusters as follows. Firstly, bidentate phosphines dppR (R = organic spacer) bridge two copper centers at the periphery of the polynuclear complex or cluster molecule and therefore simultaneously act as protecting groups. Secondly, selenolato ligands SeR<sup>-</sup> usually behave like dppR molecules although they are able to bridge two or three metal centers. Additionally, they *can* be terminally bonded, as found in 39 when the Cu–Cu distance (9.01 Å) is too large for a  $\mu_2$ -SeR bridge. Thirdly, tertiary phosphines PR<sub>2</sub>R' act exclusively as terminal ligands, and thus the copper atoms in 38 are held by SePh<sup>-</sup> fragments at a distance of 2.846(1) Å. The molecular structure of 40 [22] also follows these patterns, again with the final purpose of optimal protection of the heavy atom framework by organic groups. Compounds 41 [30] and 42 [30] are the only examples that could be isolated by employing the bidentate amine ligand bipyridyl (41) or diphenylphosphino acid Ph<sub>2</sub>PO<sub>2</sub>H (42). Cluster 41 seems to represent a “snapshot” molecule of cluster growth, since two [Cu(bipy)]<sup>+</sup> fragments are unsymmetrically attached to a quite regular cluster center. The latter is formed from a distorted tetrahedron Cu<sub>4</sub> (Cu–Cu: 2.650(4)–2.824(4) Å) whose six edges are  $\mu_2$ -bridged by SePh<sup>-</sup> ligands.

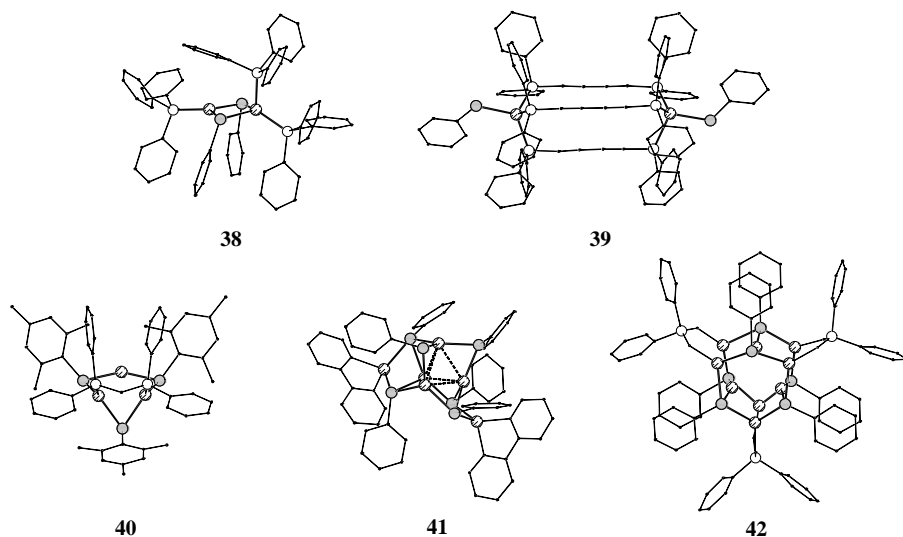


**Fig. 3-47** Molecular structures of  $[\text{Cu}_2(\text{SePh})_2(\text{PPh}_3)_3]$  (**38**),  $[\text{Cu}_2(\text{SePh})_2(\text{dppbd})_3]$  (**39**),  $[\text{Cu}_3(\text{SeMes})_3(\text{dppm})]$  (**40**),  $[\text{Cu}_6(\text{SePh})_6(\text{bipy})_2]$  (**41**), and  $[\text{Cu}_9(\text{SePh})_6(\text{O}_2\text{PPh}_2)_3]$  (**42**) (without hydrogen atoms).

Four of the phenyl selenolato groups, however, act as  $\mu_3$  bridges, since each pair binds to the additional  $\text{Cu}(\text{bipy})^+$  units. Much higher molecular and crystallographic symmetry is found for **42**. Two six-membered  $\text{Cu}_3(\text{SePh})_3$  rings are conjunct by three “naked” copper centers leading to a  $\mu_3$  bridging function of the  $\text{SePh}^-$  groups. Additionally, the rings are held by three  $\text{Ph}_2\text{PO}_2^-$  ligands that bind to the six copper atoms. Twelve phenyl groups envelop the uncharged cluster and therefore enable the termination of atomic aggregation and crystallization in THF.

As for the copper chalcogenide clusters **1–37**, the nature of the phosphine ligands plays a key role in the size and structures of the observed product molecules – even though they are no longer the only protective groups at the cluster peripheries. Success in the synthesis of copper selenide/selenolate clusters was achieved by the use of bidentate phosphines. The variation of organic spacers between the two ligating  $[\text{Ph}_2\text{P}]$  fragments replaces the former variation of organic substituents  $\text{R}$  of  $\text{PR}_2\text{R}'$  with the selenolato-free clusters. Again, one given  $\text{dppR}$  ligand does not necessarily restrict the synthesis to the formation of one single cluster product. Outer reaction conditions rather select between several potential compounds that can all be conveniently protected by the phosphine employed. Thus, with ethane, propane, butane, acetylene or benzene spacers, one obtains clusters with 16, 25, 36, 38, or 58 copper centers (**43** [20], **44** [22], **46–50** [22, 30], **52** [22]). The only tertiary phosphine  $\text{PR}_3$  that was successfully used for the formation of higher nuclearity  $\text{Se}^{2-}/\text{SePh}^-$ -bridged copper clusters is  $\text{P}(\text{iPr})_3$ . The synthesis of molecules featuring thirty-two, fifty, or even seventy-three metal centers (**45**, **51**, **53**) [23] was observed by variation of the reaction conditions with this phosphine. Figure 3-48

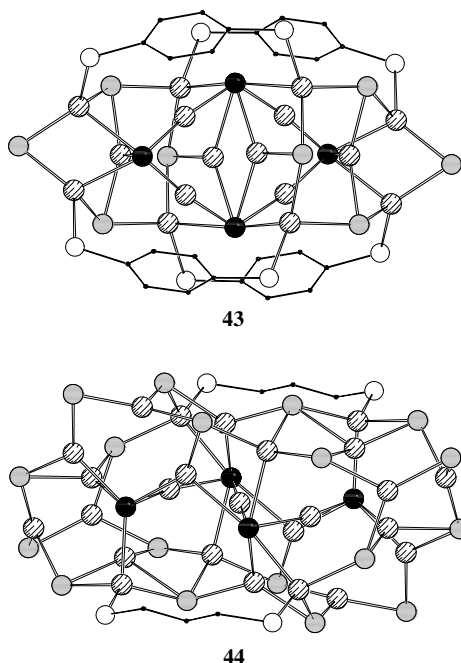


**Fig. 3-48** Molecular structures of  $[\text{Cu}_{16}\text{Se}_4(\text{SePh})_8(\text{dppbe})_4]$  (**43**) and  $[\text{Cu}(\text{dppp})_2][\text{Cu}_{25}\text{Se}_4(\text{SePh})_{18}(\text{dppp})_2]$  (**44**) (without terminal phenyl groups).

shows the molecular structures of **43** and the anion in **44**, the only ionic copper selenide cluster compound isolated to date via this synthetic method.

Both clusters **43** and **44** are oblong in shape. The selenium substructure of **43** can, however, be viewed as a beginning of hexagonal packing of selenium atoms. The middle “layer” consists of six atoms arranged in zigzag fashion, the two enclosing “layers” each containing three selenium centers occupying the *quasi A* position with respect to the *quasi B* position of the atoms in between. Four of the chalcogen ( $\text{Se}^{2-}$ ) bridges act as  $\mu_4$  or  $\mu_6$  bridging ligands. The  $\text{SePh}^-$  ligands are bonded to two or three copper neighbors each and at the same time contribute to the protection of the Cu–Se core by means of their organic substituents. Six copper atoms are surrounded linearly by two selenium ligands: two show an almost trigonal planar  $[\text{Se}_3\text{Cu}]$  coordination, whereas the remaining eight metal centers occupy the centers of slightly distorted  $[\text{Se}_3\text{P}]$  tetrahedra. In contrast to **43**, the chalcogen framework of **44** rather represents an ellipsoid-type deltahedron of four  $\text{Se}^{2-}$  ligands and 18 selenium atoms of the  $\text{SePh}^-$  groups. Again, the bridging grade of the chalcogen centers is higher for the “naked” ligands ( $\mu_5$  or  $\mu_7$ ) than for the  $\text{SePh}^-$  fragments ( $\mu_2$ – $\mu_4$  with regard to the Cu–Se bonds). There are eighteen copper atoms positioned at the cluster periphery, and these belong to almost planar  $[\text{Se}_3\text{Cu}]$  or distorted tetrahedral  $[\text{Se}_3\text{CuP}]$  units. The observation that no linear  $[\text{Se}_2\text{Cu}]$  arrangements are present in **44** underlines the trend to higher coordina-



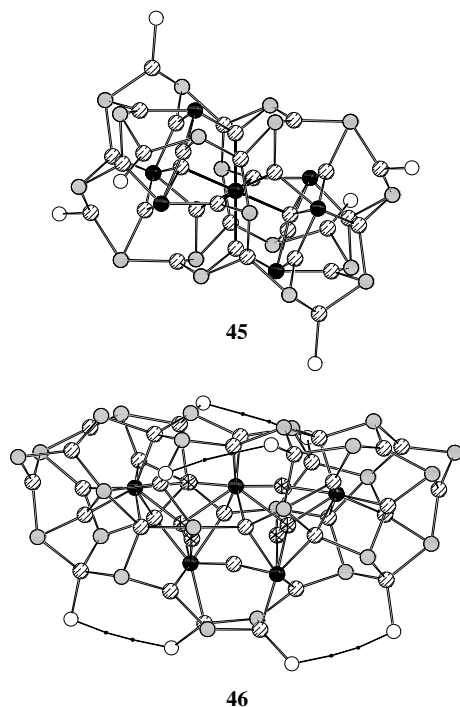


**Fig. 3-49** Molecular structures of  $[\text{Cu}_{32}\text{Se}_7(\text{SenBu})_{18}(\text{PiPr}_3)_6]$  (**45**) and  $[\text{Cu}_{36}\text{Se}_5(\text{SePh})_{26}(\text{dppa})_4]$  (**46**) (without *n*-butyl, *i*-propyl or phenyl groups). Three copper atoms (marked with a cross) in the cluster center of **46** are distributed over six sites with an occupation of 0.5.

tion numbers at the metal center with increasing molecular size as reported for the copper selenide clusters without selenolato ligands. The cluster corpus is large enough to accommodate some inner copper atoms that are either two-, three-, or – rarely – five-coordinated by selenium neighbors. Comparing the compositions of **43** and the anion in **44**, one perceives an increasing preference for the ligation by  $\text{SePh}^-$  ligands rather than the ligation by phosphine donors. This may be explained by the ambivalent character of the  $\text{SePh}^-$  groups, which firstly form fairly stable Cu–Se cluster bonds and secondly carry protective organic substituents. Thus, the ratio of “terminally ligating selenium atoms” to phosphorus atoms increases from 1:1 in **43** to 4.5:1 in **44**.

The molecular structures of the cluster compounds **45** and **46** are given in Figure 3-49. Figure 3-50 shows the packing of selenium atoms in **45** and the selenium substructure in **46**.

As for the comparison of **43** and **44**, one can discuss a smaller cluster whose structure is based on a regular packing of selenium atoms in layers (**45**) and a larger, rather spherically shaped compound, that features a polyhedral selenium framework (**46**). The selenium layers in the  $\text{SenBu}^-$ -bridged species **45** are packed

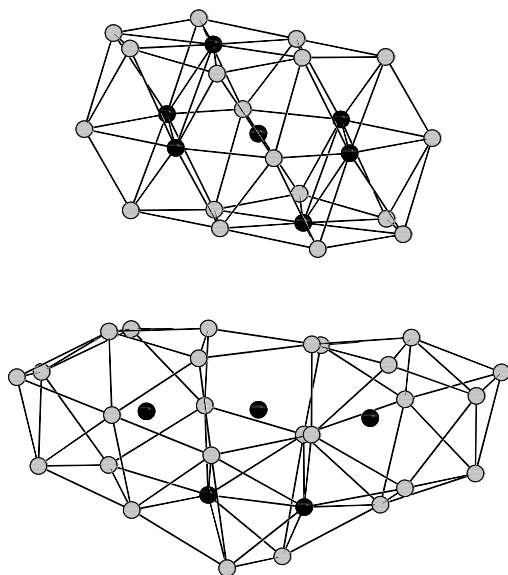


**Fig. 3-50** Selenium substructures in **45** (top) and **46** (bottom). The drawn Se–Se contacts do not represent bonding interactions, but only serve to visualize the A–B–C packing of selenium atoms in three layers in **45** or explain the geometry of the polyhedron in **46**.

in an A–B–C fashion similar to the  $\text{Cu}_2\text{Se}$  solid state structure, which is so far unparalleled for all known copper chalcogenide clusters. This similarity between the atomic arrangement of a cluster molecule and the *non-molecular*  $\text{Cu}_2\text{Se}$  suggests that a fragment of a bulk structure may indeed be stabilized to nano-size by coating the surface with suitable groups. This tendency is also observed in three silver selenide/selenolate clusters,  $[\text{Ag}_{112}\text{Se}_{32}(\text{SenBu})_{48}(\text{PtBu}_3)_{12}]$ ,  $[\text{Ag}_{114}\text{Se}_{34}(\text{SenBu})_{46}(\text{PtBu}_3)_{14}]$ , and  $[\text{Ag}_{172}\text{Se}_{40}(\text{SenBu})_{92}(\text{dppp})_4]$  (see section 3.1.3.3) [53]. Cluster **45** is the only copper selenide/selenolate compound that contains  $\text{SenBu}^-$  groups like these silver clusters. It is not yet proven, but it is at least possible, that the packing of the selenium atoms may be influenced by the nature of the organic group attached to the selenolato ligand. The chalcogen layers in **45** are centered by a large planar rhombus of nine selenium atoms. Five of these are “naked”  $\text{Se}^{2-}$  ligands in the cluster network, while the four vertex atoms are  $\text{SenBu}^-$  groups. Above and below this middle layer, one finds two truncated rhombuses consisting of only eight selenium atoms, the “central” ones not being bonded to organic substituents. However, the size dependency of structural properties seems to be different from that of the selenolato-free copper clusters: layer-type structures are observed even for smaller molecules like **43** or **45** in addition to larger, spherical ones. A reversion to lower average coordination numbers in larger clusters may also appear, as observed in **45**. Of the 32 copper atoms in **45**, twelve have a trigonal planar coordination geometry and two show an ideal tetrahedral environment. The remaining

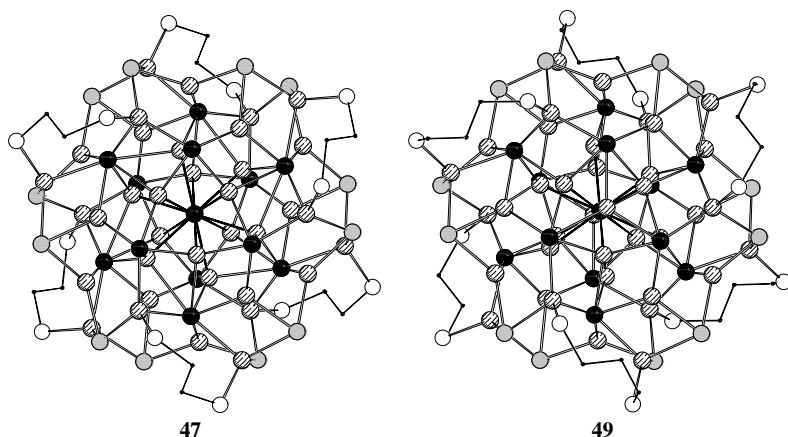


**Fig. 3-51** Molecular structures of  $[\text{Cu}_{36}\text{Se}_{13}(\text{SePh})_{12}(\text{dppe})_6]$  (**47**) and  $[\text{Cu}_{38}\text{Se}_{13}(\text{SePh})_{12}(\text{dppp})_6]$  (**49**) (without phenyl groups).

eighteen metal atoms are shifted away from the centers of tetrahedral holes. Hence, each of them displays only three normal Cu–Se bonds, with the fourth Cu–Se distance being relatively long (3.18–3.35 Å). The tendency to occupy tetrahedral holes – even without perfect realization – again correlates with the structural properties of bulk  $\text{Cu}_2\text{Se}$ . In **46**, five inner  $\text{Se}^{2-}$  ligands are enclosed by a shell of twenty-six  $\text{SePh}^-$  fragments. The bridging grades of the  $\text{Se}^{2-}$  ligands amount to  $\mu_7$  or  $\mu_8$  whereas the selenium atoms of the  $\text{SePh}^-$  groups act only as  $\mu_2$ – $\mu_4$  bridges between next copper atoms. The copper centers feature coordination numbers of two, three, or four, within  $[\text{Se}_2\text{Cu}]$ ,  $[\text{Se}_3\text{Cu}]$ ,  $[\text{Se}_4\text{Cu}]$ , or  $[\text{Se}_3\text{CuP}]$  units, respectively. Depending on their position inside the cluster or at the surface, the selenium neighbors of the metal atoms are either exclusively  $\text{Se}^{2-}$  or a combination of  $\text{Se}^{2-}$  and  $\text{SePh}^-$  ligands. As for the **43** and **44**, the number of terminal selenolato groups is a multiple of the number of ligating phosphorus atoms (SeR:P ratios are 3:1 in **45**, 3.25:1 in **46**).

Four closely related Cu–Se–SePh clusters are formed in the presence of either dppe, dppp, or dppb (**47**–**50**). The syntheses of isomeric, mixed valence compounds **47** and **48** containing 36 copper centers were carried out in THF; the isomeric “ $\text{Cu}_{38}$ ” clusters **49** and **50** that formally display exclusively  $\text{Cu}^+$  crystallize from toluene. As well as being performed in different solvents, the reactions producing the dppp-ligated compounds **48** or **50** differed in the  $\text{CuCl}:\text{dppp}$  ratios (3.1:1 for **48**, 5:1 for **50**). In Figure 3-51, the molecular structures of **47** and **49** are given as examples.

Cluster **47** crystallizes in the trigonal space group  $R\bar{3}$ , whereas **48**–**50** crystallize in triclinic space ( $P\bar{1}$ ). Despite the different crystallographic symmetry, all four compounds display very similar structural properties. A closer look at the atomic arrangements helps to put the preference of this prototypic cluster framework

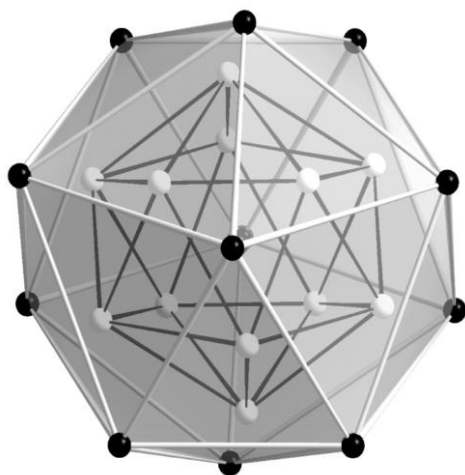
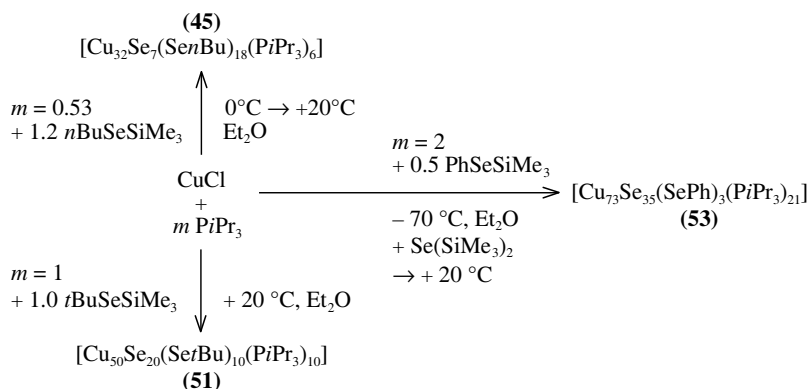


**Fig. 3-52** Central  $[\text{Se}_{13}\text{Cu}_{12}]$  unit in **47**. The drawn lines only represent polyhedral edges and do not specify bonding interactions.

down to highly symmetric substructures. A central selenium atom positioned on the inversion centers of the clusters is surrounded by a distorted icosahedron of twelve copper atoms. The latter is itself enclosed by another distorted  $\text{Se}_{12}$  icosahedron. An alternate packing of  $\text{Cu}_{12}$  and  $\text{Se}_{12}$  icosahedra has already been discussed for the Cu–Se clusters **14** and **15** (Figures 3-34 and 3-35). In these compounds, one polyhedron is positioned with its edges perpendicular to the edges of the polyhedron below. In contrast to this pattern, the  $\text{Se}_{12}$  and  $\text{Cu}_{12}$  icosahedra in **47–50** are arranged such that one of the idealized fivefold axes of one polyhedron parallels one of the idealized threefold axes of the other and vice versa. The central  $[\text{Se}_{13}\text{Cu}_{12}]$  unit of **47** is shown as an example in Figure 3-52.

In this way, six edges and six faces of the  $\text{Cu}_{12}$  icosahedron are bridged by the selenide ligands that form the  $\text{Se}_{12}$  polyhedron. The cluster core expands out to the periphery by coordination of the  $\text{Se}_{12}$  substructure to another 24 copper atoms, twelve of which are bonded to the six dppR ligands. These copper atoms are bridged by twelve  $\mu_3\text{-SePh}^-$  groups that are positioned at the cluster surface with the phosphine molecules. Except for the  $\mu_{12}$  bridging central selenium atom, the selenide ligands act as  $\mu_6$  (each six in **47** and **48**, all in **49** and **50**) or  $\mu_5$  bridges (each six in **47** and **48**) between copper centers. The different numbers of copper neighbors per selenium atom in **47** and **48** on the one hand and **49** and **50** on the other hand is caused by two copper atoms being formally “missing” in the molecular structures of **47** or **48**, resulting in the mixed-valence situation. The metal centers are distorted trigonal planar or tetrahedrally surrounded. All Cu–Se distances in the mixed-valence clusters lie within the range of the Cu–Se bond lengths in all four clusters (2.301(4)–2.888(3) Å) and thus give no evidence of any localization of the  $\text{Cu}^{2+}$  centers. However, the range of the Cu–Cu contacts in **47** or **48** (2.511(3)–2.943(4) Å) is somewhat narrower than that found in **49** or **50**



**Scheme 3-6** Synthesis of various selenido/selenolato-bridged copper clusters in the presence of  $\text{PiPr}_3$  under different reaction conditions.

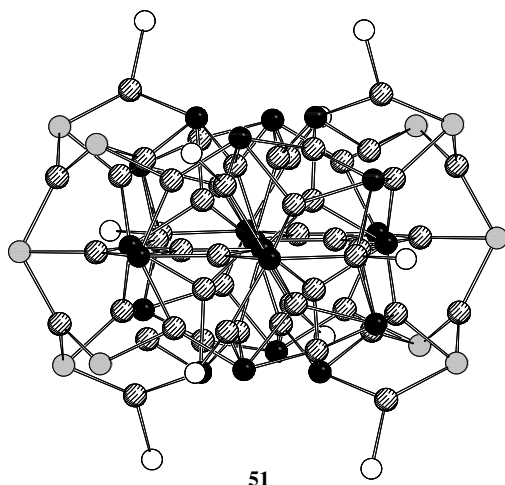


**Fig. 3-53** Molecular structure of  $[\text{Cu}_{50}\text{Se}_{20}(\text{SetBu})_{10}(\text{PiPr}_3)_{10}]$  (51) (without organic groups).

(2.305(4)–3.040(3) Å). The spherical, somewhat oblate molecules show maximum diameters of 23.9–25.7 Å.

The use of different selenolato sources and different optimized reaction conditions leads to three various copper selenide/selenolate clusters with terminal  $\text{PiPr}_3$  ligands, 45 (Figures 22 and 23), 51, and 53. The latter is synthesized in an uncommon manner by the use of both  $\text{PhSeSiMe}_3$  and  $\text{Se}(\text{SiMe}_3)_2$  in the same reaction and is discussed below. Scheme 3-6 summarizes the syntheses of the  $\text{PiPr}_3$ -clad clusters, specifying the reaction conditions in detail, and Figure 3-53 shows the molecular structure of compound 51.

Examining Figure 3-53, one surmises that a “normal” cluster growth occurred in the presence of a tertiary phosphine – indeed under Se–C bond cleavage

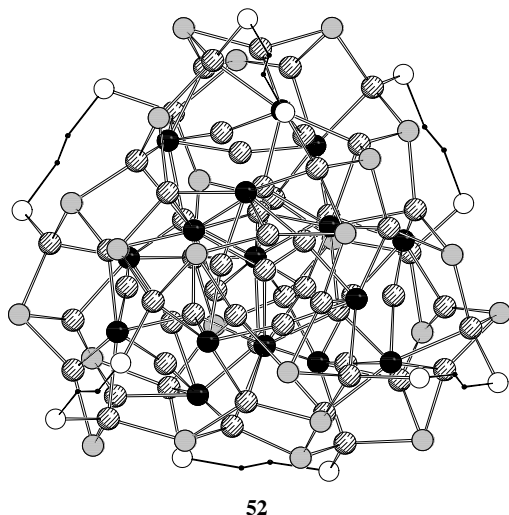
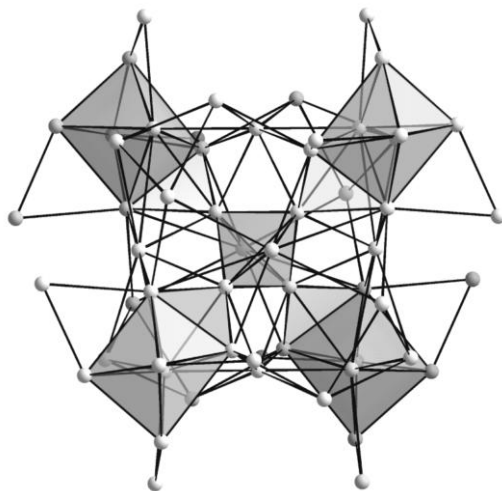


Fig. 3-54 Molecular structure of  $[\text{Cu}_{58}\text{Se}_{16}(\text{SePh})_{24}(\text{dppa})_6]$  (**52**) (without phenyl groups).

conditions – to result in the formation of a copper selenide cluster which is represented by the  $[\text{Cu}_{40}\text{Se}_{20}]$  central unit of **51**. Only the sidewise attachment of two symmetry equivalent  $[\text{Cu}_5(\text{Se}t\text{Bu})_5]$  fragments reflects the presence of the selenolato reactant. This is in contrast to the related  $\text{PiPr}_3$ -ligated structure of **45**, which shows only seven  $\text{Se}^{2-}$  ligands with eighteen  $\text{Se}t\text{Bu}^-$  groups. A definite correlation between the significantly different course of the cluster formation and the respective reaction conditions cannot be evaluated based on the low statistic, but it is very likely that the Cu:P ratio of the reactants and the temperature play an important role. The copper atoms in **51** bind to  $\text{Se}^{2-}$ ,  $\text{SePh}^-$ , and  $\text{PiPr}_3$  ligands in different ratios to achieve coordination numbers of two (with a bend coordination geometry indicating a weak third interaction), three, and four. The selenium atoms that carry *t*-butyl groups act as  $\mu_3$  bridges between copper atoms, whereas the  $\text{Se}^{2-}$  ligands bridge between five, six or seven copper neighbors. The molecules are regularly protected by  $\text{PiPr}_3$  ligands and the organic substituents of the  $\text{Se}t\text{Bu}^-$  groups.

The molecular structure of another dppR-ligated copper cluster ( $\text{R} = \text{a} = \text{acetylene}$ ) with both selenido and selenolato ligands, **52**, again displays high symmetry, and here the molecular symmetry is underlined by very high crystallographic symmetry. The compound crystallizes in the cubic space group  $F\bar{4}3c$  and is thus the second copper chalcogenide cluster known besides **14** (space group  $Fm\bar{3}$ ) with a cubic crystal lattice. The molecular structure of **52** is illustrated in Figure 3-54.

As observed for **47–50**, the cluster core is oblate in shape. However, in contrast to **47–50**, it is not based on icosahedral fragments. Instead, one perceives a central tetrahedron  $\text{Cu}_4$  sharing its corners with four further  $\text{Cu}_4$  units that themselves share the *trans* face with each octahedral  $\text{Cu}_6$ . The remaining 30 copper atoms are



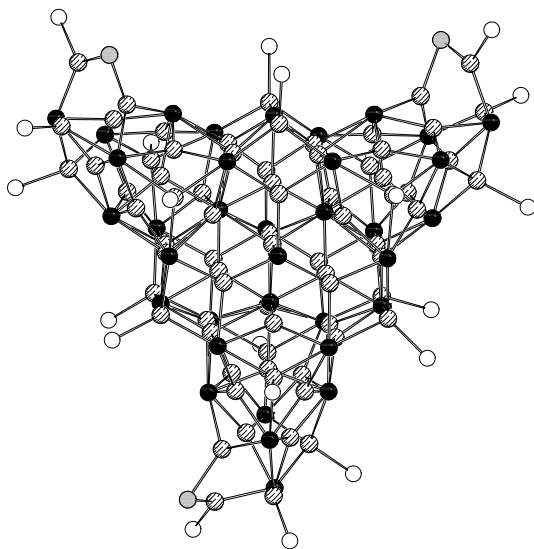
**Fig. 3-55** Copper substructure in **52**. The connected tetrahedra  $\text{Cu}_4$  and octahedra  $\text{Cu}_6$  are highlighted by gray shading. Cu–Cu distances are drawn up to 301.2(4) Å.

situated between these polyhedra or are connected at the outside of the polyhedral arrangement. The copper substructure of **52** is given in Figure 3-55.

Even though the  $\text{Cu}_{58}$  substructure has to be assigned the formal charge  $56+$  (assuming  $\text{Se}^{2-}$  and  $\text{SePh}^-$  ligands as well as electroneutrality in the sum), which leads to an extraordinary mixed valence  $\text{Cu}^+/\text{Cu}^0$  compound, one does not find any hints of exceptional Cu–Cu binding interactions. The Cu–Cu distances lie within the usual range of 2.540(3) and 3.012(4) Å. Thus, the cluster core is habitually held together by bridging selenido or selenolato ligands. The former act as  $\mu_5$  or  $\mu_6$  bridges, and the latter are  $\mu_3$  bridges between next neighboring copper atoms. Despite the large cluster size, near-linear as well as trigonal planar or tetrahedrally coordinated metal centers are observed. Therefore, it is again proved that the size-dependence of the structural principles discussed for chalcogenolato-free copper sulfide or copper selenide clusters are widely invalid in the Cu–Se–SeR cluster systems. Six dppa ligands and 24 phenyl groups of the  $\text{SePh}^-$  fragments ligate the cluster molecule. Hence **52** continues the series of compounds that show a significant preference for protection by  $\text{SeR}^-$  groups rather than phosphine ligands. The clusters **43** and **47–51** represent exceptions to this series, as their SeR:P ratios are all 1:1.

The largest copper cluster with both  $\text{Se}^{2-}$  and  $\text{SeR}^-$  ligands in the framework is **53**. Its molecular structure is shown in Figure 3-56.

The cluster displays a  $[\text{Cu}_{70}\text{Se}_{35}]$  core that is identical to that observed in **28** or **29** (Figures 15 and 16). Only three additional Cu–SePh fragments positioned at the corners of the triangular molecule distinguish **53** from the slightly smaller clusters. The fact that one observes a typical copper selenide cluster structure with only a few selenolato groups present is surprising, since  $\text{PhSeSiMe}_3$  was the first sele-



53

Fig. 3-56 Molecular structure of  $[\text{Cu}_{73}\text{Se}_{35}(\text{SePh})_3(\text{PiPr}_3)_{21}]$  (**53**) (without organic groups).

nium source added during the synthesis. This indicates again the distinct preference for the “ $\text{Cu}_{70}$ ” molecular structure that is formed whenever the reaction conditions (Scheme 3-6) and the solubility situation enables the cluster growth to proceed until crystallization of this large cluster compound can occur.

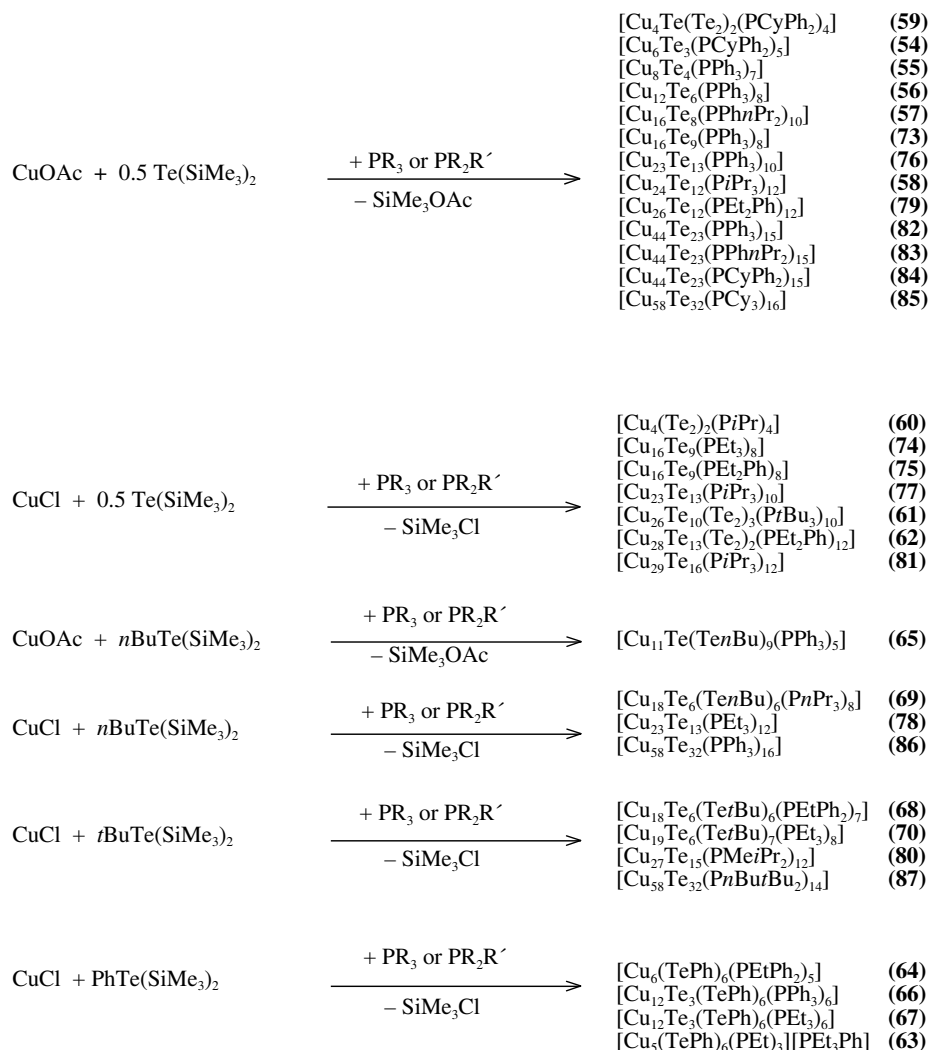
### Tellurium-Bridged Copper Clusters

In this section, we focus on the description of the syntheses and structures of ligand-stabilized copper telluride cluster molecules. Solid-state copper tellurides as well as ternary alkali metal copper telluride compounds, which consist of  $n$ -dimensionally linked copper telluride clusters, are beyond the scope of this review. Their syntheses have accelerated lately, although only a limited number exist up to now, e.g.,  $\text{KCuTe}$  [54],  $\text{NaCuTe}$  [55],  $\text{KCu}_3\text{Te}_2$  [56],  $\text{NaCu}_3\text{Te}_2$  [57],  $\text{K}_2\text{Cu}_5\text{Te}_5$  [58], and  $\text{K}_4\text{Cu}_8\text{Te}_{11}$  [59], all of which have been prepared by means of melt reactions. The recently synthesized compound  $\text{K}_3\text{Cu}_{11}\text{Te}_{16}$  [60] is the first example of a ternary alkali metal copper telluride crystallized from supercritical 1,2-diaminoethane.

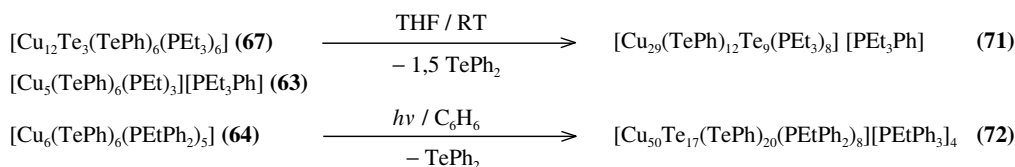
According to the general reaction pathway given in Scheme 3-7 and 3-8, the syntheses of ligand-stabilized copper telluride clusters have mainly been achieved in one of three different ways [11, 16, 19, 20, 24, 25, 31, 61].

Reaction of copper(I) acetate with  $\text{Te}(\text{SiMe}_3)_2$  at low temperatures ( $-50$  to  $-20$  °C) yields smaller cluster compounds with stoichiometric composition. At higher reaction temperatures, up to  $25$  °C, larger clusters can be isolated that are mostly of the mixed-valence type. Similar mixed-valence compounds have also been isolated from reactions of copper(I) chloride with  $\text{Te}(\text{SiMe}_3)_2$  at lower





**Scheme 3-7** Survey of the reaction pathways for the synthesis of ligand-stabilized tellurido or tellurido/telluroloato-bridged copper clusters.



**Scheme 3-8** Reaction pathways for the formation of larger telluride/telluroloato-bridged copper clusters starting from cluster precursors.

temperatures (down to  $-70\text{ }^{\circ}\text{C}$ ). By treating copper(I) chloride or copper(I) acetate with telluroate compounds  $\text{RTeSiMe}_3$  ( $\text{R} = t\text{Bu}, n\text{Bu}, \text{Ph}$ ), one obtains clusters which contain both  $\text{RTe}^-$  and  $\text{Te}^{2-}$  ligands as a result of the facile cleavage of the Te–C bond. In some cases, we isolated clusters featuring Te–Te bridges. Examples of syntheses of larger copper telluride clusters starting from cluster precursors are light-induced formation of  $[\text{Cu}_{50}\text{Te}_{17}(\text{TePh})_{20}(\text{PEtPh}_2)_8][\text{PEtPh}_3]_4$  (**72**) from  $[\text{Cu}_6(\text{TePh})_6(\text{PEtPh}_2)_5]$  (**64**) in benzene [19] and the co-condensation of  $[\text{Cu}_{12}\text{Te}_3(\text{TePh})_6(\text{PEt}_3)_6]$  (**67**) with  $[\text{Cu}_5(\text{TePh})_6(\text{PEt}_3)_3][\text{PEt}_3\text{Ph}]$  (**63**) to form  $[\text{Cu}_{29}(\text{TePh})_{12}\text{Te}_9(\text{PEt}_3)_8][\text{PEt}_3\text{Ph}]$  (**71**) as outlined in Scheme 3-8 [61].

Table 3-1 summarizes all the Cu–Te cluster compounds that have been synthesized and structurally characterized by single-crystal X-ray diffraction analysis to date. The species can be subdivided into four main groups, three of which consist of stoichiometric compositions  $[\text{Cu}_n\text{Te}_{n-x}(\text{TeR})_{2x}(\text{PR}_2\text{R}')_m]$  that differ in the nature of their tellurium ligands, while the fourth represents the group of mixed-valence clusters.

The structures of the tellurium-bridged copper clusters (Figures 3-57–3-61, see below) differ from those of the copper sulfide or selenide clusters, with the exception of some smaller ones. This can be understood against the background of the larger atomic and ionic radii of the tellurium atoms compared to the lighter chalcogen atoms, allowing higher coordination numbers and therefore new binding geometries which lead to different structures. In addition, one finds a greater tendency to form mixed-valence clusters. This is in line with the existence of many stable binary compounds with compositions  $\text{Cu}_{2-x}\text{Te}$  [40] and with the situation found in the ternary alkali copper telluride compound  $\text{K}_2\text{Cu}_5\text{Te}_5$  [58].

In the case of copper telluride clusters, we have not yet reached the turning point in size where the whole core structures display bulk structure characteristics, as seen for the copper selenide species. Nevertheless, the tellurium frameworks in the largest cluster compounds, **85–87** display hexagonal structure properties. Powder diffraction patterns of  $\text{Cu}_2\text{Te}$  could be also indexed on the basis of a hexagonal cell of tellurium atoms. However, the structural details for bulk  $\text{Cu}_2\text{Te}$  have not yet been completely established [40b].

In all the copper tellurium cluster molecules, the tellurium atoms form polyhedra with triangular faces. In the larger ones, some of the tellurium atoms are located inside the polyhedra. For smaller cluster molecules, the tellurium polyhedra can usually be derived from classical polyhedra (Figure 3-57). Those of the larger ones often show unusual cage structures. The distances between the tellurium atoms are usually non-bonding, except the Te–Te units in **59–62**.

The copper atoms reside in the holes and on the surface of the polyhedra and are coordinated by either two, three, or four tellurium atoms, with some being additionally coordinated by one further phosphine ligand.

The Cu–Te distance ranges that are regarded as bonding contacts range from 2.403 to 3.337 Å for all the clusters under discussion. Even though coordination numbers ( $CN$ ) for  $\text{Te}^{2-}$  ligands range from 4 to 12 and those for  $\text{TeR}^-$  are usually smaller ( $CN = 2, 3, 4$ ), there is no significant difference between the average Cu–Te distances for  $\text{Te}^{2-}$  and  $\text{TeR}^-$  ligands.

Tab. 3-1 Classification of copper telluride into stoichiometric or mixed valence according to the types of tellurium ligands.

stoichiometric				
only with $Te^{2-}$ ligands	with additional $Te-Te$ bridges	with additional $TeR$ ligands	mixed-valence	
$[Cu_6Te_3(PCyPh_2)_5]$	(54) [31] $[Cu_4Te(Te_2)(PCyPh_2)_4]$	(59) [31] $[Cu_5(TePh)_6(PEt)_3][PEt_3Ph]$	(63) [61] $[Cu_{16}Te_9(PPh_3)_8]$	(73) [24]
			$[Cu_{16}Te_9(PEt_3)_8]$	(74) [11]
$[Cu_8Te_4(PPh_3)_7]$	(55) [24] $[Cu_4(Te_2)_2(PtPr_3)_4]$	(60) [11] $[Cu_6(TePh)_6(PEtPh_2)_5]$	$[Cu_{16}Te_9(PEt_2Ph)_8]$	(75) [11]
			$[Cu_{23}Te_{13}(PPh_3)_{10}]$	(76) [24]
			$[Cu_{23}Te_{13}(PPr_3)_{10}]$	(77) [11]
			$[Cu_{23}Te_{13}(PEt_3)_{12}]$	(78) [16]
$[Cu_{12}Te_6(PPh_3)_8]$	(56) [24] $[Cu_{26}Te_{10}(Te_2)_3(PtBu_3)_{10}]$	(61) [11] $[Cu_{11}Te(TerBu)_9(PPh_3)_5]$	$[Cu_{26}Te_{12}(PEt_2Ph)_{12}]$	(79) [24]
$[Cu_{16}Te_8(PPhnPr_2)_{10}]$	(57) [24] $[Cu_{28}Te_{13}(Te_2)_2(PEt_2Ph)_{12}]$	(62) [11] $[Cu_{12}Te_3(TePh)_6(PEt_3)_6]$	$[Cu_{27}Te_{15}(PMeiPr_2)_{12}]$	(80) [25]
				(67) [61]
$[Cu_{24}Te_{12}(PPr_3)_{12}]$	(58) [24]	$[Cu_{18}Te_6(TerBu)_6(PEtPh_2)_7]$	$[Cu_{29}Te_{16}(PPr_3)_{12}]$	(81) [11]
		$[Cu_{18}Te_6(TerBu)_6(PnPr_3)_8]$		(68) [25]
		$[Cu_{19}Te_6(TerBu)_7(PEt_3)_8]$		(69) [16]
			$[Cu_{44}Te_{23}(PPh_3)_{15}]$	(82) [24]
			$[Cu_{44}Te_{23}(PPhnPr_2)_{15}]$	(83) [24]
			$[Cu_{44}Te_{23}(PCyPh_2)_{15}]$	(84) [24]
		$[Cu_{29}(TePh)_{12}Te_9(PEt_3)_8][PEt_3Ph]$	$[Cu_{58}Te_{32}(PCy_3)_{16}]$	(85) [31]
			$[Cu_{58}Te_{32}(PPh_3)_{16}]$	(86) [16]
		$[Cu_{50}Te_{17}(TePh)_{20}(PEtPh_2)_8][PEtPh_3]_4$	$[Cu_{58}Te_{32}(PnBu_2Bu)_{14}]$	(87) [25]
				(72) [19]

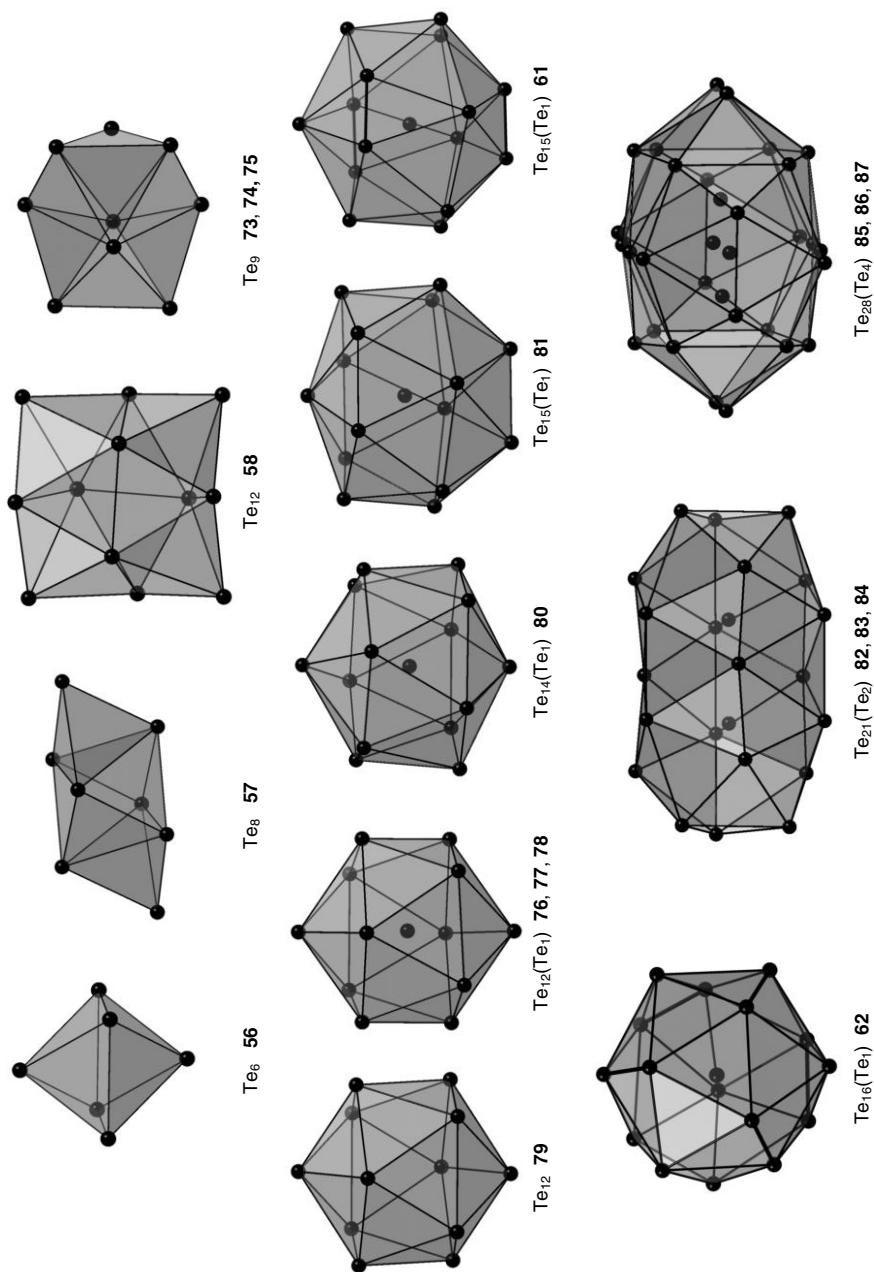


**Fig. 3-57** Tellurium polyhedra in copper telluride clusters. Connections to the central tellurium atoms are omitted for clarity. Direct Te–Te bonds in **61** and **62** are drawn thicker.

Those tellurium atoms that are located in the center of the cluster molecules tend to bond to a large number of copper atoms. In some compounds, the copper atoms themselves form polyhedra, which can be described as Frank-Kasper polyhedra [62]. In these cases, the clusters consist of interpenetrating Frank-Kasper polyhedra, which are well known from a number of intermetallic phases (e.g., Laves Phases).

However, the observed Cu–Cu distances give no indication of strong metal-metal (i.e.  $d^{10}$ – $d^{10}$ ) interactions. Theoretical investigations point to the same conclusions [34b, 63]. The shortest Cu–Cu contacts were observed in the molecular structures of **62** (2.383 Å), and **78** (2.382 Å), but these involve copper atoms which exhibit elongated thermal ellipsoids. Aside from these, the shortest Cu–Cu distances are interestingly observed for the largest clusters, namely **85** (2.426 Å), **86** (2.448 Å), and **87** (2.433 Å).

In the following section, all cluster structures will be briefly described and discussed according to the division into four groups indicated in Table 3-1.

The molecular structures of the stoichiometric copper telluride clusters **54**–**58** are shown in Figure 3-58.

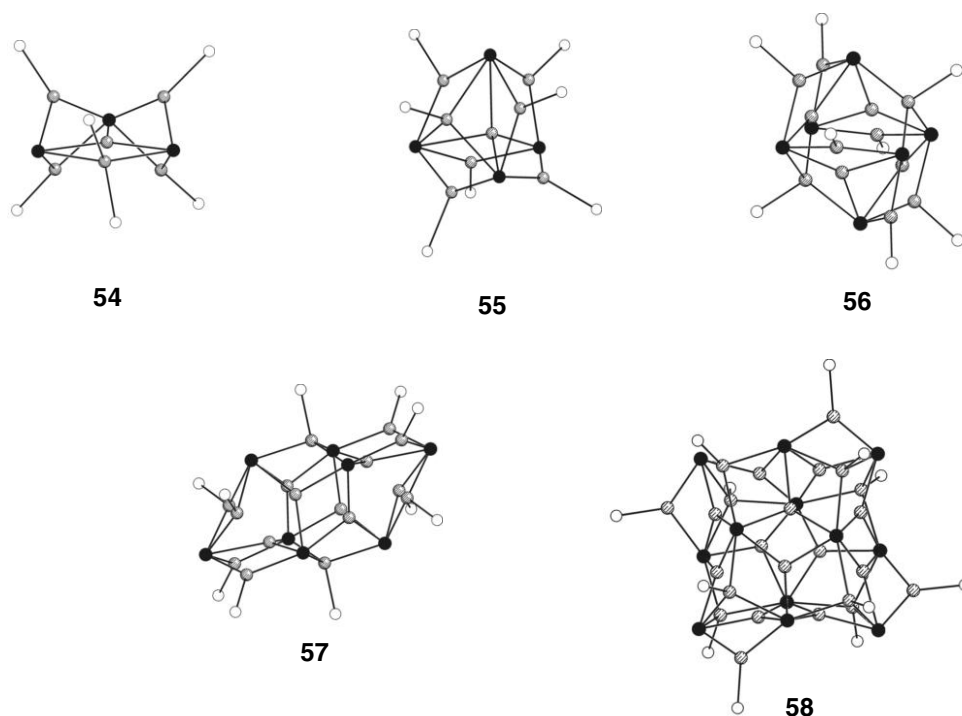


**Fig. 3-58** Molecular structures of stoichiometric copper telluride clusters  $[\text{Cu}_6\text{Te}_3(\text{PCyPh}_2)_5]$  (**54**),  $[\text{Cu}_8\text{Te}_4(\text{PPh}_3)_7]$  (**55**),  $[\text{Cu}_{12}\text{Te}_6(\text{PPh}_3)_8]$  (**56**),  $[\text{Cu}_{16}\text{Te}_8(\text{PPhnPr}_2)_{10}]$  (**57**), and  $[\text{Cu}_{24}\text{Te}_{12}(\text{PiPr}_3)_{12}]$  (**58**). C and H atoms are omitted for clarity.

In **54**, three tellurium atoms form a triangle, in the center of which a copper atom is coordinated in a slightly distorted triangular fashion. Four [CuPPh<sub>2</sub>Cy] units are doubly bridging two of the edges. The third edge is bridged by a copper atom which is bonded to two phosphine ligands.

The tellurium atoms in **55** form a tetrahedron, the six edges of which are bridged by [CuPPh<sub>3</sub>] groups. An additional  $\mu_3$ -[CuPPh<sub>3</sub>] fragment is bonded to a Te<sub>3</sub> face, and one naked copper atom is located in the center of the Te<sub>4</sub> tetrahedron.

Cluster **56** features a Te<sub>6</sub> octahedron. Six [CuPPh<sub>3</sub>] groups act as  $\mu_2$ -bridges above six of the octahedral edges. Two further [CuPPh<sub>3</sub>] groups are coordinated by three tellurium atoms, giving a tetrahedral environment around the copper atoms. The other four copper atoms are each coordinated by three tellurium atoms. Thus, **56** represents a novel isomer of the [Cu<sub>12</sub>E<sub>6</sub>(PR<sub>3</sub>)<sub>8</sub>] clusters (see above) which was not observed for E = S, Se.

An octahedron of tellurium atoms is also found in **57**. However, two further tellurium atoms additionally cap two opposite triangular faces. Eight [CuPPh<sub>2</sub>Pr<sub>2</sub>] groups are bonded along edges of this polyhedron. Of the other eight copper centers, two are tetrahedrally coordinated by one phosphine and a Te<sub>3</sub> face. The six remaining metal atoms are bonded in a distorted trigonal planar mode by three tellurium atoms and are located inside the cluster cavity.

The Te<sub>12</sub> substructure of **58** cannot be described as a classical deltahedron, but rather shows an arrangement of two highly distorted face-sharing tetragonal antiprisms. Four [CuPiPr<sub>3</sub>] groups bridge one Te–Te non-bonding edge each, and eight [CuPiPr<sub>3</sub>] units act as  $\mu_3$ -bridges above Te<sub>3</sub> faces. The other twelve copper atoms are each surrounded by three tellurium atoms and are slightly shifted away from the Te<sub>3</sub> planes toward the center of the molecule.

Some reactions of copper(I) chloride or copper(I) acetate lead to the formation of copper telluride clusters that contain Te–Te bridges (**59**–**62**, Figure 3-59).

In **59**, three tellurium atoms form an approximate isosceles triangle with a Te–Te bond along the short edge (Te–Te: 2.791 Å). The two longer edges of the triangle are bridged by one [CuPPh<sub>2</sub>Cy] unit each. The two other copper atoms are located above and below the triangular face and are additionally coordinated by phosphine ligands.

The four copper atoms in **60** form a “butterfly” structure bridged by two ditelluride ligands (Te–Te 2.800–2.812 Å). Every copper atom is additionally coordinated by a phosphine ligand.

Clusters **61** and **62** are spherical molecules based on tellurium polyhedra, parts of which are strongly distorted because of the presence of Te–Te bonds. Both compounds display Frank-Kasper polyhedra containing 15 (**61**) or 16 (**62**) tellurium atoms centered by one additional tellurium ligand. The tellurium polyhedron of **61** is similar to that observed in **20**, although it differs in the presence of three Te–Te bonds (2.936–3.011 Å). The copper atoms are bonded to the tellurium atoms in a different arrangement to that in **20**. Eight [CuP<sup>*t*</sup>Bu<sub>3</sub>] units are situated above Te<sub>3</sub> faces of the polyhedron, while two such units are edge-bridging. Eleven further copper atoms are coordinated by three tellurium atoms, eight of which are localized below Te<sub>3</sub> faces, while the other three bind between the central tellurium

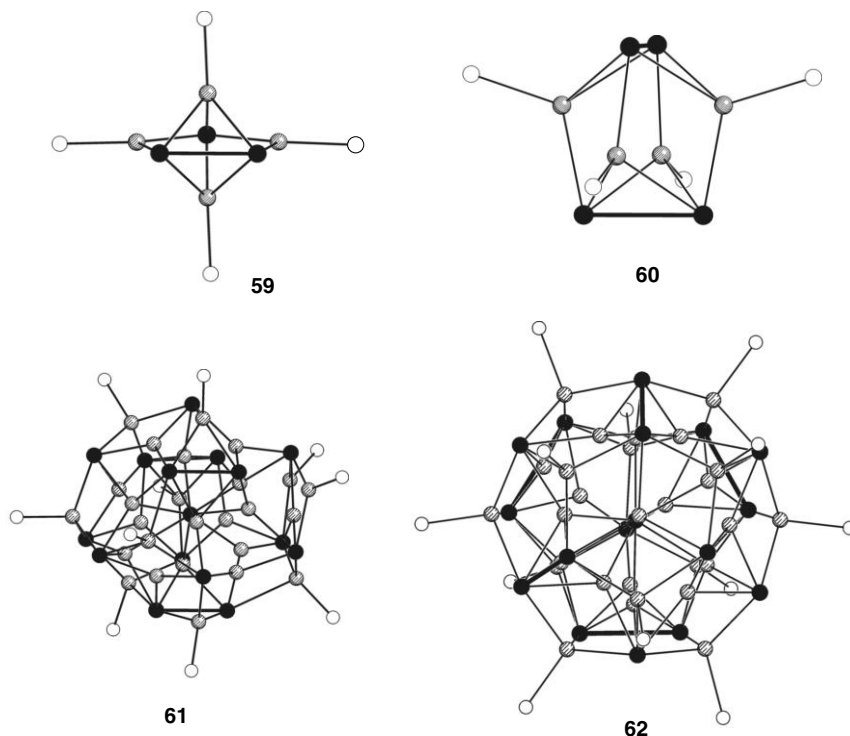


**Fig. 3-59** Molecular structures of stoichiometric copper telluride clusters  $[\text{Cu}_4\text{Te}(\text{Te}_2)_2(\text{PCyPh}_2)_4]$  (**59**),  $[\text{Cu}_4(\text{Te}_2)_2(\text{PiPr})_4]$  (**60**),  $[\text{Cu}_{26}\text{Te}_{10}(\text{Te}_2)_3(\text{PtBu}_3)_{10}]$  (**61**), and  $[\text{Cu}_{28}\text{Te}_{13}(\text{Te}_2)_2(\text{PEt}_2\text{Ph})_{12}]$  (**62**) containing Te–Te bridges. C and H atoms are omitted for clarity.

atom and the tellurium atoms of the polyhedron. The remaining copper atoms are localized in the center of the molecule and are each tetrahedrally surrounded by four tellurium atoms.

In **62**, two of the copper centers display relatively high thermal parameters, from which it can be concluded that their positions are only partly occupied. A deficiency of electrons at the tellurium atoms resulting from the partial occupation of copper sites could either be formally delocalized in the valence band or localized as a ditelluride group following a structural deformation similar to a Peierls deformation [64]. Considering the tellurium polyhedra, the molecular structure of **62** shows two short Te–Te bonds (2.848 and 2.876 Å) and four Te–Te distances in the range 3.150–3.351 Å. The latter tellurium atoms have thermal ellipsoids which are elongated in the direction of the formal Te–Te bond. As Te–Te bonds and copper centers seem to be disordered to a certain extent in **62**, the given formula represents the idealized composition of a stoichiometric cluster compound with three Te–Te bonds. The situation in **62** can therefore be viewed as being somewhat sim-

ilar to that in CuS, a well-known mixed-valence compound that can be described as  $(\text{Cu}^+)_2\text{Cu}^{2+}(\text{S}_2)^{2-}\text{S}^{2-}$  or as  $(\text{Cu}^+)_3(\text{S}_2)^{2-}\text{S}^-$  [65].

In a different approach to the synthesis of copper telluride cluster compounds, we used alkyl- and aryl-(trimethylsilyl)tellurium compounds  $\text{RTeSiMe}_3$  ( $\text{R}$  = organic group). Because of the facile cleavage of the carbon-tellurium bond, one obtains clusters featuring either exclusively  $\text{TeR}^-$  ligands, a mixture of  $\text{TeR}^-$  and  $\text{Te}^{2-}$  ligands, or solely  $\text{Te}^{2-}$  ligands. The tellurium atoms of the tellurolato ligands bridge two or three copper atoms at most, whereas “naked”  $\text{Te}^{2-}$  ligands can coordinate to up to seven copper atoms. The polyhedra of tellurium atoms usually possess unusual structures, even in the smaller clusters. In the larger clusters one already observes characteristics of layer type arrangements of tellurium atoms. As in the cluster compounds discussed earlier, the copper atoms are coordinated in linear, trigonal or tetrahedral geometries by tellurium atoms. Metal centers coordinated by two or three chalcogens may also be ligated by a phosphine ligand. The molecular structures of the copper telluride/tellurolate clusters **63**, **64**, **66**, **71** and **72** are given in Figure 3-60.

The ionic cluster compound **63** contains six  $\text{TePh}^-$  ligands, the tellurium atoms of which define an octahedron. In contrast to **64** (see below), all tellurolato ligands act as  $\mu_2$ -bridges. There are two distinct coordination geometries around the copper. Two of the metal centers are located inside the cluster below  $\text{Te}_3$  faces. The others are coordinated by three tellurium atoms above  $\text{Te}_3$  faces and are also each ligated by one phosphine ligand each.

The structure of **64** is also based on a non-bonded octahedral array of tellurolato ligands. With the exception of one tellurium atom which forms two Cu–Te bonds, all of these are bridging three copper sites. Four of the copper atoms adopt tetrahedral geometries, either with three tellurium atoms and one phosphorus or through two Cu–Te and two Cu–P bonds. The other two copper atoms lie in opposite deltahedral  $\text{Te}_3$  faces of the  $\text{Te}_6$  octahedron. **64** is therefore related to the recently published homoleptic hexanuclear copper selenolate complex  $[\text{Cu}_6\{\text{Se}(2,4,6\text{-iPr}_3\text{C}_6\text{H}_2)\}_6]$  [8].

Clusters **66** and **67** are identical except for the organic groups  $\text{R}$  of the  $\text{PR}_3$  ligands. Both contain two tellurolato layers of three  $\text{TePh}^-$  groups each and one central tellurido layer of three  $\text{Te}^{2-}$  ligands. The resulting  $\text{Te}_9$  polyhedron can alternatively be viewed as two face-sharing  $\text{Te}_6$  octahedra. Six of the twelve copper atoms are coordinated in a distorted trigonal fashion by three tellurium atoms, resulting in shorter contacts to  $\text{Te}^{2-}$  ligands than to the  $\text{TePh}^-$ . The other six copper atoms are tetrahedrally surrounded by three tellurium atoms and one phosphine ligand. Compounds **66** and **67** may be viewed as condensation products of two  $(\text{TePh})_6$  frameworks like those found in **64**.

The synthesis of the ionic cluster compound **71** is the only example to date of a co-condensation reaction of two smaller clusters, namely **67** and **63**, to form a larger one. However, the structure of **71** cannot be considered as being built up from recognizable structural fragments of the precursor compound. The tellurium atoms form an unusual polyhedron consisting of twelve  $\text{TePh}^-$  ligands and nine  $\text{Te}^{2-}$  ligands. Two of the tellurolato ligands act as a  $\mu_4$ -bridges, while the other ten



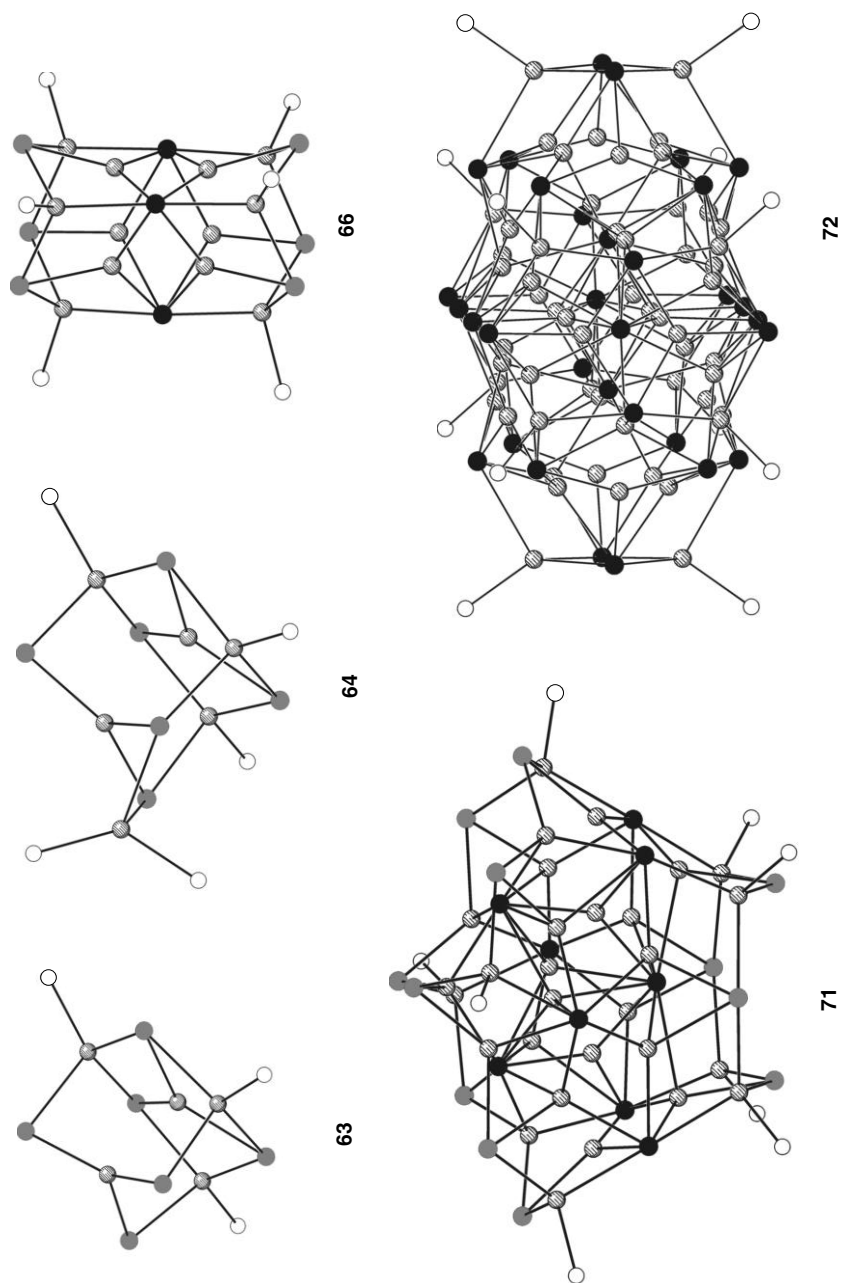


**Fig. 3-60** Molecular structures of stoichiometric copper telluride/telluroate clusters  $[\text{Cu}_5(\text{TePh})_6(\text{PET}_3)_3][\text{PET}_3\text{Ph}]$  (**63**),  $[\text{Cu}_6(\text{TePh})_6(\text{PETPh}_2)_5]$  (**64**),  $[\text{Cu}_{12}\text{Te}_3(\text{TePh})_6(\text{PPh}_3)_6]$  (**66**),  $[\text{Cu}_{29}(\text{TePh})_{12}\text{Te}_9(\text{PET}_3)_8][\text{PET}_3\text{Ph}]$  (**71**), and  $[\text{Cu}_{50}\text{Te}_{17}(\text{TePh})_{20}(\text{PETPh}_2)_8][\text{PETPh}_3]_4$  (**72**) containing  $\text{TeR}^-$  ligands. C and H atoms are omitted for clarity.

act as  $\mu_3$ -bridging atoms between the copper centers. The telluride ligands each coordinate six, seven, eight, or ten copper atoms with Cu–Te distances between 2.58 and 3.14 Å. Eight of the copper atoms which are bonded to phosphine ligands cap  $\text{Te}_3$  faces at the cluster surface, while four further copper atoms without phosphine ligands are coordinating to  $\text{Te}_3$  faces from the inside of the cluster core. The remaining seventeen copper atoms are surrounded in a tetrahedral manner in the center of the molecule. Interestingly, a structurally related silver tellurium compound,  $[\text{Ag}_{30}(\text{TePh})_{12}\text{Te}_9(\text{PEt}_3)_{12}]$  [71] can be prepared by the direct reaction of AgCl with  $\text{Te}(\text{SiMe}_3)_2/\text{PhTeSiMe}_3$ , which is in contrast to the synthesis of **71**. This cluster represents the only example of a copper-telluride-telluroate cluster yet isolated with a distinct structural relationship with its silver analog.

Upon standing in daylight, solutions of **64** in benzene gradually darken to a brown color. Over the course of several days, brown platelets of the ionic, mixed tellurido/telluroate cluster **72** crystallize from these solutions. On the other hand, when solutions of **64** in benzene are protected from light, they show no sign of darkening even after several weeks at room temperature. The detection of a  $^{125}\text{Te}\{^1\text{H}\}$ -NMR-signal at  $\delta = 688$  ppm reveals the formation of  $\text{TePh}_2$  in the solution, giving good evidence for the mechanism of formation of the naked tellurido ligands. The most striking feature of the cluster core is the manner in which the tellurium ligands are arranged: the molecule consists of “top” and “bottom” layers of  $\mu_3\text{-TePh}^-$  ligands with a central tellurido ( $\text{Te}^{2-}$ ) layer. Sandwiched between these are the 50 copper atoms along with the remaining seven tellurido ligands. The 20 phenyltelluroate ligands are each bonded to three copper atoms and, in conjunction with the eight coordinated  $\text{PEt}_2\text{Ph}$  ligands, serve to effectively stabilize the inner copper telluride core. The telluride ligands of the middle  $\text{Te}_{10}$  layer act as  $\mu_6$ - and  $\mu_7$ -bridges between the copper sites. The seven remaining  $\text{Te}^{2-}$  centers function as  $\mu_6$ -,  $\mu_7$ - or  $\mu_8$ -ligands. Eight of the copper atoms are bonded to  $\text{Te}_3$  faces at the surface of the cluster molecule and to one phosphine ligand. The 42 copper atoms in the center of the molecule are either trigonally (18) or tetrahedrally (24) coordinated by the tellurium neighbors.

Counting the electrons for **73–85** on the assumption of  $\text{Te}^{2-}$  and  $\text{Cu}^+$  leads to an overall electron excess for **79** and an electron deficiency for the other compounds. These compounds can therefore be thought of as being of mixed-valence type. The molecular structures of **73**, **76**, **79**, **83**, and **85** are depicted in Figure 3-61.

The smallest mixed-valence cluster molecules, **73–75**, feature 16 copper atoms arranged around a  $\text{Te}_9$  polyhedron. However, the tellurium substructure cannot be derived from the skeleton of **57** by simply adding one tellurium atom, as one might have assumed. Two of the copper atoms that carry a phosphine ligand bridge  $\text{Te}$ – $\text{Te}$  non-bonding edges. The other six  $[\text{CuPR}_2\text{R}']$  units bridge three tellurium atoms, the copper atoms thus being tetrahedrally coordinated. The remaining eight copper atoms are coordinated by three tellurium atoms in a distorted trigonal planar manner. Assuming that the tellurium atoms have a formal charge of  $-2$ , one can formally assign fourteen  $\text{Cu}^{1+}$  centres and two  $\text{Cu}^{2+}$ . However, the co-existence of  $\text{Cu}^{2+}$  with  $\text{Te}^{2-}$  is unlikely for thermodynamical reasons because of an electron transfer process from the reducing  $\text{Te}^{2-}$  ligand to the oxi-

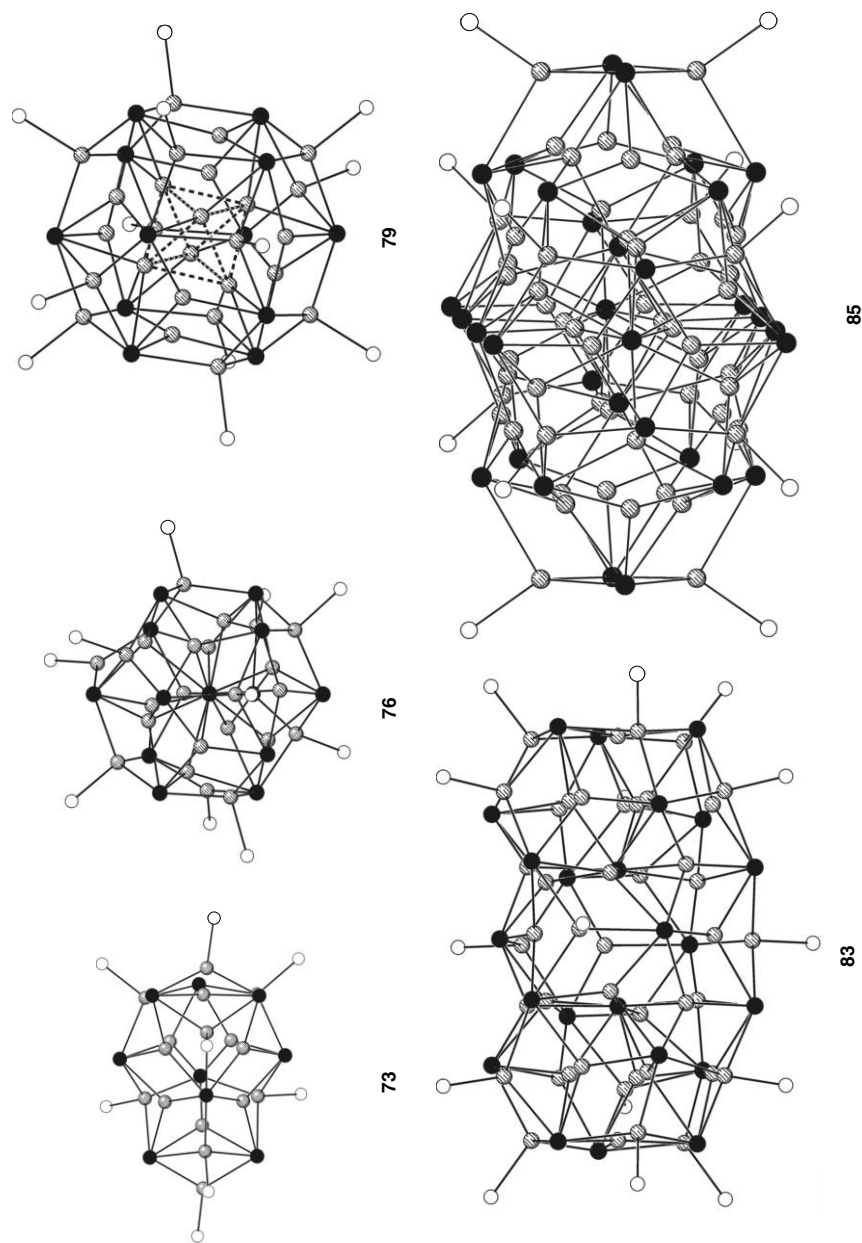


**Fig. 3-61** Molecular structures of mixed-valence copper telluride clusters  $[\text{Cu}_{16}\text{Te}_9(\text{PPh}_3)_8]$  (**73**),  $[\text{Cu}_{23}\text{Te}_{13}(\text{PPh}_3)_{10}]$  (**76**),  $[\text{Cu}_{26}\text{Te}_{12}(\text{PEt}_2\text{Ph})_{12}]$  (**79**),  $[\text{Cu}_{44}\text{Te}_{23}(\text{PPhnPr}_2)_{15}]$  (**83**), and  $[\text{Cu}_{58}\text{Te}_{32}(\text{PCy}_3)_{16}]$  (**85**). C and H atoms are omitted for clarity.

dizing  $\text{Cu}^{2+}$  center. An assignment of 16  $\text{Cu}^+$ , seven  $\text{Te}^{2-}$  and two  $\text{Te}^{1-}$  is not supported by structural means. The compounds should therefore rather be described in terms of a “pure”  $\text{Cu}^+$  substructure, ligated by tellurium centers with an average charge of  $-1.78$ . This electron deficiency can be delocalized in the valence band of the compound, as has recently been shown by calculations on the electron-rich compound **79** (see below) [66].

Thirteen tellurium atoms form a distorted, centered icosahedron in the closely related compounds **76–78**. Ten of the 20  $\text{Te}_3$  faces are bridged by copper-phosphine units, whereas ten more copper atoms are situated below the remaining faces, either trigonally coordinated or tetrahedrally surrounded, because of an additional Cu–Te bond to the central tellurium atom. Compound **78** needs twelve phosphine ligands for a sufficient shielding of the cluster core. This can be put down to the smaller steric demand of the phosphine  $\text{PEt}_3$  compared to  $\text{PPh}_3$ . As a result, in **78**, twelve of the copper atoms are coordinated above  $\text{Te}_3$  faces and eight below. The three remaining copper atoms in all three compounds are positioned inside the icosahedron. They each have three tellurium neighbors, two of which belong to the  $\text{Te}_{12}$  shell, while one is the central tellurium ligand. Formal counting of charges leads to an electron excess of three, and, assigning a charge of  $+1$  to every copper atom as discussed above, an average charge of  $-1.77$  is obtained for the 13 tellurium ligands.

An icosahedron of tellurium atoms is also found in **79**, but, in contrast to those observed in **76–78**, it does not contain a central atom. The arrangement of the copper atoms above the  $\text{Te}_3$  faces is similar to that found in **78**. This might have been anticipated, given the Tolman angle for both phosphines. Twelve  $[\text{CuPEt}_2\text{Ph}]$  units are bonded above  $\text{Te}_3$  faces, and eight copper atoms cap the other  $\text{Te}_3$  faces from the interior. In contrast to the situation in **76–78**, in **79** six rather than three copper atoms are located in the center of the cluster molecule forming an octahedron with intermetallic distances between 2.592 and 2.607 Å. These distances lie within the range of Cu–Cu distances measured in the other copper telluride clusters under investigation. Therefore, it cannot be determined from these distances whether  $d^{10}\text{--}d^{10}$  interactions are present within the  $\text{Cu}_6$  octahedron. However, it is remarkable that two of the copper atoms must be formally uncharged  $\text{Cu}^0$  atoms lying alongside 24  $\text{Cu}^+$  centers, if one assigns a formal charge of  $2-$  to all the tellurium ligands. Calculations of the electronic band structure reveal that a localization of the oxidation states does not occur and that the excess electron density cannot be assigned to  $d^{10}\text{--}d^{10}$  interactions [66]. The “additional” electron pair, which arises if one assigns exclusively  $\text{Cu}^+$  and  $\text{Te}^{2-}$  centers, is better described as an MO embedded in the valence band of tellurium 5p orbitals and copper 4s orbitals.

The largest copper telluride cluster molecules synthesized to date are also mixed-valence compounds. Compounds **82–87** display ellipsoidal tellurium deltahedra with an increasing number of inner tellurium atoms, ranging from two inner tellurium atoms in **82–84** to four such tellurium atoms in the centers of the molecular structures of **85–87**. As usual, the copper atoms that are coordinated by phosphine ligands are coordinated above the  $\text{Te}_3$  triangles at the cluster surface. The

other copper atoms are either coordinated by three or, especially in the cluster center, by four tellurium ligands. The structures of **85–87** already suggest the formation of distorted layers of tellurium atoms showing incipient characteristics of bulk  $\text{Cu}_2\text{Te}$  [40]. However, the turning point has not yet been reached for copper telluride cluster compounds. In view of the reported tendency for ever bigger molecules to be necessary in order that bulk structure properties will be observed on going from  $\text{Cu-S}$  to  $\text{Cu-Se}$  clusters, the cluster size that might begin to show bulk  $\text{Cu}_2\text{Te}$  structural characteristics should in fact be considerably larger than a “ $\text{Cu}_{58}$ ” species and probably even larger than a “ $\text{Cu}_{70}$ ” analog of the turning point to “large” clusters found for the copper selenide system.

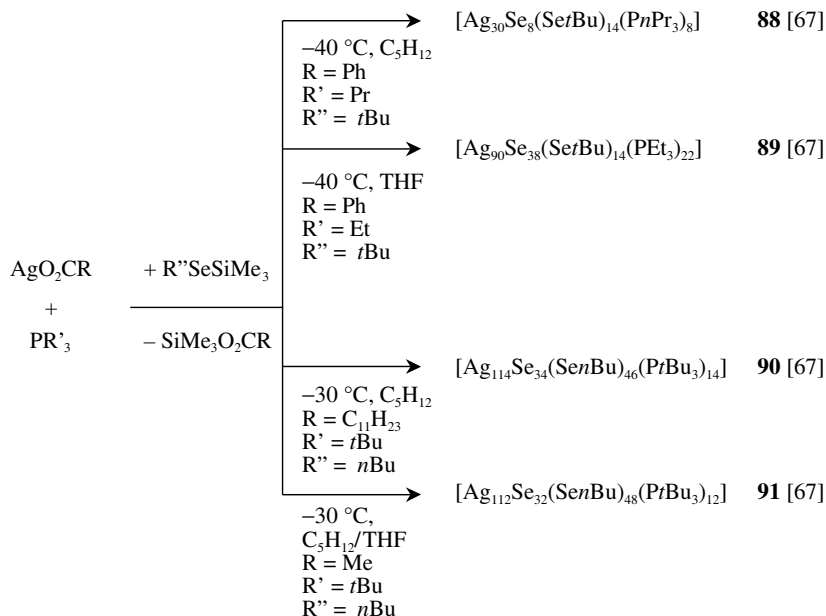
### 3.1.3.3 Chalcogen-Bridged Silver Clusters

The development of the chemistry of  $\text{Cu}_2\text{S}$ ,  $\text{Cu}_2\text{Se}$  and  $\text{Cu}_2\text{Te}$  complexes has yet to be mirrored for the heavier metals Ag and Au. Monodentate phosphine ligands have generally been shown to be incapable of providing a kinetically stabilizing sphere when  $\text{Ag(I)}$  and  $\text{Au(I)}$  salts are reacted with  $\text{E}(\text{SiMe}_3)_2$ , and these reactions lead instead to the formation of amorphous binary solids.

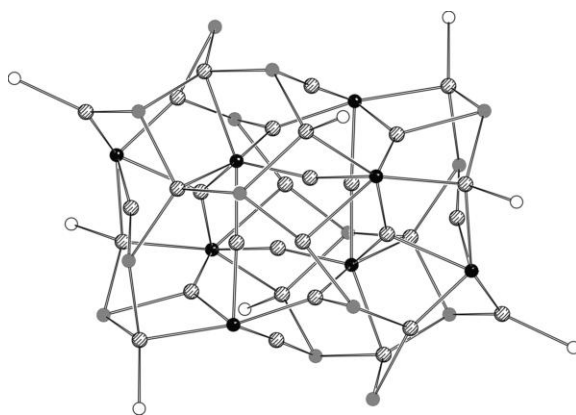
It is clear from the development of the chemistry of the copper chalcogenide cluster complexes described above that (i) the incorporation of additional surface ligands in the form of  $\text{SeR}$  and  $\text{TeR}$  functionalities and/or (ii) the use of bidentate phosphine ligands offer additional structural flexibility. Additionally, they may be used to stabilize  $\text{AgSe}$ ,  $\text{AgTe}$  and  $\text{AuSe}$  cluster cores, themselves synthesized with bis(silylated) reagents. The use of monosilylated chalcogen reagents, as the hydrocarbon moiety is relatively inert and unreactive toward metal salts, could thus aid in inhibiting the formation of the bulk, amorphous solids. Furthermore, the reaction chemistry of metal-selenolate and -tellurolate complexes can also provide the source of  $\text{E}^{2-}$  ligands required for the formation of larger polynuclear complexes [19, 61]. Thus, the use of monosilylated reagents  $\text{RESiMe}_3$  ( $\text{R} = \text{aryl, alkyl}$ ) has led to the development of nanometer scale  $\text{Ag/Se/SeR}$  and  $\text{Ag/Te/TeR}$  complexes. The carbon chain on the chalcogen center is readily modified, and, as discussed below, this plays an important role in governing the structures formed.

### Silver-Selenium Clusters

The reaction chemistry of  $\text{Ag(I)}$  and  $\text{RESiMe}_3$  complexes in the presence of tertiary phosphine ligands is summarized in Scheme 3-9. Of note is the requirement for acetate salts of silver for the successful isolation of polynuclear complexes, as  $\text{AgCl}$  invariably leads to  $\text{Ag}_2\text{Se}$  formation. This contrasts with the reaction chemistry of  $\text{Cu(I)}$  described above and also with the chemistry of silver-tellurium complexes (see below). Of equal importance is the facile formation of selenide ( $\text{Se}^{2-}$ ) ligands from  $\text{RSe}$  fragments, as this allows for the formation of extremely large  $\text{Ag-Se}$  frameworks. Although this reactivity limits the number of low nuclearity complexes that can be isolated, and thus limits the amount of information that can be obtained about condensation pathways, it offers the distinct advantage of the formation of the largest structurally characterized metal-chalcogenide complexes reported to date.



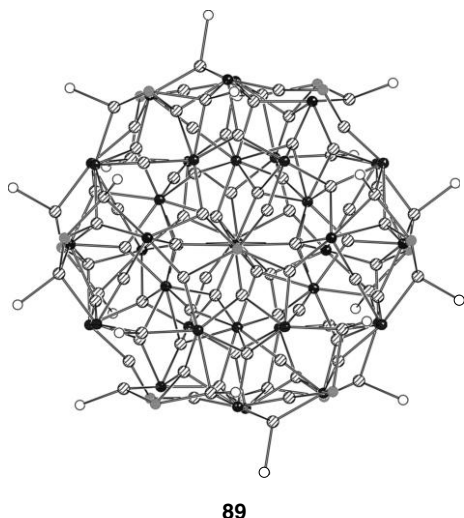
**Scheme 3-9** The synthesis of selenido/selenolato-bridged silver clusters with monodentate  $\text{PR}_3$  ligands.



**88**

**Fig. 3-62** The molecular structure of  $[\text{Ag}_{30}\text{Se}_8(\text{SetBu})_{14}(\text{PPr}_3)_8]$  (**88**).

The reaction of silver benzoate with  $t\text{BuSeSiMe}_3$  and  $\text{PPr}_3$  at  $-40\text{ }^\circ\text{C}$  in pentane solvent affords the light-sensitive, spherical cluster  $[\text{Ag}_{30}\text{Se}_8(\text{SetBu})_{14}(\text{PPr}_3)_8]$  **88** in good (60%) yield [67]. The structure of **88** (Figure 3-62) illustrates the surface groups ( $\text{PR}_3$  and  $t\text{Bu}$ ) stabilizing the  $\text{AgSe}$  core. The  $\text{SetBu}$  ligands bridge two and three silver centers and the  $\text{Se}^{2-}$  ligands adopt coordination numbers five and six.



89

**Fig. 3-63** The core atoms in  $[\text{Ag}_{90}\text{Se}_{38}(\text{SeiBu})_{14}(\text{PEt}_3)_{22}]$  (**89**).

There are ten silver centers that are two-coordinate, bonded to two  $\text{SeiBu}$  ligands, two  $\text{Se}^{2-}$  ligands, or one  $\text{SeiBu}$  ligand and one  $\text{Se}^{2-}$  ligand. The remaining twenty silver atoms, including the eight that are bonded to  $\text{PPr}_3$  ligands, exhibit distorted trigonal planar or tetrahedral coordination geometries. As is the case for the stoichiometric copper-chalcogenide complexes described in the preceding sections, the shortest non-bonding contacts (2.904–2.991 Å) between the metal centers are consistent with the +1 oxidation states assigned to all Ag atoms.

A similar reaction for the formation of **88** with  $\text{PEt}_3$  in THF leads to the larger cluster  $[\text{Ag}_{90}\text{Se}_{38}(\text{SeiBu})_{14}(\text{PEt}_3)_{22}]$  (**89**) in 60% yield (Figure 3-63) [67]. The similar basicities and Tollman cone angles [42] for  $\text{PPr}_3$  and  $\text{PEt}_3$  suggest that the use of a different phosphine ligand for **89** does not account for the different product formation. A more likely reason is the combination of a different solvent (THF vs pentane) with higher reaction/crystallization temperatures ( $-20^\circ\text{C}$  for **89**;  $-60^\circ\text{C}$  for **88**). Higher reaction temperatures for these clusters lead to the formation of bulk  $\text{Ag}_2\text{Se}$  and other unidentified amorphous materials. The thirty-eight  $\text{Se}^{2-}$  ligands in the core of **89** result in a larger, pseudo-spherical framework with core dimensions of  $1.1 \times 1.7 \times 1.9 \text{ nm}^3$ . The 90 Ag centers are ligated to the 38  $\text{Se}^{2-}$  and 14  $\text{SeiBu}$  groups, with 22 also bonded to the surface  $\text{PEt}_3$  ligands. The metal atoms display linear, trigonal planar, and tetrahedral coordination. The  $\text{SeiBu}^-$  groups ligate in  $\mu_2$ - and  $\mu_3$ -fashion, and the  $\text{Se}^{2-}$  centers also exhibit varying coordination modes, with those in the outer shell bridging four and five silver atoms and the core ligands forming five to eight bonds to the metals. The arrangement of the selenium centers in **89** is best described in two ways (Figure 3-64). The projection at the top of Figure 3-64 illustrates the approximately  $D_{6h}$  symmetry found in the non-bonded  $\text{Se}_{52}$  polyhedron, forming two “belts” of selenium ligands. The outer belt consists of 12  $\text{SeiBu}^-$  and 18  $\text{Se}^{2-}$ , whereas the inner one is

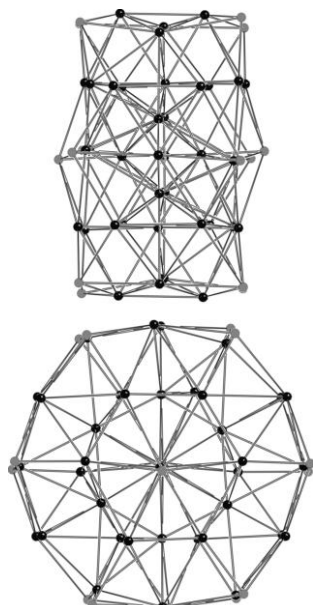


Fig. 3-64 Two projections of the  $\text{Se}_{52}$  selenium sub-structure in **89**.

composed exclusively of  $18 \text{ Se}^{2-}$ . A perpendicular view of the Se framework emphasizes the development of a layered arrangement of these ligands, which dominates the overall structural motif observed in the larger Ag–Se cluster complexes described below.

The  $2.3 \times 2.3 \times 2.5 \text{ nm}^3$  AgSe core in  $[\text{Ag}_{114}\text{Se}_{34}(\text{SenBu})_{46}(\text{PtBu}_3)_{14}]$  **90** (Figure 3-65) is reproducibly formed from the reaction of silver laurate ( $\text{C}_{11}\text{H}_{23}\text{CO}_2\text{Ag}$ ),  $\text{PtBu}_3$  and  $n\text{BuSeSiMe}_3$  in pentane at  $-30^\circ\text{C}$  [67]. The increased size of **90** compared with **88** and **89** is accompanied by a rather marked change in the gross structural features exhibited. Specifically, the arrangement of Se atoms in **90** (Figure 3-66) corresponds to a distorted cubic-centered structure that is also observed in solid  $\text{Ag}_2\text{Se}$ . The Ag atoms have trigonal and tetrahedral coordination and are distributed between the layers of Se, which is also consistent with the structural features observed in the bulk solid. This “transition”, i.e. the size-dependent structural changes, is also observed in the  $\text{PR}_3$ -stabilized  $\text{Cu}_2\text{Se}$  clusters, where a clear relationship between molecule and bulk is observed for structures containing 70 or more Cu atoms, as described in the preceding sections. One cannot ignore, however, the effect of the different substituents on the selenolate ligands ( $n\text{Bu}$  vs  $t\text{Bu}$ ), which cannot be discounted. The  $n\text{BuSe}^-$  ligands in **90** bridge three and four Ag(I) centers, and the selenide ligands again are within the bonding distance range to 5, 6, 7 and 8 metals.

The cluster  $[\text{Ag}_{112}\text{Se}_{32}(\text{SenBu})_{48}(\text{PtBu}_3)_{12}]$  **91** (Figure 3-65) is closely related to that of **90**, and is formed from the reaction of  $\text{AgOAc}$ ,  $\text{PtBu}_3$  and  $n\text{BuSeSiMe}_3$  in pentane/THF mixtures at  $-30^\circ\text{C}$  [67]. The number of selenium atoms in **90** and



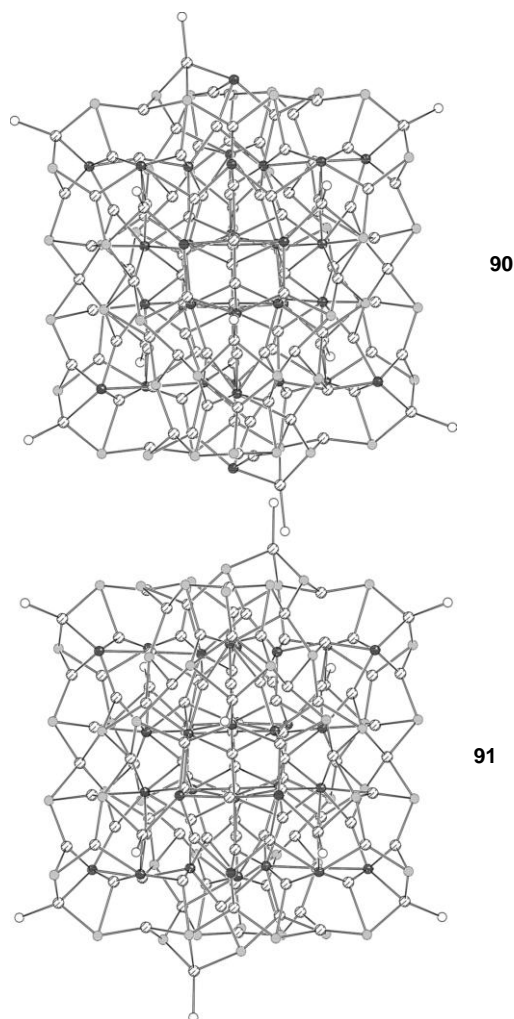


**Fig. 3-65** The core structures in  $[\text{Ag}_{114}\text{Se}_{34}(\text{SenBu})_{46}(\text{P}t\text{Bu}_3)_{14}]$  (**90**) (top) and  $[\text{Ag}_{112}\text{Se}_{32}(\text{SenBu})_{48}(\text{P}t\text{Bu}_3)_{12}]$  (**91**) (bottom).

**91** is identical; however, the number of surface selenolate groups is greater in the latter (48 vs 46), with a concomitant reduction in the number of  $\text{P}t\text{Bu}_3$  ligands (12 vs 14). Two fewer (112) Ag centers in **91** relative to **90** is consistent with the lower  $\text{Se}^{2-}:n\text{BuSe}^-$  ratio in the former (32:48 and 34:46, respectively).

Bidentate phosphine ligands have been successfully employed for the synthesis of Cu/E/ER complexes ( $\text{E} = \text{Se}, \text{Te}$ ) from silylated reagents, as described above. Their utility in stabilizing Ag/SeR and Ag/Se/SeR frameworks using analogous reaction strategies is demonstrated and summarized in Scheme 3-10.

The use of bidentate phosphine ligands in conjunction with low temperature conditions is apparently sufficient in enabling the isolation of low-nuclearity Ag/

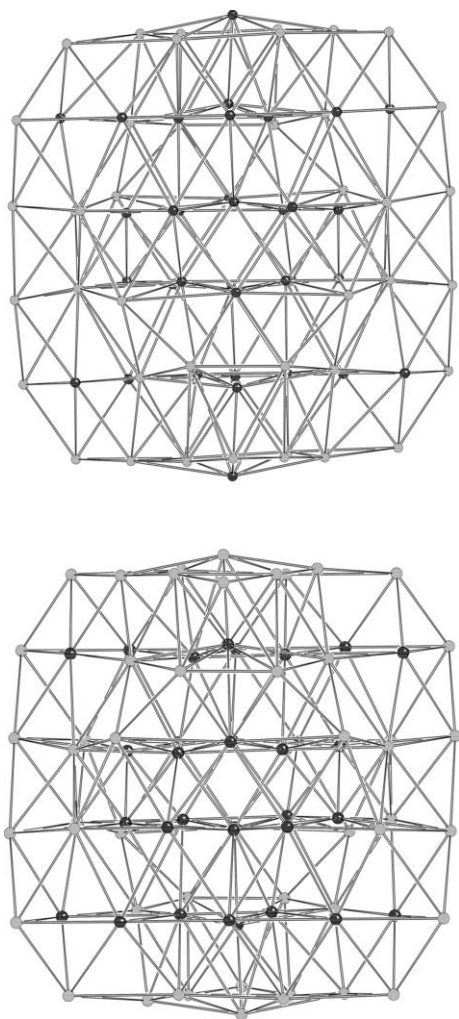
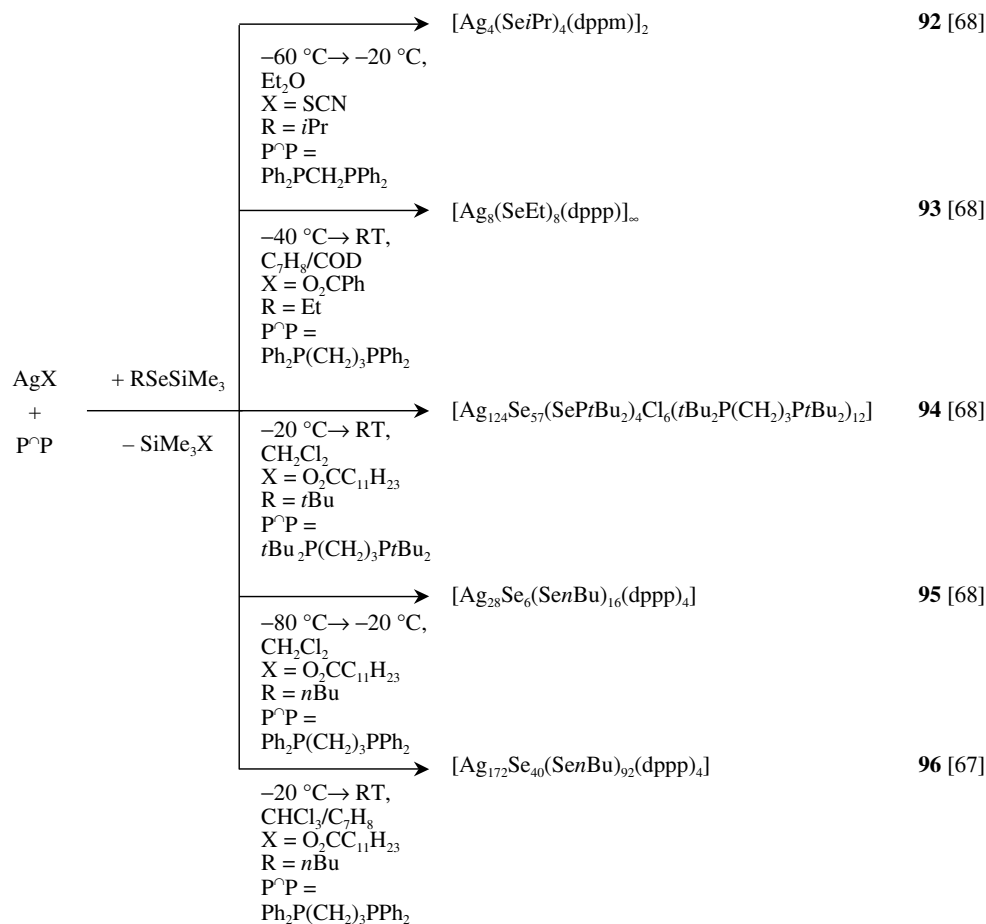


Fig. 3-66 The selenium frameworks in **90** (top) and **91** (bottom).

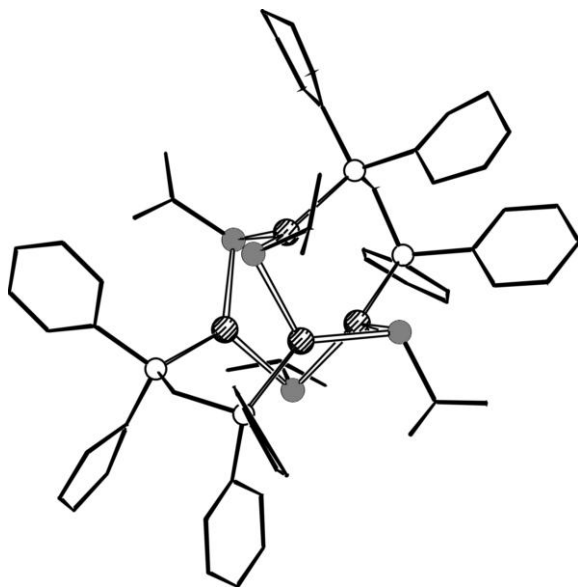
SeR complexes from Ag(I) salts and  $\text{RESiMe}_3$ , hitherto impossible when working with  $\text{PR}_3$  ancillary ligands. For example, the cluster  $[\text{Ag}_4(\text{SeiPr})_4(\text{Ph}_2\text{PCH}_2\text{PPh}_2)_2]$  (**92**) is isolated in 45% yield from silver thiocyanate (or silver benzoate), bis-(diphenylphosphino)methane and  $i\text{PrSeSiMe}_3$  at low temperatures [68]. Cluster **92** (Figure 3-67) consists of an  $\text{Ag}_4$  tetrahedron with each non-bonded  $\text{Ag} \cdots \text{Ag}$  edge bridged by a  $\mu_2$ - $i\text{PrSe}^-$  ligand. The trigonal planar coordination geometry about the Ag(I) centers is completed via coordination to a phosphine ligand.

The  $\mu_3$ -bridging capacity of alkylselenolate ligands and the flexible coordination ability of bis(diphenylphosphino)propane ligands lead to an infinite repeat of  $[\text{Ag}_8(\text{SeEt})_8(\text{Ph}_2\text{PCH}_2\text{CH}_2\text{CH}_2\text{PPh}_2)]$  units (Figure 3-68) in **93** [68]. This poly-



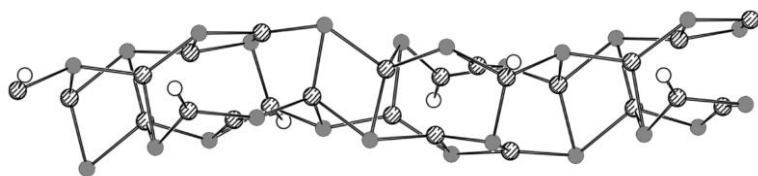
**Scheme 3-10** The synthesis of selenido/selenolato-bridged silver clusters with bidentate phosphine ligands.

meric structure consists of a strand of distorted  $\text{Se}_6$  octahedral arrangements of ethylselenolate ligands, each of the  $\text{EtSe}^-$  ligands functioning as  $\mu_3$ -bridges to the  $\text{Ag(I)}$  centers. There is no discrepancy between “intra” and “inter” unit bonding distances, which range from 2.509(4) to 2.847(3) Å. In contrast to  $\text{Ag}_4$  cluster **92**, the silver atoms in the  $\text{Ag}_8$  cluster **93** display different coordination geometries: a linearly coordinated Ag is bonded to two EtSe ligands above an edge and a trigonal planar Ag center resides in a deltahedral face of the  $\text{Se}_6$  octahedron; two additional silver atoms show trigonal planar geometry “between” the octahedral subunits; the remaining silver atoms are three- and four-coordinate, occupying positions above and within the  $\text{Se}_6$  octahedra. Although the ethyl groups bonded to the selenium sites have poor shielding ability, the AgSe strand is effectively insulated and stabilized by the DPPP ligands (Figure 3-69).



92

Fig. 3-67 The molecular structure of  $[\text{Ag}_4(\text{SeiPr})_4(\text{Ph}_2\text{PCH}_2\text{PPh}_2)_2]$  (**92**).



93

Fig. 3-68 A projection of the infinite repeat in  $[\text{Ag}_8(\text{SeEt})_8(\text{Ph}_2\text{PCH}_2\text{CH}_2\text{CH}_2\text{PPh}_2)]_\infty$  (**93**).

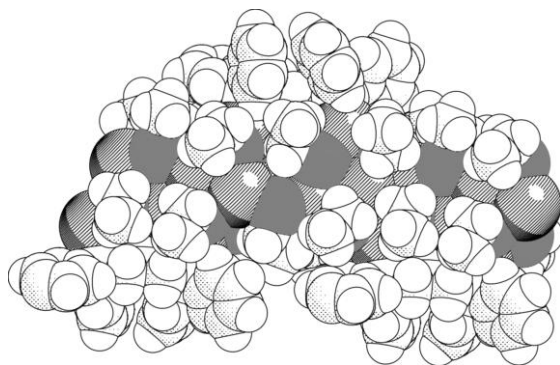
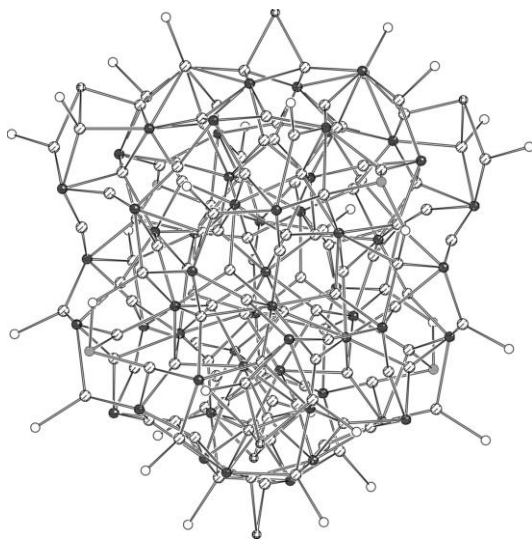


Fig. 3-69 A space-filling model of polymeric **93**.



94

**Fig. 3-70** A projection of the molecular structure of  $[\text{Ag}_{124}\text{Se}_{57}(\text{SePtBu}_2)_4\text{Cl}_6(\text{tBu}_2\text{P}(\text{CH}_2)_3\text{PtBu}_2)_{12}]$  (**94**) (carbon atoms omitted).

Much larger Ag–Se frameworks are formed using bidentate ligands if reaction conditions and the selenium reagent are modified. The cluster  $[\text{Ag}_{124}\text{Se}_{57}(\text{SePtBu}_2)_4\text{Cl}_6(\text{tBu}_2\text{P}(\text{CH}_2)_3\text{PtBu}_2)_{12}]$  (**94**, Figure 3-70) is isolated as black crystals from the reaction of silver laurate, 1,3-bis(*di**tert*butylphosphino)propane, and *tert*-butylselenotrimethylsilane in methylene chloride at  $-20^\circ\text{C}$  [68]. Cluster **94**, with a spherical  $\sim 2$  nm AgSe core, is a very unusual member of the series of high-nuclearity silver selenide clusters, bears no structural relationship to the clusters **90** and **91** described above, and displays no structural characteristics of the bulk phases of  $\text{Ag}_2\text{Se}$ .

The important structural features of **94** are the Frank-Kasper polyhedra surrounding the central selenide ligand. A non-bonded ( $\text{Se}\cdots\text{Se} = 4.93\text{--}5.36\text{ \AA}$ )  $\text{Se}_{16}$  polyhedron surrounds the central  $\text{Se}^{2-}$  and is itself enveloped by 44 selenium centres, four of which are from the surface  $\text{SePtBu}_2^-$  ligands (Figure 3-71). This defined  $\text{Se}_{44}$  polyhedron ( $\text{Se}\cdots\text{Se} = 3.80\text{--}5.99\text{ \AA}$ ) possesses 84  $\Delta_3$  faces that can be described as a growth of the inner  $\text{Se}_{16}$  deltahedron. The  $\text{Se}^{2-}$  ligands in **94** act as  $\mu_3$ ,  $\mu_4$ ,  $\mu_5$ ,  $\mu_6$ ,  $\mu_7$  or  $\mu_8$  bridges to the silver atoms, with the Ag–Se distances ranging from 2.491(3) to 3.101(3)  $\text{\AA}$ . The four selenod*tert*butylphosphido ligands,  $\text{SePtBu}_2^-$ , are  $\mu_3\text{-}\eta^1(\text{P})\text{:}\eta^2(\text{Se})$  bonded to 12 Ag(I) centers. The formation of these ligands from the reaction conditions must result from the decomposition of the  $\text{tBuSeSiMe}_3$  and  $\text{tBu}_2\text{P}(\text{CH}_2)_3\text{PtBu}_2$  ligands. For their part, the six surface chlorides, which arise from the reaction solvent methylene chloride, are  $\mu_3$  and  $\mu_2$  bridging to the silver centers.

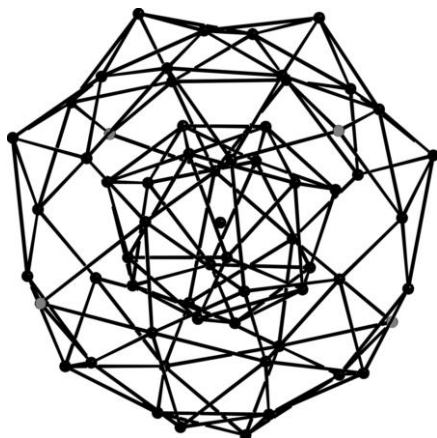


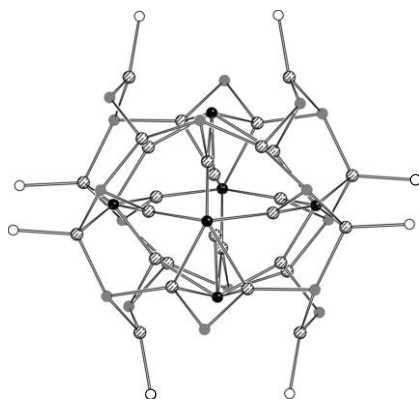
**Fig. 3-71** The selenium substructure in **94**. The central Se is surrounded by the Se<sub>16</sub> Frank-Kasper polyhedron, which is itself surrounded by the Se<sub>44</sub> polyhedron in a second coordination sphere.

The combination of 57 Se<sup>2-</sup>, 6 Cl<sup>-</sup> and 4 SePtBu<sub>2</sub><sup>-</sup> ligands again allows for +1 oxidation states to be assigned to the silver atoms. The 124 Ag(I) centers are distributed as follows: twelve of the 28 tetrahedral sites of the central Se<sub>16</sub> delta-hedron surrounding the central Se are occupied by silver atoms in distorted geometries; 80 silver atoms located between the Se<sub>16</sub> and Se<sub>44</sub> polyhedra exhibit linear, trigonal planar and tetrahedral coordination, and the remaining 32 silver atoms are located at the cluster surface with coordination numbers three and four.

The effects of solvent and reaction/crystallization conditions on product formation are clearly evident in the syntheses of [Ag<sub>28</sub>Se<sub>6</sub>(SenBu)<sub>16</sub>(dppp)<sub>4</sub>] (**95**) and [Ag<sub>172</sub>Se<sub>40</sub>(SenBu)<sub>92</sub>(dppp)<sub>4</sub>] (**96**). The former is obtained in 45% yield from 1:0.25:1 mixtures of AgO<sub>2</sub>CC<sub>11</sub>H<sub>23</sub>:Ph<sub>2</sub>P(CH<sub>2</sub>)<sub>3</sub>PPh<sub>2</sub>:*n*BuSeSiMe<sub>3</sub> in CH<sub>2</sub>Cl<sub>2</sub> at -80 °C, slowly rising to -20 °C [68]. In contrast, the same combination of reagents in CHCl<sub>3</sub>/toluene at -20 °C generates cluster **96** in 20% yield when reaction solutions are allowed to warm to room temperature [67].

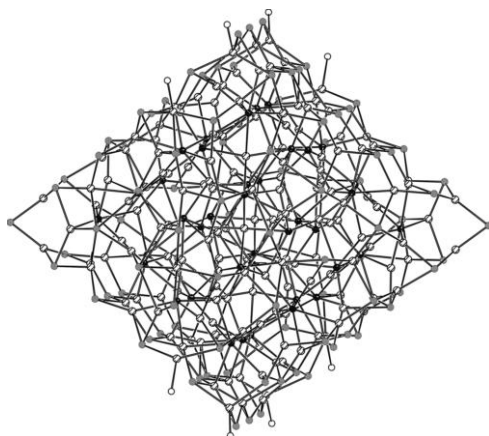
The red crystals of **95** formed from the reaction mixtures are very sensitive and decompose at temperatures above -10 °C. X-ray analysis on the highly solvated crystals is possible, however, and the structure of **95** (Figure 3-72) displays the features expected for a “medium-sized” Ag–Se complex and is not structurally dissimilar to [Ag<sub>30</sub>Se<sub>8</sub>(SetBu)<sub>14</sub>(PPr<sub>3</sub>)<sub>8</sub>] (**88**). Each of the *n*BuSe<sup>-</sup> ligands is μ<sub>3</sub>-bonded on the surface of the cluster, and the six Se<sup>2-</sup> atoms are arranged to form a non-bonded octahedron at the center of the cluster. For their part, the Ag(I) atoms display the (distorted) linear, trigonal planar and tetrahedral coordination geometries expected in such a medium-sized cluster.

The cluster 2.4 × 2.4 × 2.0 nm<sup>3</sup> AgSe core in [Ag<sub>172</sub>Se<sub>40</sub>(SenBu)<sub>92</sub>(dppp)<sub>4</sub>] **96** represents the largest structurally characterized metal-selenide complex reported to



95

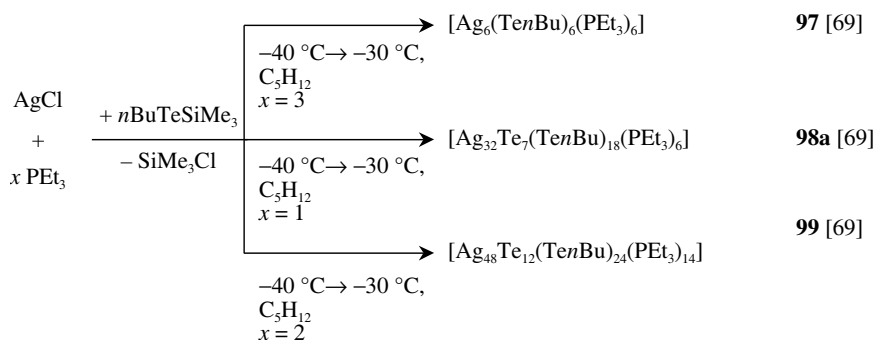
Fig. 3-72 A projection of the core atoms in  $[\text{Ag}_{28}\text{Se}_6(\text{SenBu})_{16}(\text{dppp})_4]$  (**95**).



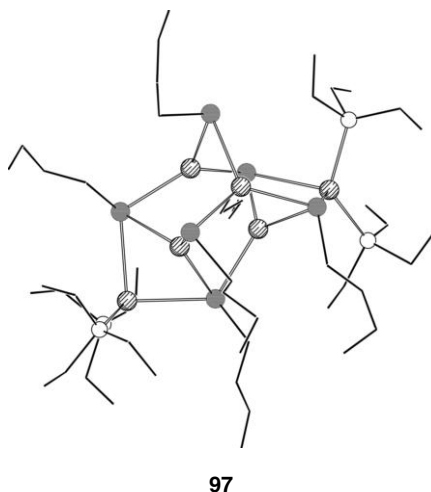
96

Fig. 3-73 The Ag, Se and P atoms in the  $2.4 \times 2.4 \times 2.0 \text{ nm}^3$  AgSe core in  $[\text{Ag}_{172}\text{Se}_{40}(\text{SenBu})_{92}(\text{dppp})_4]$  (**96**).

date (Figure 3-73) [67]. With increasing cluster size, the distribution of the silver centers appears to become chaotic, and the refinement of the X-ray data for **96** is correspondingly problematic. In this respect, **96** reflects the structure of solid  $\text{Ag}_2\text{Se}$ , where the  $\text{Ag}^+$  cations are also disordered. On the cluster surface, 92  $n\text{BuSe}$  ligands are  $\mu_3$ - and  $\mu_4$ -bonded to the silver atoms ( $\text{Se}-\text{Ag} = 2.498(3)\text{--}3.064(3) \text{ \AA}$ ). Noteworthy is the fact that there are only eight phosphine-silver bonds (four DPPP ligands) on the surface, as the butyl chains of the selenolate ligands provide the majority of the stabilization of the silver-selenide core. The 40  $\text{Se}^{2-}$  ligands act as  $\mu_5$ ,  $\mu_6$ ,  $\mu_7$  and  $\mu_8$  bridges ( $\text{Ag}-\text{Se} = 2.44\text{--}3.30 \text{ \AA}$ ) and are arranged with the Se centers of the  $n\text{BuSe}^-$  groups to form layered arrangements of selenium.



**Scheme 3-11** A summary of the reaction chemistry of  $\text{Et}_3\text{P}/\text{AgCl}$  and  $n\text{BuTeSiMe}_3$ .

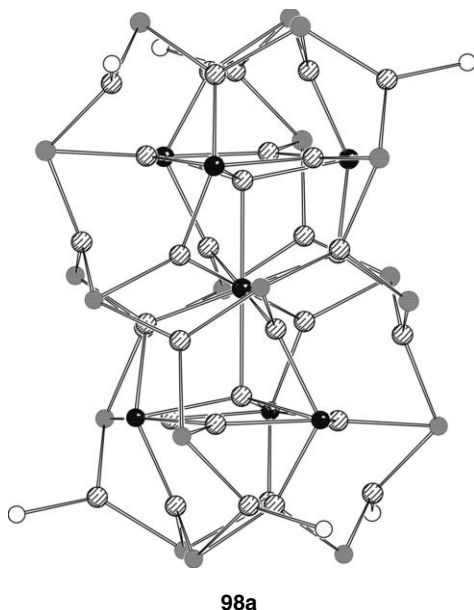


**Fig. 3-74** The molecular structure of  $[\text{Ag}_6(\text{TenBu})_6(\text{PEt}_3)_4]$  (**97**).

### Silver-Tellurium Clusters

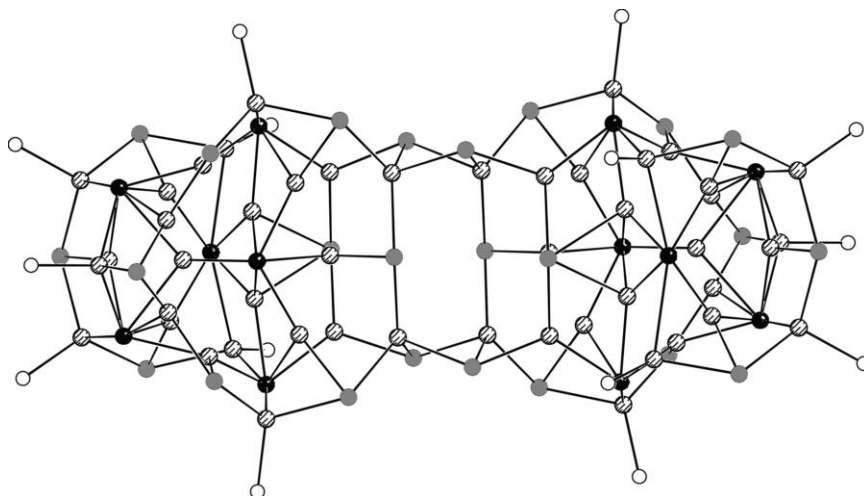
Silver chloride is dissolved readily in ether or hydrocarbon solvents using excess trialkylphosphine ligands. At room temperature, the addition of  $n\text{BuTeSiMe}_3$  to these solutions proceeds with the precipitation of insoluble, brick-red, amorphous materials or the formation of  $\text{Ag}_2\text{Te}$ . Low-temperature reactions again provide a route to access crystalline products suitable for X-ray analysis (Scheme 3-11) [69]. The addition of  $n\text{BuTeSiMe}_3$  to pentane solutions of a 1:3 mixture of  $\text{AgCl}:\text{PEt}_3$  at  $-40^\circ\text{C}$  yields a gold-colored solution from which bright yellow crystals of  $[\text{Ag}_6(\text{TenBu})_6(\text{PEt}_3)_4]$  (**97**, Figure 3-74) grow within several days in modest yield (30%). The six tellurolate ligands define a non-bonded octahedron, with four of the  $n\text{BuTe}^-$  ligands  $\mu_3$ -bonded and two  $n\text{BuTe}^-$  ligands bridging two Ag atoms. Two  $\text{Ag}(\text{I})$  centers are tetrahedral, bonded to two  $\text{PEt}_3$  and two  $n\text{BuTe}^-$  ligands, and the four remaining silver atoms are trigonal planar and bonded to the butyl-tellurolate ligands only, residing in the deltahedral faces of the  $\text{Te}_6$  polyhedron. The





**Fig. 3-75** The molecular structure of  $[\text{Ag}_{32}(\text{TenBu})_{18}\text{Te}_7(\text{PEt}_3)_6]$  (**98a**) (carbon atoms omitted).

importance of phosphine:metal ratio in the synthesis of metal-chalcogenide complexes with silylated reagents is again highlighted with the synthesis of  $[\text{Ag}_{32}(\text{TenBu})_{18}\text{Te}_7(\text{PEt}_3)_6]$  (**98a**): if the ratio of phosphine to silver is only 1:1, there is no evidence of **97**, and cluster **98a** is formed in low yield. The projection illustrates the layered nature of cluster **98a**, which resides on a crystallographic inversion centre (Figure 3-75). The “top” layer of **98a** consists of three  $\mu_3\text{-}n\text{Te}(\text{Bu})^-$  groups, whereas the second tellurium-rich layer contains three  $\mu_3$ -telluroate and three  $\mu_5$ -telluride ( $\text{Te}^{2-}$ ) ligands. The latter form a nearly planar hexagonal  $\text{Te}_3\text{Ag}_3$  ring (max. dev. = 0.10 Å), which lies above (0.61 Å) a tetrahedral Ag center. The central tellurium layer contains six  $\mu_3\text{-}n\text{Te}(\text{Bu})^-$  ligands and one, central  $\text{Te}^{2-}$  atom, which is within the range of bonding distances to eight silver atoms. The arrangement of Te is repeated in the bottom half of the structure. The result is that 24 Ag atoms all form three bonds to neighbouring Te atoms and six Ag atoms achieve trigonal planar coordination by bonding to two telluroate ligands and one phosphine ligand. The butyltelluroate ligands in **98** symmetrically bridge three metal centers. The combination of eighteen telluroate ( $18^-$ ) and seven telluride ligands ( $14^-$ ) again suggests a +1 oxidation state for the thirty-two silver atoms. The yield of cluster **98a** is low (~5%), although the synthesis is reproducible. There appears to be some inherent stability associated with the Ag–Te framework, as analogous  $[\text{Ag}_{32}(\text{TenBu})_{18}\text{Te}_7(\text{PR}_3)_6]$  clusters can be isolated using other tertiary phosphine ligands, and  $[\text{Ag}_{32}(\text{TenBu})_{18}\text{Te}_7(\text{PEt}_2\text{Ph})_6]$  (**98b**),  $[\text{Ag}_{32}(\text{TenBu})_{18}\text{Te}_7(\text{P}n\text{Pr}_3)_6]$  (**98c**) and  $[\text{Ag}_{32}(\text{TenBu})_{18}\text{Te}_7(\text{PiPr}_3)_6]$  (**98d**) are also similarly prepared. Unlike **98a–98c**, for which yields are low, the yield of cluster **98d** (R = *i*Pr) is rela-



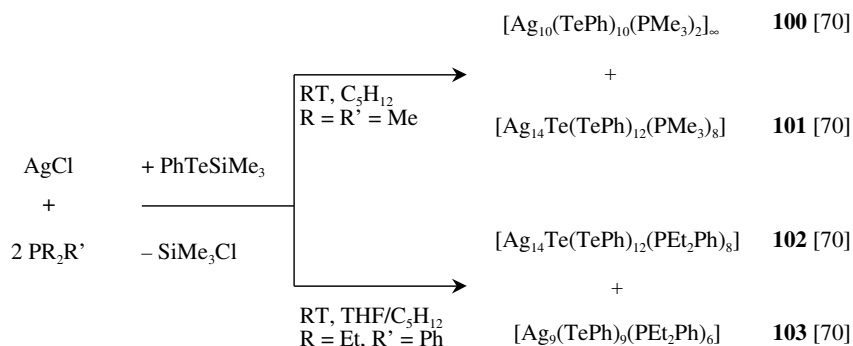
99

Fig. 3-76 The molecular structure of  $[\text{Ag}_{48}(\text{TenBu})_{24}\text{Te}_{12}(\text{PEt}_3)_{14}]$  (**99**) (carbon atoms omitted).

tively good (40%), as reaction solutions (of  $\text{AgCl}$ ,  $\text{PiPr}_3$  and  $n\text{BuTeSiMe}_3$ ) can be stirred at room temperature prior to crystallization without the formation of insoluble, solid materials. Presumably this facilitates the formation of additional  $\text{Te}^{2-}$  ions via tellurium-carbon bond cleavage of butyltellurolate moieties. The range of cone angles of the phosphines  $132\text{--}160^\circ$  for which identical cluster frameworks are observed illustrates the prominent role the alkyl chains on the Te centers play in stabilizing the cluster core, consistent with the limited number (six) of phosphines on the surface of the cluster. Attempts to improve the yields of clusters **98a–d** by using a mixture of  $n\text{BuTeSiMe}_3$  and  $\text{Te}(\text{SiMe}_3)_2$  does not yield any crystalline materials.

Modifying the ratio of triethylphosphine to silver chloride such that  $\text{AgCl}:\text{PEt}_3:n\text{BuTeSiMe}_3$  is 1:2:1, the cluster  $[\text{Ag}_{48}(\text{TenBu})_{24}\text{Te}_{12}(\text{PEt}_3)_{14}]$  (**99**, Figure 3-76) is isolated as dark red crystals after several days at low temperatures. The cluster consists of two spherical  $\text{Ag}_{24}\text{Te}_{16}$  sub-units linked by four  $\mu_3\text{-TenBu}^-$  ligands about a crystallographic inversion center. In contrast to **98**, the fourteen  $\text{Ag-PEt}_3$  centres in **99** are all tetrahedral. The remaining silver atoms within the cluster core have coordination number three (trigonal planar) or four (tetrahedral), and longer  $\text{Ag}\cdots\text{Te}$  contacts also suggest intermediate bonding descriptions. The 24  $n\text{BuTe}^-$  ligands and 12  $\text{Te}^{2-}$  atoms are in agreement with a +1 oxidation state to be assigned to the Ag sites, and the  $\text{Ag(I)}\cdots\text{Ag(I)}$  contacts range between 2.802(2) and 3.222(2) Å.

Although the synthesis of butyltellurolate-silver complexes requires low temperatures to avoid the precipitation of amorphous solids and we have isolated relatively few structural types of these compounds (see above), the chemistry of phenyltellurolate-silver complexes from  $\text{PhTeSiMe}_3$  and  $\text{AgCl}$  is rich and varied with respect to the polynuclear frameworks formed. These aryltellurolate reagents can



**Scheme 3-12** The synthesis of tellurido/telluroato-bridged silver clusters with monodentate  $\text{PR}_3$  ligands.

also be classified as “gentler” in that reactions between the phosphine-solubilized metal salt and the silylated chalcogens can often be performed at room temperature to yield medium-sized polynuclear complexes.

The reaction of a suspension of  $\text{AgCl}:2 \text{PMe}_3$  with  $\text{PhTeSiMe}_3$  yields two products,  $[\text{Ag}_{10}(\mu_3\text{-TePh})_{10}(\text{PMe}_3)_2]_{\infty}$  (**100**) and  $[\text{Ag}_{14}\text{Te}(\text{TePh})_{12}(\text{PMe}_3)_8]$  (**101**) and in 40% and 20% yield respectively (Scheme 3-12) [70].

Complex **100** consists of a polymeric one-directional arrangement, in which the  $\text{PhTe}^-$  ligands serve as both intra- and intermolecular bridges. A crystallographic inversion center relates the two halves of the  $\text{Ag}_{10}$  cluster frame (Figure 3-81), which is repeated to form the polymeric chain. All  $\text{PhTe}^-$  ligands are bonded to three  $\text{Ag}(\text{I})$  atoms, and the silver centers are three-coordinate and trigonal planar (sum of the angles =  $350.3\text{--}357.2^\circ$ ) with the exception of those bonded to the  $\text{PMe}_3$  ligand, which adopt a tetrahedral coordination geometry. There is no significant difference in length between the inter- and intracluster  $\text{Te-Ag}$  contacts. The structure of **100** consists of a rather shell-like make-up: the inner core consists of silver atoms surrounded by a  $\text{Te/Ag}$  layer which is itself surrounded by  $\text{PMe}_3$  and  $\text{Ph}$  ligands (Figure 3-77). The structure consists of a repeating clustered arrangement of silver and tellurium forming an  $\text{AgTe}$  “wire”.

The second product formed in the reaction of  $\text{AgCl}:2 \text{PMe}_3$  with  $\text{PhTeSiMe}_3$  is the molecular complex  $[\text{Ag}_{14}\text{Te}(\text{TePh})_{12}(\text{PMe}_3)_8]$  (**101**) [70]. In **101** (Figure 3-78), the fourteen silver centers are bonded to  $\mu_3$ -, three  $\mu_4$ - and two  $\mu$ - $\text{TePh}^-$  ligands with a central  $\mu_6\text{-Te}^{2-}$ . The  $\text{Ag-Te}$  distances associated with the two  $\mu$ - $\text{TePh}$  ligands are the shortest (on average) within the cluster. The non-bonded  $\text{Te}_{13}$  framework can be described as a capped, centered icosahedron in which one  $\mu_5$ -vertex is missing. The eight silver centers bonded to phosphine ligands exhibit tetrahedral coordination geometry, the remaining sites being either trigonal planar or tetrahedral.

The highly distorted and asymmetric nature of the cluster **101** can be contrasted with the framework observed in  $[\text{Ag}_{14}\text{Te}(\text{TePh})_{12}(\text{PEt}_2\text{Ph})_8]$  (**102**, Figure 3-79). Although the ratio of  $\text{Ag:TeR:Te:PR}_3$  is the same in **101** and **102**, there are marked differences in the structures of the two clusters [70]. The eight  $\text{PEt}_2\text{Ph}$  ligands in

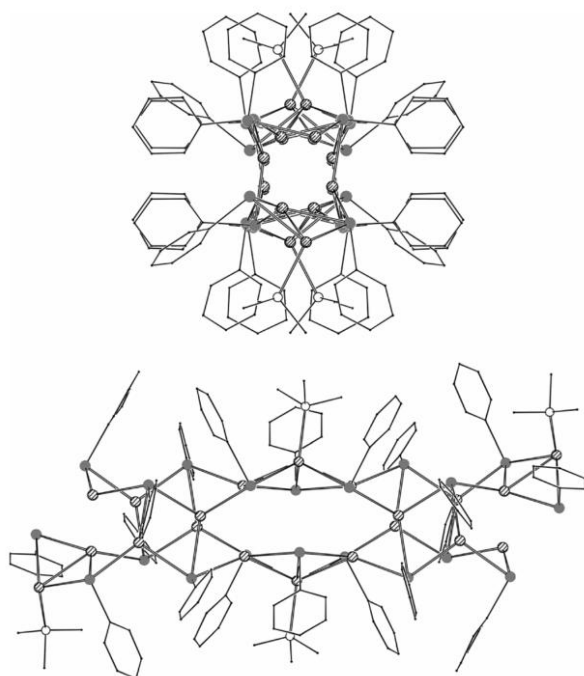
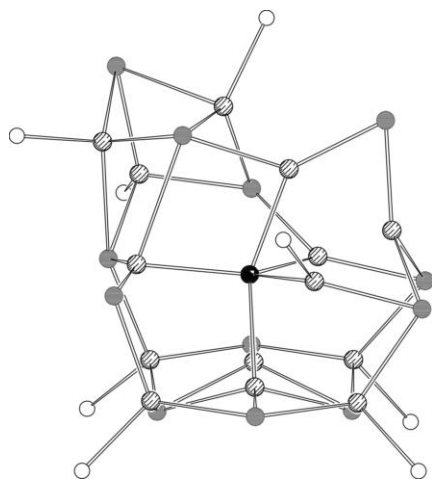
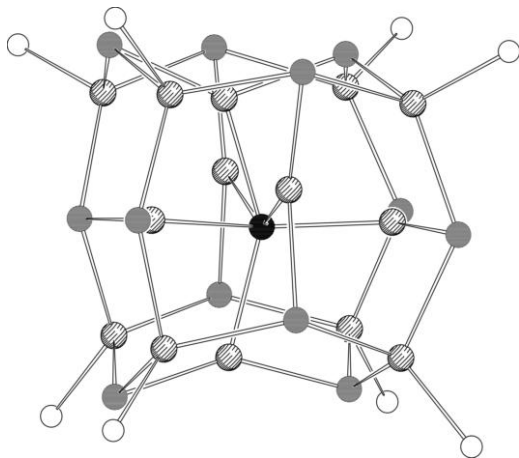


**Fig. 3-77** Two different projections of the infinite repeat observed in  $[\text{Ag}_{10}(\mu_3\text{-TePh})_{10}(\text{PMe}_3)_2]_{\infty}$  (**100**).



**101**

**Fig. 3-78** The Ag-Te-P framework in  $[\text{Ag}_{14}\text{Te}(\text{TePh})_{12}(\text{PMe}_3)_8]$  (**101**).



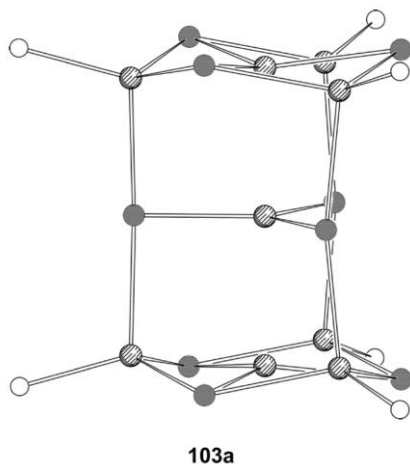
102

Fig. 3-79 The Ag–Te–P framework in  $[\text{Ag}_{14}\text{Te}(\text{TePh})_{12}(\text{PEt}_2\text{Ph})_8]$  (**102**).

**101** are located at the corners of a cube, and the twelve  $\text{TePh}^-$  ligands are evenly distributed, forming three (distorted) layers and each bonded to three silver atoms. The central telluride is within the range of bonding distances (2.768(1)–2.825(1) Å) to six silver atoms. The  $\text{Te}_{13}$  framework can be described as a highly distorted centered icosahedron. Of the twenty deltahedral faces of the icosahedron, eight are capped by the tetrahedral  $\text{Ag}(\text{PEt}_2\text{Ph})$  sites. The Ag–Te distances at these four-coordinate silver sites are longer than the six three-coordinate  $\text{Ag}(\text{I})$ , which lie within the  $\text{Te}_{13}$  frame: these latter have Ag–Te contacts ranging from 2.660(1) to 2.825(1) Å, and for the former set the Ag–Te contacts are longer, ranging from 2.838(1) to 3.026(1) Å. The coordination about the three-coordinate silver centers is, however, highly asymmetric, as invariably one of the Te–Ag–Te angles lies close to 90°.

The second, and major, product (60%) from the reaction of  $\text{AgCl}:\text{PEt}_2\text{Ph}$  with  $\text{Te}(\text{Ph})\text{SiMe}_3$  is the cluster  $[\text{Ag}_9(\text{TePh})_9(\text{PEt}_2\text{Ph})_6]$  (**103a**) (Scheme 3-12) [70]. The Ag–Te framework (Figure 3-80) sits on a 3-fold rotation axis that bisects three three-coordinate  $\text{Ag}(\text{I})$  atoms in the center of the rather columnar cluster that are bonded to three  $\text{TePh}^-$  ligands in trigonal planar fashion. The other six silver atoms are each bonded to one  $\text{PEt}_2\text{Ph}$  and three  $\text{TePh}^-$  ligands, and are tetrahedral. All  $\text{TePh}^-$  groups bridge three  $\text{Ag}(\text{I})$  atoms. The coordination environment about the three central  $\text{TePh}^-$  ligands is unusual in the Ag–TePh clusters described, as it consists of “T-shaped” coordination about tellurium. The central layer consists of a planar  $\text{Ag}(\text{TePh})_3$  arrangement, with the three phenyl rings lying in this plane. The extended packing arrangement of **103a** results in the central  $\text{Ag}(\text{TePh})_3$  layers being aligned, in a mixed aromatic–Ag–Te infinite repeat.

With the exception of  $[\text{Ag}_{32}(\text{Te}^i\text{Bu})_{18}\text{Te}_7(\text{PiPr}_3)_6]$  (**98d**), systematically accessing higher nuclearity, nanoscale AgTe clusters in good yield using monosilylated re-

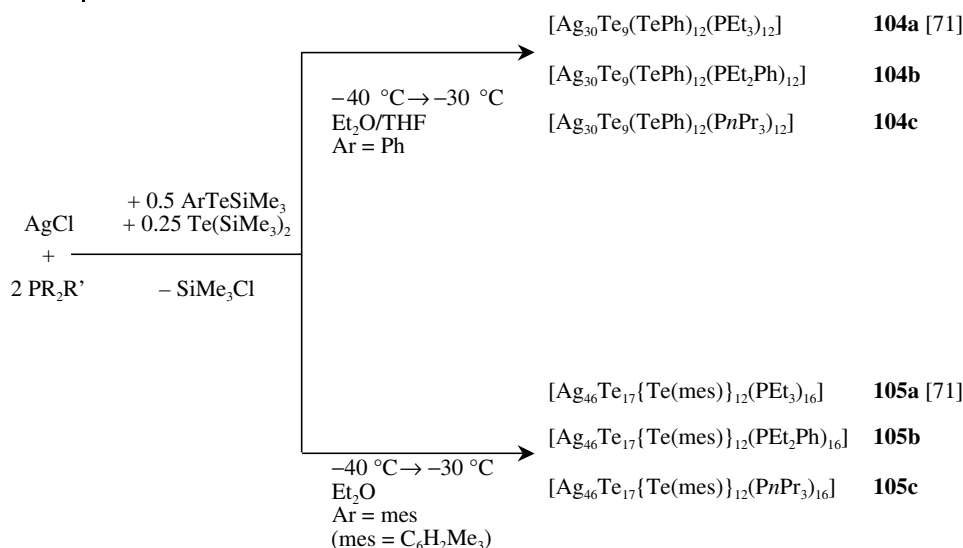


**Fig. 3-80** The Ag–Te–P framework in  $[\text{Ag}_9(\text{TePh})_9(\text{PEt}_2\text{Ph})_6]$  (**103a**).

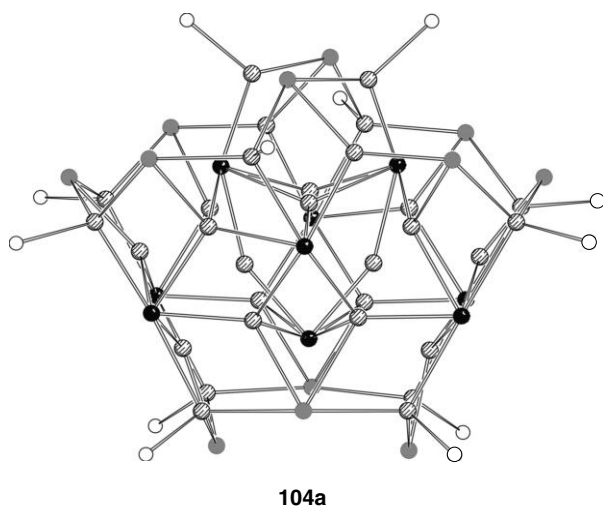
agents  $\text{R}/\text{ArTeSiMe}_3$  is not as effective as the corresponding technique for Cu–Te or Ag–Se complexes. Using a combination of silylated tellurium sources, however, (i.e.  $\text{ArTeSiMe}_3$  and  $\text{Te}(\text{SiMe}_3)_2$ ) to access metal-telluride clusters in good yield can be used if the substituent on the telluroate ligand is an aryl group. Thus, although the reaction of  $\text{AgCl}:\text{PR}_3$  solutions and  $\text{Te}(\text{SiMe}_3)_2$  leads to the formation of bulk  $\text{Ag}_2\text{Te}$ ,  $\text{AgCl}$  dissolved in ethereal solvents with triethylphosphine reacts with a combination of  $\text{Te}(\text{SiMe}_3)_2$  and  $\text{ArTeSiMe}_3$  ( $\text{Ar} = \text{Ph}$ , mes; mes =  $\text{C}_6\text{H}_2\text{Me}_3$ ) to yield the cluster complexes  $[\text{Ag}_{30}(\text{TePh})_{12}\text{Te}_9(\text{PEt}_3)_{12}]$  (**104a**) and  $[\text{Ag}_{46}(\text{Temes})_{12}\text{Te}_{17}(\text{PEt}_3)_{16}]$  (**105a**), respectively (Scheme 3-13) [71].

When an  $\text{AgCl}:\text{PET}_3$  (1:2) solution is treated with 0.5 equivalents of  $\text{PhTeSiMe}_3$  and 0.25 equivalents of  $\text{Te}(\text{SiMe}_3)_2$  at  $-40^\circ\text{C}$ , red crystals of **104a** form within a few days at  $-30^\circ\text{C}$  in fair yield (20%). The  $\sim 1.3 \times 1.1 \times 0.8 \text{ nm}^3$  cluster core is comprised of 12 telluroate ( $\text{PhTe}^-$ ), 9 telluride ( $\text{Te}^{2-}$ ), and 30 silver atoms (Figure 3-81). Similar complexes can be prepared using the different phosphine ligands ( $\text{PET}_2\text{Ph}$  (**104b**),  $\text{PnPr}_3$  (**104c**)).

The order of addition of the silylated reagents does not affect the yield of product. The phenyltelluroate ligands in **104a** act as both  $\mu_3$ - and  $\mu_4$ -bridges between the Ag(I) centers. Each of the nine  $\text{Te}^{2-}$  atoms forms six bonding contacts to the Ag centers ( $\text{Ag}-\text{Te} = 2.703(3)\text{--}3.185(3) \text{ \AA}$ ). Of the twelve phosphine-bonded silver sites, all but two, which are trigonal planar, exhibit tetrahedral coordination. The coordination environments of the silver atoms bonded only to tellurium are varied: two silver atoms form two bonds, each [ $\angle(\text{Te}-\text{Ag}-\text{Te}) = 153.1(1)\text{--}153.22(9)^\circ$ ], eight silver atoms are three-coordinate and six are tetrahedral. This varied coordination geometry about silver in the cluster contrasts with the trigonal planar geometry of the majority of the silver centers in **98** and **99**, but is consistent with the more close-packed nature of the AgTe framework in **104** and the higher coordination modes of the interstitial Te ligands. Similar varied coordination geometries have been observed for the copper-chalcogenide clusters described in the preceding sec-

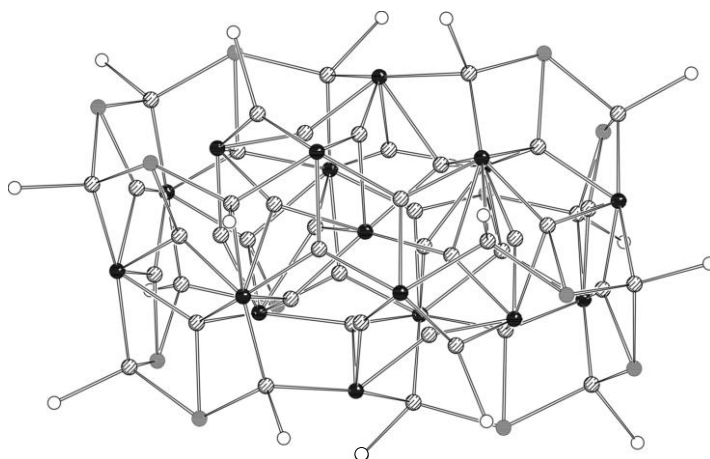


**Scheme 3-13** The synthesis of higher nuclearity tellurido/tellurolato-bridged silver clusters from AgCl, Te(SiMe<sub>3</sub>)<sub>2</sub>, and ArTeSiMe<sub>3</sub>.



**Fig. 3-81** A projection of the core atoms in [Ag<sub>30</sub>(TePh)<sub>12</sub>Te<sub>9</sub>(PEt<sub>3</sub>)<sub>12</sub>] (**104a**).

tions: whereas for copper-sulfide clusters containing up to 28 Cu centres, near linear S–Cu–S and trigonal planar S<sub>2</sub>–Cu–P arrangements are observed, the copper centres in larger selenium clusters exhibit tetrahedral and trigonal planar coordination. Cluster **104a** is structurally related to the copper-tellurium cluster [Cu<sub>29</sub>·(TePh)<sub>12</sub>Te<sub>9</sub>(PEt<sub>3</sub>)<sub>8</sub>][PEt<sub>3</sub>Ph] (**71**), which is formed from the co-condensation reaction of the two smaller clusters [Cu<sub>12</sub>Te<sub>3</sub>(TePh)<sub>6</sub>(PEt<sub>3</sub>)<sub>6</sub>] (**63**) and [Cu<sub>5</sub>(TePh)<sub>6</sub>·

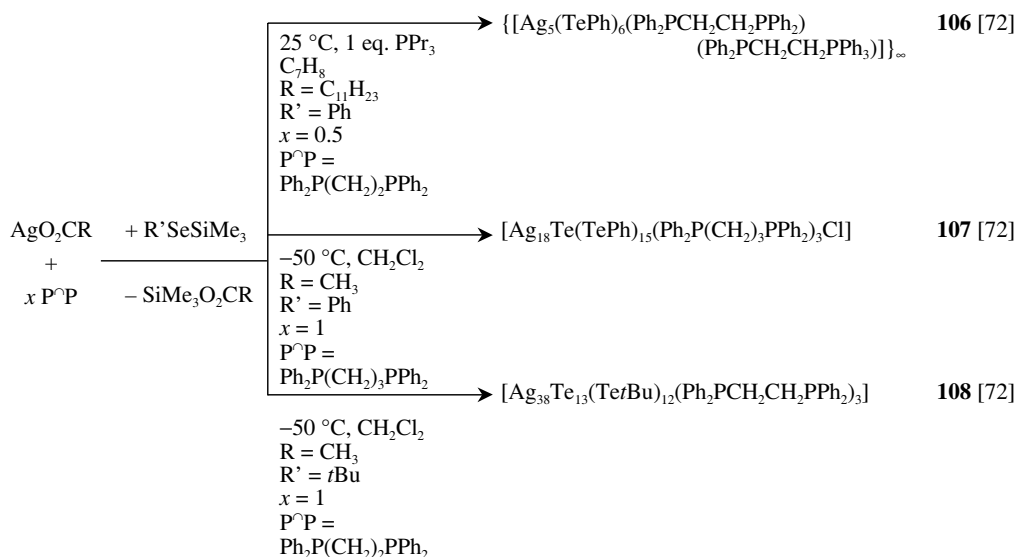
**105a**

**Fig. 3-82** The molecular structure of  $[\text{Ag}_{46}(\text{Temes})_{12}\text{Te}_{17}(\text{PEt}_3)_{16}]$  (**105a**) (carbon atoms omitted).

$(\text{PEt}_3)_3][\text{PEt}_3\text{Ph}]$  (**67**) [61]. This is the only example identified to date where there is a distinct structural relationship between a copper-telluride-telluroate nanocluster and a silver analog. There are four additional  $\text{PEt}_3$  ligands on the surface of **104a** vs **63** and the phosphine-bonded silver centers lie well “outside” of the tellurium polyhedron, whereas the copper atoms “missing” the phosphine in **63** are drawn into the cluster framework. The near linear coordination geometries of the two two-coordinate Ag centers in **104a** are replaced with trigonal planar copper sites in **63**, and this is accompanied by an increase in the coordination numbers of two telluride ligands.

The substituted aryl ligand  $2,4,6\text{-Me}_3\text{C}_6\text{H}_2\text{Te}^-$  ( $\text{mesTe}^-$ ) is also suitable for stabilizing polymetallic AgTe frameworks. Thus, in an analogous reaction to that for **104**,  $\text{AgCl}:\text{PR}_3$  ( $\text{PR}_3 = \text{PEt}_3, \text{P}n\text{Pr}_3, \text{PEt}_2\text{Ph}$ ) solutions in ether solvents are reacted with a combination of  $\text{Te}(\text{mes})\text{SiMe}_3$  and  $\text{Te}(\text{SiMe}_3)_2$ . The clusters  $[\text{Ag}_{46}(\text{Temes})_{12}\text{Te}_{17}(\text{PR}_3)_{16}]$  (**105**) are formed as dark red/black crystals in excellent yield (80–85%) [71]. Cluster **105a** ( $\text{PR}_3 = \text{PEt}_3$ ) contains a distribution of telluride ligands (Figure 3-82) in the central portion of the cluster, and telluroate groups and  $\text{PEt}_3$  are on the cluster surface. About the central  $\text{Te}^{2-}$  are 12 additional telluride ligands arranged to form a distorted [non-bonded  $\text{Te} \cdots \text{Te} = 4.523(2)\text{--}5.288(2)\text{ \AA}$ ] centered icosahedron. The central atom telluride is within the range of bonding distances to eight silver metal atoms [ $2.814(2)\text{--}3.198(2)\text{ \AA}$ ], which occupy positions within the  $\text{Te}_{13}$ -centered icosahedron, and an additional six Ag atoms reside within its delta-hedral faces. This central  $\text{Ag}_{34}\text{Te}_{13}$  unit is surrounded by 12  $\mu_3\text{-Te}(\text{mes})^-$ , 4  $\text{Te}^{2-}$ , and 12 Ag centers. The coordination number about the 46 silver atoms in **105a** varies from two (linear) to four (tetrahedral). The more condensed nature of the framework in **105a** is reflected in its color of dark red/black as compared with the more lightly coloured (red) **104a**.





**Scheme 3-14** The synthesis of tellurido/tellurolato-bridged silver clusters with bidentate phosphine ligands.

Bidentate phosphine ligands have also been shown to be effective in stabilizing AgTe polynuclear frameworks, and, as in the case of AgSe complexes, they can serve as both inter- and intracuster bridges. Unlike the entry into  $\text{PR}_3/\text{Ag}/\text{Te}/\text{TeR}$  complexes, where AgCl is used as a source of Ag(I), the successful preparation of  $\{[\text{Ag}_5(\text{TePh})_6(\text{Ph}_2\text{PCH}_2\text{CH}_2\text{PPh}_2)(\text{Ph}_2\text{PCH}_2\text{CH}_2\text{PPh}_3)]\}_\infty$  (**106**),  $[\text{Ag}_{18}\text{Te}(\text{TePh})_{15}(\text{Ph}_2\text{P}(\text{CH}_2)_3\text{PPh}_2)_3\text{Cl}]$  (**107**), and  $[\text{Ag}_{38}\text{Te}_{13}(\text{Te}t\text{Bu})_{12}(\text{Ph}_2\text{PCH}_2\text{CH}_2\text{PPh}_2)_3]$  (**108**) requires carboxylate salts of Ag(I) (Scheme 3-14) [72].

A suspension of silver laurate and half an equivalent of dppe in toluene can be solubilized via the addition of one equivalent of tri-*n*-propylphosphine. The addition of  $\text{PhTeSiMe}_3$  at room temperature to this solution results in the crystallization of  $\{[\text{Ag}_5(\text{TePh})_6(\text{Ph}_2\text{PCH}_2\text{CH}_2\text{PPh}_2)(\text{Ph}_2\text{PCH}_2\text{CH}_2\text{PPh}_3)]\}_\infty$  (**106**) in moderate yield (28%) after several days [72]. The structure of **106** (Figure 3-83) consists of  $[\text{Ag}_5(\text{TePh})_6]$  units linked by a dppe ligand. The arrangement of silver centers and tellurolate ligands is similar to that observed in the copper-tellurium complex  $[\text{Cu}_5(\text{TePh})_6(\text{PET}_3)_3][\text{PET}_3\text{Ph}]$ . There are three  $\mu_3$ -TePh groups ( $\text{Ag}-\text{Te} = 2.786\text{--}2.993\text{ \AA}$ ) around the “base” of the cluster and three  $\mu_2$ -TePh bridges ( $\text{Ag}-\text{Te} = 2.662\text{--}2.837\text{ \AA}$ ), the Te centers arranged to form a distorted non-bonded  $\text{Te}_6$  octahedron. There are four silver atoms in the base of the cluster and a lone, trigonal planar silver atom bonded to the three  $\mu_2$ -TePh bridges. The lone Ag atom centered in the base of the cluster has noticeably shorter  $\text{Ag}\cdots\text{Ag}$  contacts to the other three basal Ag sites ( $2.815(7)\text{--}2.870(6)\text{ \AA}$ ) than do the other silver atoms in **106** ( $>3.1\text{ \AA}$ ). The three additional Ag(I) atoms are tetrahedral, bonded to one  $\text{PPh}_2\cdot(\text{CH}_2)$ -group. The dppe ligand serves as an intercluster bridge between two  $[\text{Ag}_5(\text{TePh})_6]^-$  cluster units, to form the infinite repeat observed in **106**. The pen-

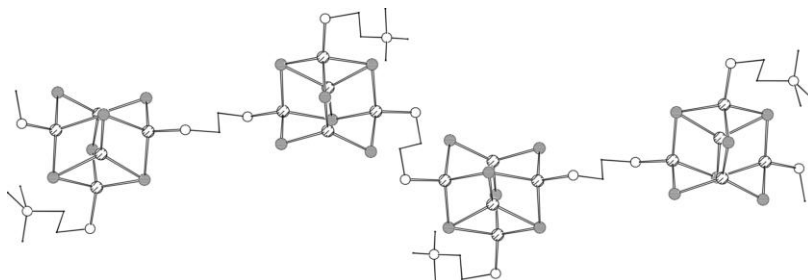
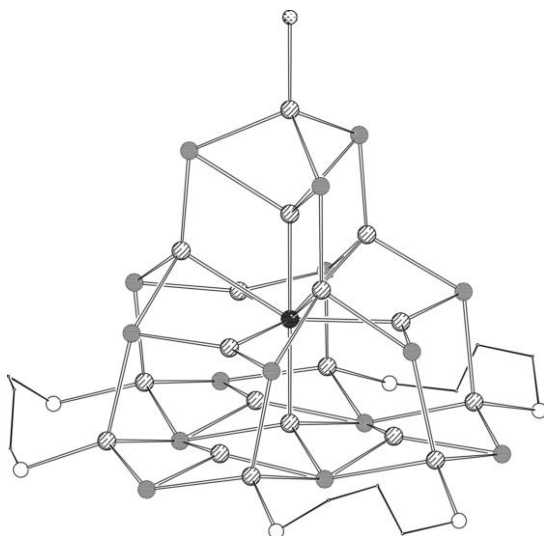


**Fig. 3-83** A projection of the polymeric repeat in  $\{[\text{Ag}_5(\text{TePh})_6(\text{Ph}_2\text{PCH}_2\text{CH}_2\text{PPh}_2)(\text{Ph}_2\text{PCH}_2\text{CH}_2\text{PPh}_3)]\}_\infty$  (**106**). For clarity, only the *ipso* carbon atoms of the  $-\text{PPh}_3^+$  centers and the C atoms of the methylene units on phosphorus are illustrated.



**107**

**Fig. 3-84** The core atoms in  $[\text{Ag}_{18}\text{Te}(\text{TePh})_{15}(\text{Ph}_2\text{P}(\text{CH}_2)_3\text{PPh}_2)_3\text{Cl}]$  (**107**).

dant  $[\text{Ph}_2\text{PCH}_2\text{CH}_2\text{PPh}_3]^+$  cation balances the negative charge on the cluster framework. Although the origin of this cation is difficult to rationalize, the generation of phosphonium centers during photochemically induced condensation reactions of Cu–TePh complexes is well established [19, 61].

$[\text{Ag}_{18}\text{Te}(\text{TePh})_{15}(\text{Ph}_2\text{P}(\text{CH}_2)_3\text{PPh}_2)_3\text{Cl}]$  (**107**) is synthesized by the 1:1:1 reaction of AgOAc,  $\text{Ph}_2\text{P}(\text{CH}_2)_3\text{PPh}_2$  and  $\text{PhTeSiMe}_3$  in  $\text{CH}_2\text{Cl}_2$ , the highly symmetric cluster residing on a crystallographic  $C_3$  axis (Figure 3-84) [72]. Cluster **107** possesses a pseudo close-packed arrangement of Te centers, with a central telluride ligand present from  $\text{Te}-\text{C}_{\text{phenyl}}$  bond cleavage of a TePh fragment. The five silver

atoms within the range of bonding distances to this central  $\text{Te}^{2-}$  are arranged to form nearly perfect trigonal bipyramidal coordination geometry about the tellurium. The  $\text{PhTe}^-$  ligands bridge either three or four Ag atoms, and, consistent with the rather open nature of the Ag–Te framework, the majority (nine) of the 11 interstitial silver atoms are three-coordinate, the other two adopting tetrahedral coordination. All phosphine-bonded Ag(I) sites and the lone Ag–Cl fragment are also bonded to three  $\text{PhTe}^-$  ligands. The dppp ligands are located exclusively around the “base” of the pyramidal AgTe framework, with the chloride occupying the apical position on the cluster.

The largest structurally characterized Ag/Te/TeR cluster stabilized with bidentate phosphine ligands,  $[\text{Ag}_{38}\text{Te}_{13}(\text{TetBu})_{12}(\text{Ph}_2\text{PCH}_2\text{CH}_2\text{PPh}_2)_3]$  (**108**) is obtained without the use of  $\text{Te}(\text{SiMe}_3)_2$  as a source of telluride ligands [72]. Cluster **108** forms as small, black crystals in ~50% yield from the reaction of AgOAc, dppe and  $t\text{BuTeSiMe}_3$  in a 4:4:3 ratio at low temperatures (Scheme 3-14). Gradual warming of reaction solutions to room temperature leads to the formation of **108** over several weeks, and the stability of these solutions at higher temperature (vs the precipitation of amorphous solids) accounts for the formation of such a “telluride-rich” cluster.

The structure of **108** (Figure 3-85) contains a spherical Ag–Te framework. The 13  $\text{Te}^{2-}$  ligands are spatially arranged in the cluster core to form a centered icosahedron, as is observed in  $[\text{Ag}_{46}(\text{Temes})_{12}\text{Te}_{17}(\text{PR}_3)_{16}]$  (**105**) [71]. The central telluride ligand of this deltahedral sub-unit forms eight Ag–Te bonding interactions (3.049–3.199 Å), and the polyhedron is in fact surrounded by twelve Ag(I) atoms, themselves arranged to form an  $\text{Ag}_{12}$  (non-bonded) icosahedron. The outer  $\text{Te}_{12}$  and inner  $\text{Ag}_{12}$  “shells” are then surrounded by the 12  $\mu_3$ - $t\text{BuTe}^-$  surface ligands and the additional 26 Ag(I) atoms. The twelve phosphine-bonded silver atoms have tetra-

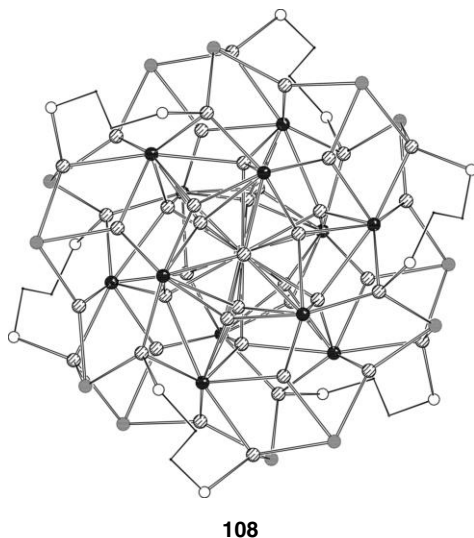


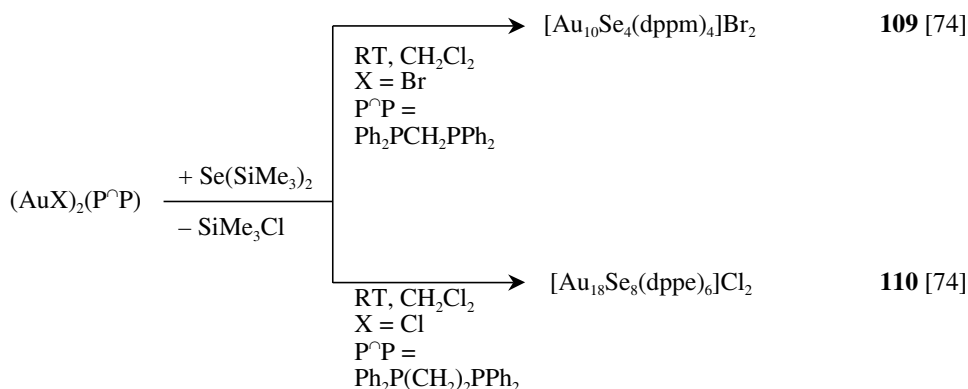
**Fig. 3-85** The core atoms in  $[\text{Ag}_{38}\text{Te}_{13}(\text{TetBu})_{12}(\text{Ph}_2\text{PCH}_2\text{CH}_2\text{PPh}_2)_3]$  (**108**).

hedral coordination as they are each also bonded to three Te centers. Sixteen of the remaining Ag(I) atoms are trigonal planar, and ten Ag(I) atoms are tetrahedrally coordinated to four Te ligands in asymmetric fashion.

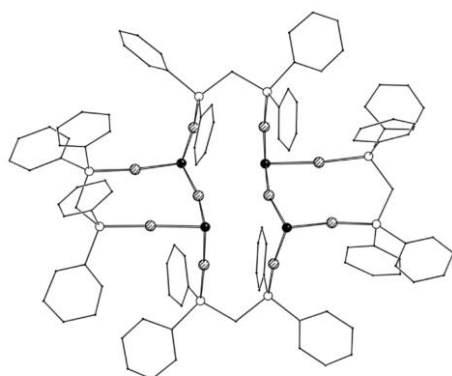
### 3.1.3.4 Selenium-Bridged Gold Clusters

The growing interest in gold-chalcogenide polynuclear chemistry can be attributed partly to the demonstration that these systems exhibit rich photoluminescence behavior and partly to the interesting structural frameworks that are generated as a result of weak Au(I)  $\cdots$  Au(I) interactions [73].

The utility of bidentate phosphine ligands in stabilizing metal-chalcogenide cores is again demonstrated by the synthesis of  $[\text{Au}_{10}\text{Se}_4(\text{Ph}_2\text{PCH}_2\text{PPh}_2)_4]\text{Br}_2$  (**109**) and  $[\text{Au}_{18}\text{Se}_8(\text{Ph}_2\text{PCH}_2\text{CH}_2\text{PPh}_2)_6]\text{Cl}_2$  (**110a**, Scheme 3-15) from the reaction of  $\text{Se}(\text{SiMe}_3)_2$ ,  $[(\text{AuBr})_2(\text{dppm})]$  and  $[(\text{AuCl})_2(\text{dppe})]$  at ambient temperature, respectively. The complex dication **109** is illustrated in Figure 3-86 and features



**Scheme 3-15** The synthesis of selenido-bridged gold clusters with bidentate phosphine ligands.



**109**

**Fig. 3-86** The molecular structure of the cationic framework in  $[\text{Au}_{10}\text{Se}_4(\text{Ph}_2\text{PCH}_2\text{PPh}_2)_4]\text{Br}_2$  (**109**).

four  $\mu_3$ -selenide ligands and four bidentate DPPM ligands bonded to ten Au(I) centers. The  $\mu_3$ -Se<sup>2-</sup> ligands are symmetrically bonded to three gold atoms (Se–Au = 2.423(1)–2.461(1) Å), with two ligands on either side of the Au<sub>10</sub> “plane”. The arrangement of the ten gold atoms has eight Au(I) atoms forming an outer, corrugated octahedron that surrounds two central Au(I) atoms. The molecule can also be regarded as consisting of two [Au<sub>5</sub>Se<sub>2</sub>]<sup>+</sup> units held together by two dppm ligands together with a contribution from the aurophilic interaction of the central Au(I)···Au(I) atoms (3.127(1) Å). These two gold atoms are bonded to two selenide ligands, with a noticeable deviation from linear geometry (164.7(1)–168.6(1)°) due to the metal-metal interaction. The eight additional gold sites are each bonded to one phosphorus and one selenium ligand, again with moderate deviations from linear geometries ( $\angle$ P–Au–Se = 168.5(1)–177.2(2)°) and Au(I)···Au(I) distances of 3.031(1)–3.364(1) Å similar to those observed in the structurally related complex [Au<sub>12</sub>(dppm)<sub>6</sub>S<sub>4</sub>]<sup>4+</sup>.

The larger gold-selenide cluster [Au<sub>18</sub>Se<sub>8</sub>(Ph<sub>2</sub>PCH<sub>2</sub>CH<sub>2</sub>PPh<sub>2</sub>)<sub>6</sub>]Cl<sub>2</sub> (**110a**) (Figure 3-87) is prepared in 90% yield from [(AuCl)<sub>2</sub>(dppe)] and Se(SiMe<sub>3</sub>)<sub>2</sub>. The structure of the complex dication **110** consists of two [Au<sub>9</sub>( $\mu_3$ -Se)<sub>4</sub>(dppe)<sub>3</sub>]<sup>+</sup> fragments formed from three Au<sub>4</sub>Se<sub>3</sub>dppe “rings”. Each of these forms a catenated structure with the corresponding ring in the second Au<sub>9</sub> fragment such that there are three pairs of interlocked rings, resulting in a central Au<sub>6</sub>Se<sub>2</sub> heterocubane unit. The six gold atoms in this heterocubane are two-coordinate, each linearly bonded to two selenide ligands ( $\angle$ Se–Au–Se = 173.7(1)–174.9(1)°). The Au(I)···Au(I) distances in the Au<sub>6</sub>Se<sub>2</sub> unit are in the range 2.940(2)–3.002(2) Å, and in the rest of the cluster are in the range 2.948(2)–3.327(3) Å. The remaining twelve Au(I) centers display the same, expected coordination geometries, as they are bonded to one phosphine and one selenide ligand ( $\angle$ P–Au–Se = 166.8(1)–173.1(1)°). The  $\mu_3$ -Se ligands symmetrically bridge the Au(I) centers (2.430(2)–2.481(3) Å), with six

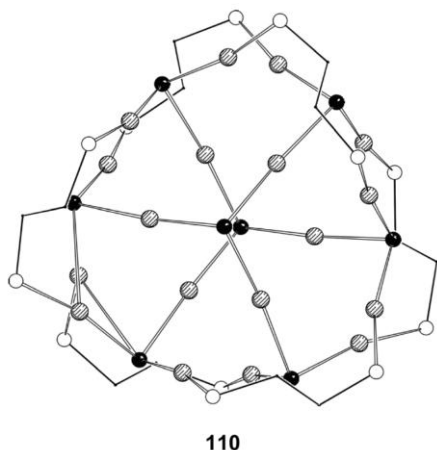


**Fig. 3-87** A projection of the molecular structure of [Au<sub>18</sub>Se<sub>8</sub>(Ph<sub>2</sub>PCH<sub>2</sub>CH<sub>2</sub>PPh<sub>2</sub>)<sub>6</sub>]<sup>2+</sup> (**110**, phenyl rings omitted for clarity).

of the selenide ligands distributed around the periphery of the AuSe frame. It is noteworthy that reactions of  $[(\text{AuCl})_2(\text{dppe})]$  with  $\text{RESiMe}_3$  ( $\text{R} = \text{Et}, i\text{Pr}, t\text{Bu}, n\text{Bu}$ ) invariably lead to the formation of  $[\text{Au}_{18}\text{Se}_8(\text{dppe})_6]\text{Cl}_2$  (**110a**) via Se–C bond cleavage, with no evidence to date of any intermediate, Au–SeR, containing complexes that can be isolated. Although the chloride counterions are easily substituted via the reaction of **110a** with  $\text{KPF}_6$  and  $\text{NaBPh}_4$  to yield  $[\text{Au}_{18}\text{Se}_8(\text{dppe})_6](\text{PF}_6)_2$  (**110b**) and  $[\text{Au}_{18}\text{Se}_8(\text{dppe})_6](\text{BPh}_4)_2$  (**110c**), respectively.

High-resolution electrospray ionization mass spectrometric investigations of **110b** display the expected isotopic distribution centered around  $m/z$  3283.89, corresponding to the dication **110**, with no evidence of fragmentation. Controlled, collision-induced fragmentation reactions of **110** with argon indicate that the preferred dissociation path is into two Au–Se fragments,  $[\text{Au}_{13}\text{Se}_6(\text{dppe})_3]^+$  and  $[\text{Au}_5\text{Se}_2(\text{dppe})_2]^+$ , with the concomitant loss of dppe. These experiments suggest similar Au–Se and Au–P binding energies in **110**.

## References

- 1 V. A. FEDORIN, *Semiconductors* **1993**, 27, 196.
- 2 (a) B. A. MANSOUR, S. E. DEMIAN, H. A. ZAYED, *J. Mater. Sci.* **1992**, 3, 249; (b) Z. VUČIĆ, O. MILAT, V. HORVATIĆ, Z. OGORELEK, *Phys. Rev.* **1981**, B 24, 5398.
- 3 (a) G. NIMTZ, P. MARQUARD, H. GLEITER, *J. Cryst. Growth* **1988**, 86, 66; (b) J. KOUTECKY, P. FANTUCCI, *Chem. Rev.* **1986**, 86, 539; (c) M. D. MORSE, *Chem. Rev.* **1986**, 86, 1049; (d) M. M. KAPPES, *Chem. Rev.* **1988**, 88, 369; (e) H. WELLER, *Angew. Chem.* **1993**, 105, 43.
- 4 (a) H. WELLER, *Angew. Chem.* **1998**, 110, 1748; (b) A. P. ALIVISATOS, *Science* **1996**, 271, 933; (c) H. WELLER, *Angew. Chem.* **1996**, 108, 1159; (d) G. SCHMID (Ed.): "Clusters and Colloids", VCH, Weinheim, 1995.
- 5 (a) J. P. FACKLER JR., D. COUCOUVANIS, *J. Am. Chem. Soc.* **1966**, 88, 3913; (b) L. E. MCCANDLISH, E. C. BISSELL, D. COUCOUVANIS, J. P. FACKLER, K. KNOX, *J. Am. Chem. Soc.* **1968**, 90, 7357.
- 6 I. G. DANCE, *Aust. J. Chem.* **1978**, 31, 617.
- 7 P. BETZ, B. KREBS, G. HENKEL, *Angew. Chem.* **1984**, 96, 293; P. BETZ, B. KREBS, G. HENKEL, *Angew. Chem. Int. Ed. Engl.* **1984**, 23, 311.
- 8 D. OHLMANN, H. PRITZKOW, H. GRÜTZMACHER, M. ANTHAMATTEN, P. GLASER, *J. Am. Chem. Soc. Chem. Commun.* **1995**, 1011.
- 9 Recent review: S. DEHNEN, A. EICH-HÖFER, D. FENSKE, *Eur. J. Inorg. Chem.* **2002**, 279–317.
- 10 (a) D. FENSKE, H. KRAUTSCHEID, S. BALTER, *Angew. Chem.* **1990**, 102, 799; (b) D. FENSKE, H. KRAUTSCHEID, *Angew. Chem.* **1990**, 102, 1513.
- 11 D. FENSKE, J. C. STECK, *Angew. Chem. Engl.* **1993**, 32, 238.
- 12 H. KRAUTSCHEID, D. FENSKE, G. BAUM, M. SEMMELMANN, *Angew. Chem.* **1993**, 105, 1364.
- 13 S. DEHNEN, A. SCHÄFER, D. FENSKE, R. AHLRICHS, *Angew. Chem.* **1994**, 106, 786.
- 14 S. DEHNEN, D. FENSKE, *Angew. Chem.* **1994**, 106, 2369–2372.
- 15 S. DEHNEN, D. FENSKE, A. C. DEVESON, *J. Clust. Sc.* **1996**, 7(3), 351–369.
- 16 J. F. CORRIGAN, S. BALTER, D. FENSKE, *J. Chem. Soc. Dalton Trans.* **1996**, 729.
- 17 S. DEHNEN, D. FENSKE, *Chem. Eur. J.* **1996**, 2, 1407–1416.
- 18 A. DEVESON, S. DEHNEN, D. FENSKE, *J. Chem. Soc., Dalton Trans.* **1997**, 4491.
- 19 J. F. CORRIGAN, D. FENSKE, *Angew.*

- Chem.* **1997**, 109, 2070, *Angew. Chem. Int. Ed. Engl.* **1997**, 36, 1981.
- 20 M. SEMMELMANN, D. FENSKE, J. F. CORRIGAN, *J. Chem. Soc., Dalton Trans.* **1998**, 2541.
  - 21 A. EICHHÖFER, D. FENSKE, *J. Chem. Soc., Dalton Trans.* **1998**, 2969.
  - 22 M. BETTENHAUSEN, A. EICHHÖFER, D. FENSKE, M. SEMMELMANN, *Z. Anorg. Allg. Chem.* **1999**, 625, 593.
  - 23 N. ZHU, D. FENSKE, *J. Chem. Soc., Dalton Trans.* **1999**, 1067.
  - 24 A. EICHHÖFER, J. F. CORRIGAN, D. FENSKE, E. TRÖSTER, *Z. Anorg. Allg. Chem.* **2000**, 626, 338.
  - 25 N. ZHU, D. FENSKE, *J. Clust. Sci.* **2000**, 11, 135.
  - 26 H. KRAUTSCHEID, *Ph.D. Thesis*, University of Karlsruhe **1991**.
  - 27 J. C. STECK, *Ph.D. Thesis*, University of Karlsruhe **1992**.
  - 28 S. BALTER, *Ph.D. Thesis*, University of Karlsruhe **1994**.
  - 29 S. DEHNEN, *Ph.D. Thesis*, University of Karlsruhe **1996**.
  - 30 M. SEMMELMANN, *Ph.D. Thesis*, University of Karlsruhe **1997**.
  - 31 A. EICHHÖFER, D. FENSKE, *unpublished results*.
  - 32 J. H. EL NAKAT, I. G. DANCE, K. J. FISHER, G. D. WILLET, *Inorg. Chem.* **1991**, 30, 2957.
  - 33 (a) D. VAN DER PUTTEN, D. OLEVANO, R. ZANONI, H. KRAUTSCHEID, D. FENSKE, *J. Electron. Spectrosc. Relat. Phenom.* **1995**, 76, 207; (b) A. ENDERLE, *Diploma Thesis*, University of Karlsruhe **1993**; (c) U. STÖHR, *Diploma Thesis*, University of Karlsruhe **1993**.
  - 34 (a) A. SCHÄFER, C. HUBER, J. GAUSS, R. AHLRICHS, *Theor. Chim. Acta* **1993**, 87, 29; (b) A. SCHÄFER, R. AHLRICHS, *J. Am. Chem. Soc.* **1994**, 116, 10686.
  - 35 S. DEHNEN, A. SCHÄFER, R. AHLRICHS, D. FENSKE, *Chem. Eur. J.* **1996**, 2, 429.
  - 36 K. EICHKORN, S. DEHNEN, R. AHLRICHS, *Chem. Phys. Lett.* **1998**, 284, 287.
  - 37 A. SCHÄFER, *Ph.D. Thesis*, University of Karlsruhe **1994**.
  - 38 (a) A. F. WELLS: "Structural Inorganic Chemistry", 5<sup>th</sup> Edn., Clarendon Press, Oxford (1984); (b) H. T. EVANS, *Z. Kristallogr.* **1979**, 150, 299.
  - 39 (a) R. D. HEYDING, R. M. MURRAY, *Can. J. Chem.* **1976**, 54, 841; (b) P. RAHLFS, *Z. Phys. Chem.* **1936**, B31, 157; (c) W. BORCHERT, *Z. Kristallogr.* **1945**, 106, 5; (d) A. L. N. STEVELS, *Philips Res. Rep. Suppl.* **1969**, 9, 124; (e) A. L. N. STEVELS, F. JELLINEK, *Recl. Trav. Chim.* **1971**, 90, 273; (f) A. TONJEC, Z. OGORELEC, B. MESTNIK, *J. Appl. Crystallogr.* **1975**, 8, 375.
  - 40 (a) R. BLACHNIK, M. LASOCKA, U. WALBRECHT, *J. Solid State Chem.* **1983**, 48, 431; (b) Y. G. ASADOV, L. V. RUSTAMOVA, G. B. GASIMOV, K. M. JAFAROV, A. G. BABAJEV, *Phase Transitions* **1992**, 38, 247.
  - 41 G. H. AYLWARD, T. J. V. FINDLAY, *Datensammlung Chemie*, VCH, Weinheim, **1986**, p. 125.
  - 42 C. A. TOLMAN, *Chem. Rev.* **1977**, 77, 313.
  - 43 (a) G. WILKINSON (Ed.), *Comprehensive Coordination Chemistry*, Vol. 5, Pergamon Press, Oxford **1987**, p. 583f; (b) M. G. B. DREW, A. H. B. OTHMAN, D. A. EDWARDS, R. RICHARDS, *Acta Crystallogr. Sect.* **1975**, B31, 2695.
  - 44 (a) R. AHLRICHS, M. BÄR, M. HÄSER, H. HORN, C. KÖLMEL, *Chem. Phys. Lett.* **1995**, 242, 652; (b) O. TREUTLER, R. AHLRICHS, *J. Chem. Phys.* **1995**, 102, 346; (c) A. SCHÄFER, H. HORN, R. AHLRICHS, *J. Chem. Phys.* **1992**, 97, 2571.
  - 45 (a) K. EICHKORN, O. TREUTLER, H. ÖHM, M. HÄSER, R. AHLRICHS, *Chem. Phys. Lett.* **1995**, 242, 652; (b) O. TREUTLER, R. AHLRICHS, *J. Chem. Phys.* **1995**, 102, 346; (c) K. EICHKORN, F. WEIGEND, O. TREUTLER, R. AHLRICHS, *Theor. Chim. Acta* **1997**, 97, 119.
  - 46 C. MÖLLER, M. S. PLESSET, *Phys. Rev.* **1934**, 46, 618.
  - 47 R. G. PARR, W. YANG, *Density Functional Theory of Atoms and Molecules*, Oxford University Press, New York **1988**.
  - 48 T. ZIEGLER, *Chem. Rev.* **1991**, 91, 651.
  - 49 E. LAX, *Taschenbuch für Chemiker und Physiker*, Vol. I, Springer, Berlin, Heidelberg **1967**, p. 324.
  - 50 E. LAX, *Taschenbuch für Chemiker und Physiker*, Vol. I, Springer, Berlin, Heidelberg **1967**, p. 326.

- 51 A. F. HOLLEMAN, E. WIBERG, *Lehrbuch der Anorganischen Chemie*, W. de Gruyter, Berlin **1985**, p. 148.
- 52 G. WEDLER, *Lehrbuch der Physikalischen Chemie*, VCH, Weinheim **1987**, p. 168.
- 53 D. FENSKE, N. ZHU, T. LANGETEPE, *Angew. Chem.* **1998**, *110*, 2784; *Angew. Chem. Int. Ed.* **1998**, *37*, 2640.
- 54 Y. PARK, *Ph.D. Thesis*, Michigan State University **1992**.
- 55 G. SAVELSBERG, H. SCHÄFER, *Z. Naturforsch.* **1978**, *B33*, 711.
- 56 K. O. KLEPP, *J. Less-Common Met.* **1987**, *128*, 79.
- 57 G. SAVELSBERG, H. SCHÄFER, *Mater. Res. Bull.* **1981**, *16*, 1291.
- 58 Y. PARK, D. C. DEGROOT, J. SCHINDLER, C. R. KANNEWURF, M. G. KANATZIDIS, *Angew. Chem. Int. Ed. Engl.* **1991**, *30*, 1325.
- 59 (a) Y. PARK, M. G. KANATZIDIS, *J. Chem. Mater.* **1991**, *3*, 781; (b) X. ZHANG, Y. PARK, T. HOGAN, J. L. SCHINDLER, C. R. KANNEWURF, S. SEONG, T. ALBRIGHT, M. G. KANATZIDIS, *J. Am. Chem. Soc.* **1995**, *117*, 10300.
- 60 M. EMIRDAG, G. L. SCHIMEK, J. W. KOLIS, *J. Chem. Soc., Dalton Trans.* **1999**, 1531.
- 61 M. W. DEGROOT, M. W. COCKBURN, M. S. WORKENTIN, J. F. CORRIGAN, *Inorg. Chem.* **2001**, *40*, 4678.
- 62 (a) F. C. FRANK, J. S. KASPER, *Acta Cryst.* **1958**, *11*, 184; (b) F. C. FRANK, J. S. KASPER, *Acta Cryst.* **1959**, *12*, 483.
- 63 (a) C. KÖLMEL, R. AHLRICHS, *J. Phys. Chem.* **1990**, *94*, 5536; (b) F. A. COTTON, X. FENG, M. MATUSZ, R. POLI, *J. Am. Chem. Soc.* **1988**, *110*, 7077; (c) K. M. MERZ, R. HOFFMANN, *Inorg. Chem.* **1988**, *27*, 2120.
- 64 U. MÜLLER, *Anorganische Strukturchemie*, 2<sup>nd</sup> Edn., B.G. Teubner, Stuttgart **1991**, p. 101f.
- 65 (a) JELLINEK in D. W. SHARP (Eds.): *MTP International Review of Science, Inorganic Chemistry Series One*, Vol. 5, Butterworths, London **1972**, p. 339; (b) C. W. FOLMER, F. JELLINEK, *J. Less Common Met.* **1980**, *76*, 153.
- 66 R. AHLRICHS, J. BESINGER, A. EICH-HÖFER, D. FENSKE, A. GBURECK, *Angew. Chem.* **2000**, *112*, 4089.
- 67 D. FENSKE, N. ZHU, T. LANGETEPE, *Angew. Chem. Int. Ed. Engl.* **1998**, *37*, 2640.
- 68 D. FENSKE, T. LANGETEPE, *Angew. Chem. Int. Ed. Engl.* **2002**, *41*, 300.
- 69 J. F. CORRIGAN AND D. FENSKE, *Chem. Commun.* **1996**, 943.
- 70 J. F. CORRIGAN, D. FENSKE, W. P. POWER, *Angew. Chem. Int. Ed. Engl.* **1997**, *36*, 1176.
- 71 J. F. CORRIGAN, D. FENSKE, *Chem. Commun.* **1997**, 1837.
- 72 T. LANGETEPE, D. FENSKE, *Z. Anorg. Allg. Chem.* **2001**, *627*, 820.
- 73 (a) H. SCHMIDBAUR, *Gold: Progress in Chemistry, Biochemistry, and Technology*, Wiley, New York, **1999**. (b) V. W.-W. YAM, C.-L. CHAN, C.-K. LI, K. M.-C. WONG, *Coord. Chem. Rev.* **2001**, *216*, 173 and references therein.
- 74 D. FENSKE, T. LANGETEPE, M. M. KAPPES, O. HAMPE, P. WEIS, *Angew. Chem. Int. Ed. Engl.* **2000**, *39*, 1857.

### 3.2

#### Synthesis of Metal Nanoparticles

Section 3.2 is divided into two parts, the first of which considers particles mainly consisting of noble metals, except for a few examples. Nanoparticles of noble metals have an especially long tradition, and fundamental synthetic strategies have therefore been known for some decades. The purpose of this part is therefore not to describe the huge number of synthetic pathways to metal nanoparticles, but rather to summarize the known syntheses. However, novel procedures are included if they complement traditional ones.



The second part of Section 3.2 deals exclusively with magnetic particles, since these species have attracted a lot of attention during the last decade. The reason is to be seen in the manifold future applications in nanodevices. In contrast to the part dealing with noble metal nanoparticles, this second part will also describe the most important properties of the particles.

### 3.2.1

#### Noble Metal Nanoparticles

*John S. Bradley and Günter Schmid*

##### 3.2.1.1 Introduction

The advancement of the understanding of small-particle science and the potential for new materials science based on the chemistry and physics of nanoscale metal clusters rests on the measurement and application of useful size-dependent properties of small metal nanoparticles. Ideally this requires the preparation and isolation of monodisperse metal particles with a great degree of control over size, structure and composition. Metals in varying levels of dispersion have a long history in many technological applications, but the methods of preparation used are usually determined by the intended use for the metal and are not necessarily developed with the aim of preparing well-defined metal particles. For example, highly dispersed metal catalysts are usually prepared by high-temperature reduction of metal precursors on oxide supports. These severe preparative conditions tend to yield metal particles with ranges of sizes and morphologies broad enough to hide the potentially unique properties which a monodisperse nanoscale sample could exhibit.

With these considerations in mind, synthetic chemists have begun to address the needs of metal particle research by developing the synthetic chemistry of colloidal metals, with a view to using the strategies of molecular chemistry to prepare well-defined metal particles. The goal may be stated as the search for synthetic methods for preparing metal particles stabilized in the 1–20 nm size range, and these synthesis approaches will be covered in this chapter. This area was discussed in a recent book giving a broad review of metal colloid chemistry [1], and is brought up to date here with a particular focus on synthetic methods.

##### 3.2.1.2 History and Background

Metal colloid science (as opposed to alchemical and aesthetic investigations) can be said to have begun with the experiments of Michael Faraday on gold sols in the mid-nineteenth century [2]. Deep red solutions of colloidal gold were prepared by the reduction of chloroaurate  $[\text{AuCl}_4]^-$  solutions using phosphorus as a reducing agent. (Recently these preparations have been reproduced in Faraday's original laboratory at the Royal Institution in London by J. M. Thomas, who has demonstrated that the gold sols thus produced contain particles of diameter 3–30 nm [3]. The work of Zsigmondy at the turn of the century put the physical investigation of

colloidal solutions (or suspensions – he used the terms interchangeably but with frequent comment as to the most appropriate term) on a firm basis, and his invention of the ultramicroscope enabled careful studies of the effect of preparation conditions on particle size to be carried out [4]. Many methods for the preparation of colloidal metals have been developed over the years since Faraday's experiments. A summary of the research on the preparation of metal sols in the first half of the century can be found in the 1951 paper of Turkevitch and coworkers [5], which describes detailed synthesis conditions and early electron microscopic characterization of gold sols prepared by the methods of Faraday (see above), Bredig (electric arc between gold electrodes under water), and Donau (action of carbon monoxide on chloroauric acid), and by a number of other related methods involving the action of reducing agents on chloroaurate solutions. These preparations introduce many of the methods used today in preparative metal colloid chemistry. Turkevitch's long study of this system yielded detailed knowledge of the nucleation, growth, and agglomeration of colloidal metals and has also allowed the reproducible preparation of gold sols with narrow particle size distributions in a range of mean sizes [6]. Figure 3-88 shows a TEM image of typical, very narrowly size-distributed 18 nm gold nanoparticles prepared by the Turkevitch method.

In general, the particle sizes found for these and related colloids can be varied over the range ca. 2–100 nm, depending on preparative conditions, with most examples falling in the large diameter range.

Inorganic colloid chemistry in the last two decades has focused on inorganic chalcogenides [7, 8] in approaches to quantum-confined semiconductor particles, and has progressed to the point where truly monodisperse II–VI semiconductor colloids in size ranges from 12 to 115 Å have been isolated and their size-dependent optical and other physical properties measured [9, 10]. The synthetic chemistry of metal colloids has now reached this degree of refinement, and after a lengthy period in which highly dispersed metals were widely exploited in specific technological applications such as photography and catalysis, the resurgence of interest in the intrinsic chemistry and physics of small metal particles has fostered the establishment of a new synthetic metal colloid chemistry.

### 3.2.1.3 Generation of Metal Particles

The successful establishment of this new area of inorganic materials chemistry will depend first of all on the control of particle size, morphology and composition of metal nanoparticles in syntheses which produce chemically significant quantities. So, for our purposes, the preparation of size-selected particles in a molecular beam experiment, although elegant, is not relevant to materials chemistry. The problem of preparing isolable yields of uniform samples is also one which was central to the development of synthetic organometallic cluster chemistry. The obvious difference between molecular synthesis and molecular approaches to colloidal metals is that with the former it is the constant aim of the organometallic chemist to maintain metals in complexed molecular form, whereas with the latter the goal is reversed, and we seek controlled methods for metal formation from molecular or ionic precursors. A reaction which results in the formation of ele-

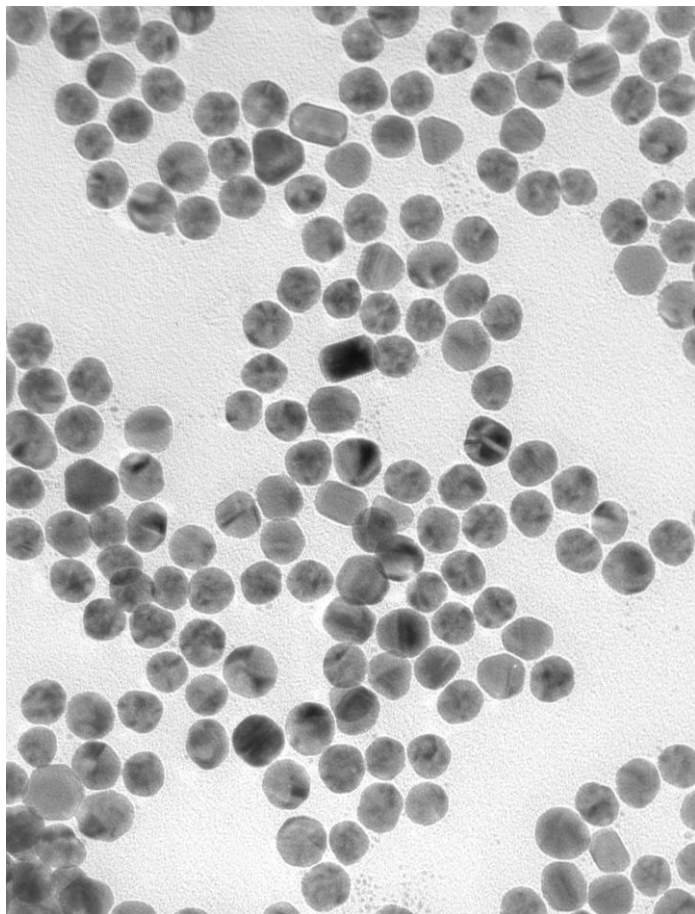


**Fig. 3-88** Transmission electron micrograph of a monodisperse 18 nm gold hydrosol prepared by citrate reduction of  $\text{HAuCl}_4$ .

mental metal in the laboratory of the synthetic molecular chemist is a failure, but it is also a potential source of colloidal metal. Such a process would normally lead to the formation of a metallic precipitate or mirror, but, in the presence in solution of an appropriate stabilizing agent, aggregation of the metal atoms can be arrested at an early stage, and the metal particles are preserved in suspension in the organic liquid.

A survey of the literature reveals that many of the various methods reported for the preparation of metal nanoparticles are applicable to a number of metals across the periodic table. For example, salt reduction using main group hydride reducing agents has been used for the preparation of many metals in colloidal form, not only those cited in this review. It is not the goal of this chapter to provide a direc-

tory of all reports of colloid syntheses, but only to give examples of the principal types of preparative methods which can be used.

### 3.2.1.4 Stabilization of Colloidal Metal Particles in Liquids

Before beginning a description of synthetic methods, a general and crucial aspect of colloid chemistry should be considered, and that is the means by which the metal particles are stabilized in the dispersing medium, since small metal particles are unstable with respect to agglomeration to the bulk. At short interparticle distances, two particles would be attracted to each other by van der Waals forces and in the absence of repulsive forces to counteract this attraction an unprotected sol would coagulate. This counteraction can be achieved by two methods, *electrostatic stabilization* and *steric stabilization* [11]. In classical gold sols, for example, prepared by the reduction of aqueous  $[\text{AuCl}_4]^-$  by sodium citrate, the colloidal gold particles are surrounded by an electrical double layer formed by adsorbed citrate and chloride ions and cations which are attracted to them. This results in a Coulombic repulsion between particles, and the net result is shown schematically in Figure 3-89.

The weak minimum in potential energy at moderate interparticle distance defines a stable arrangement of colloidal particles which is easily disrupted by medium effects and, at normal temperatures, by the thermal motion of the particles. Thus, if the electric potential associated with the double layer is sufficiently high, electrostatic repulsion will prevent particle agglomeration, but an electrostatically

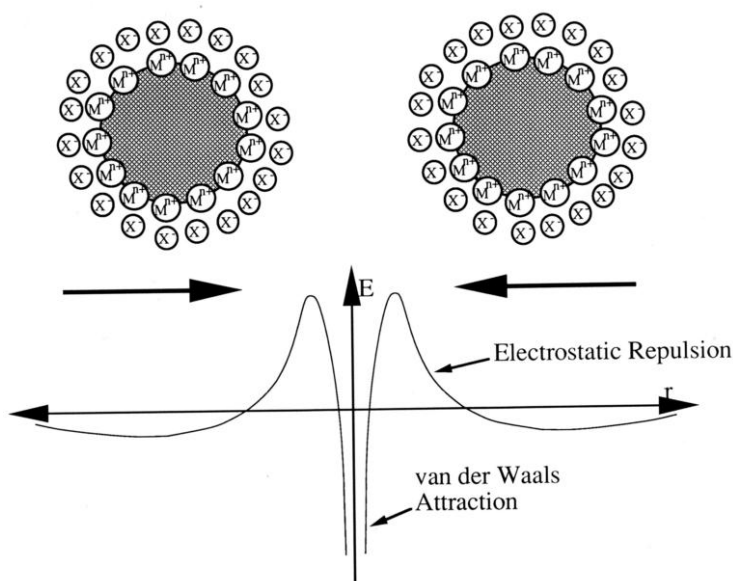


**Fig. 3-89** Electrostatic stabilization of metal colloid particles. Attractive van der Waals forces are outweighed by repulsive electrostatic forces between adsorbed ions and associated counterions at moderate interparticle separation.

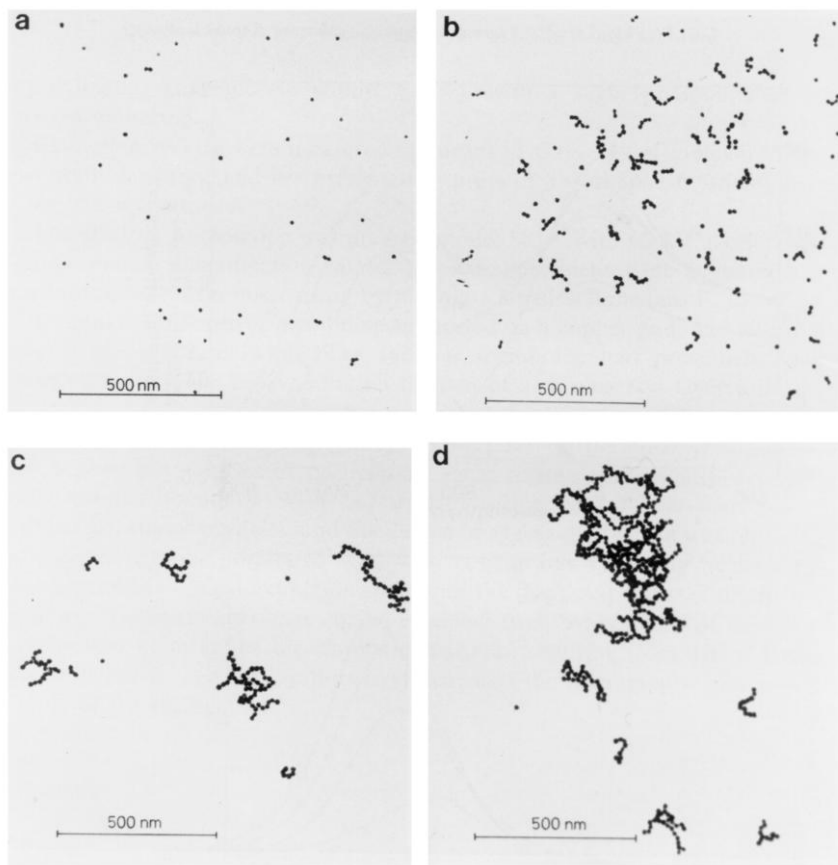


**Fig. 3-90** Aggregation of an electrostatically stabilized 12–18 nm gold hydrosol caused by the addition of pyridine, a neutral ligand (reproduced with permission from [12]).

stabilized sol can be coagulated if the ionic strength of the dispersing medium is increased sufficiently. If the surface charge is reduced by the displacement of adsorbed anions by a more strongly binding neutral adsorbate, the colloidal particles can now collide and agglomerate under the influence of the van der Waals attractive forces. This phenomenon is nicely demonstrated by the addition of pyridine to a gold sol of the type mentioned above, as shown in Figure 3-90 [12].

Even in organic media, in which electrostatic effects might not normally be considered to be important, the development of charge has been demonstrated on inorganic surfaces, including metals, in contact with organic phases such as solvents and polymers [13]. For example, the acquisition of charge by gold particles in organic liquids has been demonstrated, and the sign and magnitude of the charge has been found to vary as a function of the donor properties of the liquid [14]. Thus, even for colloidal metals in suspension in relatively non-polar liquids, the

possibility cannot be excluded that electrostatic stabilization contributes to the stability of the sol.

A second means by which colloidal particles can be prevented from aggregating is by the adsorption of molecules such as polymers, surfactants or ligands at the surface of the particles, thus providing a protective layer. Polymers are widely used, and it is obvious that the protectant, in order to function effectively, must not only coordinate to the particle surface, but must also be adequately solvated by the dispersing fluid – such polymers are termed amphiphilic. The choice of polymer is determined by consideration of the solubility of the metal colloid precursor, the solvent of choice, and the ability of the polymer to stabilize the reduced metal particles in the colloidal state. Natural polymers such as gelatin and agar were often used before the advent of synthetic polymer chemistry, and related stabilizers such as cellulose acetate, cellulose nitrate [15], and cyclodextrins [16] have been used more recently. Thiele [17] proposed the *Protective Value* as a measure of the ability of a polymer to stabilize colloidal metal. It was defined, similarly to the older *Gold Number* of Zsigmondy, as the weight of the polymer which would stabilize 1 g of a standard red gold sol containing 50 mg/L gold against the coagulating effect of 1% sodium chloride solution. Several other studies have been performed on the relative ability of polymers to act as steric stabilizers [18–20], and, despite the fact that these quite subjective studies focus on very specific (and quite different) sol systems, it seems that, of the synthetic polymers considered, vinyl polymers with polar side groups such as poly(vinylpyrrolidone) (PVP) and poly(vinyl alcohol) are especially useful in this respect.

The use of copolymers introduces another degree of variability to colloidal stabilization, as the comonomer ratio can be varied. For example, the use of vinylpyrrolidone-vinyl alcohol copolymers is reported for the preparation of platinum and silver hydrosols [21]. The silver sols were stable only in the presence of the copolymer, and the size of the silver particles decreased with an increase in vinylpyrrolidone content of the copolymer.

Electrostatic and steric stabilization are in a sense combined in the use of long-chain alkylammonium cations and surfactants, either in single-phase sols or in reverse micelle synthesis of colloidal metals. Examples will be described below. A new class of metal colloids has recently been established in which the surface of the particle is covered by relatively small ligand molecules such as sulfonated triphenylphosphine [22] or alkane thiols, and examples will be given below [23].

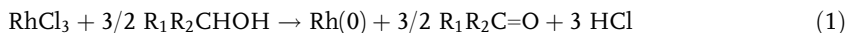
#### 3.2.1.5 Synthetic Methods for the Preparation of Colloidal Transition Metals

The synthetic methods which have been used include modern versions of established methods of metal colloid preparation such as the mild chemical reduction of solutions of transition metal salts and complexes and newer methods such as radiolytic and photochemical reduction, metal atom extrusion from labile organometallics, and the use of metal vapor synthesis techniques. Some of these reactions have been in use for many years, and some are the results of research stimulated by the current resurgence in metal colloid chemistry. The list of preparative methods is being extended daily, and, as examples of these methods are described be-

low, the reader will quickly be made aware that almost any organometallic reaction or physical process which results in the deposition of a metal is in fact a resource for the metal colloid chemist. The acquisition of new methods requires only the opportunism of the synthetic chemist in turning a previously negative result into a synthetic possibility.

### Salt Reduction

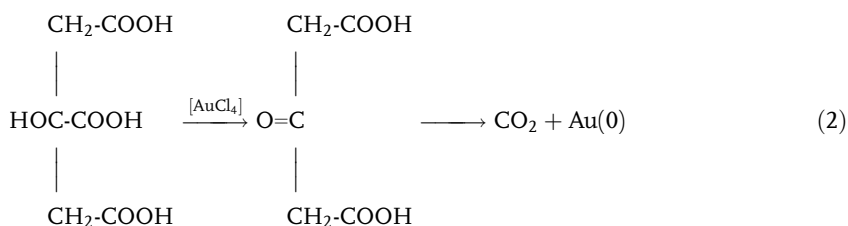
The reduction of transition metal salts in solution is the most widely practiced method of generating colloidal suspensions of the metals. In aqueous systems, the reducing agent must be added or generated *in situ*, but in non-aqueous systems the solvent and the reducing agent can be one and the same. Easily oxidized solvents such as alcohols can thus function both as reducing agents and as the colloid diluent, and these have been used widely in colloid preparations. Hirai and Toshima developed the so-called “alcohol reduction process”, which is a very general process for the production of metal nanoparticles, often stabilized by organic polymers such as poly(vinylpyrrolidone), poly(vinyl alcohol), and poly(methyl vinyl ether) [24–31]. In general, the alcohols which were useful reducing agents contained  $\alpha$ -hydrogen (tert-butanol, for example, was not effective) and were oxidized to the corresponding carbonyl compounds (methanol to formaldehyde, ethanol to acetaldehyde, *iso*-propanol to acetone) which were detected during the reaction [Eq. (1)].



Palladium acetate has been compared with palladium chloride as a starting material for PVP-stabilized colloidal palladium and was found to give smaller particles and better control of particle size distribution, and the effect of Pd/PVP ratio was also investigated [32]. Palladium organosols have been prepared by the reduction of palladium acetate in refluxing methanol or at a higher temperature in 2-ethoxyethanol, both in the presence of PVP, which yields ca. 6.5 nm particles [33, 34]. Organosols of platinum and palladium have been synthesized by heating salts of the metals in long-chain aliphatic alcohols like 1-decanol, which not only reduce the salts to the metal but also act as stabilizers for the colloid particles [35]. Esumi has reported the use of several alcohols in a comparative synthetic study in which  $\text{C}_1$ – $\text{C}_5$  aliphatic alcohols,  $\alpha$ -phenylethanol,  $\beta$ -phenylethanol, and benzyl alcohol were used as solvent and reducing agent for palladium acetate in the presence of PVP, giving particle sizes in the 1–4 nm range [36]. A review reports on the generation of bimetallic nanoparticles [24].

The reduction of metal salts by added reducing agents in non-reducing solvents is the oldest established procedure for the preparation of aqueous suspensions of colloidal metals. A wide range of reducing agents have been used in metal colloid syntheses, and they are frequently interchangeable from metal to metal. Thus, hydrazine hydrate has been used in preparations of colloidal platinum [37], gold [38], copper [39], and palladium-platinum alloy [40]. A catalog of preparations will not be presented here, but examples of the use of typical reducing agents will be given.

Faraday reduced aqueous solutions of  $[\text{AuCl}_4]^-$  with phosphorus vapor to produce gold hydrosols [2], and a variety of reducing agents have subsequently been used with tetrachloroaurate, both with and without protective polymers, to give colloidal gold with particle sizes from one to several hundred nanometers in diameter. Turkevitch and his coworkers reproduced many of these methods [5] and have established reliable preparative procedures for the preparation of gold sols with quite precisely defined particle sizes. The 20 nm gold sol prepared by the reduction of  $[\text{AuCl}_4]^-$  by sodium citrate has become a standard for histological staining applications. The mechanism of the reduction of metal salts by citrate was also studied by the same authors [5], who demonstrated that, in the reduction of  $[\text{AuCl}_4]^-$ , an induction period which was present when citrate was the reducing agent was absent when  $[\text{AuCl}_4]^-$  was reduced by acetone dicarboxylate (an oxidation product of citrate), and a rapid formation of colloidal gold resulted.



A similar mechanism may be postulated for other reductions with citrate, and this method has been widely used for the preparation of other metal sols, such as platinum [41–43], and can be added as an ionic stabilizer in preparations which require an additional reducing agent. The use of formate, citrate, and acetone dicarboxylate as reducing agents at various pH values was reported to give good control over particle size in the preparation of a series of platinum hydrosols [44].

A study by Glaunsinger and coworkers [37] has been reported on the reduction of chloroplatinic acid by a variety of reducing agents including sodium borohydride, hydroxylamine hydrochloride, dimethylamine borane, sodium citrate, hydrazine monohydrate, sodium formate, trimethylamine borane, sodium trimethoxyborohydride, and formaldehyde.

Among the various reducing agents,  $\text{BH}_4^-$  plays a dominant role. Brust et al. [45] introduced this method to reduce gold salts in the presence of alkanethiols, resulting in 1–3 nm Au particles. Variations in the thiol concentrations provide good size control of the particles, between 2 and 5 nm [46]. Thiol-stabilized Au particles became available by following a seeding growth approach starting with 3.5 nm colloids [47]. Nanoparticles of gold in the size range of 10 to about 30 nm have become known using mercaptosuccinic acid for stabilization and  $\text{BH}_4^-$  as the reducing species. Variations in the ratio  $[\text{AuCl}_4]^-$ : succinic acid allow the specific synthesis of 10.2, 10.8, 12.8, 19.4, and 33.6 nm colloids [48].

The generation of a reducing agent *in situ* was recently used for the preparation of gold hydrosols from  $[\text{AuCl}_4]^-$ . Tetrakis(hydroxymethyl)phosphonium chloride (THPC) hydrolyzes under alkaline conditions to eliminate formaldehyde, and



under hydrolysis conditions  $[\text{AuCl}_4]^-$  oxidizes THPC with the formation of small (1–2 nm) colloidal gold clusters [49–51]. The mechanism of this reaction is not known, but it is known that under high pH conditions THMP yields formaldehyde and subsequently hydrogen, either of which could be the reducing agent.

Hydrogen has been used effectively as a reducing agent for metal salts in electrostatically stabilized metal sol syntheses. Hydrosols of palladium, platinum, rhodium, and iridium, stabilized with poly(vinyl alcohol), were prepared by hydrogen reduction of the metal hydroxides [52–56].

Moiseev et al. used hydrogen to synthesize Pd nanoclusters of very uniform size and composition, so that these particles can be described by a rather precise formula:  $\text{Pd}_{561}\text{L}_{\approx 60}(\text{OAc})_{\approx 180}$  ( $\text{L}$  = phenanthroline, bipyridine) [57–62]. Pd nanoclusters, also of discrete size, shape, and composition have been described by Schmid et al., also using  $\text{H}_2$  to reduce Pd salts:  $\text{Pd}_{561}\text{phen}_{36}\text{O}_{\approx 200}$ ,  $\text{Pd}_{1415}\text{phen}_{60}\text{O}_{\approx 1100}$ ,  $\text{Pd}_{2057}\text{phen}_{84}\text{O}_{\approx 1600}$  (phen = phenanthroline) [63–65].

These nanoclusters belong to the family of so-called full-shell clusters, meaning that their metal nuclei consist of a number of atoms that follows hexagonal or cubic close packing. The coordination number 12 in such metallic structures leads to a first full-shell cluster of  $1 + 12 = 13$  atoms, followed by another shell of 42 atoms, resulting in 55 atoms, etc. Generally, a nanocluster of  $n$  shells consists of  $10n^2 + 2$  atoms. So, the above-mentioned Pd clusters correspond to five shells (561), seven shells (1415), and eight shells (2057). Of course, with increasing size, the exact number of atoms can in practice deviate from the ideal number. However, it has to be stated that the full-shell clusters that have become known up to the present time are indeed more or less monodisperse, especially compared to the huge number of larger nanoparticles, which usually show size distributions of at least  $\pm 10\%$ .

The  $\text{Au}_{13}$  and  $\text{Au}_{55}$  clusters at the very beginning of this row of full-shell clusters have to be discussed.  $\text{Au}_{13}$  clusters were first described in 1981 [66, 67] and were found to form icosahedral structures, whereas the two-shell clusters with  $\text{Au}_{55}$  cores exhibit cubic close-packed (ccp) structures like bulk gold.

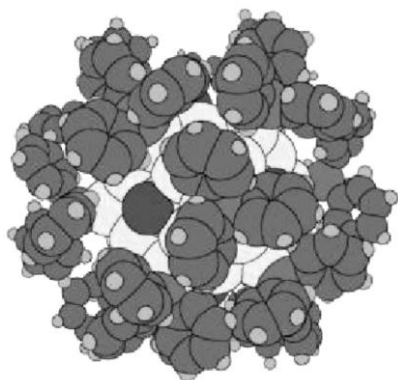
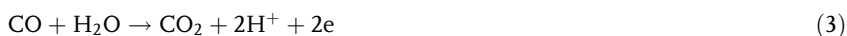


**Fig. 3-91** Model of  $\text{Au}_{55}(\text{PPh}_3)_{12}\text{Cl}_6$ .

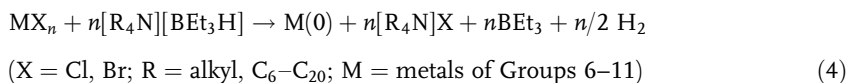
$\text{Au}_{55}(\text{PPh}_3)_{12}\text{Cl}_6$  is probably the most frequently investigated full-shell cluster, since its size definitely represents the transition from bulk to molecule (represented by ligand-protected  $\text{Au}_{13}$  clusters), so that it represents the prototype metallic quantum dot [68–117]. Chapters 4 and 5 deal intensively with this cluster and some of its ligand-modified relatives. The synthesis of  $\text{Au}_{55}(\text{PPh}_3)_{12}\text{Cl}_6$  occurs by a very special reduction method.  $\text{B}_2\text{H}_6$  is used to react with  $\text{Ph}_3\text{PAuCl}$  in warm benzene or toluene [68, 69]. Diborane not only acts as a reducing agent but also traps excess  $\text{PPh}_3$  to give  $\text{Ph}_3\text{P}\cdot\text{BH}_3$ . Numerous derivatives of the  $\text{PPh}_3$ -stabilized cluster are available by ligand exchange reactions. For instance,  $\text{Ph}_2\text{PC}_6\text{H}_4\text{SO}_3\text{Na}$  removes  $\text{PPh}_3$  quantitatively and makes the compound water-soluble [73]. Thiols are best suited to substitute  $\text{PPh}_3$  because  $\text{Au-S}$  bonds are stronger than  $\text{Au-P}$  bonds [102, 103, 118]. The only four-shell cluster that has become known is  $\text{Pt}_{309}\text{phen}^*_{36}\text{O}_{30\pm 10}$  ( $\text{phen}^* = 4,7\text{-C}_6\text{H}_4\text{SO}_3\text{Na}$ -substituted 1,10-phenanthroline) [119]. It is prepared from  $\text{Pt(II)}$  acetate, which is reduced by hydrogen at room temperature in acetic acid solution in the presence of equivalent amounts of ligand. Under these conditions, the oxygen-free cluster is formed first, and this is then carefully treated with oxygen to give the air-stable final product. The nature of the oxygen is probably (as in the above-mentioned  $\text{Pd}$  full-shell clusters) super-oxidic or peroxidic. It can easily be removed from the surfaces of the clusters by hydrogen. The structure of the  $\text{Pt}_{309}$  core is ccp, as in the case of the  $\text{Au}_{55}$ , the  $\text{Pd}_{561}$ , the  $\text{Pd}_{1415}$ , and the  $\text{Pd}_{2057}$  nanoclusters, as has been shown by X-ray diffraction and high-resolution electron microscopic (TEM) studies. More structural details are described in [120].

A remarkable type of rather well-defined nanoclusters has been described by Finke et al. [121–123]. Polyoxoanion-supported  $\text{Ir(I)}$  complexes, e.g.,  $(\text{Bu}_4\text{N})_5\text{Na}_3\cdot[(1,5\text{-COD})\text{Ir}\cdot\text{P}_2\text{W}_{15}\text{Nb}_3\text{O}_{62}]$ , are reduced in solution by hydrogen to give  $\text{Ir}$  nanoclusters with  $\text{Ir}$  cores containing ca. 300–900 atoms, protected by an assembly of polyoxoanions.

Carbon monoxide/water was used to reduce  $\text{PtO}_2$  to nanoparticles, effectively using a water gas shift reaction to provide reducing equivalents of electrons from the reaction [124].



Remarkable contributions to the synthetic field of transition metal nanoparticles came from Bönemann's group. Their work has recently been reviewed [31]. Some details will be discussed in the following. Tetraalkylammonium hydrotriorganoborates  $[\text{R}_4\text{N}]^+ [\text{BR}'_3\text{H}]^-$  as reducing species for transition metal salts turned out to result in numerous valuable  $[\text{NR}_4]^+$ -stabilized metal nanoparticles [31, 125–128]. Equation (4) represents the general formation of metal nanoparticles following this route.



The ammonium salts accomplish two functions: the hydride reduces the positively charged metal in  $\text{MX}_n$  and the  $[\text{R}_4\text{N}]^+$  cations stabilize the metal nanoparticles.

The  $[\text{BEt}_3\text{H}]^-$  anion as the potassium salt even reduces salts of the early transition metals, only stabilized by THF. So, Ti, V, and Nb colloids could be obtained [123].

A rather unexpected reaction happens between metal salts  $\text{MX}_n$  ( $\text{M}$  = metals of Groups 6–11,  $\text{X}$  = halogen, acetylacetonate,  $n = 2\text{--}4$ ,  $\text{R} = \text{C}_1\text{--}\text{C}_8$  alkyl) and  $\text{AlR}_3$ , giving particles in the size range 1–12 nm [129, 130]. It is suggested that a not precisely determinable layer of organoaluminum species covers the nanoparticles.

Silanes have also found use in colloid preparation, and an interesting example of the use of organosilanes in the formation of organosols of transition metals is the reduction of platinum, palladium, and rhodium salts to colloidal particles by trialkoxysilanes and trialkylsilanes. This was reported by Lewis and coworkers [131–133], who demonstrated that presumably homogeneous hydrosilylation catalysts formed from platinum compounds in the presence of silanes were in fact colloidal in nature, raising the prospect of colloid activity in many ostensibly homogeneous catalyst systems. Silanes and Si–H-containing polymers have been used to reduce  $\text{Pd}(\text{hfacac})_2$  ( $\text{hfacac}$  = hexafluoroacetylacetonate) to colloidal palladium in organic solvents [134].

Alkanethiols have been used as phase transfer stabilizers for gold colloids. The thiols were added to THF-water solutions of a preformed gold sol (prepared by the citrate method) from which adsorbed anions had been removed by treatment with an ion exchange resin, resulting in a cyclohexane-soluble sol [23]. This was a particularly useful procedure in that the colloidal gold particles of various sizes could be deposited electrophoretically in ordered close-packed two-dimensional lattices with spacings correlating to the length of the alkyl chain of the thiol.

Surfactants such as water soluble-phosphines, e.g., sodium salts of sulfonated triphenylphosphine,  $\text{P}(m\text{-C}_6\text{H}_4\text{SO}_3\text{Na})_3$ , and alkyltriphenyl-methyltrisulfonates,  $\text{RC}(p\text{-C}_6\text{H}_4\text{SO}_3\text{Na})_3$ , function as stabilizers for hydrosols of colloidal rhodium, prepared by hydrogen reduction of aqueous  $\text{RhCl}_3 \cdot 3\text{H}_2\text{O}$  in the presence of the surfactant [135, 136]. The colloidal material is described as a polyhydroxylated rhodium particle, implying considerable oxidation of the rhodium surface to  $\text{Rh}(\text{I})$ , and is stabilized by interaction between the anionic head of the surfactant and the  $\text{Rh}(\text{I})$  sites at the colloid surface. Conversely, if the rhodium sol is prepared by aqueous borohydride reduction of  $\text{RhCl}_3 \cdot 3\text{H}_2\text{O}$ , the colloidal particles are thought to be zero-valent rhodium metal, stabilized by interaction with the hydrophobic alkyl group on the surfactant [137]. Analogous colloids of gold were prepared by Schmid by citrate reduction of chloroaurate followed by addition of  $(\text{C}_6\text{H}_5)_2\text{P-}p\text{-C}_6\text{H}_5\text{SO}_3\text{Na}$ , giving a water-soluble gold colloid which can be isolated as a solid and redissolved without aggregation [22].

Just as the use of a surfactant salt of triethylborohydride introduces reducing agent and stabilizer in a single reagent [125–128], polymeric reducing agents can be used which also can function as polymeric stabilizers. Examples include the use of polyethyleneimine in the preparation of colloidal silver [17, 138].

A chemical analog of the preparation of metal colloids by the reduction of metal salts by radiolytically produced radicals and electrons (see below) can be found in

recent reports by Dye et al. [139, 140], who used alkalides and electrides as homogeneous reducing agents to reduce main group and transition metal salts in aprotic solvents. These reducing agents are crystalline salts of alkali metal anions or trapped electrons of the form  $K^+[(\text{crown})_2K]^-$  or  $K^+[(\text{crown})_2e]^-$  prepared by reaction of the alkali metal with a crown ether. In solvents such as dimethyl ether or THF these remarkable compounds reduce metal salts to the colloidal metal state with particle sizes in the nanoscale range. For example,  $\text{AuCl}_3$  is reduced to an unstable colloidal gold by  $K^+[(15\text{-crown-5})K]^-$  in dimethyl ether. The familiar stable ruby red hydrosol is produced by dissolving the reaction product in water.

Electrons have been used in the more traditional form in the electrolytic reduction of metal salts to metal nanoparticles [141–147]. The relevant metal is dissolved from the anode, and reduction at the cathode in the presence of tetraalkylammonium salts results in the formation of metal nanoparticles. The most significant aspect of this method is that the size of the resulting metal particles is determined by the current density, with the smallest particles (1.4 nm) being produced at the highest current density.

Ti, Fe, Co, Ni, Pd, Pt, Ag, and Au nanoparticles became available in preparative amounts by this method with yields of >95%. The electrochemical method also opens pathways to bimetallic nanoparticles such as Pd/Ni, Fe/Co, and Fe/Ni by using two sacrificial  $M_{\text{bulk}}$  anodes [145].

### Thermolysis

Since many organometallic compounds of transition metals decompose thermally to their respective metals under relatively mild conditions, these compounds provide a rich source of nanoparticle precursors. The method is widely applicable. The thermolysis of carbonyl-containing complexes of rhodium, iridium, ruthenium, osmium, palladium, and platinum in polymer solutions has been used to prepare polymer-stabilized colloidal metals with particle sizes in the range 1–10 nm, possibly by decomposition of polymer-bound organometallic intermediates [148–152].

Organosols of palladium and platinum [153–158] have been synthesized by the thermolysis of precursors such as palladium acetate, palladium acetylacetonate and platinum acetylacetonate in high boiling organic solvents such as methylisobutylketone, and bimetallic colloids of copper and palladium have been prepared by the thermolysis of mixtures of their acetates in similar solvents. These preparations were performed in the absence of stabilizing polymers, and as a result relatively broad size distributions and large particles were observed. A preparation of bimetallic PVP-stabilized copper-palladium particles with diameters of 1–4 nm has been reported by Toshima, in which palladium acetate and cupric sulfate are transformed first to the colloidal hydroxides by treatment of an ethylene glycol solution of these salts with sodium hydroxide solution in the presence of PVP [159]. The colloidal mixed hydroxide was then heated to 198 °C under nitrogen, yielding a stable bimetallic sol.

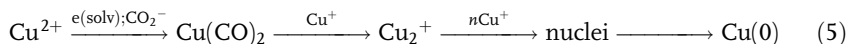
In view of the extensive literature on the syntheses and structures of bimetallic metal carbonyl clusters, it is even more surprising that few attempts have been reported to use the facile decomposition of these compounds in the preparation of

bimetallic colloids. Although this would be an unnecessarily complicated route for colloids of miscible metals if their salts could be coreduced to the same end, there remains the possibility of preparing bimetallic particles of immiscible metals starting from well-defined molecular bimetallic clusters of immiscible metals. Such clusters are known to exist despite the immiscibility of their constituent metals in the bulk, and there is reason to believe that bulk immiscibility might not apply to very small particles because of the importance of surface effects.

### Photolysis and Radiolysis

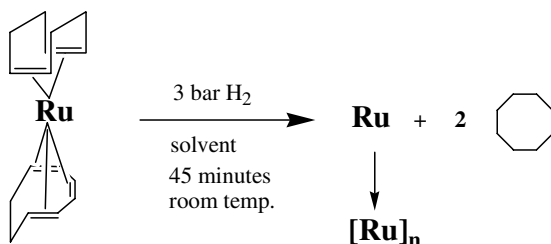
Photochemical colloid syntheses fall into two categories: the reduction of metal salts by radiolytically produced reducing agents such as solvated electrons and free radicals, and the photolysis of photolabile metal complexes. Again, the essence of the preparative procedure is the generation of zero-valent metal under conditions which prevent or at least retard the formation of bulk metal precipitates.

The method has of course a long and important history in the formation of photographic images in silver halide emulsions. Research over the past decades, predominantly that of Henglein and of Belloni, has established a wide range of colloidal metals prepared by this method, encompassing both main group metals such as cadmium, thallium, and lead, and other noble and non-noble transition metals [160–175]. Radiolytic methods differ in the identity of the reducing species formed under irradiation, this being a function of solvent and any added solute. The radiolysis of aqueous solutions of metal ions produces solvated electrons, which may react either with the dissolved metal ions directly or with other solutes to produce secondary radicals, which then reduce the metal cation. For example, irradiation of solutions of  $\text{Cu}(\text{ClO}_4)_2$  containing  $\text{HCOONa}$  yields colloidal copper [173] via reduction of  $\text{Cu}^{2+}$  by both solvated electrons and  $\text{CO}_2^-$ :



An advantage of radiolytic methods of colloidal metal synthesis lies in the fact that a large number of metal nuclei are produced homogeneously and instantaneously, a condition favorable for the formation of very highly dispersed particles. In addition, the reducing agents are formed *in situ*, and thus chemical compatibility of added reducing agents ( $\text{BH}_4^-$ ,  $\text{Et}_3\text{BH}^-$ , etc.) with other components of the colloid system is not an issue, although the possibility of photolysis of those components exists, as does the possibility of their reaction with primary photolysis or radiolysis products.

The photolysis of metal complexes and salts is also an effective and clean method for the generation of colloidal metals, and it is amenable to all of the experimental protocols used for stabilization of the resulting particles. For example, gold, silver or platinum salts may be subjected to UV-visible irradiation in inverse microemulsions, surfactant solutions or polymer solutions [176–181]. In a comparative study of hydrogen reduction vs photoreduction of chlorplatinic acid in the presence of surfactants it was found that photoreduction produced smaller platinum particles with a narrower size distribution [176].



**Scheme 3-16** Formation of Ru nanoparticles from Ru(COD)(COT).

### Ligand Reduction and Ligand Displacement from Organometallics

Reduction of the metal can be carried out prior to colloid preparation, giving a zero-valent metal complex as the immediate colloid precursor. The synthesis of metal carbonyls and their subsequent thermolysis in nanoparticle synthesis is an example of this approach. In a further refinement, the supporting ligands in the zero-valent complex can be removed by ligand displacement with an excess of a weakly bound ligand or by ligand reduction, thus generating metal particles at low temperatures. The organometallic literature is replete with examples of reactions of organometallic complexes with hydrogen to give metal deposits, and some of these reactions have been applied to colloid synthesis.

The zero-valent palladium and platinum complexes with dibenzylideneacetone Pd(dba)<sub>2</sub> and M<sub>2</sub>(dba)<sub>3</sub> (M = Pd, Pt) have been known since 1970 to react under mild conditions with either hydrogen or carbon monoxide with the formation of metal [182].

Meanwhile, there exists a long series of examples where CO and H<sub>2</sub> are used to decompose organometallic precursor molecules [183–200]. As a very recent example, the decomposition of Ru(COD)(COT) (COD = cyclooctadiene, COT = cyclooctatriene) in an atmosphere of hydrogen should be mentioned [201, 202].

The precursor molecule is dissolved in a methanol/THF mixture and is contacted with H<sub>2</sub> at 3 bar and room temperature for at least 45 min. Depending on the MeOH/THF mixture, the Ru particle size can be set at a value between 3 and 86 nm.

#### 3.2.2

### Synthesis and Characterization of Magnetic Nanoparticles

*Dmitri V. Talapin, Elena V. Shevchenko, Horst Weller*

#### 3.2.2.1 Introduction

Magnetic particles of micro- and nanometer size are attracting growing fundamental and technological interest. Magnets are important for motors, electrical power transformation, data storage devices, electronics, etc. Miniaturization, one of the important features of modern technology, requires extremely small magnets of

micro- or even nanometer size. How to prepare such materials? Which properties can one expect from an extremely small piece of a material which is ferromagnetic in the bulk state? In this Section we will focus on the nanoparticles of ferromagnetic metals, their preparation, and their structural and magnetic characterization. In nature there are only three ferromagnetic elements at room temperature: iron, cobalt and nickel (one can also include in this series gadolinium which is ferromagnetic below 16 °C). Additionally, some compounds and alloys of manganese, chromium, and europium can exhibit ferro- or ferrimagnetic behavior [203]. The exciting discovery that rhodium clusters ( $\text{Rh}_n$  with  $n = 12\text{--}32$ ) are ferromagnetic [204] shows the non-trivial scaling behavior of magnetism and demonstrates that magnetic nanomaterials can reveal novel unexpected phenomena.

Magnetic metal nanoparticles could find future applications also as catalysts [205] and single-electron devices [206–209]. Monodisperse magnetic nanoparticles can organize themselves into highly ordered superstructures and even form macroscopic “crystals” with nanoparticles as building blocks. The electron spins inside a nanoparticle can be aligned in a certain direction by applying an external magnetic field. Thin granular films of ferromagnetic nanocrystals are already the basis of conventional magnetic storage media (hard drives). It is expected that the advanced magnetic media based on ordered arrays of monodisperse nanocrystals could reach magnetic recording densities in the range of 100 Gb/in<sup>2</sup> and 1 Tb/in<sup>2</sup> [210]. Spin-dependent tunneling electron transport has recently been demonstrated in an array of close-packed cobalt nanoparticles [206]. Granular materials consisting of nanometer-sized magnetic particles in a dielectric or nonmagnetic metal matrix exhibit outstanding magnetoresistive properties [211–215].

Magnetic colloids, or ferrofluids, are based on magnetic nanoparticles coated with a layer of surfactant dispersed in a carrying solvent. The molecules of surfactant (further referred to as “stabilizing agents” or “stabilizers”) bind to the nanoparticle surface preventing coagulation and providing solubility and desired surface properties. Moreover, stabilizers protect the particle from oxidation and can strongly affect the magnetic properties [216–218]. Ferrofluids have been extensively studied and harnessed in a variety of applications [219–221]. For example, the magnetorheological properties of magnetic colloids are exploited in high-performance bearings and seals [222–224]. There are several reviews on the properties and technological applications of ferrofluids [219–224].

A possibility of manipulating nanoparticles at a distance by applying an external magnetic field opens up a broad field for biomedical applications of magnetic nanoparticles. Specific surface groups of the stabilizers can be used for linking different species to the nanoparticle surface. Drugs, antibodies, etc. can be attached to the surface of colloidal magnetic nanoparticles and can be steered into regions of the body where they are required by means of an applied magnetic field [203]. Functionalized magnetic nanoparticles can be specifically attached to a cancer tumor and heated up by an a.c. magnetic field, resulting in thermoablation of the tumor (magnetic fluid hyperthermia) [225]. Magnetic nanoparticles coupled with oligonucleotides were used as a nanosensor for the detection and separation of complementary specific oligonucleotides [226].

The preparation of nanoparticles of desired sizes is the first and very important step, being a prerequisite of their further investigation and use in practice. Narrow size distribution or monodispersity is highly desirable because magnetic properties become strongly size dependent in the nanometer size range. The magnetic behavior of nanoparticles depends not only on their chemical composition and size, but also on their crystalline modification and the presence of structural defects like stacking faults or twinned planes [210]. Murray et al. proposed the use of the term “nanocrystals” for crystalline particles with low concentrations of defects, while the more general term “nanoparticle” also includes particles containing gross internal grain boundaries, fractures, or internal disorder [227]. In the case of granular films composed of magnetic nanoparticles, the interparticle spacing strongly affects the magnetic and charge transport properties [228].

Since the different preparation methods lead to magnetic nanoparticles with differences in crystalline structure, surface chemistry, shape, etc., the fabrication technique has a great influence on the magnetic properties of the materials obtained [229], and, indeed, many examples are reported where differently prepared nanocrystalline materials with similar grain sizes exhibit very different magnetic properties [230]. Numerous physical and chemical methods have been employed to produce magnetic nanostructures. *Molecular beam epitaxy* [231], *chemical vapor deposition* [232], *normal incident pulsed laser deposition* [233, 234], *sputtering* [235], and *electrodeposition* [236, 237] are widely used for the preparation of thin magnetic films. Separated nanometer-sized nanoparticles of Fe, Co and Ni can be prepared by the *inert gas condensation* technique, where metal is evaporated at a very high temperature ( $\sim 1500^\circ\text{C}$ ) into a high purity gas (e.g., helium) [238, 239]. Upon collision with the inert gas, metal atoms lose their kinetic energy and condense on a cold finger in the form of an ultrafine powder. A modification of this method is based on the evaporation of metals by arc discharge into a circulating gas mixture of  $\text{H}_2$  and Ar and is used for the large-scale preparation of 20–30 nm particles of Fe, Ni and Fe–Ni alloys. Usually the nanoparticles synthesized by this approach are amorphous, and some amount of oxide is present at their surface [238, 239]. An *arc discharge* technique similar to that used in the fullerene synthesis was applied for the preparation of carbon-encapsulated Ni, Co or Fe nanoparticles. *Laser pyrolysis* is a technique based on heating, with a laser beam, an organometallic reactant vapor, e.g., a metal carbonyl mixed with an inert gas. Reactant vapors rapidly decompose to give the atoms, which form clusters upon collision with inert gas molecules [229]. Nanoparticles of iron and iron carbides have been prepared in this way. More detailed information about these methods can be found in [229].

Solution phase chemical syntheses are commonly used for preparation of colloids of magnetic metal nanoparticles. There are several general approaches used for controlling the size and shape of nanoparticles in solution phase synthesis. Thus, the water-in-oil microemulsion (*reverse micelles*) technique is based on using droplets of water sustained in an organic phase by a surfactant. A metal salt dissolved in the nanodroplets can be reduced, inside these nanometer-sized reactors, to metal nanoparticles. The amount of metal precursor available for the particle growth is limited by the volume of the micelle, which can be varied by tailoring the



water-to-surfactant ratio. This technique has been employed for the preparation of nanoparticles of magnetic metals [240, 241], metal alloys [242], core-shell structures [243], and oxides [244, 245]. Thus, Pileni et al. synthesized nanoparticles of Co, Fe or Fe–Cu alloy in water-in-isooctane microemulsion by the reduction of metal salts using hydrazine or sodium borohydride in the presence of sodium bis(2-ethylhexyl)sulfosuccinate, Na(AOT), as a surfactant [240]. The size of the metal nanoparticles increased with increasing water-to-surfactant ratio ( $[\text{H}_2\text{O}]/[\text{AOT}]$ ) [246]. Synthesis in the reverse micelles is a fairly simple method and does not require special costly equipment; however, several drawbacks of this approach should be mentioned. First, the size distribution of nanoparticles is usually rather broad ( $\sim 21\%$ ) [247]. This means that monodisperse colloids can be obtained only after costly post-preparative size-selective fractionation procedures [248]. Another important problem is that nanoparticles of the magnetic metals do not crystallize well at room temperature [249], and annealing at 200–300 °C is required in order to prepare nearly defect-free nanocrystals [250]. The reactions in the reverse micelles occur at relatively low temperatures (below 100 °C), and the resulting material is usually poorly crystalline [251].

*Sonochemical synthesis* is based on the decomposition of metal precursor (usually a metal carbonyl complexes) dissolved in a high-boiling solvent under irradiation with high intensity ultrasound. Ultrasonic treatment initiates acoustic cavitation, i.e. the formation, growth, and collapse of bubbles within a liquid. The collapse of these bubbles locally heats up the media to thousands of kelvin. Volatile organometallic compounds rapidly decompose inside the collapsing bubbles, yielding the individual metal atoms. In the presence of stabilizing agents these atoms agglomerate to nanosized particles [252]. This technique has been developed by Suslick et al. for the preparation of Ni [253], nanostructured silica-supported Fe and Fe–Co alloys [254], and Fe [252] nanoparticles. Sonochemical synthesis usually yields amorphous, rather polydisperse nanoparticles, and further high-temperature heating is required for their crystallization [252–254].

Among various solution phase approaches, the recently developed *colloidal organometallic syntheses* seem to be the most promising routes to the preparation of high-quality magnetic nanocrystals. These methods are based on the reduction of metal salts or the thermolysis of zero-valent organometallic precursors in the medium of a high-boiling solvent in the presence of special stabilizing agents which adsorb reversibly to the nanoparticle surface, mediating the growth rate. The proper choice of surfactants, precursors, and temperature regime allows the successful preparation of monodisperse colloids of highly crystalline magnetic nanoparticles, as described in the next Section.

### 3.2.2.2 Organometallic Synthesis of Magnetic Nanoparticles

Most of the high-quality colloidal magnetic nanoparticles were synthesized via the organometallic routes based on the thermolysis or reduction of organometallic precursors in the presence of ligand molecules, so-called stabilizing agents which bind to the nanoparticle surface, preventing its further growth and coagulation with other particles. The proper choice of the stabilizing agents is of great impor-

tance, as the attractive magnetic interactions between nanocrystals tend to decrease the overall stability of the magnetic colloids. A high reaction temperature (150–300 °C) allows the annealing of crystalline defects and, consequently, is important for the preparation of highly crystalline nanoparticles. In this Section we discuss the main peculiarities of the organometallic synthetic approach using Co and CoPt<sub>3</sub> nanocrystals as the examples. Cobalt nanocrystals are probably the most extensively studied nanocrystalline elemental magnetic materials, and CoPt<sub>3</sub> can be regarded as a model system for magnetic alloy nanocrystals.

### General Remarks on the Synthesis of Co and CoPt<sub>3</sub> Nanocrystals

The organometallic synthesis of magnetic metal nanocrystals usually requires a rigorously air-free atmosphere and is carried out under a dry inert gas using Schlenk line technique or a glovebox.

The size and size distribution of the nanoparticles are usually determined by the kinetics of the particle nucleation and growth [255]. A narrow particle size distribution can be obtained if a temporally discrete nucleation event is followed by controlled growth on the preformed nuclei [256]. Temporally discrete nucleation in the organometallic synthesis can be attained by the hot injection technique schematically shown in Figure 3-92. A solution of organometallic precursors or a reducing agent (solution A) is rapidly injected into a hot solution containing stabilizing agents (solution B), resulting in explosive nucleation, and this is followed by a temperature drop and slow growth of pre-formed nuclei. The optimized injection temperature, duration of heating and the proper choice of the precursors and stabilizing agents are the prerequisites for a successful synthesis of magnetic nanoparticles with controllable size and shape and narrow size distribution.

If the synthesis does not yield nanoparticles of the desired monodispersity, the size distribution of the as-prepared nanoparticles can be narrowed by a size-selective precipitation procedure which exploits the difference in the solubility of

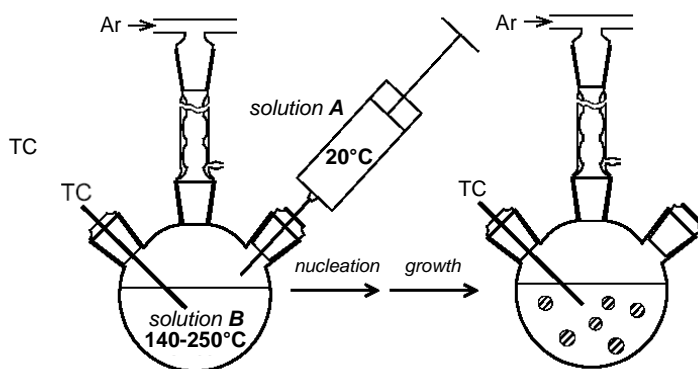


**Fig. 3-92** Schematic representation of the hot injection technique usually employed in the organometallic synthesis of magnetic nanocrystals. A thermocouple (TC) controls

the temperature in the reaction vessel. The compositions of solutions A and B are detailed in the text for each particular recipe.

smaller and larger particles [248, 257]. A typical example of a method of carrying out the size-selective precipitation of a nanoparticle colloid is as follows. A sample of as-prepared nanoparticles with a broad size distribution is dispersed in an appropriate solvent, and a non-solvent is added dropwise, gradually destabilizing the colloidal dispersion until the solution becomes slightly turbid. The largest nanoparticles in the sample exhibit the greatest attractive van der Waals and magnetic forces and tend to aggregate before the smaller particles. The aggregates consisting of the largest nanoparticles can be isolated by centrifugation or filtration and redissolved in any appropriate solvent. A further portion of the non-solvent is added to the supernatant to isolate the second size-selected fraction, and so on. For magnetic nanoparticles, the size-selective precipitation can also be performed by applying an external magnetic field, as the larger particles precipitate in the magnetic field before the smaller ones [227]. These procedures repeated several times allow a series of monodisperse fractions to be obtained with a near-Gaussian size distribution and a standard deviation below 5% ( $\pm 1$  atomic layer).

### Synthesis of Cobalt Nanoparticles with Different Crystalline Modifications

Cobalt nanoparticles can be synthesized in three different crystalline modifications: hexagonal close-packed (hcp), face-centered cubic (fcc) and epsilon ( $\epsilon$ ). The  $\epsilon$ -Co structure, which is not observed in the bulk, consists of a twenty-atom unit cell with cubic symmetry, similar to the structure of  $\beta$ -Mn [258]. The hcp structure is the most stable phase for bulk cobalt at room temperature. Despite this fact, experimental data repeatedly show that  $\epsilon$ -Co is the most often found crystalline structure in nanoparticles prepared by wet chemistry [259].

The  $\epsilon$ -Co nanoparticles can be synthesized via reduction of a cobalt salt by superhydride ( $\text{LiBEt}_3\text{H}$ ) in the presence of stabilizing agents [227]. Injection of the solution of superhydride in dioctylether (solution A) into the hot (200 °C) solution of  $\text{CoCl}_2$  in dioctylether also containing oleic acid and trioctylphosphine (TOP) as stabilizing agents (solution B) yields relatively monodisperse  $\epsilon$ -Co nanoparticles (Figure 3-93a) [210]. HRTEM measurements (Figure 3-94b) and simulations of X-ray powder data indicate that the  $\epsilon$ -Co nanoparticles are nearly perfect single crystals [260]. The width of the XRD reflexes decreases coarsely with increase of the nanoparticle size, as shown in Figure 3-93a for the (221), (310) and (311) reflexes. The average nanocrystal size can be tuned from  $\sim 2$  up to 6 nm by tailoring the concentration of stabilizers. Increasing the concentration of oleic acid and TOP yields a smaller mean particle size. In order to prepare  $\epsilon$ -Co nanocrystals larger than 6 nm, one has to use less bulky stabilizers which can effectively cap particles with lower surface curvature. Thus, substitution of tributylphosphine (TBP) for TOP results in the formation of larger, 7–11 nm  $\epsilon$ -Co nanocrystals [227, 261]. Fine tuning of the particle size can be performed by size fractionation of crude solutions, yielding a series of nearly monodisperse  $\epsilon$ -Co nanocrystals (Figure 3-94a).

Another method of preparation of cobalt nanoparticles is based on the thermal decomposition of  $\text{Co}_2(\text{CO})_8$  in the presence of surfactants [227]. A typical recipe involves the injection of a solution of  $\text{Co}_2(\text{CO})_8$  in diphenylether (solution A) into the hot (200 °C) mixture of oleic acid and TOP or TBP, also dissolved in diphenyl-

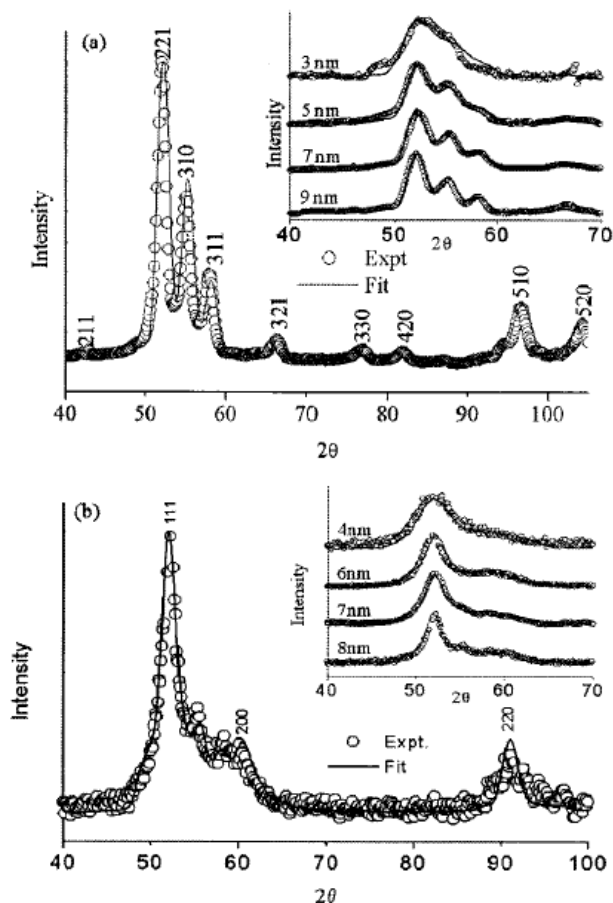


**Fig. 3-93** X-ray data (circles) for cobalt nanoparticles and their corresponding simulations (solid lines) using atomic-level models of the particles. **a** fcc-Co particles, **b** mt-fcc particles. The insets are X-ray data

and simulations for several particle sizes. Reproduced from [260], Copyright 2001, with permission from the American Chemical Society.

ether (solution B). The injection is followed by heating at 200 °C for 15–20 minutes. Decomposition of cobalt carbonyl under the conditions described above results in the formation of Co nanoparticles with a so-called multi-twinned face-centered cubic (mt-fcc) lattice (Figures 6b and 7d). The multi-twinned particles are composed of domains with a distorted fcc lattice. This structure is similar to that observed in multiply-twinned, icosahedral gold particles [227]. Post-preparative size selection procedures allow the isolation of fairly monodisperse fractions of mt-fcc Co nanocrystals (Figure 3-94c). Depending on the reaction medium and stabilizers, thermal decomposition of cobalt carbonyl can also yield nanoparticles of other crystalline phases [259, 262–264].

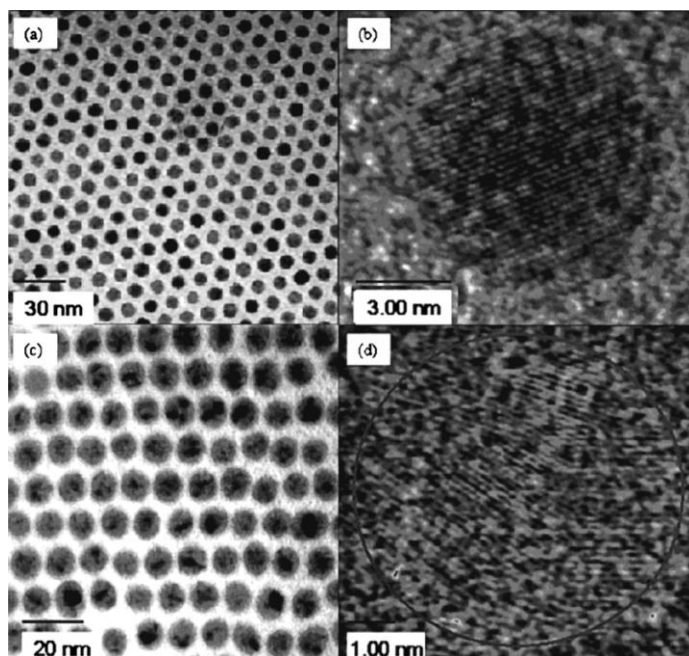


**Fig. 3-94** TEM images of cobalt nanoparticles. **a** Low magnification image of  $\epsilon$ -Co. The even contrast across the individual particles implies a uniform crystalline structure for this phase. **b** HRTEM image of  $\epsilon$ -Co showing perfect crystallographic coherence and discrete faceting. **c** Low-magnification image of the mt-fcc structure. Contrast changes within

particles indicate they are composed of crystal domains. **d** HRTEM image showing the domains within a single mt-fcc particle. These domains correspond to a multiply twinned structure. Reproduced from [260], Copyright 2001, with permission from the American Chemical Society.

Annealing of  $\epsilon$ -Co nanocrystals at 300 °C under vacuum converts them into the hcp-Co phase (Figure 3-95), which has higher magnetocrystalline anisotropy than that of  $\epsilon$ - and mt-fcc cobalt modifications [261]. Alternatively, the hcp-Co nanoparticles can be synthesized in solution by reduction of cobalt acetate by 1,2-dodecanediol at 250 °C in diphenylether medium in the presence of oleic acid and TOP as stabilizing agents [227, 261].

As shown above, an optimized combination of precursors ( $\text{CoCl}_2$ ,  $\text{Co}(\text{CH}_3\text{COO})_2$  or  $\text{Co}_2(\text{CO})_8$ ) with reducing agents (superhydride or polyalcohol) allows the selective preparation of monodisperse cobalt nanoparticles with a desired crystalline phase. Such behavior shows that solution-phase chemical synthesis of magnetic nanocrystals is not thermodynamically controlled and thus can enable the preparation of crystal phases which are metastable, like the  $\epsilon$ -Co structure [210]. The control of size and crystalline phase of nanoparticles is important, because these parameters strongly affect their magnetic properties, as discussed in Section 3.2.2.3 below.

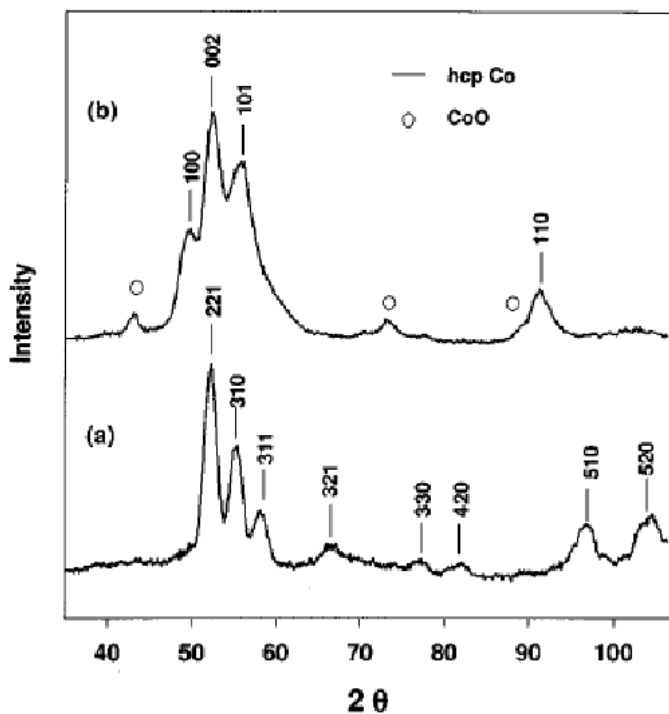


**Fig. 3-95** XRD patterns of  $\epsilon$ -Co particles before and after annealing: **a** 9 nm particles as synthesized and **b** after annealing at 300 °C under vacuum for 3 h. Reproduced from [210], Copyright 1999, with permission from the American Institute of Physics.

A serious drawback of cobalt and other elemental magnetic nanoparticles (Fe, Ni, etc.) is their relatively low stability toward oxidation under ambient conditions. Thus, the exposure of cobalt nanoparticles to air results in the formation of a shell of  $\sim 1$ – $2$  monolayers of cobalt oxide. This shell of anti-ferromagnetic cobalt oxide considerably disturbs the magnetic properties of the cobalt core. Additionally, the intrinsic coercivity of elemental cobalt is too low for Co nanoparticles to be considered as candidates for advanced magnetic recording media. Nanoparticles of more stable materials with higher coercivity are highly desirable. Intermetallic materials such as  $\text{Co}_x\text{Pt}_{1-x}$  and  $\text{Fe}_x\text{Pt}_{1-x}$  seem to satisfy both the requirements mentioned above. They are considerably more stable than elemental cobalt or iron and can have crystalline modifications with very high magnetocrystalline anisotropy (e.g.  $\text{L1}_0$ ).

#### The Synthesis of $\text{CoPt}_3$ Magnetic Alloy Nanocrystals

The synthetic approach developed for the preparation of elemental nanoparticles can be further extended to intermetallic compounds. Thus, high-quality  $\text{CoPt}_3$  nanocrystals can be synthesized via the simultaneous reduction of platinum acetylacetonate and thermal decomposition of cobalt carbonyl in the presence of 1-

adamantanecarboxylic acid (ACA) and hexadecylamine (HDA) as stabilizing agents [265].

In a typical preparation, the mixture of platinum acetylacetonate, 1,2-hexadecanediol, 1-adamantanecarboxylic acid, and hexadecylamine (solution B in Figure 3-92) was heated to a certain temperature in the range 140–220 °C, and solution A, prepared by dissolving cobalt carbonyl in 1,2-dichlorobenzene, was swiftly injected into solution B with vigorous stirring. The temperature of injection of the stock solution is henceforth referred to as the “reaction temperature”. After injection, the color changes from pale yellowish to black, indicating the formation of CoPt<sub>3</sub> nanocrystals. Further heating was usually continued for 1 h at the injection temperature and was followed by annealing at refluxing temperature (~275–285 °C) for 1 h. The annealing stage is necessary to improve the crystallinity of the as-formed CoPt<sub>3</sub> nanoparticles.

Information about nanoparticle crystallinity can be obtained by comparison of the average particle sizes estimated by powder XRD and TEM methods. The width of the XRD reflexes provides information about the X-ray coherence length, which is close to the average size of the single crystalline domain inside the nanocrystal, whereas TEM images show the total size of a nanoparticle. Nanocrystal sizes estimated by these methods are referred to as “XRD-size” and “TEM-size”, respectively. For CoPt<sub>3</sub> nanoparticles prepared at 140–200 °C, the XRD-size is considerably smaller than the TEM-size (Figure 3-96a), because of the internal structural defects (stacking faults, twinned planes, etc.) present within as-formed particles. Annealing of CoPt<sub>3</sub> nanoparticles at the boiling point of the crude solution (~275–285 °C) for ~30 min results in an increase in the XRD-size, whereas no significant change in the TEM-size is observed. The annealing process requires relatively high temperatures (200–300 °C) to trigger atom diffusion inside the nanocrystals. After annealing, the XRD-size becomes almost equal to the TEM-size (Figure 3-96b), in-

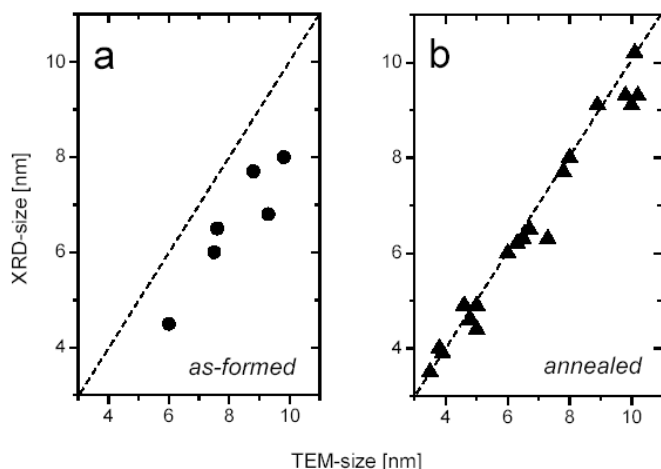


**Fig. 3-96** *In situ* annealing of CoPt<sub>3</sub> nanoparticles. Comparison of the XRD-size and TEM-size before and after annealing. Reproduced from [255], copyright 2003, with permission from the American Chemical Society.

dicating that most of nanocrystals are single crystallites with a nearly perfect lattice. High-resolution TEM (HRTEM) investigations additionally confirm the excellent crystallinity of annealed  $\text{CoPt}_3$  nanocrystals (Figure 3-97). Almost all particles possess lattice fringes without stacking faults or other defects. From a practical point of view, perfect crystallinity of magnetic nanoparticles is important, because the structural defects considerably reduce coercivity, the parameter determining the applicability of a material for magnetic recording and storage [210].

Tuning of the size of  $\text{CoPt}_3$  nanoparticles can be achieved by control over nucleation and growth rates, as illustrated in Scheme 3-17. Fast nucleation provides a

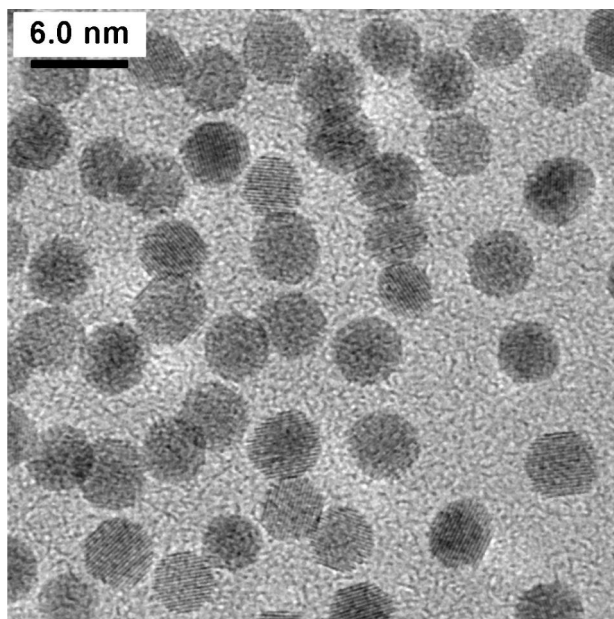
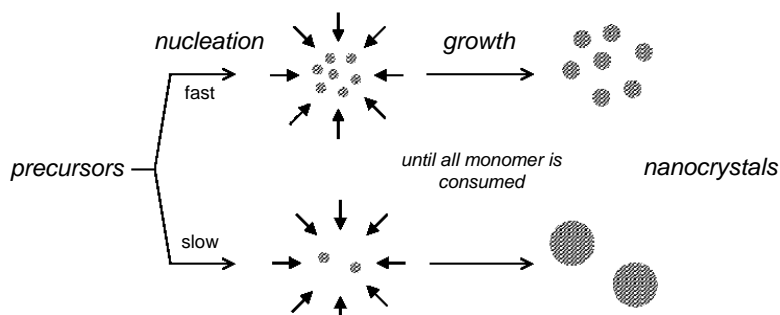


**Fig. 3-97** An HRTEM image of annealed  $\text{CoPt}_3$  nanocrystals. Note that almost all nanoparticles possess the lattice fringes without stacking faults or other defects.



**Scheme 3-17** Schematic representation of the synthesis of  $\text{CoPt}_3$  nanocrystals. Reproduced from [255], copyright 2003, with permission from the American Chemical Society.



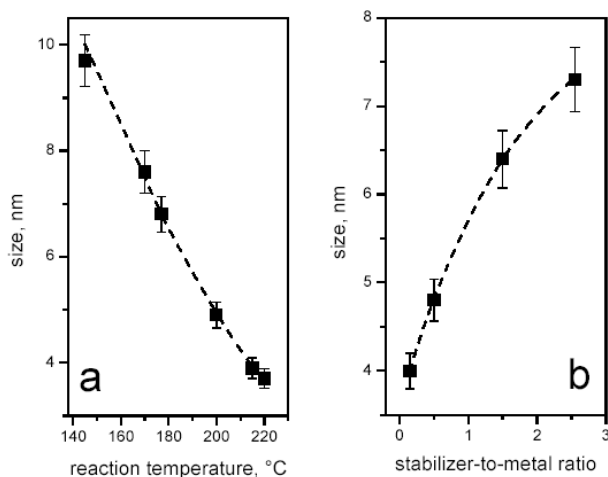


**Fig. 3-98** **a** Dependence of CoPt<sub>3</sub> nanocrystals size on the reaction temperature. **b** Influence of initial amount of stabilizing agent (1-adamantanecarboxylic acid) on the size of the nanocrystals. Reproduced from [255], copyright 2003, with permission from the American Chemical Society.

high concentration of nuclei, ultimately yielding smaller nanocrystals, whereas slow nucleation provides a low concentration of seeds consuming the same amount of precursors, thus resulting in larger particles [255].

The balance between nucleation and growth rates can be tuned by changing the reaction temperature, because the activation energy for homogeneous nucleation is usually much higher than that for particle growth [266]. This means that the nucleation rate is much more sensitive to changes in temperature than the growth rate. At higher reaction temperature, more nuclei are formed, and, according to the scheme in Figure 3-96, the final particle size is smaller. Indeed, an increase in temperature from 145 to 220 °C allows the average size of the CoPt<sub>3</sub> nanocrystal to be reduced from ~10 nm to 3 nm, i.e., it permits the preparation of nanocrystals in a wide range of sizes (Figure 3-98a). This concept of size tuning implies that Ostwald ripening, i.e. the growth of large particles with concomitant dissolution of small ones, is very slow. As reported in [249, 255], this is indeed the case in the most organometallic preparations of metal particles.

The nanoparticle size can also be tuned by tailoring the concentration of the stabilizing agents. The effect of varying the concentration of stabilizers on the size of the magnetic nanocrystals can be different for different systems. Thus, an increase in the concentration of the stabilizers resulted in smaller nanocrystals in the case of Co [227, 267] and Ni [227], whereas an opposite behavior was observed for iron [268] and CoPt<sub>3</sub> [255] nanocrystals (Figure 3-98b).

For the kinetically driven synthesis of nanoparticles, a decrease in the mean particle size with increasing stabilizer concentration can take place if strong passivation of the nanocrystal surface results in slowing the growth rate, whereas the nucleation rate remains less influenced (Scheme 3-17). An opposite situation can

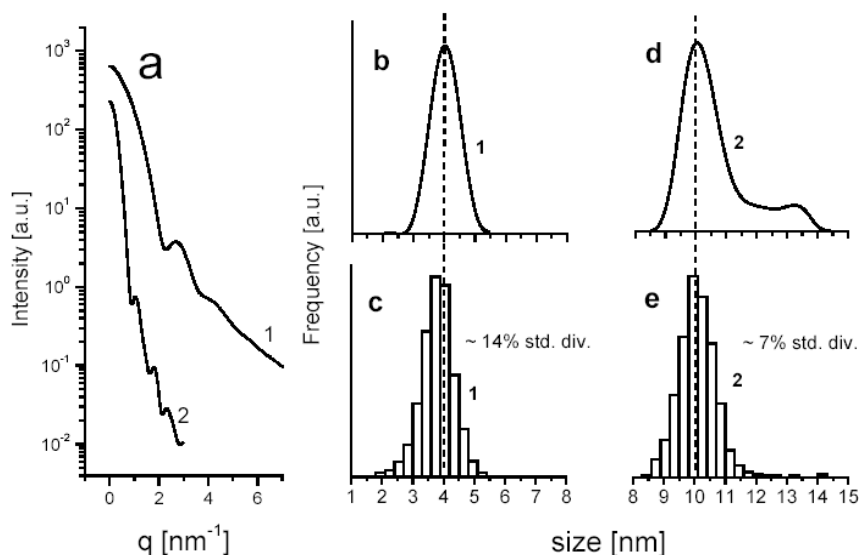


**Fig. 3-99** a Angular dependence of scattered X-ray intensity (SAXS) from two samples of as-prepared  $\text{CoPt}_3$  nanocrystals with mean size (1)  $\sim 4$  nm and (2)  $\sim 10$  nm. b and d: Particle volume fraction vs size curves calculated from the SAXS data shown in part a. c and e: Particle size distribution histograms estimated for the same samples from TEM images. Reproduced from [255], copyright 2003, with permission from the American Chemical Society.

also be realized, as was recently observed for  $\text{CoPt}_3$  [255] and Fe-oxide [268] nanocrystals. Stabilizing agents like 1-adamantanecarboxylic acid (ACA) and primary amines can also form stable complexes with individual metal atoms of a molecular precursor. Thus, the platinum precursor (platinum acetylacetonate) decomposed in the hexadecylamine (HDA)/diphenyl ether/1,2-hexadecandiol mixture at  $\sim 130^\circ\text{C}$ , whereas addition of ACA increased the decomposition temperature to  $\sim 220^\circ\text{C}$ . Similar behavior was observed for the cobalt precursor: addition of ACA drastically enhanced the stability of the cobalt carbonyl solution toward thermal decomposition. Formation of these complexes precedes the nucleation step [269] and decreases the monomer reactivity. Therefore, an increase in the amount of ligand would be expected to decrease nucleation rate. In accordance with Scheme 3-17, slowing the nucleation rate will result in a larger final size of the nanocrystals, and this was also observed experimentally (Figure 3-98).

Information about the *in situ* size distribution of  $\text{CoPt}_3$  nanoparticles can be obtained by statistical evaluation of all nanocrystals in a representative TEM micrograph, or from small-angle X-ray scattering (SAXS) data by the indirect Fourier transformation technique [270, 271]. The latter method provides the information averaged over a huge number of nanoparticles and, moreover, allows the *in situ* investigation of particle aggregation. Figure 3-99a shows the SAXS patterns for two samples of as-prepared  $\text{CoPt}_3$  nanocrystals with mean sizes of  $\sim 4$  and  $10$  nm. The nanocrystal size was tuned by varying the reaction temperature ( $215^\circ\text{C}$  and  $145^\circ\text{C}$ ). Figures 12b and c show the particle size distribution functions of as-prepared  $\sim 4$  nm  $\text{CoPt}_3$  nanocrystals as obtained from the SAXS and TEM data,

respectively. The SAXS data provide evidence that small  $\text{CoPt}_3$  nanocrystals form stable suspensions of isolated nanoparticles (single-particle population) [272, 273]. Both SAXS and TEM measurements confirm a relatively narrow and nearly symmetric particle size distribution for as-prepared  $\sim 4$  nm  $\text{CoPt}_3$  nanocrystals (Figures 12b and c), whereas a minor deviation between the mean sizes estimated by these methods was observed. HRTEM always provided lower estimates of particle size compared to SAXS, because the size distribution from SAXS is a volume (or mass) distribution, whereas that from microscopy is a number distribution. The difference between volume and number distribution is negligible when the distribution is narrow. However, in broad distributions or in the presence of a few aggregates, the larger particles count visibly more in volume distributions (SAXS) than in number distributions (TEM).

In the case of  $\sim 10$  nm  $\text{CoPt}_3$  nanocrystals, the SAXS size distribution curve is superimposed on a peak, corresponding to the single-particle population and a tail in the large size region (Figure 3-99d). The TEM investigations of the same sample revealed a symmetrical size distribution curve without any features around 12–13 nm (Figure 3-99e). This allows us to assume partial aggregation of  $\sim 10$  nm  $\text{CoPt}_3$  at room temperature [272]. The long-term stability of the colloidal solutions as well as the absence of agglomerates in the TEM images provides evidence that the aggregation is reversible.

The absolute width of the particle size distribution is nearly constant for both the  $\sim 4$  nm and the  $\sim 10$  nm samples (Figure 3-99). This means that the relative size distribution of as-prepared  $\sim 4$  nm  $\text{CoPt}_3$  nanocrystals is much broader than that of  $\sim 10$  nm nanocrystals ( $\sim 14\%$  and  $\sim 7\%$  of standard deviation, respectively). The general tendency is a narrowing of the size distribution with increase in particle size, as observed for all samples irrespective of the method of size control. Progressive narrowing of the particle size distribution with increasing mean size is due to the faster growth of the smaller particles compared with that of the larger ones [266]. This growth regime was recently observed for ensembles of CdSe nanocrystals and was called “focusing” of size distribution [274].

A combination of the methods of size control described above allows us to obtain a series of nearly monodisperse  $\text{CoPt}_3$  nanocrystals ranging from  $\sim 3$  to 17 nm. It was found that different experimental conditions (reaction temperature, ratio between the cobalt and platinum precursors, etc.) yielded nanocrystals of identical chemical composition. Figures 3-100 and 3-101 show the systematic evolution of XRD patterns and HRTEM images of  $\text{CoPt}_3$  nanocrystals with increase in their size.

$\text{CoPt}_3$  nanocrystals with sizes smaller than  $\sim 7$  nm are usually spherical (Figures 3-97 and 3-101). However, further increase in the nanocrystal size results in a rather abrupt transition from spherical to cubic, truncated cubic or, in some cases, plate-like shapes, as shown in Figure 3-100. Annealing at  $\sim 275$  °C results in smoothing of the edges of cubic nanocrystals formed at 145 °C (cf. Figures 3-101 and 3-102). Each side of the cubic crystal lattices corresponds to the [100] direction of the fcc nanocrystal lattice. Cubic particles can be formed if the growth rate in the [111] direction is higher than that in the [100] direction [275].

Generally, shape anisotropy of magnetic nanocrystals can result in advanced magnetic properties and is therefore of great practical interest [230]. The shape of a

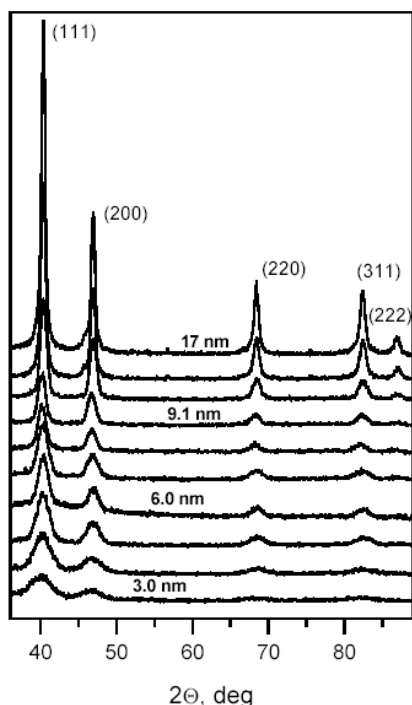


**Fig. 3-100** Size-dependent XRD patterns of  $\text{CoPt}_3$  nanocrystals. The average nanocrystal sizes were calculated using the Debye-Scherrer equation. Reproduced from [255], copyright 2003, with permission from the American Chemical Society.

colloidal nanoparticle can be controlled by selective adsorption of organic surfactants onto particular crystallographic facets in order to inhibit the particle growth in a particular crystallographic direction. This approach to shape control is based on the presence of chemically dissimilar lattice faces, e.g., the unique (001) face of an hcp lattice. Shape-controlled colloidal syntheses were recently developed for semiconductor ( $\text{CdSe}$  [276, 277],  $\text{PbS}$  [278],  $\text{ZnO}$  [279]) and noble metal ( $\text{Pt}$  [248],  $\text{Au}$  [249]) nanoparticles.

A possibility for achieving shape control was also reported for Co nanocrystals [259, 263, 264]. Thus, decomposition of cobalt carbonyl in the presence of primary amines (e.g., octadecylamine) together with TOPO or oleic acid yields nanodisks of hcp-cobalt (Figure 3-103) [264]. Alkylamines inhibit the growth of the unique (001) face of hcp-Co upon increase of the particle size in a kinetic regime. Both length and diameter of the nanodisks can be controlled by tailoring the reaction time as well as by variation of the precursor-to-surfactant ratios. The long-term heating of hcp-Co nanodisks (thermodynamic limit) results in the transformation of the thermodynamically stable spherical nanoparticles of the  $\epsilon$ -Co phase. The nanodisks are ferromagnetic and can spontaneously self-assemble into long ribbons formed from stacked nanodisks lying perpendicular to the substrate. Note that a side view of the nanodisks in transmission electron microscopy (TEM) images (Figure 3-103)

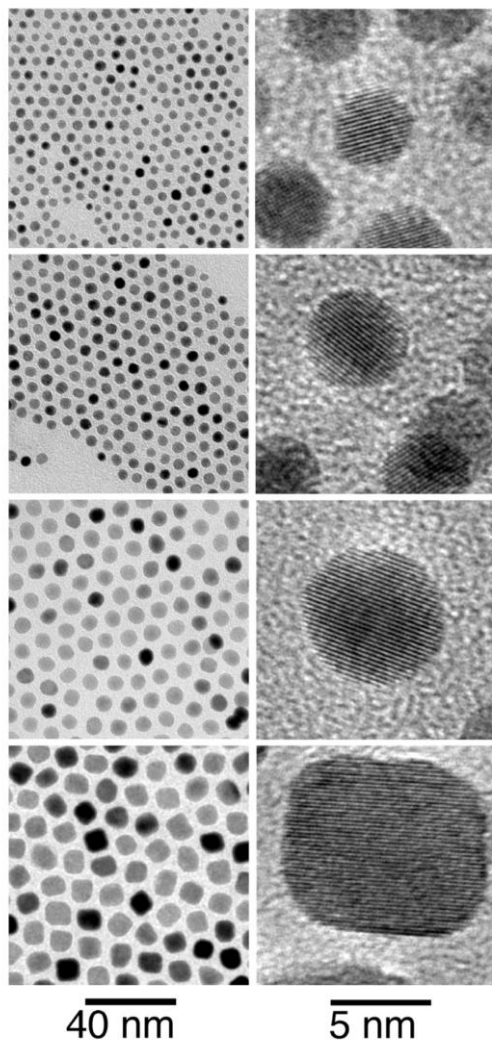


**Fig. 3-101** TEM and HRTEM images showing the effect of reaction temperature on the mean size and size distribution of 3.7 nm, 4.9 nm, 6.3 nm, and 9.3 nm CoPt<sub>3</sub> nanocrystals prepared at 220, 200, 170, and 145 °C. Molar

ratio of Pt:Co:ACA is 1:3:6 for all samples. Reproduced from [255], copyright 2003, with permission from the American Chemical Society.

strongly resembles nanorods, and TEM tilting experiments are necessary to verify the disk shape [264].

The synthesis of hcp-Co nanorods and nanowires was also reported [283]. Thermal decomposition of the organometallic cobalt precursor, [Co( $\eta^3$ -C<sub>8</sub>H<sub>13</sub>)( $\eta^4$ -C<sub>8</sub>H<sub>12</sub>)], in the presence of oleic acid and oleylamine under a pressure of 3 bar H<sub>2</sub> yielded ~3 nm spherical hcp-Co nanoparticles, which were further transformed into uniform nanorods (Figure 3-104) after heating for 48 h at 150 °C. Both lengths

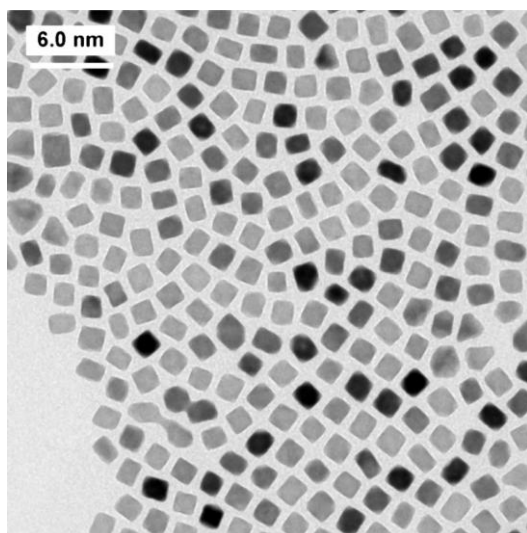


**Fig. 3-102** TEM overview image of faceted  $\text{CoPt}_3$  nanocrystals prepared at 145 °C. Shape-controlled synthesis of magnetic nanoparticles.

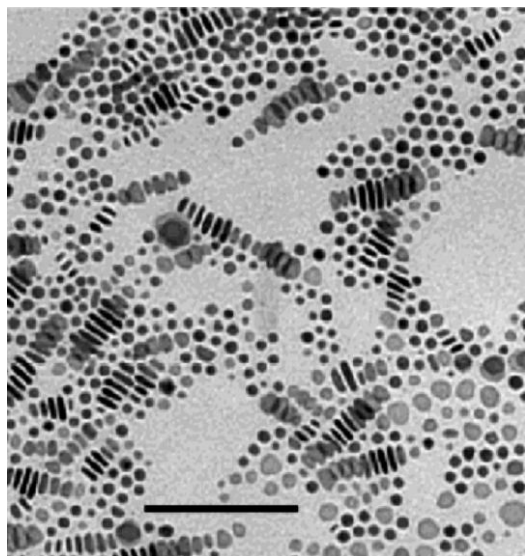


**Fig. 3-103** TEM image of partially self-assembled Co nanodisks. Bar is 100 nm. Reproduced from [264], Copyright 2002, with permission from the American Chemical Society.

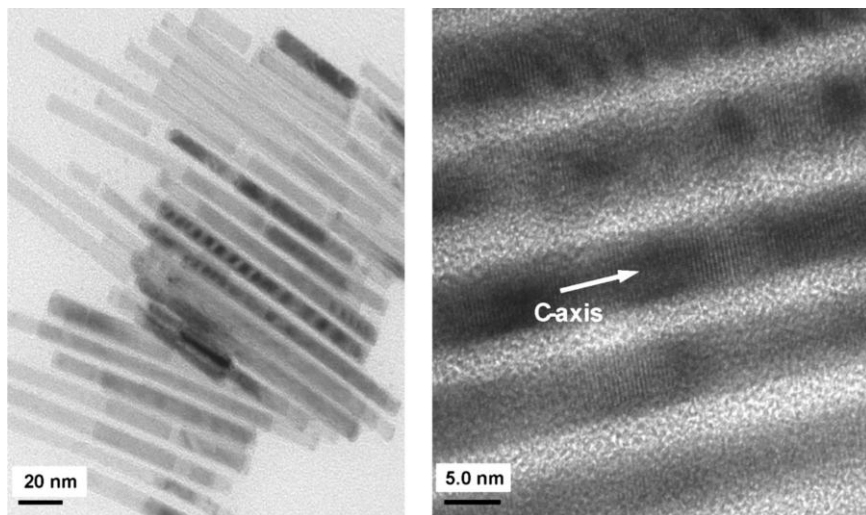


**Fig. 3-104** TEM and HRTEM micrographs of cobalt nanorods. Courtesy of Dr. B. Chaudret.

and diameters of the hcp-Co nanorods can be varied by tailoring the nature and concentration of the stabilizing agents. Thus, increasing the concentration of oleic acid allows the preparation of very long (micron range) nanowires of diameter 4 nm. Conversely, replacing oleylamine by octylamine results in smaller and wider Co nanoparticles (17 nm  $\times$  10 nm). The mechanism of transformation of the initially formed  $\sim 3$  nm spherical nanoparticles into rods and wires is still unclear. In principle, the nanorods could be obtained either through coalescence of spherical particles followed by fusion [279–284] or by using the initial particles as nuclei for an anisotropic growth process [285].

Colloidally synthesized  $\text{CoPt}_3$  nanocrystals possess chemically disordered face-centered cubic (fcc) structure which has no unique crystallographic direction. Despite this, the formation of  $\text{CoPt}_3$  nanowires took place if the reaction was performed at a relatively low temperature ( $\sim 100$ – $130$   $^{\circ}\text{C}$ ) in the presence of 1-adamantanecarboxylic acid and hexadecylamine as stabilizing agents [265]. The  $\text{CoPt}_3$  nanowire-rich fraction (Figure 3-105a) can be isolated from the crude solution by centrifugation. The wires typically comprised two “heads”, the ends of which were approximately the same size as the spherical particles present in the same sample, and a “body” with some bulges (Figure 3-105b). The concentration of wires and their length decreased drastically upon prolonged heating of the reaction mixture. After continuous heating at  $280$   $^{\circ}\text{C}$  the quantity of nanowires became negligible (Figure 3-105c).

#### **Other Metal Magnetic Nanoparticles Synthesized by the Methods of Colloid Chemistry**

In the previous Section we described the colloidal synthesis of Co and  $\text{CoPt}_3$  nanocrystals and showed the great potential of the organometallic approach to the preparation of high-quality magnetic nanoparticles. These synthetic schemes can

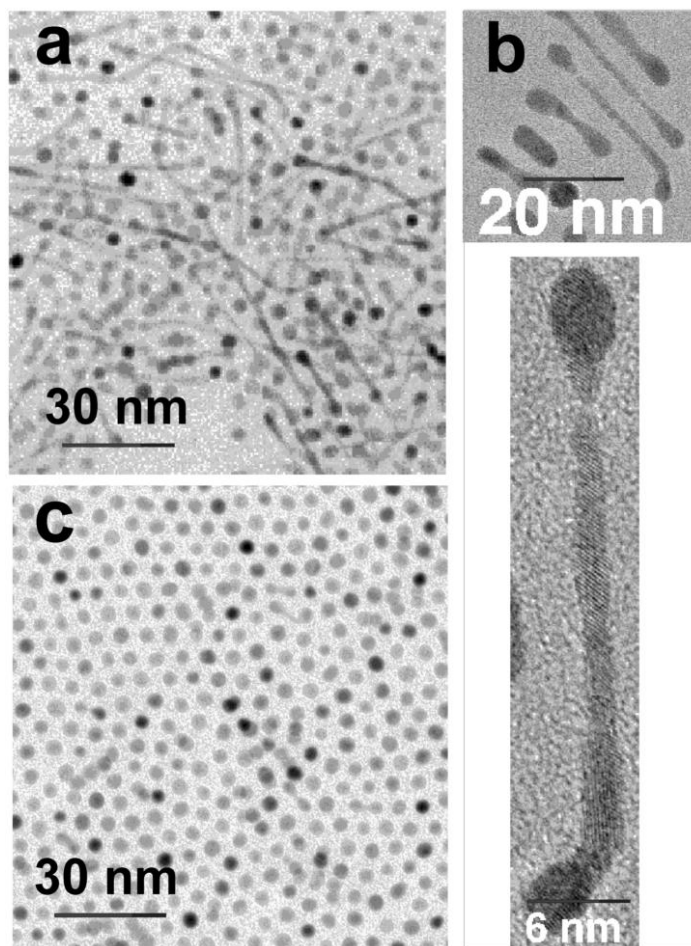


**Fig. 3-105** TEM images of  $\text{CoPt}_3$  nanocrystals grown in a 1-adamantanecarboxylic acid-hexadecylamine-diphenyl ether mixture: **a** nanowire-rich  $\text{CoPt}_3$  fraction; **b** enlarged views of nanowires; **c** spherical  $\text{CoPt}_3$  nanocrystals

formed from the nanowire-rich sample after refluxing for 3 h. Reproduced from [265], Copyright 2002, with permission from the American Chemical Society.

also be adopted for the preparation of nanoparticles of different magnetic materials. In this Section, we briefly describe the preparation of some other important magnetic nanoparticles.

Murray et al. reported the synthesis of monodisperse iron nanoparticles by the thermal decomposition of  $\text{Fe}(\text{CO})_5$  under an inert atmosphere in the presence of oleic acid/tri-butyl phosphines [227]. These  $\sim 6$  nm Fe nanoparticles have a structure resembling the bulk bcc lattice with some disorder and are very sensitive to oxidation. Even a short contact of a nanoparticle surface with air resulted in the formation of oxide with a thickness of  $\sim 2$  nm [227]. Thermal decomposition of



iron carbonyl in tri-*n*-octylphosphine oxide at 320–340 °C yielded ~2 nm iron nanoparticles [264]. Hyeon et al. used them as building blocks for the formation of iron nanorods [286]. Thus, refluxing the 2 nm nanoparticles in pyridine in the presence of didodecyldimethylammonium bromide (DDAB) resulted in the formation of uniform rod-shaped iron particles of diameter 2 nm and length varying from 11 to 27 nm, depending on the concentration of the DDAB in solution in pyridine. The electron diffraction pattern of the obtained nanorods exhibited a body-centered cubic (bcc) structure of  $\alpha$ -Fe. The transformation of nanospheres to nanorods was explained by the oriented attachment of several 2 nm spherical particles followed by their fusion. The shape-dependent magnetic properties of iron nanoparticles is discussed in the next Section. Practical applications of iron nanoparticles are impractical because of their chemical instability under ambient conditions. On the other hand, monodisperse iron particles can be gently oxidized by trimethylamine *N*-oxide to form stable monodisperse magnetic  $\gamma$ -Fe<sub>2</sub>O<sub>3</sub> nanocrystals [268].

Spherical nickel nanoparticles have been synthesized by the reduction of nickel salts by polyalcohols [227]. The mixture of oleic acid, tri-butylphosphine (TBP) and tri-butylamine (TBA) as stabilizing agents favors the formation of ~12–13 nm nanoparticles. Increasing the length of alkyl chains in the stabilizing agents results in a decrease in the nanoparticle size. Thus, replacing TBP and TBA with TOP and tri-octylamine (TOA) results in 8–10 nm Ni nanoparticles. Decomposition of Ni(cycloocta-1,5-diene)<sub>2</sub> in the presence of HDA as the stabilizing and shape-controlling agent yielded Ni nanorods [287]. Simultaneous reduction of nickel and cobalt salt was used to prepare cobalt-nickel alloy nanoparticles with the fcc structure [227]. Nickel is more readily incorporated into the growing nanoparticles, and so employing equal amounts of nickel and cobalt precursors leads to the formation of an Ni-rich alloy (~Ni<sub>60</sub>Co<sub>40</sub>).

Some of the most promising magnetic nanoparticle materials, which may give a boost to data storage technology, are the iron-platinum alloys [288]. The classical synthesis by Sun et al. is based on the simultaneous high-temperature reduction of platinum acetylacetonate and decomposition of iron pentacarbonyl in the presence of oleic acid and oleyl amine as stabilizing agents [289]. The size of the PtFe nanocrystals can be controlled by first growing ~2.5–3 nm monodisperse seed particles and then adding more reagents to enlarge the existing seeds until the desired size, ~10 nm, is reached [289]. The chemical composition of Fe<sub>*x*</sub>Pt<sub>1-*x*</sub> binary alloy nanocrystals can be tuned between *x* = 0.48 and *x* = 0.7 by controlling the molar ratio of iron carbonyl to platinum salt.

As-prepared FePt nanoparticles exhibit the chemically disordered fcc structure. fcc FePt nanoparticles are superparamagnetic at room temperature and can be handled in the form of a colloidal solution for casting films, making self-assembled arrays, etc. (Figure 3-106). Further, the FePt nanoparticles can be annealed at 550–600 °C under an inert atmosphere. This annealing induces the iron and platinum atoms to rearrange, converting the particles to the chemically ordered face-centred tetragonal (fct) phase (Figure 3-107). Room temperature coercivity of the arrays of fct FePt nanocrystals is high enough to use them in a data storage device [289].

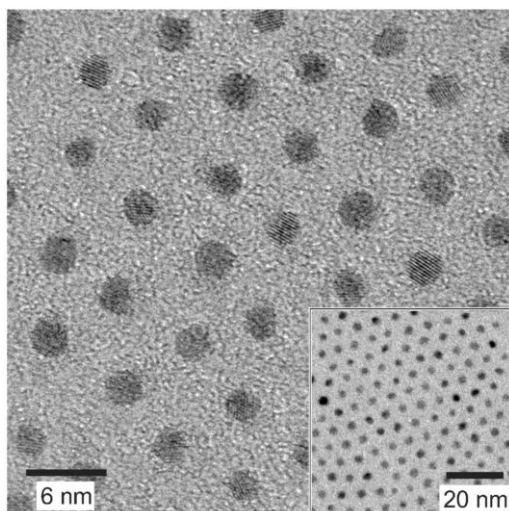


Fig. 3-106 Hexagonal close-packed 2D array of FePt nanocrystals on a TEM grid.

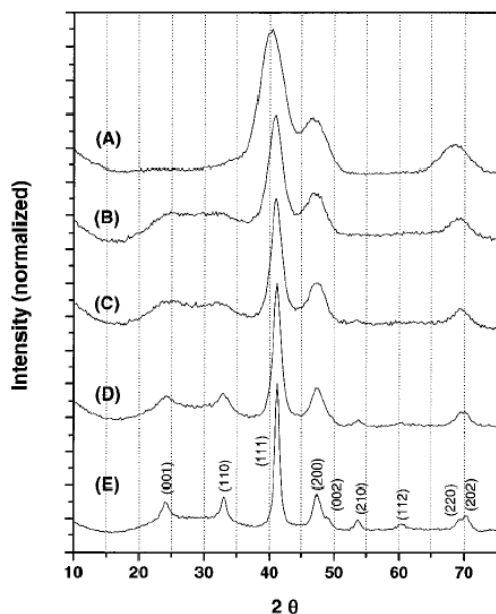


Fig. 3-107 XRD patterns (A) of as-synthesized 4-nm  $\text{Fe}_{52}\text{Pt}_{48}$  particle assemblies and a series of similar assemblies annealed under atmospheric  $\text{N}_2$  gas for 30 min at temperatures of (B) 450 °C, (C) 500 °C, (D) 550 °C, and (E) 600 °C. The indexing is based on tabulated fct FePt reflections (25). Reproduced from [289], Copyright 2000, with permission.

Depending on the  $\text{Fe}_x\text{Pt}_{1-x}$  stoichiometry and nanocrystal size, the transition temperature was in the range 500–700 °C [290], while for the bulk material the reported value was 1300 °C [291]. In order to further reduce the phase transition temperature, it was proposed to introduce silver atoms into the lattice of FePt nanocrystals during their synthesis [292]. Incorporation of Ag promotes the transition from fcc to the tetragonal phase, reducing the transition temperature by ~100–150 °C compared to the pure FePt nanocrystals. It was suggested that Ag atoms leave the FePt lattice at temperature of less than 400 °C, and that the vacancies formed increase the mobility of the Fe and Pt atoms, accelerating the phase transformation.

The synthetic approach developed for the synthesis of platinum-iron binary alloy nanoparticles was adopted for the preparation of several other binary alloy nanoparticles, such as FePd [293] or MnPt [294]. However, these alloys require further structural characterization as well as further development of the methods of control of particle size, shape and composition.

The possibility of preparing “core-shell”-type magnetic nanoparticles was reported [295, 296]. These core-shell nanoparticles can be prepared by a two-step synthesis in which nanoparticles of one metal serve as seeds for the growth of a shell from another metal. Thus, reduction of platinum salts in the presence of the Co nanoparticles enabled the preparation of air-stable Co-core/Pt-shell nanoparticles [295]. Thermal decomposition of cobalt carbonyl in the presence of silver salt led to the formation of  $\text{Ag}_{\text{core}}\text{Co}_{\text{shell}}$  nanoparticles [296].

Summarizing, a combination of organometallic and colloid chemistry gives a powerful method of preparation of monodisperse magnetic nanoparticles with controllable size, shape, composition, and crystalline modification. The present state of the art in the synthesis of magnetic nanoparticles allows us to provide a palette of high-quality materials for investigations of nanomagnetism as well as for various applications. In spite of the progress in the synthesis of magnetic nanocrystals, there is still a lack of theoretical understanding of the processes occurring during the growth of nanoparticles in colloidal solutions and of the problem of keeping the particle size distribution narrow. Further synthetic progress will definitely depend on our ability to understand and control the parameters governing the properties of colloiddally grown nanocrystals.

### 3.2.2.3 Size- and Shape-Dependent Magnetic Properties of Ferromagnetic Metal Nanoparticles

Magnetism is a result of moving charges. Additionally, elementary particles, e.g., electrons, have an intrinsic magnetic moment (spin), which determine their quantum state. The magnetic properties of materials arise mainly from the motion of electrons: the orbital motion and the spin motion. Other contributions such as that from nuclear magnetic effects are usually much smaller than that from the electron. The electronic structure of a nanometer-sized metal particle is strongly size dependent (see, e.g., Chapter 5.2), resulting in size-dependent magnetic behavior. Many physical phenomena (magnetic domain size, exchange coupling effects, etc.), which determine experimentally observable magnetic properties of ma-

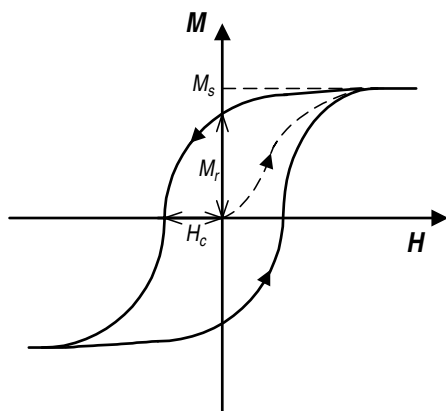


**Fig. 3-108** A typical hysteresis loop for a ferromagnetic material and the important magnetic parameters which can be obtained from the hysteresis loop. Dashed line shows the first scan.

materials, have natural length scales lying in the nano- and micrometer size range. What happens if the size of a ferromagnetic material is shrunk below 10 nm? In this Section we intend to show the effect of particle size, shape, and structure on magnetic properties of nanomaterials. The reader can find a more detailed description of the physical aspects of nanoscale magnetism in several excellent books [203, 229, 297] and journal reviews [227, 230].

First, we would like to very briefly introduce the reader to the commonly measured magnetic parameters. All materials interact with a magnetic field, and this interaction can be either attractive toward a magnetic pole (ferro- and paramagnetism) or repulsive (diamagnetism). The application of a magnetic field ( $H$ ) results in magnetization ( $M$ ) of a sample, which can be measured by, e.g., a superconductive quantum interference device (SQUID), one of the most popular and sensitive methods of investigating magnetic properties. When a ferromagnetic material is magnetized by an increasing applied field and then the field is decreased, the magnetization does not follow the initial magnetization curve obtained during the increase. This irreversibility is called hysteresis [203]. A typical hysteresis loop arises from measuring the magnetization of the material as a function of magnetic field applied in positive and negative directions, i.e., the response of the material follows two distinct paths on magnetization and demagnetization (Figure 3-108). At large fields, the magnetization approaches the maximum value, called the saturation magnetization ( $M_s$ ). Magnetic materials in a ferromagnetic state have a residual magnetization at zero external field, called the remanent magnetization ( $M_r$ ). Coercivity ( $H_c$ ) characterizes the reverse-field strength needed to reduce the magnetization to zero. Thus, hysteresis measurements allow us to obtain information about coercivity, remanent magnetization, and saturation magnetization of a given material (Figure 3-108).

Tab. 3-2 Magnetic units and unit conversions.

Magnetic units		cgs	SI	Conversion
Magnetic field strength	$H$	Oe (oersted)	A/m	$1 \text{ Oe} = 10^3/4\pi \text{ A/m}$
Magnetization	$M$	emu/cm <sup>3</sup>	A/m	$1 \text{ emu/cm}^3 = 10^3 \text{ A/m}$
Magnetic flux density (induction)	$B$	G (gauss) $B = H + 4\pi M$	T (tesla) $B = \mu_0(H + M)$	$1 \text{ T} = 10^4 \text{ G}$
Induction constant	$\mu_0$	G/Oe	T/(A/m)	$\mu_0 = 1 \text{ G/Oe}$ $4\pi \cdot 10^{-7} \text{ T/(A/m)}$

It is still common to use the old cgs (centimetre, gram, second) system for magnetic units in scientific and engineering literature. As a consequence, there are two widely used systems of units, the cgs and the SI system. Thus, the magnetic field strength  $H$  can be measured in Oe (cgs) or in A/m (SI). Moreover, the applied field can be multiplied by the induction constant  $\mu_0$  and given in units of Gauss (cgs) or Tesla (SI). The magnetization  $M$  is measured in emu/cm<sup>3</sup> (cgs) or A/m (SI) or, being multiplied by  $\mu_0$ , can also be given in Gauss or Tesla. Also note that in the cgs system the magnetization can also be written per gram of substance. Table 3-2 presents the magnetic units used in cgs and SI systems and some unit conversions.

To minimize their energy, macroscopic ferromagnetic materials are divided up into domains of parallel magnetic moments. Within a domain, the magnetic moments orient in one direction, while the alignment of spins in neighboring domains is usually antiparallel. The oppositely aligned magnetic domains are separated from each other by a domain wall (Bloch wall). As the particle size decreases below some critical value, the formation of domain walls become energetically unfavorable, and the ferromagnetic particle can support only a single domain. This critical size depends on the material and is usually on the order of tens of nanometers, varying from  $\sim 14 \text{ nm}$  for Fe up to  $\sim 170 \text{ nm}$  for  $\gamma\text{-Fe}_2\text{O}_3$ . One can see that magnetic particles of nanometer size are usually a single domain [227].

The dimensionless parameter – magnetic susceptibility ( $\chi$ ) defined as  $\chi = \partial M / \partial H$  is used to estimate the efficiency of the applied magnetic field for magnetizing a material. In many cases, the susceptibility of a material depends on the direction in which it is measured. Such a situation is called magnetic anisotropy. The physical origin of magnetic anisotropy can be, e.g., the symmetry of the crystalline lattice or the shape of a particular piece of magnetic material, as is considered below in more detail. Now we would only like to emphasize that the anisotropy is an extremely important parameter determining the behavior of a ferromagnetic material. When magnetic anisotropy exists, the total magnetization of a system will prefer to lie along a special direction, called the easy axis of magnetization. For a small single-domain particle, the energy associated with this alignment is called the anisotropy energy and can be written in the simplest uniaxial approximation as  $E_a = KV \sin^2 \theta$ , where  $K$  is the anisotropy constant,  $V$

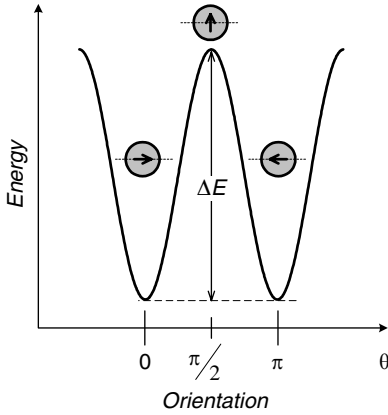


**Fig. 3-109** The energy associated with rotation of a magnetization direction for a uniaxial magnetic particle. The minima correspond to alignment of the magnetization along the easy axis (schematically shown by dotted lines).  $\Delta E$  represents the energy barrier to the rotation of magnetization.

the particle volume, and  $\theta$  the angle between the moment and the easy axis (Figure 3-109) [227].

When an external magnetic field interacts with the single-domain particle, an additional potential energy of  $E_f = -\vec{M}_s \cdot \vec{H}$  is supplied. Depending on the direction of the magnetic field with respect to the particle easy axis, the response of the particle moment to an applied field is different. Thus, if the field is applied perpendicular to the easy axis, the dependence of the particle potential energy on the direction of magnetization varies with the strength of applied field as shown in Figure 3-110a. The equilibrium direction of the magnetic moment, corresponding to the minimum of the total alignment energy  $E_{\text{tot}} = E_a + E_f$ , turns toward the field to the angle  $\theta = \arcsin(M_s H / (2KV))$ . At  $H = 2KV/M_s$  the moment aligns perpendicular to the easy axis (i.e. along the applied field) and magnetization approaches saturation. In the  $M$  vs.  $H$  scans, the magnetization component parallel to the applied field changes linearly from  $-M_s$  to  $+M_s$  as shown in Figure 3-110c. Note that no magnetization hysteresis is observed if the magnetic field is applied perpendicular to the easy axis of a uniaxial single-domain particle.

If a magnetic field is applied parallel to the easy axis, the particle moment can align either parallel or antiparallel to the field direction. The latter case is considered in Figure 3-110b. The alignment of the particle magnetization along the field is energetically favorable; however, in a relatively weak field the energy barrier blocks the magnetization reversal. The height of the barrier decreases with increasing field strength (Figure 3-110b). At  $H = 2KV/M_s$  the barrier vanishes and the particle magnetic moment jumps from antiparallel to parallel alignment. This behavior leads to a square hysteresis loop with coercivity  $H_c = 2KV/M_s$  as shown in Figure 3-110d. The effect of magnetic field applied at any other angle to the particle easy axis can be evaluated in a similar manner.

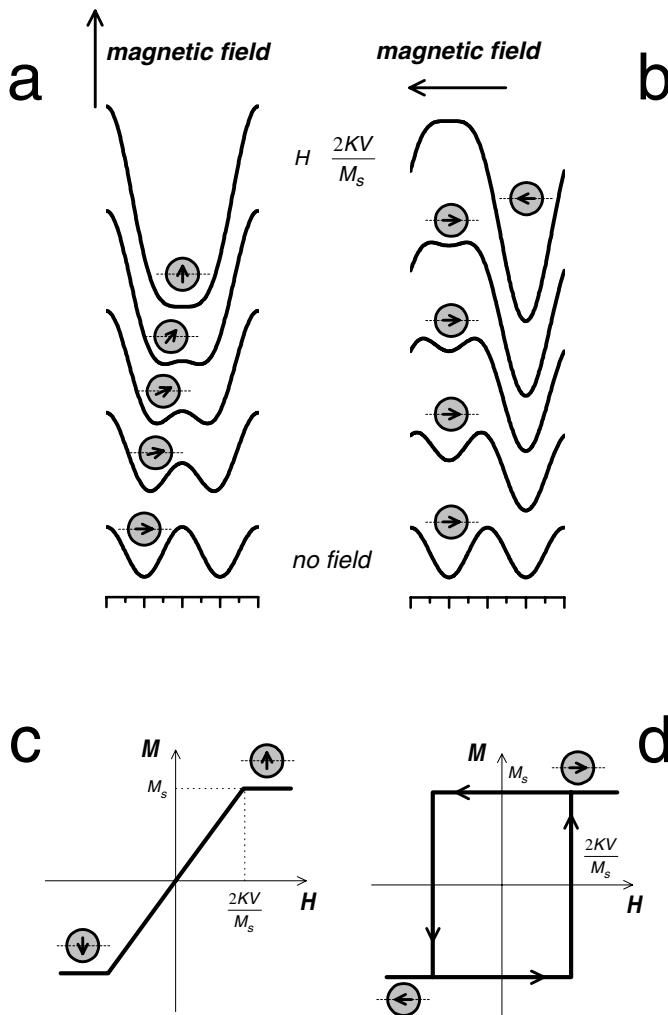


**Fig. 3-110** a,b Dependence of potential energy on the direction of a particle magnetic moment in the presence of external magnetic fields applied (a) perpendicular and (b) parallel to the easy magnetization axis. The lower curves correspond to zero magnetic field and the upper ones correspond to the saturation magnetization when the magnetic moments align along the field. c and d: Hysteresis loops for applied fields perpendicular (c) and parallel (d) to the easy axis of a uniaxial single-domain particle. The direction of the axis of easy magnetization is shown by dotted lines.

As one can see, the response of an individual single-domain particle crucially depends on the direction of the applied magnetic field. The two situations considered above represent the extreme cases of the possible hysteresis curves, totally closed (no hysteresis) and totally open (square). Other orientations yield hysteresis curves between these limits. In reality, an ensemble of many particles has ran-

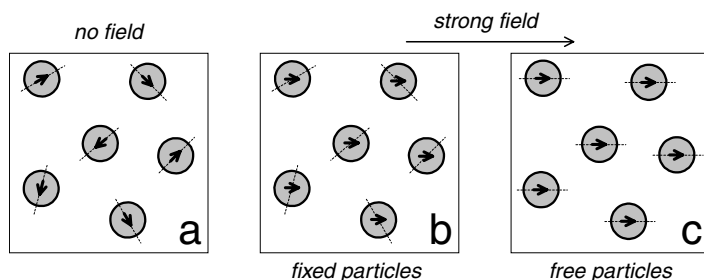


**Fig. 3-111** **a** An ensemble of magnetic particles with randomly distributed axes of easy magnetization. **b** Magnetization of a particle ensemble in a strong field via rotation of the particle magnetic moments. **c** Magnetic

particles dispersed in a liquid can align their easy axes along the applied field. Directions of particle easy magnetization axes are shown by dotted lines.

domly oriented easy axes (Figure 3-111a), and the measured hysteresis loop is the result of averaging over all possible orientations. In an extremely strong magnetic field all particles align their moments along the field, approaching the largest (saturation) magnetization. If the particles are fixed, e.g., dispersed in a solid non-magnetic matrix, the easy axes are randomly aligned and the magnetization occurs through rotation of the particle moments (Figure 3-111b). The time scale of this process is approx.  $10^{-9}$  s. However, the particles dispersed in a liquid can considerably decrease the potential energy aligning their easy axes along the external field (Figure 3-111c). This alignment occurs via the Brownian motion process in which the particles' collision rate with solvent molecules is much slower ( $\sim 10^{-7}$  s for solvents like hexane) than the rate of rotation of magnetic moment inside the particle.

Let us now consider the role of thermal fluctuations in the behavior of very small magnetic particles. In zero magnetic field, the energy barrier  $\Delta E$  has to be overcome in order to rotate the magnetization of a single-domain particle (Figure 3-109). The height of this barrier  $\Delta E = KV$  is proportional to the particle volume, and, as the particle size decreases,  $\Delta E$  may become comparable to the thermal energy ( $k_B T$ , where  $k_B$  is the Boltzmann's constant). In this case, the energy barrier can no longer pin the direction of magnetization to the time scale of observation, and rotation of the direction of magnetization occurs due to thermal fluctuations. Such a particle is said to be *superparamagnetic*. The coercivity of a superparamagnetic particle is zero ( $H_c = 0$ ), because thermal fluctuations prevent the existence of a stable magnetization. Cooling of a superparamagnetic particle reduces the energy of thermal fluctuations, and, at a certain temperature, the free movement of magnetization becomes blocked by anisotropy. The temperature of the transition from the superparamagnetic to the ferromagnetic state is called the blocking temperature ( $T_B$ ). The blocking temperature is related to the particle volume and the anisotropy constant. The latter can be calculated as  $K = 25k_B T_B / V$  [203].

The coercivity of a magnetic particle strongly depends on its size. Thus, if the particle is large enough to support a multidomain structure, magnetization rever-



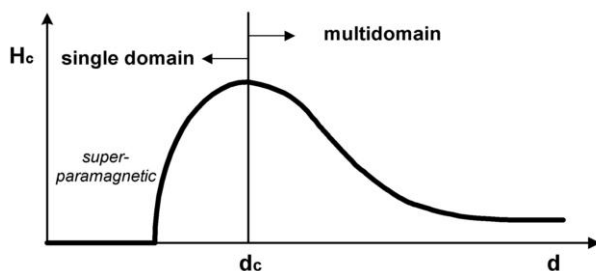


**Fig. 3-112** Particle coercivity vs size. The largest coercivity is observed at the particle size  $d_c$  corresponding to the transition from multidomain to single-domain structure.

sal occurs through a domain walls motion [230]. This is relatively easy, and hence the coercivity is low. On the other hand, in a single-domain particle the change of direction of magnetization can occur only by coherent rotation of spins, resulting in considerably higher coercivity of single-domain particles than that of multidomain particles (Figure 3-112) [203]. Upon further decrease of the particle size, the coercivity falls off because of the progressively increasing role of thermal fluctuations, leading to superparamagnetism, with  $H_c = 0$  (Figure 3-112).

In general, a magnetic nanoparticle is a single-domain magnet. To investigate the magnetic properties inherent in independent nanoparticles, the measurements have to be performed on an ensemble of uniform non-interacting nanoparticles. All sources of sample inhomogeneity (particle size and shape distribution, presence of particles with different crystalline modifications, etc.) must be minimized. Interparticle interactions can be reduced by dissolving the particles in an appropriate solvent at a low concentration [227]. If a distribution of particle sizes is present, the initial susceptibility is more sensitive to the larger particles present, whereas the approach to saturation is sensitive to the smallest particles of the sample [230]. In addition to hysteresis measurements, which allow the coercivity and specific magnetization of a sample to be estimated, zero-field-cooled (ZFC) and field-cooled (FC) measurements provide information about the blocking temperature ( $T_B$ ). In ZFC scans, a sample is cooled under zero applied magnetic field to a temperature well below the suspected  $T_B$ . The system is then warmed up, and the magnetization is measured as a function of temperature by applying a relatively low external magnetic field. As the thermal energy increases, the nanoparticles align with the applied field and the magnetization increases. At the blocking temperature the magnetization is maximal. Further increase in temperature above  $T_B$  results in decrease in the magnetization because the thermal energy causes fluctuation of magnetic moments of nanoparticles. In the field-cooled (FC) scans, a sample is cooled in a small magnetic field, freezing-in a net alignment of the nanoparticle moments. The field is then removed, and the magnetization is measured as the sample is slowly warmed up. Thermal energy unpins and randomizes the nanoparticle moments, lowering the sample's net magnetization. Be-

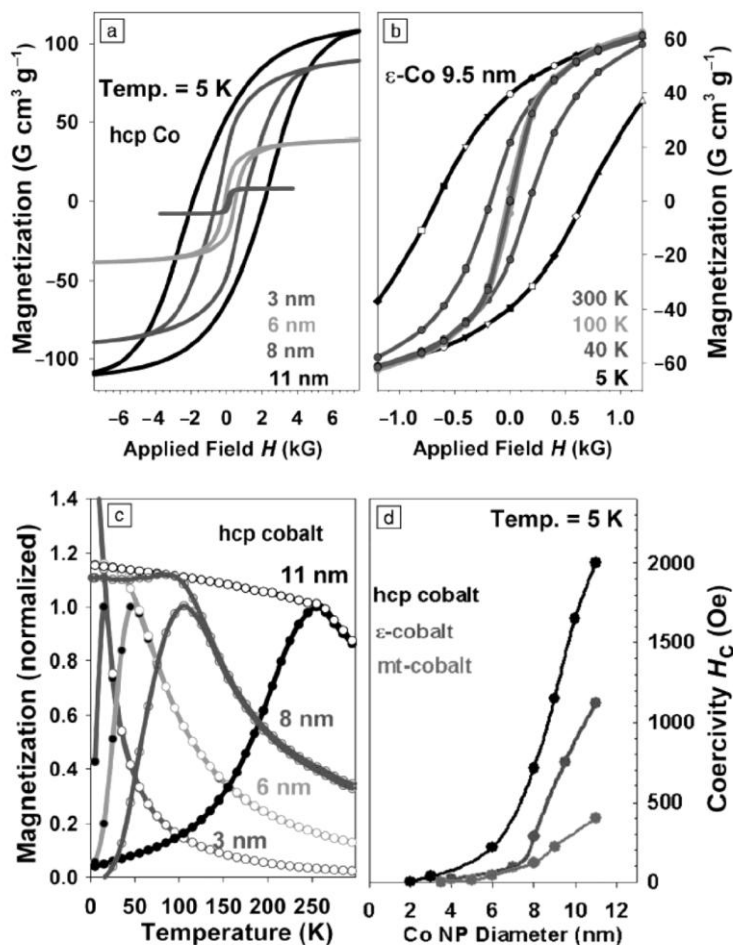
low  $T_B$  the free movement of magnetic moments is “blocked” by the anisotropy, so that the particles are in a ferromagnetic state, whereas above  $T_B$  the particles are characterized by superparamagnetic behavior [247]. At the blocking temperature the ZFC and FC curves converge [227]. The blocking temperature in a superparamagnetic system decreases with increasing applied measuring fields, and is proportional to  $H^{2/3}$  at large magnetic fields and to  $H^2$  at lower fields [230].

Figure 3-112 shows a set of measurements performed for the characterization of magnetic properties of cobalt nanoparticles [227]. As was discussed in Section 3.2.2.2, size series of monodisperse cobalt nanoparticles can be synthesized with three different intrinsic crystal structures: hexagonal (hcp),  $\epsilon$ , and multi-twinned face-centred cubic (mt-fcc). All investigated sizes are far below the critical single domain size which is, e.g., 70 nm for the hcp cobalt phase, and the particles are small enough to be superparamagnetic at room temperature. The hysteresis measurements performed at 5 K on hcp-Co nanoparticles of different sizes revealed a strong decrease in coercivity with decreasing particle size (Figures 26a and 26d). As already discussed, the number of spins coupled by exchange interaction decreases with the size of the single-domain particle, leading to an easier spontaneous reorientation of magnetization at a given temperature and thus to a decrease in coercivity [227].

Reducing the size of a single-domain particle decreases the number of spins exchange-coupled to resist spontaneous reorientation of its magnetization at a given temperature [227]. The drop in saturation magnetization with decreasing nanoparticle size (Figure 3-113a) was attributed to increase in nanoparticle surface-to-volume ratio [227]. The measurements of the hysteresis loop at different temperatures show the transition from ferromagnetic to superparamagnetic behavior in 9.5 nm  $\epsilon$ -Co nanocrystals (Figure 3-113b). Increasing thermal energy results in fluctuations of direction of magnetization of the nanoparticles, reducing coercivity and leading to superparamagnetic behavior at temperatures above 125 K. More precise information about the blocking temperature can be obtained from ZCF and FC scans, shown in Figure 3-110c for a size series of hcp-Co nanocrystals. The blocking temperature estimated from the peak magnetization on the ZCF scans increases with the particle size from 20 K for 3 nm up to 240 K for 11 nm hcp-Co nanoparticles. The increase in blocking temperature, magnetization, and coercivity with increase in nanoparticle size was observed for all crystalline modifications. Similar behavior was also observed for CoPt<sub>3</sub> nanocrystals [255].

The magnetic anisotropy of nanocrystalline materials originates from the influence of crystal symmetry, shape, and surface (or grain boundaries) effects. The most common anisotropies in the case of magnetic nanoparticles are *magnetocrystalline* and *shape* anisotropies.

*Magnetocrystalline anisotropy* arises from the coupling of the electron spins to the electronic orbit, which, in turn, is coupled to the crystal lattice. The magnetization is energetically favorable to alignment along a specific crystallographic direction called the easy axis of the material. In the case of hexagonal cobalt, the easy axis of magnetization is the  $c$  axis. Magnetocrystalline anisotropy is intrinsic to a given material and independent of particle shape [230] but dependent on temperature.



**Fig. 3-113** **a** Magnetization versus applied-field hysteresis loops at 5 K for 3, 6, 8, and 11 nm hcp cobalt nanocrystals. **b** Comparison of the hysteresis loops for 9.5 nm  $\epsilon$ -Co nanocrystals measured at 5, 40, 100, and 300 K. **c** A series of zero-field-cooled (ZFC) and field-cooled (FC) magnetization scans for hcp-Co nanocrystals of different sizes (3, 6, 8, and 11 nm). **d** Dependence of coercivity on nanoparticle size for a collection of hcp-Co,  $\epsilon$ -Co, and mt-fcc Co samples. Reproduced from [227], Copyright 2001, with permission.

In a cubic lattice, symmetry creates multiple easy axes. At room temperature, the easy magnetization axes of cubic Ni and Fe are  $\langle 111 \rangle$  and  $\langle 100 \rangle$  axes, respectively [298].

The highest magnetization and coercivity were achieved in the case of hcp cobalt nanoparticles (Figure 3-113d), because this structure has greater magnetocrystalline anisotropy than that of the mt-fcc and  $\epsilon$ -Co phases [227]. For each system, coercivity is lower than that predicted for idealized nanocrystals, as internal structural defects (stacking faults, twinned planes) reduce  $H_c$  [210]. Future ultrahigh-density

recording media will require uniform particles (size distribution less than 10%) with an average diameter of  $<6$  nm and a room temperature  $H_c$  of 3000–5000 Oe [227]. The coercivity is proportional to the anisotropy constant, so monodisperse nanoparticles of materials with high intrinsic magnetocrystalline anisotropy (e.g., platinum-iron and cobalt-platinum binary alloys) are essential [230].

Cobalt nanoparticles have a strong tendency to become oxidized in air, and their surface is usually covered with a layer of anti-ferromagnetic cobalt oxide, which influences the magnetic properties [230]. The influence of this oxide layer is especially noticeable in the case of the small nanoparticles with an extremely high surface-to-volume ratio. Thus, the coercivity of the smallest nanoparticles in the size series shown in Figure 3-110d is dominated by coupling to the surface CoO layer [227, 230]. The phenomenon is called *exchange anisotropy* [299] and occurs when a ferromagnet is in close proximity to an antiferromagnet or ferrimagnet [230]. Exchange anisotropy arises as a consequence of the interfacial, exchange coupling. This effect was discovered in oxide-coated cobalt particles (with sizes in the range 10–100 nm), and since then it has been observed in a variety of other systems.

Some molecular species adsorbed on the surface of nanoparticles can also significantly influence the magnetic behavior through the quenching of the surface atom contribution. Complete quenching of the magnetic moment of the surface nickel atoms was reported for small nickel particles and  $\text{Ni}_{38}\text{Pt}_6$  clusters coated with carbonyl ligands [217].

Non-spherical nanoparticles can also possess *shape anisotropy*. Shape anisotropy accounts for preferential orientation of the magnetization along the long axis of an elongated particle. The demagnetization field is less in the long direction, because the induced poles at the surface are further apart [203]. Shape anisotropy is comparable to magnetocrystalline anisotropy and can produce large coercive forces. Thus, the blocking temperature of Fe nanorods (2 nm  $\times$  11 nm) is nearly one order of magnitude higher than that of 2 nm spherical nanoparticles (Figure 3-114) [286]. The advanced magnetic properties of non-spherical nanoparticles has led to great attention being paid to shape-controlled colloidal synthesis. The syntheses of Co nanodisks [264], Co nanorods [283], Fe nanorods,  $\text{CoPt}_3$  nanocubes [255], and  $\text{CoPt}_3$  nanowires [265] have been recently reported. Progress in the synthesis of monodisperse non-spherical magnetic particles is the most important prerequisite for the investigation of shape-dependent magnetic properties.

If the concentration of nanoparticles in a sample is high, magnetic moments of individual nanoparticles can interact, and these dipolar interactions strongly affect the magnetic behavior of the sample [300]. Interparticle interactions in 2D and 3D assemblies of magnetic nanoparticles result in the shift of blocking temperature to higher values. Thus, a 5 K increase in the  $T_b$  was observed for 5.8 nm cobalt particles when they were arranged in a 2D network instead of being isolated non-interacting particles [247]. Also, an increase in the blocking temperature and broadening of the ZFC/FC scans was found in close-packed assemblies of monodisperse nickel [227] and  $\text{CoPt}_3$  nanoparticles. Dilution of a close-packed film of 9 nm cobalt particles ( $T_b = 165$  K) with 1-octadecylamine reduced the magnetostatic

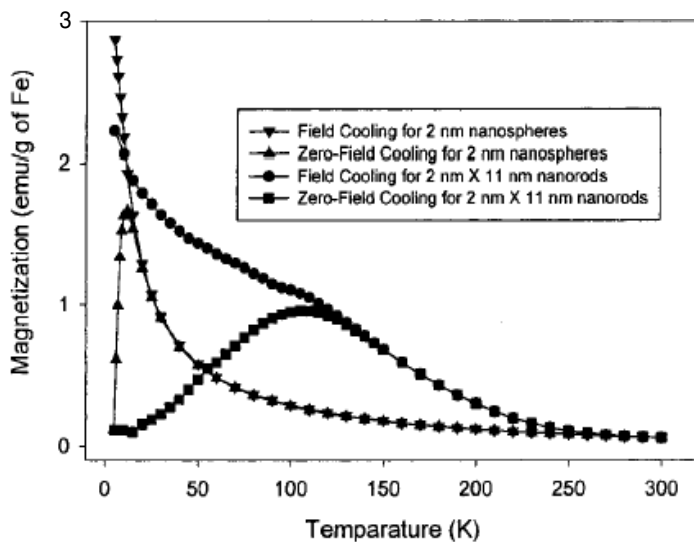


**Fig. 3-114** Zero-field-cooled (ZFC) and field-cooled (FC) magnetization scans for 2 nm spherical iron nanoparticles and 2 nm  $\times$  11 nm iron nanorods at an applied magnetic field of 100 Oe. Reproduced from [286], Copyright 2000, with permission from the American Chemical Society.

coupling of the particles and resulted in a sharper transition from the superparamagnetic to the ferromagnetic state at 105 K [210].

## References

- 1 J. S. BRADLEY, in *Clusters and Colloids*, G. SCHMID (ed.) VCH, Weinheim, 1993, p. 459.
- 2 M. FARADAY, *Phil. Trans. Roy. Soc.* **1857**, 147, 145.
- 3 J. M. THOMAS, *Pure Appl. Chem.* **1988**, 60, 1517.
- 4 R. ZSIGMONDY, *Colloids and the Ultra-microscope (English Edition)*; Wiley, New York, 1909.
- 5 J. TURKEVITCH, P. C. STEVENSON, J. HILLIER, *Disc. Faraday Soc.* **1951**, 11, 55.
- 6 J. TURKEVITCH, *Gold Bulletin* **1985**, 18, 86.
- 7 M. L. STEIGERWALD, L. E. BRUS, *Annu. Rev. Mater. Sci.* **1989**, 19, 471.
- 8 A. HENGLEIN, *Top. Curr. Chem.* **1988**, 143, 113.
- 9 C. B. MURRAY, D. J. NORRIS, M. G. BAWENDI, *J. Am. Chem. Soc.* **1993**, 115, 8706.
- 10 D. J. NORRIS, A. SACRA, C. B. MURRAY, M. G. BAWENDI, *Phys. Rev. Lett.* **1994**, 72, 2612.
- 11 J. T. G. OVERBEEK, in *Colloidal Dispersions*, J. W. GOODWIN (ed.), Royal Society of Chemistry, London, 1981, p. 1.
- 12 C. G. BLATCHFORD, J. R. CAMPBELL, J. A. CREIGHTON, *Surface Science* **1982**, 120, 435.
- 13 M. E. LABIB, *Colloids and Surfaces* **1988**, 29, 293.

- 14 M. E. LABIB, R. WILLIAMS, *J. Colloid Interface Sci.* **1984**, 97, 356.
- 15 A. DUTEIL, R. QUÉAU, B. M. CHAUDRET, C. ROUCAU, J. S. BRADLEY, *Chem. Mater.* **1993**, 5, 341.
- 16 M. KOMIYAMA, H. HIRAI, *Bull. Chem. Soc. Jpn.* **1983**, 56, 2833.
- 17 V. H. THIELE, J. KOWALLIK, *J. Colloid Sci.* **1965**, 20, 679.
- 18 P. H. HESS, P. H. PARKER, *J. Appl. Polymer. Sci.* **1966**, 10, 1915.
- 19 H. HIRAI, Y. NAKAO, N. TOSHIMA, *J. Macromol. Sci. Chem.* **1979**, 13, 727.
- 20 H. HIRAI, *Macromol. Chem. Suppl.* **1985**, 14, 55.
- 21 K. MEGURO, Y. NAKAMURA, Y. HAYASHI, M. TORIZUKA, K. ESUMI, *Bull. Chem. Soc. Jpn.* **1988**, 61, 347.
- 22 G. SCHMID, A. LEHNERT, *Angew. Chem.* **1989**, 101, 773; *Angew. Chem. Int. Ed. Engl.* **1989**, 28, 780.
- 23 M. GIERSIG, P. MULVANEY, *Langmuir* **1993**, 9, 3408.
- 24 N. TOSHIMA, T. YONEZAWA, *New. J. Chem.* **1998**, 1179.
- 25 H. HIRAI, Y. NAKAO, N. TOSHIMA, K. ADACHI, *Chem. Lett.* **1976**, 905.
- 26 H. HIRAI, Y. NAKAO, N. TOSHIMA, *Chem. Lett.* **1978**, 545.
- 27 H. HIRAI, Y. NAKAO, N. TOSHIMA, *J. Macromol. Sci. Chem.* **1978**, A 112, 1117.
- 28 H. HIRAI, Y. NAKAO, N. TOSHIMA, *J. Macromol. Sci. Chem.* **1979**, A 13, 727.
- 29 N. TOSHIMA, K. HIRAKAWA, *Polymer J.* **1999**, 31, 1127.
- 30 P. LU, T. TERAMISHI, K. ASAKURA, M. MIYAKE, N. TOSHIMA, *J. Phys. Chem. B.* **1999**, 103, 9673.
- 31 H. BÖNNEMANN, R. M. RICHARDS, *Eur. J. Inorg. Chem.* **2001**, 2455.
- 32 F. PORTA, F. RAGAINI, S. CENINI, G. SCARI, *Gazz. Chim. Ital.* **1992**, 122, 361.
- 33 J. S. BRADLEY, J. M. MILLAR, E. W. HILL, *J. Am. Chem. Soc.* **1991**, 113, 4016.
- 34 J. S. BRADLEY, E. W. HILL, S. BEHAL, C. KLEIN, B. CHAUDRET, A. DUTEIL, *Chem. Mater.* **1992**, 4, 1234.
- 35 D. MANDLER, I. WILLNER, *J. Phys. Chem.* **1987**, 91, 3600.
- 36 K. ESUMI, T. ITAKURA, K. TORIGOE, *Colloids Surfaces A* **1994**, 82, 111.
- 37 P. R. VAN RHEENEN, M. J. MCKELVEY, W. S. GLAUNSINGER, *J. Solid State Chem.* **1987**, 67, 151.
- 38 H. ISHIZUKA, T. TANO, K. TORIGOE, K. ESUMI, K. MEGURO, *Colloids Surf.* **1992**, 63, 337.
- 39 A. C. CURTIS, D. G. DUFF, P. P. EDWARDS, D. A. JEFFERSON, B. F. G. JOHNSON, A. I. KIRKLAND, A. S. WALLACE, *J. Phys. Chem.* **1988**, 92, 2270.
- 40 R. TOROUDE, P. GIRARD, G. MAIRE, M. KIZLING, M. BOUTONNET-KIZLING, P. STENIUS, *Colloids Surf.* **1992**, 67, 19.
- 41 D. N. FURLONG, A. LAUNIKONIS, W. H. F. SASSE, J. V. SAUNDERS, *J. Chem. Soc., Faraday Trans.* **1984**, 80, 571.
- 42 A. HARRIMAN, G. R. MILLWARD, P. NETA, M. C. RICHOUX, J. M. THOMAS, *J. Phys. Chem.* **1988**, 92, 1286.
- 43 J. TURKEVICH, R. S. J. MINER, I. OKURA, S. NAMBA, *Proc. Swed. Symp. Catal.* **1981**, 111.
- 44 J. TURKEVITCH, G. KIM, *Science* **1970**, 169, 873.
- 45 M. BRUST, A. WALKER, D. BETHELL, D. J. SCHIFFRIN, R. WHYMAN, *Chem. Commun.* **1994**, 801.
- 46 M. J. HOSTETTLER, J. E. WINGATE, C. J. ZHONG, J. E. HARRIS, R. W. VACHET, M. R. CLARK, J. D. LONDONO, S. J. GREEN, J. J. STOKES, G. D. WIGNALE, G. L. GLISH, M. D. PORTER, N. D. EVANS, R. W. MUARRY, *Langmuir* **1998**, 14, 17.
- 47 N. R. JANA, L. GEARHEART, C. J. MURPHY, *Langmuir*, **2001**, 17, 6782.
- 48 S. CHEN, K. KIMURA, *Langmuir* **1999**, 15, 1075.
- 49 D. G. DUFF, A. BAIKER, P. P. EDWARDS, *Chem. Commun.* **1993**, 96.
- 50 D. G. DUFF, A. BAIKER, P. P. EDWARDS, *Langmuir* **1993**, 9, 2301.
- 51 D. G. DUFF, A. BAIKER, P. P. EDWARDS, *Langmuir* **1993**, 9, 2310.
- 52 L. D. RAMPINO, F. F. NORD, *J. Am. Chem. Soc.* **1941**, 63, 2745.
- 53 L. D. RAMPINO, F. F. NORD, *J. Am. Chem. Soc.* **1941**, 63, 3268.
- 54 K. E. KAVANAGH, F. F. NORD, *J. Am. Chem. Soc.* **1943**, 65, 2121.
- 55 L. HERNANDEZ, F. F. NORD, *J. Colloid Sci.* **1948**, 3, 363.

- 56 W. P. DUNSWORTH, F. F. NORD, *J. Am. Chem. Soc.* **1950**, 72, 4197.
- 57 M. N. VARGAFTIK, V. P. ZARGORODNIKOV, I. P. STOLAROV, I. I. MOISEEV, V. A. LIKHOLOBOV, D. I. KOCHUBEY, A. L. CHUVILIN, V. I. ZAIKOVSKY, K. I. ZAMARAEV, G. I. TIMOFEEVA, *Chem. Commun.* **1985**, 937.
- 58 M. N. VARGAFTIK, V. P. ZARGORODNIKOV, I. P. STOLAROV, I. I. MOISEEV, D. I. KOCHUBEY, V. A. LIKHOLOBOV, A. L. CHUVILIN, K. I. ZARNARAEV, *J. Mol. Catal.* **1989**, 53, 315.
- 59 V. V. VOLKOV, G. VAN TENDELOO, G. A. TSIRKOV, N. V. CHERKASHAIN, M. N. VARGAFTIK, I. I. MOISEEV, V. M. NOVOTORTSEV, A. V. KRIT, A. L. CHUVILIN, *J. Cryst. Growth*, **1996**, 163, 377.
- 60 I. I. MOISEEV, M. N. VARGAFTIK, V. V. VOLKOV, G. A. TSIRKOV, N. V. CHERKASHINA, V. M. NOVOTORTSEV, O. G. ELLETT, I. A. PETRUNENKA, A. L. CHUVILIN, A. V. KRIT, *Mendeleev Commun.* **1995**, 87.
- 61 V. OLESHKO, V. VOLKOV, W. JACOB, M. VARGAFTIK, I. I. MOISEEV, G. VAN TENDELOO, *Z. Phys. D*, **1995**, 34, 283.
- 62 I. I. MOISEEV, M. N. VARGAFTIK, T. V. CHERNYSHEVA, T. A. STROMNOVA, A. E. GEKHAM, G. A. TSIRKOV, A. M. MAKHLINA, *J. Mol. Catal. A: Chem.* **1996**, 108, 77.
- 63 G. SCHMID, B. MORUN, J.-O. MALM, *Angew. Chem.* **1989**, 101, 772; *Angew. Chem. Int. Ed. Engl.* **1989**, 28, 778.
- 64 G. SCHMID, *Mater. Chem. Phys.* **1991**, 29, 133.
- 65 G. SCHMID, M. HARMS, J.-O. MALM, J.-O. BOVIN, J. VAN RUITENBECK, H. W. ZANDBERGEN, W. T. FU, *J. Am. Chem. Soc.* **1993**, 115, 2046.
- 66 C. E. BRIANT, B. R. C. THEOBALD, J. W. WHITE, C. K. BELL, D. M. P. MINGOS, *Chem. Commun.* **1981**, 201.
- 67 J. W. A. VAN DER VELDEN, F. A. VOLLENBROEK, J. J. BOUR, P. I. BEURSKENS, J. M. M. SMITS, W. P. BOSMAN, *Rec. J. R. Neth. Chem. Soc.* **1981**, 100, 148.
- 68 G. SCHMID, R. BOESE, R. PFEIL, F. BANDERMANN, S. MEYER, G. H. M. CALIS, J. W. A. VAN DER VELDEN, *Chem. Ber.* **1981**, 114, 3634.
- 69 G. SCHMID, *Inorg. Synth.* **1990**, 7, 214.
- 70 G. SCHMID, "The Way to Large Clusters", *Structure and Bonding* **1985**, 62, 51.
- 71 M. P. J. VAN STAVEREN, H. B. BROM, L. J. DE JONGH, G. SCHMID, *Solid State Commun.* **1986**, 60, 319.
- 72 A. H. A. SMIT, R. C. THIEL, L. J. DE JONGH, G. SCHMID, N. KLEIN, *Solid State Commun.* **1988**, 65, 915.
- 73 G. SCHMID, N. KLEIN, L. KORSTE, U. KREIBIG, D. SCHÖNAUER, *Polyhedron* **1988**, 7, 605.
- 74 G. SCHMID, *Polyhedron* **1988**, 7, 2321.
- 75 R. E. BENFIELD, J. A. CREIGHTON, D. G. EADON, G. SCHMID, *Z. Phys. D* **1989**, 12, 533.
- 76 M. C. FAIRBANKS, R. E. BENFIELD, R. J. NEWPORT, G. SCHMID, *Solid State Commun.* **1990**, 73, 431.
- 77 H. FELD, A. LEUTE, D. RADING, A. BENNINGHOVEN, G. SCHMID, *Z. Phys. D* **1990**, 17, 73.
- 78 G. SCHMID, *Endeavour* **1990**, 14, 172.
- 79 H. FELD, A. LEUTE, D. RADING, A. BENNINGHOVEN, G. SCHMID, *J. Am. Chem. Soc.* **1990**, 112, 8166.
- 80 C. BECKER, Th. FRIES, K. WANDELT, U. KREIBIG, G. SCHMID, *J. Vac. Sci. Technol.* **1991**, B9, 810.
- 81 U. KREIBIG, K. FAUTH, C.-G. GRANQVIST, G. SCHMID, *Z. Phys. Chem. Neue Folge*, **1990**, 169, 11.
- 82 K. FAUTH, U. KREIBIG, G. SCHMID, *Z. Phys. D* **1991**, 20, 297.
- 83 M. QUINTEN, I. SANDER, P. STEINER, U. KREIBIG, K. FAUTH, G. SCHMID, *Z. Phys. D* **1991**, 20, 377.
- 84 L. E. C. VAN DE LEEMPUT, J. W. GERRITSEN, P. H. H. RONGEN, R. T. M. SMOKERS, H. A. WIERINGA, H. VAN KEMPEN, G. SCHMID, *J. Vac. Sci. Technol.* **1991**, B9, 814.
- 85 B. DUSEMUND, A. HOFFMANN, T. SALZMANN, U. KREIBIG, G. SCHMID, *Z. Phys. D* **1991**, 20, 305.
- 86 G. SCHMID, *Chem. Rev.* **1992**, 92, 1709.
- 87 G. SCHMID, in *Physics and Chemistry of Metal Cluster Compounds*. J. DE JONGH (ed.), Kluwer, **1994**, 107.
- 88 U. SIMON, G. SCHMID, G. SCHÖN, *Angew. Chem.* **1993**, 105, 264; *Angew. Chem. Int. Ed. Engl.* **1993**, 32, 250.

- 89 F. M. MULDER, E. A. v. d. ZEEUW, R. C. THIEL, G. SCHMID, *Solid State Commun.* **1993**, 85, 93.
- 90 M. HERRMANN, U. KREIBIG, G. SCHMID, *Z. Phys. D*, **1993**, 26, 1.
- 91 J. BAAK, H. B. BROM, L. J. DE JONGH, G. SCHMID, *Z. Phys. D*, **1993**, 26, 30.
- 92 H. B. BROM, J. BAAK, L. J. DE JONGH, F. M. MULDER, R. C. THIEL, G. SCHMID, *Z. Phys. D*, **1993**, 26, 27.
- 93 P. D. CLUSKEY, R. J. NEWPORT, R. E. BENFIELD, ST. J. GURMANN, G. SCHMID, *Z. Phys. D* **1993**, 26, 8.
- 94 R. HOUBERTZ, T. FEIGENSPAN, F. MIELKE, U. MEMMERT, U. HARTMANN, U. SIMON, G. SCHÖN, G. SCHMID, *Europhys. Lett.* **1994**, 28, 641.
- 95 B. A. SMITH, J. Z. ZHANG, U. GIEBEL, G. SCHMID, *Chem. Phys. Lett.* **1997**, 270, 139.
- 96 T. TOMINAGA, Sh. TENMA, H. WATANABE, U. GIEBEL, G. SCHMID, *Chem. Lett.* **1996**, 1033.
- 97 V. RUFFIEUX, G. SCHMID, P. BRAUNSTEIN, J. ROSÉ, *Chem. Eur. J.* **1997**, 6, 3, 900.
- 98 A. BEZRYADIN, C. DEKKER, G. SCHMID, *Appl. Phys. Lett.* **1997**, 71, 1273.
- 99 L. F. CHI, M. HARTIG, T. DRECHSLER, Th. SCHWAACK, C. SEIDEL, H. FUCHS, G. SCHMID, *Appl. Phys. A* **1998**, 66, 187.
- 100 G. SCHMID, L. F. CHI, *Adv. Mater.* **1998**, 10, 515.
- 101 G. SCHMID, *J. Chem. Soc., Dalton Trans.* **1998**, 1077.
- 102 G. SCHMID, R. PUGIN, J.-O. MALM, J.-O. BOVIN, *Eur. J. Inorg. Chem.* **1998**, 813.
- 103 G. SCHMID, R. PUGIN, W. MEYER-ZAIKA, U. SIMON, *Eur. J. Inorg. Chem.* **1999**, 2051.
- 104 G. SCHMID, R. PUGIN, T. SAWITOWSKI, U. SIMON, B. MARLER, *Chem. Commun.* **1999**, 303.
- 105 G. SCHMID, W. MEYER-ZAIKA, R. PUGIN, T. SAWITOWSKI, J.-P. MAJORAL, A.-M. CAMINADE, C.-O. TURRIN, *Chem. Eur. J.* **2000**, 6, 1693.
- 106 M. HERRMANN, R. KOLTUN, U. KREIBIG, G. SCHMID, G. GÜNTHERODT, *Adv. Funct. Mater.* **2001**, 11, 202.
- 107 V. TORMA, G. SCHMID, U. SIMON, *Chem. Phys. Chem.* **2001**, 5, 321.
- 108 V. TORMA, T. REUTER, O. VIDONI, M. SCHUMANN, C. RADEHAUS, G. SCHMID, *Chem. Phys. Chem.* **2001**, 8/9, 546.
- 109 Y. LIU, M. SCHUMANN, T. RASCHKE, C. RADEHAUS, G. SCHMID, *Nano Lett.* **2001**, 8, 405.
- 110 T. SAWITOWSKI, Y. MIQUEL, A. HEILMANN, G. SCHMID, *Adv. Funct. Mater.* **2001**, 11, 435.
- 111 H.-G. BOYEN, G. KÄSTLE, F. WEIGL, P. ZIEMANN, G. SCHMID, M. G. GARNIER, P. OELHAFEN, *Phys. Rev. Lett.* **2001**, 87, 276401.
- 112 H.-G. BOYEN, G. KÄSTLE, F. WEIGL, B. KOSLOWSKI, C. DIETRICH, P. ZIEMANN, J. P. SPATZ, S. RIETHMÜLLER, C. HARTMANN, M. MÖLLER, G. SCHMID, M. G. GARNIER, P. OELHAFEN, *Science* **2002**, 297, 1533.
- 113 V. TORMA, O. VIDONI, U. SIMON, G. SCHMID, *Eur. J. Inorg. Chem.* **2003**, 1121.
- 114 H. ZHANG, G. SCHMID, U. HARTMANN, *Nano Lett.* **2003**, 3, 305.
- 115 G. SCHÖN, U. SIMON, *Colloid Polymer Sci.* **1995**, 273, 101.
- 116 G. SCHÖN, U. SIMON, *Colloid Polymer Sci.* **1995**, 273, 202.
- 117 U. SIMON, *Adv. Mater.* **1998**, 10, 1487.
- 118 L. O. BROWN, J. E. HUTCHISON, *J. Am. Chem. Soc.* **1997**, 119, 12384.
- 119 G. SCHMID, B. MORUN, J.-O. MALM, *Angew. Chem.* **1989**, 101, 772; *Angew. Chem. Int. Ed. Engl.* **1989**, 28, 778.
- 120 G. SCHMID, in *Clusters and Colloids – From Theory to Applications*, G. SCHMID (ed.), VCH, Weinheim, **1994**.
- 121 Y. LIU, R. G. FINKE, *J. Am. Chem. Soc.* **1994**, 116, 8335.
- 122 M. A. WATZKY, R. G. FINKE, *J. Am. Chem. Soc.* **1997**, 119, 10382.
- 123 J. D. AIKEN III, R. G. FINKE, *J. Mol. Catal. A*, **1999**, 145, 1.
- 124 M. R. MUCALO, R. P. COONEY, *Chem. Commun.* **1989**, 94.
- 125 H. BÖNNEMANN, W. BRIJOUX, R. BRINKMANN, R. FRETZEN, T. JOUSSEN, R. KÖPPLER, P. NEITELER, J. RICHTER, *J. Mol. Catal.* **1994**, 86, 129.
- 126 H. BÖNNEMANN, G. BRAUN, W. BRIJOUX, R. BRINKMANN, A. SCHULZE



- TILLING, K. SEEVOGEL, K. SIEPEN, *J. Organometal. Chem.* **1996**, 520, 143.
- 127 H. BÖNNMANN, W. BRIJOUX, in *Active Metals*, A. FÜRSTER (ed.), VCH, Weinheim, **1996**, p. 339.
  - 128 H. BÖNNEMANN, W. BRIJOUX, R. BRINKMANN, E. DINJUS, T. JOUSSEN, B. KORALL, *Angew. Chem.* **1991**, 103, 1344; *Angew. Chem. Int. Ed. Engl.* **1991**, 30, 1312.
  - 129 H. BÖNNEMANN, W. BRIJOUX, R. BRINKMANN, U. ENDRUSCHAT, W. HOFSTADT, K. ANGERMUND, *Rev. Roum. Chim.* **1999**, 44, 1003.
  - 130 J. SINZIG, L. J. DE JONGH, H. BÖNNEMANN, W. BRIJOUX, R. KÖPPLER, *Appl. Organomet. Chem.* **1998**, 12, 387.
  - 131 L. N. LEWIS, N. LEWIS, *Chem. Mater.* **1989**, 1, 106.
  - 132 L. N. LEWIS, *J. Am. Chem. Soc.* **1990**, 112, 5998.
  - 133 L. N. LEWIS, N. LEWIS, *J. Am. Chem. Soc.* **1986**, 108, 7228.
  - 134 L. FOWLEY, D. MICHOS, X. LIANG, R. H. CRABTREE, *Tetrahedron Lett.* **1993**, 34, 3075.
  - 135 C. LARPENT, H. PATIN, *J. Mol. Catal.* **1988**, 44, 191.
  - 136 C. LARPENT, F. BRISSÉ-LEMENN, H. PATIN, *New J. Chem.* **1991**, 15, 361.
  - 137 C. LARPENT, F. BRISSÉ-LEMENN, H. PATIN, *J. Mol. Catal.* **1991**, 65, 35.
  - 138 D. G. DUFF, A. C. CURTIS, P. P. EDWARDS, D. A. JEFFERSON, B. F. G. JOHNSON, D. E. LOGAN, *Chem. Commun.* **1987**, 1264.
  - 139 J. L. DYE, K. L. TSAI, *Faraday Discuss. Chem. Soc.* **1991**, 92, 45.
  - 140 K. L. TSAI, J. L. DYE, *Chem. Mater.* **1993**, 5, 540.
  - 141 M. T. REETZ, W. HELBIG, *J. Amer. Chem. Soc.* **1994**, 116, 7401.
  - 142 M. T. REETZ, W. HELBIG, S. A. QUAISER, in A. FÜRSTNER (ed.), *Active Metals*, VCH, Weinheim, **1996**, p. 279.
  - 143 J. A. BECKER, R. SCHÄFER, W. FESTAG, W. RULAND, J. H. WENDORF, J. PEBLER, S. A. QUAISER, W. HELBIG, M. T. REETZ, *J. Chem. Phys.* **1995**, 103, 2520.
  - 144 M. T. REETZ, S. A. QUAISER, C. MERK, *Chem. Ber.* **1996**, 129, 741.
  - 145 M. T. REETZ, W. HELBIG, S. A. QUAISER, *Chem. Mater.* **1995**, 7, 2227.
  - 146 M. T. REETZ, S. A. QUAISER, *Angew. Chem.* **1995**, 107, 2461; *Angew. Chem. Int. Ed. Engl.* **1995**, 34, 2240.
  - 147 U. KOLB, S. A. QUAISER, M. WINTER, M. T. REETZ, *Chem. Mater.* **1996**, 8, 1889.
  - 148 T. W. SMITH, *US Patent* 4252674 **1981**.
  - 149 T. W. SMITH, *US Patent* 4252673 **1981**.
  - 150 T. W. SMITH, *US Patent* 4252671 **1981**.
  - 151 T. W. SMITH, *US Patent* 4252672 **1981**.
  - 152 T. W. SMITH, *US Patent* 4252678 **1981**.
  - 153 T. TANO, K. ESUMI, K. MEGURO, *J. Colloid Interface Sci.* **1989**, 133, 530.
  - 154 K. ESUMI, T. TANO, K. MEGURO, *Langmuir* **1989**, 5, 268.
  - 155 K. ESUMI, T. TANO, K. TORIGOE, K. MEGURO, *Chem. Mater.* **1990**, 2, 564.
  - 156 K. ESUMI, M. SUZUKI, T. TANO, K. TORIGOE, K. MEGURO, *Colloids Surf.* **1991**, 55, 9.
  - 157 K. ESUMI, N. SATO, K. TORIGOE, K. MEGURO, *J. Colloid Interface Sci.* **1992**, 149, 295.
  - 158 K. ESUMI, O. SADAKANE, K. TORIGOE, K. MEGURO, *Colloids Surf.* **1992**, 62, 255.
  - 159 N. TOSHIMA, Y. WANG, *Chem. Lett.* **1993**, 1611.
  - 160 A. HENGLEIN, A. HOLZWARATH, P. MULVANEY, *J. Phys. Chem.* **1992**, 96, 8700.
  - 161 A. HENGLEIN, J. LILLE, *J. Phys. Chem.* **1981**, 85, 1246.
  - 162 J. BUTLER, A. HENGLEIN, *Radiat. Phys. Chem.* **1980**, 15, 603.
  - 163 B. G. ERSHOV, A. HENGLEIN, *J. Phys. Chem.* **1993**, 97, 3434.
  - 164 A. HENGLEIN, P. MULVANEY, A. HOLZWARATH, T. E. SOSEBEE, A. FOJTIK, *Ber. Bunsenges. Phys. Chem.* **1992**, 96, 754.
  - 165 A. HENGLEIN, *Ber. Bunsenges. Phys. Chem.* **1977**, 81, 556.
  - 166 A. HENGLEIN, R. TAUSCH-TREML, *J. Coll. Interfac. Sci.* **1981**, 80, 84.
  - 167 S. MOSSERI, A. HENGLEIN, E. JANATA, *J. Phys. Chem.* **1989**, 93, 6791.
  - 168 J. BELLONI, M. D. DELCOURT, C. LECLERC, *Nouv. J. Chim.* **1982**, 6, 507.

- 169 G. MILLS, A. HENGLEIN, *Radiat. Phys. Chem.* **1984**, 26, 385.
- 170 M. O. DELCOURT, N. KEGHOUCHE, J. BELLONI, *Nouv. J. Chim.* **1983**, 7, 131.
- 171 M. O. DELCOURT, J. BELLONI, J.-L. MARIGNIER, C. MORY, C. COLLIEX, *Radiat. Phys. Chem.* **1984**, 23, 485.
- 172 J. L. MARIGNIER, J. BELLONI, M. O. DELCOURT, J. P. CHEVALIER, *Nature* **1985**, 317, 344.
- 173 B. G. ERSHOV, E. JANATA, M. MICHAELIS, A. HENGLEIN, *J. Phys. Chem.* **1991**, 95, 8996.
- 174 B. G. ERSHOV, E. JANATA, A. HENGLEIN, *Radiat. Phys. Chem.* **1992**, 39, 123.
- 175 A. HENGLEIN, M. GUTTIEREZ, E. JANATA, B. G. ERSHOV, *J. Phys. Chem.* **1992**, 96, 4598.
- 176 N. TOSHIMA, T. TAKAHASHI, H. HIRAI, *Chem. Lett.* **1985**, 1245.
- 177 Y. YONEZAWA, T. SATO, M. OHNO, H. HADA, *J. Chem. Soc., Faraday Trans.* **1987**, 83, 1559.
- 178 P. BARNICKEL, A. WOKAUN, *Mol. Phys.* **1990**, 69, 1.
- 179 K. TORIGOE, K. ESUMI, *Langmuir* **1992**, 8, 59.
- 180 Y. YONEZAWA, T. SATO, S. KURODA, K. KUGE, *J. Chem. Soc., Faraday Trans* **1991**, 87, 1905.
- 181 T. SATO, S. KURODA, A. TAKAMI, Y. YONEZAWA, H. HADA, *Appl. Organomet. Chem.* **1991**, 5, 261.
- 182 Y. TAKAHASHI, T. ITO, S. SAKAI, Y. ISHII, *Chem. Commun.* **1970**, 1065.
- 183 C. AMIENS, D. DE CARO, B. CHAUDRET, J. S. BRADLEY, *J. Amer. Chem. Soc.* **1993**, 115, 11638.
- 184 D. DE CARO, H. WALLY, C. AMIENS, B. CHAUDRET, *Chem. Commun.* **1994**, 1891.
- 185 A. RODRIGUEZ, C. AMIENS, B. CHAUDRET, M.-J. CASANOVE, P. LECANTE, J. S. BRADLEY, *Chem. Mater.* **1996**, 8, 1978.
- 186 M. BARDAJI, O. VIDONI, A. RODRIGUEZ, C. AMIENS, B. CHAUDRET, M.-J. CASANOVE, P. LECANTE, *New J. Chem.* **1997**, 21, 1243.
- 187 J. S. BRADLEY, E. W. HILL, S. BEHAL, C. KLEIN, B. CHAUDRET, A. DUTEIL, *Chem. Mater.* **1993**, 4, 1234.
- 188 A. DUTEIL, R. QUÉAU, B. CHAUDRET, R. MAZEL, C. ROUCAU, J. S. BRADLEY, *Chem. Mater.* **1993**, 5, 341.
- 189 D. DE CARO, V. AGELOU, A. DUTEIL, B. CHAUDRET, R. MAZEL, Ch. ROUCAU, J. S. BRADLEY, *New J. Chem.* **1995**, 19, 1265.
- 190 F. DASSENOY, K. PHILIPPOT, T. OULD ELY, C. AMIENS, P. LECANTE, E. SNOECK, A. MOSSET, M.-J. CASANOVE, B. CHAUDRET, *New J. Chem.* **1998**, 19, 703.
- 191 J. OSUNA, D. DE CARO, C. AMIENS, B. CHAUDRET, E. SNOECK, M. RESPAUD, J.-M. BROTO, A. FERT, *J. Phys. Chem.* **1996**, 100, 14571.
- 192 T. OULD ELY, C. AMIENS, B. CHAUDRET, E. SNOECK, M. VERELST, M. RESPAUD, J. M. BROTO, *Chem. Mater.* **1999**, 11, 526.
- 193 J. S. BRADLEY, E. W. HILL, B. CHAUDRET, A. DUTEIL, *Langmuir* **1995**, 11, 693.
- 194 F. DASSENOY, M.-J. CASANOVE, P. LECANTE, M. VERELST, E. SNOECK, A. MOSSET, T. OULD ELY, C. AMIENS, B. CHAUDRET, *J. Chem. Phys.* **2000**, 112, 8137.
- 195 M. VERELST, T. OULD ELY, C. AMIENS, E. SNOECK, P. LECANTE, A. MOSSET, M. RESPAUD, J.-M. BROTO, B. CHAUDRET, *Chem. Mater.* **1999**, 11, 2702.
- 196 K. SOULANTICA, A. MAISONNAT, M. FROMEN, M. CASANOVE, P. LECANTE, B. CHAUDRET, *Angew. Chem.* **2001**, 113, 462; *Angew. Chem. Int. Ed.* **2001**, 40, 448.
- 197 C. NAYRAK, E. VIALA, P. FAU, F. SENOCQ, J. JUMAS, A. MAISONNET, B. CHAUDRET, *Chem. Eur. J.* **2000**, 6, 4082.
- 198 S. GOMEZ, K. PHILIPPOT, V. COLLIÈRE, B. CHAUDRET, F. SENOCQ, P. LECANTE, *Chem. Commun.* **2000**, 19, 1945.
- 199 F. FASSENOY, M. CASANOVE, P. LECANTE, M. VERELST, E. SNOECK, A. MOSSET, T. OULD ELY, C. AMIENS, B. CHAUDRET, *J. Chem. Phys.* **2000**, 112, 8137.
- 200 C. PAN, F. DASSENOY, M. CASANOVE, K. PHILIPPOT, C. AMIENS, P. LECANTE, A. MOSSET, B. CHAUDRET, *J. Phys. Chem. B*, **1999**, 103, 10098.
- 201 K. PEIZER, O. VIDONI, K. PHILIPPOT, B. CHAUDRET, *Adv. Funct. Mater.* **2003**, 13, 118.

- 202 K. PELZER, K. PHILIPPOT, B. CHAUDRET, W. MEYER-ZAIKA, G. SCHMID, *ZAAC*, **2003**, 629, 1217.
- 203 C. M. SORENSEN (Magnetism), in *Nanoscale Materials in Chemistry*, K. J. KLABUNDE (ed.), John Wiley, **2001**, pp. 162–221.
- 204 A. J. COX, J. G. LOUDERBACK, L. A. BLOOMFIELD, *Phys. Rev. Lett.* **1993**, 71, 923.
- 205 U. A. PAULUS, A. WOKAUN, G. G. SCHERER, T. J. SCHMIDT, V. STAMENKOVIC, V. RADMILOVIC, N. M. MARKOVIC, P. N. ROSS, *J. Phys. Chem. B* **2002**, 106, 4181.
- 206 C. T. BLACK, C. B. MURRAY, R. L. SANDSTROM, S. SUN, *Science* **2000**, 290, 1131.
- 207 R. C. DOTY, H. YU, C. K. SHIH, B. A. KORGEL, *J. Phys. Chem. B* **2001**, 105, 8291.
- 208 G. SCHMID, Y.-P. LIU, M. SCHUMANN, T. RASCHKE, C. RADEHAUS, *Nano Lett.* **2001**, 1, 405.
- 209 R. PARTHASARATHY, X.-M. XIAO-MIN LIN, H. M. JAEGER, *Phys. Rev. Lett.* **2001**, 87, 186807.
- 210 S. SUN, C. B. MURRAY, *J. Appl. Phys.* **1999**, 85, 4325.
- 211 C. L. CHIEN, *J. Appl. Phys.* **1991**, 69, 5267.
- 212 A. E. BERKOWITZ, J. R. MITCHELL, M. J. CAREY, A. P. YOUNG, S. ZHANG, F. E. SPADA, F. T. PARKER, A. HUTTEN, G. THOMAS, *Phys. Rev. Lett.* **1992**, 68, 3745.
- 213 J. Q. XIAO, J. S. JIANG, C. L. CHIEN, *Phys. Rev. Lett.* **1992**, 68, 3749.
- 214 H. J. LIPKIN, *Phys. Rev. Lett.* **1987**, 58, 425.
- 215 S. TAKAHASHI, S. MAEKAWA, *Phys. Rev. Lett.* **1998**, 80, 1758.
- 216 V. RUSSIER, C. PETIT, J. LEGRAND, M. P. PILENI, *Phys. Rev. B* **2000**, 62, 3910.
- 217 D. A. VAN LEEUWEN, J. M. VAN RUITENBEEK, L. J. DE JONGH, A. CERIOTTI, G. PACCHIONI, *Phys. Rev. Lett.* **1994**, 73, 1432.
- 218 F. BØDKER, S. MØRUP, S. LINDEROTH, *Phys. Rev. Lett.* **1994**, 72, 282.
- 219 S. A. ZAHN, K. E. SHENTON, *IEEE Trans. Magn.* **1980**, 16, 387.
- 220 K. O'GRADY, R. W. CHANTRELL, *Magnetic Properties of Fine Particles*, Elsevier, Amsterdam, **1992**, p. 93.
- 221 A. AHARONY, *Introduction to the Theory of Ferromagnetism*, Oxford University Press, New York, **1996**, p. 133.
- 222 E. BLUMS, A. CEBERS, M. M. MAIORIV, *Magnetic Fluids*, Walter de Gruyter, New York, **1997**, p. 343.
- 223 R. E. ROSENWIEG, *Ferrohydrodynamics*, Dover Publishing, New York, **1998**.
- 224 B. M. BERKOVSKII, V. G. BSHTOVIO, *Magnetic Fluids and Applications Handbook*, Begell House, New York, **1996**.
- 225 A. JORDAN, R. SCHOLZ, P. WUST, H. FÄHLING, R. J. FELIX, *Magn. Mater.* **1999**, 201, 413.
- 226 L. JOSEPHSON, J. M. PEREZ, R. WEISSLEDER, *Angew. Chem.* **2001**, 113, 3304; *Angew. Chem. Int. Ed.* **2001**, 40, 3204.
- 227 C. B. MURRAY, S. SUN, H. DOYLE, T. BETLEY, *MRS Bulletin* **2001**, 985.
- 228 C. P. COLLIER, R. J. SAYKALLY, J. J. SHIANG, S. E. HENRICH, J. R. HEATH, *Science* **1997**, 277, 1978.
- 229 C. J. O'CONNOR AND J. TANG (Nanostructured magnetic materials), in *Magnetism: Molecules to Materials III*, J. ZHANG, J. S. MILLER, M. DRILLON (eds.), Wiley-VCH, Weinheim, **2001**, p. 1.
- 230 D. L. LESLIE-PELECKY, R. D. RIEKE, *Chem. Mater.* **1996**, 8, 1770.
- 231 M. DUMM, M. ZÖFL, R. MOOSBÜHLER, M. BROCKMANN, T. SCHMIDT, G. BAYREUTHER, *J. Appl. Phys.* **2000**, 87, 5457.
- 232 S. W.-K. CHOI, J. PUDDIPHATT, *Chem. Mater.* **1997**, 9, 1191.
- 233 I. J. JEON, D. KIM, J. S. SONG, J. H. HER, D. R. LEE, K. B. LEE, *Appl. Phys. A* **2000**, 70, 235.
- 234 I. J. JEON, D. W. KANG, D. E. KIM, D. H. KIM, S. B. CHOE, S. C. SHIN, *Adv. Mater.* **2002**, 14, 1116.
- 235 L. M. FALICOV, D. T. PIERCE, S. D. BADER, R. GRONSKY, K. B. HATHAWAY, H. J. HOPSTER, D. N. LAMBETH, S. S. P. PARKIN, G. PRINZ, M. SALAMON, I. K. SCHULLER, R. H. VICTORA, *J. Mater. Res.* **1990**, 5, 1299.
- 236 C. CHEUNG, P. NOLAN, U. ERB, *Mater. Lett.* **1994**, 20, 135.

- 237 J. L. DELPLANCHE, O. BOUESNARD, J. REISSE, R. WINAND, *Mater. Soc. Symp. Proc.* **1997**, 451, 383.
- 238 J. F. LÖFFLER, P. SCHERRER, J. P. MEIER, B. DOUDIN, J.-P. ANSERMET, W. WAGNER, *Phys. Rev. B* **1998**, 57, 2915.
- 239 C. PRADOS, M. MULTIGNER, A. HERNANDO, J. C. SÁNCHEZ, A. FERNÁNDEZ, C. F. CONDE, A. CONDE, *J. Appl. Phys.* **1999**, 85, 6118.
- 240 J. TANORI, N. DUXIN, C. PETIT, P. BONVILLE, C. COLLIEX, M. P. PILENI, *Colloid Polym. Sci.* **1995**, 273, 886.
- 241 N. DUXIN, O. STEPHAN, C. PETIT, P. BONVILLE, C. COLLIEX, M. P. PILENI, *Chem. Mater.* **1997**, 9, 2096.
- 242 E. E. CARPENTER, C. T. SEIP, C. J. O'CONNOR, *J. Appl. Phys.* **1999**, 85, 5184.
- 243 E. E. CARPENTER, C. J. O'CONNOR, C. SANGREGORIO, *IEEE Trans. Magn.* **1999**, 35, 3496.
- 244 S. LI, V. T. JOHN, S. H. RACHAKONDA, G. C. IRVIN, G. L. MCPHERSON, C. J. O'CONNOR, *J. Appl. Phys.* **1999**, 85, 5178.
- 245 N. MOUMEN, M. P. PILENI, *Chem. Mater.* **1996**, 8, 1128.
- 246 J. TANORI, M. P. PILENI, *Langmuir* **1997**, 13, 639.
- 247 C. PETIT, A. TALEB, M. P. PILENI, *Adv. Mater.* **1998**, 10, 259.
- 248 A. CHEMSEDDINE, H. WELLER, *Ber. Bunsenges. Chem.* **1993**, 97, 636.
- 249 C. B. MURRAY, C. R. KAGAN, M. G. BAWENDI, *Annu. Rev. Mater. Sci.* **2000**, 30, 545.
- 250 M. H. YANG, C. P. FLYNN, *Phys. Rev. Lett.* **1989**, 62, 2476.
- 251 C. PETIT, A. TALEB, M. P. PILENI, *J. Phys. Chem. B* **1999**, 103, 1805.
- 252 K. SUSLICK, M. FANG, T. HYEON, *J. Am. Chem. Soc.* **1996**, 118, 11960.
- 253 S. RAMESH, Y. KOLTYPIN, R. PROZOROV, A. GEDANKEN, *Chem. Mater.* **1997**, 9, 546.
- 254 K. S. SUSLICK, T. HYEON, M. FANG, *Chem. Mater.* **1996**, 8, 2172.
- 255 E. V. SHEVCHENKO, D. V. TALAPIN, H. SCHNABLEGGER, A. KORNOWSKI, O. FESTIN, P. SVEDLINDH, M. HAASE, H. WELLER, *J. Am. Chem. Soc.*, **2003**, 125, 9090.
- 256 V. K. LA MER, R. H. DINEGAR, *J. Am. Chem. Soc.* **1950**, 72, 4847.
- 257 C. B. MURRAY, D. J. NORRIS, M. G. BAWENDI, *J. Am. Chem. Soc.* **1993**, 115, 8706.
- 258 D. P. DINEGA, M. G. BAWENDI, *Angew. Chem.* **1999**, 111, 1906; *Angew. Chem. Int. Ed.* **1999**, 38, 1788.
- 259 V. F. PUNTES, K. M. KRISHAN, A. P. ALIVISATOS, *Science* **2001**, 291, 2115.
- 260 M. R. DIEHL, J.-Y. YU, J. R. HEATH, G. A. HELD, H. DOYLE, S. SUN, C. B. MURRAY, *J. Phys. Chem. B* **2001**, 105, 7913.
- 261 S. SUN, C. B. MURRAY, H. DOYLE, *Mater. Res. Soc. Symp. Proc.* **1999**, 577, 385.
- 262 O. KITAKAMI, H. SATO, Y. SHIMADA, F. SATO, M. TANAKA, *Phys. Rev. B* **1997**, 56, 13849.
- 263 V. F. PUNTES, K. M. KRISHAN, A. P. ALIVISATOS, *Top. Catal.* **2002**, 19, 145.
- 264 V. F. PUNTES, D. ZANCHET, C. K. ERDONMEZ, A. P. ALIVISATOS, *J. Am. Chem. Soc.* **2002**, 124, 12874.
- 265 E. V. SHEVCHENKO, D. V. TALAPIN, A. L. ROGACH, A. KORNOWSKI, M. HAASE, H. WELLER, *J. Am. Chem. Soc.* **2002**, 124, 11480.
- 266 T. SUGIMOTO, *Monodisperse Particles*, Elsevier, **2001**.
- 267 J. I. PARK, N. J. KANG, Y. JUN, S. J. OH, H. C. RI, J. CHEON, *Chem. Phys. Chem.* **2002**, 3, 543.
- 268 T. HYEON, S. S. LEE, J. PARK, Y. CHUNG, H. B. NA, *J. Am. Chem. Soc.* **2001**, 123, 12798.
- 269 W. W. YU, X. PENG, *Angew. Chem.* **2002**, 114, 2474; *Angew. Chem. Int. Ed.* **2002**, 41, 2368.
- 270 O. GLATTER, *J. Appl. Cryst.* **1977**, 10, 415.
- 271 O. GLATTER, *J. Appl. Cryst.* **1980**, 13, 7.
- 272 B. A. KORGEL, S. FULLAM, S. CONNOLLY, D. FITZMAURICE, *J. Phys. Chem. B* **1998**, 102, 8379.
- 273 H. MATTOUSSI, A. W. CUMMING, C. B. MURRAY, M. G. BAWENDI, R. OBER, *J. Chem. Phys.* **1996**, 105, 9890.
- 274 X. PENG, J. WICKHAM, A. P. ALIVISATOS, *J. Am. Chem. Soc.* **1998**, 120, 5343.
- 275 Z. L. WANG, *Adv. Mater.* **1998**, 10, 13.

- 276 X. PENG, L. MANNA, W. YANG, J. WICKHAM, E. SCHER, A. KADAVANICH, A. P. ALIVISATOS, *Nature* **2000**, 404, 59.
- 277 L. MANNA, E. C. SCHER, A. P. ALIVISATOS, *J. Am. Chem. Soc.* **2000**, 122, 12700.
- 278 S. M. LEE, Y. W. JUN, S. N. CHO, J. CHEON, *J. Am. Chem. Soc.* **2002**, 124, 11244.
- 279 C. PACHOLSKI, A. KORNOWSKI, H. WELLER, *Angew. Chem.* **2002**, 114, 1234; *Angew. Chem. Int. Ed.* **2002**, 41, 1188.
- 280 T. S. AHMADI, Z. L. WANG, A. HENGLEIN, M. A. EL-SAYED, *Chem. Mater.* **1996**, 8, 1161.
- 281 N. R. JANA, L. GEARHEART, C. J. MURPHY, *J. Phys. Chem. B* **2001**, 105, 4065.
- 282 M. P. PILENI, *Nat. Mater.* **2003**, 2, 145.
- 283 F. DUMESTRE, B. CHAUDRET, C. AMIENS, M. C. FROMEN, M.-J. CASANOVE, P. RENAUD, P. ZURCHER, *Angew. Chem.* **2002**, 114, 4462; *Angew. Chem. Int. Ed.* **2002**, 41, 4286.
- 284 Z. TANG, N. A. KOTOV, M. GIERSIG, *Science*, **2002**, 297, 237.
- 285 X. PENG, L. MANNA, W. YANG, J. WICKHAM, E. SCHER, A. KADAVANICH, A. P. ALIVISATOS, *Nature*, **2000**, 404, 59.
- 286 S. J. PARK, S. KIM, S. LEE, Z. G. KHIM, K. CHAR, T. HYEON, *J. Am. Chem. Soc.* **2000**, 122, 8581.
- 287 N. CORDENTE, M. RESPAUD, F. SENOCQ, M.-J. CASANOVE, C. AMIENS, B. CHAUDRET, *Nano Lett.* **2001**, 1, 565.
- 288 R. F. SERVICE, *Science* **2000**, 287, 1902.
- 289 S. SUN, C. B. MURRAY, D. WELLER, L. FOLKS, A. MOSER, *Science* **2000**, 287, 1989.
- 290 Z. R. DAI, S. SUN, Z. L. WANG, *Nano Lett.* **2001**, 1, 443.
- 291 M. HANSEN, *Constitution of Binary Alloys*, McGraw-Hill, New York, **1958**, pp. 492.
- 292 S. KANG, J. W. HARRELL, D. E. NIKLES, *Nano Lett.* **2002**, 2, 1033.
- 293 M. CHEN, D. E. NIKLES, *Nano Lett.* **2002**, 91, 8477.
- 294 K. ONO, R. OKUDA, S. KAMIMIRA, M. OSHIMA, *J. Phys. Chem. B* **2003**, 107, 1941.
- 295 J.-I. PARK, J. CHEON, *J. Am. Chem. Soc.* **2001**, 123, 5743.
- 296 N. SOBAL, M. HILGENDORFF, H. MÖHWALD, M. GIERSIG, M. SPASOVA, T. RADETIC, M. FARLE, *Nano Lett.* **2002**, 2, 621.
- 297 W. A. DEHEER (NANOMAGNETISM), in *Characterisation of Nanophase Materials*, Z. L. WANG (ed.), Wiley-VCH, Weinheim, **2000**, p. 289.
- 298 C. KITTEL, *Introduction to solid state physics*, John Wiley & Sons, New York, Singapore, **1996**.
- 299 W. H. MEIKLEJOHN, C. P. BEAN, *Phys. Rev.* **1957**, 105, 904.
- 300 G. A. HELD, G. GRINSTEIN, H. DOYLE, S. SUN, C. B. MURRAY, *Phys. Rev. B* **2001**, 64, 012408.

## 4

## Organization of Nanoparticles

## 4.1

### Semiconductor Nanoparticles

*Alexander Eychmüller*

Once formed in solution or as powders, semiconductor nanocrystals may become building blocks for larger supramolecular units. These units may form “automatically”, i.e. by crystallization or self-assembly, or they may be formed “intentionally” using one of several techniques, and these methods of formation are discussed here. Structures of semiconductor nanoparticles as large as several hundreds of microns can be formed as crystals (Section 4.1.1) or superlattices (Section 4.1.2), depending on fine adjustment of the experimental conditions. Section 4.1.3 deals with a number of experimental techniques, e.g., the Langmuir-Blodgett and layer-by-layer techniques, which have in common the build-up of layered structures consisting of disordered particles, while Section 4.1.4 is devoted to the coupling (either ionic or covalent) of semiconductor particles.

## 4.1.1

#### Molecular Crystals

One of the very interesting developments of the last decade is the merging of the colloidal preparation of nanostructures with synthetic approaches that stem from advanced inorganic chemical routes (see, e.g., Section 3.1.3), both leading to very similar nanoparticles. Both routes yield species that crystallize into superstructures with sizes reaching some hundreds of microns. Single-crystal X-ray diffraction is performed on these macroscopic crystals, yielding the exact positions of every single atom in the superstructures.

Based on the works of Strickler [1] and Dance and coworkers [2–5] in 1993, Herron et al. reported on the crystallization of  $[\text{Cd}_{32}\text{S}_{14}(\text{SPh})_{36}] \cdot 4\text{DMF}$  ( $\text{Ph} = \text{C}_6\text{H}_5$ , DMF = dimethyl formamide) as pale yellow cubes [6]. The structure unraveled by single-crystal X-ray diffraction consists of an 82-atom CdS core that is a piece of the bulk cubic lattice appearing as a tetrahedron whose points are capped by DMF solvent molecules. The cluster remains soluble, and as such retains properties of a discrete molecule. From the point of view of a nanocrystal chemist in-

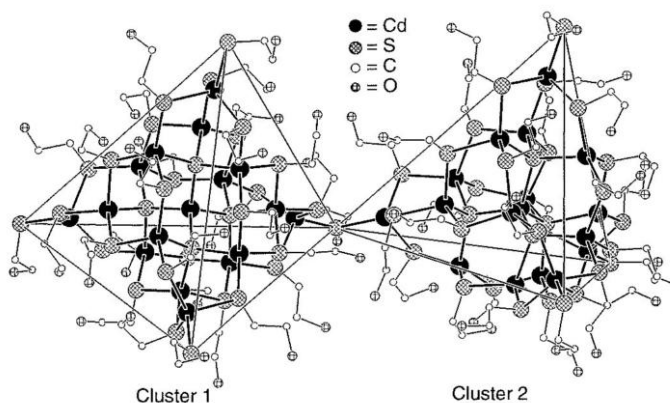


Fig. 4-1 Structures of two covalently linked  $[\text{Cd}_{17}\text{S}_4(\text{SCH}_2\text{CH}_2\text{OH})_{26}]$  clusters [7].

terested in studying the properties of particles as a function of size, the “ $\text{Cd}_{32}$ -cluster” produced is exceptional because, unlike all other colloiddally prepared samples, it has no size distribution. Its structure is a larger homolog of the  $[\text{Cd}_{17}\text{S}_4(\text{SPh})_{28}]^{2-}$  cluster prepared by Lee et al. [5]. This compound is obtained by recrystallization from hot  $\text{CH}_3\text{CN}$  of the mixed products of the reaction of  $\text{PhSH}$ ,  $\text{Et}_3\text{N}$ ,  $\text{Cd}^{2+}$ ,  $\text{Na}_2\text{S}$ , and  $\text{Me}_4\text{NCl}$  in methanol/acetonitrile. As in the case of the “ $\text{Cd}_{32}$ -cluster”, this “ $\text{Cd}_{17}$ -cluster” appears as a noncovalently bound cluster in the crystal. An identical cluster core was prepared by Vossmeier et al. but via a distinctly different route and with another superstructure in the evolving crystals [7]. The preparative route was essentially described earlier as a colloid-chemical one in which  $\text{Cd}(\text{ClO}_4)_2$  and 2-mercaptoethanol were dissolved in water, followed by  $\text{H}_2\text{S}$  injection in alkaline solution [8]. Exhaustive dialysis against water yields crystalline material which first appears as needles and evolves as blocky crystals after standing in mother liquor for some weeks. Figure 4-1 displays the structures of two  $[\text{Cd}_{17}\text{S}_4(\text{SCH}_2\text{CH}_2\text{OH})_{26}]$  clusters that form the basic units of the superlattice. In contrast to the above-mentioned clusters, here intermolecular bridges are formed that build up a superlattice framework.

Smaller thiophenolate-capped clusters containing zinc, e.g.  $[\text{Zn}_4(\mu_2\text{-SPh})_6 \cdot (\text{SPh})_4]^{2-}$ ,  $[\text{Zn}_{10}(\mu_3\text{-S})_4(\mu_2\text{-SPh})_{12}]$ , and  $[\text{Zn}_{10}(\mu_3\text{-S})_4(\mu_2\text{-SPh})_{12}(\text{SPh})_4]^{4-}$ , are prepared as supertetrahedral fragments and possible molecular models for cubic  $\text{ZnS}$ , and their electronic structure is evaluated theoretically [9].

As mentioned above, very similar structures are obtained via organometallic synthetic routes. Clusters derived in this manner include  $[\text{Cd}_{32}\text{Se}_{14}(\text{SePh})_{36} \cdot (\text{PPh}_3)_4]$  [10] and its mercury analog, which display exactly the same internal structure as the above-mentioned sulfur-containing clusters. Other crystalline material consists of  $[\text{Cd}_{17}\text{Se}_4(\text{SePh})_{24}(\text{PPh}_2\text{Pr})_4]^{2+}[\text{Cd}_8\text{Se}(\text{SePh})_{12}\text{Cl}_4]^{2-}$  [11] ( $\text{Pr} = n$ -propyl) and the smaller cluster  $[\text{Cd}_{10}\text{Se}_4(\text{SPh})_{12}(\text{PPr}_3)_4]$  [12]. The latter work also contains results concerning the cluster compound  $[\text{Cd}_{16}(\text{SePh})_{32}(\text{PPh}_3)_2]$ , which lacks a central atom, in contrast to the “ $\text{Cd}_{17}$ ” cluster, thus forming a structure similar to that of Koch pyramids [13].

Together with the Banin group, the authors of [10–12] performed optical spectroscopy on some of the cluster molecules gained [14–16]. They were treated as the molecular limit of the bulk semiconductor CdSe, and issues like the oscillator strength, the steady-state and time-resolved photoluminescence and the photoluminescence excitation were addressed. Additionally, emission-mediating vibrational modes were detected, and photobleaching effects were observed.

Although not yielding II–VI cluster crystals, yet another series of crystallized nanoparticles seems to be interesting because of a possible transfer of the synthetic approach to the II–VI semiconductor materials also. Crystals of supertetrahedra of, e.g.,  $[\text{Cd}_4\text{In}_{16}\text{S}_{33}(\text{H}_2\text{O})_{20}(\text{C}_{10}\text{H}_{28}\text{N}_4)_{2.5}]$  [17] were obtained in a high-temperature synthesis involving elemental indium and sulfur together with a cadmium salt. Mn, Co or Zn may be introduced into the clusters instead of Cd [18]. Even larger particles are formed without the incorporation of divalent metal ions like the cluster  $[\text{In}_{34}\text{S}_{54}]^{6-}$  [19]. These structures also lack an interior core atom and form three-dimensional superlattices together with the smaller  $[\text{In}_{10}\text{S}_{18}]^{6-}$  species. A cluster (namely  $[\text{In}_{28}\text{Cd}_6\text{S}_{54}]^{12-}$ ) with the same tetrahedral shape and also with a missing central atom is also formed by the incorporation of Cd-ions [20].

In a study dealing with the particle-particle interaction in semiconductor nanocrystal assemblies, Döllefeld et al. investigated, among other structures, the crystalline superstructure of  $[\text{Cd}_{17}\text{S}_4(\text{SCH}_2\text{CH}_2\text{OH})_{26}]$  depicted in Figure 4-1 [21].

In Figure 4-2 the UV-Vis absorption spectrum of this compound in solution (dotted line) and diffuse reflectance spectrum of the crystalline material. It is clearly seen that in the spectra of the crystalline material the first electronic transition

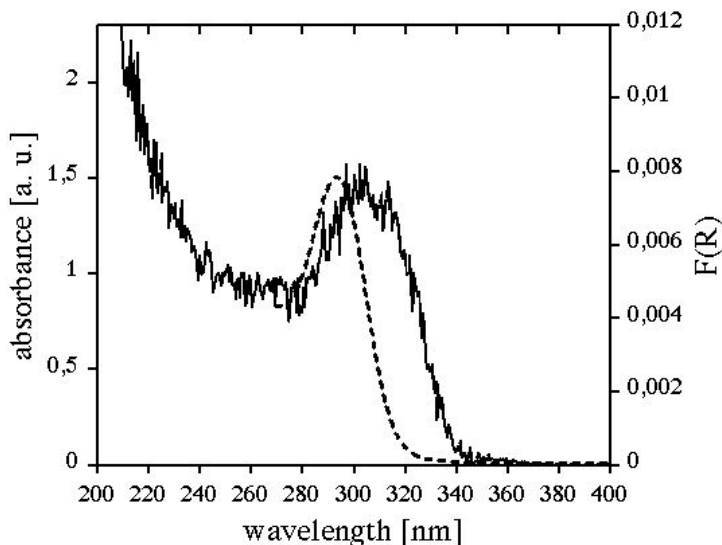


**Fig. 4-2** Absorption spectrum of the  $[\text{Cd}_{17}\text{S}_4(\text{SCH}_2\text{CH}_2\text{OH})_{26}]$  cluster compound in solution (dotted line) and diffuse reflectance spectrum of the crystalline superstructure of the same compound (cf. also Figure 4-1) [21].



is shifted to lower energies by about 150 meV. Additionally, the transition is broadened from a full width at half maximum of about 390 meV to about 520 meV. Most probably, a complete description of the interaction of semiconductor nanocrystals in crystalline superstructures includes both electronic and dipole-dipole interaction. The electronic coupling may be introduced by the covalent bridging of the nanocrystals in the crystalline superstructure, but detailed theoretical studies would help for a more quantitative picture. First attempts in this direction were reported recently [22].

#### 4.1.2

#### **Superlattices of Semiconductor Nanoparticles**

Yet another development of remarkable nanostructured materials yields superlattices of nanosized objects. Since there is no clear distinction between “molecular crystals” and “superlattices” formed from nanoparticles, here we decide to refer to structures composed of very similar but most probably not exactly identical nanoparticles, namely colloidal particles in the size range 2–10 nm.

Two excellent reviews by leading experts in the field were published in 1998 and 2000 [23, 24]. The titles of these articles contain the terms “nanocrystal superlattices” and “close-packed nanocrystal assemblies”, which are in line with the above-outlined delimitation, although Collier et al. also report on molecular crystals as is done here in the preceding chapter. The two articles comprise roughly 100 pages with some 300 references and summarize the state of the art at that time in exemplary fashion. The topics include preparative aspects of the formation of monodisperse nanoparticles of various compositions including metals, the superlattice formation itself with some theoretical background, covalent linking of nanocrystals (see below), and an appropriate description of the physical properties and the characterization of the nanocrystal superlattices.

Naturally, both survey papers refer to the pioneering work of Murray et al. from 1995, in which the self-organization of CdSe nanocrystals into three-dimensional colloidal crystals is demonstrated [25] (see also [26, 27]). A prerequisite for superlattice formation is the high degree of monodispersity of the particles, a result of synthetic advances. The characterization of the evolving structures is performed by absorption and emission spectroscopy, high-resolution scanning and transmission electron microscopy, electron diffraction, and, very impressively, X-ray diffraction, giving clear-cut evidence of both long range order and tunability of the interdot spacing by variation of the size and nature of the capping agents.

A very fine example of superlattice formation is reported by Talapin et al. [28, 29]. In Figure 4-3, the concept of the nucleation procedure is depicted: a nonsolvent (methanol) for the CdSe particles dispersed in toluene diffuses either directly (left tube in Figure 4-3a) or slowed down through a buffer layer (propan-2-ol, right tube) into the colloidal solution. Over weeks, this leads to irregularly shaped crystals in the case of fast diffusion (Figure 4-3b) or to perfectly faceted hexagonal colloidal crystals with sizes of about 100  $\mu\text{m}$  (Figure 4-3c) consisting of about  $10^{12}$  individual 3.5 nm CdSe particles.

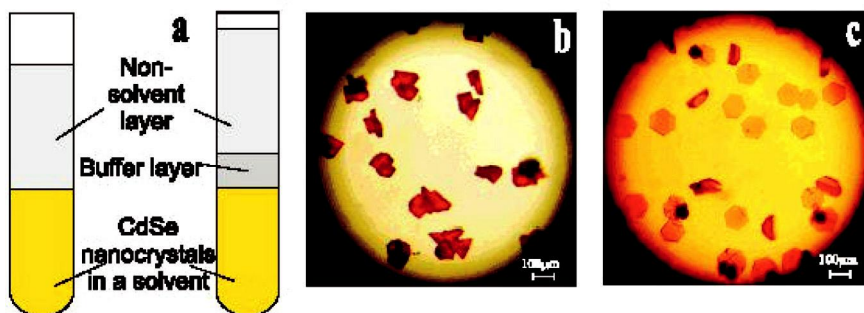


Fig. 4-3 Schematic illustration of superlattice formation from colloidal solutions of 3.5 nm CdSe nanocrystals in toluene (a). Optical micrographs of the evolving nanocrystal superlattices after fast (b) and slow (c) nucleation [28].

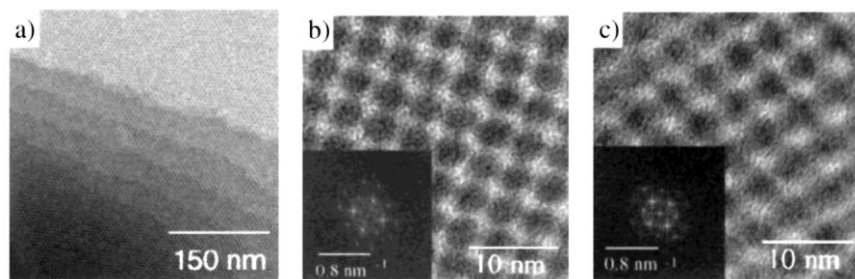


Fig. 4-4 Transmission electron microscopic images of superlattices formed from CdSe nanocrystals. Different orientations of the CdSe nanocrystal superlattice with corresponding Fast Fourier Transforms as insets leading to the assignment of fcc-like packing of the particles [28].

In Figure 4-4, transmission electron microscopic images are displayed. Image (a) reveals a close packing of up to seven monolayers of CdSe particles, demonstrating the earliest stages of 3D superlattice formation starting from a 2D lattice. Images (b) and (c) with their corresponding Fast Fourier Transforms (insets) display differently oriented segments of the evolving superlattices, leading to the assignment of the 3D alignment of the particles to fcc-like.

There exist other approaches to the formation of superlattices aside from pure self-organization, e.g., the use of bacterial S-layers as templates for the nucleation of ordered two-dimensional arrays of CdS nanocrystals [30], crystallization on other periodically patterned surfaces [31], or the “lost-wax approach” reported recently, in which first polymer templates are formed from silica colloidal crystals with subsequent filling of the evolving voids of the porous polymer with a variety of colloidal particles [32]. Filling of voids of “artificial opals” (periodic structures formed from, e.g., SiO<sub>2</sub>, latex, or polymethylmethacrylate spheres) with semiconductor nanocrystals like CdSe [33] or CdTe [34] followed by the destruction

of the template leads to so-called inverse opals, which are of eminent interest in the evolving field of photonics. Another procedure yields CdS nanoparticles inside 3D hexagonal mesoporous silica films [35]. An area still to be approached with II–VI semiconductor materials is the “nanotectonic” approach, in which three-dimensional objects are formed by the template-directed assembly using nanocrystals as building units [36].

Based on work on the formation of amorphous three-dimensional arrays of CdSe nanocrystals [37] and of compact round disks of similar particles [38], a step forward was made by Ge and Brus, who reported planar monolayer aggregates consisting of 80–100 identical 4 nm CdSe nanocrystals diffusing on planar graphite surfaces [39]. It is, thus, an investigation into the collective motion of a very small nanocrystal superlattice, which opens up yet another new field of research.

#### 4.1.3

##### Layers of Semiconductor Nanocrystals

Layers of semiconductor nanoparticles are made in various ways, either from pre-formed colloids with the aid of techniques like spin-coating or layer-by-layer assembly or from ionic, atomic or molecular precursors via, e.g., electrodeposition, chemical vapor deposition (CVD), or metal-organic chemical vapor deposition (MOCVD). From the wealth of literature, selected examples of layered structures are shown here as examples, together with some attempts at characterization.

Relatively early in the development of the field, the Langmuir-Blodgett (LB) technique was recognized as a useful tool for preparing thin layers of nanocrystalline material and for controlling parameters like film composition and thickness. Based on earlier work [40–44] in 1992, Grieser et al. utilized the LB technique for the generation of multilayer films of CdS, CdSe and CdTe and of the mixed crystal compounds  $\text{CdS}_x\text{CdSe}_{1-x}$ ,  $\text{CdS}_x\text{CdTe}_{1-x}$  and  $\text{CdSe}_x\text{CdTe}_{1-x}$  [45]. Most of the films are formed from multilayers of cadmium arachidate that are exposed to  $\text{H}_2\text{X}$  ( $\text{X} = \text{S}, \text{Se}, \text{Te}$ ), resulting in the formation of the respective CdX particles within the matrix of the LB films. The best characterization concerning the particle sizes is based on the relationship between absorption energy and size, whilst direct methods like atomic-force microscopy (AFM) and TEM do not yield unambiguous results. A fine example of an early application of a local probe technique on colloido-chemically derived nanostructures was presented by Facci and coworkers on similarly derived LB films of CdS particles [46]. Again, cadmium arachidate films of various thicknesses were formed, followed by exposure to an  $\text{H}_2\text{S}$  atmosphere. The film formation was monitored by X-ray diffraction, absorption spectroscopy, nanogravimetry, and scanning tunneling microscopy (STM). In Figure 4-5 STM images from this study are shown. In the upper panel an image of a  $48.5 \times 64 \text{ nm}^2$  cutout of a CdS film formed from 20 bilayers of cadmium arachidate is presented, showing a structure formed by interconnected particles 4–5 nm in size. For washing purposes the layer was treated with chloroform, which induces particle growth and aggregation, observed in the STM experiment and consistent with the absorption spectra data. From a flat zone in the upper panel a

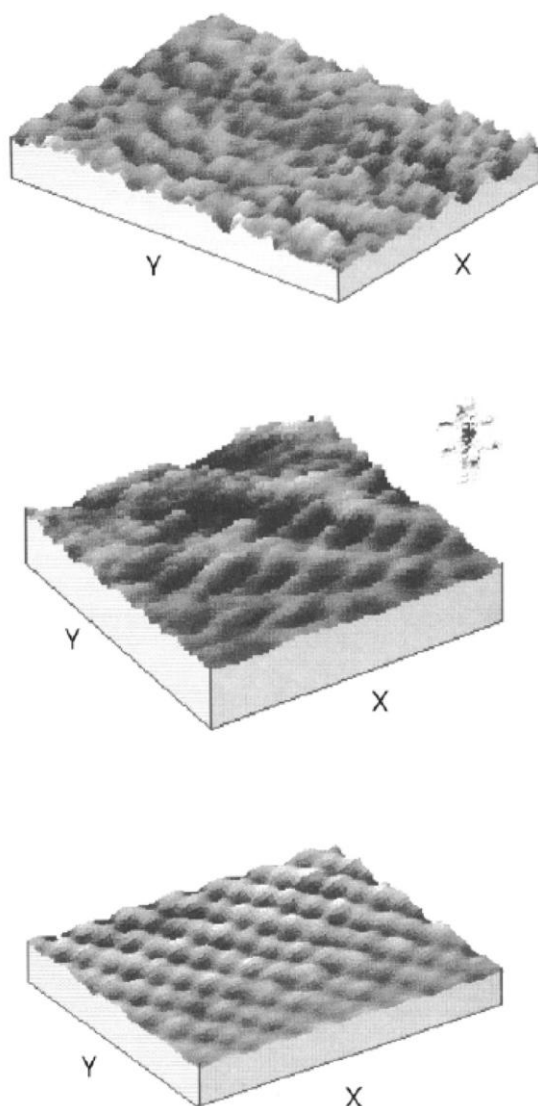


**Fig. 4-5** STM images of a CdS film formed from 20 bilayers of cadmium arachidate (top), small cutout of the upper panel (middle, cf. text), and highly oriented pyrolytic graphite acting as the substrate (bottom) [46].

$2.1 \times 2.5 \text{ nm}^2$  area is displayed (middle) showing the CdS hexagonal lattice with a period of 0.42 nm. For comparison in the lower panel, a high-resolution image of a  $2.0 \times 1.9 \text{ nm}^2$  area of the supporting highly oriented pyrolytic graphite lattice is shown, which exhibits a lattice constant of 0.246 nm. The organometallically derived TOP/TOPO-capped CdSe particles described in Section 3.1.1.3 are also suit-

able to be applied as monolayer-forming elements on the water surface of an LB trough, as demonstrated by Bawendi and coworkers [47]. The absorption and luminescence studies indicate that the monolayers retain the optical properties of the isolated crystallites, while TEM investigations reveal the formation of two-dimensional hexagonal close-packed regions. Fendler et al. also reported on studies of LB-derived films of CdS nanoparticles [48] and other sulfides and selenides [49]. The characterization of the films included surface pressure vs surface area isotherms as well as Brewster angle microscopy, while the focus of [48] is mainly on the emission properties (spectral and time-resolved) of the films and that of [49] on methodic issues of the *in situ* generation of size-quantized semiconductor particulate films. The emission properties of LB-derived nanocrystal monolayers are also the field of investigations reported by Cordero et al. [50].

By comparing wet and dry films of CdSe particles with and without illumination, it is concluded that water molecules adsorbed on the surface of the quantum dots act firstly to passivate surface traps, accompanied by increased emission, and secondly to oxidize the surface species, introducing new surface defects which results in a decrease of luminescence quantum yield. As demonstrated by Heath et al., the application of the LB technique in conjunction with semiconductor nanoparticles may lead to the generation of tunnel diodes [51]. These devices consist of a monolayer of 3.8 nm CdSe nanocrystals and an insulating bilayer of eicosanoic acid sandwiched between an Au and an Al electrode. Advanced spectroscopic techniques like attenuated low-energy photoelectron spectroscopy were also applied to LB-derived multilayered nanostructured assemblies of different-sized CdS particles [52].

Chemical solution deposition (CD) and electrodeposition (ED), two other techniques of film formation, make use of neutral and charged species in solution. These sorts of film making are inseparably linked to the name of Gary Hodes. A long list of publications could be named here (e.g. the review [53]), but instead we refer to a few examples showing the basic ideas. The basis of CD is a reaction between a slowly produced anion (e.g. sulfide from thiourea or selenide from selenourea or selenosulfate) with a free metal cation in low concentration, which is accomplished by complexation [54]. The nanoparticles are formed either by an ion-by-ion reaction at the substrate or by homogenous nucleation in solution followed by diffusion of the semiconductor crystallites to the substrate. Figure 4-6 displays a number of transmission spectra of CdSe films chemically deposited at various temperatures, with the dashed line representing particles formed at the lowest deposition temperature (274 K) and the long-short-long dashed line those formed at the highest temperature (334 K). Obviously, smaller particles are formed at lower temperatures, which might be explained by a quite complex reaction mechanism involving the formation of the reacting species in solution, nucleation and growth of crystals and the redissolution of small ones, and aggregation or coalescence of the particles [54]. While most of the CD preparations are performed in aqueous solution, the ED method often relies on nonaqueous electrolytes like dimethyl sulfoxide or diethylene glycol, the chalcogen being present in its elemental form [55, 56]. The crystallite sizes typically are in a range around 5 nm for CdS and

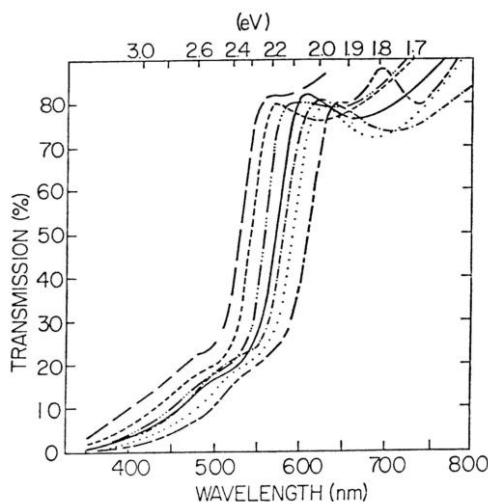


**Fig. 4-6** Transmission spectra of chemically deposited CdSe films. Deposition temperatures vary from 274 K (dashed line) to 334 K (long-short-long dashed line) [54].

CdSe, and the properties of the films are qualitatively similar to those of the respective CD films. Differences in crystal structure are observed: whereas ED shows hexagonal CdSe and CdS, CD shows cubic CdSe [54].

A method of film formation gaining considerable interest in recent years is named “Layer-by-Layer” assembly, abbreviated LbL. The method stems from G. Decher [57], is based on alternating adsorption of oppositely charged species, and was originally developed for positively and negatively charged polyelectrolytes. It is also a useful tool for the assembly of nanoparticles as shown, e.g., in a study of the electroluminescence of negatively charged CdSe particles embedded in poly(*p*-phenylene vinylene) [58], in work on graded semiconductor films from nanocrystals [59], and on films of IR-emitting quantum dots of HgTe [60, 61]. Because of its universality, simplicity, and low cost, the LbL method has gained such widespread application that even including the literature on the subject would make this chapter excessively long. Instead, only a single example is shown from the recent literature. A paper of Gao et al. [62] is devoted to lateral patterning of CdTe nanocrystal films by a modification of the conventional LbL technique, namely by using an electric field. The idea is that the electric field will direct the spatially selective deposition of the LbL films. Binary patterned arrays of such films containing two differently sized CdTe nanocrystals and a polyelectrolyte are obtained on conductive indium-tin-oxide electrodes in a multistep process. Figure 4-7 displays the impressive results of these operations. Samples a and b represent the differently sized negatively charged CdTe nanocrystals which are deposited on either the upper (red emitting particles) or the lower (green emitting particles) biased electrode. Both sorts of particles are also found in the unbiased marginal regions, which finally leads to orange emission in the case of successive deposition of both

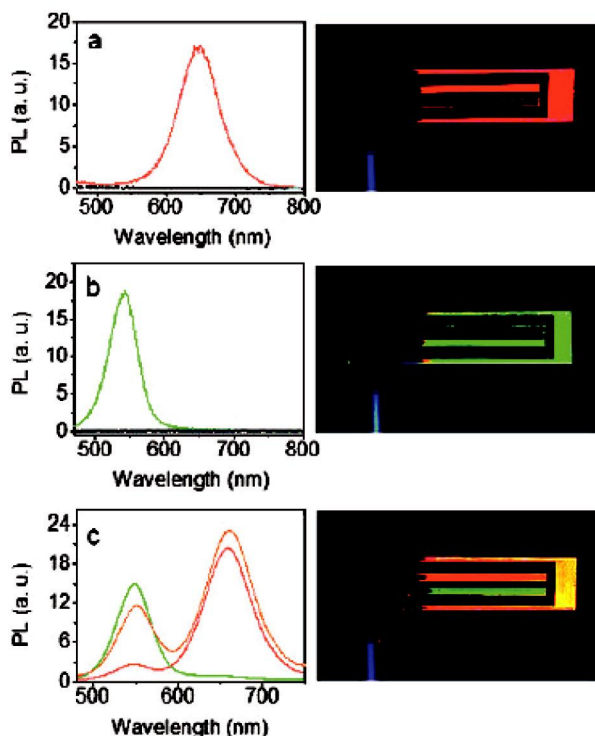


Fig. 4-7 Photographs of lateral structures selectively formed by green- and red-luminescing CdTe nanocrystals via electric field-directed layer-by-layer assembly and the corresponding emission spectra [62].

sorts (cf. panel c and the corresponding emission spectrum on the left-hand side of Figure 4-7).

Several other techniques have also been utilized for film formation: drop casting (e.g., CdSe on a Pt electrode in order to study electrochromic effects in nanocrystal films [63]), spin casting (e.g., composite films of CdSe and electron transporting block copolymers [64]), and photochemical deposition (e.g., CdSe films from aqueous solution [65]) and electrospray organometallic chemical vapor deposition for the formation of quantum dot composites [66].

Regardless of the film formation procedure, the question of the interaction of semiconductor nanocrystal assemblies arises and has been tackled by a number of groups in recent years. In 1994, Vossmeier et al. reported on the absorption properties of very small CdS nanoparticles [8]. A red shift of the first electronic transition with respect to the transition observed in solution is observed when compact layers are formed from the material by spin coating. A comparatively small red shift in the emission spectra of the crystalline superstructure of CdSe nanoparticles, mentioned in Section 4.2.2, with respect to the emission peaks in solution is explained by small size deviations of the particles within the sample result-

ing in energy transfer from the smaller to the larger particles [25, 67, 68]. Similar observations were made for III–V semiconductor nanocrystals of InP [69]. Artemyev et al. prepared unstructured solids also from CdSe nanoparticles with polymers acting as spacers in order to control the distance between the particles [70–72]. The pure solid built up by drop casting solutions of semiconductor nanoparticles shows very broad transitions bearing a resemblance to a bulk spectrum rather than to isolated absorption bands. Micic et al. obtained similar results in disordered films of InP nanoparticles [73]. After studies on the photoconductivity in CdSe quantum dot solids [74], Leatherdale et al. reported on CdSe particles in different dielectrics [75]. In agreement with the results in [8], a red shift of the first electronic transition was found exhibiting no significant broadening. Kim et al. presented studies of pressure dependency in solutions and compact layers of semiconductor nanoparticles of CdSe [76]. Different stabilizing agents were used, and, in contrast to the results of Leatherdale et al., no red shift was found for the compact layers of TOP/TOPO-stabilized CdSe particles. Only for particles stabilized with pyridine was a shift to lower transition energies observed. Again, no significant broadening of the electronic transitions was noted. As shown in Section 4.2.1, Figure 4-2, reflection spectroscopy on the cluster crystal compound  $\text{Cd}_{17}\text{S}_4(\text{SCH}_2\text{CH}_2\text{OH})_{26}$  reveals substantial broadening and a low-energy shift of the first absorption band, which in a first step is explained by both dipole-dipole interaction and electronic coupling of the nanocrystals in the crystalline superstructure. When comparing these results with those from disordered solids obtained by spin-coating concentrated solutions of the same material, it was found that extreme care has to be taken in order to avoid measuring artifacts [77]. Misinterpretations of observed alterations of transition energies in these structures are avoided by the choice of an integrating sphere as the experimental setup. The resulting “real” red shift of the transition energy is explainable in a simple picture by dipole-dipole interactions of the semiconductor nanocrystals in the films. More elaborate theoretical work covers topics like exciton dissociation and interdot transport [78], takes into account the dielectric medium surrounding the nanoparticles [79], and explains an observed solvatochromism in CdSe colloidal quantum dots, also taking into account the screening of the ligand shell [75], and, for example, uses pair potentials to predict the phase behavior and thermodynamics of small particles [80]. Because of its potential applications (based also on experimental studies of, e.g., fast kinetics [81] and electronic transport in films of colloidal particles [82–86], this research area will remain active in the coming years.

#### 4.1.4

#### Coupling of Semiconductor Nanocrystals

Probably one of the most demanding challenges in current preparational research is the directed coupling of semiconductor nanoparticles. If the quantum dots were called “artificial atoms”, this endeavor would yield “artificial molecules”, and the challenge is to create such quantum dot molecules in a desired manner to form, e.g., dimers (“two-atomic quantum dot molecules”) of various compositions,  $\text{AB}_4$



molecules, etc. The field is about to grow out of its infant status, and so the very first attempts in this direction are reported here.

Couplings of semiconductor nanocrystals to, e.g., small particles of metals [87] or insulators [88, 89] is beyond the scope of this chapter. Additionally, couplings of semiconductor nanoparticles to DNA [90–94] and to other biological systems [95–100], as well as those to organic [101] or metal-organic fluorophores [102], are excluded here, and the literature can therefore be more clearly arranged.

A recent paper by Kolny, Kornowski and Weller reports on the use of the electrostatic interaction between oppositely charged CdS nanocrystals [103]. It is shown by absorption spectroscopy, X-ray diffraction, and high-resolution electron microscopy that two types of aggregates may be formed: complex-like structures are obtained when a large excess of one kind of particles is used, whereas a three-dimensionally ordered solid evolves when comparable amounts of the constituents are mixed. Additionally, the strength of the interaction between the particles is controllable by adjusting the ionic strength of the solution. Another approach relies on the covalent bonding of different [104, 105] or similar [106] semiconductor nanocrystals. The latter work describes the synthesis, isolation and characterization of CdSe-homodimers. Monodisperse CdSe particles capped with TOPO were treated with various surface-active species. Thiols proved to be a good choice for passivation of the surfaces. For coupling of the nanocrystals, bis(acylhydrazine) was used, a compound bridging two semiconductor nanocrystals via its two terminating  $\text{NH}_2$ -groups. Size-selective precipitation finally leaves mostly homodimers in solution. The covalent coupling of different CdTe nanocrystals is reported in [104]. The CdTe particles are stabilized with thioacids or aminothiols, which form an amide bond using carbodiimide as a mediating agent. Thus, in this case, the stabilizing ligands are directly used for the coupling without a bridging molecule, in contrast to the above-mentioned case and the work of Trindade et al. [105], in which the coupling of PbS particles to CdS or CdSe nanocrystals via the bridging ligand 2,2'-bipyrimidine is outlined. Figure 4-8 displays the infrared transmission spectra of a sample containing only a mixture of the two kinds of nanocrystals (dotted line) and of a sample of the coupled particles (solid line). A careful analysis of these spectra, together with those of the bare particles, reveals the existence of the N–H vibrations within the amide group and the diminishing of the O–H vibration in the carbonyl group due to the coupling reaction (see the arrows in Figure 4-8). The authors also state that a possible alternative interpretation needs to be considered. In their own words: “Since the nanocrystalline powders are washed with buffer solution and dried in a vacuum in order to perform the IR measurements, the existence of coupled stabilizers without connection to at least one nanocrystalline surface can be excluded. However, it is conceivable that some of these “amide bridges” fall off the nanocrystal on one side. Since the S–H bond vibrations are detected in neither Raman nor IR spectroscopy, this hypothesis cannot yet be verified.”

Together with theoretical investigations [22, 107, 108], this sub-field of nanoscience is expected to continue and to grow as more sophisticated preparational attempts are launched and new demands from the applications area are imposed.

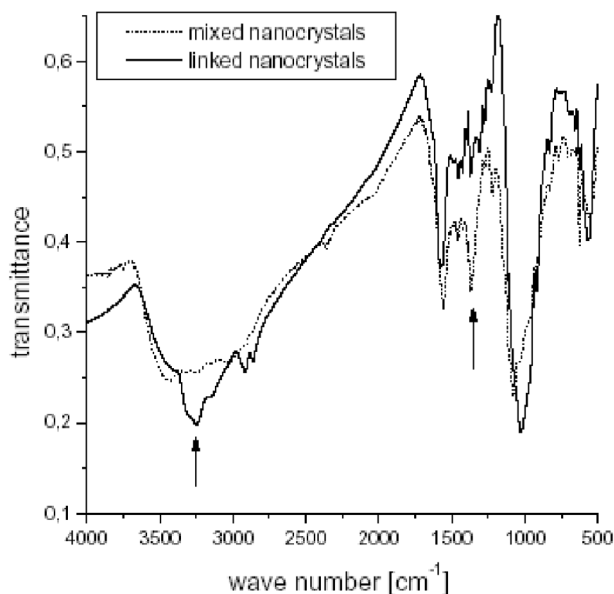


Fig. 4-8 Infrared transmission spectra of mixed and linked CdTe nanocrystals [104].

## 4.2

### Metal Nanoparticles

*Günter Schmid, Dmitri V. Talapin, and Elena V. Shevchenko*

The organization of metal nanoparticles is, like that of semiconductor nanoparticles, of vital relevance. The ultimate goal of all efforts in making and investigating semiconducting or metal nanoparticles is their use in optoelectronics, nanoelectronics, storage systems, etc., based on the size-quantized properties of these miniaturized materials. The fact that the electronic properties of metal particles dramatically change if their size falls below a well-defined limit makes them very promising candidates for single-electron switches, transistors, etc. Organization of the particles in three (3D), two (2D) or even in one (1D) dimension(s) seems indispensable if specific functions are to be called upon. This chapter therefore reports on the present state of the art with respect to 3D, 2D, and 1D arrangements of metal nanoparticles.

#### 4.2.1

##### Three-dimensional Organization of Metal Nanoparticles

In principle, 3D organization of building blocks of matter happens simply by nature: we call it crystallization. Why do we have to devote a special chapter to 3D organization of metal nanoparticles? Typically, ions and molecules forming 3D

crystals are identical in every respect and so enable them to be arranged periodically in three dimensions. This is usually not the case for building blocks on the nanometer scale. Nanoparticles, traditionally also called “colloids”, usually differ not only in size, but also in shape and structure. The surprising discovery with respect to crystal formation of nanoparticles during the last decade was that, in spite of not having fully identical building blocks, 3D organizations and (as will be shown in the following sections) 2D and even 1D arrangements become available if specific conditions are fulfilled. Of course, there is a continuous transition from 1D to 2D and from 2D to 3D. In the following, we will consider assemblies of some monolayers as quasi-two-dimensional systems or thin films rather than as 3D architectures. Three-dimensional crystals are considered to exhibit dimensions in the *a*, *b*, and *c* directions of the same order of magnitude.

Usually, nanoparticles to be 3D assembled to superlattices are covered by a shell of stabilizing ligand molecules, protecting the particles from coalescence and, furthermore, making them soluble in appropriate solvents.

Gold nanoparticles, stabilized by alkylthiolates  $RS^-$  ( $R = n\text{-C}_{12}\text{H}_{25}$ ) and rather narrowly distributed in size, could be obtained by repeated fractional crystallization of a mixture of 1.5–3.5 nm particles from nonpolar solvents. The success of the fractionation was controlled by mass spectroscopy [109]. Based on these data, definite numbers of atoms could be assigned to the particles of distinct fractions, e.g., 140, 225, 314, and 459, all consisting of fcc-structured octahedra. Solutions of these remarkably well-defined particles can be used for generating 2D assemblies (see Section 4.2.2) and also for growing 3D crystals of considerable extension. The  $\text{Au}_{459}$  fraction forms well-shaped crystals up to ca. 40  $\mu\text{m}$  in length [109]. Obviously no coalescence is happening during crystal formation, since the crystals are highly soluble in nonpolar solvents. The assembly of nanoparticles changes from the well-known purple color of individual colloids to a metallic-like luster.

Superlattices of 5.0 nm silver nanoparticles have also become available from alkylthiolate protected colloids [110–112]. From high-resolution electron microscopy (TEM), quite precise information about the architecture of the crystals could be deduced. They consist of highly ordered truncated octahedra, as is formally shown in Figure 4-9.

Crystals of up to ca. 5  $\mu\text{m}$  edge length could be grown on the TEM copper grid from solution. 3D superlattices of thiol-stabilized 5–6 nm gold particles have also been described [113].

Micron-sized 3D crystals of the well-known gold cluster compound  $\text{Au}_{55}(\text{PPh}_3)_{12}\text{Cl}_6$  are formed from dichloromethane solution, simply by evaporating the solvent [114]. This is no surprise, since these very small nanoparticles are indeed identical in size and shape. The growth of larger crystals fails because of the fast decomposition of these clusters in solution in the course of hours. The fast removal of the solvent results in small crystals, which, however, are more or less perfectly organized, as can be followed from TEM and small-angle X-ray diffraction (SARXD) measurements. The  $2\theta$  angle of  $4.3^\circ$  corresponds with a  $d$  value of 2.05 nm, in agreement with an fcc arrangement of the clusters of an effective size of 2.3–2.4 nm including the ligand shell. From TEM, the hexagonally close-packed

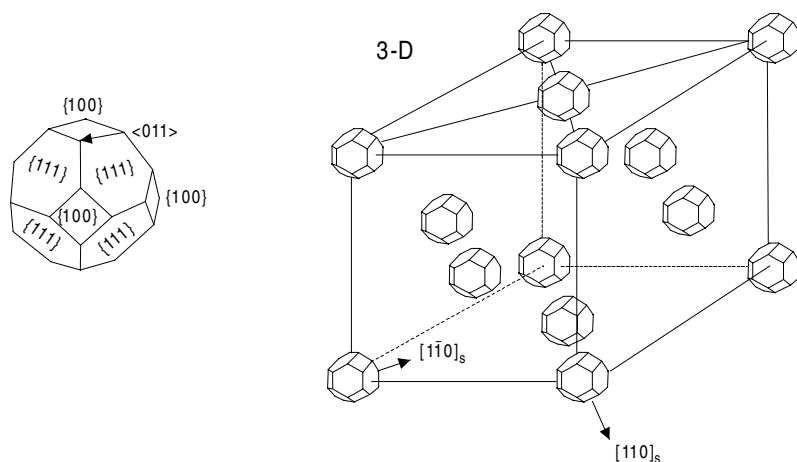


Fig. 4-9 Sketch of a superlattice of truncated octahedral 5.0 nm Ag nanoparticles.

arrangement of the clusters can also be deduced, in agreement with the SAXRD result.

Independent of the dimensionality, the organization of metal nanoparticles seemed to be linked to the existence of a protecting ligand shell enveloping the particles' surfaces. The most important reason for this condition was seen as the necessity to grow the arrangements from solution.

The soft removal of the ligands from protected particles in solution could be one way to realize the generation of defined naked nanoparticles. On the other hand, it is known that a quantitative elimination of a ligand shell cannot be induced by heat treatment. As early as 1986, the first hints emerged that naked metal clusters could organize themselves in an ordered manner. Mild electrochemical decomposition of  $\text{Au}_{55}(\text{PPh}_3)_{12}\text{Cl}_6$  in solution resulted in the formation of naked  $\text{Au}_{13}$  clusters (the inner cores of  $\text{Au}_{55}$ ) together with  $\text{Ph}_3\text{PAuCl}$  and bulk gold. The  $\text{Au}_{13}$  clusters were found to build up clusters of clusters of the type  $(\text{Au}_{13})_n$  [115, 116]. Secondary ion mass spectrometric (SIMS) investigations of  $\text{Au}_{55}(\text{PPh}_3)_{12}\text{Cl}_6$  resulted in similar species, identified by masses corresponding to  $(\text{Au}_{13})_n$  with  $n$  values up to 55 [117, 118].

The generation of bare  $\text{Au}_{55}$  clusters under mild conditions has later become possible by a surprising reaction: a thiol-terminated fourth generation dendrimer with 96 SH groups ( $\text{G4-SH}$ ) on its surface reacts with  $\text{Au}_{55}(\text{PPh}_3)_{12}\text{Cl}_6$  in solution with quantitative elimination of  $\text{PPh}_3$  and  $\text{Cl}$  ligands [119].

The reason for the removal of the ligand shell is to be seen in a formal substitution of the phosphines by the stronger thiol groups of the dendrimers, which are used in large excess. Ligand-free clusters on the dendrimers' surface are obviously not irreversibly fixed, but can move on the equivalent surface positions to finally get contact with a second, third etc. other bare cluster, with formation of strong metal-metal bonds. The process can be described as a crystal growth in a matrix of

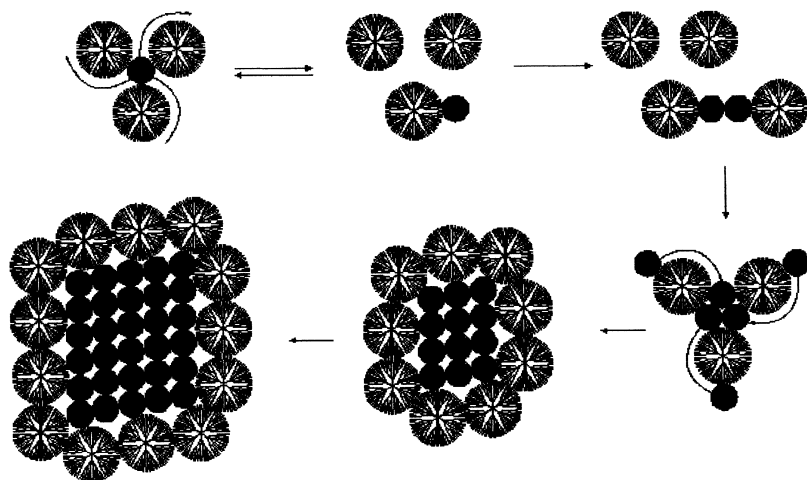


**Fig. 4-10** Illustration of the formation of  $\text{Au}_{55}$  microcrystals inside a matrix of G4-SH dendrimers.

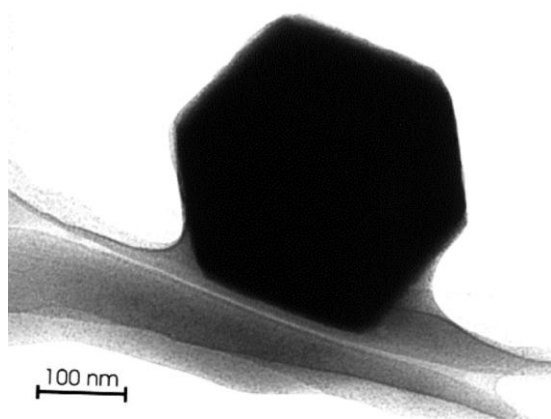


**Fig. 4-11** TEM image of an  $\text{Au}_{55}$  microcrystal with a skin of G4-SH dendrimer molecules.

organic material. The growth continues until the solubility is exceeded. Figure 4-10 illustrates in a very simplified manner the possible formation of the isolated microcrystals consisting of only  $\text{Au}_{55}$  building blocks. One of these perfectly shaped crystals is shown in Figure 4-11.

Surprisingly, not only are the  $\text{PPh}_3$  ligands removed and can be detected in solution, but also the Cl atoms have disappeared, recognizable in the lack of the characteristic Au–Cl vibration at  $274\text{ cm}^{-1}$  in the IR spectrum.

The most important question is, how do the bare  $\text{Au}_{55}$  clusters organize themselves to give the perfect-looking microcrystals? Detailed TEM and small- and wide-angle X-ray diffraction (SAXRD, WAXRD) finally showed that the cuboctahedrally shaped  $\text{Au}_{55}$  clusters obviously touch each other via their edges in a very regular

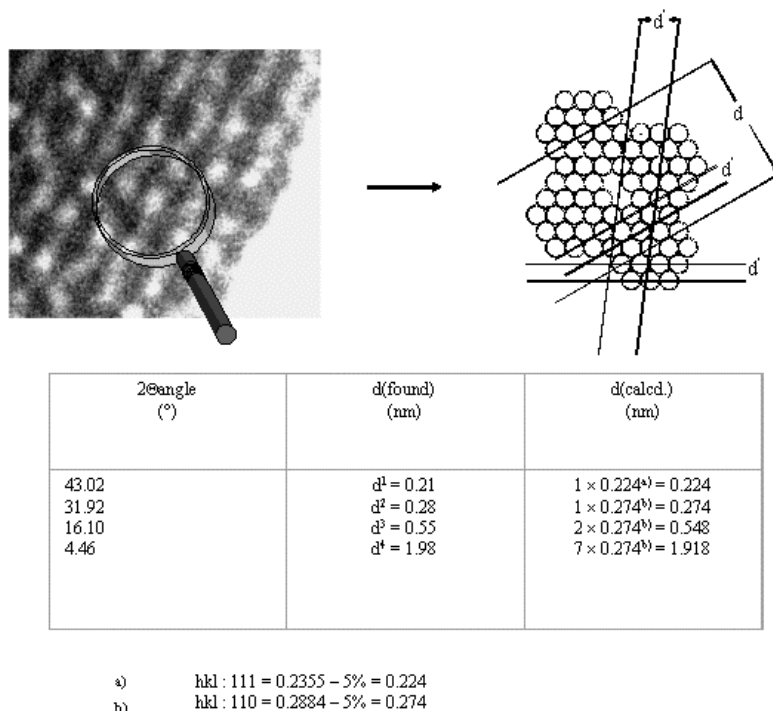


**Fig. 4-12** Magnified TEM image of an  $\text{Au}_{55}$  microcrystal and crystallographic data from SAXRD and WAXRD. The  $hkl$  values 111 and 110 are reduced by 5% because of size-determined contraction of Au–Au distances in small particles.

manner to build up superlattices of an architecture schematically shown in Figure 4-12.

These results show impressively that the organization of metal nanoparticles need not be limited to ligand-protected ones, but that ligand-free particles can also be three-dimensionally organized to build up new modifications of metals, in this case gold.

In contrast to the microcrystals formed of  $\text{Au}_{55}(\text{PPh}_3)_{12}\text{Cl}_6$ , which have been intensively investigated with respect to their electronic characteristics, the 3D assemblies of bare  $\text{Au}_{55}$  clusters have up to now not been subject of physical investigations.

Self-assembly of monodisperse nanoparticles into ordered 3D superstructures is usually achieved by slowly destabilizing a colloidal dispersion. Indeed, if the evaporation rate of a solvent is relatively high, close-packed glassy films of nanoparticles with short-range order are formed [120]. On the other hand, superlattices with low concentrations of lattice defects and a long-range order of nanocrystal arrangement can be formed if the particles are mobile and have enough time to find their lowest energy sites in the superstructure. For example, slow evaporation of a high-boiling carrier solvent at elevated temperatures (50–60 °C) was used to form ordered su-

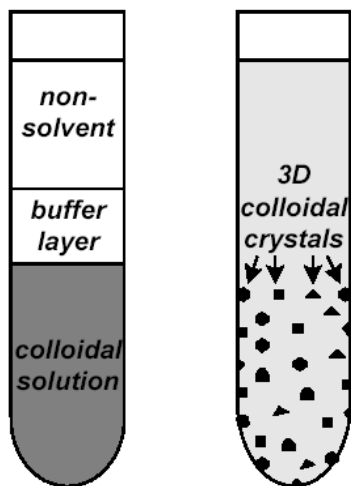


**Fig. 4-13** Schematic outline illustrating the concept of the three-layer oversaturation technique used for the crystallization of monodisperse FePt and CoPt<sub>3</sub> nanoparticles.

perstructures of monodisperse cobalt [120–123], nickel [121], and magnetite [124] nanoparticles. Recently, the technique for growing macroscopic crystals (so-called colloidal crystals) consisting of monodisperse semiconductor or metal nanoparticles as building blocks has been developed [125–127]. The method is based on gentle destabilization of a colloidal solution induced by slow diffusion of a non-solvent into a concentrated solution of monodisperse nanoparticles inside a vertically positioned glass tube, as shown in Figure 4-13. The colloidal crystals nucleate and grow preferentially on the walls of a glass tube. The growing process usually takes several weeks. The spatial distribution of local oversaturations caused by the diffusion of a nonsolvent determines the quality of the colloidal crystals. To make the oversaturation front less sharp than in the case of a direct solvent-nonsolvent contact, a buffer layer with low, but not negligible, solubility for nanocrystals was inserted between solvent and nonsolvent layers. This technique allowed preparation of perfectly faceted colloidal crystals with sizes from tens of microns up to a hundred microns from monodisperse CdSe [125], FePt [126], and CoPt<sub>3</sub> [128] nanocrystals.

Figures 4-14a and b show optical micrographs of FePt colloidal crystals adhering to the glass. The crystals grew preferably in the form of faceted triangular or hexagonal platelets, 10–30  $\mu\text{m}$  in size, on a slide. Crystals with a pyramidal-like shape were also observed. Scanning electron microscopy (SEM) provides a closer look at the morphology of colloidal crystals. In the case of FePt, faceted triangular platelets, incomplete hexagonal platelets, and tetrahedral colloidal crystals with imperfect sides showing terraces and cleaved ledges (Figure 4-14c–e) were clearly distinguishable. Figure 4-14 shows a TEM image taken from a small fragment of the

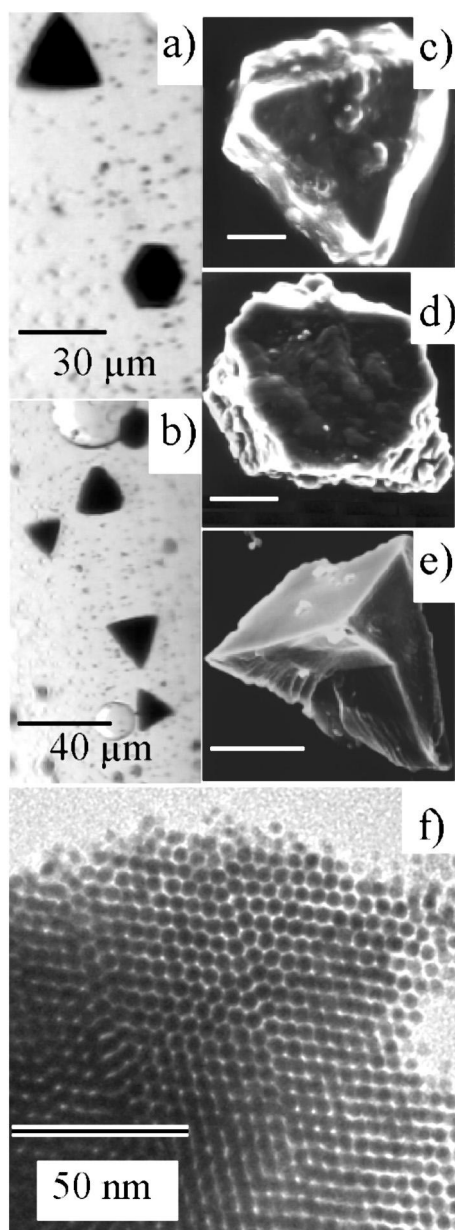


**Fig. 4-14** Optical micrographs (a, b) and SEM images (c, d, e) of colloidal crystals of FePt nanocrystals illustrating their different shapes. TEM image (f) of the fragment of an FePt colloidal crystal. Reproduced from [126], Copyright 2001, with permission from Wiley-VCH.



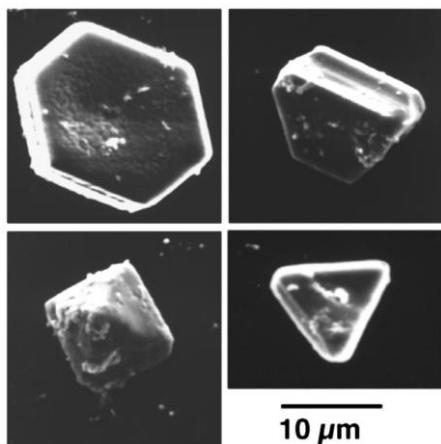


**Fig. 4-15** SEM images of colloidal crystals of CoPt<sub>3</sub> nanoparticles illustrating their different shapes. Reproduced from [128], Copyright 2002, with permission from the American Chemical Society.

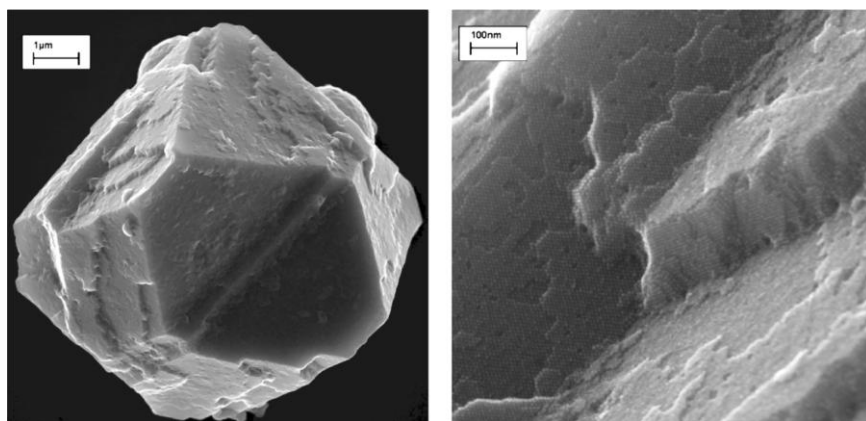


**Fig. 4-16** HRSEM images of the surface of a CoPt<sub>3</sub> colloidal crystal.

FePt colloidal crystal obtained by mechanical grinding and treatment in an ultrasonic bath. Hexagonal arrangements of nanocrystals, i.e. building blocks of the colloidal crystals, are clearly seen at the edges of the crystalline pieces. Figure 4-15 shows SEM images of well-faceted hexagonal, triangular, and pyramid-like colloidal crystals built of CoPt<sub>3</sub> nanocrystals.

The arrangement of nanocrystals at the surface of colloidal crystals can be investigated using HRSEM (Figure 4-16). Thus, the ledges and terraces of ordered CoPt<sub>3</sub> nanoparticles are clearly seen at the surface of colloidal crystal. These 6.3 nm CoPt<sub>3</sub> nanoparticles are superparamagnetic, with the blocking temperature of 19 K. However, in 3D ordered structures dipolar interactions between adjacent

particles can orient the magnetic moments of individual nanocrystals, and ferromagnetic domains can appear within the supercrystal resulting in considerable increase of the blocking temperature [123, 129].

The self-assembly of magnetic nanocrystals can also be affected by applying an external magnetic field. We have found that relatively large external magnetic fields disturb the crystallization of magnetic nanoparticles into macroscopic colloidal crystals, causing the formation of glass-like solids rather than 3D ordered superlattices.

The direction of the applied magnetic field influences the morphology of self-assembled structures of magnetic nanoparticles [121, 130, 131]. When the field was applied in the plane of the substrate, deposition of Co nanoparticles led to spindle-shaped superlattices with their long axes aligned along the external magnetic field [121, 132]. Within these spindle-shaped aggregates, individual magnetic nanoparticles showed nearly perfect long-range order [121]. CoPt<sub>3</sub> nanocrystals slowly precipitated in the external magnetic field of 0.5 T applied parallel to the substrate, organizing themselves into parallel equidistant stripes, as shown in Figure 4-17a. In such structures, the periodic stripes of close-packed CoPt<sub>3</sub> nanocrystals were separated from each other by regions where no nanocrystals were deposited. The period of these self-assembled gratings decreased with increase in the strength of the external magnetic field.

A magnetic field applied perpendicularly to the substrate induces the formation of 2D hexagonal superlattices of individual Co nanoparticles [132]. Pileni et al. [130] observed the formation of a hexagonal network of ca. 1  $\mu\text{m}$  dot-shaped aggregates made of 8 nm cobalt nanoparticles. CoPt<sub>3</sub> nanocrystals (4 nm) deposited under the magnetic field of 0.9 T applied perpendicularly to the substrate can self-assemble into needles of diameter 0.1–2  $\mu\text{m}$  and length up to 100  $\mu\text{m}$  (Figure 4-17b). HRSEM investigation revealed no long-range ordering of CoPt<sub>3</sub> nanoparticles inside these needles.

Self-organization phenomena in colloids of magnetic nanoparticles (ferrofluids) induced by external magnetic fields have attracted considerable attention because of their importance from both fundamental and an applied perspectives [133]. However, the lack of systematic investigations and some contradictory published results can be noticed, probably because of the relative novelty of this subject. Wirtz et al. [134] suggested that the formation of macroscopic one-dimensional periodic patterns composed of high- and low-concentration regions in a ferrofluid is possible only in an oscillating magnetic field. On the other hand, Wang et al. succeeded in forming periodic branched structures similar to those shown in Figure 17a under a constant magnetic field [135]. Recently, Wen et al. modeled the self-assembly of planar magnetic colloidal crystals under an external magnetic field using glass microspheres coated with nickel floating at the interface of two immiscible liquids of different densities [136]. A hexagonal lattice with the lattice constant steeply increasing with increase of magnetic field strength was observed when the magnetic field was applied perpendicularly to the plane of the magnetic particles. Tilting the magnetic field at an angle of 60° away from the normal projection transformed the hexagonally ordered monolayer into equidistant straight

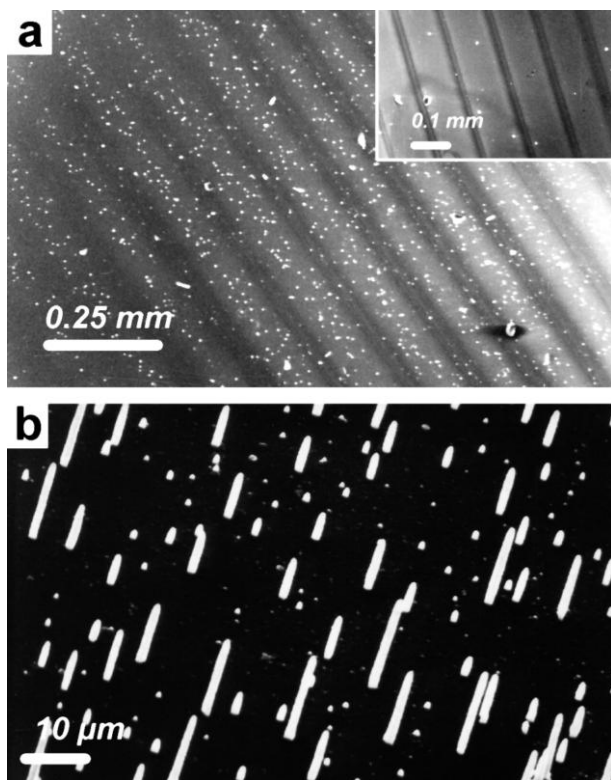


**Fig. 4-17** **a** Stripes of 9 nm CoPt<sub>3</sub> nanocrystals deposited in a magnetic field of 0.5 T applied parallel to a glass substrate. **b** Needles composed of 4.0 nm CoPt<sub>3</sub> nanocrystals deposited in the magnetic field of 0.9 T applied perpendicularly to a glass substrate. The image was acquired at a 40° tilt of the substrate.

chains of particles aligned along the field [136]. Studying self-organization phenomena in ferrofluids requires extremely monodisperse samples of magnetic nanoparticles, because the magnetic dipole moment of a single-domain nanoparticle is proportional to the third power of the radius, and therefore particles of different sizes have different susceptibilities to the magnetic field. The considerable progress in the preparation of monodisperse magnetic nanocrystals achieved during recent years will probably help our further understanding self-organization and phase behavior of ferrofluids.

#### 4.2.2

##### Ordered Monolayers of Metal Nanoparticles

Nature tends to organize materials three-dimensionally. This is why 2D assemblies usually do not grow except within special experimental conditions. As already mentioned in the previous section on 3D structures, it turned out that formation of

2D assemblies can be achieved without having identical building blocks. More than that, the tolerance with respect to deviations from size and shape is found to be even larger than in the 3D case. The formation of 2D structures of metal nanoparticles has therefore developed into a broad field in nanoscience, with promising aspects regarding future applications.

The present section deals with the different techniques of making ordered monolayers. Double and multiple layers up to thin films will also be considered here, since these systems are not covered by the definition of 3D crystals given in Section 4.2.1.

The generation of ordered 2D structures of metal nanoparticles can be achieved by very different techniques:

- self-assembly from solution
- use of pre-prepared templates
- writing structures with special techniques.

In the following, examples of these three principal routes will be presented and discussed.

#### 4.2.2.1 Self-Assembly

Self-assembly of nanoparticles on appropriate substrates is, without doubt, the simplest way to make monolayers. However, there are several disadvantages associated with this method: there is little or no influence on the structure and extension of the monolayers. Formation of self-assembled monolayers (SAMs) depends on experimental conditions, making reproducibility difficult. Nevertheless, many quite impressive 2D structures of metal nanoparticles have become known in the course of the last decade.

One of the first hints that gold nanoparticles can be deposited in an ordered manner came from Schiffrin et al. [137]. Gold particles (8 nm), prepared in a two-phase liquid-liquid system and stabilized by dithiols [138], gave cross-linked assemblies whose quality of ordering was rather limited compared with recent results. However, these very first results showed that 2D self-assembled arrays can be produced.

This research group and others contributed considerably to the improvement of 2D architectures by varying the experimental conditions [139]. Instead of dithiols, tetraalkylammonium bromides [140],  $[R_4N]^+Br^-$ , are used, whereby the separation of the clusters depends on the chain length of R in  $[R_4N]^+$ . Bilayered structures also became available with these particles, forming unusual patterns owing to the occupancy of 2 gold saddle sites, and leading to linear and circular arrangements. The reason for this unexpected structure is to be seen in the balance between local electrostatic repulsion and dispersion forces between the ammonium stabilized particles.

Schiffrin et al., also for the first time, made another important discovery: they fabricated bimodal ensembles of nanosized gold particles. Alkanethiol-stabilized gold nanoparticles of different but well-defined sizes can organize two-

dimensionally, namely with size segregation, each region consisting of hexagonally close-packed structures, randomly positioned particles, and, most importantly, ordered bimodal arrays also.

“Alloy-like” bimodal 2D structures, consisting of two different metals, are likewise available, as was shown for silver and gold [141, 142]. There seems to be a relationship between the geometrical packing of these sphere-like particles and that of intermetallic alloys on an atomic scale. This follows the well-known Laves rules [143], which describe the ratio of the atomic radii  $r_A$  and  $r_B$  of two metallic species  $r_A/r_B$  (where  $r_A > r_B$ ) and of the local number ratio of the two metals  $n_A/n_B$ . Furthermore, there are polarizability components to be considered. In the case of only one metal of two different particle sizes ( $< 10$  nm), the 2D lattice structures mainly depend on the ratios  $n_A/n_B$  and  $r_A/r_B$ , since polarization effects can be neglected.  $AB_2$  structures are formed if  $n_A/n_B = 0.5$  and  $0.482 < r_A/r_B < 0.624$ . If, however,  $n_A/n_B = 1$  and  $0.27 < r_A/r_B < 0.425$ , AB lattices with the NaCl structure result. Both alternatives are sketched in Figure 4-18.

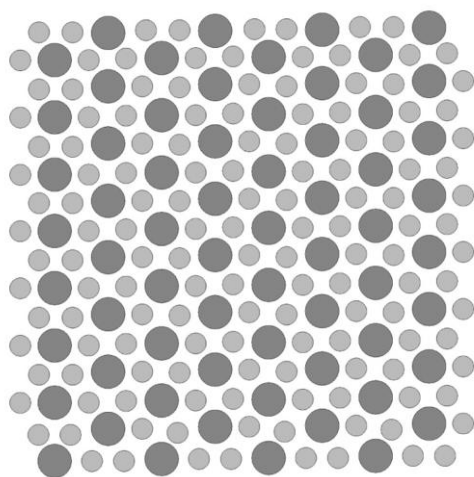
An Au/Ag mixture whose particles are of approximately the same size gives only randomly oriented colloids. However, an Au/Ag 10:1 mixture with 8 nm Au and 5 nm Ag particles results in an  $AB_2$  superlattice, in agreement with the Laves alloy rules. It should be stated that these comparisons of true alloys with mixtures of nanoparticles of different sizes are not really permissible, since the conditions do not correspond. For instance, the fact that the nanoparticles are ligand-stabilized means that the metal cores do not really touch each other. However, as a simple model to understand the different structures of the 2D superlattices it works quite satisfactorily.

When two monodisperse colloids of  $CoPt_3$  nanocrystals (4.5 nm and 2.6 nm in diameter) were mixed together, followed by slow evaporation of the solvent, an  $AB_5$ -type superlattice analogous to the structure of the intermetallic compound  $CaCu_5$  [144] was obtained (Figure 4-19) [128]. A similar structure was observed for binary mixtures of latex spheres of two different sizes [145, 146]. In the first plane of this lattice (Figure 4-19), each 4.5 nm  $CoPt_3$  nanocrystal is surrounded with a hexagon formed by 2.6 nm nanocrystals. The second plane consists only of hexagons of small particles, and the third plane repeats the first.

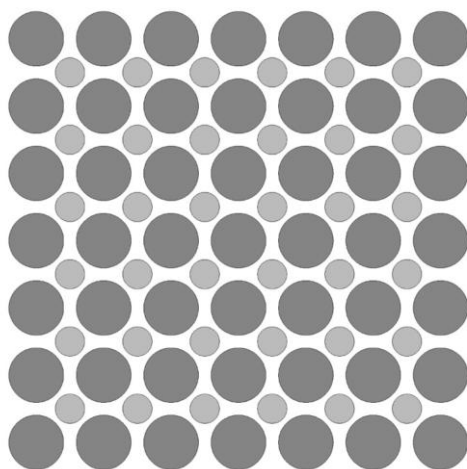
Well-ordered and largely extended (up to 1  $\mu m$ ) 2D superlattices formed by self-organization of silver and gold nanoparticles protected by alkylthiolates were found by Whetten et al. in connection with the formation of 3D assemblies (see Section 4.2.1) [109, 110]. The Ag particles were produced by a special aerosol technique in which elementary silver was evaporated at 1200–1500 K into an atmosphere of helium, followed by a cooling step to give 4–5 nm Ag particles. These were finally cocondensed with an excess of alkylthiols ( $C_{12}$  chains) [110].

The gold nanoparticles were the same as those used for the fabrication of 3D crystals [109]. Fcc-structured monolayers and multilayers were formed, from solution, on carbon-coated copper grids. Detailed structural investigations are described in the original literature.

Other groups also contributed to this development in the second half of the 1990s, mostly also using the noble metals silver and gold [147–149, 113].



a)



b)

**Fig. 4-18** Sketch of 2D AB<sub>2</sub> (a) and AB (b) superlattices.

Spontaneous self-assembly was observed when colloidal solutions of CoPt<sub>3</sub> nanocrystals were spread onto a substrate, with subsequent slow evaporation of the carrier solvent [127, 128]. Depending on the particle size and conditions of solvent evaporation, several kinds of self-organized superstructures were obtained. Figure 4-20a shows a TEM overview image of a close-packed monolayer of 4.8 nm CoPt<sub>3</sub> nanocrystals. If the surface coverage with nanocrystals was thicker than one monolayer, nanocrystals of the second layer occupied positions between the nanocrystals in the first layer (Figure 4-20b, c). Owing to the relatively large interparticle spacing

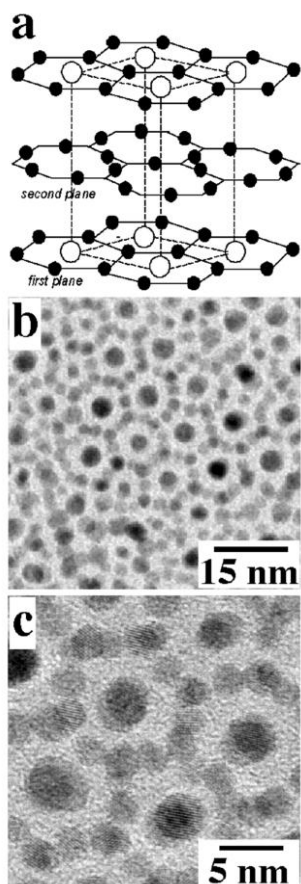


**Fig. 4-19** a Schematic view of an intermetallic compound  $\text{CaCu}_5$ . b, c TEM images illustrating  $\text{AB}_5$ -type superstructure formed by  $\text{CoPt}_3$  nanocrystals with bimodal size distribution. Reproduced from [128], Copyright 2002, with permission from the American Chemical Society.

(ca. 2.5 nm) maintained by the bulky ACA capping ligands, two layers of  $\text{CoPt}_3$  nanocrystals formed the above mentioned structure, observable for different nanocrystal sizes. The third layer of nanocrystals occupied the positions typical of the cubic close packing (ccp) structure (Figure 4-20d, e). Figure 4-20e shows a magnified image of a three-layered assembly of ca. 4.0 nm  $\text{CoPt}_3$  nanocrystals. The difference between the phase contrast of the two underlying layers and that of the darker third layer allows us to attribute each nanocrystal to the layer it is placed in and to conclude that  $\text{CoPt}_3$  nanocrystals are packed into a ccp-like superlattice where the nanocrystals are separated from each other by thick (2.5 nm) organic shells. Figure 4-20f shows a TEM image of a multilayer 3D superlattice where the 4.5 nm  $\text{CoPt}_3$  nanocrystals are arranged in a nearly defect-free 3D structure, ex-

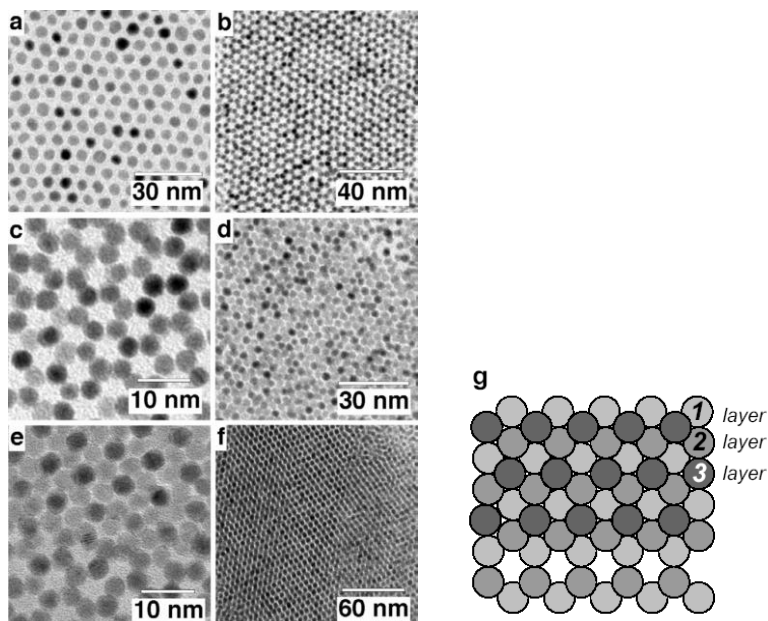


**Fig. 4-20** TEM images of (a) a monolayer of 4.8 nm CoPt<sub>3</sub> nanoparticles; (b) and (c) two layers of 3.6 and 4.0 nm CoPt<sub>3</sub> nanoparticles; (d) three layers of 3.6 nm CoPt<sub>3</sub> nanoparticles; (e) three layers of 4.0 nm CoPt<sub>3</sub> nanoparticles; (f) more than five layers of 4.5 nm CoPt<sub>3</sub> nanoparticles;

(g) graphical illustration of a three-layer arrangement of CoPt<sub>3</sub> nanocrystals. Reproduced from [128], Copyright 2002, with permission from the American Chemical Society.

hibiting long-range order. The graphical illustration (Figure 4-20g) clarifies the three-layer arrangement of CoPt<sub>3</sub> nanocrystals.

The shape of the individual nanocrystals can strongly affect the morphology of self-assembled structures [150–152]. In the case of spherical particles, the crystal-line lattices of individual nanocrystals are as a rule randomly oriented within a superstructure. However, faceted and, in particular, cubic nanocrystals can form “lattice-matched superstructures”, in which each nanocrystal has the same orientation as its neighbors (Figure 4-21). Such superstructures are of interest for creating materials with a high magnetic anisotropy constant, because of the possibility of aligning the axes of easy magnetization of individual nanocrystals.

The high magnetic anisotropy of CoPt<sub>3</sub> nanocrystals [153] makes them superior candidates for realizing this new kind of artificial solid.

Another exciting example of the effect of particle shape on self-assembly is the formation of the cobalt nanorod superstructures observed by Chaudret et al. [154]. Exceptionally monodisperse cobalt nanorods were synthesized by thermal decomposition of Co( $\eta_3$ -C<sub>8</sub>H<sub>13</sub>)( $\eta_4$ -C<sub>8</sub>H<sub>12</sub>) organometallic precursor in anisole at 150 °C in the presence of hexadecylamine and stearic acid under hydrogen at a pressure of 3 bar. Upon aging the colloidal solution, the Co nanorods stuck to each other, forming a superstructure consisting of perfectly aligned nanorods (Figure 4-22).



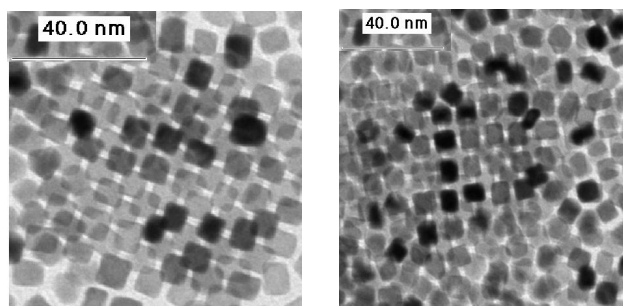


**Fig. 4-21** TEM images of self-assembled structures of cubic  $\text{CoPt}_3$  nanocrystals.

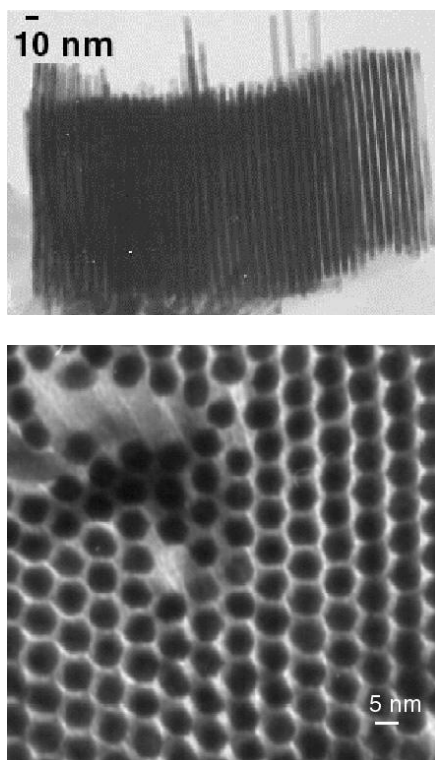


**Fig. 4-22** 3D organization of hcp cobalt nanorods. Side and top views. Courtesy of Dr. B. Chaudret.

Note that the axes of easy magnetization of individual nanorods are aligned in one direction, so that one would expect high magnetic anisotropy and very high coercivity of the material obtained.

The wetting properties of the substrate can influence the superlattice morphology [121]. If the colloidal solution of nanoparticles wets the substrate, a 2D superlattice grows preferentially, forming a monolayer. As the surface coverage in-

creases, the nanocrystals adsorb to the ledges and kinks of the growing structure, forming terraces that extend laterally across the substrate. If the colloidal solution does not wet the substrate, a 3D superlattice grows preferentially, with facets reflecting the packing symmetry inherent in the nanocrystals. Annealing of the superlattice can change the packing symmetry of self-assembled magnetic nanocrystals. Upon annealing of 2D arrays of  $\epsilon$ -Co nanoparticles under vacuum or inert atmosphere at ca. 300 °C, the packing symmetry of 3D ordered regions was converted from the original hexagonal to cubic [122]. The internal transition of the nanocrystal structure from cubic  $\epsilon$ -Co to hcp-Co was responsible for this change. Further annealing of Co nanoparticles led to dramatic change of the crystalline core, fusing and sintering of nanoparticles, and destruction of the superlattice. The temperature of nanocrystal coalescence may depend on the substrate. Thus no obvious aggregation of PtFe nanocrystals in a monolayer was observed even at 700 °C on an SiO<sub>2</sub> substrate, while on an amorphous carbon surface the particles coalesced at ca. 530 °C [150, 155].

The monolayers described so far are all grown by self-assembly processes where ligand-stabilized metal nanoparticles are deposited on “innocent” surfaces from solution, and this is followed by a more or less fast evaporation of the solvent. Depending on concentration and other experimental conditions, those procedures may sometimes also result in multilayers or even in small 3D microcrystals. Self-assembly processes can, however, also be supported by chemical, electrochemical, magnetic, or mechanical effects. Some examples of these are given in the following sections.

The organization of metal nanoparticles on surfaces is based not only on the presence of almost identical building blocks and attractive forces between them, but also on the interaction between particles and surface. Strong bonds between nanoparticle and surface do not usually lead to ordered structures of any appreciable extension. The reason is that chemically bound particles cannot move sufficiently to support the organization process. For instance, only very small areas of ordered Au<sub>55</sub>(PPh<sub>2</sub>C<sub>6</sub>H<sub>4</sub>SO<sub>3</sub>H)<sub>12</sub>Cl<sub>6</sub> clusters could be obtained on poly(ethyleneimine)-modified surfaces, since the relatively strong acid-base interactions between clusters and surface disturb the organization process [156]. On the other hand, the lack of any interaction between surface and particle may also be disadvantageous, since there is no reason to deposit from solution as long as solvent is present. These conditions often end up in the formation of circles of particles owing to the drying mechanism of the solvent. It turned out that moderate attraction between nanoparticles and surface are best suited to generate ordered areas of remarkable extent. The following examples illustrate these findings.

Au<sub>55</sub>(PPh<sub>3</sub>)<sub>12</sub>Cl<sub>6</sub>, dissolved in dichloromethane, can be distributed in a very thin film on a water surface. The particles self-assemble on this surface, resulting in relatively small hexagonal or square structured islands that can be transferred to TEM grids for imaging [157]. Figure 4-23 shows some of these small islands. This self-assembly process can be drastically improved if the attraction between the surface and the nanoparticles is slightly increased. A monomolecular film of appropriate polymer molecules at the water-dichloromethane phase transition sup-

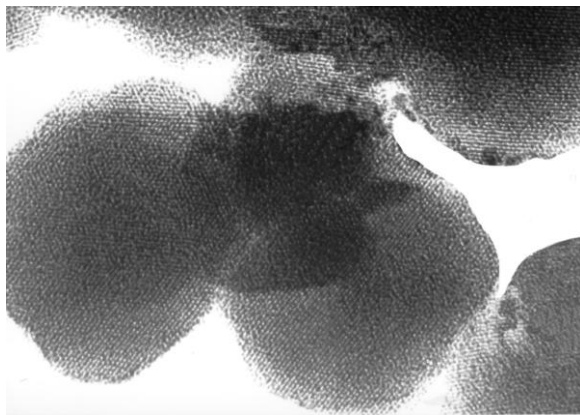


**Fig. 4-23** TEM image of  $\text{Au}_{55}(\text{PPh}_3)_{12}\text{Cl}_6$  clusters, self-assembled on a water surface from dichloromethane solution.

ports the attraction. Molecules with an extended  $\pi$  electron system, interacting with the electronic  $\pi$  system of the phenyl rings of the  $\text{PPh}_3$  ligands, turned out to work best. Examples are poly(*p*-phenyleneethynylene) (PPE) derivatives, but poly(vinylpyrrolidone) (PVP) and several other polymers gave comparable results [158, 159]. In addition, these polymer films act as a kind of “carpet”, supporting the transfer to solid substrates. Figure 4-24 impressively demonstrates the difference between self-assembled areas without (Figure 4-23) and with polymers.

The relevance of the weak particle-surface interaction could also be demonstrated when alkyl- instead of aryl-substituted ligands were used: there was no ordering process at all. However, if the same clusters with an “alkyl surface” were used in combination with saturated polymers such as poly(methylmethacrylate) (PMMA), reasonable ordering could be observed again [157].

Independently of the polymer, two different arrangements of  $\text{Au}_{55}(\text{PPh}_3)_{12}\text{Cl}_6$  were observed: hexagonal and square. The reason for this is not quite clear; however, it can be postulated that the very first contact between a few clusters will be decisive for the formation of the one or the other structure, since the orientation of the  $\text{PPh}_3$  ligands between different clusters could determine the further growth. Figure 4-25a illustrates the situation schematically, while Figure 4-25b shows a simulation of a full space model, elucidating the different densities [160]. Indeed, statistics calculated from many different TEM images clearly show different cluster-cluster distances, depending on the structure of the monolayers, as indicated in Figure 4-25a.

The TEM image in Figure 4-26 shows a cutout of a perfectly square-packed monolayer of  $\text{Au}_{55}(\text{Ph}_2\text{PC}_6\text{H}_4\text{SO}_3\text{H})_{12}\text{Cl}_6$  clusters [158].

#### 4.2.2.2 Guided Self-Assembly

A “guided” self-assembly of gold nanoparticles on patterned GaAs surfaces has been elaborated by R. P. Andres et al. for developing arrays electronically to

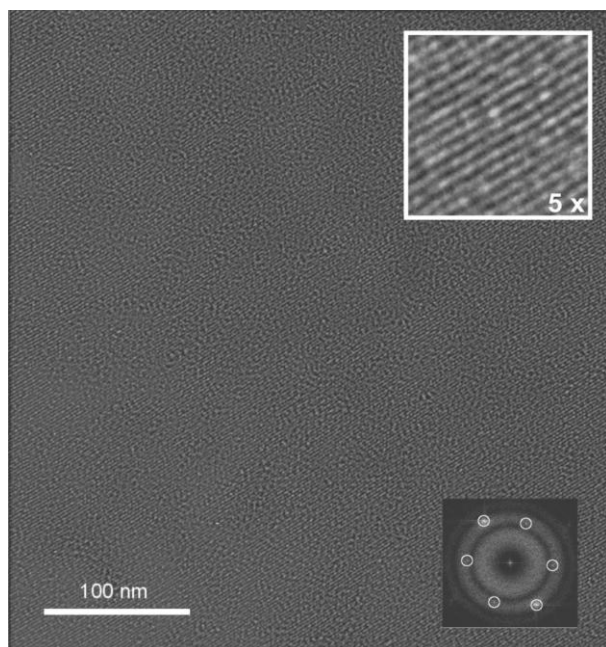


**Fig. 4-24** TEM image of a cutout of extended self-assembled  $\text{Au}_{55}(\text{PPh}_3)_{12}\text{Cl}_6$  arrangements, deposited on a polymer film as support.

form semiconductor device layers [166]. A structured Be-doped GaAs layer is covered by a monolayer of xylyl dithiol,  $\text{HS}-\text{CH}_2-\text{C}_6\text{H}_4-\text{CH}_2-\text{SH}$ . If a solution of dodecanethiol-protected 5 nm Au nanoparticles in hexane is spread on a convex water surface, a uniform monolayer of nanoparticles is formed, in accordance with the procedure described above. If the modified GaAs surface is caused to briefly touch the nanoparticle monolayer, this is transferred to the substrate. It is assumed that dodecanethiol ligand molecules are partially substituted by the xylyl dithiol covering the surface. The quality of the hexagonal close-packed monolayer of gold nanoparticles was controlled by transferring samples to TEM grids. It can be assumed that the quality of the monolayer does not change if the thiol-modified GaAs surface is used instead of the grid. This procedure could be of particular interest, since the self-organization happens on a water surface, and the monolayer is then strongly fixed onto another surface by covalent bonds. Rinsing of the surface by hexane only removes particles that are not tethered, but not the chemically fixed ones.

Langmuir-Blodgett (LB) techniques have also been used to fabricate ordered 2D structures of metal nanoparticles. Several approaches have become known using particles in the size range 3–5 nm [162–168]. J. R. Heath et al. reported [163] that success in the organization of alkanethiolate-protected nanoparticles using LB techniques typically depends on the ratio of ligand length to surface pressure.

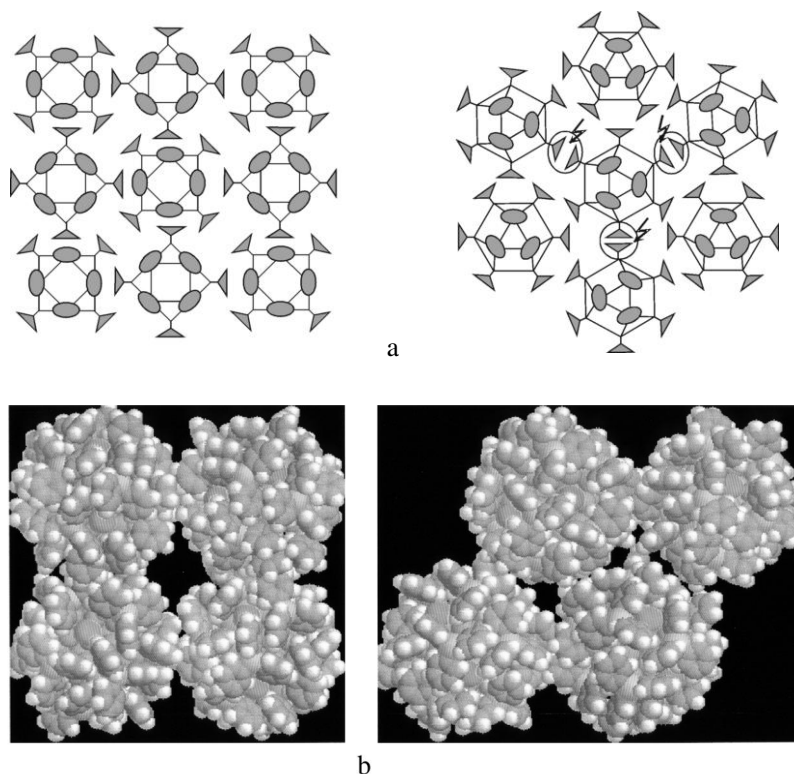


**Fig. 4-25** Sketch of variously oriented  $\text{Au}_{55}(\text{PPh}_3)_{12}\text{Cl}_6$  clusters, indicating the  $\text{PPh}_3$  shapes and their positionings towards each other, resulting in square or hexagonal closed-packed structures (a). Full space models of both orientations (b).

Ligand-stabilized  $\text{Au}_{55}$  clusters only ca. 2 nm in size were first organized in LB films in 2000 [169], but only relatively small ordered areas were observed. Much better results were obtained when the surface pressure was increased. Under these conditions,  $\text{Au}_{55}$  clusters coated with  $\text{PPh}_3$  ligands, some of which had been substituted by hydrophilic derivatives to make the particles amphiphilic, formed much larger areas of ordered particles [170]. Repeated compression of the films to 35 mN/m with alternating relaxation gave quite adequately ordered films of dimensions  $0.25\ \mu\text{m} \times 0.35\ \mu\text{m}$ .

From the moment of introduction of the photonic bandgap concept by Jabolonovitch and John [171, 172], materials possessing a three-dimensional periodicity of the dielectric constant have attracted increasing attention. The periodically varying index of refraction in photonic crystals causes a redistribution of the density of photonic states due to Bragg diffraction, which is associated with stop bands for light propagation. Chemical self-assembly (bottom-up) methods have been utilized for making 3D photonic crystals (so called artificial opals) from colloidal silica or

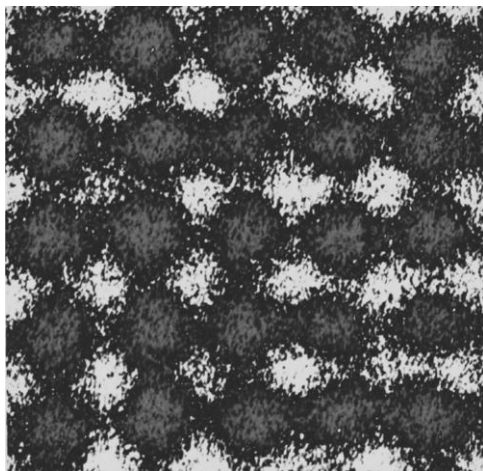


**Fig. 4-26** TEM image of a magnified cutout of perfectly square-packed  $\text{Au}_{55}(\text{Ph}_2\text{PC}_6\text{H}_4\text{SO}_3\text{H})_{12}\text{Cl}_6$  clusters.

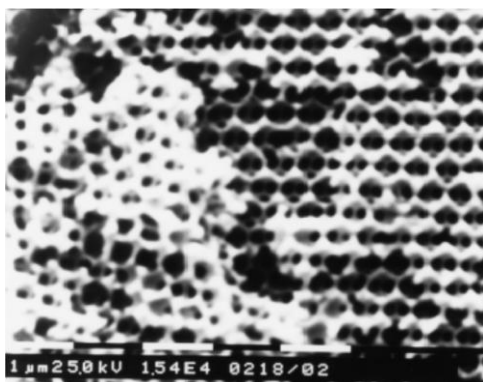


**Fig. 4-27** SEM image of an inverse colloidal crystal made from PtFe nanocrystals. Courtesy of Dr. N. Gaponik.

micron-size polymer spheres. Using artificial opals as templates, so-called “inverse opals” possessing pronounced photonic bandgap can be prepared by impregnation of voids with different materials followed by removal of the spheres by annealing or dissolution, which can give a complete photonic bandgap [173]. Magnetic nanocrystals can be used for the fabrication of metal-dielectric inverse opals addressable through an external magnetic field. Figure 4-27 shows an SEM image of an inverse FePt colloidal crystal obtained by complete impregnation of a 3D template of monodisperse latex microspheres with FePt nanocrystal followed by dissolution of polymer spheres in toluene.

Self-assembled structures are quite suitable for the study of the electronic behavior of ordered monomolecular films and have contributed considerably to a

better understanding of the quantum size nature of metal nanoparticles. On the other hand, it is quite clear that metal particles in future nanoelectronic devices should be in structures in which the quantum dots are not self-arranged, but are placed at definite positions. This is a big problem that will only be solved by techniques other than self-assembling.

The use of appropriate templates is one possible way to succeed; however, the generation of the templates needs to be developed. Remarkable progress in the organization of metal nanoparticles to form given structures involved the use of micelles. M. Möller et al. have contributed to this development in numerous ways. They use micellar structures in block copolymers as nano reaction vessels to generate and to organize metal nanoparticles. Although this technique is not based on the self-assembling of metal nanoparticles, it is linked with the organization of the micelles in the polymers. This technique differs from the self-assembly processes described above, but it cannot be considered to solve the problem of creating artificial architectures. However, compared with the classical self-assembly procedures, the application of preformed micelles opens up novel routes for handling nanoparticles.

A-B diblock copolymers can be used to form micelles which allow the preparation of thin, coherent films of well-developed structure [174–180]. Poly(styrene)-block (b)-poly(ethylene oxide) as well as poly(styrene)-b-poly(2-vinylpyridine) turned out to act as useful combinations for generating well-ordered compartments in which metal nanoparticles can be fabricated in various ways. Figure 4-28a illustrates the formation of diblock copolymers from polymer A and polymer B ending with nanospheres which can be transferred to films of highly ordered micelles. Figure 4-28b shows schematically the formation of metal nanoparticles inside the micelles.

As a typical example, the formation of gold nanoparticles will be described [181]. Both of the above-mentioned block copolymers can be treated with  $\text{HAuCl}_4$  or  $\text{LiAuCl}_4$ . The tetrachloroaurates penetrate into the micelles in nonpolar solution to form thermodynamically stable dispersions inside the holes. The solubilization can be supported by ultrasound irradiation. Subsequent reduction of the gold salts results in formation of nanoparticles. Suitable reducers are hydrazine and  $\text{NaBH}_4$ . The dispersion of the generated nanoparticles can be controlled by the domain structure of the block copolymer [175, 176]. Because of the reduction mechanisms it is not possible to prepare one single gold monocrystal per micelle by this method, but instead multiple nanoparticle formation in each domain is observed. Figure 4-29 shows a TEM image of an ordered array of micelles, each loaded with several gold particles [176]. One single nanoparticle per micelle can be obtained, even with systematic variation of particle size, if the process is performed at the glass transition temperature (90 °C) of the poly(ethylene oxide). Particles of 6, 4, and 2.5 nm diameter have been prepared by variable loading ratios and micelle size and are shown in Figures 4-30a, b, and c.

Self-assembling processes leading to film formation usually occur by evaporation of the solvent from solutions containing loaded micelles. Micellar film formation can also be brought about by dipping platelets of different materials such as GaAs,

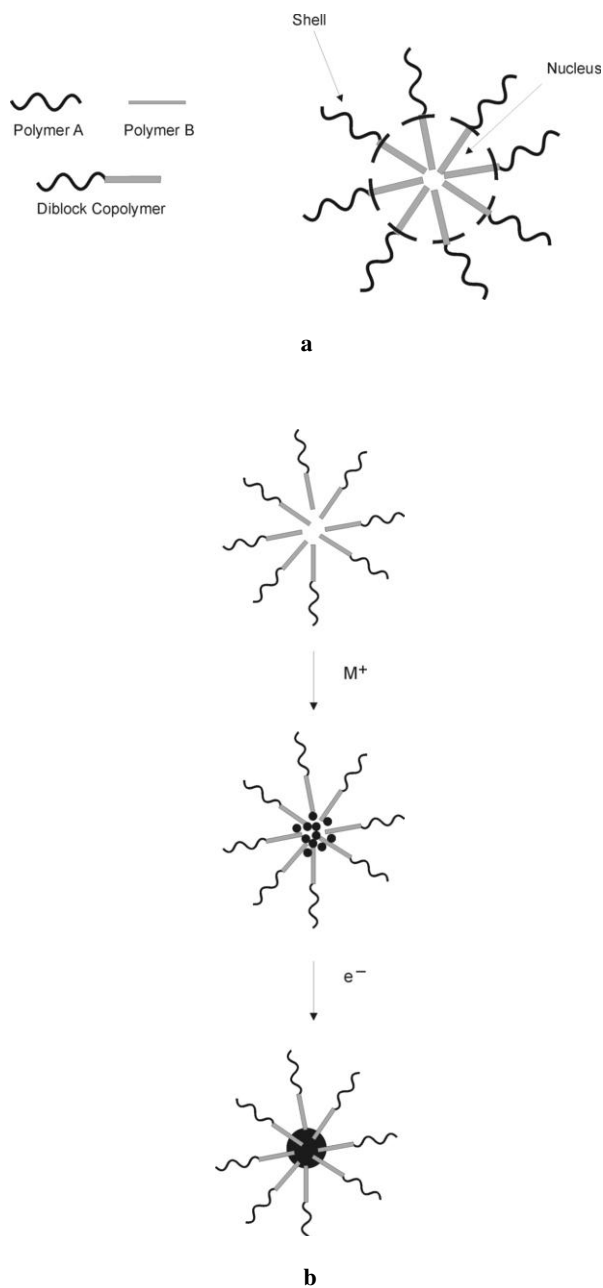


**Fig. 4-28** Formation of diblock copolymers from polymer A and polymer B, resulting in micelles (a). Formation of metal nanoparticles inside the micelles (b).



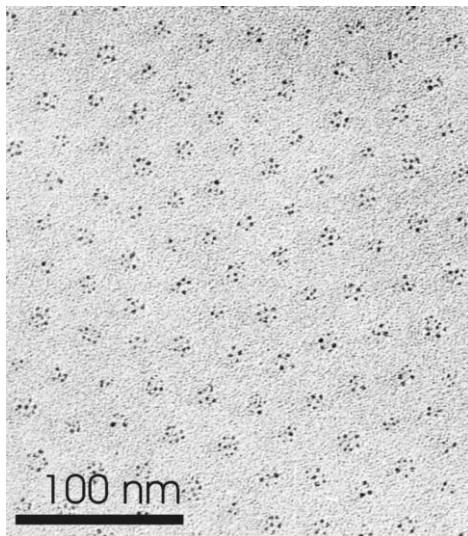


**Fig. 4-29** Gold particles inside of an ordered array of micelles.

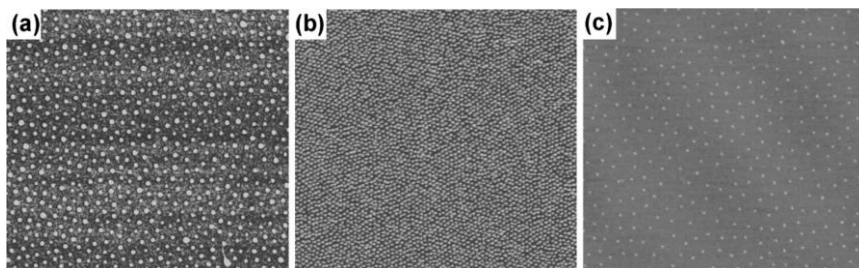


**Fig. 4-30** TEM images of gold nanoparticles of various sizes generated in micelles of different sizes and by different loading ratios, **a** 6 nm, **b** 4 nm, and **c** 2.5 nm.

InP, glass or carbon-coated copper grids into a corresponding solution and withdrawing them [182].

So, using the four kinetically controlled steps, namely reduction, mineralization, coagulation, and film formation, the structure of nanoparticle-loaded block copolymer composites becomes available, and further use of these materials can be expected.

Gold is by no means the only material that can be incorporated into block copolymer micelles. Other metals such as palladium, silver, and cobalt have been successfully applied, and even nanoparticles of CdS and PbS have been generated inside micelles [183].

An interesting and important continuation of this development is the possibility of removing the diblock copolymer material without losing the ordering of the nanoparticles, so generating nanostructures on different surfaces and with varying

inter-particle distances. Möller et al. developed an elegant method to routinely generate these materials by the use of an oxygen plasma [184–186].

If ordered micellar films on glass or mica, containing either gold nanoparticles or even the non-reduced tetrachloroaurates, are treated by an oxygen plasma at 200 W for 20 min, bare nanoparticles are deposited on the surfaces without any loss of the original order. The formation of nanoparticles from  $\text{AuCl}_4^-$  during the plasma process is traced back to the existence of intermediate oxidation products of the polymer, like CO, and also free electrons. XPS experiments prove the absence of any residual polymer. The as-prepared particles are strongly fixed on the surfaces and cannot be removed by rinsing with solvents or by rubbing with a soft tissue. Another remarkable advantage is associated with this method of depositing metal nanoparticles on surfaces: the particle size, the inter-particle distances and thereby the particle density can be varied, and additionally the extension of the covered surfaces is in principle not limited. The three examples in Figure 4-31 are cutouts of  $3\text{ cm} \times 3\text{ cm}$  areas and demonstrate the versatility of this method.

The important point is to use diblock copolymers of different molecular weights and different gold contents. A poly[styrene(800)-b-2-vinylpyridine( $\text{HAuCl}_4$ )<sub>0.5</sub>(860)] (number of monomer units in brackets) gives gold colloids 12 nm in height (AFM) and a periodicity of 80 nm (Figure 4-31a). A styrene:vinylpyridine ratio of 325:75 with the same equivalent of  $\text{HAuCl}_4$  results in 2 nm particles with 30 nm distances (Figure 4-31b), whereas a change to 1700:450 with only 0.1 equivalent of gold acid gives 1 nm particles of 140 nm periodicity (Figure 4-31c) [184].

Other diblock copolymers and metal compounds such as  $\text{H}_2\text{PtCl}_6$ ,  $\text{Pd}(\text{Ac})_2$ ,  $\text{TiCl}_4$  or  $\text{FeCl}_3$  have been successfully used. The less noble metals Ti and Fe are deposited as oxides after plasma treatment.

Gold nanoparticles containing films of diblock copolymers can be used for nanolithographic structuring of surfaces and so may contribute to the search for techniques that allow routine fabrication of nanostructured surfaces. Semiconductor substrates such as GaAs, InP, or layered systems can be covered by micellar films containing gold nanoparticles. If such composites are etched by an  $\text{Ar}^+$  beam, nanostructured surfaces are generated owing to the fact that the nanoparticulated gold is much more rapidly etched than bulk gold or than pure poly(styrene) and poly(vinylpyridine), so that all positions containing gold can be transferred into holes in the underlying semiconductor, as illustrated in Figure 4-32.

In contrast, if a hydrogen plasma is used instead of argon, all organic material is removed first, so that only the metal nanoparticles remain. On subsequent etching by an ion beam chlorine plasma, GaAs cylinders of up to 80 nm in height could be prepared [187]. Gold nanoparticles, generated from a gold-loaded diblock copolymer film by an oxygen plasma, also act as a mask during continued etching by oxygen [188]. As a result, gold-capped diamond pillars with a diameter roughly corresponding to the size of the gold particles are generated.

The use of so-called S-layers [189] is a combination of self-organization and spatial patterning. S-layers consist of two-dimensional protein crystals. They are formed by nature as the outermost cell surface layer (S-layer) of prokaryotic or-

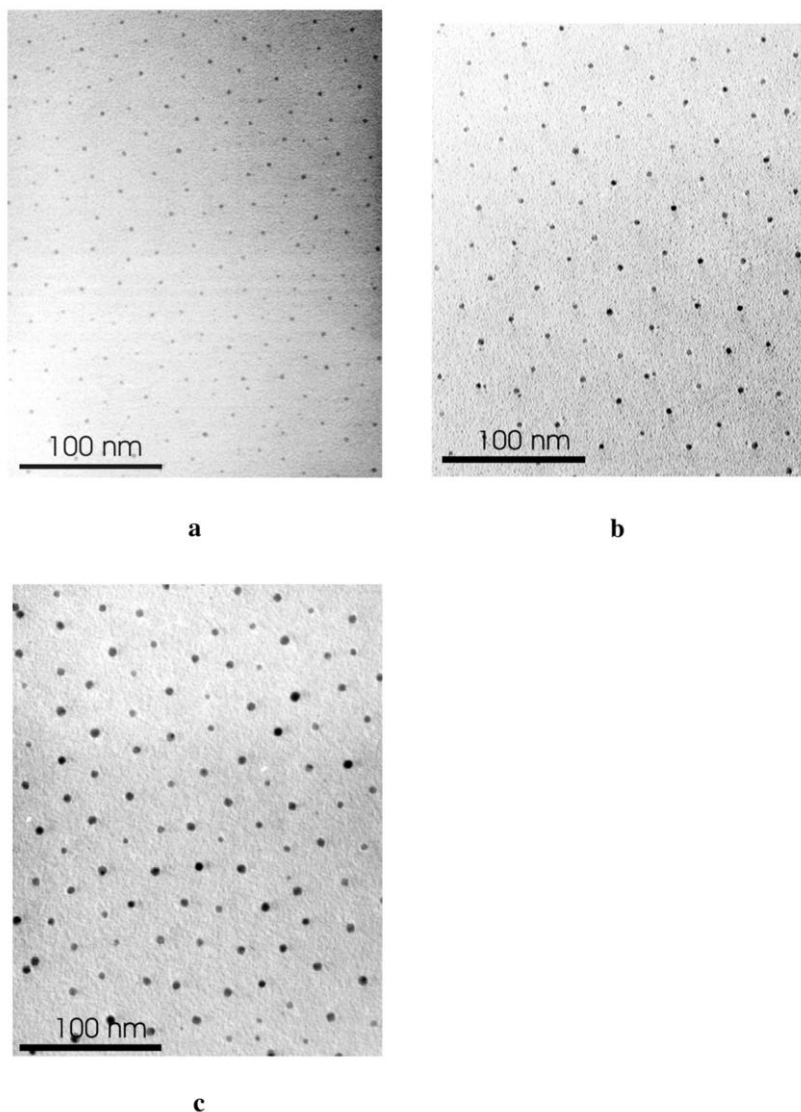


**Fig. 4-31** TEM images of cutouts of  $3 \times 3 \text{ cm}^2$  areas of gold nanoparticles produced in diblock copolymers of different molecular weights and different gold contents.

ganisms. The subunits can recrystallize into nanoporous monolayers in suspension, at liquid-surface interfaces, on lipid films, or on solid substrates. S-layers of *Bacillus sphaericus* CCM 2177 have been used to generate ordered arrays of 4–5 nm gold particles, with a 13.1 nm repeat distance, from  $\text{AuCl}_4^-$  ions [190]. Spontaneous self-assembly processes of 5 nm gold nanoparticles occur at the S-layer of

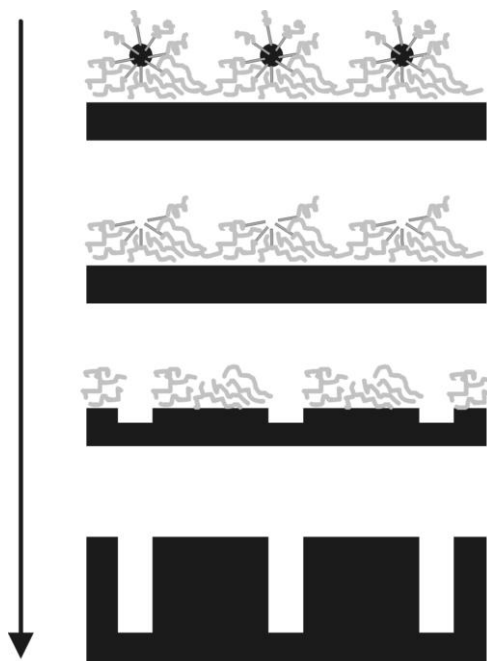


**Fig. 4-32** Scheme of etching semiconductor substrates starting with gold nanoparticles containing micellar films and followed by  $\text{Ar}^+$  beam etching to remove the gold nanoparticles. This forms holes in the substrate with the same diameter as that of the gold nanoparticles.

*Deinococcus radiodurans* to give micron-sized ordered domains [191]. Arrays of 1.9 nm platinum particles were achieved from Pt salts in the S-layer of *Sporosarcina ureae* [191]. These are of square symmetry with a lattice constant of 13.2 nm.

#### 4.2.2.3 Aimed Structures

Up to now we have discussed only two-dimensional arrangements of metal nanoparticles that were based on self-assembly mechanisms, although, as in the case of micellar films, some influence on particle size and periodicity was possible. Arrangements of nanoparticles that are completely free of natural self-assembly processes, thus allowing the formation of arbitrary arrays, seems possible, since Mirkin et al. developed so-called dip-pen nanolithography [192, 193]. This technique is based on the transport of molecules from an atomic force microscope tip through a water meniscus onto a flat surface that attracts the molecules by chemical bonding. The water meniscus is naturally formed in the laboratory's atmosphere. So, moving the tip over the surface, the corresponding molecules are transported to the surface to form programmed patterns. Gold surfaces are very much suited to be decorated with thiol molecules from the tip. The general method of depositing regularly oriented nanoparticles on a surface is shown in Figure 4-33 [194].

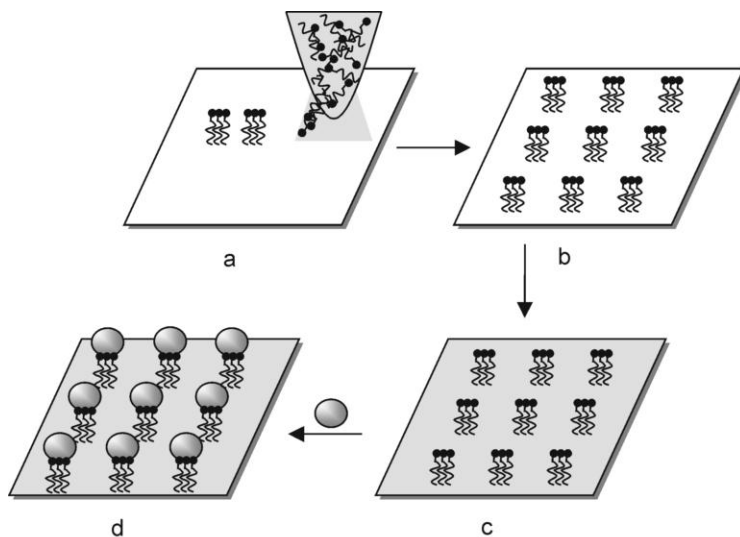


**Fig. 4-33** Formal illustration of dip-pen nanolithography. An AFM tip is loaded by thiol molecules, here 16-thiohexadecanoic acid. Because of the presence of a “natural” water meniscus, the thiols are transported onto a gold surface via the moving tip (a) to form

any kind of pattern (b). Passivation of the unpatterned regions by alkylthiols (c) enables the deposition of nanospheres with basically modified surfaces by interactions with the carboxylic groups (d).

An array of dots of molecules that will attract the nanoparticles in a second step are deposited on the substrate. 16-thiohexadecanoic acid has been used to bind positively charged particles such as protonated amine or amidine-modified polystyrene spheres as building blocks from solution. Beforehand, the unpatterned regions of the gold substrate were passivated by an alkanethiol.

Orthogonal gold assemblies have been fabricated by varying this method in such a way that, after patterning of the gold surface with 16-thiohexadecanoic acid and passivation of the unpatterned regions with 1-octadecanethiol, alkylamine-modified oligonucleotide ( $a = \text{TCTCAACTCGTAA}_{10}$ ) is then chemically bound to the carboxylic groups. Several steps of rinsing with buffer solutions, washing with deionized water, and drying follow. The superiority of the dip-pen technique is impressively demonstrated by adding a second orthogonal structure to the first one: it is possible to replace 1-octadecanethiol by 16-thiohexadecanoic acid molecules coming from the AFM tip under usual writing conditions (0.5 nN, 55% humidity, 23 °C). A second, but different, alkylamine-modified oligonucleotide ( $b = \text{A}_{10}\text{CGCATTGAGGAT}$ ) is then combined with the acid functions, as in the first step. So, two nanopatterns, consisting of two different oligonucleotide sequences, can be created. The  $a,b$ -modified substrate is then treated with  $a'b' = \text{TACGAGTTGAGAATCCTGAATGCG}$  with  $a'$  and  $b'$  complementary to  $a$  and  $b$ . The deposition of gold nanoparticles of two different sizes happens by adding  $a$ - and  $b$ -substituted 13 nm and 30 nm particles. The complement of  $a$  and  $a'$  and  $b$

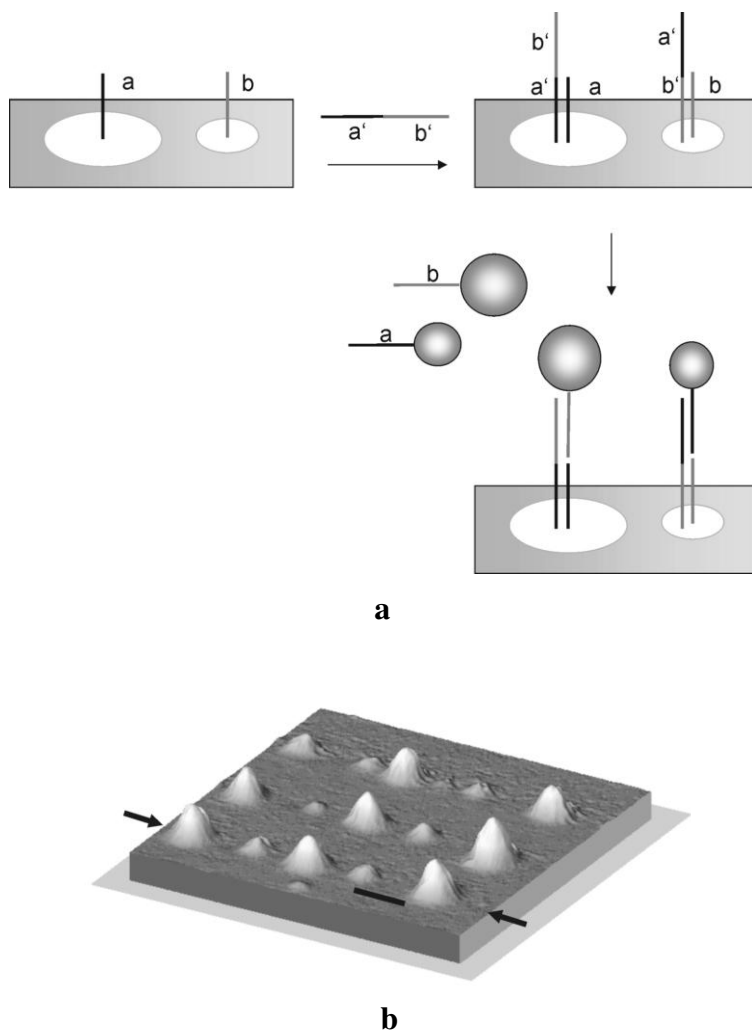


**Fig. 4-34** **a** Schematic illustration of the formation of gold-nanostructures via complementary oligonucleotides. **b** AFM image of as-prepared patterns consisting of gold nanoparticles of different sizes.

and  $b'$  respectively ends up with a regular pattern of both types of nanoparticles [195]. Of course, the fabrication of 2D arrangements of only one type of particle is possible as well. Figure 4-34a illustrates schematically the formation of the nanostructures via complementary oligonucleotides. Figure 4-35b shows an AFM topography image of different Au particles after the orthogonal assembly process.

It can be foreseen that not only can two different sizes of the same kind of metal be used to generate these or other structures, but that different metals can be used as well, opening up manifold possibilities with respect to future applications.

At this point we can conclude that the two-dimensional organization of metal nanoparticles has developed very promisingly. From very simple self-organization via guided self-assembling to the controlled patterning of surfaces, there is a wide variety of routes available now that should in principle make applications in nanoelectronics possible. It should be stated, however, that not all of the organized particles mentioned above can really be used as quantum dots since they are still too big to exhibit those very special electronic properties that are needed for single-electron transitions at room temperature. The quantum-sized characteristics are discussed in detail in Section 5.2.

#### 4.2.3

#### One-dimensional Arrangements

The expression “one-dimensional” is not very well defined. In principle, one-dimensionality could be reduced to the atomic scale, simply considering atoms as the smallest building blocks of wires. In practice this very stringent definition would not make much sense. Nanoparticles as building blocks arranged in only one direction justifies the term “one-dimensional” just as well. However, how do we consider structures of two, three or four parallel rows of “one-dimensional” chains of nanoparticles? It seems reasonable to consider the aspect ratio, i.e. the ratio of length to width of an assembly of building blocks. Three times three particles could be considered as a small two-dimensional area, whereas a structure of three times a hundred or a thousand nanoparticles is better described as one-dimensional. In some cases, if the building blocks are rather big (or are very small three-dimensional particles) or the aspect ratio is not very well expressed, one also speaks of *quasi* one-dimensional structures. Therefore, in the following, there will no longer be a distinction between a truly one-dimensional assembly of nanoparticles and a merely *quasi* one-dimensional assembly.

The one-dimensional organization of metal nanoparticles can be achieved via appropriate templates or by special techniques to be discussed below. There is a very important difference between these and 2D arrangements, where self-assembly processes can be initiated without specific templates.

Templates to organize metal nanoparticles in one direction are rare. Steps on crystal surfaces have occasionally been observed to adsorb nanoparticles in preference to flat terraces, so giving rise to 1D orientations. However, this route has not yet been developed into a common and routinely applicable procedure.

Nanopores are in principle promising candidates if they can be filled with nanoparticles in such a way that the resulting composites can be used for planned investigations or applications. In this connection, nanoporous alumina plays a certain role, since it can easily be prepared as thin films equipped with  $10^9$ – $10^{11}$  pores per  $\text{cm}^2$ , all running parallel through the membrane. These films are formed by anodic oxidation of aluminum surfaces in polyprotic aqueous acids, the applied voltage determining the pore width. The pore length simply depends on the anodization time. So, pores from about 10 up to 200 nm in width and up to some hundreds of  $\mu\text{m}$  in length are available [196–200]. Indeed, several attempts

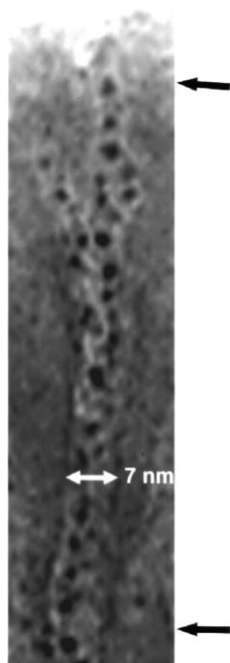


**Fig. 4-35** A 7 nm pore in a nanoporous alumina membrane filled with  $\text{Au}_{55}$  gold clusters, imaged by TEM after sectioning.

have been made to fill these pores with metal nanoparticles [196, 201–203]. Pre-formed particles can be transferred into the pores from solution by vacuum induction, or they can be generated inside the pores by decomposition of previously deposited appropriate complexes. Figure 4-35 shows a TEM image of a sectioned piece of a membrane filled with gold nanoparticles [196].

However, as it turned out, these templates did not yet lead to fully convincing results, i.e., to the perfect wires of nanoparticles which are necessary to study electronic conduction mechanisms, since the lack of only one particle in a row would interrupt the electric conductance. Among other causes of this difficulty, the main one was the length of the pores. For instance, in a pore of a 1  $\mu\text{m}$  thick membrane (a minimum thickness that could still be handled), 500 particles of size 2 nm have to be arranged without defects. This is practically impossible.

Polymer molecules could be promising alternative templates for assembling metal nanoparticles on their surfaces. DNA is one of several candidates for assemblies of up to several microns [204]. Ligand-protected platinum particles of 2–3 nm do in fact add to natural DNA in buffer solution in a very regular fashion and can easily be observed by TEM [211]. Figure 4-36 shows an assembly of DNA strands covered with Pt nanoparticles. These results indicate that DNA might indeed act as a suitable template.



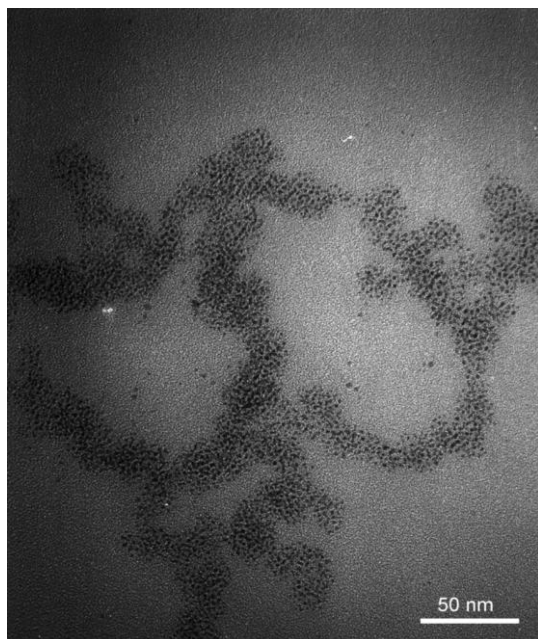


**Fig. 4-36** Double-stranded  $\lambda$ -DNA decorated by 2–3 nm Pt particles bearing a ligand shell of (–)-cinchonidine and acetic acid.

$\lambda$ -DNA has also been used for covering with 3–5 nm Pd particles [206]. Here, preformed particles were not used, but were generated on the DNA surface by reduction of  $\text{Pd}(\text{CH}_3\text{COO})_2$  with a mixture of sodium citrate, lactic acid, and dimethylamine borane.

Colloidal platinum particles have also been generated on DNA, starting with an impregnation step with dichloro(2,2':6',2''-terpyridine)platinum(II) or  $\text{cis-Pt}(\text{NH}_3)_2\text{Cl}_2$ , followed by reduction with  $\text{NaBH}_4$  [207]. Water-soluble thiol-stabilized ca. 2 nm Au particles and  $\lambda$ -DNA combine to form real 1D assemblies or bundles of these filaments [208].

All these methods give *quasi* one-dimensional, but more or less disordered, structures. A rather interesting route to ordered arrangements of gold nanoparticles in combination with DNA has recently become known [209]. The method is based on Coulomb interactions between the negatively charged phosphate backbone of synthetic and natural DNA and positively charged 3.5 nm gold nanoparticles prepared from  $\text{HAuCl}_4$  and  $\text{NaBH}_4$  and capped with lysine molecules. TEM investigations of these hybrid systems indeed prove the formation of equidistant rows of nanoparticles between parallel DNA sequences, as sketched in Figure 4-37.

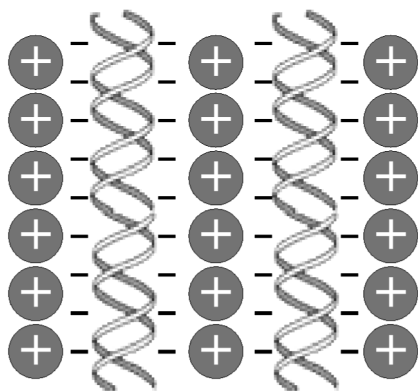


**Fig. 4-37** Sketch of an arrangement of DNA/Au nanoparticles. Positively charged 3.5 nm gold nanoparticles, capped with lysine, add to the negatively charged phosphate backbones of DNA to build up equidistant rows.

A unique kind of one-dimensionally organized metal nanoparticles in connection with DNA as templating material was observed when  $\lambda$ -DNA was reacted with  $\text{Au}_{55}(\text{Ph}_2\text{PC}_6\text{H}_4\text{SO}_3\text{H})_{12}\text{Cl}_6$  [210]. As it turned out, these clusters do not only interact with DNA, like the above-mentioned 2–3 nm Pt particles, by assembling along the double-stranded DNA, but occupy the major grooves of B-DNA, the preferred DNA version in aqueous solution. Molecular dynamics simulations indicated that bare  $\text{Au}_{55}$  clusters 1.4 nm in diameter fit perfectly into the grooves. The loss of parts or even all of the original phosphine ligands can be understood as a substitution reaction of phosphines by phosphates of the DNA backbone, acting as a kind of polydentate system. This can be seen from Figure 4-38a. However, the surprising effect is the degradation of these 1.4 nm particles in the B-DNA major grooves to 0.6–0.7 nm particles in ultra-high vacuum, probably due to the shrinkage of the major grooves of B-DNA, which changes to A-DNA under these conditions. Again, the grooves of this type of DNA fit perfectly to the observed size of particles, which correspond reasonably with  $\text{Au}_{13}$ . This situation is shown in Figure 4-38b. Moreover, these  $\text{Au}_{13}$ -DNA hybrid systems organize in such a way that, probably via gold-gold interactions, equidistant wires of nanoparticles result. The ordering parameter is without any doubt the A-DNA. The simulation and the experimental result are shown in Figure 4-38c.

The formation of the nanowires obviously occurs during drying on the grid used for transmission electron microscopy.  $\text{Au}_{55}$  clusters have never been observed to degrade under comparable conditions. This is obviously a unique instance of a change of a molecular conformation leading to a controlled degradation of nanoparticles. Under the conditions of electron beam irradiation, however, the cluster-DNA hybrid system is rather unstable. In the course of seconds, the lines break

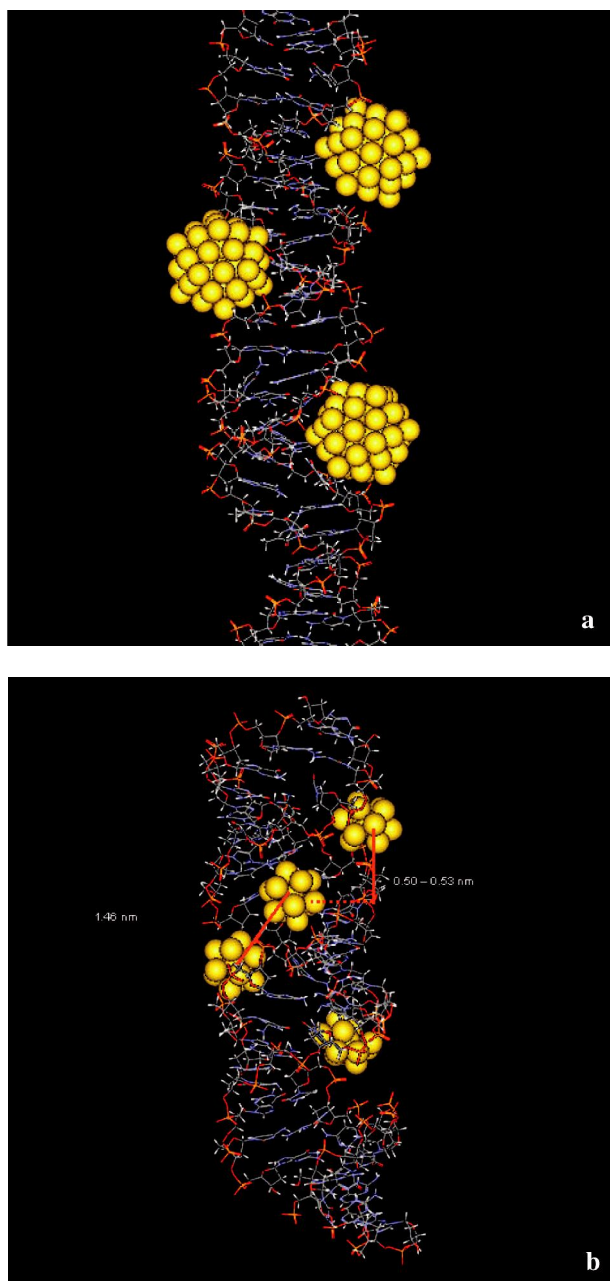


**Fig. 4-38** **a** Molecular modeling resulting from the combination of B-DNA with bare Au<sub>55</sub> clusters trapped in the major groves. **b** Transition from B- to A-DNA, linked with shrinking of the major groves from 1.4 to

0.7 nm causes the degradation of the Au<sub>55</sub> clusters to 0.6–0.7 nm particles. These hybrid systems then combine to give equidistant wires (**c**).

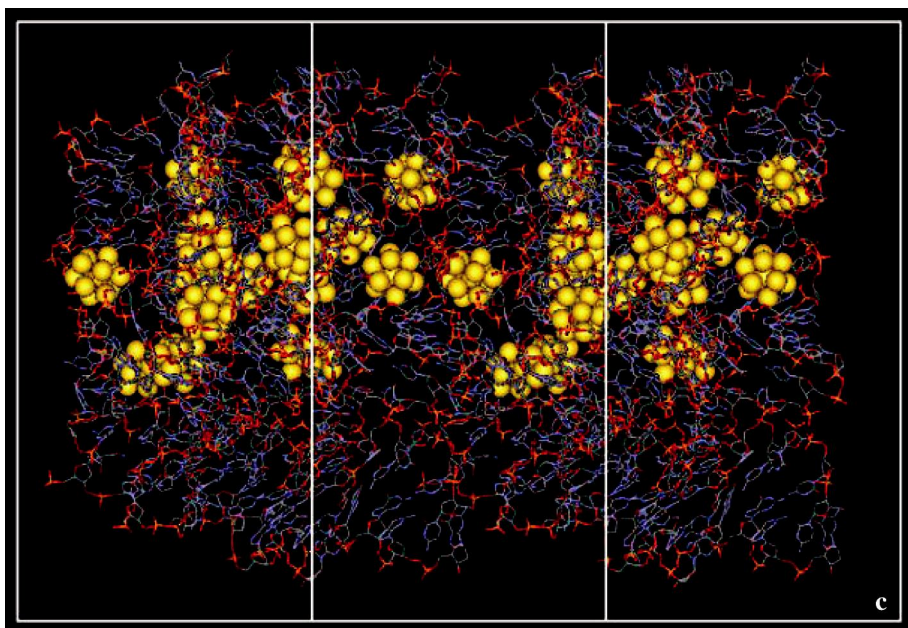
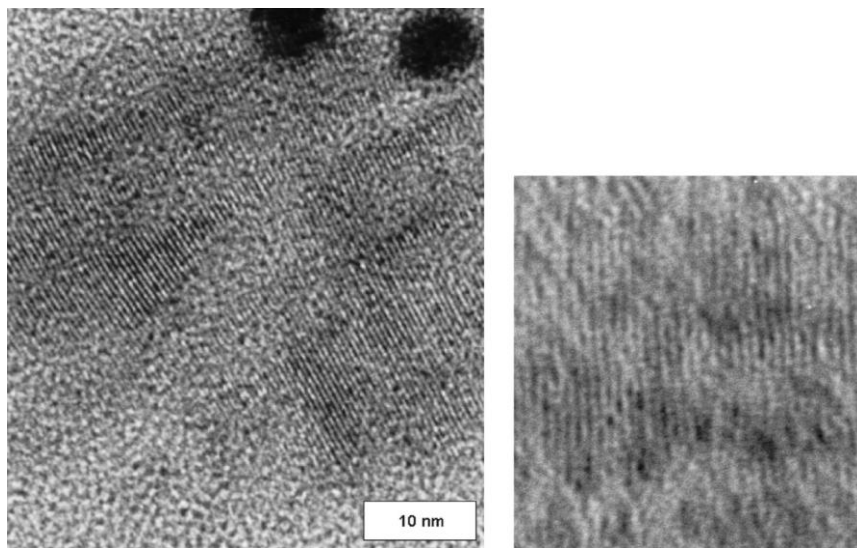


Fig. 4-38 (continued)

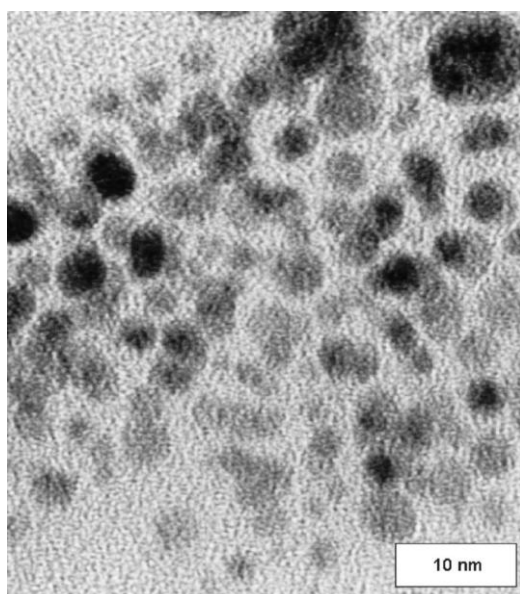
down to form larger gold particles, the formation of which can be observed under the microscope. It is not clear whether a beam-conditioned decomposition of DNA, of the wires or of both causes the degradation. Figure 4-39b shows the situation after the decomposition of the same area shown in Figure 4-39a.

One-dimensional arrangements of metal nanoparticles using templates other than DNA have also been generated successfully. Polymer molecules were used in two cases for decoration with  $\text{Au}_{55}(\text{PPh}_3)_{12}\text{Cl}_6$  clusters. Substituted poly(*p*-phenyleneethynylenes) turned out to readily chemisorb the clusters, probably owing to  $\pi$ - $\pi$  interactions between the electron-rich polymer and the phenyl groups in the clusters' ligand shells. In the special case of the 1-octyl-substituted derivative (PPE-I-oct), small bundles of polymer molecules can be generated in very dilute solutions [211]. PPE-I-oct (0.5  $\mu\text{g}$  per liter dichloromethane) forms bundles of diameter ca. 10–12 nm and length 250 nm. These thin chains of polymers are able to adsorb the clusters in a truly one-dimensional manner, as can be seen from Figure 4-40.

Another polymer suitable for collecting the same nanoparticles is poly(vinylpyrrolidone) (PVP). Distributed in a thin dichloromethane film on a water surface in a Langmuir-Blodgett trough, cluster-covered individual polymer molecules can be imaged by AFM. However, when surface pressure is increased, the PVP-nanoparticle wires continuously form dense filaments, which show numerous knots, leading to a two-dimensional network [212]. It is assumed that these knots consist of gold nanoparticles, since PVP, imaged under the same conditions, does



**a**



**b**

**Fig. 4-39** **a** TEM image of gold nanowires consisting of 0.6–0.7 nm particles (see magnified cutout) arranged equidistantly (0.5 nm). **b** The same area after continued e-beam irradiation, showing the formation of large gold nanoparticles from the wires.

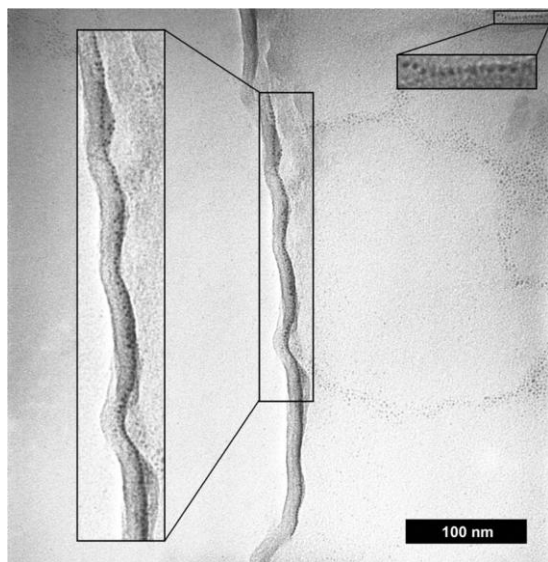


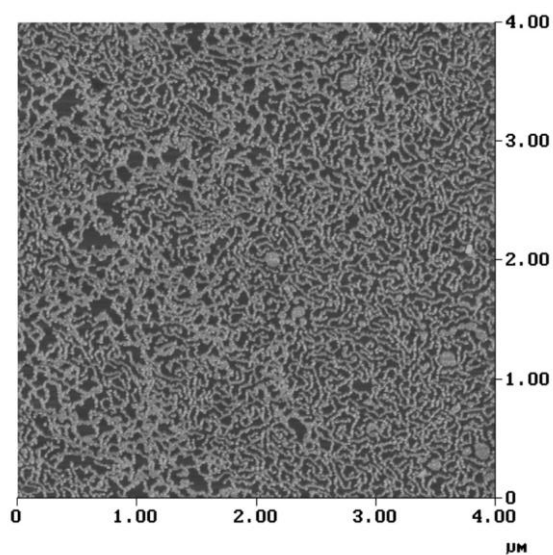
**Fig. 4-40** TEM image of one-dimensional arrangements of  $\text{Au}_{55}(\text{PPh}_3)_{12}\text{Cl}_6$  clusters along chains of poly(*p*-phenyleneethynylenes).

not exhibit corresponding behavior. Figure 4-41 shows the formation of these filaments, which can be transferred to solid substrates without degradation because of the linkage via nanoparticles.

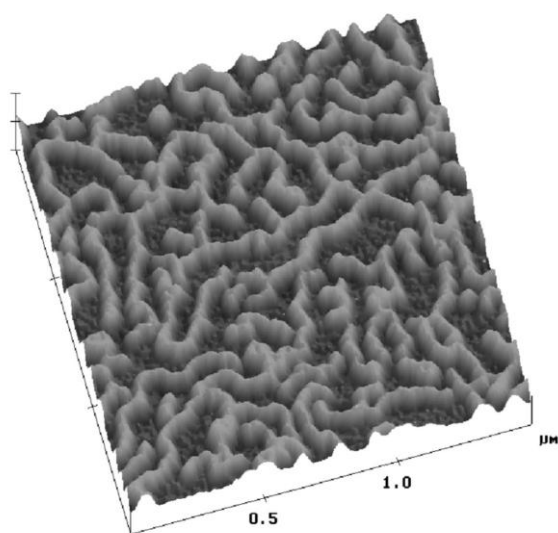
Arrangements like these could be of interest with respect to future nanoelectronic devices using  $\text{Au}_{55}$  clusters as quantum dots.

A template-free fabrication of one-dimensionally organized  $\text{Au}_{55}$  clusters using a controlled degradation of ordered monolayers has been found. As described in Section 4.2.2.1, islands of square and hexagonal structures of  $\text{Au}_{55}(\text{PPh}_3)_{12}\text{Cl}_6$  clusters are formed on the surface of water, which was previously covered with a thin film of clusters in dichloromethane, when the solvent is evaporated. If these islands are transferred to solid substrates under well-defined conditions, they are degraded into strictly parallel stripes, each consisting of 3–4 rows of clusters [213]. The transfer conditions found to work best consist of a  $20^\circ$  withdrawal angle and a speed of  $10 \text{ cm min}^{-1}$ . The formation of these patterns is explained by the oscillation of the water meniscus at the water-substrate boundary. The complex mechanism is illustrated in Figure 4-42. The monolayer is divided parallel to the transfer direction. Figure 4-43 shows a TEM image of an as-prepared pattern of stripes of  $\text{Au}_{55}$  clusters.

This kind of organization of nanoparticles is related to a method based on wetting instabilities of monomolecular layers when transferred onto solid substrates. Low-pressure monolayers of  $\text{L-}\alpha$ -dipalmitoyl-phosphatidylcholine (DPPC) on water degrade, forming a pattern with parallel hydrophilic channels 200–300 nm in



**a**



**b**

**Fig. 4-41** **a** AFM image of  $\text{Au}_{55}(\text{PPh}_3)_{12}\text{Cl}_6$  clusters decorating chains of poly(vinylpyrrolidone) forming a 2D network.  
**b** A magnified cutout.

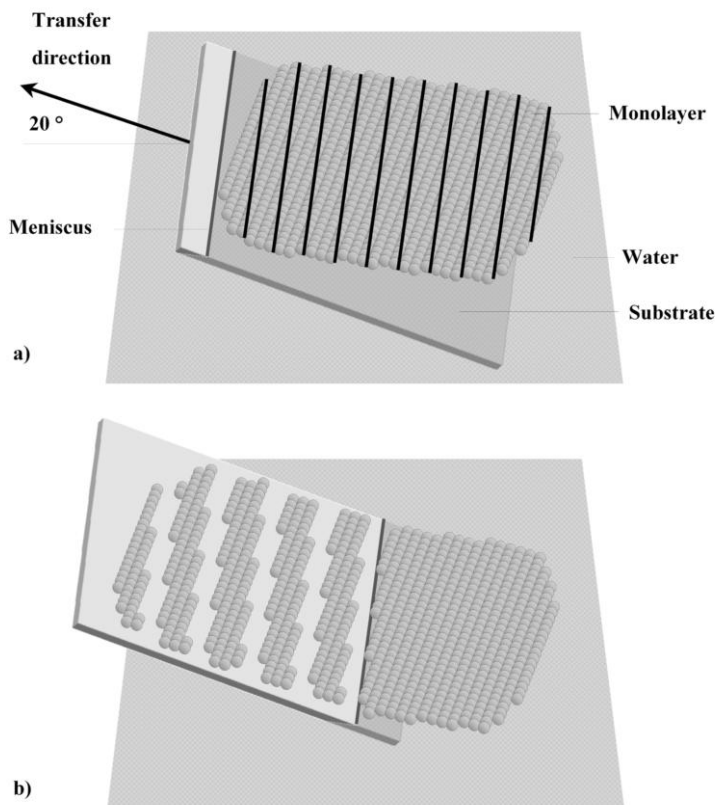


**Fig. 4-42** Sketch of the mechanism generating stripes of  $\text{Au}_{55}(\text{PPh}_3)_{12}\text{Cl}_6$  chains by the division of ordered islands into sections caused by the oscillating meniscus at the water-substrate boundary.

width when transferred to mica at a speed of  $1 \text{ mm s}^{-1}$  [214]. The channels of such structures can be used to deposit nanoparticles in one direction. Thiol-stabilized  $\text{Au}_{55}$  clusters, dissolved in 1-phenyloctane, were used to fill the channels, aggregates being formed during removal of the solvent. The DPPC areas are almost completely free of clusters owing to their nonwettability.

Because of the magnetic dipolar interactions, one-dimensional self-assembly is rather typical for magnetic nanoparticles. For a magnetic single-domain nanoparticle of radius  $r$ , the magnetic dipole moment arising from the alignment of electron spins is  $\mu = 4\pi r^3 M_s / 3$ , where  $M_s$  is the saturation magnetization of the respective bulk material. The dipole-dipole interaction between two magnetic particles at contact is proportional to  $\mu^2 / \sigma^3 \propto r^6 / \sigma^3$ , here  $\sigma$  is the effective hard sphere diameter, consisting of the magnetic core diameter and the thickness of



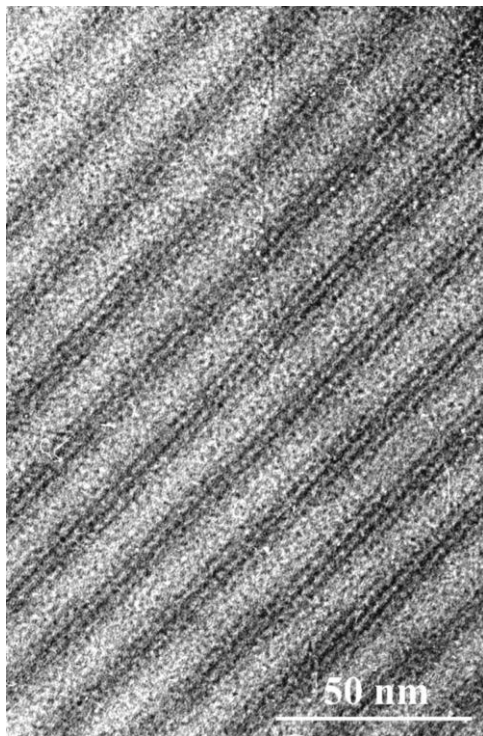


**Fig. 4-43** TEM image of equidistant stripes of Au<sub>55</sub>(PPh<sub>3</sub>)<sub>12</sub>Cl<sub>6</sub> clusters consisting of 3–4 individual 1D chains.

the surfactant layer [215]. These dipolar interactions favoring the head-to-tail arrangement of dipoles can compete with nondirectional van der Waals forces and steric repulsion, inducing anisotropic agglomeration of nanoparticles. In 1970, de Gennes and Pincus [216] theoretically predicted that colloidal particles with a magnetic dipole moment should be able to minimize the magnetostatic energy via self-assembly into flexible chains, as schematically shown in Figure 4-44a. Simulations show that such chains can be present in colloids of superparamagnetic particles even in zero magnetic field [217, 218]. Only in 2003 did Butter et al. [219] provide direct *in situ* observation of such linear chains of particles present in a dispersion of iron nanoparticles at zero field. They used a cryogenic TEM technique based on fast vitrification of the colloidal solution followed by low-dose TEM imaging of metal nanoparticles inside the vitrified film. A clear transition from a single particle population observed for 4 nm iron nanoparticles to a system of worm-like chains for particles larger than ca. 12 nm was observed, and this was explained by rapid increase of dipolar interaction with particle size.

Unpaired dipoles present at the ends of a linear chain of nanoparticles can pair, yielding the closed ring shown in Figure 4-44b. Such structures were observed by

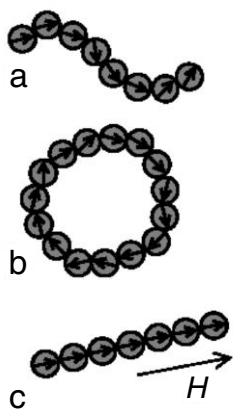


**Fig. 4-44** Dipolar chains formed by magnetic particles. **a** A semi-flexible chain of magnetic colloidal particles showing the head-to-tail, paired dipoles in the middle section and the unpaired dipoles at the ends. **b** A self-

assembled closed ring of magnetic particles allows all magnetic dipoles to be paired.

**c** Straight chains of magnetic particles can form and align in a magnetic field.

Tripp et al. [220] for 27 nm cobalt nanoparticles (weakly ferromagnetic at room temperature), which self-assemble into bracelet-like rings. Typically, the rings consisted of 5–12 particles and were 50–100 nm in diameter. The key point for selective formation of the nanoparticle rings instead of large aggregates was increased viscosity of solvent during an earlier stage of drying the colloidal solution on a TEM grid.

An external magnetic field orients the magnetic dipoles of individual nanoparticles in one direction, facilitating the formation of linear head-to-tail superstructures. The chain of dipole-dipole interacting nanoparticles will align itself in the direction of an externally applied magnetic field, as shown in Figure 4-44c. Another striking effect of the magnetic field is the dependence of the lateral width of 1D-nanoparticle aggregates on the strength of the applied field, as was demonstrated by Giersig et al. using the example of cobalt nanoparticles (Figure 4-45) [132]. Progressive increase in the width of nanoparticle chains with increasing magnetic field can be explained by the attractive chain-chain interactions between parallel dipolar chains of particles aligned by the magnetic field [219, 221]. In the case of a substrate positioned vertically, the self-assembly of magnetic nanoparticles into 1D chains of variable width has been explained as a cooperative effect of the external magnetic field and the force of gravity [222].

The shape of the magnetic nanoparticles can also affect the preferential dimensionality of self-assembled superstructures. Thus, hcp-Co nanodisks synthesized by Puentes et al. show a clear predisposition to stack face-to-face and remain perpendicular to the substrate, forming long ribbons (Figure 4-45) [223]. In the TEM images, these resemble ribbons of nanorods. However, tilting of the TEM grid shows that the standing disks vary in thickness when tilted in the short direction

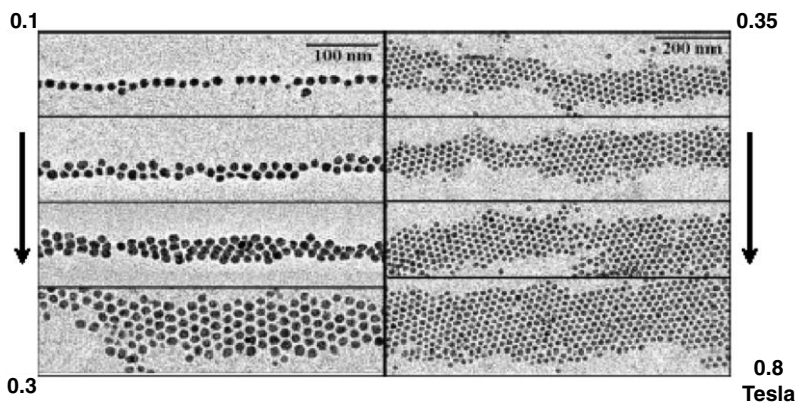


**Fig. 4-45** TEM images of 1D ordered cobalt nanoparticles self-assembled in magnetic fields of different strengths. Reproduced from [132], Copyright 2002, with permission from Elsevier Science.

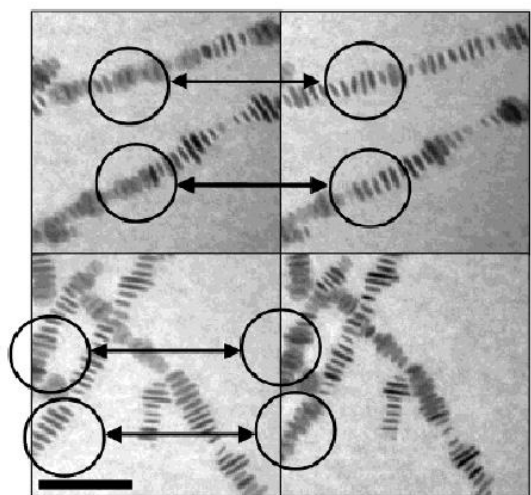
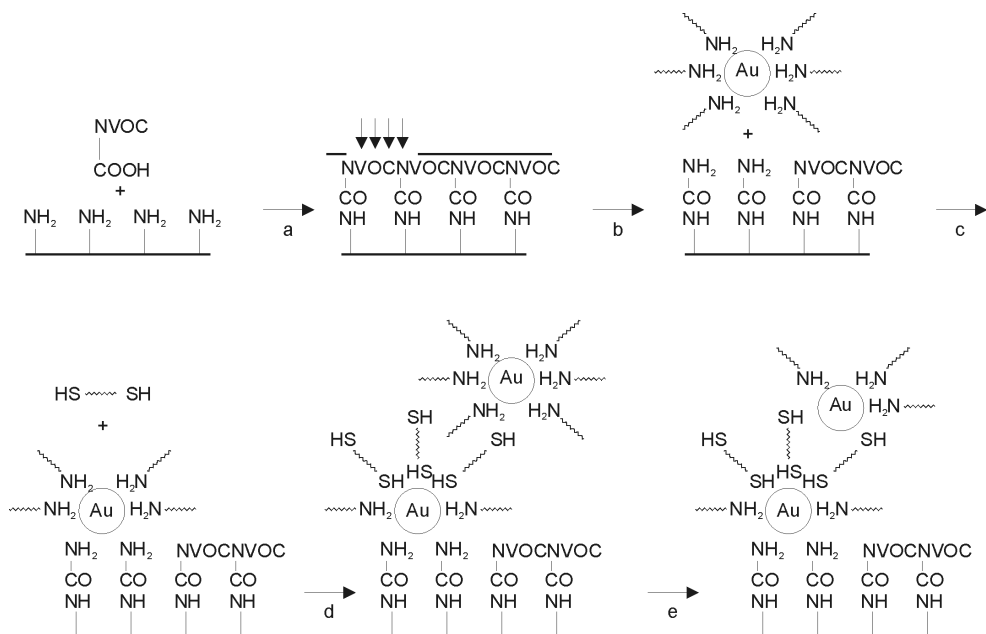


**Fig. 4-46** TEM picture of stacked face-to-face hcp-Co nanodisks. The pictures on the left correspond to no tilt and those on the right to a 25° tilt. The bar is 200 nm. Tilting direction corresponds with the double arrows. Reproduced from [223], Copyright 2002, with permission from the American Chemical Society.

and remain of constant length when tilted in the long direction (Figure 4-46), verifying the disk shape.

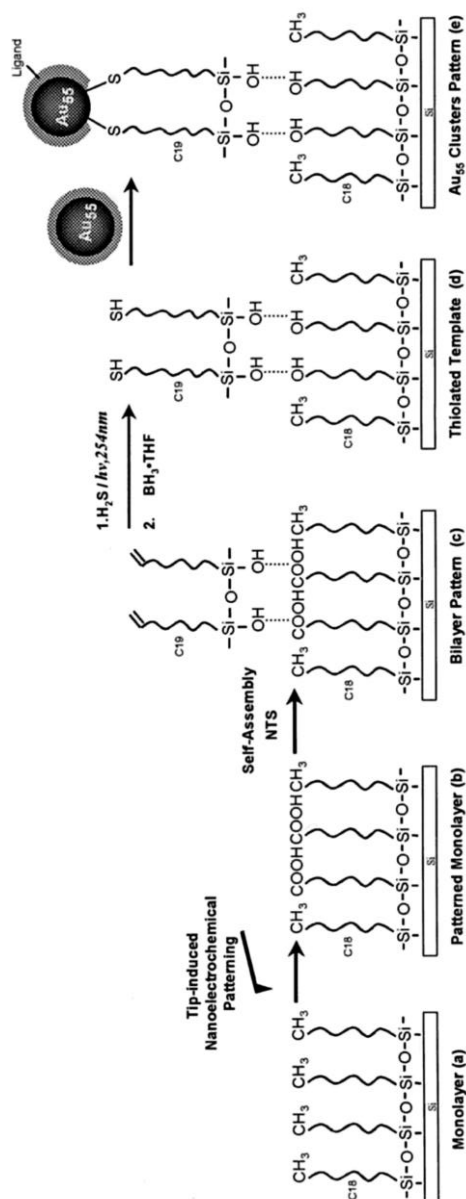
More or less all attempts to organize nanoparticles are driven by their possible use in future nanoelectronic devices, above all as miniaturized transistors. This highly desirable goal can only be reached if we succeed in generating structures



**Scheme 4-1** Process of formation of light-induced positions to add 2.6 nm gold nanoparticles by ligand exchange (a–c). Additional gold nanoparticles can be coordinated via the removal by dithiols of more weakly bound amines.

which are not made by nature, but instead follow complex designs. The precise placement of nanoparticles, acting as single electron transistors, is therefore the ultimate dream of any research in that field.

The very first attempts have been made. The present state of the art is based on the use of appropriately nanostructured surfaces that are chemically modified in such a way as to irreversibly bind nanoparticles onto the structure. One possible route has been pointed out by J. R. Heath et al. However, it still leads to rather broad structures [224]. They used light-controlled arrangement of gold nanoparticles on glass and silicon substrates. These are first covered with a monolayer of (3-aminopropyl)ethoxydimethylsilane, and this is followed by the addition of nitroveratryloxycarbonyl glycine (NVOC-GLY) to yield a surface with light-sensitive NVOC functions. Exposure to UV/Vis light through a mask results in a pattern of free and protected amino groups. Gold particles (2.6 nm), protected by a shell of 1-dodecylamine, are then used for addition to the free amino groups. Ligand exchange reactions between the 1-dodecylamine and the free amine groups of the surface lead to the decoration of the exposed areas with gold nanoparticles. The process is illustrated in Scheme 4-1. As can also be seen from this figure, additional particles can be placed in successive steps via dithiol ligands removing more weakly bound amines.



**Scheme 4-2** Generation of  $\text{Au}_{55}$  patterns on a prestructured surface. An alkyl-terminated self-assembled monolayer (a) is oxidized along traces by a metalized AFM tip inducing electric pulses (b). Alkene-terminated silanes are then added specifically to the COOH functions (c). This is followed by thiolization of the C=C double bonds (d) and addition of water-soluble  $\text{Au}_{55}$  ( $\text{Ph}_2\text{PC}_6\text{H}_4\text{SO}_3\text{Na})_{12}\text{Cl}_6$  clusters (e).

The best existing tool for fabricating nanostructured surfaces is, without doubt, the AFM tip. Mirkin et al. used it to develop so-called dip-pen nanolithography to deposit thiol molecules on gold surfaces [192, 193].

Conductive AFM tips can be used to emit electrical pulses to affect the top functions of ordered monolayers [225–227]. Here, the tip operates as a nanoelectrical pen, inscribing chemical information into appropriate surfaces. These traces, chemically modified, can then be used to deposit nanoparticles for further applications.

As can be seen from Scheme 4-2, a  $C_{18}$  alkyl monolayer on silicon has been oxidized by a tip-induced nanoelectrical reaction, generating carboxylic functions [228]. A second self-assembled monolayer, produced by nonadecenyltrichlorosilane, on top of the COOH groups functionalizes the carboxylic tracks by  $C=C$

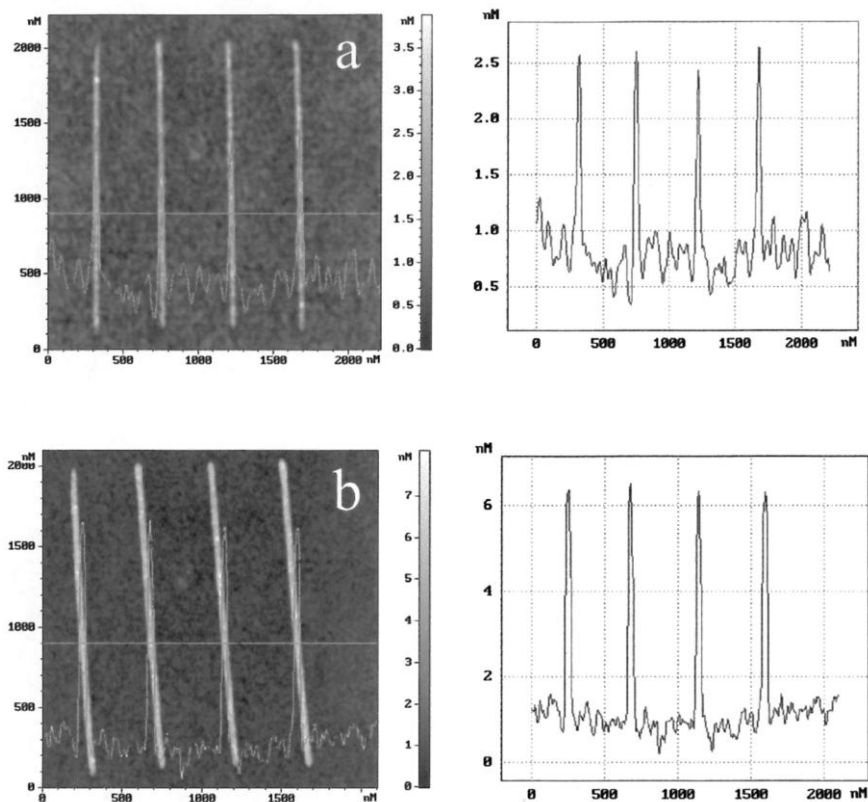


**Fig. 4-47** a Lines of SH functionalized traces corresponding to step **d** in Scheme 4-2 and height profile. b  $Au_{55}$ -decorated lines corresponding to step **e** in Scheme 4-2. The height profile agrees well with the addition of ca. 2.5 nm to the 2 nm height of the thiol-functionalized traces.

double bonds that can be attacked photolytically by  $\text{H}_2\text{S}$  to give the corresponding thiol-functionalized pattern. The purpose of using  $\text{BH}_3$  is to reduce S–S bonds, possibly formed during the process. The water-soluble gold cluster  $\text{Au}_{55}(\text{Ph}_2\text{PC}_6\text{H}_4\text{SO}_3\text{Na})_{12}\text{Cl}_6$  was used for deposition on the thiolated traces. The structures are remarkably thermally stable, as was shown by annealing up to  $120^\circ\text{C}$ .

With this technique, J. Sagiv et al. generated a series of planned patterns of 1.4 nm gold particles, whose electronic properties are known to make them promising candidates for future single-electron switches. Figures 4-47 to 4-50 show some of these structures. AFM analyses of the patterns indicate the existence of single-cluster layers. Figure 4-47 demonstrates a pattern of parallel wires and the corresponding distance-height profiles. The wires in (a) consist of the bilayer system only (step d in Scheme 4-2), whereas (b) images the same pattern after the addition of the gold clusters (step e in Scheme 4-2). As can be seen from the distance-height profiles, there is an increase in height from ca. 2 nm in (a) to ca. 5 nm in (b), corresponding to a particle height of ca. 3 nm. Considering the inherent limitations of AFM height determination, this value agrees quite well with the cluster size of ca. 2.5 nm.

Details cannot be distinguished in Figure 4-47. However, in the magnified cut-outs in Figure 4-48, gold clusters placed in two densely packed parallel rows can be observed. The clusters seem to be arranged along the periphery of the tracks.

Figure 4-49 shows a pattern of dots, each consisting of assemblies of 2–3 partially resolved clusters.

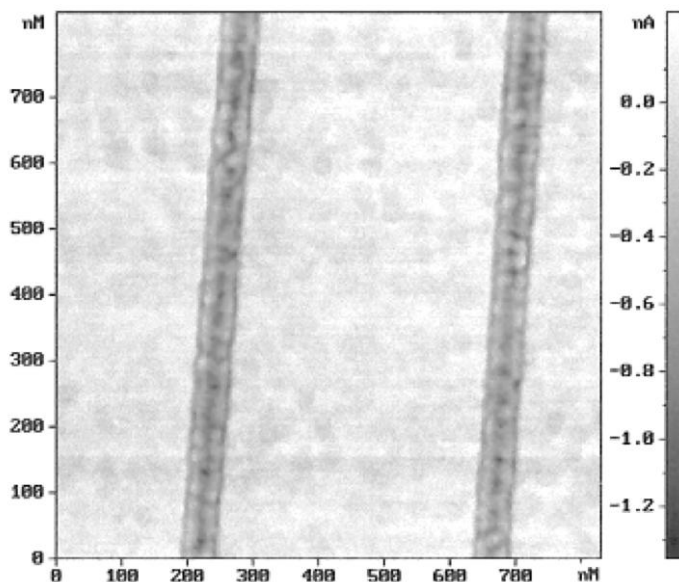


Fig. 4-48 Magnified pieces of  $\text{Au}_{55}$  cluster-decorated lines of Figure 4-47, indicating 2 rows of clusters per line.

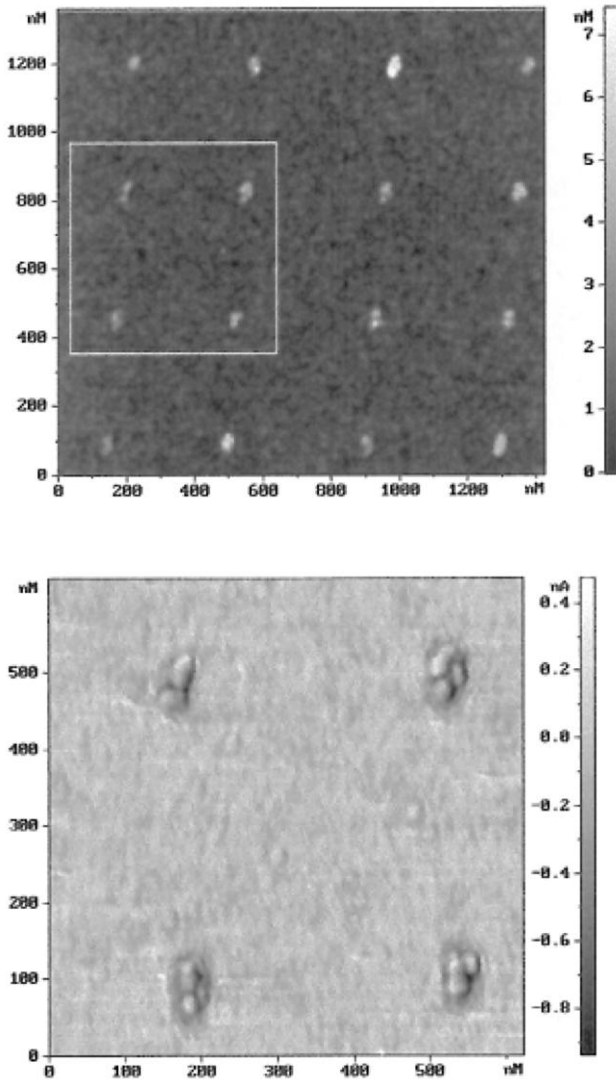


Fig. 4-49 AFM images of a regular arrangement of dots of Au<sub>55</sub> clusters, each dot consisting of 2–3 clusters.

The capabilities of this method, provided that the experimental conditions are optimized, can be seen from Figure 4-50. Ideal one-dimensional wires of individual particles become available, and it would even be possible to place single clusters in predefined intrawire gaps.

So far, this route represents the most promising recipe for the creation of planned architectures of quantum dots. Of course, there is still a long way to go before practical applications become realizable. On the other hand, there exists no



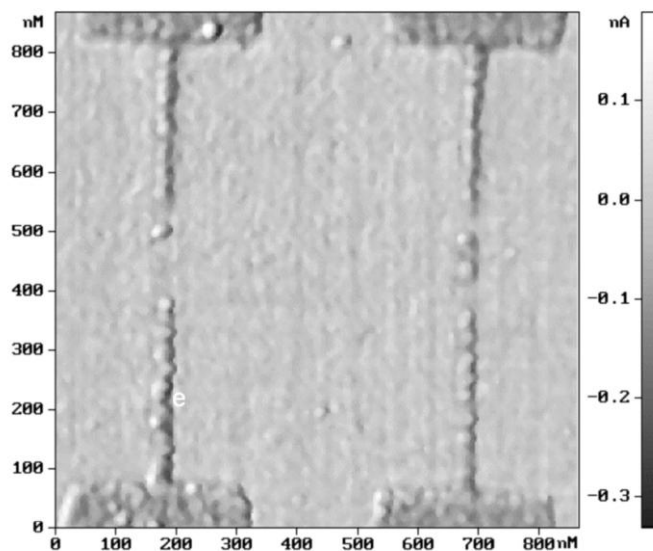


Fig. 4-50 Optimized pattern of ideal 1D cluster wires and single clusters in predefined intrawire gaps.

other system which could be built up from particles as small as the 1.4 nm gold particles mentioned above and which is electronically exposed in such a manner that single electrons can be used to switch, even at room temperature. This vision justifies any efforts to further improve the techniques to build up working constructions.

## References

- 1 P. STRICKLER, *J. Chem. Soc., Chem. Commun.* **1969**, 655.
- 2 I. G. DANCE, M. L. SCUDDER, R. SECOMB, *Inorg. Chem.* **1983**, 22, 1794.
- 3 I. G. DANCE, A. CHOY, M. L. SCUDDER, *J. Am. Chem. Soc.* **1984**, 106, 6285.
- 4 I. G. DANCE, *Polyhedron* **1986**, 5, 1037.
- 5 G. S. H. LEE, D. C. CRAIG, I. MA, M. L. SCUDDER, T. D. BAILEY, I. G. DANCE, *J. Am. Chem. Soc.* **1988**, 110, 4863.
- 6 N. HERRON, J. C. CALABRESE, W. E. FARNETH, Y. WANG, *Science* **1993**, 259, 1426.
- 7 T. VOSSMEYER, G. RECK, L. KATSIKAS, E. T. K. HAUPT, B. SCHULZ, H. WELLER, *Science* **1995**, 267, 1476.
- 8 T. VOSSMEYER, L. KATSIKAS, M. GIERSIG, I. G. POPOVIC, K. DIESNER, A. CHEMSEDDINE, A. EYCHMÜLLER, H. WELLER, *J. Phys. Chem.* **1994**, 98, 7665.
- 9 R. BERTONCELLO, M. BETTINELLI, M. CASARIN, C. MACCATO, L. PANDOLFO, A. VITTADINI, *Inorg. Chem.* **1997**, 36, 4707.
- 10 S. BEHRENS, M. BETTENHAUSEN, A. C. DEVESON, A. EICHHÖFER, D. FENSKE, A. LOHDE, U. WOGGON, *Angew. Chem.* **1996**, 108, 2360; *Angew. Chem. Int. Ed. Engl.* **1996**, 35, 2215.
- 11 S. BEHRENS, D. FENSKE, *Ber. Bunsenges. Phys. Chem.* **1997**, 101, 1588.
- 12 S. BEHRENS, M. BETTENHAUSEN, A. EICHHÖFER, D. FENSKE, *Angew. Chem.* **1997**, 109, 2874; *Angew. Chem. Int. Ed. Engl.* **1997**, 24, 2797.
- 13 V. PTATSCHEK, T. SCHMIDT, M. LERCH, G. MÜLLER, L. SPANHEL, A. EMMERLING, J. FRICKE, A. H. FOIZIK, E.

- LANGER, *Ber. Bunsenges. Phys. Chem.* **1998**, 102, 85.
- 14 V. N. SOLOVIEV, A. EICHHÖFER, D. FENSKE, U. BANIN, *J. Am. Chem. Soc.* **2000**, 122, 2673.
  - 15 V. N. SOLOVIEV, A. EICHHÖFER, D. FENSKE, U. BANIN, *Phys. Stat. Sol. B* **2001**, 224, 285.
  - 16 V. N. SOLOVIEV, A. EICHHÖFER, D. FENSKE, U. BANIN, *J. Am. Chem. Soc.* **2001**, 123, 2354.
  - 17 H. LI, J. KIM, T. L. GROV, M. O'KEEFE, O. M. YAGHI, *J. Am. Chem. Soc.* **2001**, 123, 4867.
  - 18 C. WANG, Y. LI, X. BU, N. ZHENG, O. ZIVKOVIC, C.-S. YANG, P. FENG, *J. Am. Chem. Soc.* **2001**, 123, 11506.
  - 19 C. WANG, X. BU, N. ZHENG, P. FENG, *J. Am. Chem. Soc.* **2002**, 124, 10268.
  - 20 W. SU, X. HUANG, J. LI, H. FU, *J. Am. Chem. Soc.* **2002**, 124, 12944.
  - 21 H. DÖLLEFELD, H. WELLER, A. EYCHMÜLLER, *Nano Lett.* **2001**, 1, 267.
  - 22 Y. NOSAKA, H. TANAKA, *J. Phys. Chem. B* **2002**, 106, 3389.
  - 23 C. P. COLLIER, T. VOSSMEYER, J. R. HEATH, *Annu. Rev. Phys. Chem.* **1998**, 49, 371.
  - 24 C. B. MURRAY, C. R. KAGAN, M. G. BAWENDI, *Annu. Rev. Mater. Sci.* **2000**, 30, 545.
  - 25 C. B. MURRAY, C. R. KAGAN, M. G. BAWENDI, *Science* **1995**, 270, 1335.
  - 26 J. R. HEATH, *Science* **1995**, 270, 1315.
  - 27 H. WELLER, *Angew. Chem.* **1996**, 108, 1159; *Angew. Chem., Int. Ed. Engl.* **1996**, 35, 1079.
  - 28 D. V. TALAPIN, E. V. SHEVCHENKO, A. KORNOWSKI, N. GAPONIK, M. HAASE, A. L. ROGACH, H. WELLER, *Adv. Mater.* **2001**, 13, 1868.
  - 29 A. L. ROGACH, D. V. TALAPIN, E. V. SHEVCHENKO, A. KORNOWSKI, M. HAASE, H. WELLER, *Adv. Funct. Mater.* **2002**, 12, 653.
  - 30 W. SHENTON, D. PUM, U. B. SLEYTR, S. MANN, *Nature* **1997**, 389, 585.
  - 31 K.-H. LIN, J. C. CROCKER, V. PRASAD, A. SCHOFIELD, D. A. WEITZ, T. C. LUBENSKY, A. G. YODH, *Phys. Rev. Lett.* **2000**, 85, 1770.
  - 32 P. JIANG, J. F. BERTONE, V. L. COLVIN, *Science* **2001**, 291, 453.
  - 33 Y. A. VLASOV, N. YAO, D. J. NORRIS, *Adv. Mater.* **1999**, 11, 165.
  - 34 N. GAPONIK, S. ROMANOV, A. L. ROGACH, C. SOTOMAYOR-TORRES, A. EYCHMÜLLER, unpublished.
  - 35 S. BESSON, T. GACOIN, C. RICOLLEAU, C. JACQUIOD, J.-P. BOILLOT, *Nano Lett.* **2002**, 2, 409.
  - 36 S. A. DAVIDS, M. BREULMANN, K. H. RHODES, B. ZHANG, S. MANN, *Chem. Mater.* **2001**, 13, 3218.
  - 37 B. S. KIM, L. AVILA, L. E. BRUS, I. P. HERMAN, *Appl. Phys. Lett.* **2000**, 76, 3715.
  - 38 G. GE, L. E. BRUS, *J. Phys. Chem. B* **2000**, 104, 9573.
  - 39 G. GE, L. E. BRUS, *Nano Lett.* **2001**, 1, 219.
  - 40 E. S. SMOTKIN, C. LEE, A. J. BARD, A. CAMPION, M. A. FOX, T. E. MALLOUK, S. E. WEBBER, J. M. WHITE, *Chem. Phys. Lett.* **1988**, 152, 265.
  - 41 H. CHEN, X. CHAI, Q. WEI, Y. JIANG, T. LI, *Thin Solid Films* **1898**, 178, 535.
  - 42 C. ZYLBERAJCH, A. RUADEL-TEIXIER, A. BARRAUD, *Thin Solid Films* **1989**, 179, 9.
  - 43 X. K. ZHAO, Y. X. YUAN, J. H. FENDLER, *J. Chem. Soc. Chem. Commun.* **1990**, 1248.
  - 44 D. J. SCOBURG, F. GRIESER, D. N. FURLONG, *J. Chem. Soc., Chem. Commun.* **1991**, 515.
  - 45 F. GRIESER, D. N. FURLONG, D. SCOBURG, I. ICHINOSE, N. KIMIZUKA, T. KUNITAKE, *J. Chem. Soc. Faraday Trans.* **1992**, 88, 2207.
  - 46 P. FACCI, V. EROKHIN, A. TRONIN, C. NICOLINI, *J. Phys. Chem.* **1994**, 98, 13323.
  - 47 B. O. DABBOUSI, C. B. MURRAY, M. F. RUBNER, M. G. BAWENDI, *Chem. Mater.* **1994**, 6, 216.
  - 48 Y. C. TIAN, C. J. WU, J. H. FENDLER, *J. Phys. Chem.* **1994**, 98, 4913.
  - 49 J. H. FENDLER, *Isr. J. Chem.* **1993**, 33, 41.
  - 50 S. R. CORDERO, P. J. CARSON, R. A. ESTABROOK, G. F. STROUSE, S. K. BURATTO, *J. Phys. Chem. B* **2000**, 104, 12137.
  - 51 S.-H. KIM, G. MARKOVICH, S. REZVANI, S. H. CHOI, K. L. WANG, J. R. HEATH, *Appl. Phys. Lett.* **1999**, 74, 317.

- 52 A. SAMOKHVALOV, M. BERFELD, M. LAHAV, R. NAAMAN, E. RABANI, *J. Phys. Chem. B* **2000**, 104, 8631.
- 53 G. HODES, *Solar Energy Materials and Solar Cells* **1994**, 32, 323.
- 54 G. HODES, *Isr. J. Chem.* **1993**, 33, 95.
- 55 A. S. BARANSKI, W. R. FAWCETT, *J. Electrochem. Soc.* **1980**, 127, 766.
- 56 G. HODES, A. ALBU-YARON, *Proc. Electrochem. Soc.* **1988**, 88-14, 298.
- 57 G. DECHER, *Science* **1997**, 277, 1232.
- 58 M. GAO, B. RICHTER, S. KIRSTEIN, H. MÖHWALD, *J. Phys. Chem. B* **1998**, 102, 4096.
- 59 A. A. MAMEDOV, A. BELOV, M. GIERSIG, N. N. MAMEDOVA, N. A. KOTOV, *J. Am. Chem. Soc.* **2001**, 123, 7738.
- 60 A. L. ROGACH, D. S. KOKTYSH, M. HARRISON, N. A. KOTOV, *Chem. Mater.* **2000**, 12, 1526.
- 61 A. L. ROGACH, N. A. KOTOV, D. S. KOKTYSH, A. S. SUSHA, F. CARUSO, *Colloids Surf. A* **2002**, 202, 135.
- 62 M. GAO, J. SUN, E. DULKEITH, N. GAPONIK, U. LEMMER, J. FELDMANN, *Langmuir* **2002**, 18, 4098.
- 63 C. WANG, M. SHIM, P. GUYOT-SIONNEST, *Appl. Phys. Lett.* **2002**, 80, 4.
- 64 H. MATTOUSSI, L. H. RADZIŁOWSKI, B. O. DABBOUSI, D. E. FOGG, R. R. SCHROCK, E. L. THOMAS, M. F. RUBNER, M. G. BAWENDI, *J. Appl. Phys.* **1999**, 86, 4390.
- 65 M. ICHIMURA, K. TAKEUCHI, A. NAKAMURA, E. ARAI, *Thin Solid Films* **2001**, 384, 157.
- 66 M. DANEK, K. F. JENSEN, C. B. MURRAY, M. G. BAWENDI, *Chem. Mater.* **1996**, 8, 173.
- 67 C. R. KAGAN, C. B. MURRAY, M. NIRMAL, M. G. BAWENDI, *Phys. Rev. Lett.* **1996**, 76, 3043.
- 68 C. R. KAGAN, C. B. MURRAY, M. G. BAWENDI, *Phys. Rev. B* **1996**, 54, 8633.
- 69 O. I. MICIC, K. M. JONES, A. CAHILL, A. J. NOZIK, *J. Phys. Chem. B* **1998**, 102, 9791.
- 70 M. V. ARTEMYEV, A. I. BIBIK, L. I. GURINOVICH, S. V. GAPONENKO, U. WOGGON, *Phys. Rev. B* **1999**, 60, 1504.
- 71 M. V. ARTEMYEV, U. WOGGON, H. JASCHINSKI, L. I. GURINOVICH, S. V. GAPONENKO, *J. Phys. Chem.* **2000**, 104, 11617.
- 72 M. V. ARTEMYEV, A. I. BIBIK, L. I. GURINOVICH, S. V. GAPONENKO, H. JASCHINSKI, U. WOGGON, *Phys. Stat. Sol. B* **2001**, 224, 393.
- 73 O. I. MICIC, S. P. AHRENKIEL, A. J. NOZIK, *Appl. Phys. Lett.* **2001**, 78, 4022.
- 74 C. A. LEATHERDALE, C. R. KAGAN, N. Y. MORGAN, S. A. EMPEDOCLES, M. A. KASTNER, M. G. BAWENDI, *Phys. Rev. B* **2000**, 62, 2669.
- 75 C. A. LEATHERDALE, M. G. BAWENDI, *Phys. Rev. B* **2001**, 63, 165315.
- 76 B. S. KIM, M. A. ISLAM, L. E. BRUS, I. P. HERMAN, *J. Appl. Phys.* **2001**, 89, 8127.
- 77 H. DÖLLEFELD, H. WELLER, A. EYCHMÜLLER, *J. Phys. Chem. B* **2002**, 106, 5604.
- 78 A. FRANCESCHETTI, A. ZUNGER, *Phys. Rev. B* **2001**, 63, 153304.
- 79 E. RABANI, B. HETENYI, B. J. BERNE, L. E. BRUS, *J. Chem. Phys.* **1999**, 110, 5355.
- 80 S. RAMAKRISHNAN, C. F. ZUKOSKI, *J. Chem. Phys.* **2000**, 113, 1237.
- 81 P. MALY, J. KUDRNA, F. TROJANEK, D. MIKES, P. NEMEC, A. C. MACIEL, J. F. RYAN, *Appl. Phys. Lett.* **2000**, 77, 2352.
- 82 D. VANMAEKELBERGH, P. E. DE JONGH, *J. Phys. Chem. B* **1999**, 103, 747.
- 83 E. A. MEULENKAMP, *J. Phys. Chem. B* **1999**, 103, 7831.
- 84 A. SOLBRAND, A. HENNINGSSON, S. SÖDERGREN, H. LINDSTRÖM, A. HAGFELDT, S.-E. LINDQUIST, *J. Phys. Chem. B* **1999**, 103, 1078.
- 85 V. NOACK, H. WELLER, A. EYCHMÜLLER, *J. Phys. Chem. B* **2002**, 106, 8514.
- 86 N. Y. MORGAN, C. A. LEATHERDALE, M. DRNDIC, M. V. JAROSZ, M. A. KASTNER, M. G. BAWENDI, *Phys. Rev. B* **2002**, 66, 075339.
- 87 M. BRUST, D. BETHELL, D. J. SCHIFFRIN, C. J. KIELY, *Adv. Mater.* **1995**, 7, 795.
- 88 K. R. GOPIDAS, M. BOHORQUEZ, P. V. KAMAT, *J. Phys. Chem.* **1990**, 94, 6435.
- 89 D. LAWLESS, S. KAPOOR, D. MEISEL, *J. Phys. Chem.* **1995**, 99, 10329.
- 90 T. TORIMOTO, M. YAMASHITA, S. KUWUBATA, T. SAKATA, H. MORI, H. YONEYAMA, *J. Phys. Chem. B* **1999**, 103, 8799.

- 91 A. N. SHIPWAY, E. KATZ, I. WILLNER, *ChemPhysChem* **2000**, 1, 18.
- 92 C. A. MIRKIN, *Inorg. Chem.* **2000**, 39, 2258.
- 93 C. M. NIEMEYER, *Angew. Chem.* **2001**, 113, 4643; *Angew. Chem., Int. Ed. Engl.* **2001**, 40, 4128.
- 94 W. J. PARAK, D. GERION, D. ZANCHET, A. S. WOERZ, T. PELLEGRINO, C. MICHEEL, S. C. WILLIAMS, M. SEITZ, R. E. BRUEHL, Z. BRYANT, C. BUSTAMANTE, C. R. BERTOZZI, A. P. ALIVISATOS, *Chem. Mater.* **2002**, 14, 2113.
- 95 M. BRUCHEZ JR., M. MORONNE, P. GIN, S. WEISS, A. P. ALIVISATOS, *Science* **1998**, 281, 2013.
- 96 S. MANN, W. SHENTON, M. LI, S. CONNOLLY, D. FITZMAURICE, *Adv. Mater.* **2000**, 12, 147.
- 97 I. SONDI, O. SIIMAN, S. KOESTER, E. MATIJEVIC, *Langmuir* **2000**, 16, 3107.
- 98 N. N. MAMEDOVA, N. A. KOTOV, A. L. ROGACH, J. STUDER, *Nano Lett.* **2001**, 1, 281.
- 99 S. J. ROSENTHAL, *Nature Biotech.* **2001**, 19, 621.
- 100 M. HAN, X. GAO, J. Z. SU, S. NIE, *Nature Biotech.* **2001**, 19, 631.
- 101 O. SCHMELZ, A. MEWS, T. BASCHE, A. HERRMANN, K. MÜLLEN, *Langmuir* **2001**, 17, 2861.
- 102 T. NI, D. K. NAGESHA, J. ROBLES, N. F. MATERER, S. MÜSSIG, N. A. KOTOV, *J. Am. Chem. Soc.* **2002**, 124, 3980.
- 103 J. KOLNY, A. KORNOWSKI, H. WELLER, *Nano Lett.* **2002**, 2, 361.
- 104 K. HOPPE, E. GEIDEL, H. WELLER, A. EYCHMÜLLER, *Phys. Chem. Chem. Phys.* **2002**, 4, 1704.
- 105 T. TRINDADE, P. O'BRIAN, X.-M. ZHANG, *J. Mater. Res.* **1999**, 14, 4140.
- 106 X. PENG, T. E. WILSON, A. P. ALIVISATOS, P. G. SCHULTZ, *Angew. Chem., Int. Ed. Engl.* **1997**, 36, 145.
- 107 U. LANDMAN, R. N. BARNETT, A. G. SCHERBAKOV, P. AVOURIS, *Phys. Rev. Lett.* **2000**, 85, 1958.
- 108 E. RABANI, S. A. EGOROV, *Nano Lett.* **2002**, 2, 69.
- 109 R. L. WHETTEN, J. T. KHOURY, M. M. ALVAREZ, S. MURTHY, I. VEZMAR, Z. L. WANG, P. W. STEPHENS, C. L. CLEVELAND, W. D. LUEDTKE, U. LANDMANN, *Adv. Mater.* **1996**, 8, 428.
- 110 St. A. HARFENIST, Z. L. WANG, M. M. ALVAREZ, I. VEZMAR, R. L. WHETTEN, *J. Phys. Chem.* **1996**, 100, 13904.
- 111 St. A. HARFENIST, Z. L. WANG, R. L. WHETTEN, I. VEZMAR, M. M. ALVAREZ, *Adv. Mater.* **1997**, 9, 817.
- 112 Z. L. WANG, *Adv. Mater.* **1998**, 10, 13.
- 113 J. E. MARTIN, J. P. WILCOXON, J. ODINEK, P. PROVENCIO, *J. Phys. Chem.* **2000**, 104, 9475.
- 114 G. SCHMID, R. PUGIN, T. SAWITOWSKI, U. SIMON, B. MARLER, *Chem. Commun.* **1999**, 1303.
- 115 G. SCHMID, N. KLEIN, *Angew. Chem., Int. Ed. Engl.* **1986**, 25, 922.
- 116 G. SCHMID, *Polyhedron* **1988**, 7, 2321.
- 117 H. FELD, A. LEUTE, D. RADING, A. BENNINGHOVEN, G. SCHMID, Z. *Physik D*, **1990**, 17, 73.
- 118 H. FELD, A. LEUTE, D. RADING, A. BENNINGHOVEN, G. SCHMID, *J. Am. Chem. Soc.* **1990**, 112, 8166.
- 119 G. SCHMID, W. MEYER-ZAIKA, R. PUGIN, T. SAWITOWSKI, J.-P. MAJORAL, A.-M. CAMINADE, C.-O. TURRIN, *Chem. Eur. J.* **2000**, 6, 1693.
- 120 C. B. MURRAY, C. R. KAGAN, M. G. BAWENDI, *Annu. Rev. Mater. Sci.* **2000**, 30, 545.
- 121 C. B. MURRAY, S. SUN, H. DOYLE, T. BETLEY, *MRS Bulletin* **2001**, 985.
- 122 S. SUN, C. B. MURRAY, H. DOYLE, *Mater. Res. Soc. Symp. Proc.* **1999**, 577, 385.
- 123 S. SUN, C. B. MURRAY, *J. Appl. Phys.* **1999**, 85, 4325.
- 124 S. SUN, H. ZENG, *J. Am. Chem. Soc.* **2002**, 124, 8204.
- 125 D. V. TALAPIN, E. V. SHEVCHENKO, A. KORNOWSKI, N. P. GAPONIK, M. HAASE, A. L. ROGACH, H. WELLER, *Adv. Mater.* **2001**, 13, 1868.
- 126 E. V. SHEVCHENKO, D. V. TALAPIN, A. KORNOWSKI, F. WIEKHORST, J. KÖTZLER, M. HAASE, A. L. ROGACH, H. WELLER, *Adv. Mater.* **2001**, 14, 287.
- 127 A. L. ROGACH, D. V. TALAPIN, E. V. SHEVCHENKO, A. KORNOWSKI, M. HAASE, H. WELLER, *Adv. Funct. Mater.* **2002**, 12, 653.
- 128 E. V. SHEVCHENKO, D. V. TALAPIN, A. L. ROGACH, A. KORNOWSKI, M.

- HAASE, H. WELLER, *J. Am. Chem. Soc.* **2002**, 124, 11480.
- 129 C. PETIT, A. TALEB, M. P. PILENI, *Adv. Mater.* **1998**, 10, 259.
  - 130 M. P. PILENI, *J. Phys. Chem. B* **2001**, 105, 3358.
  - 131 A. T. NGO, M. P. PILENI, *Adv. Mater.* **2000**, 12, 276.
  - 132 M. GIERSIG, M. HILGENDORFF, *Colloids Surf. A* **2002**, 202, 207.
  - 133 S. A. SAFRAN, *Nat. Mater.* **2003**, 2, 71.
  - 134 D. WIRT, M. FERMIGIER, *Phys. Rev. Lett.* **1994**, 72, 2294.
  - 135 H. WANG, Y. ZHU, C. BOYD, W. LUO, A. CEBERS, R. E. ROSENSWEIG, *Phys. Rev. Lett.* **1994**, 72, 1929.
  - 136 W. WEN, L. ZHANG, P. SHENG, *Phys. Rev. Lett.* **2000**, 85, 5464.
  - 137 M. BRUST, D. BETHELL, D. J. SHIFFRIN, C. J. KIELY, *Adv. Mater.* **1995**, 7, 795.
  - 138 M. BRUST, M. WALKER, D. BETHELL, D. J. SCHIFFRIN, R. WHYMAN, *J. Chem. Soc. Chem. Commun.* **1994**, 801.
  - 139 J. FINK, C. J. KIELY, D. BETHELL, D. J. SCHIFFRIN, *Chem. Mater.* **1998**, 10, 922.
  - 140 M. T. REETZ, M. WINTER, B. TESCHE, *Chem. Commun.* **1997**, 147.
  - 141 C. J. KIELY, J. FINK, M. BRUST, D. BETHELL, D. J. SCHIFFRIN, *Nature* **1998**, 396, 444.
  - 142 C. J. KIELY, J. G. ZHENG, J. FINK, M. BRUST, D. BETHELL, D. J. SCHIFFRIN, *Adv. Mater.* **2000**, 12, 640.
  - 143 F. LAVES, *The Theory of Alloy Phases*, American Society for Metals, Cleveland, OH **1956**, 124–129.
  - 144 W. B. PEARSON, *Crystal Chemistry and Physics of Metals and Alloys*, Wiley-Interscience, London **1972**.
  - 145 S. HACHISU, S. YOUSHIMURA, *Nature* **1980**, 283, 188.
  - 146 S. YOUSHIMURA, S. HACHISU, *Prog. Colloid Polym. Sci.* **1983**, 68, 59.
  - 147 R. P. ANDRES, J. D. BIELEFELD, J. I. HENDERSON, D. B. JANES, V. R. KOLAGUNTA, C. P. KUBIAK, W. J. MAHONEY, R. G. OSIFCHIN, *Science* **1996**, 273, 1690.
  - 148 B. A. KORGEL, D. FITZMAURICE, *Adv. Mater.* **1998**, 10, 661.
  - 149 J. P. WILCOXON, J. E. MARTIN, P. PROVENCIO, *J. Chem. Phys.* **2001**, 115, 998.
  - 150 Z. R. DAI, S. SUN, Z. L. WANG, *Nano Lett.* **2001**, 1, 443.
  - 151 Z. L. WANG, *Adv. Mater.* **1998**, 10, 13.
  - 152 Z. L. WANG, Z. DAI, S. SUN, *Adv. Mater.* **2000**, 12, 1944.
  - 153 F. WIEKHORST, E. V. SHEVCHENKO, H. WELLER, J. KÖTZLER, *Phys. Rev. B*, **2003**, 67, 224416.
  - 154 F. DUMESTRE, B. CHAUDRET, C. AMIENS, M.-C. FROMEN, M.-J. CASANOVE, P. RENAUD, P. ZURCHER, *Angew. Chem. Int. Ed.* **2002**, 41, 4286.
  - 155 S. SUN, C. B. MURRAY, D. WELLER, L. FOLKS, A. MOSER, *Science* **2000**, 287, 1989.
  - 156 G. SCHMID, St. PESCHEL, *New J. Chem.* **1998**, 7, 669.
  - 157 N. BEYER, Diploma Thesis, University of Essen, **1997**.
  - 158 G. SCHMID, M. BÄUMLE, N. BEYER, *Angew. Chem.* **2000**, 112, 187; *Angew. Chem., Int. Ed. Engl.* **2000**, 39, 181.
  - 159 G. SCHMID, N. BEYER, *Eur. J. Inorg. Chem.* **2000**, 835.
  - 160 Simulations performed by M. BÜHL and F. TERSTEGEN, Max Planck Institut für Kohlenforschung, Mülheim, Germany.
  - 161 J. LIU, T. LEE, D. B. JANES, B. L. WALSH, M. R. MELLOCH, J. M. WOODALL, R. REIFENBERGER, R. P. ANDRES, *Appl. Phys. Lett.* **2000**, 77, 373.
  - 162 P. C. OHARA, J. R. HEATH, W. M. GELBART, *Angew. Chem.* **1997**, 109, 1120; *Angew. Chem., Int. Ed. Engl.* **1997**, 36, 1078.
  - 163 J. R. HEATH, C. M. KNOBLER, D. V. LEFF, *J. Phys. Chem. B* **1997**, 101, 189.
  - 164 W. M. GELART, R. P. SEAR, J. R. HEATH, *Faraday Discuss.* **1999**, 112, 299.
  - 165 R. P. SEAR, S. W. CHUNG, G. MARKOVICH, *Phys. Rev. E* **1999**, 59, R 6255.
  - 166 R. L. WHETTEN, M. N. SHAFIGULLIN, J. T. KHOURY, *Acc. Chem. Res.* **1999**, 32, 397.
  - 167 C. GUTIERREZ-WING, P. SANTIAGO, J. A. ASCENCIO, A. COMACHO, M. JOSE-YACAMAN, *Appl. Phys. A* **2000**, 71, 237.
  - 168 P. C. OHARA, D. V. LEFF, J. R. HEATH, W. M. GELBART, *Phys. Rev. Lett.* **1995**, 75, 3466.
  - 169 L. F. CHI, S. RAKERS, M. HARTIG,

- M. GLEICHE, H. FUCHS, G. SCHMID, *Colloids Surf.* **2000**, 171, 241.
- 170 J. J. BROWN, J. A. PORTER, C. P. DAGHLIAN, U. J. GIBSON, *Langmuir* **2001**, 17, 7966.
  - 171 E. YABLONOVITCH, *Phys. Rev. Lett.* **1987**, 58, 2059.
  - 172 S. JOHN, *Phys. Rev. Lett.* **1987**, 58, 2486.
  - 173 A. BLANCO, E. CHOMSKI, S. GRABTCHAK, M. IBISATE, S. JOHN, S. W. LEONARD, C. LOPEZ, F. MESEGUER, H. MIGUEZ, J. P. MONDIA, G. A. OZIN, O. TOADER, H. M. VAN DRIEL, *Nature* **2000**, 405, 437.
  - 174 J. P. SPATZ, A. ROESCHER, M. MÖLLER, *Polymer Reprints, Am. Chem. Soc.* **1996**, 36, 409.
  - 175 J. P. SPATZ, S. SHEIKO, M. MÖLLER, *Macromolecules*, **1996**, 29, 3220.
  - 176 J. P. SPATZ, A. ROESCHER, M. MÖLLER, *Adv. Mater.* **1996**, 8, 337.
  - 177 J. P. SPATZ, S. MÖßNER, M. MÖLLER, *Angew. Chem.* **1996**, 108, 1673; *Angew. Chem., Int. Ed. Engl.* **1996**, 35, 1510.
  - 178 J. P. SPATZ, S. SHEIKO, M. MÖLLER, *Adv. Mater.* **1996**, 8, 513.
  - 179 J. P. SPATZ, M. MÖLLER, P. ZIEMANN, *Physikal. Blätter* **1999**, 55, 1.
  - 180 J. P. SPATZ, P. EIBECK, S. MÖßNER, M. MÖLLER, T. HERZOG, P. ZIEMANN, *Adv. Mater.* **1998**, 10, 849.
  - 181 M. MÖLLER, J. P. SPATZ, A. ROESCHER, S. MÖßNER, S. T. SELVAN, H.-A. KLOK, *Macromol. Symp.* **1997**, 117, 207.
  - 182 M. MÖLLER, J. P. SPATZ, *Curr. Opin. Colloid Interface Sci.* **1997**, 2, 177.
  - 183 J. P. SPATZ, T. HERZOG, S. MÖßNER, P. ZIEMANN, M. MÖLLER, *Adv. Mater.* **1999**, 11, 149.
  - 184 J. P. SPATZ, T. HERZOG, S. MÖßNER, P. ZIEMANN, M. MÖLLER, in H. ITO, E. REICHMANIS, O. NALAMASU, T. UENO (eds.) ACS Symposium Series, Micro- and Nanopatterning Polymers, **1997**, 706, 12.
  - 185 J. P. SPATZ, S. MÖßNER, M. MÖLLER, T. HERZOG, A. PLETTL, P. ZIEMANN, *J. Luminescence* **1998**, 76, 77, 168.
  - 186 J. P. SPATZ, S. MÖßNER, C. HARTMANN, M. MÖLLER, T. HERZOG, M. KRIEGER, H.-G. BOYEN, P. ZIEMANN, B. KABIUS, *Langmuir* **2000**, 16, 407.
  - 187 M. HAUPT, S. MILLER, K. BITZER, K. THONKE, R. SAUER, J. P. SPATZ, S. MÖßNER, C. HARTMANN, M. MÖLLER, *Phys. Status Solidi* **2001**, 224, 867.
  - 188 B. KOSLOWSKI, S. STROBEL, T. HERZOG, B. HEINZ, H. G. BOYEN, R. NOTZ, P. ZIEMANN, J. P. SPATZ, M. MÖLLER, *J. Appl. Phys.* **2000**, 87, 7533.
  - 189 S. DIELUWEIT, D. PUM, U. B. SLEYTR, *Supramolec. Sci.* **1998**, 5, 15.
  - 190 S. R. HALL, W. SHENTON, H. ENGELHARDT, S. MANN, *Chem. Phys. Chem.* **2001**, 2, 194.
  - 191 M. MERTIG, R. KIRSCH, W. POMPE, H. ENGELHARDT, *Euro. Phys. J. D.* **1999**, 9, 45.
  - 192 R. D. PINER, J. ZHU, F. XU, S. HONG, C. A. MIRKIN, *Science* **1999**, 283, 661.
  - 193 S. HONG, J. ZHU, C. A. MIRKIN, *Science* **1999**, 286, 523.
  - 194 L. M. DEMERS, C. A. MIRKIN, *Angew. Chem* **2001**, 113, 3159; *Angew. Chem. Int. Ed. Engl.* **2001**, 40, 3069.
  - 195 L. M. DEMERS, S.-J. PERK, T. A. TATON, Z. LI, C. A. MIRKIN, *Angew. Chem.* **2001**, 113, 3161; *Angew. Chem., Int. Ed. Engl.* **2001**, 40, 3071.
  - 196 G. SCHMID, *J. Mater. Chem.* **2002**, 12, 1231.
  - 197 J. W. DIGGLE, T. C. DOWNIE, C. W. GOULDING, *Chem. Rev.* **1969**, 69, 365.
  - 198 J. P. O. SULLIVAN, G. C. WOOD, *Proc. R. Soc. London* **1970**, 317, 511.
  - 199 G. E. THOMPSON, G. C. WOOD, *Sci. Technol.* **1983**, 23, 205.
  - 200 M. M. LOHRENGEL, *Mater. Sci. Engl.* **1993**, 17, 202.
  - 201 G. C. HORNYAK, M. KRÖLL, R. PUGIN, Th. SAWITOWSKI, G. SCHMID, J.-O. BOVIN, G. KARSSON, H. HOFMEISTER, S. HOPFE, *Chem. Eur. J.* **1997**, 3, 1951.
  - 202 Th. SAWITOWSKI, Y. MIQUEL, A. HEILMANN, G. SCHMID, *Adv. Funct. Mater.* **2001**, 11, 435.
  - 203 P. BRAUNSTEIN, H.-P. KORMANN, W. MEYER-ZAIKA, R. PUGIN, G. SCHMID, *Chem. Eur. J.* **2000**, 6, 4637.
  - 204 C. M. NIEMEYER, *Curr. Opin. Chem. Biol.* **2000**, 4, 609.
  - 205 N. BEYER, PhD Thesis, University of Essen **2000**.
  - 206 J. RICHTER, R. SEIDEL, R. KIRSCH, M. MERTIG, W. POMPE, J. PLASCHKE, H. K. SCHACHERT, *Adv. Mater.* **2000**, 12, 507.
  - 207 W. E. FORD, O. HARNACK, A. YASUDA,

- J. M. WESSELS, *Adv. Mater.* **2001**, *13*, 1793.
- 208 M. G. WARNER, J. E. HUTCHISON, *Nat. Mater.* **2003**, *2*, 272.
- 209 A. KUMAR, M. PATTARKINE, M. BHADBHADHE, A. B. MANDELA, K. N. GANESH, S. S. DATAR, C. V. DHARMADHIKARI, M. SASTRY, *Adv. Mater.* **2002**, *13*, 341.
- 210 Y. LIU, W. MEYER-ZAIKA, S. FRAUZKA, G. SCHMID, M. TSOLI, H. KUHN, *Angew. Chem.* **2003**, *115*, 2959; *Angew. Chem. Int. Ed.* **2003**, *42*, 2853.
- 211 D. WYRWA, N. BEYER, G. SCHMID, *Nano Lett.* **2002**, *2*, 419.
- 212 T. REUTER, O. VIDONI, V. TORMA, G. SCHMID, L. NAN, M. OLEICHE, L. CHI, H. FUCHS, *Nano Lett.* **2002**, *2*, 709.
- 213 O. VIDONI, T. REUTER, V. TORMA, W. MEYER-ZAIKA, G. SCHMID, *J. Mater. Chem.* **2001**, *11*, 3188.
- 214 M. GLEICHE, L. F. CHI, H. FUCHS, *Nature*, **2000**, *403*, 173.
- 215 P. C. SCHOLTEN, in *Magnetic Properties of Fine Particles* (eds. J. L. DORTMANN, AND D. FIORANI) Elsevier, Amsterdam, The Netherlands, **1992**.
- 216 P. G. DE GENNES, P. A. PINCUS, *Phys. Kondens. Mater.* **1970**, *11*, 189.
- 217 R. W. CHANTRELL, A. BRADBURY, J. POPPLEWELL, S. W. CHARLES, *J. Appl. Phys.* **1982**, *53*, 2742.
- 218 J. M. TAVARES, J. J. WEIS, M. M. TELO DA GAMA, *Phys. Rev. E* **2002**, *65*, 061201.
- 219 K. BUTTER, P. H. H. BOMANS, P. M. FREDERIK, G. J. VROEGE, A. P. PHILIPSE, *Nature Mater.* **2003**, *2*, 8891.
- 220 S. L. TRIPP, S. V. PUSZTAY, A. E. RIBBE, A. WEI, *J. Am. Chem. Soc.* **2002**, *124*, 7914.
- 221 T. C. HALSEY, *Science* **1992**, *258*, 761.
- 222 M. HILGENDORFF, B. TESCHE, M. GIERSIG, *Aust. J. Chem.* **2001**, *54*, 497.
- 223 V. F. PUNTES, D. ZANCHET, C. K. ERDONMEZ, A. P. ALIVISATO, *J. Am. Chem. Soc.* **2002**, *124*, 12874.
- 224 T. VOSSMEYER, E. DELONNO, J. R. HEATH, *Angew. Chem., Int. Ed. Engl.* **1997**, *36*, 1080.
- 225 R. MAOZ, S. R. COHEN, J. SAGIV, *Adv. Mater.* **1999**, *11*, 55.
- 226 R. MAOZ, E. FRYDMAN, S. R. COHEN, J. SAGIV, *Adv. Mater.* **2000**, *12*, 424.
- 227 R. MAOZ, E. FRYDMAN, S. R. COHEN, J. SAGIV, *Adv. Mater.* **2000**, *12*, 725.
- 228 S. LIU, R. MAOZ, G. SCHMID, J. SAGIV, *Nano Lett.* **2002**, *2*, 1055.

## 5

## Properties

### 5.1

### Semiconductor Nanoparticles

#### 5.1.1

#### Optical and Electronic Properties of III–V and II–VI Nanoparticles

*Uri Banin and Oded Millo*

##### 5.1.1.1 Introduction

Semiconductor nanocrystals are novel materials with properties lying between the molecular and solid-state regimes, these properties, uniquely, being controlled by size and shape [1–8]. Containing hundreds to thousands of atoms, 20–200 Å in diameter, nanocrystals maintain a crystalline core with the periodicity of the bulk semiconductor. However, as the wave functions of electrons and holes are confined by the physical nanometric dimensions of the nanocrystals, the structure of the electronic levels and the resultant optical and electrical properties are greatly modified. Upon reducing the semiconductor size to the nanocrystal regime, a characteristic blue shift of the band gap appears, and a discrete level structure develops as a result of the “quantum size effect” in these quantum structures [9]. In addition, because of their small size, the charging energy associated with the addition or removal of a single electron is very high, leading to pronounced single-electron tunneling effects [10–12]. These phenomena provide ample scope for basic scientific research, which has attracted and continues to attract considerable attention. Because of their unique optical and electrical properties, nanocrystals are likely to play a key role in the emerging new field of nanotechnology in applications ranging from lasers [13, 14] and other opto-electronic devices [15–17] to biological fluorescence marking [18–20]. Here we discuss the optical and electronic properties of colloiddally grown quantum dots (QDs) and quantum rods (QRs). In the present chapter, particular attention is focused on the intuitive and appealing “artificial atom” picture of the electronic structure of semiconductor nanocrystals. In this respect, the combination of tunneling and optical spectroscopy methods has proven to be a powerful approach to the study of size- and shape-dependent level structure and single-electron charging in these systems.

Colloiddally grown nanocrystals have several favorable features such as con-



tinuous size control and chemical accessibility resulting from their overcoating with organic ligands. This chemical compatibility enables powerful chemical or biochemical means to be used to assemble nanocrystals in a controlled manner [21–27]. Further powerful control, of optical and electronic properties of nanocrystals has been achieved using colloidal synthesis. Heterostructured nanocrystals consisting of semiconductor shells grown on a core were developed [28–36]. Enhanced fluorescence and increased stability can be achieved in these particles compared with cores overcoated by organic ligands. Shape control was also achieved by suitable modification of the synthesis, allowing the preparation of rod-shaped particles – quantum rods (QRs) [6, 37, 38]. These manifest the transition from 0-D quantum dots to 1-D quantum wires in the sense that strong quantum confinement holds for the radial direction but weak confinement for the axial direction [39, 40]. QRs exhibit electronic and optical properties differing from those of QDs, e.g., polarized emission [41], which leads to polarized lasing [14]. Additionally, the rod geometry was found to be advantageous in polymer nanocrystal-based solar cells, because of improvement in charge transport properties [42].

In this chapter we deal with the electronic structure and the optical and electrical properties of colloiddally grown semiconductor nanocrystals, and concentrate on the application of tunneling and optical spectroscopy to this problem. In Section 5.1.1.2, we describe the application of optical and tunneling spectroscopy to the study of semiconductor nanocrystals, using the artificial atom analogy to represent their level structure. In Section 5.1.1.3, the modifications associated with core/shell nanocrystals are discussed, and, in particular, the atomic-like envelope wave functions are visualized using scanning tunneling microscopy. Section 5.1.1.4 discusses the electronic properties of quantum rods, and Section 5.1.1.5 describes recent results on optical gain and lasing obtained with semiconductor nanocrystals.

#### 5.1.1.2 Semiconductor Nanocrystals as Artificial Atoms

From the early work on the quantum confinement effect in colloidal semiconductor QDs, electronic levels have been assigned according to the spherical symmetry of the electron and hole envelope functions [9, 43]. The simplistic “artificial atom” model of a particle in a spherical box predicts discrete states with atomic-like state symmetries, e.g., *s* and *p*. To probe the electronic structure of II–VI and III–V semiconductor nanocrystals, a variety of “size-selective” optical techniques have been used, mapping the size dependence of dipole allowed transitions [44–48]. Theoretical models based on an effective mass approach with varying degree of complexity [45, 49] as well as pseudopotentials [50, 51] were used to assign the levels. A model system that was studied extensively in this context is that of CdSe nanocrystals, for which spectroscopic mapping of electronic states using PLE (photo luminescence excitation) was performed by Bawendi and coworkers [44, 45]. The size-selective PLE method was also utilized to examine the size-dependent level structure of InAs QDs, an additional system that has attracted interest [47, 48]. InAs is a narrow-gap semiconductor ( $E_g = 0.418$  eV) with a large Bohr radius  $a_0$  of 340 Å, whereas CdSe has a significantly larger band gap,  $E_g = 1.84$  eV and

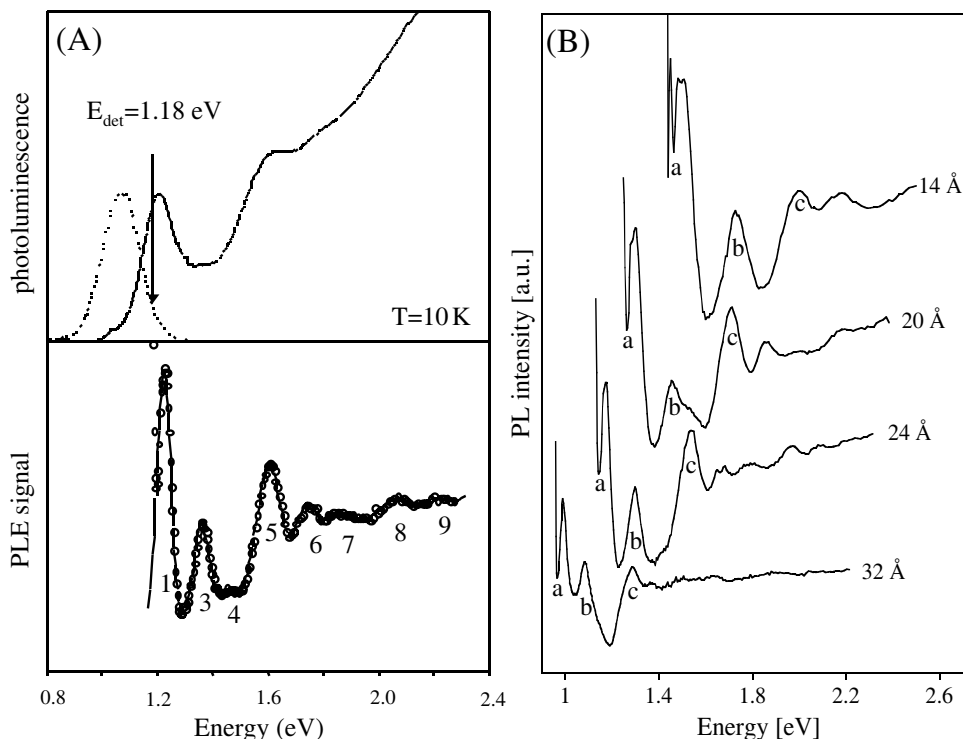


**Fig. 5-1** **A** Optical spectroscopy of InAs nanocrystals with a mean radius of 2.5 nm. The top frame shows the absorption (solid line) and the PL (dotted line) for the sample. The lower frame shows a size-selected PLE spectrum, where eight transitions are resolved, measured with a narrow detection window

positioned as indicated by the arrow in the top panel. The weak transition  $E_2$  is not detected in this QD size. **B** Size-dependent PLE spectra for four representative InAs QD radii. The band gap transition (a), and two strong excited transitions (b and c) are indicated.

smaller Bohr radius ( $a_0 = 55 \text{ Å}$ ). Therefore both systems serve as a prototypical framework for the study of quantum confinement effects.

Figure 5-1A shows the typical spectral features measured at 10 K for a sample of InAs nanocrystals with a mean radius of 2.5 nm. The absorption onset exhibits a  $\sim 0.8 \text{ eV}$  blue shift from the bulk band gap. A pronounced first peak and several features at higher energies are observed in the absorption spectra. Band edge luminescence is observed, with no significant red-shifted (deep-trapped) emission. In the PLE spectrum, a set of up to eight transitions are resolved. The full size dependence was measured by changing the detection window and by using different samples, and a representative set of such PLE spectra is shown in Figure 5-1B [47].

The map of excited transitions for InAs nanocrystals was extracted from such PLE data, and the levels were assigned using an eight-band effective mass model [47]. Briefly, in this approach, each electron ( $e$ ), and hole ( $h$ ) state, is characterized by its parity and its total angular momentum  $\mathbf{F} = \mathbf{J} + \mathbf{L}$ , where  $\mathbf{J}$  is the Bloch band

edge angular momentum ( $1/2$  for the conduction band (CB),  $3/2$  for the heavy and light hole bands, and  $1/2$  for the split-off band) and  $\mathbf{L}$  is the angular momentum associated with the envelope function. The standard notation for the electron and hole states is  $nQ_F$ , where  $n$  is the main quantum number, and  $Q = S, P, D, \dots$ , denotes the lowest  $L$  in the envelope wave function. The calculated level separations were found to closely reproduce the observed strong transitions.

Tunneling transport through semiconductor nanocrystals can yield complementary information on their electronic properties which cannot be probed in the optical measurements. While, in the optical spectra, allowed valence band (VB) to conduction band (CB) transitions are detected, in tunneling spectroscopy the CB and VB states can be separately probed. In addition, the tunneling spectra may show effects of single-electron charging of the QD. Such interplay between single-electron charging and resonant tunneling through the QD states can provide unique information on the degeneracy and therefore the symmetry of the levels.

The interplay between single-electron tunneling (SET) effects and quantum size effects in isolated nanoparticles can be experimentally observed most clearly when the charging energy of the dot by a single electron,  $E_c$ , is comparable to the electronic level separation  $\Delta E_L$ , and both energy scales are larger than  $k_B T$  [10, 52, 53]. These conditions are met by semiconductor nanocrystals in the strong quantum confinement regime, even at room temperature, while for metallic nanoparticles,  $E_c$  is typically much larger than  $\Delta E_L$ . SET effects are relevant to the development of nano-scale electronic devices, such as single-electron transistors [54, 55].

However, for small colloidal nanocrystals, the task of wiring up the QD between electrodes for transport studies is exceptionally challenging. To this end, various mesoscopic tunnel junction configurations have been employed, such as the double barrier tunnel junction (DBTJ) geometry, where a QD is coupled via two tunnel junctions to two macroscopic electrodes [10, 11, 56, 57]. Klein et al. achieved this by attaching CdSe quantum dots to two lithographically prepared electrodes, and have observed SET effects [58]. In this device, a gate voltage can be applied to modify the transport properties. An alternative approach to achieving electrical transport through single QDs is to use scanning probe methods. Alpers et al. observed SET effects at room temperature in electrochemically deposited CdSe nanocrystals using conductive atomic force microscopy (AFM) [59].

A most useful approach for tunneling-transport spectroscopy on single nanocrystals is based on using the scanning tunneling microscope (STM). For such measurements, the nanocrystals can be linked to a gold film via hexanedithiol (DT) molecules [12, 60], enabling the realization of a DBTJ, as shown schematically in Figure 5-2A. An STM topographic image of an isolated InAs QD, 32 Å in radius, is presented in Figure 5-2A (left inset). Also shown is a tunneling current-voltage ( $I-V$ ) curve that was acquired after positioning the STM tip above the QD. A region of suppressed tunneling current is observed around zero bias, followed by a series of steps at both negative and positive bias. Figure 5-2B shows the  $dI/dV$  versus  $V$  tunneling conductance spectrum, which is proportional to the tunneling DOS (density of states). A series of discrete single-electron tunneling peaks is clearly observed, where the separations are determined by both  $E_c$  (addition spec-

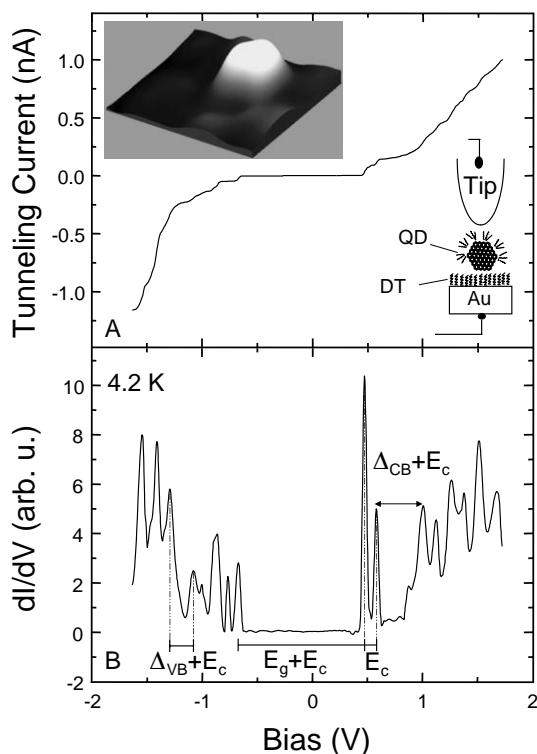


**Fig. 5-2** STM measurements on a single InAs nanocrystal of radius 3.2 nm, acquired at 4.2 K. The QDs are linked to the gold substrate by DT molecules, as shown schematically in the right inset. The left inset presents a  $10 \times 10$  nm STM topographic image of the QD. The tunneling  $I$ - $V$  characteristic is shown in **A**, and the tunneling conductance spectrum in **B**. The arrows depict the main energy separations:  $E_c$  is the single-electron charging energy,  $E_g$  is the nanocrystal band-gap, and  $\Delta_{VB}$  and  $\Delta_{CB}$  are the spacings between levels in the valence and conduction bands, respectively.

trum) and the discrete level spacings (excitation spectrum) of the QD. The  $I$ - $V$  characteristics were acquired with the tip retracted from the QD to a distance where the bias predominantly drops on the tip-QD junction. In these conditions, representing an asymmetric DBTJ, CB (VB) states appear at positive (negative) sample bias, and the excitation peak separations are nearly equal to the real QD level spacings [12, 61].

On the positive bias side of Figure 5-2B, two closely spaced peaks are observed immediately after current onset, followed by a larger spacing and a group of six nearly equidistant peaks. The doublet is assigned to tunneling through the lowest CB QD state, where the spacing corresponds to the single-electron charging energy,  $E_c$ . The observed doublet is consistent with the degeneracy of the envelope function of the first CB level,  $1S_e$  (here we revert to a simpler notation for the CB states), which has  $s$  character. In this case, a direct relationship between the degeneracy of a QD level and the number of addition peaks is expected. This is

further substantiated by the observation that the second group consists of six peaks, corresponding to the degeneracy of the  $1P_e$  state, spaced by  $E_c$ . This sequential level filling resembles the Aufbau principle of building up the lowest energy electron configuration of an atom, directly demonstrating the atomic-like nature of the QD.

The separation between the two groups of peaks is a sum of the level spacing  $\Delta_{CB} = 1P_e - 1S_e$  and the charging energy  $E_c$ . On the negative bias side, tunneling through filled dot levels takes place, reflecting the tunneling DOS of the QD valence band. Again, two groups of peaks are observed. The multiplicity in this case, in contrast to the CB, cannot be clearly assigned to specific angular momentum degeneracy. In a manner similar to that described above for the CB states, we extract a value of  $\Delta_{VB}$  for the level separation between the two observed VB states. In the region of null current around zero bias, the tip and substrate Fermi energies are located within the QD band gap where the tunneling DOS is zero, and the energy gap  $E_g$  can be extracted from the observed spacing between the highest VB and the lowest CB peaks. The gap region appears to be free of spectral features (see also Figure 5-3). Upon removing the coating ligands by pyridine treatment, sub-gap states can be observed [62], which were attributed to surface states [63].

The tunneling conductance spectra for single InAs nanocrystals spanning a size range of 10–35 Å in radius are presented in Figure 5-3. Two groups of peaks are observed in the positive bias side (CB). The first is always a doublet, consistent with the expected  $s$  symmetry of the  $1S_e$  level, while the second has a higher multiplicity of up to six, consistent with  $1P_e$ . The separation between the two groups and the spacing of peaks within each multiplet increase with decreasing QD radius. This reflects quantum size effects on the nanocrystal energy levels and its charging energy, respectively. On the negative bias side, generally two groups of peaks, which exhibit similar quantum confinement effects, are also observed. Here, variations in the group multiplicities between QDs of different sizes as well as variations in the peak energy spacings within each group are observed. This behavior is partly due to the fact that  $E_c$  is very close to  $\Delta_{VB}$ , the level spacing in the valence band, as shown in Figure 5-4B. In this case, sequential single-electron tunneling may be either addition to the same VB state or excitation with no extra charging to the next state. An atomic analogy for this situation can be found in the changing order of electron occupation when moving from the transition to the noble metals within a row of the periodic table.

The comparison between tunneling and PLE data can be used to decipher the complex QD level structure. This correlation is also important for examining possible effects of charging and tip-induced electric field in the tunneling measurements on the nanocrystal level structure. First, the size dependence of the band gap  $E_g$  as extracted from the tunneling data can be compared with the nanocrystal sizing curve (Figure 5-4A). The sizing curve (open diamonds) was obtained by correlating the average nanocrystal size, measured using transmission electron microscopy (TEM), with the excitonic band gap of the same sample [48]. To compare these data with the tunneling results, a correction term,  $1.8e^2/\epsilon r$ , was added to compensate for the electron-hole excitonic Coulomb interaction that is absent

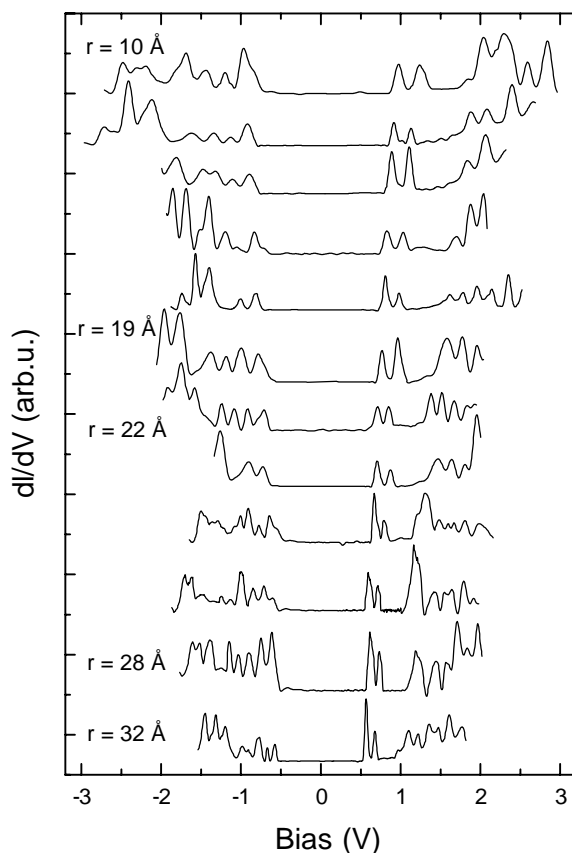


**Fig. 5-3** Size evolution of the tunneling spectra at 4.2 K of single InAs QDs, displaced vertically for clarity. The positions of the centers of the zero current gap showed non-systematic variations with respect to the zero

bias, of the order of 0.2 eV, probably due to variations of local offset potentials. For clarity of presentation, the spectra are offset along the V-direction to center them at zero bias. Representative nanocrystal radii are shown.

in the tunneling data [9]. Agreement is good for the larger nanocrystal radii, with increasing deviation for smaller nanocrystals. This deviation may be due to the difference in the estimation of QD size between the experiments, which should be more pronounced in the small-size regime [12].

Next, in Figure 5-4B, the size dependence of the higher strongly allowed optical transitions is compared with the level spacings measured by tunneling spectroscopy. The two lower data sets (II) compare the difference between the first strong excited optical transition and the band gap from PLE (b-a in Figure 5-1) with the separation  $\Delta_{VB} = 2_{VB} - 1_{VB}$  in the tunneling data (open and full squares, respectively). The excellent correlation observed enables us to assign this first excited transition in the PLE to a  $2_{VB} - 1S_e$  excitation, as shown schematically in the inset of Figure 5-4A. Strong optical transitions are allowed only between electron and hole states with the same envelope function symmetry. We thus infer that the en-

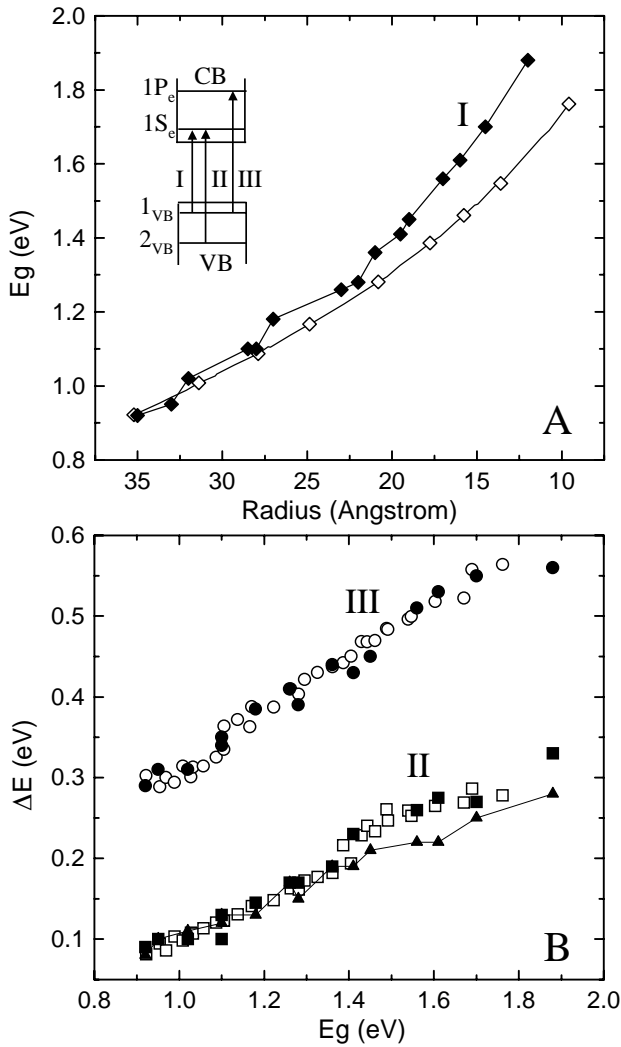


**Fig. 5-4** Correlation of optical and tunneling spectroscopy data for InAs QDs. The inset shows a schematic of the CB and VB level structure and optical transitions I, II, and III (a, b and c in Figure 5-1). **A** Comparison of the size dependence of the low-temperature optical band gap (transition I) after Coulomb correction (open diamonds) with the band gap measured by the STM (filled diamonds). **B** Excited transitions plotted versus the band gap for tunneling and optical spectroscopy: The two lower data sets (II) depict the

correlation between  $\Delta_{VB} = 1_{VB} - 2_{VB}$ , detected by tunneling spectroscopy (full squares), with the difference between transition II and the band gap transition I (open squares). The two upper data sets (III) depict the correlation between  $\Delta_{CB} = 1P_e - 1S_e$ , determined from the tunneling spectra (full circles), with the difference between optical transition III and I (open circles). Also shown is the size dependence of  $E_c$  from the tunneling data (full triangles).

velope function for state  $2\nu_B$  should have  $s$  character, and this state can be directly identified as the  $2S_{3/2}$  valence band level.

Another important comparison is depicted by the higher pair of curves, set III. The second strong excited optical transition relative to the band gap (c-a in Figure 5-1) is plotted along with the spacing  $\Delta_{CB} = 1P_e - 1S_e$  from the tunneling spectra. Again, excellent correlation is observed, which allows us to assign this peak in the PLE to the  $1\nu_B - 1P_e$  transition (Figure 5-4A, inset). The topmost VB level,  $1\nu_B$ , should thus have some  $p$  character for this transition to be allowed. From this, and considering that the band gap optical transition  $1\nu_B - 1S_e$  is also allowed, we conclude that  $1\nu_B$  has mixed  $s$  and  $p$  character, in agreement with theory [47, 64]. The good agreement between the tunneling and optical measurements indicates that charging and the tip-induced Stark effect do not significantly perturb the QD level structure.

Concerning the tunneling data, it is important to note that a detailed understanding of the role played by the double barrier tunnel junction (DBTJ) geometry and the ability to control it are essential for the correct interpretation of tunneling characteristics. In particular, the ratio between the junction capacitances determines the voltage division and therefore the observed level spacing. By varying the tip-QD distance it is possible to modify the voltage division as discussed in [65] and [66]. Additionally, the degree of single-electron charging effects depends on the ratio of the tunneling rates between the two junctions. When the rate of one of the junctions is significantly higher, charging effects are suppressed, as was achieved by depositing InAs nanocrystals on graphite (HOPG – highly oriented pyrolytic graphite) without linker molecules, leading to vanishing of the charging multiplets [61], as can be seen in Figure 5-5. A similar effect was also observed for CdSe and CdS nanocrystals by Bakkers et al. [67].

#### 5.1.1.3 Theoretical Descriptions of the Electronic Structure

The theoretical treatments for both optical and tunneling experiments on QDs first require the calculation of the level structure. Various approaches have been developed to treat this problem, including effective mass-based models, with various degrees of band-mixing effects [45, 47, 49, 68] and a more atomistic approach based on pseudo-potentials [64, 69]. Both have been successfully applied for various nanocrystal systems [50, 51, 69–72]. To model the PLE data, one has to calculate the oscillator strength of possible transitions and take into account the electron-hole Coulomb interaction which modifies the observed (excitonic) band gap. In the tunneling case, as discussed above, the device geometry should be carefully modeled, and, in addition, the effects of charging and the tip-bias on the level structure needs to be considered. The charging may affect the intrinsic level structure and also determines the single-electron addition energy, while the tip-bias may perturb the levels via the Stark effect.

Zunger and coworkers treated the effects of electron charging for a QD embedded in a homogeneous dielectric medium characterized by  $\epsilon_{out}$ . The addition energies and quasi-particle gap were calculated as a function of  $\epsilon_{out}$  [73, 74]. While this isotropic model does not represent the experimental geometry of the tunnel-



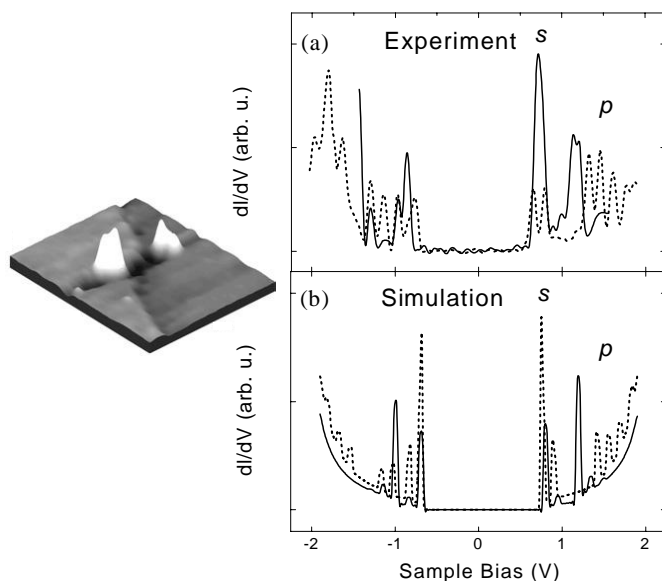


**Fig. 5-5** **a** Tunneling spectra measured on InAs QDs of radius ca. 2 nm. The solid curve was measured in the QD/HOPG geometry and the dashed curve in the QD/DT/Au geometry. **b** Calculated spectra showing the effect of tunneling-rate ratio. The dashed and solid curves were calculated with tunneling rate ratios,  $\Gamma_2/\Gamma_1$ , ca. 1 and 10, respectively. The image shows two QDs positioned near a step on HOPG.

ing measurements, the authors were able to find good agreement between the energetic positions of the peaks for several QD sizes using one value of  $\epsilon_{\text{out}}$ . These authors also noted that the charging energy contribution associated with the band-gap transition may be different from that within the charging multiplets in the excited states. This difference is, however, on the order of the peak width in our spectra.

In another approach, Niquet et al. modeled the junction parameters (capacitances and tunneling rates) and used a tight-binding model for the level structure [75, 76]. The tunneling spectra were calculated using a rate equation method. The authors were able to reproduce the experimental tunneling spectra, attributing part of the tunneling peaks at negative bias to tunneling through the CB.

#### 5.1.1.4 Atomic-like States in Core/Shell Nanocrystals – Spectroscopy and Imaging

Additional complexity and functionality are afforded for semiconductor nanocrystals through the growth of shells. Of particular interest are core/shell nanocrystals that exhibit enhanced emission quantum yield (QY) and improved stability. In such composite core/shell structures, the shell type and shell thickness provide further control for tailoring the optical, electronic, electrical and chemical properties of semiconductor nanocrystals. The growth of InAs/shell nanocrystals with high QY in the technologically important near-IR spectral range is discussed in Section 3.1.3.4 and in [34]. These nanocrystals were successfully implemented

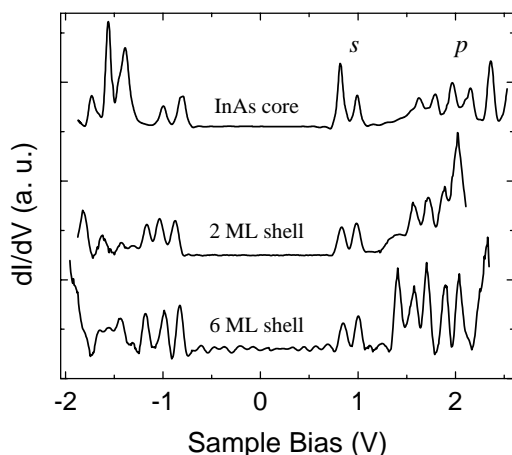


**Fig. 5-6** Tunneling conductance spectra of an InAs core QD and two core/shell nanocrystals with two and six ML shells with nominal core radii of ca. 1.7 nm. The spectra were offset along the  $V$  direction to center the observed zero current gaps at zero bias.

as chromophores in polymer-nanocrystal light emitting diodes active in the telecomm range [17]. They also constitute an important system for further investigating the evolution of level structure in QDs. The combined tunneling and optical spectroscopy approach has been further applied to investigate core/shell nanocrystals.

Figure 5-6 shows tunneling-conductance spectra measured on two InAs/ZnSe core/shell nanocrystals with 2 and 6 ML (monolayer) shells, along with a typical curve for an InAs QD of radius similar to the nominal core radius  $\sim 1.7$  nm, deposited on Au with DT linkers. The general appearance of the spectra of core and core/shell nanocrystals is similar and the band-gap is nearly identical, as observed in the optical absorption measurements [34]. In contrast, the  $s$ - $p$  level separation is substantially reduced. Both effects are consistent with a model in which the  $s$  state is confined to the InAs core region, while the  $p$  level extends to the ZnSe shell. In this case, the  $p$  state is red-shifted upon increasing shell thickness, whereas the  $s$  level does not shift, yielding a closure of the CB  $s$ - $p$  gap.

The complementary optical spectroscopy also provides evidence of the reduction of the  $s$ - $p$  spacing upon shell growth, as manifested by the PLE spectra presented in Figure 5-7. The three spectra, for cores (solid line) and core/shells with 4 ML and 6 ML shell thickness (dotted and dashed lines, respectively), were measured using the same detection window (970 nm), corresponding to the excitonic band-gap energy for InAs cores 1.7 nm in radius. The peak labeled III, which as discussed earlier corresponds in the cores to the transition from the VB edge state to the CB  $1P_e$  state, is red-shifted monotonically upon shell growth. The dependence of the difference between peak III and the band-gap transition I on shell thickness is depicted in the inset of Figure 5-7 (circles), along with the  $1S_e - 1P_e$  level spac-

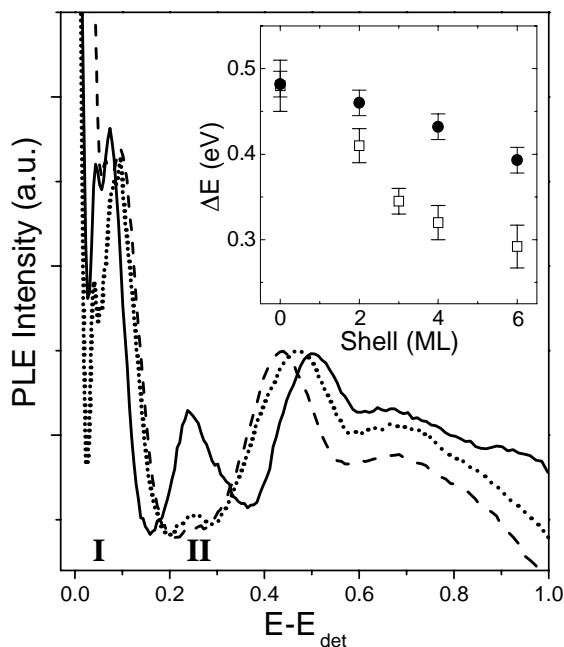


**Fig. 5-7** PLE spectra, normalized to peak III, for InAs cores (solid line) and InAs/ZnSe core/shell nanocrystals of four (dotted line) and six (dashed line) ML shells, with the zero of the energy scale taken at the detection window (970 nm). The inset depicts the dependence

on shell thickness of the  $s$ - $p$  level closure, as determined by tunneling (open squares) and PLE (solid circles). The PLE data points represent the difference between transition III and transition I (which hardly shifts upon shell growth).

ing extracted from the tunneling spectra (squares). While the qualitative trend of red shift is similar for both data sets, there is a quantitative difference, the optical shift being considerably smaller. This is in contrast to the good correlation between the optical and tunneling spectra observed for InAs cores, providing an opportunity to examine the intricate differences between these two complementary methods. While the tunneling data directly depict the spacing between the two CB states, the PLE data in the inset of Figure 5-7 represent the energy difference between two VB to CB optical transitions. Therefore, evolution of the complex VB edge states upon shell growth will inevitably affect the PLE spectra. In particular, a blue shift of the  $p$ -like component of the VB edge state upon shell growth will reduce the net observed PLE shift compared to the tunneling data, consistent with the experimental observations.

The elegant artificial atom analogy for QDs, borne out by optical and tunneling spectroscopy, can be tested directly by observing the shapes of the QD electronic wave functions, as was demonstrated by various techniques for MBE (molecular beam epitaxy) grown QDs. For colloidal free-standing nanocrystal-QDs, the unique sensitivity of the STM to the electronic density of states on the nanometer scale seems to provide an ideal probe of the wave functions. A demonstration of this

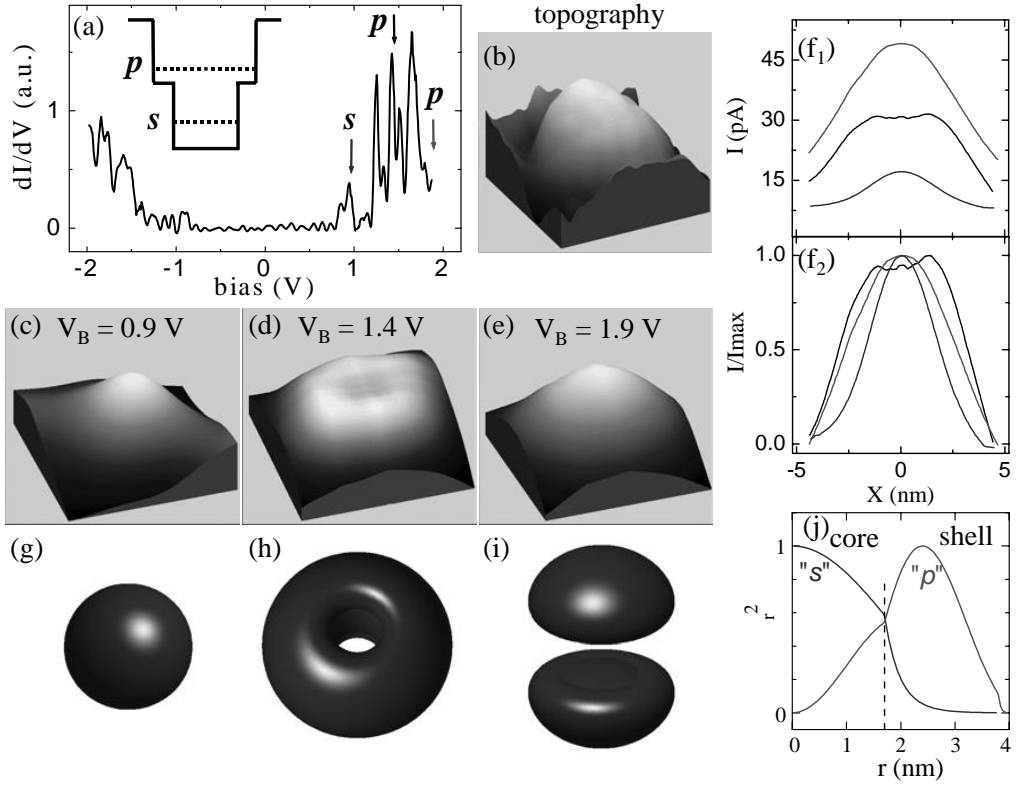


**Fig. 5-8** Wave function imaging and calculation for an InAs/ZnSe core/shell QD having a six ML shell. **a** A tunneling spectrum acquired for the nanocrystal. **b**  $8 \times 8 \text{ nm}^2$  topographic image taken at  $V_B = 2.1 \text{ V}$  and  $I_s = 0.1 \text{ nA}$ . **c–e** Current images obtained simultaneously with the topographic scan at three different bias values denoted by arrows in **a**. **f1** Cross-sections taken along the diagonal of the current images at  $0.9 \text{ V}$  (lower curve),  $1.4 \text{ V}$  (middle

curve) and  $1.9 \text{ V}$  (upper curve). **f2** The same cross-sections normalized to their maximum current values. **g–j** Envelope wave functions calculated within a “particle-in-a-sphere” model. The radial potential and the energies of the  $s$  and  $p$  states are illustrated in the inset of frame **a**. **g–i** Isoproability surfaces, showing  $s^2$  (**g**),  $p_x^2 + p_y^2$  (**h**), and  $p_z^2$  (**i**). **j** The square of the radial parts of the  $s$  and  $p$  wave functions normalized to their maximum values.

capability is given by recent work on the InAs/ZnSe core/shells discussed above. Here, the different extent of the CB  $s$  and  $p$  states, implied by the spectroscopic results, can be directly verified by using the STM to image the QD atomic-like wave functions.

Bias-dependent current imaging measurements were performed, as shown in Figure 5-8 for a core/shell nanocrystal with 6 ML shell. The  $dI/dV$  versus  $V$  spectrum is shown in Figure 5-8a, and the bias values for tunneling to the  $s$  and  $p$  states are indicated. A topographic image was measured at a bias value above the  $s$  and  $p$  states,  $V_B = 2.1 \text{ V}$  (Figure 5-8b), simultaneously with 3 current images. At each point along the topography scan the STM feedback circuit was disconnected momentarily, and the current was measured at three different  $V_B$  values:  $0.9 \text{ V}$ ,

corresponding to the CB  $s$  state (Figure 5-8c); 1.4 V, within the  $p$  multiplet (Figure 5-8d); and 1.9 V, above the  $p$  multiplet (Figure 5-8e). With this measurement procedure, the topographic and current images were all measured with the same constant local tip-QD separation. Thus, the main factor determining each current image is the local (bias-dependent) DOS, reflecting the shape of the QD electronic wave functions.

Upon comparing the current images, pronounced differences are observed in the extent and shape of the  $s$  and  $p$  wave functions. The image corresponding to the  $s$ -like wave function (Figure 5-8c) is localized to the central region of the core/shell nanocrystal, while the images corresponding to the  $p$ -like wave functions extend out to the shell (Figures 5-8d,e), consistent with the model discussed above. This can also be seen in the cross-sections presented in frame  $f_1$  taken along a common line through the center of each current image, and most clearly in frame  $f_2$ , which shows the current normalized to its maximum value along the same cuts. Figure 5-8e, taken at a voltage above the  $p$  multiplet, manifests a nearly spherical geometry similar to that of Figure 5-8c for the  $s$  state, but has a larger spatial extent. Figure 5-8d, taken with  $V_b$  near the middle of the  $p$  multiplet, is also extended but has a truncated top with a small dent in its central region.

An illustrative model aids the interpretation of the current images, assuming a spherical QD shape, with a radial core/shell potential taken as shown in the inset of Figure 5-8a [77]. The energy calculated for the  $s$  state is lower than the barrier height at the core-shell interface and has about the same values for core and core/shell QDs. In contrast, the energy of the  $p$  state is above the core-shell barrier and it red-shifts with shell growth, in qualitative agreement with our spectroscopic result discussed in the previous section. Isoprobability surfaces for the different wave functions are presented in Figures 5-8g to 5-8i, with Figure 5-8g showing the  $s$  state, Figure 5-8h the in-plane component of the  $p$  wave functions,  $p_x^2 + p_y^2$ , which has a torus-like shape, and Figure 5-8i the perpendicular component,  $p_z^2$ . The squares of the radial parts of the  $s$  and  $p$  wave functions are presented in Figure 5-8j. The calculated probability density for the  $s$  state is spherical in shape and mostly localized in the core, while the  $p$  components extend much further to the shell, consistent with the bias-dependent current images. Moreover, the different shapes observed in the current images can be assigned to different combinations of the probability density of the  $p$  components.

A filled torus shape, similar to the current image of Figure 5-8d taken at the middle of the  $p$  multiplet, can be obtained by a combination with larger weight of the  $(p_x^2 + p_y^2)$  component parallel to the gold substrate, and a smaller contribution of the  $p_z$  component. The unequal weights reflect preferential tunneling through the in-plane components. This may result from a tip-induced Stark effect leading to a small degeneracy lifting, as shown theoretically by Tews and Pfannkuche [78]. A spherical shape for the isoprobability surfaces results from summing all the  $p$  components with equal weights, consistent with the current image measured at a bias above the  $p$  manifold (Figure 5-8e). This example of wave function imaging combined with the tunneling and optical spectra provides visualization of the atomic-like character of nanocrystal quantum dots.

### 5.1.1.5 Level Structure of CdSe Quantum Rods

An additional system prepared by colloidal chemistry that is attracting considerable interest is that of quantum rods that exhibit electronic and optical properties different from QDs. For example, because of their cylindrical symmetry, QRs have linearly polarized emission, as demonstrated by fluorescence measurements on single rods [41], leading to polarized lasing [14]. The powerful combination of optical and tunneling spectroscopy discussed here was also applied to the investigation of the length and diameter dependence of the electronic level structure of CdSe quantum rods [40].

The central conclusion drawn from the spectroscopic studies, as well as from calculations employing a multiband effective mass model, is that the QR level spectrum depends mainly on the rod diameter and not on its length for CdSe rods with length above  $\sim 10$  nm [40]. This is demonstrated in Figure 5-9 by both PLE and tunneling data. PLE spectra (left frame) measured on QR samples differing considerably in length but having similar diameter look very similar, whereas the spectra measured on QRs of different radii appear to be different. This becomes evident by comparing the upper two PLE curves measured on thin rods (radii  $\sim 1.7$  nm) with the lower curves measured on thicker ones (radii  $\sim 3.1$  nm). The tunneling spectra (right frame), acquired in the regime where charging effects are suppressed, reveal a similar behavior. It can be seen here as well that the band

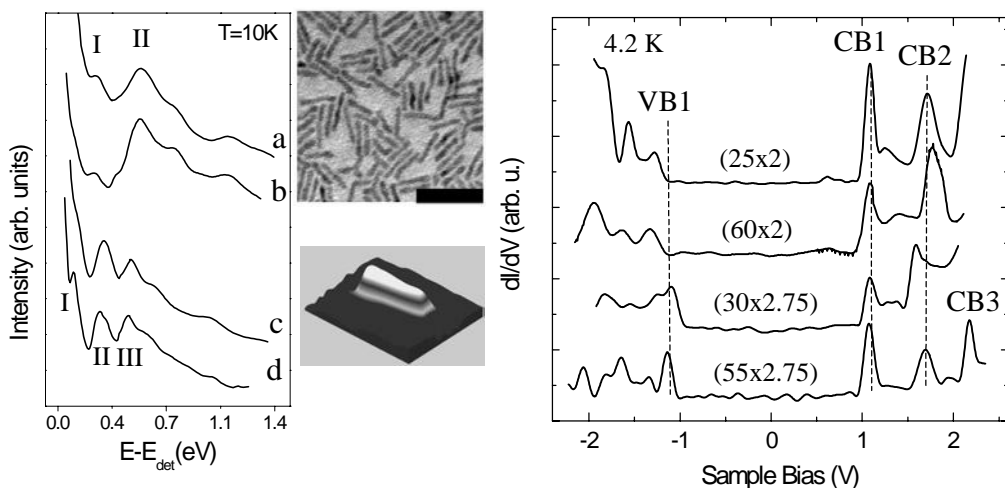


**Fig. 5-9** Optical and tunneling spectroscopy of CdSe QRs. PLE spectra for CdSe QRs are shown in the left hand frame: **a**  $31 \times 1.9$  (length times radius) nm, **b**  $11 \times 1.6$  nm, **c**  $60 \times 3.3$  nm, **d**  $11 \times 2.9$  nm, with the zero energy representing the position of the detection window. Relevant optical transitions are marked. The structure above 0.7 eV is overlapping peaks of the excitation lamp that

could not be completely normalized out. In the right hand frame, tunneling spectra for QRs of different sizes are shown. For clarity, the spectra were shifted horizontally to align the CB1 peaks. Between the left- and right-hand frames, a TEM image of a QR sample,  $31 \times 3.9$  nm (top, scale bar is 50 nm), and an STM topographic image of a single QR,  $25 \times 2$  nm (bottom), are shown.

gap depends mainly on, and decreases with, the QR radius, in agreement with the optical measurements [39].

#### 5.1.1.6 Optical Gain and Lasing in Semiconductor Nanocrystals

The broad spectral coverage for luminescence from the ultraviolet to the near infrared offered via tunability of composition, size and shape in semiconductor nanocrystals presents an obvious advantage for using such materials as tunable optical gain media and in laser applications. Furthermore, low lasing thresholds predicted for quantum dots and quantum wires compared with two-dimensionally confined quantum wells are the basis of present semiconductor diode laser devices ubiquitous in information and telecommunication technologies [79, 80].

Amplified spontaneous emission was recently observed by Bawendi, Klimov and coworkers for spherical colloidal CdSe QDs in close-packed films where pumping with an amplified femtosecond laser source was used to compete with fast non-radiative Auger decay processes [13, 81]. In further studies, films with CdSe nanocrystals were deposited on a distributed feedback grating structure to yield optically pumped lasing that was tunable through the visible range by changing the nanocrystal size [82, 83].

Lasing was also observed for semiconductor nanocrystals in solution at room temperature using a cylindrical microcavity, with nanosecond (ns) excitation. A simple microcavity set-up was used, providing uncomplicated means for screening colloidal nanocrystals as potential laser chromophores directly in solution [14].

Figure 5-10 presents results of lasing for CdSe/ZnS quantum rods, along with their structural and optical characteristics. The quantum rods were grown using the well-developed methods of colloidal nanocrystals. The rod/shell configuration was chosen, since the growth of ZnS on the organically coated CdSe quantum rods increases the fluorescence quantum yield from ~2% to 14%. A transmission electron microscope (TEM) image of the quantum rods deposited on a grid from hexane solution is presented in Figure 5-10a. Good size and shape monodispersity is observed, and the average nanorod length is 25 nm, with an average diameter of 4 nm. The monodispersity is deemed essential for achieving lasing, by reducing the inhomogeneous spectral broadening of the gain profile. The optical characteristics of the nanorod sample are summarized in Figure 5-10b.

In Figure 5-10c, emission spectra collected from the cylindrical microcavity, loaded with a quantum rod sample in hexane, is shown for several laser excitation intensities, where each spectrum corresponds to a single laser shot. The peak at 2.33 eV is due to scattering of the pump laser. At low excitation intensities (e.g. 0.016 mJ), the spectrum resembles the emission spectrum measured for the quantum rods in solution (Figure 5-10b). At higher intensities, changes in the spectral shape are observed. Most significantly, above ~0.08 mJ a narrow lasing peak clearly emerges at 1.98 eV, on the red side of the fluorescence peak. The dependence of the intensity of the lasing peak on pump power is shown in the right inset of Figure 5-10c (full squares) along with the dependence of the fluorescence peak intensity (empty circles). The lasing peak intensity exhibits an abrupt change of slope at the onset of laser action, while at the same time, the peak fluorescence

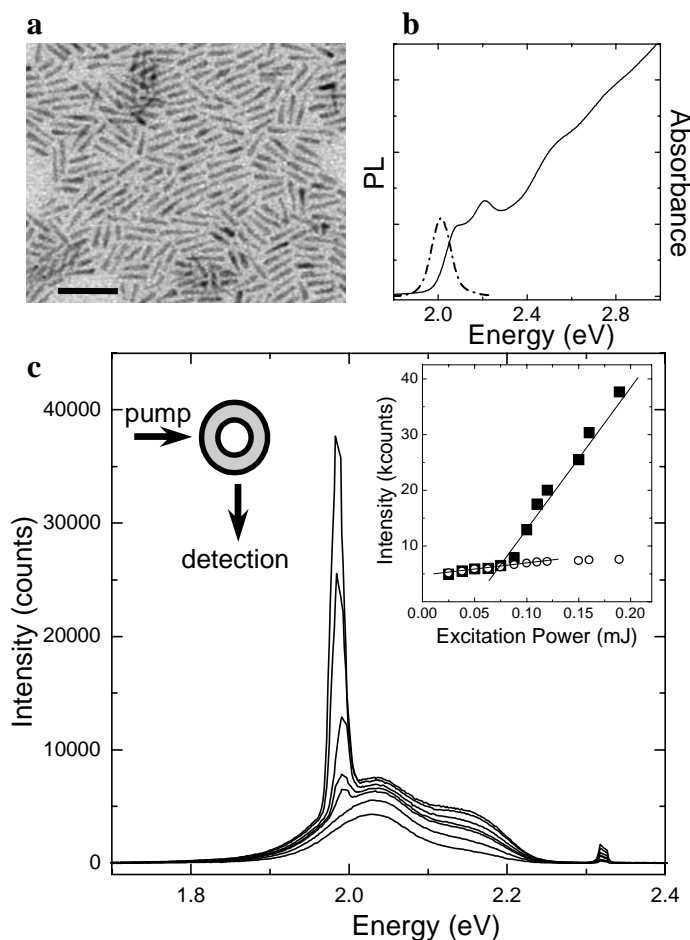


**Fig. 5-10** Frame **a** is a TEM image of the quantum rod sample (scale bar 50 nm). Frame **b** shows the absorption (solid line), and the emission (dot-dashed line) for the quantum rods in solution. Frame **c** shows emission spectra for the quantum rods loaded in the microcavity at different pump powers. The peak at 2.33 eV is the residual scattering of the pump laser. The pump intensities from low to high are: 0.016 mJ, 0.038 mJ, 0.075 mJ, 0.088 mJ, 0.10 mJ, 0.15 mJ, and 0.19 mJ. The narrow peak at 1.98 eV emerging above the

fluorescence is the laser signal that appears at a threshold pump level of  $\sim 0.08$  mJ. The inset on the right in frame **c** shows the intensity of the lasing peak (filled squares) and the fluorescence peak (empty circles) versus the pump power. Lasing shows a clear threshold behavior, as accentuated by the solid lines. The inset on the left in frame **c** is a schematic top view of the cylindrical microcavity experimental set-up, with the gray shaded area representing the quantum rod solution occupying the volume between the fiber and inner capillary walls.

intensity is in effect saturated. This threshold behavior of the lasing peak intensity provides an additional important signature of lasing [84].

Higher-resolution spectral measurements revealed that lasing occurs in a sequence of discrete modes corresponding to the whispering gallery modes of the



cylindrical microcavity. Polarized measurements of the lasing for rods versus CdSe dots in solution showed that, while for QDs the lasing is not polarized, for quantum rods, a linearly polarized laser signal directly related to their symmetry is detected [14]. These investigations into gain and lasing in semiconductor nanocrystals reveal examples that may lead to further technological developments and implementation of colloidal nanocrystals in laser and optical amplifier applications.

## Acknowledgements

We would like to thank our students and coworkers D. Katz, Y.-W. Cao, S.-H. Kan, T. Mokari, E. Rothenberg, Y. Ebenstein, M. Kazes, D. Lewis, Y. Levi, A. Sharoni and T. Wizansky for their important contributions to the work presented in this chapter. The work was supported in parts by the Israel Science Foundation, the US-Israel Binational Science Foundation, and the DIP foundation.

### 5.1.2

#### Optical and Thermal Properties of Ib–VI Nanoparticles

*Stefanie Dehnen, Andreas Eichhöfer, John F. Corrigan, and Dieter Fenske*

##### 5.1.2.1 Optical Spectra and Thermal Behavior

The discrete molecular cluster species presented are ideal subjects for the study of the molecular quantum size effect [85], which is one of the most urgent questions prompting research in this area of cluster chemistry. One has therefore to explore the electronic properties of the cluster species, beginning with the interplay of cluster size and HOMO-LUMO gap. Theoretical investigations gave preliminary answers to this question [86, 87]. The first dipole- and spin-allowed singlet or triplet excitations of selected “naked” copper selenide clusters  $[\text{Cu}_{2n}\text{Se}_n]$  (up to  $n = 15$ ) were calculated on the CIS [88, 89] level (CIS = configuration interaction considering single excitations) for structures previously optimized for the same symmetry employing the CCSD(T) [90] method (CCSD(T) = coupled cluster approximation up to single and double excitation with additional consideration of third excitations by means of perturbation theory) ( $n = 1, 2$ ) or the MP2 method (MP2 = 2<sup>nd</sup> order Møller-Plesset perturbation theory) ( $n > 2$ ). Triplet excitations were investigated in order to take into account the fact that relativistic effects (spin-orbit coupling) [91] are noticeably present in Cu–Se compounds. The results are given in Figure 5-11.

The development of the energy values for singlet or triplet excitations with increasing cluster size shows the same trend, the triplet excitation energies being 0.2–0.7 eV lower than the singlet excitation energies. The excitation energies increase with slight oscillation to a value around 6 eV for the hexamer ( $n = 3$ ) and decrease afterwards down to a value of ca. 3.8 eV for the  $[\text{Cu}_{30}\text{Se}_{15}]$  species. The initial increase in the excitation energy values can be explained firstly by a stabilization of selenium  $p$ -orbitals by an admixture of  $s$ -,  $p$ -, or  $d$ -contributions of copper

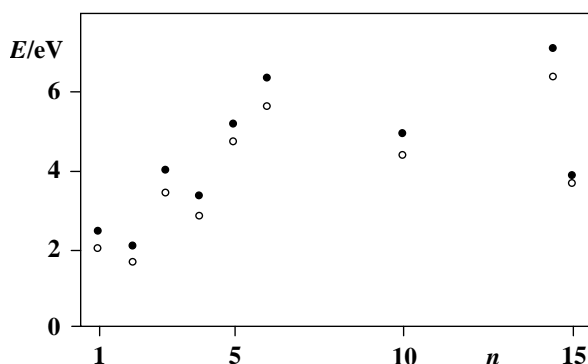


**Fig. 5-11** First dipole- and spin-allowed singlet or triplet excitations of selected “naked” copper selenide clusters  $[\text{Cu}_{2n}\text{Se}_n]$  (up to  $n = 15$ ) calculated on the CIS level (CIS = configuration interaction with single excitations) for structures previously optimized for the same symmetry employing the CCSD(T) method (CCSD(T) = coupled cluster up to single and double excitation with additional consideration of third excitations by means of perturbation theory) ( $n = 1, 2$ ) or MP2 method ( $n > 2$ ).

atoms and, secondly, by an increasing completion of the selenium shell around the copper substructure. The latter reduces the space for electrons in excited states with *s*-character. Thus, for  $[\text{Cu}_{12}\text{Se}_6]$ , significant *p*-type contributions are observed for the calculated transitions. The two exceptions ( $n = 2, 4$ ) of the described trend feature less compact molecular structures that lead to lower excitation energies. Having reached a maximum coverage of selenium atoms on the copper framework, the spatial extension of the cluster molecules gains more relevance. This confirms the assumption of the splitting of the Se-*p* and Cu-*s* states to form a valence and a conduction band. For clusters of ever-increasing size, and finally bulk  $\text{Cu}_2\text{Se}$ , the first excitation energy should approach a value of ca. 1 eV [92, 93]. According to the quantum chemical investigations, “naked” copper selenide clusters of medium size should be colorless insulators that gradually adopt *semi*-conductor properties with increasing cluster size. Calculations on small  $\text{PH}_3$ - or  $\text{PMe}_3$ -ligated copper selenide clusters show an increase in the first excitation energies. Estimating an error of about 1.5 eV, the respective transitions could indeed absorb violet light – in agreement with the red color of small experimentally observed copper selenide clusters.

The crystals that are obtained from the cluster formation reactions are intensely colored. The intensity of the color increases when going from sulfur- to selenium- to tellurium-bridged compounds (see below), as expected for an increase in the covalent or (*semi*-) metallic binding properties. Small copper sulfide and selenide clusters form light red, orange or purple crystals. With increasing cluster size, the color varies from dark red to reddish-black to (finally) black with a metallic sheen. The optical spectra of some copper selenide cluster compounds were studied by means of solid-state UV-VIS spectroscopy. The single crystalline samples were pulverized and embedded in mineral oil between two quartz plates. Figure 5-12

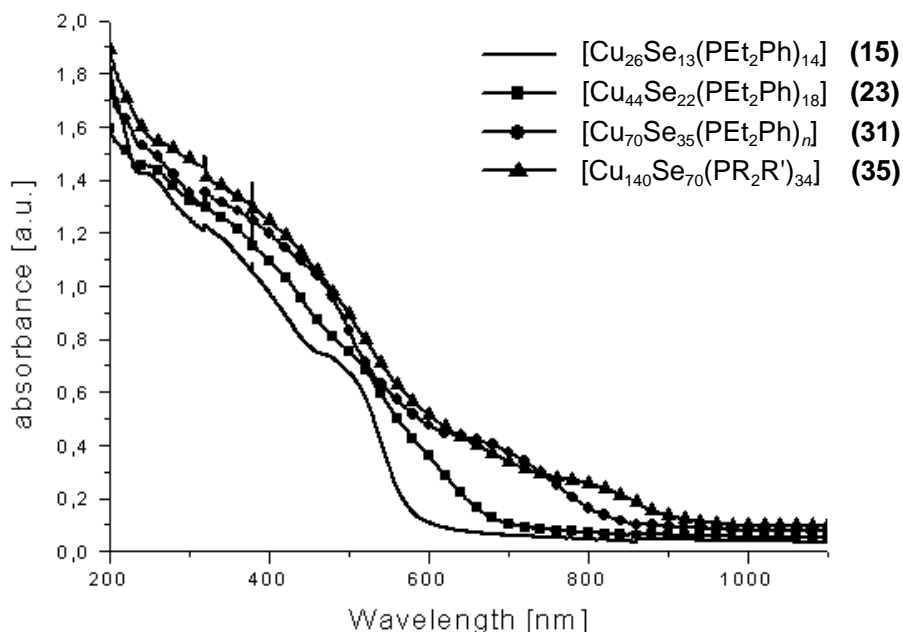


**Fig. 5-12** Solid-state absorption spectra of  $\text{PEt}_2\text{Ph}$  ligated compounds **15**, **23**, **31**, and **35**, which contain 26, 44, 70, or 140 copper atoms. For the measurements, single crystalline samples, previously pulverized in mineral oil, were placed between two quartz plates.

shows the absorption spectra of  $\text{PEt}_2\text{Ph}$ -ligated compounds  $[\text{Cu}_{26}\text{Se}_{13}(\text{PEt}_2\text{Ph})_{14}]$  (**15**),  $[\text{Cu}_{44}\text{Se}_{22}(\text{PEt}_2\text{Ph})_{18}]$  (**23**),  $[\text{Cu}_{70}\text{Se}_{35}(\text{PEt}_2\text{Ph})_n]$  ( $n = 23, 24$ ) (**31**) and  $[\text{Cu}_{140}\text{Se}_{70}(\text{Pr}_2\text{R}')_{34}]$  (**35**), which contain 26, 44, 70, and 140 copper atoms, respectively. The influence of the phosphine ligands should be roughly the same for all four clusters, and thus the increments in the measured shift of the absorption band can be ascribed solely to the increasing size and structural changes of the Cu–Se framework.

One observes a shift of the absorption band to higher wavelengths with increasing cluster size, and this agrees in principle with a decrease of the HOMO-LUMO gap in the same direction. Although the experimental value for the band gap in  $\text{Cu}_2\text{Se}$  (1.1 eV, i.e. 1127 nm, from optical measurements [93]; 0.37 eV, i.e. 3350 nm, from electrochemical measurements [94]) is not reached, the tendency can in fact be explained by the quantum size effect. An approximation of the frontier orbitals with increasing atomic number is clearly observed. The large width of the cluster spectra may be caused by the measuring temperature (room temperature) and/or the charge-transfer contribution to the observed transitions.

It has been known for several years that a Cu–P bond cleavage occurs if copper selenide clusters are heated. The residual black powders thus formed are  $\text{Cu}_2\text{Se}$  particles that convert to the  $\alpha\text{-Cu}_2\text{Se}$  phase at 600 °C. Additionally, XPS experi-

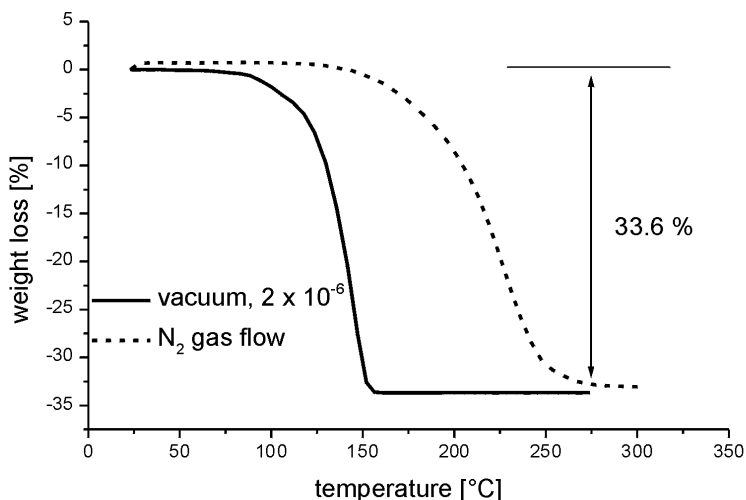


Fig. 5-13 Results of the thermogravimetry measurement of **31** under different pressures.

ments (XPS = X-ray photoelectron spectroscopy) proved that partial removal of the terminal ligands under the experimental conditions (room temperature, high vacuum) led to an aggregation of the remaining clusters to larger, still-ligated particles with a very narrow size distribution [95]. This corresponds with quantum chemical investigations which claimed that the clusters were metastable species relative to the binary chalcogenide  $\text{Cu}_2\text{E}$  and which computed very low Cu–P binding energies (see above). Thermogravimetric analyses of **35** (Figure 5-13) show that all phosphine ligands are removed in a single-step process within 20 min. The required temperature for bond breakage is also dependent on the experimental pressure.

On carrying out the experiments at ambient pressure in a nitrogen flow, the ligands dissociate at 226 °C. A reduction in the pressure down to  $2 \cdot 10^{-6}$  mbar causes a decrease in the temperature to 145 °C. The observed mass loss value of 33.6% contrasts with the figure of 35.6% for the mass that should theoretically have left the system. This observation and a 1.2% carbon residue in the formed copper selenide powders indicate a partial decomposition of the  $\text{PR}_2\text{R}'$  ligands. By following the processes by means of powder diffraction, it was observed that the intense reflections of the crystalline cluster ( $2\theta$  in the range  $2\text{--}10^\circ$ ) disappeared after the thermogravimetric experiments were undertaken. In their place, lower intensity reflections arose in a  $2\theta$  range of  $10\text{--}55^\circ$ . Sharp reflections of crystalline  $\alpha\text{-Cu}_2\text{Se}$  were eventually observed after tempering the powder to 600 °C. The Scherrer equation [96] (Eq. (5-1)) provides a relationship between the medial peak width  $\beta$  and the particle size  $D$ .

$$D = \frac{K \cdot \lambda \cdot 57.3}{\beta \cdot \cos \vartheta} \quad (5-1)$$

$D$ : average particle size perpendicular to the reflecting plane

$K$ : atomic form factor (here: 1.0)

$\lambda$ : wavelength of the X-ray radiation (here  $\text{Cu}_{K\alpha}$ :  $\lambda = 1.5418 \text{ \AA}$ )

$\beta$ : peak width measured at half maximum intensity

$\theta$ : diffraction angle

Calibrating the peak width at half maximum intensity for the used diffractometer to  $\text{LaB}_6$ , one calculates an average particle size of  $D = 117 \text{ \AA}$  for  $\text{Cu}_2\text{Se}$  powders that were generated by heating **35** up to  $150^\circ\text{C}$  at  $2 \cdot 10^{-6} \text{ mbar}$  for 20 min. This value for  $D$  is 7.8 times the size of the  $[\text{Cu}_{70}\text{Se}_{35}]$  core of **35** ( $15 \text{ \AA}$ ). The results are another indication of the partial, controlled collapse of the cluster particle lattice.

#### 5.1.2.2 Optical Spectra in the Solid State

The colors of the microcrystalline powders of various copper telluride clusters reveal differences in the electronic properties of the compounds. The larger clusters are significantly darker in color than the smaller ones. For a more detailed investigation, UV-VIS spectra of the stoichiometric clusters  $[\text{Cu}_8\text{Te}_4(\text{PPh}_3)_7]$  (**55**) and  $[\text{Cu}_{16}\text{Te}_8(\text{PPhnPr}_2)_{10}]$  (**57**), as well as for the mixed-valence compounds  $[\text{Cu}_{16}\text{Te}_9(\text{PPh}_3)_8]$  (**73**),  $[\text{Cu}_{23}\text{Te}_{13}(\text{PPh}_3)_{10}]$  (**76**),  $[\text{Cu}_{26}\text{Te}_{12}(\text{PEt}_2\text{Ph})_{112}]$  (**79**), and  $[\text{Cu}_{44}\text{Te}_{23}(\text{PPhnPr}_2)_{15}]$  (**83**) were measured in the solid state [97]. Absorption spectra of the crystalline samples were measured in transmission mode from suspension in Nujol between two quartz plates. As representative examples, the spectra of **57**, **73**, and **83** are shown in Figure 5-14.

In line with its red color, **57** exhibits charge transfer bands between 600 and 200 nm together with bands that can be assigned to transitions related to the ligands. The UV-VIS spectrum of **73** also shows similar bands between 600 and 200 nm, but additionally displays broad and weaker peaks at higher wavelengths, specifically at 670, 750, 1050 and 1350 nm. As outlined above, **73** can be described as a mixed-valence compound with an overall electron deficiency that is delocalized in the valence band. In general, compounds containing metal atoms in formally different oxidation states exhibit interesting spectroscopic behavior. Depending on the degree of delocalization of the charges over the molecular framework, one may detect additional bands in the near infrared. According to the classification of Robin and Day [98], which describes the different degrees of electron delocalization between the metal atoms, the copper telluride clusters under investigation should belong to class IIIa (metal clusters). In this class, metal centers with different valencies cannot be distinguished, and total delocalization of the charge is achieved. The larger cluster **83** also formally contains an electron deficiency of two electrons and thus shows broad peaks that are shifted even further to longer wavelengths than in the case of **73**. Since the energy of the mixed-valence transition is strongly correlated with the degree of delocalization, an even better charge delocalization – i.e. a smaller transition energy – is observed for **83**, as might have been expected for a larger cluster. In **79**, the assignment of formal charges resulted in two  $\text{Cu}^0$  atoms and 24  $\text{Cu}^+$  centers, which implies a formal electron excess of two. In principle, this should also cause mixed-valence bands. However, the ab-

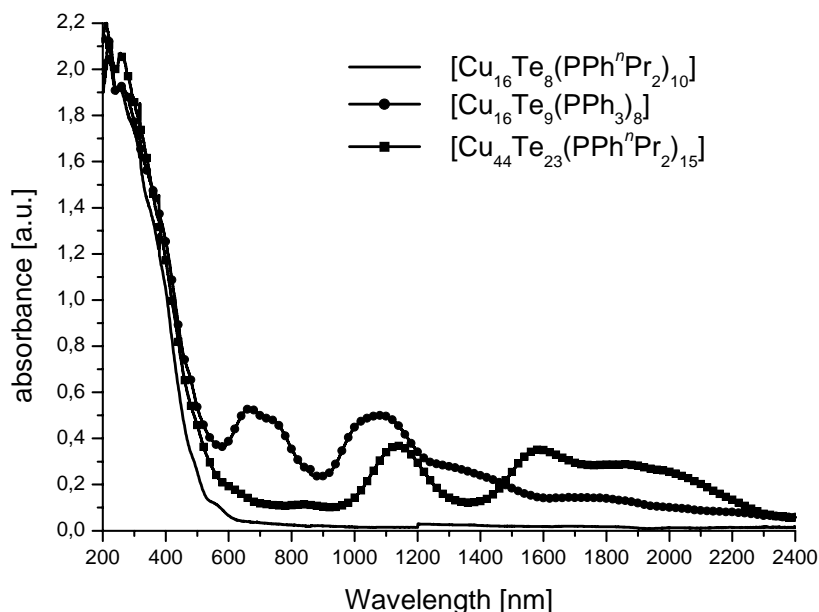
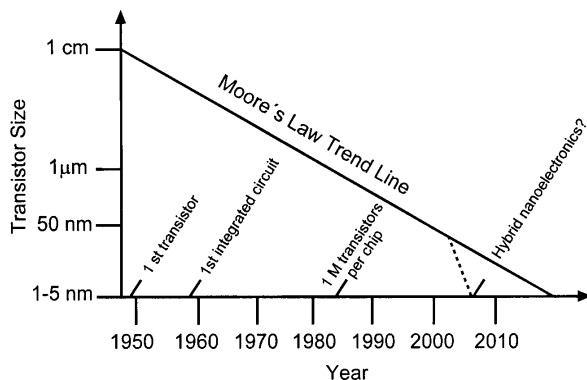


Fig. 5-14 The UV-VIS solid-state absorption spectra (mull in nujol) of copper telluride clusters  $[\text{Cu}_{16}\text{Te}_8(\text{PPh}^n\text{Pr}_2)_{10}]$  (**57**),  $[\text{Cu}_{16}\text{Te}_9(\text{PPh}_3)_8]$  (**73**), and  $[\text{Cu}_{44}\text{Te}_{23}(\text{PPh}^n\text{Pr}_2)_{15}]$  (**83**).

sorption spectrum of **79** only shows a red shift of the onset of the charge-transfer bands with respect to **57** from 600 to 800 nm. It cannot yet be established whether this is general behavior of the two different types of mixed-valence copper telluride clusters possessing either an electron deficiency or an electron excess.

Finally, one could conclude that in contrast to the clusters containing sulfur or selenium ligands, copper telluride clusters show a significant tendency to form nonstoichiometric clusters, with either an electron deficiency or an electron excess. This is not only evident from the overall charge, but it is also shown by the occurrence of intervalence bands in the optical spectra of these compounds. Structural considerations as well as calculations on the electronic band structure reveal that a localization of the different formal oxidation states is not possible. Even though **79** contains a central  $\text{Cu}_6$  octahedron with sufficiently short Cu–Cu distances, the charge excess cannot be assigned to  $d^{10}\text{--}d^{10}$  interactions. The “additional” electron pair which arises from the formal assignment of charges  $\text{Cu}^{1+}$  and  $\text{Te}^{2-}$  is rather delocalized in an MO which is embedded in the tellurium(5*d*)–copper(4*s*) valence band. The distinct differences from the  $\text{Cu}_2\text{S}$  or  $\text{Cu}_2\text{Se}$  mixed-valence cluster systems can generally be attributed to the small differences between the ionization potentials (IP), electron affinities (EA) and electronegativities (EN) of copper and tellurium, which do not allow a discrete separation into  $\text{Cu}^{1+}$  and  $\text{Te}^{2-}$  centers [IP(Cu): 745.4, IP(Te): 869.2; EA(Cu): 118.5, EA(Te): 190.2; EN(Cu, Pauling): 1.9, EN(Te): 2.1].



**Fig. 5-15** Trend line of miniaturization in microelectronics according to “Moore’s Law” as a plot of transistor size vs year. The dotted line implies that hybrid elements for nanoelectronic devices can overcome the respective size limits. See body text and the cited references (e.g. [121]) for explanation.

## 5.2

### Electrical Properties of Metal Nanoparticles

*Ulrich Simon*

#### 5.2.1

##### Introduction

Modern microelectronics continuously tends toward a higher degree of integration. Since the fabrication of the first transistor by Shockley, Brattain, and Bardeen in the late 1940s [99], transistors in microelectronic components have become smaller and smaller. This is the basis of all the present-day key technologies which play a role in all areas of our life. Figure 5-15 shows the continuous reduction in the minimum size of a transistor, known as Moore’s Law [100]. The trend line has continued since 1960, and it shows that the component size in microelectronic devices employed in present-day-technology is about 250 nm and thus about 1 million times smaller than the first transistor.

As miniaturization continues, shorter distances between the transistors and related switching elements on a chip lead to increase in the performance speed and therefore to shorter delay times in the information exchange. The availability of nanolithographic fabrication techniques makes it possible to scale down to 100 nm or less [101, 102]. This has already made a great impact on the performance of traditional semiconductor circuits as well as opening up new possibilities based upon quantum effects. However, the same has become true for so-called “metallic” electronics also. Now, following the exploitation of charging effects, or so-called Coulomb effects, in metallic circuits comprising tunnel junctions with sub-micron sizes, individual charge carriers can be handled. In metals these carriers are elec-

trons and, in the case of superconducting materials at low temperatures, they can be Cooper pairs of electrons. This field has been named Single Electronics (SE) [103].

Although charging effects were previously observed in granular thin metal films [104, 105], SE itself was born in the late eighties, when ultra-small metal-insulator-metal sandwich structures (tunnel junctions) and simple systems including these started to be intensively studied both theoretically and experimentally [106, 107]. The discreteness of the electric charge becomes essential, and the tunneling of electrons in a system of such junctions can be effected by Coulomb interaction of electrons, which can be varied by an externally applied voltage or by injected charges. A profound understanding of this phenomenon, so-called single-electron tunneling (SET), was developed, however, when the interest in this field was not a purely academic one. It is an attractive idea to exploit the principles of SE for the development of logic and memory cells, which in principle could lead to the construction of a computer working on single electrons, realizing a so-called “single-electron logic” (SEL). As the physical limits of the production technologies in device fabrication are rapidly approached, it is becoming clear that a continuous increase in the integration density requires new concepts to achieve component sizes of tens of nanometers or less, or ideally, the molecular level.

Different approaches to bridge the size gap between conventionally fabricated circuit elements and truly atomic scale components have been discussed. These include the utilization of electron transport through single molecules, the concept of molecular rectification, and the design of atomic relays or molecular shuttles. The approach that now receives the most attention among the different concepts of futuristic circuit design is circuitry based on single-electron transistors. This might justify the strong and visionary claim of Averin and Likharev that “single-charge tunneling is the only evident basis for future nanoelectronics” [108].

The aim of this Section is on the one hand to acquaint the reader with charge transport phenomena in nanoparticles, the physical principles of SET, and basic SE structures where the charging effects occur as intended. On the other hand, it will be shown by means of selected examples that in further development of the ideas of SE, Ligand-stabilized nanoparticles of noble metals have been recognized to be suitable building blocks for single-electron devices [109, 110].

### 5.2.2

#### **Physical Background and Quantum Size Effect**

The availability of small solids like transition metal clusters [111–113] offers a field of research that raises basic questions: How small must the number of atoms be for the properties of the original metal to be lost? How does an ordered accumulation of atoms behave when it is no longer under the influence of its ambient bulk matter? And, perhaps most important in the context of this chapter: What kinds of applications of these new materials in microelectronic devices can we expect in the future?

To answer these questions, we may consider the following scenario. If a metal



particle, initially having bulk properties, is reduced in size down to a few hundreds or dozens of atoms, the density of states in the valence and conduction bands decreases and the electronic properties change dramatically, i.e., conductivity, collective magnetism, and optical plasmon resonance etc. vanish. The quasi-continuous density of states is replaced by quantized levels with a size-dependent spacing. In this situation, the material chosen does not exhibit bulk metallic or semi-conducting behavior, since most of the electrons are tightly bound or localized, i.e., a small number of delocalized electrons are left to move as metallic electrons over the volume of the entire nanoparticle [114]. With respect to the size-dependent decreasing electrical conductivity, Nimtz et al. [115–117] spoke of the so-called Size-Induced Metal-Insulator Transition (SIMIT) as early as 1986. This refers to a transition due to geometrical confinement of delocalized states, with a corresponding de Broglie wavelength, when the volume of a metallic particle is strongly reduced by fractionation, from a starting diameter of 1  $\mu\text{m}$  to an experimental limit of less than 20 nm, which was quoted in these experiments. This effect was detected by measuring the dielectric absorption in the microwave range of small particles of solid or liquid indium metal dispersed in a liquid dielectric. Its explanation claims that the boundaries of these particles confine the electrons into localized states with wavelengths of multiples of half the de Broglie wavelength  $\lambda/2$ , thus leading to the picture of “particles in a box”. The corresponding level spacing was assumed to be smaller than  $k_B T$ , as the conductivity of these particles is only slightly affected by temperature. This means that the particles are still metallic, but with a limited number of electrons determined by the particle size. The first attempt to take advantage of this effect was the design of so-called Cut-Off Wavelength (COW) transistors [117].

This “size-quantization” effect may be regarded as the onset of the metal-nonmetal transition. The size at which the transition occurs depends on the type of metal and the criterion chosen for metallicity as well as the method of investigation. Remembering that the term “SIMIT” should not be restricted to the change in the electrical conductivity, but generalized by means of additional indicators at the very end of metallic behavior, the weakest-bound electrons which are confined in the quantum box occupy quantized levels analogous to the valence orbitals in ordinary atoms [114]. Therefore quantum size nanoparticles are also labeled as “artificial atoms” [118–120].

This is the great opportunity for the chemistry of nanoparticles, as the electronic properties are now tunable via the particle size. With respect to the electrical properties of nanoparticles and of all kind of arrangements built from nanoparticles, the most important property is the amount of energy needed to add one extra electron to an initially uncharged particle [121–124]. This energy is the so-called “charging energy”, it scales roughly with  $1/r$  ( $r$  = radius of the nanoparticle), and it has its atomic analog in the electron affinity of a neutral atom. Since it can be estimated from the charging energy of a macroscopic metallic sphere scaled down to the nanometer range, a physical effect like Coulomb blocking of tunneling events, which results from the huge charging energy of metal nanoparticles, is sometimes regarded as a “classical size effect”.

Based on the concept of charging energy, the following Section describes the physical principle of single-electron tunneling in terms of classical considerations.

### 5.2.3

#### Single-Electron Tunneling

The transfer of electric charges, or in other words electric current, in a metallic conductor is associated with the motion of a huge amount of free electrons over the entire conductor. Because of electron-electron and electron-phonon interaction, the effective charge which passes a cross-section of the conductor per second is a result of the displacement of individual charges. As a result, in spite of the discrete nature of the charge carriers, the current flow in a metal is averaged over a huge amount of charge carriers and is hence quasi-continuous. In contrast, if one deals with an isolated nanoscale piece of metal, the number of electrons in this is always integral. The number of electrons can be changed, e.g., by means of direct connection and then disconnection of that nanoparticle to another charged object or a lead with a different electric potential. The resulting change in the number of electrons, which is on the macroscopic scale large and uncontrollable, obviously is also integral. Therefore, the question arises how to transfer electrons in a circuit which is built up of nanoscale metallic objects one by one in a strictly controlled manner?

Physically, such a transfer of electrons can be realized by means of quantum mechanical tunneling. The probability of such a tunneling event depends on the potential applied to the circuit as well as on the distribution of excess electrons over the constituting sites. Therefore, an SET circuit should present a number of reservoirs for free electrons, which should be small and well-conducting islands separated by poorly permeable tunneling barriers. As long as the size of these so-called mesoscopic islands is larger than the atomic scale, they certainly comprise a huge amount of free charge carriers. However, handling of individual charges is still possible if the characteristic electrical capacitance ( $C$ ) of the island is small enough. In this case, the presence of one excess electron changes the electric potential  $\Delta V$  of the island considerably, i.e.,  $\Delta V = e/C$ . Then the control of single tunneling events can be realized in the following scenario. The enhanced potential could prevent further charging of the island, essentially reducing the probability of corresponding tunneling, since it would raise the energy of the whole system. If then the potential of the neighboring islands and/or gates is changed, the prob-

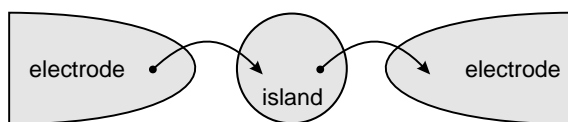


**Fig. 5-16** The tunneling of a single electron between two metal electrodes through an intermediate island can be blocked if the electrostatic energy of a single excess electron on the central island is large compared with the energy of thermal fluctuation.

ability of tunneling would be restored, and the tunneling of strictly one electron would then occur. Simply it might be concluded that SE deals with a small and defined amount of excess electrons on islands changing their distribution over the islands in time in a desirable way.

In order to realize this practically, the following two principal conditions must be fulfilled [103, 125, 126]:

First, the insulating barriers separating the conducting islands from each other as well as from the electrodes should be fairly opaque. The barrier properties determine the transport of electrons, which obey the rules of quantum mechanics and therefore are described by wave functions. The coordinate dependence of a wave function depends on the energy profile of the barrier. If the energy barrier separating the islands is high and thick enough (e.g., 1 eV and 2 nm, respectively), it provides an essential decay of the electron wave function outside the island and, as a result, only a weak overlapping of the wave functions of the neighboring islands occurs within the inter-island space. If, in addition, the number of electronic states contributing to tunneling is small enough, as is the case for nanoparticles, then the total exchange of electrons between the islands becomes negligibly small. This situation is often referred to as the case of small quantum fluctuations of charge. In spite of a relatively complex rigorous quantum mechanical consideration, quantitatively this condition can illustratively be formulated using the tunneling resistance  $R_T$  as a characteristic of the tunneling junction. It should be much higher than the characteristic resistance expressed via fundamental constants, the so-called resistance quantum,  $R_q = h/e^2 = 25.8 \text{ k}\Omega$ . Then the electrons in the island can be considered to be localized, and their number already behaves classically, although they undergo thermodynamic fluctuations just like any statistical variable.

Second, in order to have these thermal fluctuations small enough and consequently to make the exchange of electrons controllable, the energy associated with charging by one extra electron should be much greater than the characteristic thermal energy  $k_B T$ . This is the already mentioned charging energy  $E_C$  and it depends on the charge  $Q$ , on the size, and on the charge on the capacitances of any junctions, gates, conductors etc. in the vicinity of the island. As long as the size of an island exceeds the electrical screening length (a few tenths of a nanometer), the geometrical dependence of the charging energy is simply incorporated into the parameter  $C$  (the total island capacitance), and the charging energy takes the simple form  $E_C = Q^2/2C$ . Then the condition for the Coulomb energy to take precedence over the thermal energy is quantitatively expressed by  $E_C = e^2/2C \gg k_B T$ . Stated simply, the smaller the island the smaller the capacitance and the larger the  $E_C$ , as well as the temperature, at which single-electron charging can be observed experimentally.

When the above-mentioned two conditions are satisfied, the system is characterized by the set of configurations with various distributions of a small integral number of excess charges over the islands. These configurations, or states, of the system can be switched by means of tunneling of individual electrons. The characteristic time scale for the switching between the states due to externally induced

single-electron transitions depends on temperature and on the energy distribution over the whole system. This is the so-called recharging time  $\tau_R$ , and it ranges from about  $\tau_R = 10^{-11}$  s for typical values of  $R_T = 100$  k $\Omega$  and  $C = 10^{-16}$  F up to several hours with extremely large  $R_T$  in accordance with the relation  $\tau_R = R_T \cdot C$ .

If such an array is connected to a voltage source, the charge  $Q$  on the junction will increase with increasing voltage unless a tunneling event takes place. As long as  $|Q| < e/2$  the junction is in the Coulomb-blockaded state. At  $|Q| \geq e/2$  tunneling is allowed and will happen after a random amount of time because of the stochastic nature of the process. This is reflected in the current-voltage characteristic of the junction, since the Coulomb blockade appears at voltages below  $0.5 e/C$  and a corresponding shift of the tunnel current characteristic.

If the array is biased by a constant current  $I$ , at  $|Q| \geq e/2$  tunneling will appear making  $|Q|$  jump to  $-e/2$ , and a new charging cycle starts again. This leads to an oscillation of the voltage across the junction in a sawtooth-like manner with the fundamental frequency  $\nu_{SET}$ .

$$\nu_{SET} = I/e$$

In this state the tunneling of single electrons is correlated.

This gives rise to the manipulation of charges in a circuit on the single-electron level and therefore to the employment of this for the creation of, e.g., sensitive amplifiers and electrometers, switches, current standards, transistors, ultrafast oscillators, or, generally, digital electronic circuits in which the presence or absence of a single electron at a certain time and place provides the digital information.

### 5.2.3.1 Working Principles of Metal-Based Single-Electron Tunneling Devices

#### The Single-Electron Transistor

The simplest circuit which reveals the peculiarities of single-electron tunneling comprises only one Coulomb island and two leads (electrodes) attached to it. This geometry presents the double tunnel junction system. If this system works as a simple on/off switch, a gate electrode may be capacitively coupled to the island. Such a system has external control of the state of charge, often called the single-electron transistor. Applying a voltage to the outer electrodes of this circuit may cause either sequential transfer of electrons into and out of the central island or no charge transport, i.e., the transistor remains in nonconductive state. The result depends on the voltage  $U$ , applied to the electrodes as well as on the voltage  $U_g$  applied to the gate.

Because of the small total capacitance of the island,  $C = C_1 + C_2 + C_0 + C_{0'}$  ( $C_{1,2}$  are the capacitances of the junctions, which for the sake of simplicity we shall assume to be equal,  $C_1 = C_2 = C_j$ , while  $C_0$ , the capacitance with respect to the gate and  $C_{0'}$ , the capacitance with respect to other remote conducting objects, will be assumed to be much less than  $C_j$ ) the island has a large Coulomb energy, and  $E_C \gg k_B T$ . The total energy change of the system  $\Delta E$  while one electron is tunneling in one of the junctions consists of the charging energy of the island itself as

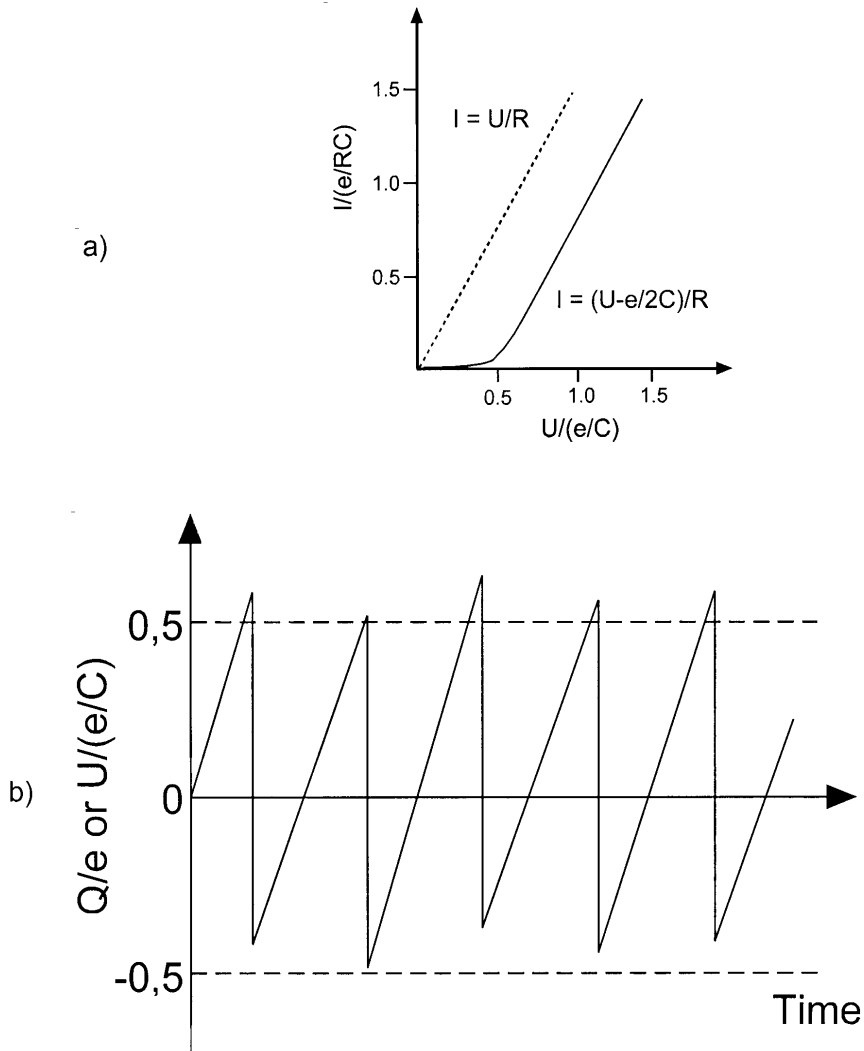


**Fig. 5-17** **a** The dependence of the time-averaged current  $I$  on  $U$  (the  $I(U)$  characteristic) for a single electron junction. Coulomb blockade appears at voltages below

$e/C$ . The dotted line indicates ohmic behavior.

**b** Time development of the junction charge or voltage imposed by a constant current source.

well as of the work done by the voltage source. For  $U_g = 0$  it is simply given by

$$\Delta E = Q_f^2/2C - Q_i^2/2C - qU,$$

where  $Q_i$  and  $Q_f$  are the initial and final charges of the island, respectively, and  $q$  is the charge (not necessarily integral) passed from the voltage source. From the elementary reasoning it is clear that if, say,  $Q_i = 0$  and  $Q_f = e$ , then  $q = \pm e/2$

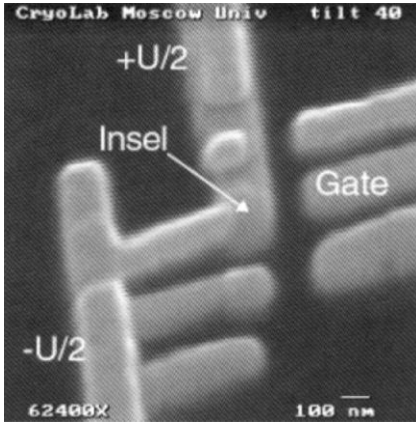


**Fig. 5-18** Scanning electron micrograph of a single-electron transistor with source and drain (+ $U/2$  and  $-U/2$  respectively) feeding the central island (marked “Insel”), which is capacitively coupled to a gate electrode. The

size of the central island is about  $60 \text{ nm} \times 60 \text{ nm}$ . (This figure is taken with permission from BMBF report *INFO PHYS TECH*, No. 22, 1998.)

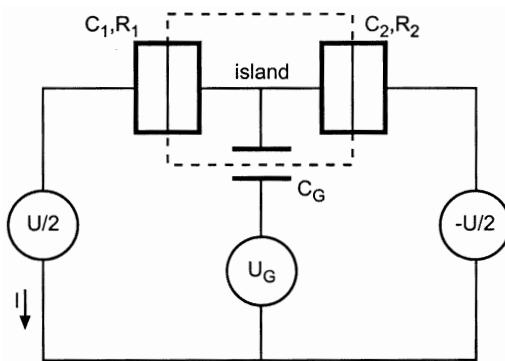


**Fig. 5-19** Circuit equivalent of a simple single-electron transistor consisting of a two-junction arrangement and a gate electrode coupled capacitively to the central island. The transport

voltage  $U$  induces a net flow of charge through the device, the volume of current  $I$  being controlled by the gate voltage  $U_g$ .

(depending on the direction of electron tunneling) and, therefore,  $\Delta E = e^2/2C \pm eU/2$ . This means that for  $-e/C$  the change of energy is positive when  $-e/C \leq U \leq e/C$ . Hence, electron tunneling would only increase the energy of the system, and this transition does not occur if the system cannot “borrow” some energy from its environment, when the temperature is assumed to be low enough. Therefore there is a Coulombically blocked state of the single-electron transistor when the voltage  $U$  is within the interval given previously and  $U_g$  is zero. Outside this range, the device conducts current by means of sequential tunneling of electrons.

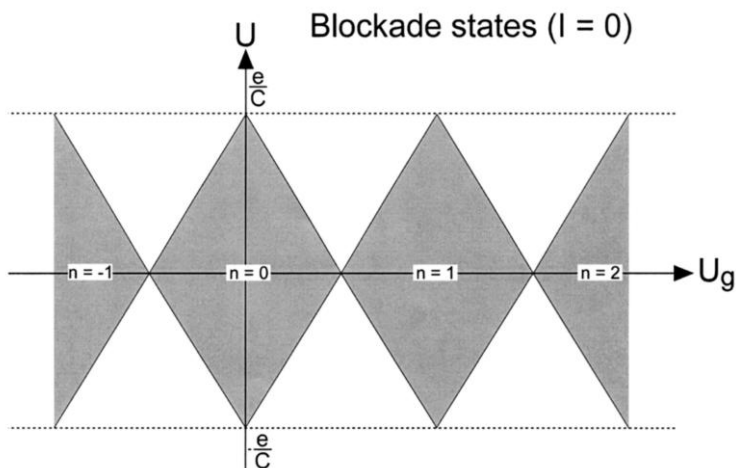


**Fig. 5-20** Idealized periodic rhomb pattern showing the Coulomb blockade region on the plane of voltages  $U$  and  $U_g$ . A transistor conducts only outside the rhombic-shaped regions. The value of the number  $n$  is the number of extra electrons trapped in the island in the blocked state.

When the gate voltage  $U_g$  is finite, the calculation of the energy change due to one electron tunneling gives another value, because of additional polarization of the island electrostatically induced by the gate. The result of this consideration is illustrated in Figure 5-20, where the  $U$  vs  $U_g$  diagram of the Coulomb blockade is shown.

The diagram reflects an interesting feature: it is periodic with respect to the voltage  $U_g$  with a period of  $e/C_0$ . This results from the fact that every new “portion” of the gate voltage of  $e/C_0$  is compensated by one extra electron on the island, and it returns to the previous conditions for electron tunneling. Therefore at constant bias  $U$ , the current through the device is alternately turning on and off with a sweep of voltage  $U_g$ .

The behavior of the transistor outside the Coulomb blockade region also shows the single-electron peculiarities, especially for the case of a highly asymmetrical junction, where  $R_1 \gg R_2$ , and  $C_1 \gg C_2$ . In Figure 5-21, one can see the  $I(U)$  characteristics with a step-like structure fading with decrease of  $U$ . This so-called Coulomb “staircase” results from the fact that an increase in  $U$  increases the number of channels for tunneling in a step-like manner, allowing an increasingly larger number of electrons to be present on the island. Another manifestation of charging effects in the SE transistor is the offset of the linear asymptotes by  $e/C$ .

The dependence of the transistor current on the gate voltage opens up the opportunity to fabricate a sensitive device which measures either directly an electric charge on the island or the charge induced on the island by the charges collected to the gate, i.e. a highly sensitive electrometer. The sensitivity of such an electrometer, which has already been reached in practice, is of the order of  $10^{-4}$ – $10^{-5}$  parts

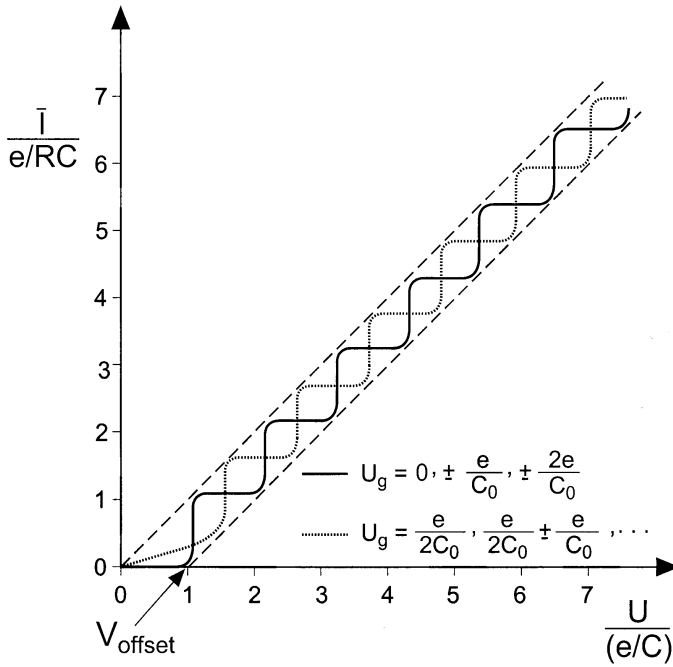


Fig. 5-21 The dependence of the time-averaged current  $\bar{I}$  vs  $U$  for an asymmetrical single-electron transistor.

of electronic charge, exceeding by far the charge sensitivity of conventional devices. And we shall see later that even the association of charges due to adsorption of molecules on the coulomb island causes the charge transport through such a single-electron transistor.

### Traps and Turnstiles

The idea of an effective control of the tunneling current by means of electrostatic gating has been developed further in multi-island systems and has opened up new possibilities for SE. An example of such a circuit is the so-called single-electron turnstile. In its simplest version, this consists of three islands aligned between two outer electrodes, as shown in Figure 5-22. It can be considered as two double junctions connected in series. The very central island of this chain is supplied by the capacitively connected gate, which controls electron tunneling in all four junctions. However, in contrast to the operation of the single-electron transistor, the additional two islands allow the realization of this condition. The central island works as a controllable trap for electrons, endowing the turnstile with its unique properties.

If the entire chain of islands is initially blocked by a small bias voltage  $U$  and the gate voltage  $U_g$  is swept, the central island first attracts one electron from the left hand side. This becomes possible because the Coulomb blockade in the left double



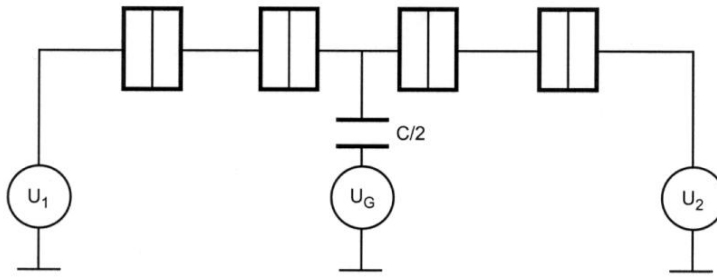


**Fig. 5-22** Circuit equivalent of a 4-junction (3-island) single-electron turnstile. The alternating voltage applied to the gate is  $U_g = U_{\text{amp}} \sin(\omega t)$ , and at its rise an electron makes a transition. The electron remains trapped in the island until the negative half-wave of  $U_g$  is diminished.

junction is lifted because of the gate voltage applied. The blockade is automatically restored after this tunneling even when  $U_g$  is increased, and the electron thereby remains trapped in the central island. If then the voltage  $U_g$  diminishes the blockade in the right double junction, the electron sequentially passes two right junctions, completing its traveling through the whole array. Hence, if one applies an alternating voltage, e.g., sinusoidal, to the gate of the turnstile, it should transfer exactly one electron during a period of the signal.

Frequency-controlled single-electron tunneling opens up an opportunity to maintain a d.c. current through a device. Its value is determined by the frequency  $\nu$  of the alternating field applied to the gate according to the fundamental relation  $I = e\nu_{\text{SET}}$ .

This is of great importance for modern quantum metrology, which could then determine the unit of d.c. current via the unit of the frequency using one universal constant, i.e. the electronic charge. In that case, taking into account the very high accuracy of the atomic standard of frequency, the accuracy of this current standard would be basically limited by the accuracy of the electron transfer cycle.

#### 5.2.4

##### Single-Electron Tunneling in Nanoparticles

The theoretical background of SET has found its experimental manifestation in lithographically fabricated capacitors, as found in conventional computer circuits. These typically have capacitances in the pF range. Because of their extremely low charging energies, they would need to be cooled down to the sub-mK range for single-electron operation. Furthermore, such a capacitor is typically driven at an operating voltage of 10–100 mV, which would lead to the storage of a few tens of thousands of electrons per charging. Going to advanced electron beam or extreme UV lithography, which allows fabrication tunnel junctions with a typical size of 50 nm × 50 nm or less, devices still have to be cooled down to at least liquid helium temperature. The utilization of SET events for applications up to the range of room

temperature leads to the necessity of decreasing the junction capacitance, at least by two orders of magnitude. As already predicted almost ten years ago, this can be realized by the use of ligand-stabilized metal nanoparticles in a size range of a few nanometers [124]. These nanoparticles are stabilized by organic molecules, the ligands which surround the metal cores and play the role of a insulating layer in contacts with neighboring clusters as well as with conducting objects. To use these particles as building blocks for a new nanoscale architecture, generally new techniques for a defined organization of such nanoparticles needed to be developed to build up single-electron circuits of different complexities. So far, these have utilized the principles of self-assembly by controlling intermolecular interaction, one of the main interests of supermolecular chemistry, and this will be a key feature in this development.

In general, the small size of the nanoparticles makes the number of electrons countable. This requires a slight modification of the two principal conditions for “classical” SET.

First of all, the standard (macroscopic) electrostatic approach, where a conductor is treated as a continuous entity with infinitely thin screening depth, fails, as the latter almost reaches the size of the object, and the number of weakly bound or metallic electrons in the object is small. As a result the electron-electron interaction is not completely screened out, so that the concept of electrical capacitances cannot strictly be applied. In this case, the calculation of the charging energy should be done by counting the energy of interacting charges. However, the Coulomb energy can still be roughly described by the same elementary formula for the charging energy of a capacitor. Then the symbol  $C$  denotes a capacitance which generally depends on the total number of interacting electrons occupying the nanoparticle.

The second point is that, because of the small size of a nanoparticle, it changes its energy spectrum essentially because of the previously mentioned quantum size effect. In contrast to a macroscopic piece of metal, which has a quasi-continuous electron energy spectrum (as assumed in the discussion of charging effects in larger structures), a metal nanoparticle presents for electrons a small potential energy well which in accordance to quantum mechanics has a set of distinctly discrete energy levels. Their density and distribution depend on the size and shape of the cluster and, consequently, the tunnel junctions. When one of its electrodes is a nanoparticle, a tunnel junction can hardly be characterized by such a simple parameter as a constant tunneling resistance  $R_T$ . Such an approximation is valid when densities of levels in both electrodes are high and independent of energy. In nanoparticles of 1–2 nm, the level spacing appears and is on the scale of the charging energy itself.

These peculiarities of metal nanoparticles do not, however, eliminate charging effects in them. Theory and experiment show that the fundamental results of single-electron tunneling still qualitatively hold true, and new features are being discovered. For example, the current-voltage characteristic of a double barrier junction with a quantum dot possesses at low temperature, as well as the Coulomb staircase, a fine structure due to energy quantization inside the dot. Nevertheless,

the interpretation of these results is complicated by the fact that the characteristic time  $R_T C$  becomes as short as the characteristic time of the energy relaxation inside the dot, and consequently the electrons no longer have the pure Fermi distribution. Thus, the tunneling characteristics of single nanoparticles provide information about their electron energy spectrum, and hence the density of levels, their degeneracy, etc.

#### 5.2.4.1 Thin Film Structures and STM Single-Electron Systems

More than a decade ago, fabrication techniques for the realization of the previously mentioned “traditional” single-electron circuits (like transistors) were developed [127, 128]. These techniques are based on the evaporation of metal (usually Al) films through a fine-pattern mask, which is often made of polymer resist, by means of an electron-beam lithographic process. The mask provides a number of thin splits, determining the sizes and shapes of resulting wires and islands, and the bridges interrupting them determine the position of the desired tunnel junctions and gates. Because of the composite polymer resist layer, which is chemically under-etched, the resulting mask is rigidly fixed above the substrate and its bridges become suspended above it. Such arrangements of splits and bridges enable metals to be evaporated onto the substrate from various angles, which allows the resulting evaporated layers to be in different positions.

In order to form a set of islands connected by tunnel junctions, the evaporation is usually made from two or three different angles in two or three steps, respectively, with an intermediate oxidation process, when aluminum is used. By adjusting the angles, the linear sizes of the resulting overlapping area of the first and the second metallic layers can be even smaller than the width of the strips, i.e., somewhat less than 100 nm. At the same time, a gate electrode coupled to the islands only capacitively should not overlap them, and this is taken into account in the mask pattern design. After double evaporation, the mask and the supporting layer are lifted off. Figure 5-18 shows such an SE transistor fabricated as an Al–Al<sub>2</sub>O<sub>3</sub>–Al stack.

The resulting barrier of Al<sub>2</sub>O<sub>3</sub>, with a desirable thickness of a few nanometers, is mechanically and chemically stable. The height of the corresponding energy barrier is about 1 eV, and this readily provides a tunnel resistance in the range of 100 k $\Omega$  for the junctions of the above-mentioned size. The resulting capacitance of such tunnel junctions is about 10<sup>–16</sup> F. This means that these circuits operate reliably only at temperatures below 1 K, which is just attainable with immense technical effort.

For essential decrease of the tunnel junction size and corresponding increase of the operating temperature, more sophisticated technologies for fabrication of SE structures are certainly needed. An alternative route is the use of ligand-stabilized metal nanoparticles as building blocks. The drastic reduction in the sizes and therefore in the capacitances of tunnel junctions are basically realized, e.g., in a double junction system consisting of a small metallic particle lying on a thin insulating film on a conducting support under the tip of the scanning tunneling microscope (STM).

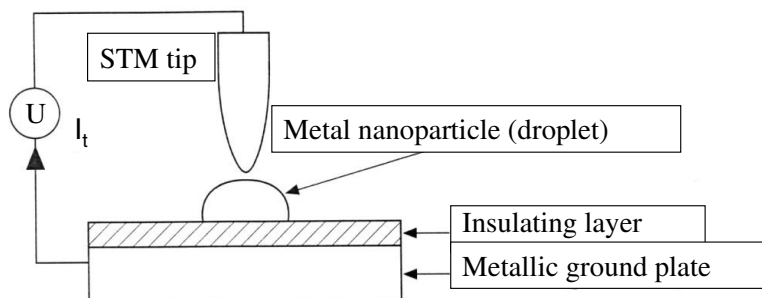


**Fig. 5-23** Single-electron two-junction system consisting of an STM tip and a metallic nanoparticle as a central electrode on a ground plane.

One of the junctions, which is between the ground plane and the metal particle, is mechanically fixed, while another one, which is between the particle and the STM tip, is adjustable.

The structures described above have been successfully and repeatedly realized in practice. As an early example, a one-dimensional arrangement forming a double-barrier SET junction working at room temperature has been realized by an STM tip above Au particles ca. 4 nm in diameter obtained by metal evaporation on a 1 nm thick layer of  $\text{ZrO}_2$  (tunnel barrier) on a flat Au substrate [129]. The experimentally determined capacitance of the nanoparticle-substrate junction is about  $10^{-18}$  F. This value is in good agreement with the theoretically estimated value based on the model of a parallel-plate capacitor with  $\text{ZrO}_2$  as a defined dielectric. Dorogi et al. prepared layers of isolated nanoparticles from a multiple expansion cluster source on self-assembled monolayers of xylene-*a,a'*-dithiol (XYL), and studied the electrical transport through the tunnel junction in an ultrahigh vacuum system with an STM. The tunneling current as a function of applied voltage yields evidence of SET at room temperature, and by fitting the  $I(U)$  curves to a Coulomb blockade model, the electrical resistance of the XYL molecules was estimated to be about 9 M $\Omega$  [130].

This result is in good agreement with most theoretical expectations of 12.5 M $\Omega$  for these molecules [131]. Based on the elastic-scattering Green's function theory, Wang et al. have developed an approach to characterize the electron transport process in molecular devices. This approach allows the description of the coupling between the molecule (forming the tunnel barrier) and metals (forming the electrodes) at the hybrid density functional theory level. For XYL,  $I(U)$  curves have been calculated, and these are found to be in good agreement with experimentally obtained ones at room temperature.

These examples show that SET in the room temperature range is accessible by means of metal nanostructures, but, for highly redundant SET devices, particle size distribution, at least with atomic precision, has to be avoided, which is not possible when metal evaporation is used as the nanoparticle source.

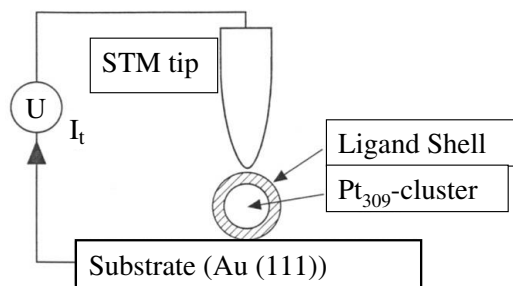


**Fig. 5-24** A single ligand-stabilized  $\text{Pt}_{309}$ -cluster between an STM tip and an Au(111) facet. The junction between the cluster and the substrate is built up by the ligand shell.

#### 5.2.4.2 SET on Single Chemically Tailored Nanoparticles

The first results obtained on single chemically tailored nanoparticles were reported by van Kempen et al. in 1995 [132, 133]. They reported scanning tunneling spectroscopy at 4.2 K on a  $\text{Pt}_{309}\text{phen}_{36}\text{O}_{20}$  cluster synthesized by Schmid and co-workers.

The  $I(U)$  characteristics exhibit clear charging effects, which indicate that the ligands are sufficiently insulating tunnel barriers between the cluster and the substrate. The experimentally observed charging energy varies from 50 to 500 meV, while a value of 140 meV would be expected assuming a continuous density of state in the particles and a dielectric constant of  $\epsilon_r = 10$  for the ligand molecules when the classical formula  $E_C = e^2/4\pi\epsilon_0\epsilon_r R$  (where  $R$  = radius of the particle) is applied.

There are different factors, affecting the variation in  $E_C$ , which have been taken into account. Since the clusters have different facets (squares and triangles)  $E_C$  will depend on the exact way in which the cluster lies on the substrate. Furthermore, the ligands, which for simplification have been assumed to be in the form of a spherical coating on the cluster, may have different orientations varying from cluster to cluster with respect to the underlying substrate, thus causing a different tunnel barrier between the cluster and the ground, and therefore a different capacitance. Finally, residual water molecules from the solvent may be physically or chemically bound on the cluster surface or on the ligand shell, and therefore the tunnel junction between cluster and substrate may differ for different clusters.

Additional structures on the charging characteristic have been observed in some cases, which might be expected from a discrete electron level spectrum in the cluster caused by the quantum size effect. The effect of discrete levels on the charging characteristics has been treated theoretically by Averin and Korotkov [134], who extended the existing “orthodox” theory of correlated SET in a double normal-metal tunnel junction to the case of a nanoscaled central electrode. According to this, the  $I(U)$  characteristics should exhibit small-scale singularities reflecting the structure of the energy spectrum of the central electrode, i.e. the

nanoparticle. Furthermore, the energy relaxation rate becomes evident because of the small recharging time,  $\tau$ , resulting from the small junction capacitance according to  $\tau = R_T \cdot C$ , where  $R_T$  is the resistance of the respective tunnel barrier and  $C$  is the capacitance of the junction. While the theoretical prediction for the level splitting  $\Delta$  according to  $\Delta = 4E_F/3N$  or to a refined approach by Halperin [135] leads to an assumed splitting of ca. 8 meV ( $E_F$  is the Fermi energy of the metal and  $N$  is the number of free electrons), the fit of the spectra lies between 20 and 50 meV. Although different reasons are discussed in the cited paper, the measurements reflect the discreteness of the level spectrum in the clusters as big as the 2.2 nm Pt<sub>309</sub> cluster.

On smaller ligand-stabilized metal clusters of 1.4 nm, i.e. Au<sub>55</sub>(PPh<sub>3</sub>)<sub>12</sub>Cl<sub>6</sub> (Au<sub>55</sub>), scanning tunneling spectroscopy (STS) could be observed up to the room temperature range. Already, cluster pellets, i.e. three-dimensional compacts of the clusters, gave hints of single-electron transfer in the  $I(U)$  curves [136] taken at room temperature. But in these investigations neither the vertical nor the lateral arrangement of the clusters is well defined, as would be the case in a one-, two- or three-dimensional superlattice. As a consequence, the charging energy has a wider spread, as would be expected from the estimation of the charging energy of a single cluster according to the formula mentioned above.

Chi et al. studied tunneling spectroscopy on Au<sub>55</sub> monolayers prepared on various technically relevant substrates [137]. The samples could be obtained utilizing a two-step self-assembly (SA) process and a combined Langmuir-Blodgett/SA-process. The spectroscopy gives clear evidence of the Coulomb blockade originating from the double barrier at the ligand-stabilized cluster as the central electrode up to the room temperature range.

From a fit of the experimental data at 90 K, the capacitance of the cluster was calculated to be  $3.9 \times 10^{-19}$  F. This value, which is very sensitive toward residual charges and nearby background charges, is close to the value of the microscopic capacitance determined earlier by temperature-dependent impedance measurements [109]. Furthermore, these results are found to be in good agreement with the capacitance data obtained on the above-mentioned gold nanoparticles on an XYL-modified Au [111] surface [130, 138].

Most recently, low-temperature tunneling spectroscopy on individual Au<sub>55</sub> clusters under ultra-high vacuum conditions have been reported [139]. In accordance with the above-mentioned results, clear evidence of the Coulomb blockade is given. In this regime the conductivity appears to be largely suppressed, but is not zero. This is attributed to a certain probability of co-tunneling within the Coulomb gap at the finite temperature of 7 K. At this temperature, thermal motion is sufficiently reduced and the molecular structure of the ligand shell is partly visible. The STM image fits the space-filling model of the cluster fairly well. Both are shown in Figure 5-26.

In this figure the two locations at which the tunneling spectra have been recorded are indicated. One location is just above a C<sub>6</sub>H<sub>5</sub> ring of the PPh<sub>3</sub> ligand and the other is next to the ring. Figure 5-27 shows the conductivity peaks, which precisely coincide for both spectra.

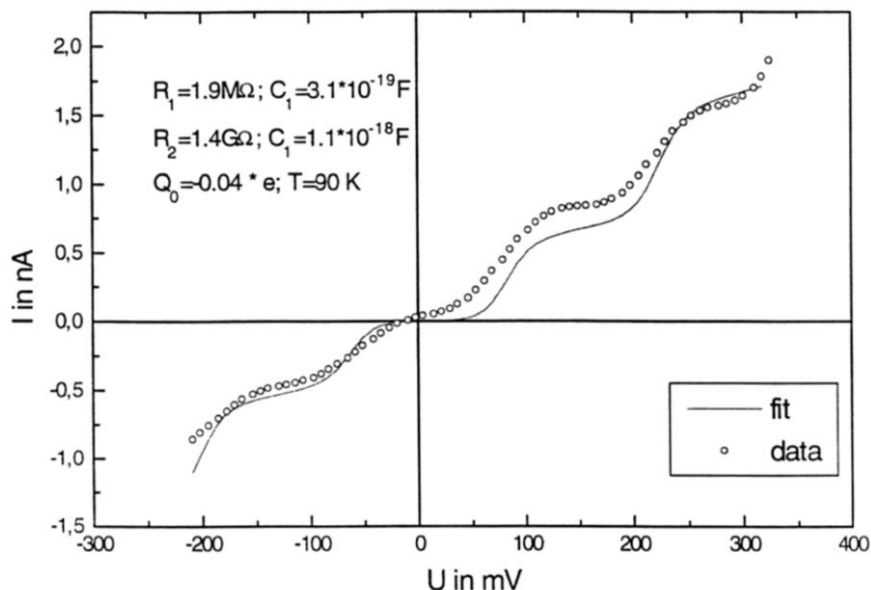


**Fig. 5-25** SET on a single-ligand-stabilized  $\text{Au}_{55}$ -cluster at 90 K.  $R_1$ ,  $C_1$  and  $R_2$ ,  $C_2$  are the junction resistance and capacitance of the junction between the cluster and the substrate

and the junction between the cluster and the STM tip.  $HC_1$  was calculated to be  $3 \times 10^{-19}$  F by fitting (reproduced with kind permission from [137]).

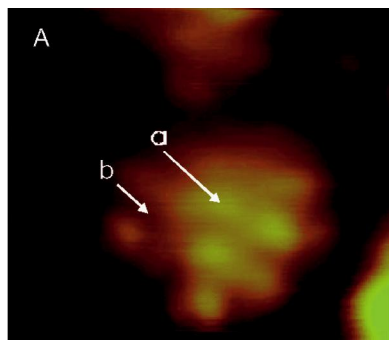
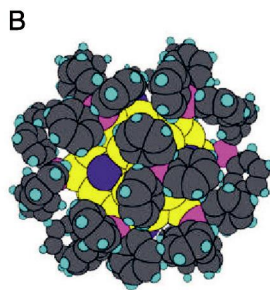


**Fig. 5-26** **A** STM image of a single  $\text{Au}_{55}[\text{P}(\text{C}_6\text{H}_5)_3]_{12}\text{Cl}_6$  cluster on an  $\text{Au}(111)$  surface at 7 K, obtained at a bias of 2 V and a current of 100 pA using a Pt-Ir tip. Image size: 3.3 nm  $\times$  2.9 nm. **B** Space-filling model of the cluster compound: cuboctahedral core with 55 Au atoms (yellow), 12  $\text{P}(\text{C}_6\text{H}_5)_3$  molecules (with P pink, C grey and H blue) bound to the



12 edges of the cuboctahedron and 6 Cl atoms (violet) located in the center of the 6 square faces of the Au core. Comparison between (a) and (b) shows that the STM resolves the  $\text{C}_6\text{H}_5$  rings. Spectroscopic data were acquired at the two distinct locations marked in **A**. (Printed with permission from [139].)

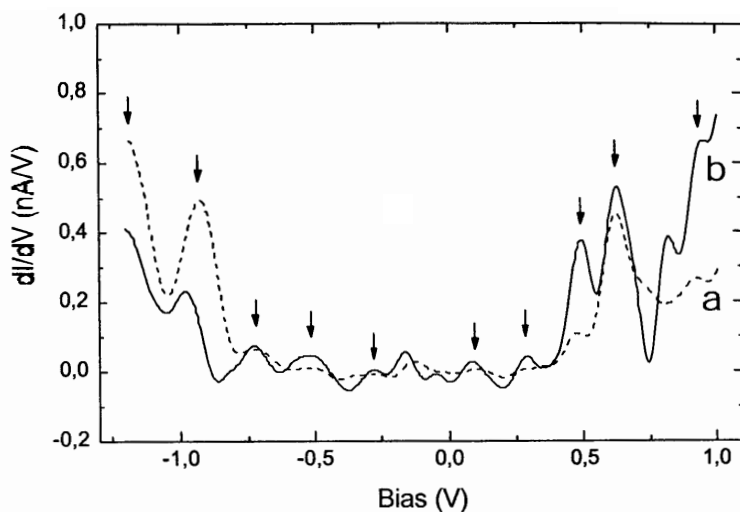


**Fig. 5-27** Tunneling spectra acquired at the two distinct locations, **a** and **b**, marked in Figure 5-26A. The dashed curve was taken just above a  $C_6H_5$  ring and the solid one next to the ring. The bias refers to the substrate potential. The arrows indicate conductivity peaks, which precisely coincide for both spectra. (Printed with permission from ref. [139].)

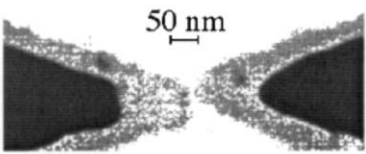
This shows that the discrete energy levels of the cluster become visible in terms of conductivity oscillations with an average level spacing of 135 meV. If this value is compared to that expected for a simple free-electron model, as described above, the “electronically apparent” cluster diameter is ca. 1.0 nm. This is significantly smaller than the geometrically determined diameter of 1.4 nm for  $Au_{55}$  and slightly larger than the expected value of 0.84 nm for  $Au_{13}$ . The author claims that the difference is most likely caused by the six Cl atoms located at the six square faces of the cuboctahedral  $Au_{55}$  surface. Since Cl has a high electronegativity it removes one electron from the  $Au_{55}$  core. Nevertheless, within the discrete energy levels the cluster exhibits metallic behavior.

#### 5.2.4.3 Metal Nanoparticles in Single-Electron Devices

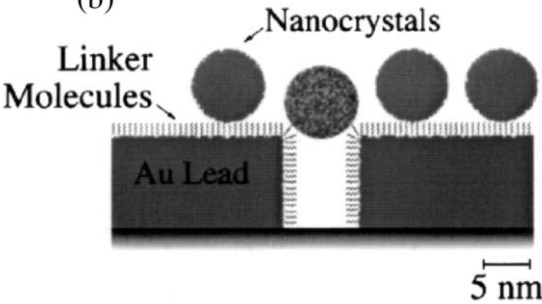
In order to utilize the opportunities which arise from the room-temperature SET peculiarities for applications beyond laboratory experimentation, two different routes have principally been followed with respect to the experimental design. On the one hand, techniques of fabricating metallic electrodes have been developed which enable the addressing of a few or even single nanoparticles by electron beam lithography. On the other hand, STS techniques have been developed further for chemical control of gating of the central island in an SET transistor or for the chemical switching of the tunneling barrier, i.e. the insulating organic molecules, separating the nanoparticles from the underlying support.



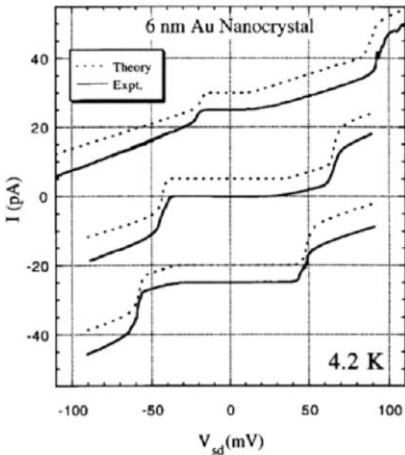
(a)



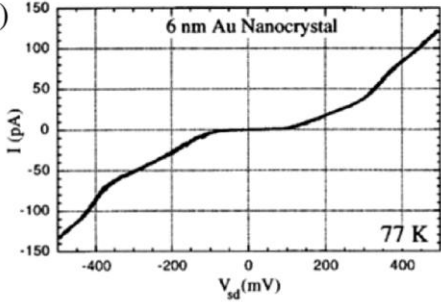
(b)



(c)



(d)



#### 5.2.4.4 Mesoscopic Arrays with Nanoelectrodes

Alivisatos and coworkers realized an electrode structure scaled down to the level of a single Au nanoparticle [140]. To fabricate this structure, they combined optical lithography and angle evaporation techniques (see previous discussion of SET device fabrication). A narrow gap of a few nanometers between two Au leads on an Si substrate was defined. The Au leads were functionalized with hexane-1,6-dithiol, which binds linearly to the Au surface. The free end, which faces the solution, was used to immobilize 5.8 nm Au nanoparticles from solution between the leads. The resulting device reveals slight current steps in the  $I(U)$  characteristic at 77 K (see Figure 5-28). By means of curve fitting to classical Coulomb blockade models, the junction capacitances were found to be  $2.1 \times 10^{-18}$  F, respectively, and the resistances 32 M $\Omega$  and 2 G $\Omega$ , respectively. In a further development of this device, a gate electrode to externally control the current flow through the central island, a CdSe nanoparticle, was applied to realize an SET transistor [141].

Sato et al. [142] reported detailed electrical characteristics an SET transistor utilizing charging effects on metal nanoparticles. This was fabricated by means of metal electrodes, formed by electron beam lithography, to which a self-assembled chain of colloidal gold nanoparticles was connected. The inter-particle connection as well as the connection to the electrodes results from a linkage by bifunctional organic molecules, which provide the tunnel barriers.

In this device, gold nanoparticles with an average diameter of 10 nm were deposited on a thermally grown SiO<sub>2</sub> surface on an Si substrate by using alkanesiloxane molecules as an adhesion agent. After formation of the Si–O–Si bond by thermal treatment, terminal amino groups of the silane became attached to gold nanoparticles to form a sub-monolayer. After this coating, where a sub-monolayer was formed, 1,6-hexanedithiol was added to interconnect the particles with a more defined spacing. With a second immersion in a gold particle solution, the coverage was complete, and the dithiol molecules maintained the distance between the particles, while the second layer filled the gaps between the particles of the first, where however, chains of 2–4 particles were formed. When this procedure was performed on an SiO<sub>2</sub> substrate equipped with source, drain and gate metal electrodes defined by electron beam lithography, the particles formed a chain of at least three particles bridging the gap between the outer driving electrodes.

← **Fig. 5-28** **a** Field emission scanning electron micrograph of a lead structure before the nanocrystals are introduced. The light gray region is formed by the angle evaporation, and is ca. 10 nm thick. The darker region is from a normal angle evaporation and is ca. 70 nm thick. **b** Schematic cross-section of nanocrystals bound via a bifunctional linker molecule to the leads. Transport between the leads occurs through the mottled nanocrystal bridging the gap. **c**  $I$ – $V_{sd}$  characteristic of a 5.8 nm diameter Au nanocrystal measured at 4.2 K. The solid lines show three  $I$ – $V$  curves measured over the course of several days. Each is offset for clarity. These different curves result from changes in the local charge distribution about the dot. The dashed lines are fits to the data using the orthodox Coulomb blockade model as discussed. **d**  $I$ – $V_{sd}$  characteristic of a 5.8 nm diameter Au nanocrystal measured at 77 K. Several Coulomb steps of period  $\Delta V_{sd} \sim 200$  mV can be seen. (Printed with permission from [140].)

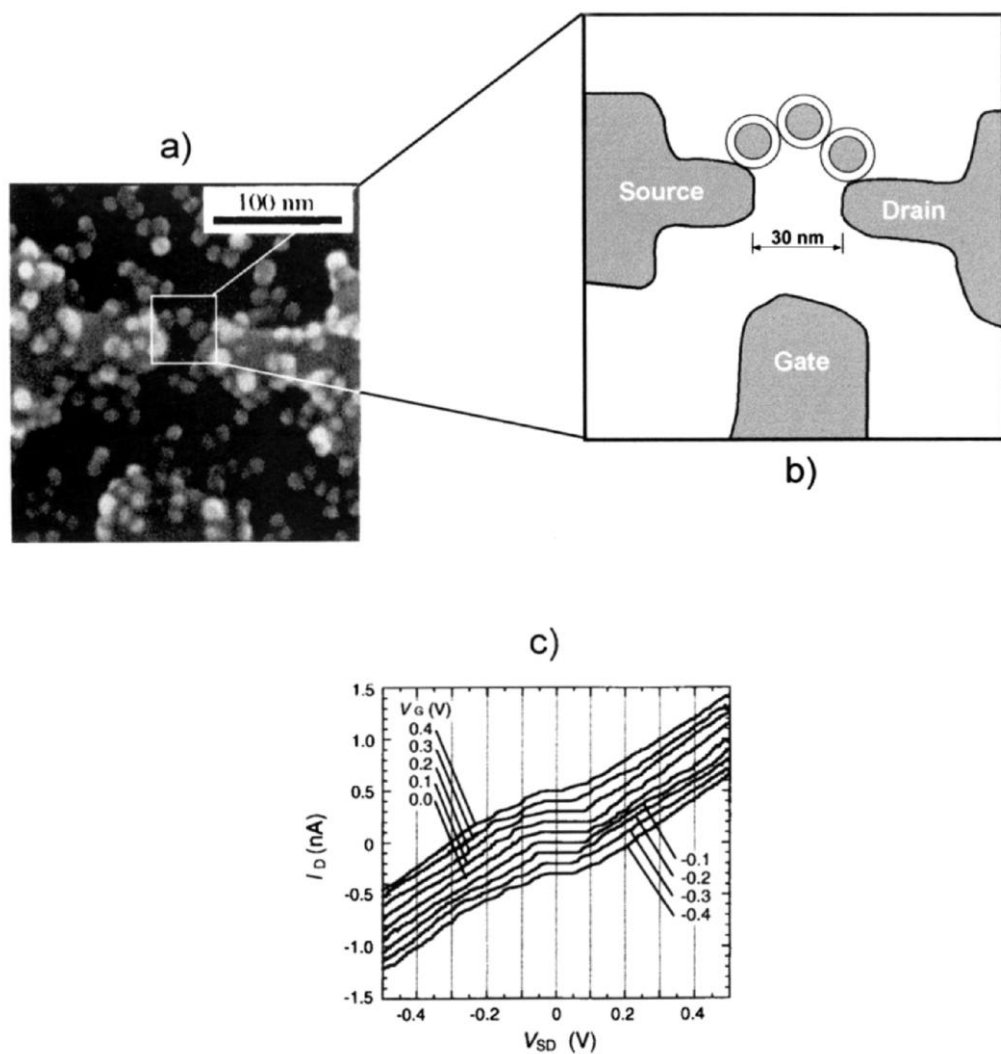


**Fig. 5-29** SET transistor, based on self-assembling of gold nanoparticles on electrodes fabricated by electron beam lithography. (Reproduced in modified form from [142].)

Since not all the steps of this procedure could be controlled in detail, the number of nanoparticles in the bridge chain differed from device to device, but in any case electron conduction dominated by single-electron charging indicated by a Coulomb gap could be observed up to 77 K, whereas the nonlinearity is smeared out at room temperature. Simulation and fitting of the data with a model circuit for a three-dot (four junction) SET-transistor indicated that the capacitance of all junctions in the chain was  $1.8\text{--}2 \times 10^{-18}$  F, and the calculated Coulomb gap was in rea-

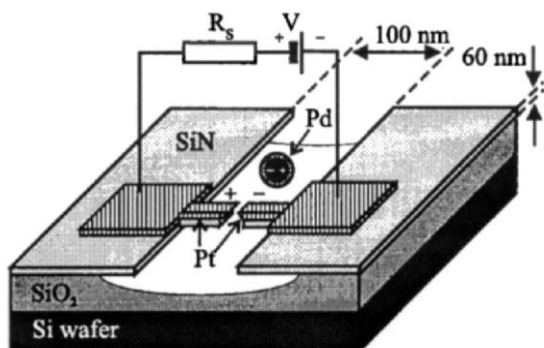


**Fig. 5-30** Schematic representation of the set-up for single particle measurements. Pt denotes two free-standing Pt electrodes (dashed region). A ligand-stabilized Pd cluster

is polarized by the applied voltage and attracted to the gap between the Pt electrodes (electrostatic trapping: ET). (Printed with kind permission from [144].)

sonably good agreement with the value of 150 mV obtained from the measured  $I(U)$  characteristic, which was systematically squeezed when a gate voltage of  $-0.4$  to  $0.4$  V was applied. The plot of the current through the device was clearly dependent on the gate voltage, showing the typical current oscillations, proving that the desired function of the single-electron transistor had been achieved. According to a Green's function-based method, which was proposed by Samanta et al. [143], the transmission function of electrons across the dithiol ligands was calculated, from which the resistance  $R$  per molecule was calculated by the Landauer formula,  $R = (h/2e^2)/T(E_g)$ , where  $T(E_F)$  is the transmission function,  $T \approx \exp[2(mE_g)^{1/2}/\hbar]$ . Assuming a barrier height of  $E_g \approx 2.8$  eV in the dithiol molecules, the resulting resistance was estimated to be  $R \approx 30$  G $\Omega$ .

Schmid and Dekker reported a new technique, which allows the controlled deposition of a single nanoparticle between two metal nanoelectrodes, i.e. the technique of electrostatic trapping (ET) [144]. The method is based on the attraction of a polarized metal nanoparticle to the strongest point of the electric field, which was applied to two Pt electrodes.

From solution, the particles can be immobilized in the gap between the Pt electrodes. The latter can be reduced down to 4 nm. The fabrication of the electrodes was by thermal growth on Si. A 60 nm SiN film was deposited on top, and electron beam lithography with PMMA and reactive ion etching was used to open a 100 nm slit in the SiN film with a local constriction with 20 nm spacing. Under-etching with HF enables free-standing SiN "fingers" to form, which were sputtered with Pt to reduce the gap down to 4 nm.

In this gap, Pd nanoparticles were trapped to study the electrical transport properties of this double-barrier system. A typical  $I(U)$  curve is shown in Figure 5-32. At 4.2 K, the most pronounced feature is the Coulomb gap at a voltage of about 55 mV, which disappears at 295 K. Furthermore, the  $I(U)$  curve is not linear above the gap

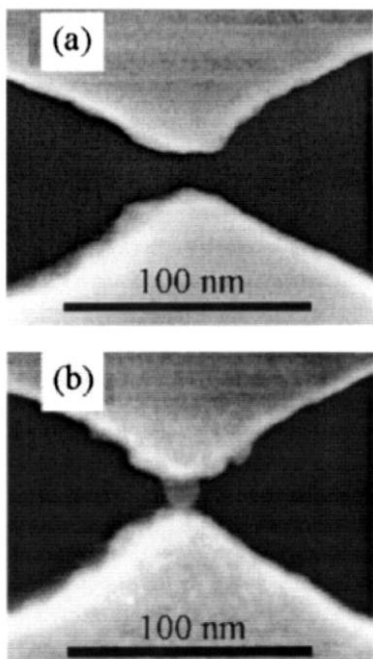


**Fig. 5-31** **a** Pt electrodes (white) separated by a ca. 14 nm gap. **b** After ET, the same electrodes are bridged by a single ca. 17 nm Pd particle (printed with kind permission from [144]).

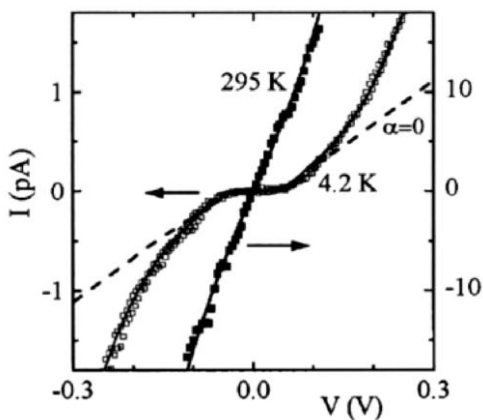


**Fig. 5-32** Current-voltage curves measured at 4.2 K (open squares) and 295 K (solid squares). The solid curves denote fits of the KN model. Fitting parameters for these curves are  $V_c = 55$  mV,  $R_0 = 1.1 \times 10^{11} \Omega$ ,  $q_0 = 0.15e$  (offset

charge), and  $a = E c / h = 0.5$ . The dashed curve ( $a = 0$ ) represents the conventional model which assumes a voltage-independent tunnel barrier (printed with kind permission from [144]).

voltage, but increases exponentially, which was explained by suppression of the effective tunnel barrier by the applied voltage.

To increase the temperature at which single-electron charging in nanoelectrode arrays may occur, smaller ligand-stabilized Au nanoparticles ( $\text{Au}_{55}(\text{PPh}_3)_{12}\text{Cl}_6$ ) were deposited by ET in a three-electrode arrangement [145]. The device consisted of three tungsten electrodes, fabricated from a 25 nm tungsten layer on an Si wafer with an 80 nm thick  $\text{SiO}_2$  layer using an electron beam lithography process. The minimum component size turned out to be 50 nm, with gaps between the contacts of about 20–50 nm. Upon ET, quasi-one-dimensional chains of the 1.4 nm Au particles are formed. These chains exhibit Coulomb blockade effects between  $-0.5$  V and  $+0.5$  V at room temperature, but without any singularities in the characteristic, which could refer to the electronic structure of the particles.

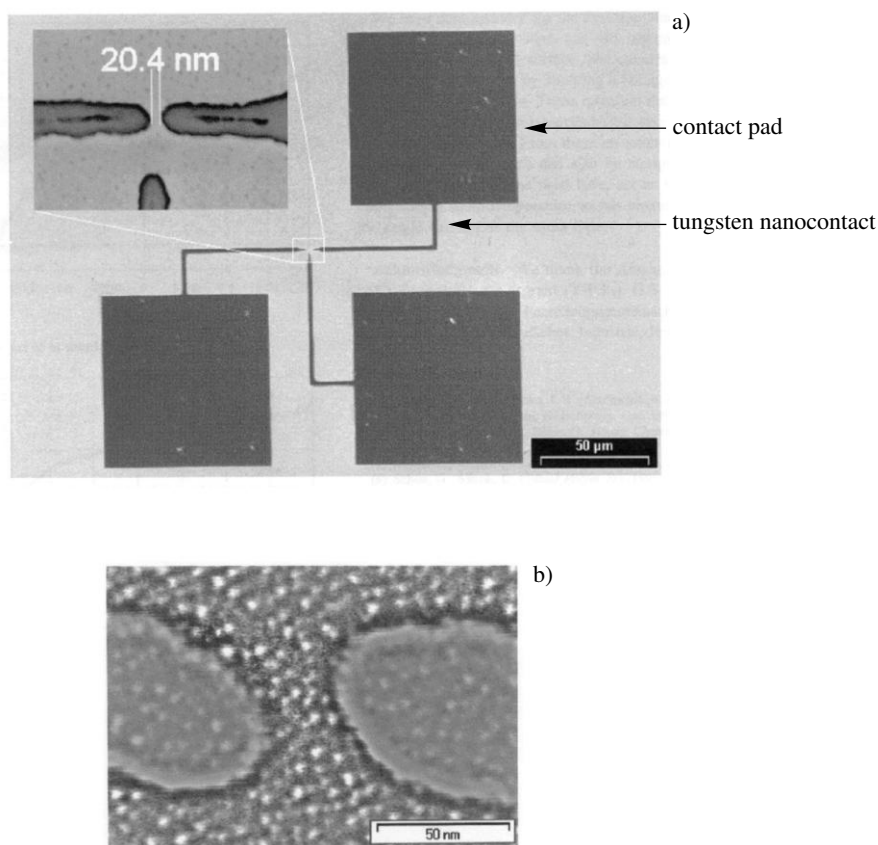


**Fig. 5-33** Complete nanostructure with contact pads (the inset is nanostructured with three nano tips). SEM image of the tungsten nanocontact (b)  $\text{Au}_{55}$  cluster deposition (printed with kind permission from [145]).

#### 5.2.4.5 Chemical Switching and Gating of Current through Nanoparticles

A significant advantage of incorporating nanoparticles in single-electron devices is the opportunity to chemically control the size of the particles as well as the thickness, composition, and state of charge of the ligand shell. The current flow through such a device will thus be very sensitive to any charges and impurities that reside on the nanoparticles or in the ligand shell. This sensitivity can be used to switch the “transparency” of the ligand shell or to use the ligands as “chemical gates” to manipulate the SET current.

Most recently, Schiffrin and coworkers have described how to control the transparency of the insulation barriers between a substrate and a nanoparticle in an STS experiment [146].

A bipyridyl moiety (viologen group,  $V^{2+}$ ) was used as a redox group incorporated in the ligand shell of the particle. Electrons were incorporated into this group under electrochemical control, while the transparency of the insulating barrier was measured by STS. They found that reduction of  $V^{2+}$  to the radical  $V^{\cdot+}$  leads to a significant decrease in the barrier height. Further reduction to  $V^0$  results in a very large increase in the barrier height. This result reflects the supporting effect of a half-filled molecular orbital in  $V^{\cdot+}$ . This might lead to an extension of the electronic wave function from the nanoparticle to the substrate via the orbitals of the radical  $V^{\cdot+}$ . As soon as  $V^0$  is formed, electron pairing in the LUMO (lowest unoccupied molecular orbital) suppresses the direct electronic interaction.

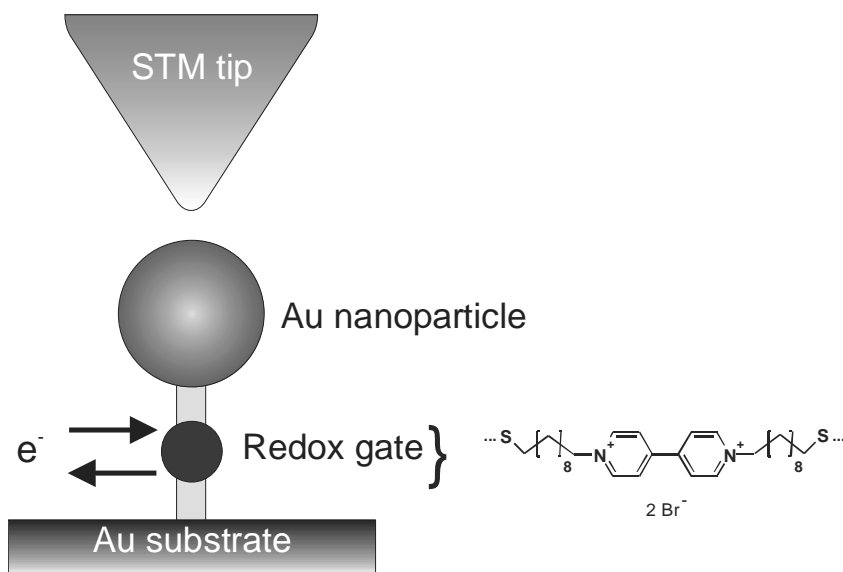


**Fig. 5-34** Scheme describing the redox switch, which is based on a viologen redox center incorporated within the nanoparticles ligand shell. For simplification the counterelectrode is not shown (adapted from [146]).

These results show impressively that switching of the SET current through a ligand-stabilized nanoparticle can be induced by electron injection into a specific redox group within the barriers of the tunnel junction. While the configuration, which was studied in this work, requires reduction by at least 30 electrons to change the transparency of the barrier in the nanoparticle layer, a great challenge will be to integrate these switching elements into a self-assembled SET circuit.

Feldheim et al. have been considering the possibility of employing particle-capping ligands as “chemical gates” to control the SET current flow in an STS configuration [147]. They reported the  $I(U)$  characteristics of ligand-stabilized Au nanoparticles in aqueous solutions, whereas octanethiol-stabilized 5 nm particles and galvinol-stabilized 3 nm particles were used at the central island. Galvinol represents a pH-active probe with  $pK_a \approx 12$ , whereas about 15 galvinol ligands were introduced into the ligand shell. Upon increasing the pH, galvinol, however, is converted to the galvinoxide anion, making the ligand shell negatively charged. The authors present a collection of  $I(U)$  characteristics for galvin and octanethiol nanoparticles in  $H_2O$  with several clear current steps and voltage plateaus, reflecting SET in the individual particles. While only small differences in the positions and magnitudes of the staircase voltage plateaus appear for octanethiol-stabilized Au upon changing the pH, galvin reacts sensitively when the pH changes from 5 to 8, 10, and finally 12. The authors point out that, firstly, a subtle shift (ca. 30 mV) in the entire staircase to positive bias potentials is noticeable from pH 5 to pH 8. The shift is even more pronounced in  $I(U)$ -curves obtained at pHs 10 and 12 (from ca. 60 to 120 mV). Secondly,  $\Delta V = e/c$  decreases in magnitude with increasing pH. Thirdly, slight peaks are evident in the  $I(U)$  curves at  $pH \geq 8$ . These chemically induced changes, which lead to an increase in the negative charge on the cluster, have two consequences: (i) the total self-capacitance of the nanoparticles decreases from ca.  $2.2 \cdot 10^{-18}$  F at pH 5 to ca.  $0.31 \cdot 10^{-18}$  F at pH 12, and (ii) the induced negative charge, by forming galvanoxide, acts like a negatively charged gate in solid-state SET devices, causing a shift of the Coulomb blockade to positive bias potentials. The authors conclude that the fact that potential shifts and capacitance changes are only observed for galvin-stabilized Au and not for octane thiol-stabilized Au supports the notion of pH-gated SET.

These results have shown for the first time that SET is dependent on the nature of the ligands stabilizing the nanoparticles as well as on the composition of the solution surrounding the function array. This will be useful in studying chemical signal transduction, where SET currents should be sensitive to single redox or analysis events.

### 5.2.5

#### From Single-Particle Properties to Collective Charge Transport

The single-particle properties discussed in the previous section showed the significance of the high charging energy of metal nanoparticles as a prerequisite for SET events at elevated temperatures. Together with the limited number of free electrons, this may lead us to regard them as artificial atoms. This raises fundamental



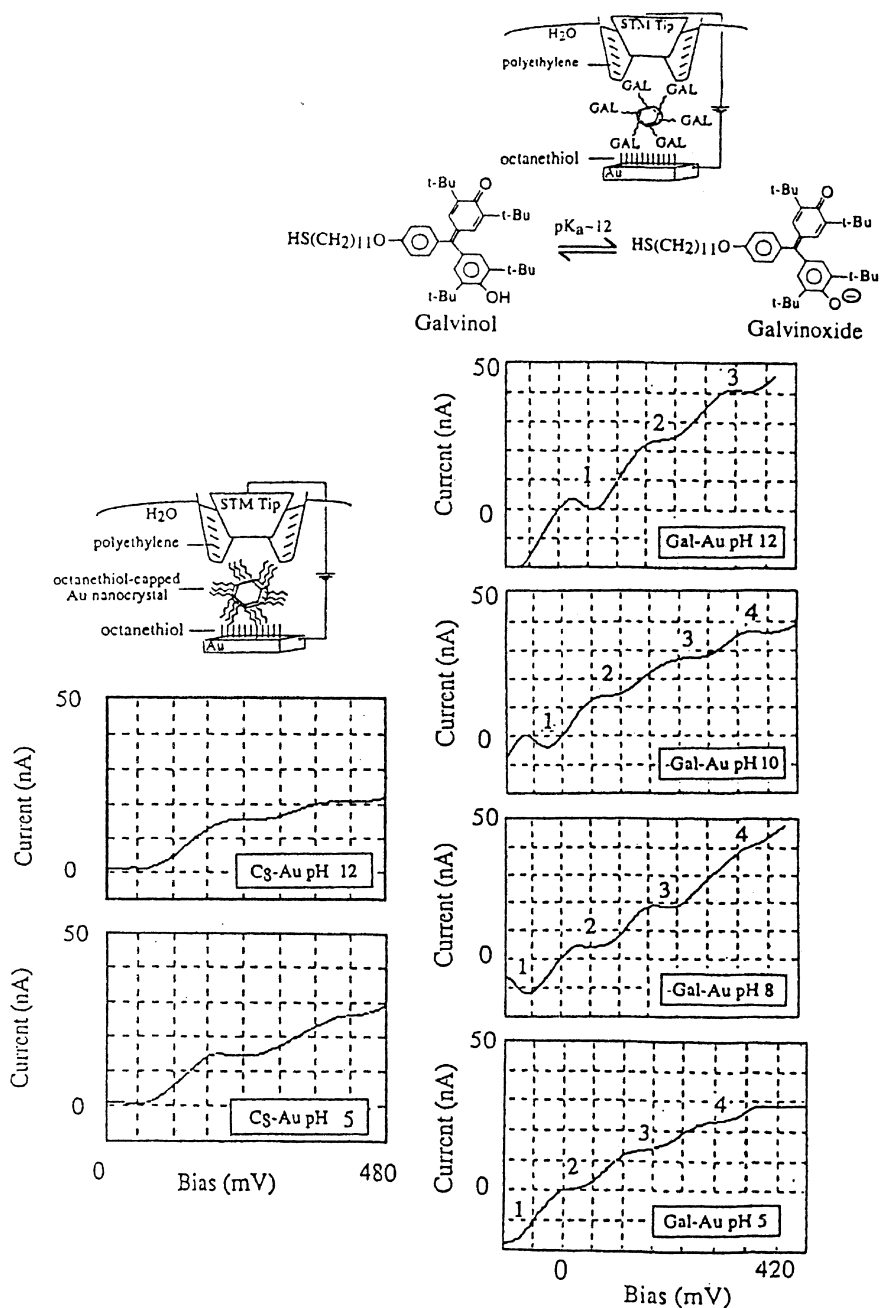


**Fig. 5-35** Current-voltage curves for  $C_8$ -Au (left) and Gal-Au (right) in  $H_2O$  as a function of pH (adjusted with phosphate buffer, see [104]). The numbers 1–4 in the Gal-Au data identify voltage plateaus. Cartoons of the experimental arrangements for measuring *I*–*V*

curves of individual nanoclusters in solution are shown at the top of each data column. The insulated STM tip, ligand-capped Au nanocluster, an octanethiol-coated planar Au substrate are shown. Length and shapes are not to scale (printed with kind permission from [147]).

questions about the design of “artificial molecules” or “artificial solids” built up from these nanoscale subunits [148–151]. Remacle and Levine reviewed these ideas associated with the use of chemically fabricated quantum dots as building blocks for a new state of matter [114].

Students in their first chemistry course learn that the simplest molecule  $H_2$  is formed by the overlap of the electron wave functions centered on the individual hydrogen atoms. Correspondingly, the wave functions of artificial atoms can also overlap, and electrons can coherently and reversibly exchange between them, which is the basis of a covalent bond. Extending this idea further, the ordered assembly of identical nanoparticles in one, two, or three dimensions represents the formation of an artificial solid or superlattice. The fabrication of two-dimensional and three-dimensional ordered superlattices has been demonstrated in several publications [152–160]. Furthermore it is possible to mix nanoparticles of different chemical compositions, of bimodal size or of different shapes to obtain tailored nanoalloys [161]. Levine called these new products “designer materials” with tunable properties [114]. Such artificial solids exhibit delocalized electron states, depending on the strength of the electronic coupling between the adjacent nanoparticles. The latter will depend on the size of the nanoparticles, the nature and the covering density of the organic ligands, the particle spacing, and the symmetry of packing.

As it is known from solid state physics, any kind of disorder affects the electronic structure of a solid. Accordingly, size distribution, packing defects, and chemical impurities lead to modification of the electronic structure of the quantum dot superlattice. And even in the case where the size of the nanoparticles is identical over microdomains of the assembly, slight deviations in the ligand density or orientation mean that the nanoparticles are not strictly the same at each lattice site, as would be the case for atoms. Therefore, solids consisting of chemically tailored nanoparticles are inherently disordered, and the loss of translational symmetry affects the extended states in the solid, which is immediately reflected in the optical and electrical properties. Remacle et al. illustrated the crucial point of symmetry breaking by comparing the experimental and theoretical second-order harmonic generation (SHG) response of a two-dimensional, hexagonal array of Ag particles ( $R = 1.5$  nm) with variable interparticle spacing  $D$  where  $D/2R$  is in the range 1.05–1.5 nm. At large interdot spacing ( $D/2R = 1.5$ ), the wave function will be localized on the individual nanoparticles. If the 2D layer is compressed, the wave function is delocalized over small domains. A quantum phase transition to a fully delocalized state is achieved for closely packed nanoparticles at  $D/2R = 1.05$  (see Figure 5-36).

A corresponding response has been obtained from complex impedance measurements on a monolayer of Ag nanoparticles with  $2R = 3.5$  nm.

Heath and coworkers, analyzing the complex dielectric modulus, which is the inverse of the complex dielectric permittivity (for details see [163]), reported a reversible metal-insulator transition. They observed a transition from RC relaxational behavior to an inductive metallic-like response, when the monolayer is compressed to decrease the interparticle spacing to  $<0.6$  nm. This suggests that a sequential transition from hopping transport between localized states via tunneling to metallic transport appears, accompanied by a rapid decay in the relaxation time, when

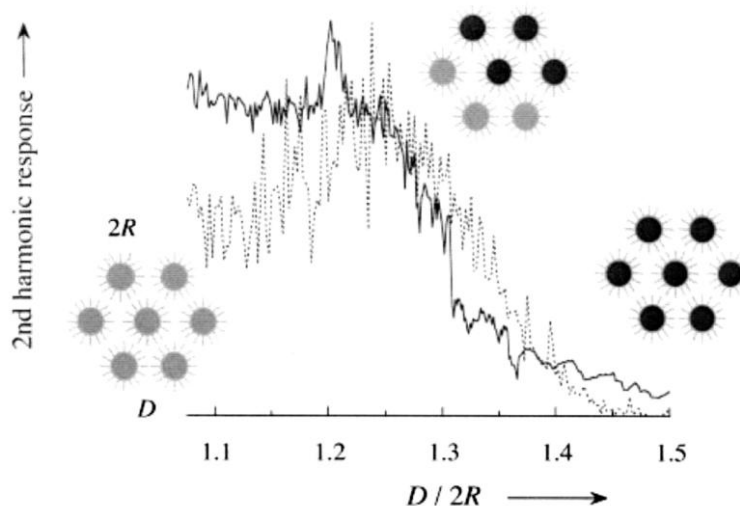


**Fig. 5-36** Transition from a localized to a delocalized state in a two-dimensional hexagonal array of ligand-stabilized 3 nm Ag particles upon mechanical compression. The

transition is probed by the second-harmonic response, which is sensitive to the extent of delocalization of the electronic wave function (printed with kind permission from [114]).

the layer is compressed. The latter may result from an increasing tunneling rate, i.e., the resistance decreases between the particles as well as in extended domains with delocalized states, and this is essentially affected by the degree of disorder.

In order to discuss the signatures of localization and delocalization and its significance to the application of nanoparticles in microelectronic devices, the following Sections give examples of the electrical properties of nanoparticle arrays, distinguished according to their dimensionality.

#### 5.2.5.1 One-Dimensional Arrangements

In the previous Sections, two examples of one-dimensional (1D) arrays of nanoparticles were described, where self-assembly or electrostatic trapping were used to address the arrays for electrical transport measurements. *A priori* it is clear that both methods cannot lead to strictly 1D defect-free arrangements. Furthermore, inherent disorder cannot be avoided.

To analyze the effect of disorder, an exact analytical solution in terms of Green's function (GF) for the potential distribution in a finite 1D array turned out to be appropriate [164, 165]. The GF approach allows the formulation the so-called partial "solitary" problem of small mesoscopic tunnel junctions, similarly to the problem of the behavior of an electron in 1D tight binding and in a set of random delta-function models.

The discussion of 1D metal cluster arrangements of ligand-stabilized nanoparticles, as reported in [164, 165], assumes that (i) either the capacitance  $C$  is the same for all junctions, whereas the self-capacitance  $C_0$  can fluctuate from site to site because of a finite size distribution or (ii) the  $C_0$  is the same, whereas  $C$  can

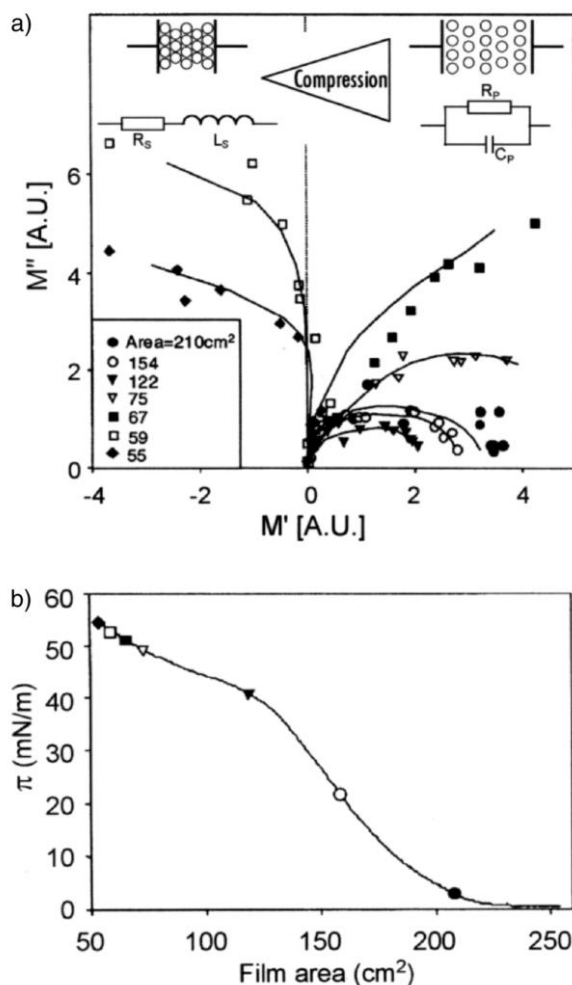


**Fig. 5-37** **a** Complex impedance response (plot of the imaginary part of the complex modulus  $M''$  vs. the real part  $M'$  in the complex plane) of a monolayer, 3.5 nm in diameter, of propanethiol-capped Ag nanoparticles. The particle film response is characterized initially by an RC circuit equivalent, in conformity with a picture of capacitively determined hopping localized conductivity. As the particles are compressed to a separation of less than 0.6 nm, the film becomes inductive,

indicating the presence of metallic-like transport in the film. **b** The Langmuir isotherm of the monolayer compression with labels corresponding to the various curves in the top graph. Although the isotherm indicates a collapse near the 130 cm<sup>2</sup> film area, the collapse is heterogeneous, occurring only at the mobile barriers. The central region of the film, where transport measurements were carried out, remains an uncollapsed monolayer (redrawn and modified from [162]).

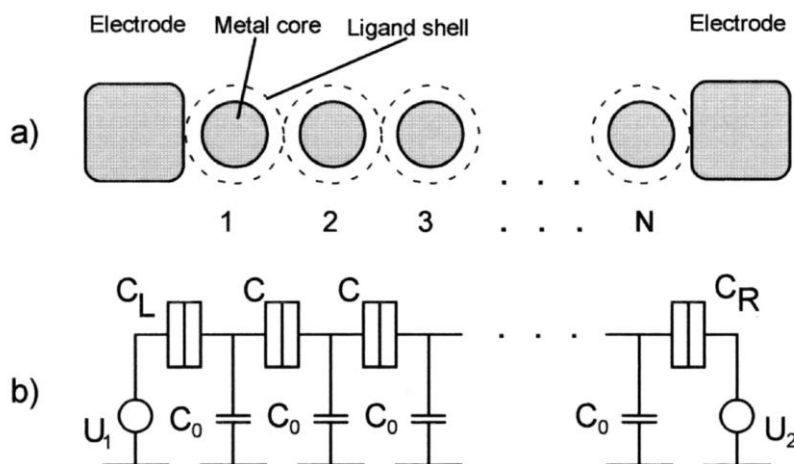


**Fig. 5-38** **a** 1D array of  $N$  ligand-stabilized metal clusters and **b** the corresponding circuit equivalent (printed with kind permission from [164]).

fluctuate from site to site because of packing defects. It has further been assumed that the metal nanoparticles have a continuous density of states, i.e., quantum size effects and their influence on the capacitance have been excluded from consideration. These simplifications illustrate the practical implications of disorder with respect to future applications in microelectronics, but generally they are not necessary assumptions for the method discussed.

The main results are that a decrease in the particle size at one position of the array increases the potential at this point, which may lead, at least, to localization, i.e., the single excess electron in the array may be trapped. As a packing defect, which affects the inter-particle capacitance at one point, acts like an inhomogeneity, the soliton will interact with its mirror-image soliton (or anti-soliton) and will therefore be attracted. This method is of practical use because the total reflection amplitude obtained by these calculations is directly related to the Landauer resistance [166–168], which increases exponentially with the number of defects. For illustration, let us consider a one-dimensional chain of 2 nm neutral particles. In this chain, a number  $N$  of the nanoparticles is replaced by smaller ones (1 nm). The 1 nm particles represent defects, which lead to a decreased transmission probability for electrons in the periodic chain, leading to an increase in the overall resistance. This situation is reflected in Figure 5-39, where the increase in resistance  $\Delta G^{-1}$  is given for this selected example, according to [169].

#### 5.2.5.2 Two-Dimensional Arrangements

Janes et al. reported the electronic conduction across a network of 4 nm gold nanoparticles interconnected by di-isonitrile ligands (1,4-di (4-isocyanophenylethynyl)-2-ethylbenzene) to produce a conjugated, rigid molecule with an approximate inter-particle spacing of 2.2 nm [170]. The two-dimensional assembly results from the

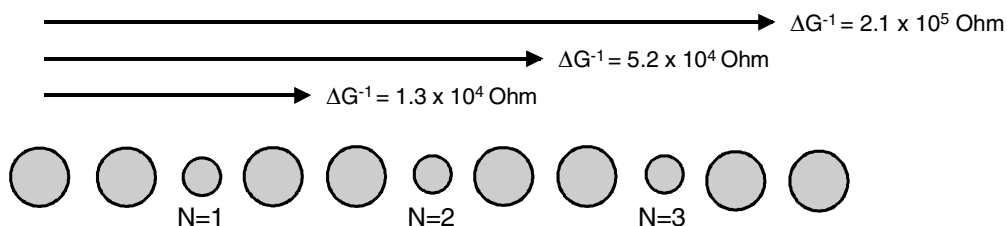


**Fig. 5-39** One-dimensional chain of 2 nm metal particles with  $N = 3$  "impurities", i.e. 1 nm metal particles. The arrows indicate that the resistance increases exponentially with  $N$ .

deposition of the nanoparticles from a colloidal solution, followed by reactive addition of the linking molecules. In order to allow electrical characterization, the layers were deposited on an  $\text{SiO}_2$ -supported GaAs wafer with gold contacts with separations of 500 nm and 450 nm, respectively.

The  $I(U)$ -characteristic of the arrays is linear over a broad voltage range. Since a dot-to-dot capacitance of  $2 \cdot 10^{-19} \text{ F}$  may be assumed, the total dot capacitance will be  $1.2 \cdot 10^{-18} \text{ F}$ , if each cluster is assumed to have six nearest neighbors. The corresponding charging energy will thus be approximately 11 meV, which is only about half of the characteristic thermal energy at room temperature. Therefore a Coulomb gap at room temperature is not apparent.

On the other hand, the charging energy of the nanoparticles has been obtained from comparable samples with two-dimensional cluster linkage by Andres et al. [171] from temperature dependent d.c. measurements. According to the Arrhenius relation  $G_0 = G_\infty \exp(-E_A/k_B T)$ , where  $G_\infty$  is the conductance as  $T \rightarrow \infty$ ,  $E_A$  is the activation energy and  $k_B$  is the Boltzmann's constant, Coulomb charging behavior with a charging energy (which corresponds to the activation energy) of  $E_A = 97 \text{ meV}$  was indicated. The interparticle resistance was revealed to be  $0.9 \text{ M}\Omega$ , from which a single-molecule resistance of  $29 \text{ M}\Omega$  is obtained. This value is in good agreement with the prediction of  $43 \text{ M}\Omega$  obtained from Hückel-MO calculations.

### 5.2.5.3 Three-Dimensional Arrangements

Signatures of a transition from single-particle properties to three-dimensional charge transport have been reported by Pileni and coworkers [172]. They reported a tunneling spectroscopy study at room temperature of 4.3 nm Ag nanoparticles stabilized in reverse micelles. The electrical transport measurements though single particles deposited on Au (111) substrates showed that, on increasing the applied voltage, the small capacitances of the double junction are charged and the detected current is close to zero because of the Coulomb blockade effect. The  $I(U)$  curve as well as the  $dI/dU$  vs  $U$  plot (insert in Figure 5-40B) clearly indicate the Coulomb blocking state, i.e., a zero bias and the onset of conductivity through the nanoparticles above the threshold voltage. When the particles are deposited from solutions at higher concentrations, they arrange in a hexagonally ordered monolayer. The tunneling current though this layer shows a less pronounced nonlinearity in

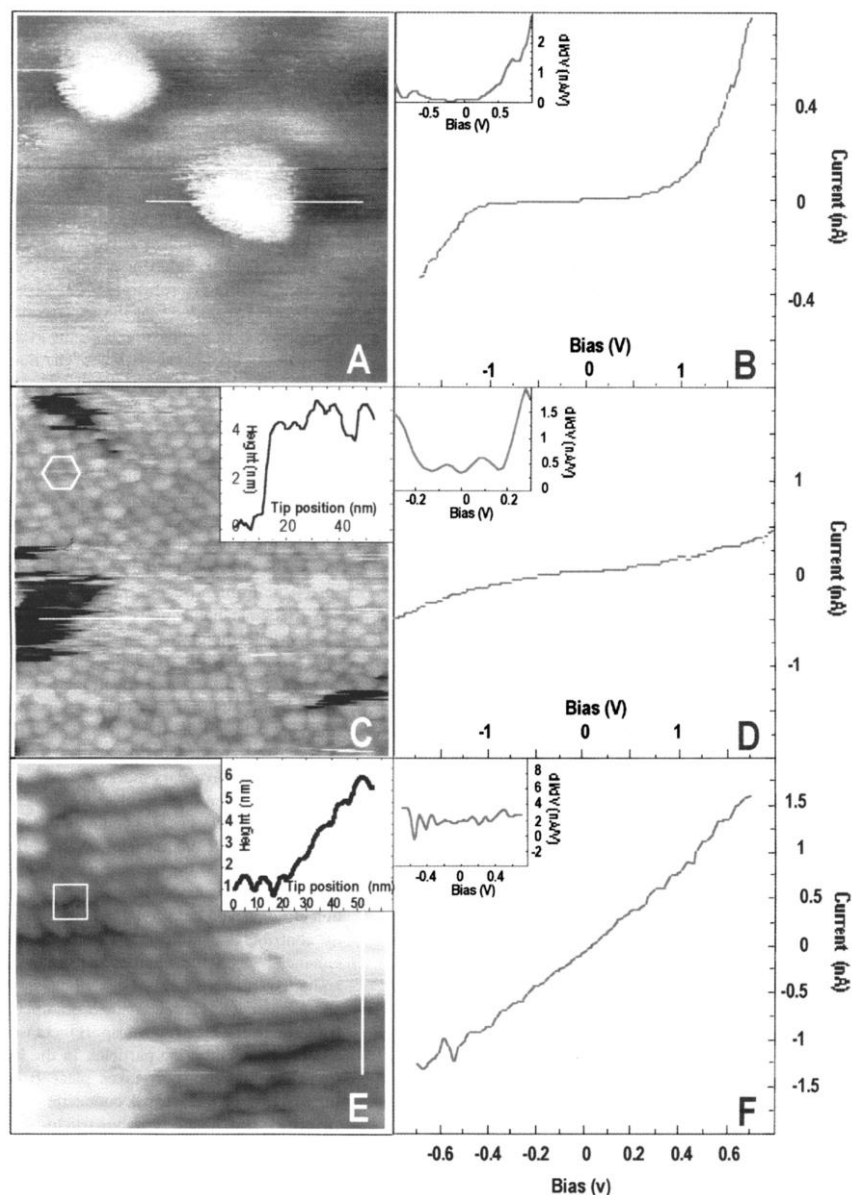


**Fig. 5-40** Constant-current mode STM images of silver nanoparticles, isolated (A), self-organized in close-packed hexagonal network (C), and in fcc structure (E), deposited on Au(111) substrate (scan size: A  $17.1 \times 17.1 \text{ nm}^2$ ,  $V_t = -1 \text{ V}$ ,  $I_t = 1 \text{ nA}$ , C  $136 \times 136 \text{ nm}^2$ ,  $V_t = -2.5 \text{ V}$ ,  $I_t = 0.8 \text{ nA}$ ,

E  $143 \times 143 \text{ nm}^2$ ,  $V_t = -2.2 \text{ V}$ ,  $I_t = 0.72 \text{ nA}$ ). The graphs are  $I$ - $V$  curves and their derivatives in the inserts of the silver nanoparticles, isolated (B), self-organized in close-packed hexagonal network (D), and in fcc structure (F), deposited on Au(111) substrate [172].

the  $I(U)$  curve as well as a smaller Coulomb gap, as compared to the isolated particles. This indicates the onset of ohmic contributions to the overall conductance of the system. Going to a three-dimensional arrangement of the particles, which form a self-organized closed-packed *fcc* structure, the Coulomb gap almost vanishes, and the  $I(U)$  characteristic is a purely ohmic one at low voltages. This reflects the fact that in the 3D systems an additional transport path for electrons appears between the adjacent nanoparticles, so that the Coulomb gap between the individual particles is smeared out because of the coupling of the electron states in the close-packed system.

The electrical behavior of the three-dimensional system is also reflected in the electrical d.c. and a.c. response of compacts of ligand-stabilized nanoparticles [109]. As a common feature, at high temperatures, i.e., several tens of Kelvin below room temperature, the temperature-dependent d.c. and a.c. conductivities follow a simply activated behavior according to the Arrhenius relation.

$$\sigma(T) = \sigma_o + \exp \frac{-E_A}{k_B T},$$

where  $E_A$  is the activation energy.  $E_A$  becomes temperature dependent when the measuring temperature is decreased. This means that down to very low temperatures the conductivity follows the Variable Range Hopping (VRH) expression proposed by Mott [173]:

$$\sigma(T) = \sigma_o + \exp \left( \frac{-T_o}{T} \right)^\gamma$$

whereas  $\gamma = 1/(d+1)$  in  $d$  dimensions. Although  $\gamma = \frac{1}{4}$  ( $d = 3$ ) might be expected from this general expression,  $\gamma = \frac{1}{2}$  is predominantly observed in the case of the compacted metal cluster compounds. This temperature dependence, as well as the electric field-dependent conductivity, which reflects pronounced non-ohmic behavior at strong electric fields, reveal a pronounced similarity to various heterogeneous materials, like cermets, doped and amorphous semiconductors, or metal- and carbon-insulator composites. This behavior was carefully analyzed by van Staveren and Adriaanse [174–176], applying different physical models of hopping conductivity, with the conclusion that the experimental data can best be fitted by a thermally activated stochastic multiple-site hopping process, whereas at high temperatures around room temperature nearest neighbor hops predominate.

This means that at low temperature the number of charge carriers participating in the hopping process does not change with temperature. Instead, at high temperatures, where  $k_B T$  becomes comparable to the charging energy  $E_c$  of the metal particle (note that  $E_c$  is determined by the total capacitance of the particle, and is therefore dependent on the particle size as well as on the inter-particle spacing, i.e. the dot-to-dot distance), thermally excited extra charge carriers are participating in the hopping process. Thus, even at high temperatures, the activation energy re-



flects the energy needed to transfer one electron from one electrically neutral particle to another. This is the charge disproportionation energy, and it has its atomic analog in the disproportionation energy of atoms or molecules in chemical redox reactions. At low temperatures, the hopping transport would be expected to become zero if all particles become electrically neutral. Since all reports on the electrical conductivity reflect a residual conductivity at very low temperatures, again it becomes obvious that packing, shape and size distribution prevent the localization sites from being identical, as has already been pointed out at the beginning of this Section.

In terms of a modified Anderson-Hubbard Hamiltonian [177, 178], orientational disorder and packing irregularities will lead to a distribution of the on-site Coulomb interaction and of the interaction of electrons on different (at least neighboring) sites. This is explicitly pointed out by Cuevas, Ortuno and Ruiz [179]. In contrast to the Coulomb-gap model of Efros and Sklovskii [180], they took into account three different states of charge of the mesoscopic particles, i.e. neutral, positively charged, and negatively charged. With this model, the VRH behavior, which dominates the electrical properties at low temperatures, can be fully explained.

Coming back to the high temperature regime, at least around 300 K, nearest-neighbor hopping is predominant. This leads to the question whether the charging energy of such cluster materials can be chemically tailored by means of bifunctional spacer molecules, which define the inter-particle spacing by the molecule length. This concept has been realized in the family of ligand-stabilized metal clusters  $\text{Au}_{55}(\text{PPh}_3)_{12}\text{C}_6$  and  $\text{Pd}_{561}(\text{phen})_{36}\text{O}_{200}$  by using bifunctional spaces with  $\text{NH}_2$ - or SH-groups on each terminus [181–183]. While the cluster size is kept constant when the cluster spacing is increased by the spacer molecules, an almost linear increase in the activation energy was observed. This can be explained by the decrease in the junction capacitance  $C$ , which scales with  $1/D$  ( $D$  = particle spacing) as long as the other geometric and dielectric parameters are kept constant.

This relationship is valid as long as the spacer molecules are not covalently bound to the cluster surface and the spacer molecules have no delocalized  $\pi$ -electron system along their backbone between the termini. As soon as covalently linking species equipped with delocalized  $\pi$  electrons enable inter-cluster electron transfer to occur, the activation energy drops, depending on the electronic structure of the molecule and its length. This shows that, at least by integral conductance measurements, the electron transport through individual organic molecules can be revealed, which is supporting information about the nature of electron transport on the molecular level.

## References

- 1 A. P. ALIVISATOS, *Science* **1996**, 271, 933.
- 2 L. E. BRUS, *Appl. Phys. A* **1991**, 53, 465.
- 3 H. WELLER, *Angew. Chem. Int. Ed. Engl.* **1993**, 32, 41.
- 4 M. NIRMAL, L. E. BRUS, *Acc. Chem. Res.* **1999**, 32, 407.
- 5 C. P. COLLIER, T. VOSSMEYER, J. R. HEATH, *Annu. Rev. Phys. Chem.* **1998**, 49, 371.
- 6 X. G. PENG, L. MANNA, W. D. YANG,

- J. WICKHAM, E. SCHER, A. V. KADAVANICH, A. P. ALIVISATOS, *Nature* **2000**, 404, 59.
- 7 C. B. MURRAY, D. J. NORRIS, M. G. BAWENDI, *J. Am. Chem. Soc.* **1993**, 115, 8706.
  - 8 A. A. GUZELIAN, U. BANIN, A. V. KADAVANICH, X. PENG, A. P. ALIVISATOS, *Appl. Phys. Lett.* **1996**, 69, 1432.
  - 9 L. E. BRUS, *J. Chem. Phys.* **1984**, 80, 4403.
  - 10 H. GRABERT, M. H. DEVORET (eds.) *Single Charge Tunneling*, New York, Plenum, 1992.
  - 11 D. V. AVERIN, K. K. LIKHAREV, in: *Mesoscopic Phenomena in Solids*, B. L. ALTSHULER, P. A. LEE, R. A. WEBB (eds.) Amsterdam, Elsevier 1991, 173.
  - 12 U. BANIN, Y. W. CAO, D. KATZ, O. MILLO, *Nature* **1999**, 400, 542.
  - 13 V. I. KLIMOV, A. A. MIKHAELOVSKY, S. XU, A. MALKO, J. A. HOLLINGSWORTH et al., *Science* **2000**, 290, 314.
  - 14 M. KAZES, D. Y. LEWIS, Y. EBENSTEIN, T. MOKARI, U. BANIN, *Adv. Mater.* **2002**, 14, 317.
  - 15 V. L. COLVIN, M. C. SCHLAMP, A. P. ALIVISATOS, *Nature* **1994**, 370, 354.
  - 16 B. O. DABBOUSI, M. G. BAWENDI, O. ONITSUKA, M. F. RUBNER, *Appl. Phys. Lett.* **1995**, 66, 1316.
  - 17 N. TESSLER, V. MEDVEDEV, M. KAZES, S. H. KAN, U. BANIN, *Science* **2002**, 295, 1506.
  - 18 M. P. BRUCHEZ, M. MORONNE, P. GIN, S. WEISS, A. P. ALIVISATOS, *Science* **1998**, 281, 2013.
  - 19 W. C. W. CHAN, S. NIE, *Science* **1998**, 281, 2016.
  - 20 G. P. MITCHELL, C. A. MIRKIN, R. L. LETSINGER, *J. Am. Chem. Soc.* **1999**, 121, 8122.
  - 21 J. E. BOWEN-KATARI, V. L. COLVIN, A. P. ALIVISATOS, *J. Phys. Chem.* **1994**, 98, 109.
  - 22 C. B. MURRAY, C. R. KAGAN, M. G. BAWENDI, *Science* **1995**, 270, 1335.
  - 23 C. P. COLLIER, T. VOSSMEYER, J. R. HEATH, *Annu. Rev. Phys. Chem.* **1998**, 49, 371.
  - 24 R. L. WHETTEN, J. T. KHOURY, M. M. ALVAREZ, S. MURTHY, I. VEZMAR et al., *Adv. Mater.* **1996**, 8, 428.
  - 25 C. T. BLACK, C. B. MURRAY, R. L. SANDSTROM, S. SUN, *Science* **2000**, 260, 1131.
  - 26 M. P. PILENI, *J. Phys. Chem. B* **2001**, 105, 3358.
  - 27 A. P. ALIVISATOS, K. P. JOHNSON, X. PENG, T. E. WILSON, C. J. LOWETH et al., *Nature* **1996**, 382, 609.
  - 28 A. MEWS, A. EYCHMÜLLER, M. GIERSIG, D. SCHOOS, H. WELLER, *J. Phys. Chem.* **1994**, 98, 934.
  - 29 Y. W. CAO, U. BANIN, *Angew. Chem. Int. Ed. Engl.* **1999**, 38, 3692.
  - 30 M. A. HINES, P. J. GUYOT-STONNIST, *J. Phys. Chem.* **1996**, 100, 468.
  - 31 X. PENG, M. C. SCHLAMP, A. V. KADAVANICH, A. P. ALIVISATOS, *J. Am. Chem. Soc.* **1997**, 119, 7019.
  - 32 B. O. DABBOUSI, J. RODRIGUEZ-VIEJO, F. V. MIKULEC, J. R. HEINE, H. MATTOUSSI et al., *J. Phys. Chem. B* **1997**, 101, 9463.
  - 33 Y. TIAN, T. NEWTON, N. A. KOTOV, D. M. GULDI, J. H. FENDLER, *J. Phys. Chem.* **1996**, 100, 8927.
  - 34 Y. W. CAO, U. BANIN, *J. Am. Chem. Soc.* **2000**, 122, 9692.
  - 35 S. V. KERSHAW, M. BURT, M. HARRISON, A. ROGACH, H. WELLER, A. EYCHMÜLLER, *Appl. Phys. Lett.* **1999**, 75, 1694.
  - 36 M. T. HARRISON, S. V. KERSHAW, A. L. ROGACH, A. KORNOWSKI, A. EYCHMÜLLER, H. WELLER, *Adv. Mater.* **2000**, 12, 123.
  - 37 L. MANNA, E. C. SCHER, A. P. ALIVISATOS, *J. Am. Chem. Soc.* **2000**, 122, 12700.
  - 38 Z. A. PENG, X. PENG, *J. Am. Chem. Soc.* **2001**, 123, 1389.
  - 39 L. S. LI, T. J. HU, W. D. YANG, A. P. ALIVISATOS, *Nano Lett.* **2001**, 1, 349.
  - 40 D. KATZ, T. WIZANSKY, O. MILLO, E. ROTHENBERG, T. MOKARI, U. BANIN, *Phys. Rev. Lett.* **2002**, 89, 86801.
  - 41 J. HU, L. S. LI, W. YANG, L. MANNA, W. WANG, A. P. ALIVISATOS, *Science* **2001**, 292, 2060.
  - 42 W. U. HUYNH, J. J. DITTMER, A. P. ALIVISATOS, *Science* **2002**, 295, 2425.
  - 43 K. J. VAHALA, P. C. SERCEL, *Phys. Rev. Lett.* **1990**, 65, 239.
  - 44 D. J. NORRIS, A. SACRA, C. B. MURRAY, M. G. BAWENDI, *Phys. Rev. Lett.* **1994**, 72, 2612.

- 45 D. J. NORRIS, M. G. BAWENDI, *Phys. Rev. B* **1996**, 53, 16338.
- 46 D. BERTRAM, O. I. MICIC, A. J. NOZIK, *Phys. Rev. B* **1998**, 57, R4265.
- 47 U. BANIN, J. C. LEE, A. A. GUZELIAN, A. V. KADAVANICH, A. P. ALIVISATOS et al., *J. Chem. Phys.* **1998**, 109, 2306.
- 48 U. BANIN, J. C. LEE, A. A. GUZELIAN, A. V. KADAVANICH, A. P. ALIVISATOS, *Superlattices and Microstructures* **1997**, 22, 559–568.
- 49 A. I. EKIMOV, F. HACHE, M. C. SCHANNE-KLEIN, D. RICARD, C. FLYTZANIS et al., *J. Opt. Soc. Am. B* **1993**, 10, 100.
- 50 H. FU, L. W. WANG, A. ZUNGER, *Appl. Phys. Lett.* **1997**, 71, 3433.
- 51 A. J. WILLIAMSON, A. ZUNGER, *Phys. Rev. B* **2000**, 61, 1978.
- 52 D. PORATH, Y. LEVI, M. TARABIAH, O. MILLO, *Phys. Rev. B* **1997**, 56, 9829.
- 53 D. PORATH, O. MILLO, *J. Appl. Phys.* **1997**, 85, 2241.
- 54 M. A. KASTNER, *Physics Today* (January, 1993).
- 55 L. KOUWENHOVEN, *Science* **1997**, 257, 1896.
- 56 M. AMMAN, K. MULLEN, E. BEN-JACOB, *J. Appl. Phys.* **1989**, 65, 339.
- 57 A. E. HANNA, M. TINKHAM, *Phys. Rev. B* **1991**, 44, 5919.
- 58 D. L. KLEIN, R. ROTH, A. K. L. LIM, A. P. ALIVISATOS, P. L. McEUEEN, *Nature* **1996**, 389, 699; D. L. KLEIN et al., *Appl. Phys. Lett.* **1996**, 68, 2574.
- 59 B. ALPERSON, S. COHEN, I. RUBINSTEIN, G. HODES, *Phys. Rev. B* **1995**, 52, R17017.
- 60 V. L. COLVIN, A. N. GOLDSTEIN, A. P. ALIVISATOS, *J. Am. Chem. Soc.* **1992**, 114, 5221.
- 61 D. KATZ, O. MILLO, S. H. KAN, U. BANIN, *Appl. Phys. Lett.* **2001**, 79, 117.
- 62 O. MILLO, D. KATZ, Y. W. CAO, U. BANIN, *J. Low Temp. Phys.* **2000**, 118, 365.
- 63 B. ALPERSON, G. HODES, I. RUBINSTEIN, D. PORATH, O. MILLO, *Appl. Phys. Lett.* **1999**, 75, 1751.
- 64 H. FU, A. ZUNGER, *Phys. Rev. B* **1998**, 57, R15064; H. FU et al., *Phys. Rev. B* **1998**, 57, 9971.
- 65 E. P. A. M. BAKKERS, D. VANMAEKELBERGH, *Phys. Rev. B* **2000**, 62, R7743.
- 66 D. KATZ, S. H. KAN, U. BANIN, O. MILLO, *Physica A* **2001**, 302, 328.
- 67 E. P. A. M. BAKKERS, Z. HENS, A. ZUNGER, A. FRANCESCHETTI, L. P. KOUWENHOVEN et al., *Nano Lett.* **2001**, 1, 551.
- 68 A. L. EFROS, M. ROSEN, *Annu. Rev. Phys. Chem.* **2000**, 30, 475.
- 69 A. FRANCESCHETTI, H. FU, L. W. WANG, A. ZUNGER, *Phys. Rev. B* **1999**, 60, 1819.
- 70 E. RABANI, B. HETENYI, B. J. BERNE, L. E. BRUS, *J. Chem. Phys.* **1999**, 110, 5355.
- 71 A. ZUNGER, *MRS Bull.* **1998**, 23, 35.
- 72 J. T. HU et al., *J. Phys. Chem.* **2002**, 106, 2447.
- 73 A. FRANCESCHETTI, A. ZUNGER, *Phys. Rev. B* **2000**, 62, 2614.
- 74 A. FRANCESCHETTI, A. ZUNGER, *Appl. Phys. Lett.* **2000**, 76, 1731.
- 75 Y. M. NIQUET, C. DELERUE, M. LANNOO, G. ALLAN, *Phys. Rev. B* **2001**, 64, 113305.
- 76 Y. M. NIQUET, C. DELERUE, G. ALLAN, M. LANNOO, *Phys. Rev. B* **2002**, 65, 165334.
- 77 D. SCHOOSS, A. MEWS, A. EYCHMÜLLER, H. WELLER, *Phys. Rev. B* **1994**, 49, 17072.
- 78 M. TEWS, D. PFANNKUCHE, *Phys. Rev. B* **2002**, 65, 73307.
- 79 M. ASADA, Y. MIYAMOTO, Y. SUEMATSU, *IEEE J. Quantum Electron.* **1986**, QE-22, 1915.
- 80 E. GRUNDMANN, *Physica E* **2000**, 5, 167.
- 81 V. I. KLIMOV, Ch. J. SCHWARZ, D. W. McBRANCH, C. A. LEATHERDALE, M. G. BAWENDI, *Phys. Rev. B* **1999**, 60, R2177.
- 82 H. J. EISLER, V. C. SUNDAR, M. G. BAWENDI, M. WALSH, H. I. SMITH, V. I. KLIMOV, *Appl. Phys. Lett.* **2002**, 80, 4614.
- 83 A. V. MALKO, A. A. MIKHAILOVSKY, M. A. PETRUSKA, J. A. HOLLINGSWORTH, H. HTOON, M. G. BAWENDI, V. I. KLIMOV, *Appl. Phys. Lett.* **2002**, 81, 1303.
- 84 A. YARIV, *Quantum Electronics*, 3rd edn., Wiley, New York, 1986.
- 85 (a) G. NIMTZ, P. MARQUARD, H. GLEITER, *J. Cryst. Growth* **1988**, 86, 66;

- (b) J. KOUTECKY, P. FANTUCCI, *Chem. Rev.* **1986**, 86, 539; (c) M. D. MORSE, *Chem. Rev.* **1986**, 86, 1049; (d) M. M. KAPPES, *Chem. Rev.* **1988**, 88, 369; (e) H. WELLER, *Angew. Chem.* **1993**, 105, 43.
- 86 (a) A. SCHÄFER, C. HUBER, J. GAUSS, R. AHLRICHS, *Theor. Chim. Acta*, **1993**, 87, 29; (b) A. SCHÄFER, R. AHLRICHS, *J. Am. Chem. Soc.* **1994**, 116, 10686.
- 87 A. SCHÄFER, *PhD Thesis*, University of Karlsruhe **1994**.
- 88 J. B. FORESMAN, M. HEAD-GORDON, J. A. POPLER, M. J. FRISCH, *J. Phys. Chem.* **1992**, 96, 135.
- 89 R. MCWHEENY, *Methods of Molecular Quantum Mechanics*, 2nd edn., Academic Press, London, 1992.
- 90 K. RAGHAVACHARI, G. W. TRUCKS, J. A. POPLER, M. HEAD-GORDON, *Chem. Phys. Lett.* **1989**, 157, 479.
- 91 F. SCHWABL, *Quantenmechanik*, Springer, Heidelberg, 1990, 189f.
- 92 A. A. VOSKANYAN, P. N. INGLIZYAN, S. P. LALYKIN, I. A. PLYUTTO, Y. M. SHEVCHENKO, *Fiz. Tekh. Poluprovodn.* **1978**, 12, 2096.
- 93 E. J. D. GARBA, R. L. JACOBS, *Physica B*, **1986**, 138, 5398.
- 94 S. N. MOSTAFA, S. A. SCHIMAN, *Ber. Bunsenges. Phys. Chem.* **1983**, 87, 113.
- 95 P. SCHERRER, *Göttinger Nachrichten*, **1918**, 2, 98.
- 96 (a) F. C. FRANK, J. S. KASPER, *Acta Cryst.* **1958**, 11, 184; (b) F. C. FRANK, J. S. KASPER, *Acta Cryst.* **1959**, 12, 483.
- 97 A. EICHHÖFER, J. F. CORRIGAN, D. FENSKE, E. TRÖSTER, *Z. Anorg. Allg. Chem.* **2000**, 626, 338.
- 98 M. B. ROBIN, P. DAY, *Adv. Inorg. Radiochem.* **1967**, 10, 248.
- 99 J. BARDEEN AND W. H. BRATTAIN, *Phys. Rev.* **1948**, 74, 230.
- 100 B. E. DEAL, *Interface*, **1997**, 6, 18.
- 101 A. QIN, Y. N. XIA, J. A. ROGERS, R. J. JACKMAN, X. M. ZHAO, G. M. WHITESIDES, *Top. Curr. Chem.* **1998**, 194, 1–20.
- 102 S. OKAZAKI, J. MOERS, in: *Nanoelectronics and Information Technology*, R. WASER (ed.), Wiley-VCH, 2003, 225–247.
- 103 M. H. DEVORET, H. GRABERT, in: *Single-charge tunneling Coulomb blockade phenomena in nanostructures*, H. GRABERT, M. H. DEVORET (eds.), Nato ASI Series, Plenum Press, New York, **1992**, 294, 1–20.
- 104 I. GIAVER, H. R. ZELLER, *Phys. Rev. Lett.* **1968**, 20, 1504.
- 105 I. GIAVER, *Phys. Rev.* **1969**, 181, 789.
- 106 K. K. LIKHAREV, *IEEE Trans. Magn.* **1987**, 23, 1142.
- 107 K. K. LIKHAREV, *IBM J. Res. Develop.* **1988**, 32(1), 144–157.
- 108 D. V. AVERIN, K. K. LIKHAREV, in: *Single charge tunneling Coulomb blockade phenomena in nanostructures*, H. GRABERT, M. H. DEVORET (eds.), Nato ASI Series, Plenum Press, New York, **1992**, 294, 311–332.
- 109 G. SCHÖN, U. SIMON, *Colloid Polym. Sci.* **1995**, 273, 101–117.
- 110 G. SCHÖN, U. SIMON, *Colloid Polym. Sci.* **1995**, 273, 202–218.
- 111 G. SCHMID, *Chem. Rev.* **1992**, 92, 1709–1727.
- 112 G. SCHMID, *Clusters and Colloids*, Wiley-VCH, 1994.
- 113 D. L. FELDHEIM, C. A. FOSS (eds.) *Metal Nanoparticles: Synthesis, Characterization and Application*, Marcel Dekker, New York, 2002.
- 114 F. REMACLE, R. D. LEVINE, *Chem. Phys. Chem.* **2001**, 2, 20.
- 115 P. MARQUARDT, L. BÖRNGEN, G. NIMTZ, H. GLEITER, R. SONNBERGER, J. ZHU, *Phys. Lett. A* **1986**, 114, 39.
- 116 G. NIMTZ, P. MARQUARDT, H. GLEITER, *J. Cryst. Growth* **1988**, 86, 66–71.
- 117 P. MARQUARDT, G. NIMTZ, *Festkörperprobleme* **1989**, 29, 317–328.
- 118 R. C. ASHOORI, *Nature* **1996**, 379, 413–419.
- 119 M. REED, *Sci. Am.* **1993**, 268(1), 98–103.
- 120 M. A. KASTNER, *Phys. Today* **1993**, 46, 24–31.
- 121 D. L. FELDHEIM, C. D. KEATING, *Chem. Soc. Rev.* **1998**, 27, 1–12.
- 122 U. SIMON, *Adv. Mater.* **1998**, 10, 1487–149; U. SIMON, in: *Metal Clusters in Chemistry*, Wiley-VCH, **1999**, 3, 1342–1359.
- 123 U. SIMON, G. SCHÖN, in: *Handbook of Nanostructured Materials and Nanotechnology*, H. S. NALWA (ed.), Academic Press, **2000**, 3, 131.

- 124 U. SIMON, G. SCHÖN, G. SCHMID, *Angew. Chem. Int. Ed. Engl.* **1993**, 2(32), 250–254; G. SCHMID, G. SCHÖN, U. SIMON, USA Patent No. 08/041,239 (1992).
- 125 G. SCHÖN, in: *Quantum Transport and Dissipation*, T. DITTRICH et al., (eds.), Wiley-VCH, 1997, 149–212.
- 126 K. UCHIDA, in: *Nanoelectronics and Information Technology*, R. WASER (ed.), Wiley-VCH, 2003, 427–443.
- 127 H. GRABERT, *Z. Phys. B* **1991**, 85, 319.
- 128 M. H. DEVORET, *Bull. Bur. Nat. Métrol.* **1991**, 22, 7.
- 129 D. ANSELMETTI, D. RICHMONT, A. BARATOFF, G. BORER, M. DREIER, M. BERNASCONI, H.-J. GÜNTHERODT, *Europhys. Lett.* **1994**, 25(4), 297–302.
- 130 M. DOROGI, J. GOMEZ, R. OSIFCHIN, R. P. ANDRES, R. REIFENBERGER, *Phys. Rev. B* **1995**, 52(12), 9071–9077.
- 131 Ch.-K. WANG, Y. FU, Y. LUO, *Phys. Chem. Chem. Phys.* **2001**, 3, 5017.
- 132 H. VAN KEMPEN, J. G. A. DUBOIS, J. W. GERRITSEN, G. SCHMID, *Physica B* **1995**, 204, 51–56.
- 133 J. G. A. DUBOIS, J. W. GERRITSEN, S. E. SHAFRANJUK, E. J. G. BOON, G. SCHMID, H. VAN KEMPEN, *Europhys. Lett.* **1996**, 33(4), 279–284.
- 134 D. V. AVERIN, A. N. KOROTKOV, *J. Low Temp. Phys.* **1990**, 3/4, 173–185.
- 135 W. P. HALPERIN, *Rev. Mod. Phys.* **1986**, 58(3), 533–606.
- 136 R. HOUBERTZ, T. FEIGENSPAN, F. MIELKE, U. MEMMERT, U. HARTMANN, U. SIMON, G. SCHÖN, G. SCHMID, *Europhys. Lett.* **1994**, 28(9), 641–646.
- 137 L. F. CHI, M. HARTIG, T. DRECHSLER, Th. SCHAAK, C. SEIDEL, H. FUCHS, G. SCHMID, *Appl. Phys. Lett. A*, **1998**, 66, 187.
- 138 R. P. ANDRES, Th. BEIN, M. DOROGI, S. FENG, J. I. HENDERSON, C. P. KUBIAK, W. MAHONEY, R. G. OSIFCHIN, R. REIFENBERGER, *Science* **1996**, 272, 1323–1325.
- 139 U. ZHANG, G. SCHMID, U. HARTMANN, *Nanoletters* **2003**, 3, 305.
- 140 D. L. KLEIN, O. L. MCEUEN, J. E. BOWENKATARI, R. ROTH, A. P. ALIVISATOR, *Appl. Phys. Lett.* **1996**, 68, 2574.
- 141 D. L. KLEIN, R. ROTH, A. LIM, A. P. ALIVISATOR, P. L. MCEUEN, *Nature*, **1997**, 389, 699–701.
- 142 T. SATO, H. AHMED, D. BROWN, B. F. H. JOHNSON, *J. Appl. Phys.* **1997**, 82(2), 696.
- 143 M. P. SAMANTA, W. TIAN, S. DATTA, *Phys. Rev. B* **1996**, 53, R7626.
- 144 A. BEZRYADIN, C. DEKKER, G. SCHMID, *Appl. Phys. Lett.* **1997**, 71, 1273.
- 145 G. SCHMID, Y.-P. LIU, M. SCHUMANN, Th. RASCHKE, Ch. RADEHAUS, *Nano Letters*, **2001**, 1(8), 405.
- 146 D. GITNIS, D. BETHELL, D. J. SCHIFFRIN, R. J. NICHOLS, *Nature*, **2000**, 408, 67.
- 147 L. C. BROUSSEAU, ILL, QI ZHAO, D. A. SCHULTZ, D. L. FELDHEIM, *J. Am. Chem. Soc.* **1998**, 120, 7645.
- 148 L. KOUWENHOVEN, *Science*, **1995**, 268, 1440–1441.
- 149 T. H. OSTERKAMP, T. FUJISAWA, W. G. VAN DER WEIL, K. ISHIBASHI, R. V. HIJMAN, S. TARUCHA, L. KOUWENHOVEN, *Nature*, **1998**, 395, 873–876.
- 150 R. H. BLICK, R. J. JANG, J. WEIS, D. PFANNKUCHE, K. VON KLITZING, K. ERBEL, *Phys. Rev. B*, **1995**, 53, 7899–7902.
- 151 C. LIVERMORE, C. H. CROUCK, R. M. WESTERVELT, K. L. KAMPMAN, A. C. GOSSARD, *Science*, **1996**, 275, 1332–1335.
- 152 C. P. COLLIER, T. VOSSMEYER, J. R. HEATH, *Annu. Rev. Phys. Chem.* **1998**, 49, 371–404.
- 153 C.-B. MURRAY, C. R. KAYAN, M. G. BAWENDI, *Science*, **1995**, 270, 1335–1338.
- 154 H. S. SUN, C. B. MURRAY, D. WELLER, C. FOLKS, A. MOSER, *Science*, **2000**, 287, 1989–1992.
- 155 C. P. COLLIER, R. J. SAYHALLY, J. J. SHIANG, S. E. HENRICKS, J. R. HEATH, *Science*, **1997**, 277, 1978–1981.
- 156 A. P. ALIVISATOR, *Science*, **1996**, 271, 933–937.
- 157 C. B. MURRAY, D. J. NORRIS, M. G. BAWENDI, *J. Am. Chem. Soc.* **1993**, 115, 8706–8715.
- 158 R. L. WHETTEN, J. T. KHONRY, M. M. ALVAREZ, S. MURTHYM, I. VEZMAR, Z. L. WANG, P. W. STEPHENS, C. L. CLEVELAND, W. D. LUETKE, U. LANDMAN, *Adv. Mater.* **1996**, 8, 428–433.

- 159 A. TALETS, V. RUSSIER, A. COURTY, M. P. PILENI, *Phys. Rev. B*, **1999**, 59, 13350–13358.
- 160 C. J. KIELEY, J. FINK, M. BRUST, D. BETHELL, D. J. SHIFFRIN, *Nature*, **1998**, 396, 444–446.
- 161 C. J. KIELEY, J. FINK, J. G. ZHENG, M. BRUST, D. BETHELL, D. J. SHIFFRIN, *Adv. Mater.* **2000**, 12, 640–643.
- 162 G. MARKOVICH, C. P. COLLIER, J. M. HEATH, *Phys. Rev. Lett.* **1998**, 80(17), 3807.
- 163 U. SIMON, M. E. FRANKE, *Microporous and Mesoporous Mater.* **2000**, 41, 1–36.
- 164 V. GASPARIAN, U. SIMON, *Physica B*, **1997**, 240, 289–297.
- 165 U. SIMON, V. GASPARIAN, *Phys. Status Solidi (b)*, **1998**, 205, 223.
- 166 R. LANDAUER, *Philos. Mag.* **1979**, 21, 863.
- 167 R. LANDAUER, *J. Phys. Cond. Mater.* **1984**, 1, 8099.
- 168 S. DATTA, *Electronic Transport in Mesoscopic Systems*, Cambridge University Press, 1995.
- 169 U. SIMON, *Habilitation Thesis*, University of Essen, 1998.
- 170 D. B. JANES, V. R. KOLAGUNTA, R. G. OSIFCHIN, J. D. BIELEFELD, R. P. ANDRES, J. I. HENDERSON, C. P. KUBIAK, *Superlattices and Microstructures* **1995**, 18(4), 275–281.
- 171 R. P. ANDRES, J. D. BIELEFELD, J. I. HENDERSON, D. B. JANES, V. R. KOLAGUNTA, C. P. KUBIAK, W. J. MAHONEY, R. G. OSIFCHIN, *Science* **1996**, 273, 1690–1693.
- 172 A. TALEB, F. SILLY, A. O. GUSEV, F. CHARRA, M.-P. PILENI, *Adv. Mater.* **2000**, 12(9), 633.
- 173 N. F. MOTT, *Philos. Mag.* **1969**, 19, 835.
- 174 M. P. J. VAN STAVEREN, H. B. BROM, L. J. DE JONGH, *Phys. Rep.* **1991**, 208, 1–96.
- 175 L. J. ADRIAANSE, *PhD Thesis*, University of Leiden, Netherlands, 1997.
- 176 L. J. DE JONGH, *Physics and Chemistry of Metal Cluster Compounds*, Kluwer Academic, Dordrecht, 1994.
- 177 P. W. ANDERSON, *Phys. Rev.* **1958**, 109, 1492.
- 178 J. HUBBARD, *Proc. Roy. Soc.* **1964**, A 277, 237.
- 179 E. CUEVAS, M. ORTUÑO, J. RUIZ, *Phys. Rev. Lett.* **1993**, 12, 1871.
- 180 A. L. EFROS, B. I. SKLOVSKII, *Phys. Status Solidi (b)*, **1976**, 76, 475.
- 181 U. SIMON, R. FLESCHE, H. WIGGERS, G. SCHÖN, G. SCHMID, *J. Mater. Chem.* **1998**, 8, 517–518.
- 182 U. SIMON, *Mater. Res. Soc. Symp. Proc.* **2000**, 581, 77–82.
- 183 V. TORMA, O. VIDONI, U. SIMON, G. SCHMID, *Eur. J. Inorg. Chem.* **2003**, 1121.

## 6

## Biomaterial-Nanoparticle Hybrid Systems: Synthesis, Properties, and Applications

*Eugenii Katz, Andrew N. Shipway, and Itamar Willner*

## 6.1

### Introduction

The unique electronic, optical and catalytic properties of metal and semiconductor nanoparticles (1–200 nm), together with the different methods available for the preparation of nanoparticles of controlled shape and size, provide exciting building blocks for nanoscale assemblies, structures and devices. Nobel Laureate Richard Feynman in his visionary lecture “There is plenty of room at the bottom” [1] inspired the concepts for the rapidly exploding research topic of nanotechnology. Although the term “nanotechnology” had not appeared on the horizon, Feynman said: “What I want to talk about is the problem of manipulating and controlling things on a small scale . . . What I have demonstrated is that there is room – that you can decrease the size of things in a practical way . . . I will not discuss how we are going to do it, but only what is possible in principle . . . We are not doing it simply because we haven’t yet gotten around to it.” Four decades later scientists have learnt that the manipulation of atoms, molecules and clusters on surfaces is feasible, and that new fundamental physics governs the properties of nano-objects.

The miniaturization of structures by conventional [2] and electron-beam lithography [3] is reaching the theoretical limits of ca. 50 nm. For the further miniaturization of chemical objects, alternative approaches must be developed. Following Feynman’s vision, one may employ atoms and molecules as building units for the “bottom-up” assembly and construction of architectures with nanometer dimensions. Nanoparticles consisting of metals [4] (e.g., Au, Ag, Pt, and Cu) or semiconductors [5–9] (e.g., PbS, Ag<sub>2</sub>S, CdS, CdSe, and TiO<sub>2</sub>) seem to be attractive units for the engineering of such structures. The unique electrical charging properties of these particles [10], as well as their optical and photophysical features [11], such as size-controlled plasmon absorbance, photonic electron-hole pair generation, and fluorescence, allow the addressing of particles by external electronic and photonic signals.

A variety of synthetic methodologies for the preparation of nanoparticles within a narrow size distribution are available [4]. Often, the nanoparticles are prepared by “wet chemistry” procedures, where the clustering of the metal atoms or semi-

conductor molecules proceeds in the presence of a surface capping ligand. This capping ligand binds to the metal/semiconductor clusters, prevents aggregation of the particles into bulk material, and controls the final dimensions of the nanoparticles. Many capping systems are available, including hydrophobic monolayers [12], positively or negatively charged monolayers [13], and polymer layers [14]. Association of molecular units to the nanoparticles introduces chemical functionalities that can provide recognition or affinity interactions between different appropriately modified particles, and thereby dictate structure when aggregation occurs [15]. New collective properties of aggregated particles [11] such as coupled plasmon absorbance, interparticle energy transfer, and electron transfer or conductivity may be observed in the clustered assemblies.

The chemical functionalities associated with nanoparticles enable the assembly of 2D and 3D nanoparticle architectures on surfaces [11]. Composite layered or aggregated structures of molecule- or macromolecule-crosslinked nanoparticles on surfaces have been prepared, and the specific sensing of substrates [16], tunable electroluminescence [17], and enhanced photoelectrochemistry [18] have been accomplished. The assembly of nanoparticle architectures on surfaces has also led to the fabrication of nanoscale devices such as single electron transistors [19], nanoparticle-based molecular switches [20], metal-insulator-nanoparticle-insulator-metal (MINIM) capacitors [21], and others. Several reviews have addressed recent advances in the synthesis and properties of nanoparticles [11, 22–24] and the progress in the integration of composite nanoparticle systems with surfaces [11, 25–27].

The conjugation of nanoparticles with biomaterials is a tempting research project that provides a route into nanobiotechnology. Evolution has optimized fascinating macromolecular structures exhibiting unique recognition, transport, and catalytic properties. The conjugation of nanoparticles with biomaterials could provide electronic or optical transduction of the biological phenomena. Enzymes, antigens and antibodies, and receptors have dimensions in the range of 2–100 nm, comparable to those of nanoparticles, and thus the two have structural compatibility. Several fundamental features show biomaterials to be important future building blocks for nanoparticle architectures:

1. Biomaterials reveal specific and strong complementary recognition interactions, e.g., antigen-antibody, nucleic-acid-DNA, hormone-receptor. The functionalization of a single kind of nanoparticle or different kinds of nanoparticles with biomaterials could lead to biomaterial-nanoparticle recognition and thus to self-assembly.
2. Various biomaterials include several binding sites, e.g., the two Fab-sites of antibodies, the four binding domains of streptavidin or concanavalin A. This allows the multidirectional growth of nanoparticle structures.
3. Proteins may be genetically engineered and modified with specific anchoring groups. This facilitates the aligned binding to nanoparticles, or the site-specific linkage of the biomaterial to surfaces. Consequently, directional growth of nanoparticle structures may be dictated. Furthermore, other biomaterials, such as double-stranded DNA, may be synthetically prepared in complex rigidified



structures that act as templates for the assembly of nanoparticles by intercalation, electrostatic binding to phosphate groups, or association to functionalities tethered to the DNA.

4. Enzymes provide catalytic tools for the manipulation of biomaterials. For example, the ligation of nucleic acids or the endonuclease scission processes of nucleic acids provide effective tools for controlling the shape and structure of biomaterial-nanoparticle hybrid systems. In this context, it is important to note that Mother Nature has developed unique biocatalytic replication processes. The use of biocatalysts for the replication of biomaterial-nanoparticle conjugates may provide an effective system for the formation of nanostructures of pre-designed shapes and compositions.

It is the aim of this chapter to review the synthesis of biomaterial-nanoparticle hybrid systems, as well as the organization of these systems as functional devices (Figure 6-1). We describe their properties, the methods of assembling two-dimensional and three-dimensional nanoparticle structures on surfaces, and the operation of these biomaterial-nanoparticle structures as functional devices. Specifically, we discuss the use of the systems as sensing devices, as building blocks for electronic circuitry, and as electronic and optoelectronic elements. It is our aim to highlight the fact that the scientific accomplishments of the past few years have already addressed important aspects of nanobiotechnology.

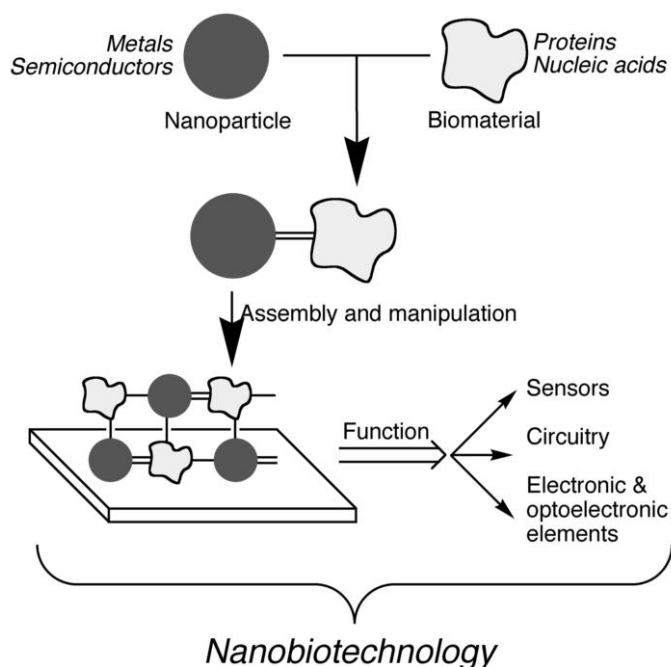


**Fig. 6-1** The conceptual generation of nanoparticle-biomaterial conjugates and their assembly to give functional devices.

## 6.2

### The Synthesis and Properties of Biomaterial-Functionalized Nanoparticles

Biological molecules have been immobilized on polymer matrices and inorganic supports by a variety of techniques, including physical adsorption, electrostatic binding, specific recognition and covalent coupling [28–32]. These supports, modified with biological molecules such as proteins/enzymes, antigens/antibodies, and DNA/oligonucleotides, have been used for numerous biotechnological applications, including affinity separations, biosensing, bioreactors, and biofuel cells. Recently, these immobilization techniques – developed for the functionalization of macro-size supports – have been applied to bring together biomolecules and nanoparticles.

#### 6.2.1

##### Functionalization by Electrostatic Adsorption

The simple adsorption of biomolecules on nanoparticles has frequently been used [28–30] and studied, these biomolecules ranging from low-molecular-weight organic substances (e.g., vitamin C [33]) to large protein/enzyme molecules [34–36]. In the case of nanoparticles that are stabilized by anionic ligands such as carboxylic acids (citrate, tartarate, lipoic acid), the adsorption of proteins originates from electrostatic interactions (Figure 6-2) [37]. For example, gold and silver nanoparticles produced by citrate reduction have been functionalized with immunoglobulin (IgG) molecules at pH values slightly above the isoelectric point of the citrate ligand [38]. This allows effective binding between the positively charged amino acid side chains of the protein and the negatively charged citrate groups of the colloids. Other examples of protein coating through electrostatic interactions include the direct adsorption of heme-containing redox enzymes at citrate-stabilized silver nanoparticles [34, 39, 40] and the binding of basic leucine zipper proteins to lipoic acid-stabilized semiconductor  $\text{CdSe}_{\text{core}}/\text{ZnS}_{\text{shell}}$  particles [41]. Differential scanning calorimetry (DSC) has been used to demonstrate the electrostatic nature of proteins adsorbed on silica particles, and allows the calculation of thermodynamic parameters [42]. The electrostatic deposition of biomolecules, particularly proteins or enzymes, can also be extended to a multi-layer level [43]. Protein molecules

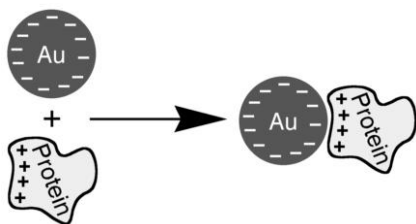


Fig. 6-2 The assembly of nanoparticle-protein conjugates by electrostatic interactions.

electrostatically attracted to the charged nanoparticles can provide a base interface for the further deposition of an oppositely charged polyelectrolyte polymer that again allows the deposition of a secondary protein layer. Multilayer films of bovine serum albumin (BSA) [44], immunoglobulin G (IgG) [44],  $\beta$ -glucosidase ( $\beta$ -GLS) [45], glucose oxidase (GOx) [46, 47], urease (Ur) [48], and horseradish peroxidase (HRP) [47] have thus been assembled on polystyrene nanoparticles by the alternate deposition of the protein and oppositely charged polymers. The protein/polymer multilayer shell could be varied from several to hundreds of nanometers in thickness. This strategy permits the preparation of functional films with a high density of enzyme molecules on nanoparticles.

Similarly, the electrostatically driven adsorption of negatively charged DNA molecules on positively charged CdS nanoparticles has been studied in detail [49–53]. An increase in the loading of nanoparticles of organic materials, upon layer-by-layer deposition, increases the sensitivity of analytical methods when these particles are utilized. For example, polystyrene particles were functionalized with a multilayer assembly of polyelectrolytes functionalized with a fluorescent dye. The assembly was terminated with an IgG layer that allowed the use of the modified particles as labels in fluorescence immunoanalysis [54]. The increase of the loading of the particles with the dye because of multilayer deposition resulted in higher fluorescence output, and thus in a higher sensitivity of the analysis.

### 6.2.2

#### Functionalization by Chemisorption of Thiol-Derivatized Biomaterials

In some cases, strong chemisorption of proteins on Au nanoparticles can originate from the binding of thiol groups (from cysteine residues) existing in the proteins (e.g., immunoglobulins (IgG) [38], serum albumin [55]) to the Au surface (Figure 6-3A). If no such residues are available in the native proteins, thiol groups can be incorporated by chemical means (e.g., with Traut's reagent, 2-iminothiolane (**1**) in Figure 6-3B) [56] or by genetic engineering. Some proteins and enzymes preserve

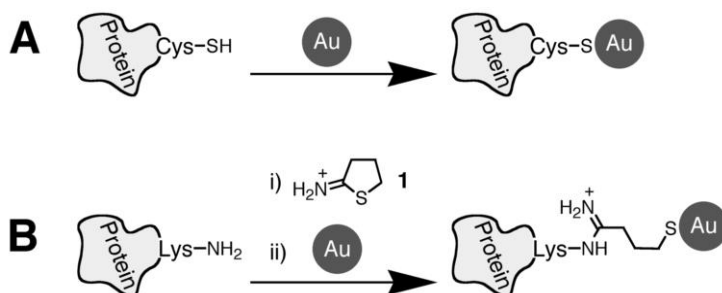


**Fig. 6-3** The formation of nanoparticle-protein conjugates by the adsorption of nanoparticles on **A** natural, and **B** synthetic thiol groups of the protein.

their native structures and activities when they are directly adsorbed on nanoparticles. For instance, a surface-enhanced resonance Raman (SERR) spectrum of native hemoglobin was obtained when it was adsorbed on citrate-stabilized Ag colloids. Reversible dioxygen and carbon monoxide binding and the R- to T-state transition were also observed [36]. A non-heme iron enzyme, chlorocatechol dioxygenase, physically adsorbed on citrate-reduced Ag colloid, also showed its native structure and biocatalytic activity upon application of SERR spectroscopy [34]. However, physically adsorbed biomolecules can be readily lost from the surface, and adsorbed proteins are often prone to denaturation, thereby losing their biocatalytic or biorecognition activities. Careful investigations of some proteins and enzymes directly adsorbed on nanoparticles demonstrate their conformational changes and loss of biological activity. For example, circular dichroism (CD), DSC, and fluorescence spectroscopy applied to bovine fibrinogen adsorbed on TiO<sub>2</sub> nanoparticles indicate that the  $\alpha$ -helix content of the protein decreases markedly upon their adsorption [35].

Nucleic acids can be synthesized with tethered alkanethiol groups by using appropriate phosphoramidate precursors in a solid-phase synthesis. The *n*-alkylthiolated nucleic acids have been used extensively in the preparation of DNA-functionalized gold nanoparticles [57, 58] and CdSe<sub>core</sub>/ZnS<sub>shell</sub> [59, 60] or CdS [52] semiconductor nanoparticles. DNA molecules functionalized with a steroid-disulfide derivative can readily bind to Au nanoparticles and demonstrate higher adsorption stability because two sulfur atoms of the disulfide anchor group are involved in the attachment process [61]. Enhanced binding of nucleic acids to metal nanoparticles may be accomplished by the use of oligonucleotides that include several adenosyl phosphothiolate residues at their ends, thus enabling multi-point attachment to the nanoparticles [62].

### 6.2.3

#### Functionalization by Specific Interactions

Nanoparticles functionalized with groups that provide sites for the affinity binding of biomolecules have been used for the specific attachment of proteins and oligonucleotides. For example, streptavidin-functionalized Au nanoparticles have been used for the affinity binding of biotinylated proteins (e.g., immunoglobulins and serum albumins [63]) or biotinylated oligonucleotides (Figure 6-4A) [64, 65]. Likewise, biotinylated CdSe/CdS/SiO<sub>2</sub> nanoparticles can be bound to streptavidin [66]. Also, nanoparticle-antibody conjugates were used for affinity binding of their respective antigens (Figure 6-4B) [67]. This may be advantageous, as antibodies associated with nanoparticles can demonstrate association constants with respective antigens that are even higher than those of the free antibody [68].

By covalently attaching proteins to nanoparticle surfaces, problems of instability, reversibility and inactivation can be overcome [43]. Low-molecular bifunctional linkers that have anchor groups for attachment to nanoparticle surfaces and functional groups for further covalent coupling to the target biomolecules were extensively used for generating covalent conjugates of biomolecules and various nano-

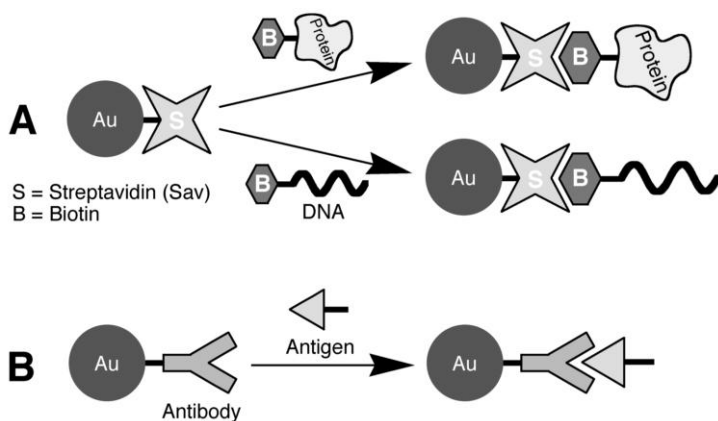


**Fig. 6-4** The assembly of nanoparticle-biomaterial conjugates by the use of bioaffinity interactions, **A** by the use of streptavidin-biotin interactions, and **B** by the use of antibody-antigen interactions.

particles [69]. Anchor groups such as thiols, disulfides, or phosphane ligands are often used for the binding of the bifunctional linkers to Au, Ag, CdS, and CdSe nanoparticles. These anchor groups readily substitute weakly adsorbed molecules stabilizing the nanoparticles, or may be incorporated in the nanoparticle synthesis, resulting in a nanoparticle surface providing functional groups for further reactions. Alkoxysilane or halogen-silane groups are used for the covalent attachment of bifunctional linkers to the surfaces of  $\text{SiO}_2$  and other oxide-coated nanoparticles. A wide variety of terminal functional groups is available in different bifunctional linkers: amino, active ester, and maleimide groups are used for the covalent coupling of biological compounds by means of carbodiimide-mediated esterification and amidation, or reaction with thiol groups [69]. Single functional groups (e.g., active ester or amino units) on Au nanoparticles are available either by a statistical approach or by the modification of chemically defined clusters. These structures provide unique synthetic routes for the covalent binding of a single target biomolecule per nanoparticle [70–72].

#### 6.2.4

#### Properties of Nanoparticle-Biomaterial Composites

The functionalization of nanoparticles with biomolecules results in changes in the properties of the nanoparticles and their interactions with the environment. Upon adsorption of vitamin C on  $\text{TiO}_2$  nanoparticles, the optical properties of the particles were red shifted by 1.6 eV. This is the result of charge transfer, and originates from the specific binding of the electron-donating modifier to corner defects on the surface of the nanoparticles [33]. The solubility of nanoparticles in water can be

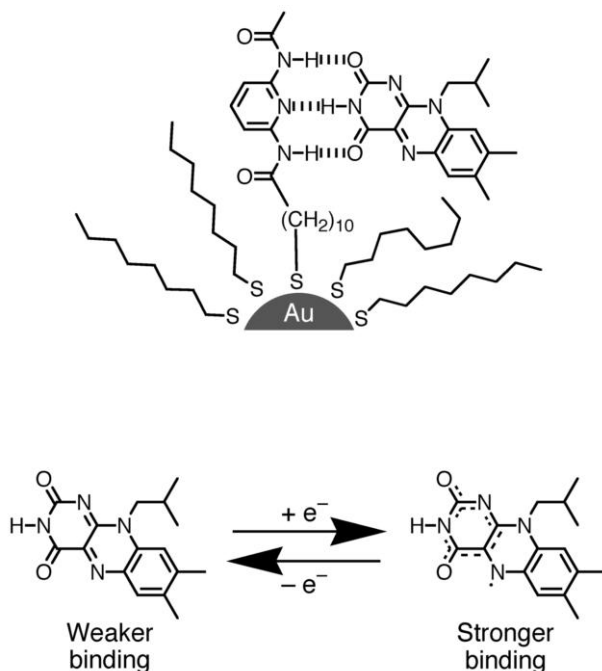


**Fig. 6-5** The electrochemically-controlled recognition of flavin by a diamidopyridine-functionalized nanoparticle.

greatly improved by the functionalization of their surfaces with highly hydrophilic biomolecules [73]. While Au nanoparticles modified with long chain alkanethiols are only soluble in low-polarity organic solvents, Au nanoparticles with  $\omega$ -carboxylic acid-functionalized alkanethiolate ligand shells are soluble in polar organic solvents such as ethanol and acetone. Au nanoparticles modified with biomolecules such as thiopronin or coenzyme A demonstrate excellent solubility in water.

Alteration of the chemical properties of the biomolecules covering nanoparticles by external signals (e.g., electrical, optical) can be used to control interactions of the modified nanoparticles with the environment, for example, to control the binding of a secondary modifier or the aggregation of the nanoparticles. Complex formation between a diaminopyridine derivative and a flavin derivative was studied at an Au nanoparticle surface [74]. It has been shown that more stable hydrogen bonding is provided when the flavin derivative is electrochemically reduced (Figure 6-5). This allows electrochemically controlled switching of the binding of the bio-organic molecules to the organic-functionalized shell of the nanoparticle.

The interactions of biomaterial-functionalized nanoparticles with other functionalized nanoparticles or other biomaterials such as proteins or DNA molecules provided by affinity properties of the biomaterial shell components are described in the following sections.

### 6.3

#### Biomaterial-Functionalized Nanoparticles for Controlled Chemical Reactivity

The interactions of functionalized nanoparticles with biomaterials or within biomaterial structures can control the chemical reactivity of the biomolecules. Alternatively, they can report on the state of the reaction or reactants, allowing control to be exercised externally. It is well known that small molecules and polymers can affect the chemical reactivity of biomolecules. If there are several possible parallel reactions, the effect produced by a promoter/inhibitor on a specific chemical reaction can change the effective chemical path of the whole process, resulting in a regulation of the biochemical system. Molecular labels (e.g., fluorescent dyes) incorporated into biomolecules can report on the state of the biomolecule, transducing the molecular operation into an output signal used, for example, in biomaterial-based diagnostics. Functionalized nanoparticles can operate in the same way, demonstrating properties of a biopromoter/bioinhibitor or a reporter, with some advantages over their molecular-sized counterparts due to the unique photophysical and electronic properties of the nanoparticles.

#### 6.3.1

##### Controlling DNA Reactivity

Biocatalytic reactions occurring at DNA molecules, such as transcription or translation, require the association of enzymes with the DNA chain. The competitive association of other molecules to the DNA chain can decrease the enzyme binding and thus inhibit the process, finally resulting in gene regulation. It has been shown that small molecules [75], dendrimers [76], and polymers [77] are capable of efficient binding to DNA that in some cases leads to inhibition of the transcription machinery. In these systems, however, the creation of suitably preorganized scaffolds for the controlled binding to DNA presents a significant design challenge. For small molecules, this challenge arises from the detailed synthesis required for a rigid scaffold containing several functional groups. For polymer systems, the precise placement of substituents along the backbone as well as the control of the polymer macro-conformation in solution are difficult to achieve. An excellent solution to these problems is the application of “mixed monolayer-protected Au clusters” (MMPCs) [78]. The self-assembled monolayer coating of the Au nanoparticles presents a highly organized surface for the recognition of DNA that is of a similar size scale (6–10 nm) to that of DNA-binding proteins. The central metal core rigidifies the particle, limiting the organic components to a much smaller subset of structures than a similarly sized polymer. The mobility of the thiols on the nanoparticle surface also allows the formation of recognition elements on the nanoparticle surface to be controlled in subsequent steps [79]. Nanoparticles for the recognition of double-stranded (ds) DNA were prepared by the partial displacement of octanethiol on the Au surface with 11-mercaptoundecyltrimethylammonium [80]. The mixed monolayer of this MMPC system is designed to interact with DNA based on the electrostatic attraction of the positively charged quater-

nary ammonium salt and the negatively charged DNA phosphate groups. These MMPCs bind to the ds-DNA in competition with the enzymes involved in gene regulation, thus resulting in effective inhibition of the biocatalytic transcription process.

### 6.3.2

#### Reporting on DNA Reactivity

DNA molecules functionalized at specific positions with a fluorescent dye and a quencher can produce a fluorescence output controlled by the distance separating the dye and the quencher, thus reporting on the conformation of the DNA chain. Au nanoparticles can quench fluorescence of chromophores to an extent that is 100-fold better than molecular quenchers, and they also have higher quenching efficiency for dyes emitting in the near infrared region. A DNA oligonucleotide was functionalized with a fluorescent dye at the 3' end, and an Au nanoparticle functionalized with a single maleimide group was covalently linked to the 5' end through a  $(\text{CH}_2)_6\text{-SH}$  group [81]. The molecule could adopt two conformations (Figure 6-6): a stem-loop structure with the fluorophore and the Au nanoparticle held in close proximity (hairpin state), and a rod-like structure with them far apart (open state). The hairpin state (2) is self-generated because of the intramolecular complementarity of the terminal parts of the DNA chain that make a ds-structure within the same molecule, whereas the open state (3) is produced upon interaction and hybridization with an analyte DNA molecule (4) that exhibits complementary to the central part of the DNA chain. This target DNA hybridizes with the modified DNA, resulting in the formation of ds-DNA, thus opening the hairpin, increasing the distance between the fluorophore and the nanoparticle, and thereby enhancing the fluorescence. The process and the reporting signal only occur in the case of complementarity between the analyte DNA and the central part of the sensing DNA. The system was thus successfully applied for single-mismatch detection in DNA sequences [81].

## 6.4

### The Aggregation of Biomaterial-Functionalized Nanoparticles

The organization and patterning of inorganic nanoparticles into two- and three-dimensional (2D and 3D) functional structures is a fundamental prerequisite for the assembly of chemical, optical, magnetic and electronic devices [11]. Many approaches have been described for the formation of 2D and 3D arrays of metal and semiconductor nanoparticles, for example, using (i) solvent evaporation of hydrophobic colloids [82–84], (ii) random inclusion of the nanoparticles into gels and glassy matrices [85], (iii) template-directed synthesis at structured surfaces [86] in porous protein crystals [87, 88] or bacterial superstructures [89], and (iv) chemical coupling in solution by means of bivalent crosslinker molecules [90–92]. An example of the latter is the alkanedithiol-directed aggregation of Au nanoparticles



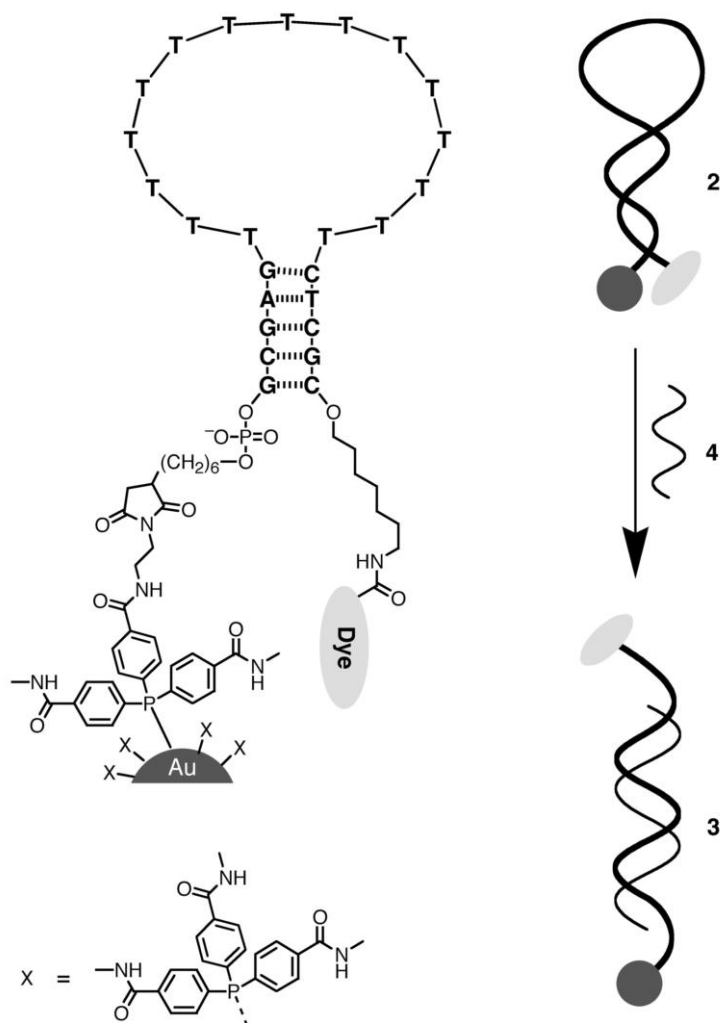


**Fig. 6-6** The change between hairpin (2) and extended (3) conformations of a DNA chain by the use of a second strand (4). In the extended conformation, the ends (which bear an Au nanoparticle and a dye) are far apart, and in the hairpin conformation they are close.

[92]. The aggregation of nanoparticles induced by specific biological interactions attracts interest as a self-assembly process for the building of complex nanostructures exhibiting new collective properties.

There are several advantages in utilizing biomaterials as building blocks of nanoparticle structures:

1. The diversity of biomaterials facilitates the selection of building units of pre-designed size, shape and functionality.
2. The availability of chemical and biological means to modify and synthesize biomaterials, e.g., synthesis of nucleic acids of pre-designed composition and shape, eliciting monoclonal antibodies, or modifying proteins by genetic engineering, pave the way to the construction of biomaterials for the assembly of nanoparticles.
3. Enzymes may act as biocatalytic tools for the manipulation of the biomaterials.
4. Hydrolysis of proteins, scission or ligation of DNA or replication of nucleic acids may be employed as assembler tools of nanoparticle architecture through the manipulation of the biomaterial.
5. Mother Nature has developed routes for the repair of biomaterials. These processes may be applied for the stabilization of the biomaterial/nanoparticle structures.
6. Crosslinking nanoparticles with enzyme units may generate biocatalytic assemblies of pre-designed functionality.

These different features of the biomaterial crosslinking units provide the flexibility for the generation of nanoparticle structures of tunable physical, chemical and functional properties. For the generation of biomaterial-crosslinked nanoparticles, two kinds of biomaterial-functionalized nanoparticles with complementary units should participate in the assembly process. Biomaterials utilized in the fabrication of such biomaterial-nanoparticle aggregates include biological protein host-guest pairs such as biotin-avidin, hapten-antibody [93] and complementary oligonucleotides [94, 95].

#### 6.4.1

#### **Receptor-Induced Aggregation of Guest-Functionalized Nanoparticles**

Protein-based recognition systems can be used to organize inorganic nanoparticles into network-aggregates, for instance with the interaction between D-biotin and the biotin-binding protein streptavidin (Sav) [93]. The recognition between water-soluble biotin and the homotetrameric protein Sav is characterized by an extraordinary affinity constant of  $K_a > 10^{14} \text{ M}^{-1}$ , which makes it the strongest ligand-receptor binding interaction presently known [96]. Another great advantage of Sav is its extreme chemical and thermal stability. The applicability of the biotin-Sav system for generating supramolecular aggregates is enhanced by the availability of various biotin analogs [97, 98] and recombinant Sav mutants [99, 100]. A wide range of rate and equilibrium constants ( $K_a$  from  $10^0$  to  $10^{15} \text{ M}^{-1}$ ) are available, allowing the construction of carefully designed nanoparticle aggregates. Many biotinylated materials are commercially available or can be prepared under mild conditions. Two routes for nanoparticle aggregation by biotin-Sav interactions are possible: (i) nanoparticles functionalized with biotin groups can be crosslinked with the tetra-valent Sav receptor (Figure 6-7A), and (ii) nanoparticles functionalized with Sav can be crosslinked with a dibiotin derivative

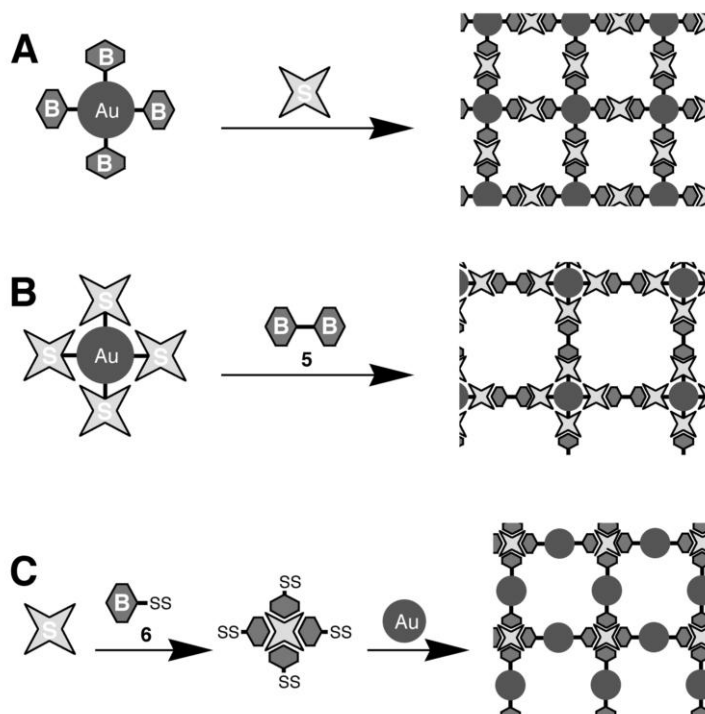


**Fig. 6-7** The use of biotin-streptavidin interactions to build nanoparticle networks, **A** using streptavidin to link biotin-functionalized nanoparticles, and **B** using a biotin dimer to

link streptavidin-functionalized nanoparticles. **C** The use of streptavidin-linked thioated biotin to build nanoparticle networks.

(5) (Figure 6-7B). Several synthetic routes can be applied to functionalize metal and semiconductive nanoparticles with biotin derivatives. In the simplest method, thiol or disulfide biotin derivatives are directly adsorbed on metal (e.g., Au, Ag) nanoparticles. Alternatively, nanoparticles can first be coated with an organic “shell” (e.g., by the polymerization of a trialkoxysilyl derivative or by polymer adsorption) and then covalently modified with biotin (e.g., by carbodiimide coupling).

Au nanoparticles functionalized with adsorbed disulfide-derivatized biotin units (6) and then crosslinked with the added Sav have been shown to yield an aggregate of Au nanoparticles with the biotin-Sav recognition pairs between the nanoparticles (Figure 6-7A) [93, 101, 102]. A similar architecture can be built by reversing the steps: Sav was interacted with the disulfide biotin derivative to produce a complex, which was then reacted with Au nanoparticles (Figure 6-7C) [101]. In both cases, fast, spontaneous aggregation of the Au nanoparticles was observed, resulting in a non-ordered network of particles. Dynamic light scattering, small-angle X-ray scattering and transmission electron microscopy were used to follow the aggregation process and to characterize the product. The kinetics of this process was fitted to the theoretical Smoluchowski model of aggregation, modified for nanoparticles [102]. This kinetic analysis allows control of the aggregate structure by optimiza-

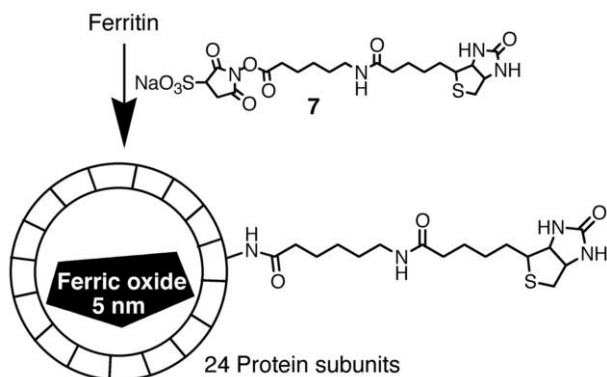
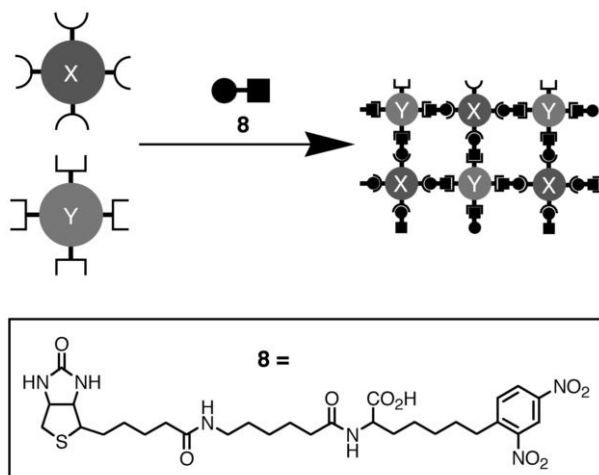


Fig. 6-8 Biotin-functionalized ferritin.

tion of the conditions (molar ratio of the biotin-functionalized nanoparticles and the Sav-crosslinker). Another example of biotin-Sav-crosslinked nanoparticles involves the native protein ferritin, which consists of a hollow polypeptide shell, 8 and 12 nm in internal and external diameters, respectively, and a 5 nm diameter ferric oxide core ( $5\text{Fe}_2\text{O}_3 \cdot 9\text{H}_2\text{O}$ ) [103]. The ferric oxide nanoparticle can easily be removed from the protein shell by reductive dissolution, and the empty cage of apoferritin can be remineralized *in vitro* with a range of inorganic oxides, sulfides or selenides (e.g.,  $\text{MnO}$ ,  $\text{FeS}$ ,  $\text{CdS}$ ,  $\text{CdSe}$ ) [104–107]. A succinimidyl active ester derivative of biotin (7) was covalently linked to the amino groups of 60–70 lysine residues provided by the polypeptide shell of ferritin, yielding a biotin-functionalized protein shell containing the ferric oxide core (Figure 6-8). Addition of Sav resulted in the crosslinking and therefore the aggregation of the functionalized ferric oxide nanoparticles [108]. Considering the library of core nanoparticles possible, this ferritin-based aggregate is a very promising material for producing electronic, magneto-electronic, and optoelectronic devices.

Nanoparticle aggregates have also been produced by means of the interaction between antigens and antibodies [93, 109]. In the simplest approach, anti-DNP IgE (DNP, dinitrophenyl) antibodies were adsorbed on 12 nm Au nanoparticles and were then crosslinked with a synthetic antigen (bis-*N*-2,4-dinitrophenyloctamethylene diamine) comprising two hapten DNP head groups separated by a spacer. A more sophisticated approach allows the association of two different kinds of nanoparticles. For this purpose, two different nanoparticles functionalized with different kinds of bioreceptors (e.g., different antibodies or an antibody and Sav) should be crosslinked with a ligand containing two different head groups providing affinity binding to the two respective receptors. For example, two kinds of Au nanoparticles were functionalized, one with anti-DNP IgE and another with Sav [93, 109]. These were crosslinked with a linker (8) containing a biotin unit and a DNP group separated with a spacer (Figure 6-9). Each ligand recognizes its respective receptor (biotin binds to Sav, DNP binds to anti-DNP IgE), thus creating a network composed of both nanoparticles.



**Fig. 6-9** Formation of a network composed of two kinds of nanoparticles functionalized with different recognition units and crosslinked with a bifunctional linker.

A novel approach to nanoparticle crosslinking involves the application of specially designed *de novo* proteins with specific affinities to inorganic crystal surfaces [69]. These structures can specifically bind directly to unmodified surfaces of various semiconductive nanoparticles, thus resulting in their bridging and aggregation. Based on a combinatorial library of about  $10^9$  random 12-mer peptides, *de novo* proteins with specific binding capabilities to single-crystal semiconductors including GaAs(100), GaAs(111), InP(100), and Si(100) have been discovered [110].

#### 6.4.2

##### Nucleic Acid-Functionalized Nanoparticles for Controlled Aggregation

DNA molecules are very powerful and versatile linkers for the controlled aggregation of nanoparticles [111, 112]. DNA chains are of a controllable length and composition, providing predictable properties and enormous control over complementarity. ds-DNA provides rigid spacers that allow control over the distance between nanoparticles. Long DNA chains can be utilized as templates ready to accommodate complementary-DNA-functionalized nanoparticles in a controlled order and with controlled distances between the nanoparticles.

In order to demonstrate the DNA-mediated binding of nanoparticles, two batches of 13 nm diameter Au nanoparticles were separately functionalized with two thiol-derivatized non-complementary DNA oligonucleotides: 3'-thiol-TACCGTTG-5' (**9**) adsorbed on nanoparticle **A** and 5'-AGTCGTTT-3'-thiol (**10**) adsorbed on nanoparticle **B** (Figure 6-10A, see p. 384) [113]. A DNA linker (**11**) was constructed, composed of ds-DNA in the center and two single-stranded fragments on the ends. These single-stranded sections were complementary to the oligonucleotides connected to the nanoparticles. Addition of the linker to a mixed solution of the two

DNA-functionalized Au nanoparticles results in crosslinking of the nanoparticles. The resulting nanoparticle aggregate should theoretically have some degree of regularity, but this could not be observed, as both nanoparticles had identical cores. Aggregation changes the color of the solution because of a collective phenomenon originating from the short-distance interparticle separation. Separate Au nanoparticles have a red color as a consequence of their plasmon absorbance, but when they are aggregated additional absorbances arise at lower energies because of interparticle plasmon coupling (Figure 6-10B). This color change can be used as a simple test for the recognition between complementary DNA sequences associated with the linker and the Au nanoparticles. The association process is temperature-dependent, and the aggregated Au nanoparticles can dissociate upon elevation of temperature and associate again upon decreasing the temperature, thus resulting in the reversible changes of the spectrum (Figure 6-10C). In a control experiment, a non-complementary linker was added to the mixed particle solution, and no color changes were observed.

In a more sophisticated investigation, a mixture of DNA-functionalized Au nanoparticles of diameters 40 nm (**A**) and 5 nm (**B**) was crosslinked with a DNA linker [114]. The larger nanoparticle (**A**) accommodates many small nanoparticles (**B**) around it, producing a so-called “satellite”  $AB_n$  system (Figure 6-10D). Interconnections between these “satellite” aggregates yield a 3D-network  $(AB_n)_m$ . An important factor controlling the network optical properties is the length of the DNA oligonucleotide: it controls not only the interparticle distances, but also the rate of aggregation and thus the number of nanoparticle per aggregate [115]. In a similar approach, DNA-functionalized CdSe/ZnS nanoparticles and Au nanoparticles were crosslinked with a complementary linker to yield a binary network [59]. Fluorescence and absorption spectroscopy indicated cooperative optical and electronic phenomena within the resulting material. Changes in the optical and electronic properties of nanoparticles upon their aggregation provide a way to detect the association process, thus allowing DNA-biosensor construction [116–119]. The application of DNA-functionalized Au nanorods instead of spherical nanoparticles results in micro-sized rods composed of many crosslinked nano-units (Figure 6-11, see p. 385) [120]. This material offers unusual anisotropic properties.

Long DNA molecules capable of accommodating several complementary DNA fragments in different domains on the strand can serve as templates for the construction of specific linear assemblies [121, 122]. In order to prevent the microscopic crosslinking of nanoparticles resulting in a network, Au nanoparticles functionalized with a single maleimide group (**12**) were reacted with thiol-derivatized DNA oligonucleotides (**13**). The resulting mono-DNA-functionalized Au nanoparticles (**14**) were associated with the respective complementary domains on the DNA template molecule (Figure 6-12). Individual placement of the nanoparticles at specific complementary domains of the template allows control of distances between them, as well as controlled placement of different kinds of nanoparticles (different sizes, different materials) on the template, which results in a variety of properties of the nanoparticles assemblies. For example, two DNA-functionalized Au nanoparticles can be placed on the DNA template with three

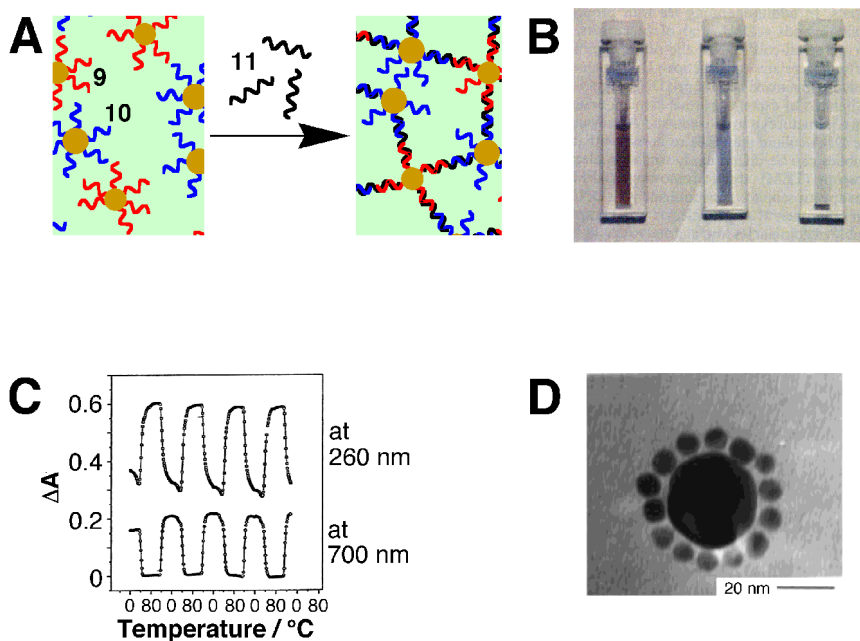


**Fig. 6-10** **A** The aggregation of oligonucleotide-functionalized nanoparticles by the addition of a DNA strand with sections complementary to the DNA on each nanoparticle. **B** Cuvettes with the Au nanoparticles and the added DNA strand responsible for the assembly process. Left cuvette, at 80 °C with DNA-functionalized nanoparticles in the unhybridized state; center, after cooling to room temperature resulting in the nanoparticle association but before the precipitate settles; and right, after the

associated nanoparticles settle to the bottom of the cuvette. **C** Variations in the absorption spectrum of DNA-linked nanoparticle networks as a function of temperature. The changes reflect different degrees of aggregation, which is controlled by DNA association (low temperature) and dissociation (high temperature). **D** A “satellite” system consisting of two different sizes of nanoparticles. (Parts **A–C** are adopted from [113], Figures 1–3; Part **D** is adopted from [114], Figure 2, with permission.)

different orientations: “head-to-head” (15), “head-to-tail” (16), and “tail-to-tail” (17), thus providing different distances between the nanoparticles.

#### 6.4.3

#### Composite Assemblies of Nucleic Acids, Proteins, and Nanoparticles

A combination of the synthetic methods to prepare biomaterial-functionalized nanoparticles (cf. Sections 6.4.1 and 6.4.2) and the application of proteins with affinity properties (e.g., Sav, antibodies), oligonucleotides and nanoparticles as building blocks, allows the construction of very sophisticated biomolecular/nanoparticle clusters (Figure 6-13A) [69]. In order to functionalize Au nanoparticles with antibodies, a multi-step procedure was performed [123]. 5'-Thiol-modified oligonucleotide (18) was covalently bound to Sav using the heterobifunctional crosslinker sulfosuccinimidyl-4-(maleimidomethyl)cyclohexane-1-carboxylate

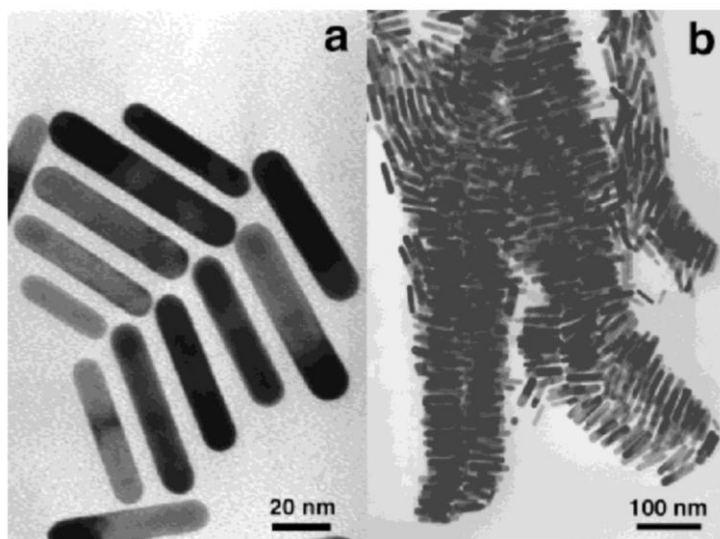


**Fig. 6-11** Transmission electron micrographs of gold nanorods organized by DNA hybridization ((a) and (b) different magnifications). (Reproduced from [120], Figure 1, with permission.)

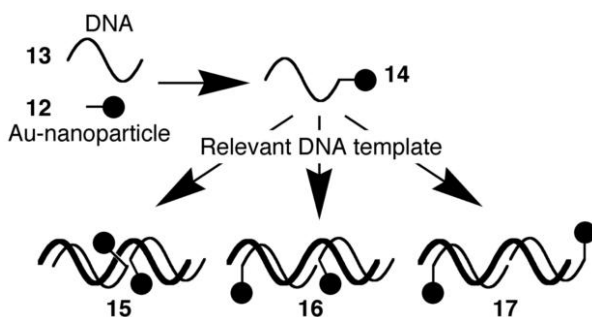


**Fig. 6-12** The assembly of controlled multiparticle composites by the use of DNA hybridization.

(19). The resulting conjugate has four binding sites for biotin ligands and one nucleic acid function. The Sav receptor sites were reacted with biotinylated antibodies (20) directed against mouse IgG ( $\alpha$ M-IgG) or rabbit IgG ( $\alpha$ R-IgG), resulting in DNA-tagged antibody conjugates that can bind to the complementary DNA from one side and to the respective antigens from the other. This architecture was reacted with Au nanoparticles functionalized with oligonucleotides complementary to the DNA tag (21), thus finally resulting in the Au nanoparticles modified with the antibody molecules. The resulting conjugate was then applied as a label for the immunoassay of the respective antigens. The linkage of the Au nanoparticle to the antigen-antibody complex was further amplified by the electroless deposition of Ag on the Au nanoparticles (Figure 6-13B) [123].



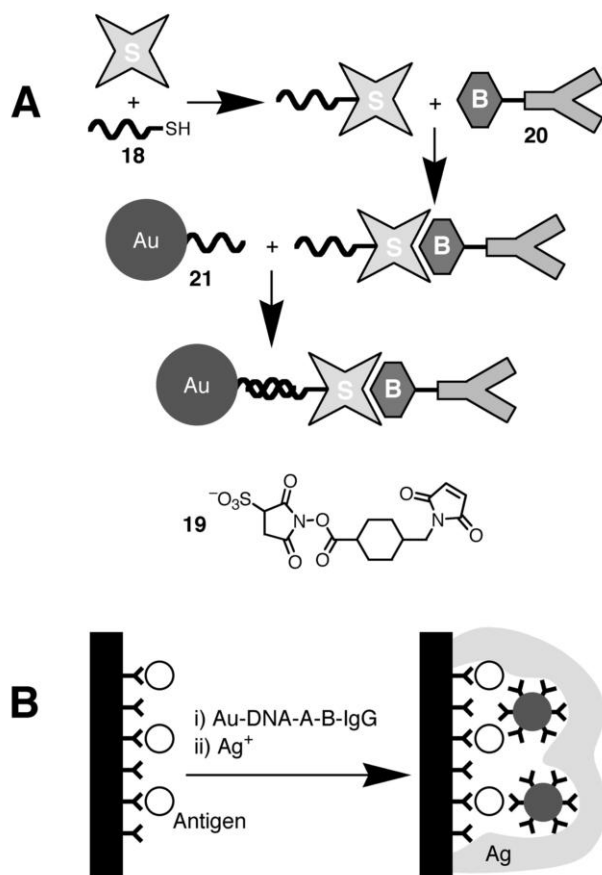


**Fig. 6-13** **A** The formation of an Au nanoparticle-IgG conjugate, and **B** its use in the sensing of antigens.

A combination of receptor proteins and oligonucleotides as binding blocks for the directed aggregation of nanoparticles allows the complex structuring of the assemblies. For example, Sav was interacted with biotinylated DNA, resulting in a four-DNA-Sav conjugate [124]. Application of this conjugate as a building block in the aggregation of DNA-functionalized Au nanoparticles yields a network with a motif different from that resulting from direct aggregation of DNA-functionalized nanoparticles bound by the complementary oligonucleotide. Even more fascinating aggregation was achieved when Au nanoparticles were primarily associated with Sav to yield nanoclusters that were then placed on a DNA template [125] (Figure 6-14). In this work, 1.4 nm Au nanoparticles with a single amino substituent were derivatized with a biotin group, and the biotin moiety was used to organize the nanoclusters into the tetrahedral superstructure defined by the ge-

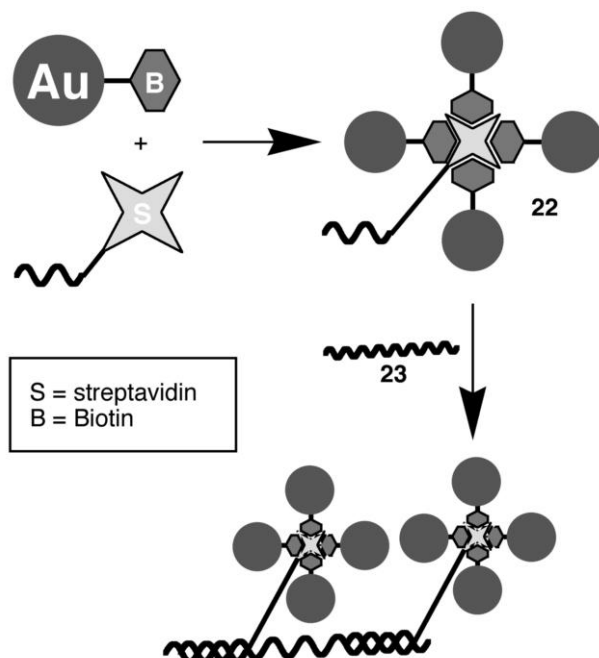


**Fig. 6-14** The construction of four-nanoparticle clusters and their assembly into linear composites along a DNA strand.

ometry of the biotin-binding sites of the Sav. Prior to cluster formation, Sav was derivatized with a single DNA molecule. The resulting tetrahedral four-Au nanoparticle clusters (22), each with a single DNA tail, were assembled on a DNA template molecule (23) with positions and distances dictated by the sequence of the DNA template. This approach could allow the formation of almost any imaginable structure composed of various nanoparticles of different sizes and materials.

An interesting application of submicron metallic “barcodes” for the analysis of biomaterials such as DNA or antigens has recently been reported [126]. “Barcodes” a few hundred nanometers across and several microns long composed of many different metals (Pt, Pd, Ni, Co, Ag, Cu and Au) were prepared by the electrochemical deposition of the metals in a porous  $\text{Al}_2\text{O}_3$  membrane (Figure 6-15A). The structure of the barcode could be identified by optical reflectivity or field emission-SEM. Figure 6-15B shows an optical image of an Au–Ag multistripe-barcode consisting of 240, 170, 110 and 60 nm Ag stripes separated by ca. 550 nm Au stripes. It was suggested that with the available optical resolution, the number of possible readable barcodes consisting of two metals with a coding length of 6.5  $\mu\text{m}$  is 4160, and for three-metal barcodes the  $8.0 \times 10^5$  distinctive striping patterns are possible. The use of a mixture of “barcodes”, each used to identify a specific biomaterial adsorbed on it, could enable the simultaneous analysis of numerous

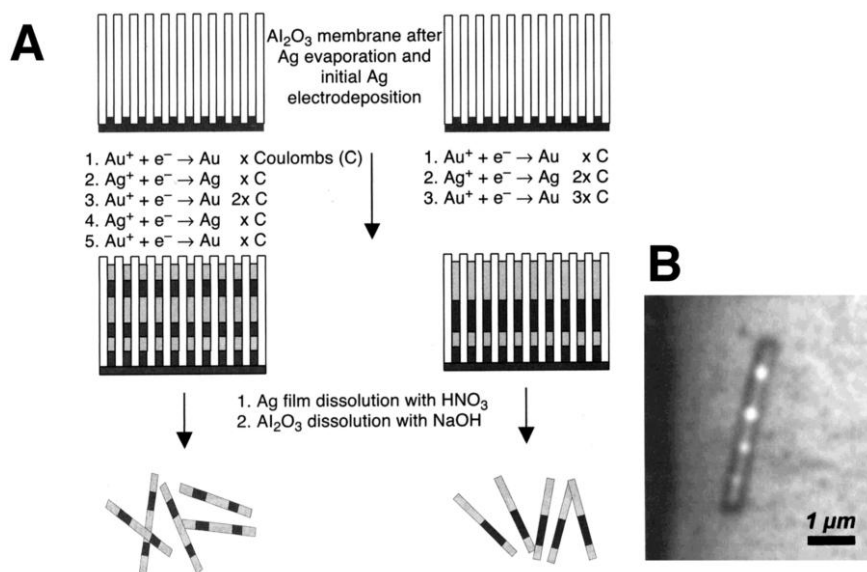


**Fig. 6-15** **A** The construction of mixed metal "barcodes" in an alumina membrane. **B** An optical image of an Au-Ag multistripe "barcode" nanorod. (Adopted from [126], Figures 1 and 3, with permission.)

components in biological mixtures. Thus, the barcode concept adds a nanoparticle-based analysis method that competes with chip-arrays and encoded microbeads. In addition, as the tag identification can be performed optically, fluorescence can be used to characterize a biorecognition event. For example, Figure 6-16A outlines the fluorescence detection of an analyte DNA (24) by a primer nucleic acid (25) linked to the Ag stripes of an Ag-Au-Ag barcode. A fluorophore labeled (TAMARA dye) nucleic acid (26) hybridizes to the free segment of the analyte DNA. Figure 6-16B shows the fluorescence image (i) and reflectivity image (ii) of the fluorescence-labeled DNA complex confined to the Ag-Au-Ag barcode. The former characterizes the binding event, and the latter identifies the "barcode" and thus the attached DNA probe. When the analyte DNA (24) is omitted, a very low fluorescence background is observed (iii), and the particles are visible only in the reflectivity image (iv). The simultaneous analysis of different biological analytes is possible with the immunoassay of human immunoglobulin G (IgG) and rabbit IgG. Two different barcodes, an Au-Ag-Au (length  $4 \mu\text{m}$ ) and an Au-Ni-Au (length  $8 \mu\text{m}$ ) were employed, where the Ag stripe of the Au-Ag-Au barcode was modified with the anti-human-IgG antibody (27), and the Au stripes of the Au-Ni-Au barcode are derivatized with the anti-rabbit-IgG antibody (28) (Figure 6-16C). Challenging of the mixture of barcodes with the mixture of antigens followed by the labeling of the antibodies with fluorescein-labeled anti-human-IgG

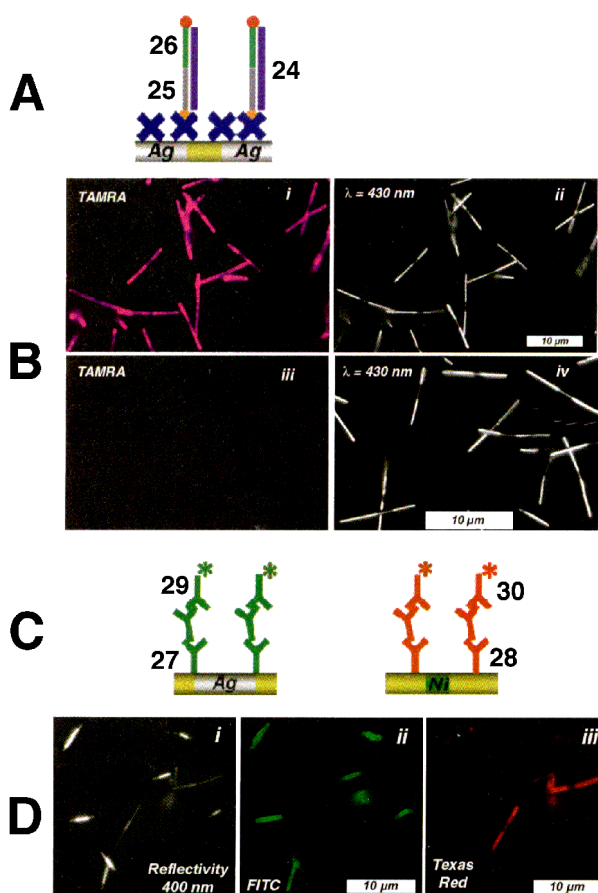


**Fig. 6-16** **A** Method of using the “barcodes” to detect DNA. **B** Fluorescence (i) and reflectivity (ii) images of “barcodes” with bound fluorescent DNA; fluorescence (iii) and reflectivity (iv) images of “barcodes” with omitted analyte DNA. **C** Method of using the “barcodes” for multiple immunoassay. **D**

Reflectivity image (i), fluorescent image produced by fluorescein-labeled anti-human-IgG (ii), and fluorescence image produced by Texas Red-labeled anti-rabbit-IgG (iii). (Adopted from [126], Figure 5, with permission.)

(29) and Texas Red-labeled anti-rabbit-IgG (30) allows the optical detection of the respective barcodes and the fluorescence detection of the two antigens. Figure 6-16D (i) shows the image of the two kinds of barcodes by optical reflectance, while Figure 6-16D (ii) shows the specific fluorescence from the Au–Ag–Au barcodes, whereas Figure 6-16D (iii) shows the specific Texas Red fluorescence from the Au–Ni–Au stripes. Thus, “solution arrays” of highly encodable and chemically diverse nanoparticles provide an interesting approach for the future analysis of complex biological samples (e.g., genomics, proteomics).

## 6.5

### Assembly of Biomaterial-Nanoparticle Architectures on Surfaces

The immobilization of biomaterials on transducers such as electrodes, piezoelectric crystals, and field-effect transistors attracts research efforts directed to the development of biosensors and bioelectronic devices [127–130]. Several methods for the surface functionalization of electronic elements have been developed, and means to couple the active sites or recognition processes of biomaterials with the electronic elements, giving electronic transduction of the biological events, have been demonstrated. Biosensors [131–133], biofuel cell elements [134–139] and optobioelectronic systems [140, 141] have been constructed. Similarly, the deposition of biomaterials on non-conductive surfaces (e.g., plastics, glass), and especially the patterning of such surfaces with biomaterials [130, 142, 143], is of high interest in tailoring protein-chips and DNA-chips for proteomic or genomic analyses. Also, diverse methods for the assembly of 2D and 3D nanoparticle structures on surfaces have been developed. Various applications of these systems in the fabrication of photoelectrochemical cells (e.g., solar cells), light-emitting diodes, electrochromic systems, and computing devices, and also the organization of different nanometric single-electron devices, have been discussed [11]. The integration of nanoparticle-biomaterial hybrid systems with surfaces paves the way for the generation of ordered architectures with new functionalities. The unique photonic properties of nanoparticles may be employed to detect and probe biological recognition events on surfaces. The spectroscopic properties of molecular adsorbates on nanoparticle surfaces such as surface plasmon resonance (SPR), surface-enhanced Raman spectroscopy (SERS), and surface-enhanced fluorescence may be used to probe biomaterial structures on surfaces. Also, the unique electronic (e.g., conductive) and catalytic properties of nanoparticles may be used to provide electron transfer from or to redox-centers of enzymes, or to enhance chemical reactivities of or on the biomaterial structures.

From another direction, biomaterial constituents on surfaces provide unique features for the formation of the hybrid biomaterial-nanoparticle structures. Biomaterials (e.g., nucleic acids, streptavidin-biotin antigen-antibody complexes) assembled on surfaces can provide templates for the immobilization of nanoparticles. Enzymes may be used as catalytic tools for the manipulation of biomaterials on surfaces. For example, the ligation, scission or polymerization of nucleic acids may be used to tailor nucleic acids of specific lengths and compositions. Thus, by the genetic manipulation of biomaterials, the synthesis of nucleic acids, and the biocatalytic manipulation of the biomaterials on surfaces, complex biomaterial-based structures on surfaces may be engineered. The incorporation and integration of nanoparticles in biological templates can then yield new functional materials. For example, the catalytic deposition of metals on nanoparticle seeds can generate circuitry with the shape of the biomaterial. Thus, hybrid biomaterial-nanoparticle composites on surfaces provide functional interfaces that could be important materials for bioelectronic, electronic, optobioelectronic and photonic applications. The following sections address the methods of organizing

these composite systems on surfaces and discuss recent activities that utilize these systems for sensoric, photoelectrochemical and electronic circuitry applications.

### 6.5.1

#### Assembly of Layered Nanoparticle-Protein Assemblies

Multilayer systems assembled on solid supports and composed of cytochrome c (Cyt c) molecules and  $\text{TiO}_2$ -nanoparticles layers have been fabricated using the layer-by-layer deposition of the biological and inorganic components [144]. The  $\text{TiO}_2$ -nanoparticle layers were deposited from aqueous solution by boric acid-promoted hydrolysis of hexafluorotitanate ion (liquid phase deposition process, LPD [145]) (Figure 6-17A). The LPD technique enables the preparation of anatase  $\text{TiO}_2$  without employing organic solvents. This is essential for co-deposition of the biomaterial. The  $\text{TiO}_2$  nanoparticles produced by this technique on the surface are negatively charged. The subsequent deposition of the positively charged protein

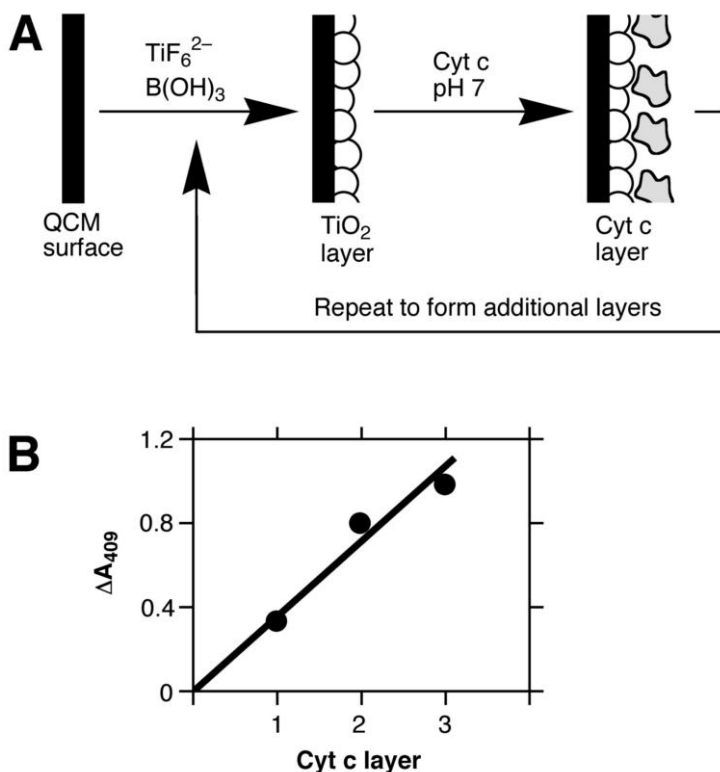


**Fig. 6-17** **A** Method for the construction of  $\text{TiO}_2$ /Cyt c multilayers on a QCM electrode. **B** Optical absorbance at 409 nm of assemblies of different thicknesses, showing the buildup of Cyt c.

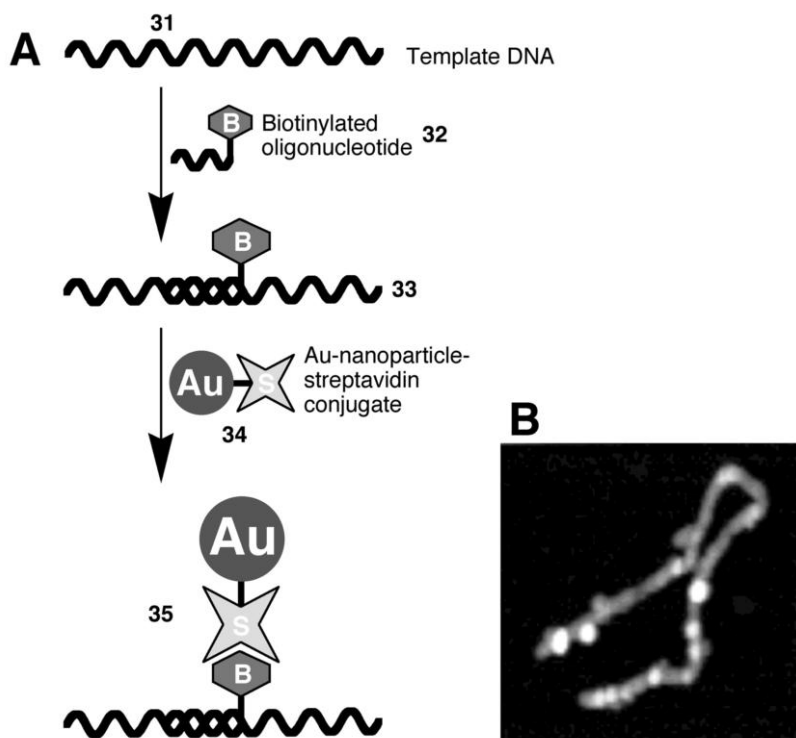
cytochrome c (isoelectric point,  $pI = 10.1$ ) results in electrostatic attraction between the  $TiO_2$  nanoparticles and the protein, allowing multilayer formation. The deposition of the multilayers was followed by quartz crystal microgravimetry (QCM), demonstrating a linear increase in the mass upon deposition of each double layer  $TiO_2$ /Cyt c, which was verified by absorbance spectroscopy (Figure 6-17B). This method could be widely extended to the preparation of other protein/metal oxide multilayers that would facilitate the creation of photo-functional protein/inorganic superlattices.

### 6.5.2

#### Nucleic Acid – Nanoparticle Architectures on Surfaces

As discussed in Chapter 6.4.2, nucleic acids can serve as templates capable of binding DNA-functionalized nanoparticles at complementary segments. When DNA templates are fixed at a surface of a solid support, the resulting assemblies of nanoparticles can yield a pattern dependent either on the shape produced by the DNA template itself or on the pattern produced upon its immobilization.

A natural single-stranded long-chain virus-DNA (M13mp18, 7246 bases) (31) was hybridized with a biotinylated short-chain target oligonucleotide (32) complementary to a specific segment of the viral DNA (Figure 6-18A) [146]. It should be noted that the template viral DNA (31) can have more than one complementary domain, and thus is capable of accommodating more than one biotinylated-DNA chain. The hybridized DNA-holding biotin units (33) were then reacted with Sav-coated Au nanoparticles (34) (5 nm). The resulting negatively charged Au nanoparticle-labeled DNA template (35) was adsorbed on a surface of positively charged  $Mg^{2+}$ -coated mica substrate and was subjected to atomic force microscopy (AFM) (Figure 6-18B). The images obtained clearly show Au nanoparticles associated with the DNA template, yet the number of Au nanoparticles per DNA chain was not perfectly defined, reflecting either incomplete hybridization of the template with the biotinylated target DNA or incomplete association of the Sav-functionalized Au with the biotinylated domains. As different biotinylated nucleic acid segments may be hybridized with the M13mp18 DNA, the entire viral DNA may be decorated with Sav-Au nanoparticles. Indeed, such an experiment revealed that the Au nanoparticle-functionalized viral DNA was formed on the solid support. The electrostatic association of CdS nanoparticles with DNA was applied as the driving force for the formation of the semiconductor nanoparticle-DNA wire on the surface [147]. Negatively charged ds-DNA molecules were located at the water-air interface containing cationic surfactant molecules (Figure 6-19). The layer at the interface was compressed using the Langmuir-Blodgett technique in order to provide a high-density packing of the DNA molecules. Negatively charged CdS nanoparticles (3 nm) capped with thiocholine were then added to the aqueous phase, resulting in their aggregation with the DNA. The obtained DNA/CdS aggregates were transferred to a solid support, and electron microscopy images revealed the formation of densely packed CdS nanoparticles along the DNA template. These generated chains are composed of semiconductive nanoparticles with a diameter of



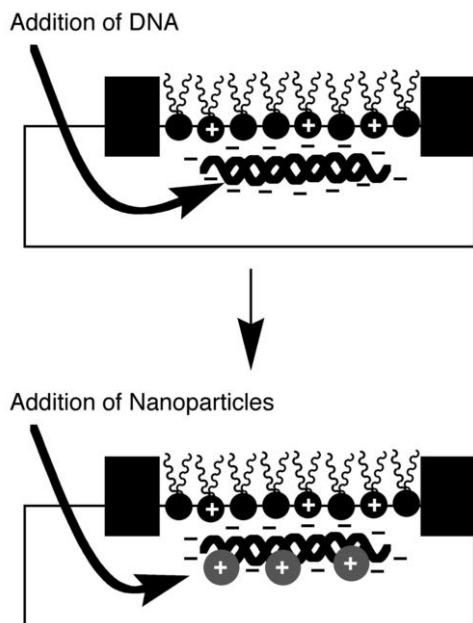
**Fig. 6-18** **A** The controlled association of Sav-coated Au nanoparticles with ss-DNA template by means of a biotinylated ss-DNA molecule hybridized with the template DNA. **B** AFM

image of a DNA strand with Au nanoparticles specifically bound to the template through the biotin-Sav interaction. (Part **B** reproduced from [146], Figure 2(a), with permission.)

ca. 3 nm, the average distance between the centers of the adjacent nanoparticles being ca. 3.5 nm.

The circular plasmid ds-DNA *pUCLeu4* (3455 base pairs) was reacted with  $\text{Cd}^{2+}$  ions, and the resulting  $\text{Cd}^{2+}$ /DNA complex was adsorbed onto a polylysine-coated glass slide by spin coating. The complexed  $\text{Cd}^{2+}$  ions were reacted with  $\text{S}^{2-}$  to yield CdS, and electron microscopy images revealed the formation of CdS nanoparticles that followed the circular shape of the DNA template [148]. In another example, positively charged lysine-capped Au nanoparticles were deposited onto a surface coated with a negatively charged thick DNA film [149, 150]. Electrostatic interaction between the positive charges on the Au nanoparticles and the negative charges on the phosphate groups of the DNA template molecules leads to the assembly of nanoparticles in linear superstructures. The DNA molecules, which are locked into a fairly rigid structure prior to addition of the lysine-capped Au nanoparticles, are rendered mobile by solvation during the addition of the nanoparticle solution to the DNA film surface. This process facilitates reorganization into highly regular linear nanoparticle superstructures during electrostatic complex-





**Fig. 6-19** Method of electrostatically depositing CdS nanoparticles on a DNA chain at the air-water interface using Langmuir-Blodgett technique.

ation. AFM and STM visualization of surface-confined DNA molecules can be greatly improved by the addition of complementary-DNA-functionalized Au nanoparticles that not only introduce clearly visible Au clusters associated with the DNA lying on the surface but can also change the orientation of the long DNA molecules at the surface, producing tethered rather than flat-lying DNA chains [151, 152]. Both these effects can facilitate the visualization of DNA molecules at surfaces.

Negatively charged DNA molecules can complex positively charged metal ions that are later reduced to the metallic state, producing a metal wire across the DNA template. For example, this was accomplished by loading the DNA template with  $\text{Pd}^{2+}$  cations and adding reductive chemicals afterwards, leading to the formation of nanoscale Pd clusters on the DNA [153]. Depending on the duration of the reduction process, well-separated Pd clusters or a quasi-continuous Pd wire with a grain-like structure could be produced.

A system utilizing DNA that crosslinks into a continuous network has been investigated in an attempt to improve structural control over a longer distance (Figure 6-20A) [154]. Three types of oligonucleotides were used, labeled **36**, **37** and **38**. Oligonucleotide **36** had a sequence of 17 bases, and its 3'-end was modified with a thiol group (5'-GTAAAACGACGACGCCAGT-SH-3'). A 57-base oligonucleotide (**37**) included a central sequence complementary to **36** and sides of alternating A and T bases. Oligonucleotide **38** was 50-base poly(dAdT). This oligo-

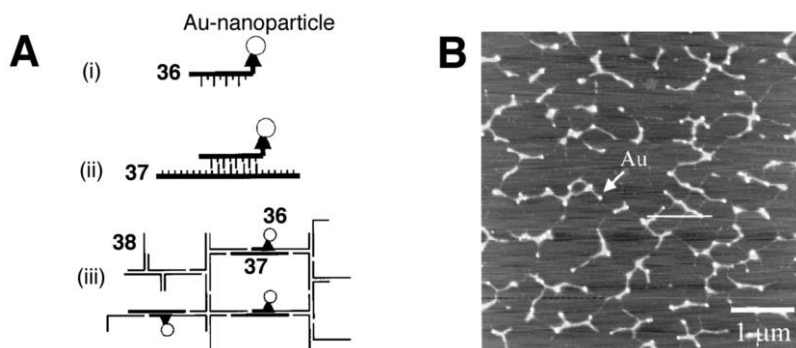


**Fig. 6-20** A Approach for two-dimensional assembly of Au nanoparticles using a DNA-based method: (i) a gold nanoparticle is attached to oligonucleotide **36** through an Au-thiol interaction; (ii) the oligonucleotide **36** is hybridized with oligonucleotide **37**

possessing a complementary base sequence; (iii) the components are built into a DNA network consisting of oligonucleotide **38**. **B** AFM image of the resulting two-dimensional Au nanoparticle-DNA network. (Adopted from [154], Figures 1 and 2(a), with permission.)

nucleotide forms a network structure and is hybridized upon contact with **37**. All three oligonucleotides were mixed with Au nanoparticles (5 nm). The resulting network was adsorbed onto a mica surface, and AFM images were obtained (Figure 6-20B). These images resembled a nanocircuit, but it lacked organization and direct contact between the Au nanoparticles. In order to construct real micro-sized DNA-templated wires, micro-wires prepared by electrochemical metal deposition in a porous alumina membrane were bound to thiolated DNA molecules and reacted with a solid support functionalized with a complementary DNA oligonucleotide [155]. The hybridization process between the surface-confined DNA and the DNA linked to the microwires yielded ds-DNA bridges binding the microwires to the surface. It should be noted that in this work the DNA molecules were used as “molecular glue” to bind micro-sized predesigned wires to the surface instead of individual nanoparticles, thus providing a significant advance in micro-scale circuitry.

Another approach to the directed placement of nanoparticles on solid supports by means of DNA is based on the micropatterning of a surface with DNA molecules. This approach provides the specific binding of complementary-DNA-functionalized nanoparticles at specific domains of the pattern. An amino-derivatized oligonucleotide was deposited onto a chemically modified glass surface in a form of a pattern by a nanoliter dispensing device, and was then covalently bound to the surface [156]. Au nanoparticles (34 nm) functionalized with a complementary oligonucleotide were then reacted with the DNA-patterned surface, yielding an Au nanoparticle pattern that follows the shape of the DNA pattern. Even more precise placement of Au nanoparticles was achieved by the “dip-pen nanolithography” that was applied for patterning the primary DNA on the surface [157]. Two kinds of amino-functionalized DNA oligonucleotides, TCTCAACTCGTAA<sub>10</sub> (**39**) and A<sub>10</sub>CGCATTCAGGAT (**40**), were deposited onto a 1,16-mercaptophex-

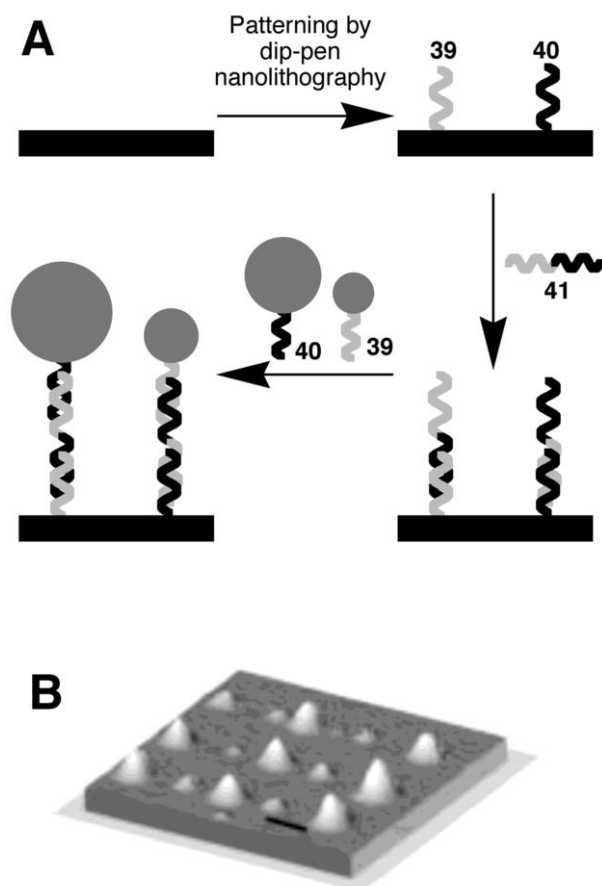


**Fig. 6-21** **A** The use of dip-pen lithography and DNA to produce a predesigned multinanoparticle pattern. **B** Noncontact AFM topography image of such an assembly consisting of large and small nanoparticles, scale bar is 1  $\mu\text{m}$ . (Part B reproduced from [157], Figure 1(C), with permission.)

adecanoic acid-functionalized Au surface, and were then covalently bound to it (Figure 6-21A). The deposition was performed in two sequential steps to yield a pattern composed of spots of both oligonucleotides. This primary pattern was reacted with an oligonucleotide of sequence TACGAGTTGAGAATCCTGAATGCG (41) composed of two domains: one complementary to 39 and the other to 40. The resulting DNA-functionalized surface provided complementary DNA chains for two kinds of DNA-functionalized Au nanoparticles: (39)-Au (13 nm) and 40-Au (31 nm). A pattern was obtained on the DNA-functionalized surface as visualized by AFM: 39-Au nanoparticles specifically bound to the spots of 40/41 and 40-Au nanoparticles bound to the spots of 39/41 periodically located on the solid support (Figure 6-21B).

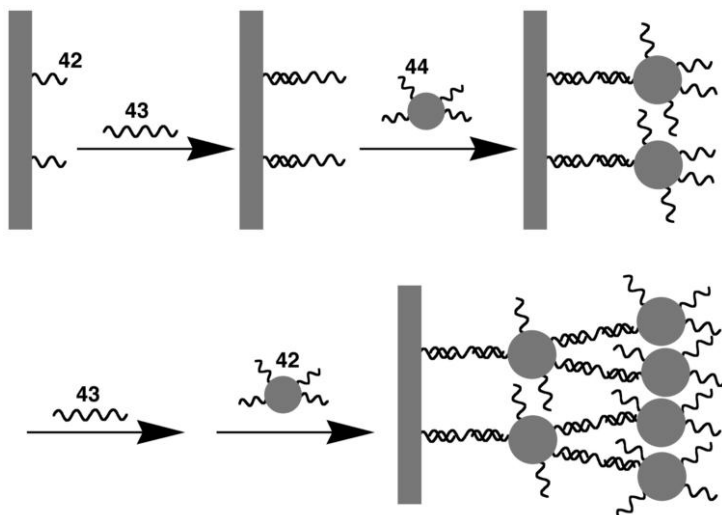


Fig. 6-22 The use of DNA as a linker to construct nanoparticle multilayers on surfaces.

Multilayers of nanoparticles can be assembled on solid supports by utilizing DNA complementarity [158]. For this purpose, a glass surface was functionalized with a monolayer of an oligonucleotide (42), and then the surface was reacted with an oligonucleotide (43) composed of two domains, one of which was complementary to 42 while the other provided complementarity for another oligonucleotide (44). Oligonucleotide 44-functionalized Au nanoparticles (13 nm) were added to yield a monolayer of ds-DNA (ds-43/44) attached to Au nanoparticles (Figure 6-22). Since many of the DNA chains (44) around the Au nanoparticle were not reacted with the surface-confined DNA (43), they could be reacted with further complementary domains of oligonucleotide 43, thus providing binding sites for 42. A second kind of Au nanoparticle modified with oligonucleotide 42 was reacted with this first layer assembly, resulting in a second layer of Au nanoparticles. The repetitive stepwise deposition of Au nanoparticles functionalized with the oligonucleotides 42 and 44 resulted in a multilayer assembly of Au nanoparticles. Each hybridized Au nanoparticle layer imparted a deeper red color onto the substrate. It should be noted that this method could allow layer-by-layer deposition of different (by size or by chemical nature, e.g., Ag, CdS, CdSe) kinds of nanoparticles.

## 6.6

### Functional Biomaterial-Nanoparticle Structures on Surfaces for Sensoric and Electronic Applications

The unique properties of nanoparticles make nanoparticle-biomaterial conjugates attractive labels for sensing applications. The optical and electronic sensing of

biomaterials on surfaces is a common practice in analytical biochemistry. Thus, the immobilization of nanoparticle-biomaterial conjugates on surfaces provides a general route for the development of optical or electronic biosensors. Also, the immobilization of metallic or semiconductor nanoparticle-biomaterial conjugates gives a method for the assembly of electronic circuitry. In such a system, the biomaterial could provide a structural template for the electronic circuitry. The photonic and optical properties of the nanoparticles enables imaging of the structural features of the circuitry, whereas the catalytic functions of the nanoparticles allow their metallic enlargement to become interconnected with long-range conductivity.

#### 6.6.1

##### **Nanoparticle-Biomaterial Conjugates for Optical Sensing and Analysis**

Au nanoparticles linked to bioreceptors provide labeled conjugates that can be used to follow the biorecognition event at a biosensor surface. Various optical methods have been employed to detect the association of Au nanoparticles to biochip domains, including, for example the scanometric detection of light scattering, surface plasmon resonance, resonance-enhanced absorption by nanoparticles, nanoparticle fluorescence, and enhanced Raman scattering. Although not limited to DNA detection, most of these detection schemes were applied for this purpose.

In a typical setup for scanometric detection, a modified glass slide was mounted on a microscope stage and illuminated in the plane of the slide with white light. In this configuration, the slide served as a planar waveguide, preventing any light from reaching the microscope objective by total internal reflection. Wherever nanoparticle probes were attached to the surface, however, evanescently coupled light was scattered out of the slide and was seen as brightly colored spots. This approach was used for the detection of Au nanoparticle-labeled DNA molecules specifically bound to a DNA-functionalized surface [159, 160]. Enlargement of the Au nanoparticles by the reduction of silver salts on them allows a 100-fold amplification of the signal, and thus increases the sensitivity. This method was used to detect single-base mismatched DNA oligonucleotides immobilized at different domains of the glass support. The high sensitivity required was provided by the silver deposition, and selectivity was achieved by examining the “melting” profiles of the spots (the mismatched spot has a lower “melt” temperature due to its lower association constant). Two different DNA sequences could be detected at once when two Au nanoparticles of different sizes were used to label different oligonucleotides [161]. Spots with different colors corresponding to two kinds of Au nanoparticles were detected on the glass support when domains functionalized with different DNA samples were reacted with the corresponding complementary DNA labeled with Au nanoparticles 50 nm and 100 nm in diameter. Ag nanoparticles have similarly been used as antibody labels for the detection of antigens. This setup provided sensitivity high enough to perform immunoassays based on single-target detection [162]. Resonance enhancement of the absorptive properties of metal nanoparticles bound to a surface by biorecognition interactions was also used as an effective means for biosensor devices [163].

Au nanoparticles have been used extensively for the detection of bioaffinity binding by virtue of enhanced surface plasmon resonance (SPR). A dramatic enhancement of SPR biosensing was achieved for immunosensing [164–166] and DNA sensing when Au nanoparticles were used [167]. A sensor interface was modified with antibody units, the surface was reacted with the complementary antigen component, and finally this affinity assembly was reacted with a secondary antibody labeled with an Au nanoparticle. The association of antigen with an antibody-functionalized surface can be detected by SPR. However, the change in the SPR spectrum is larger if the secondary antibody is bound to the surface. It should be noted that the secondary antibody was able to associate with the modified surface only when the antigen was already bound there, providing an amplification route for the primary recognition event. Amplification is dramatically increased when the secondary antibody is labeled with an Au nanoparticle. The binding of the Au nanoparticle to the immunosensing interface led to a large shift in plasmon angle, a broadened plasmon resonance, and an increase in the minimum reflectance, thereby allowing picomolar detection of the antigen. Similarly, an enhancement in sensitivity by ca. 3 orders of magnitude was obtained in DNA analysis when Au nanoparticle-functionalized DNA molecules were used as probes (Figure 6-23) [167]. Surface-enhanced Raman scattering (SERS) of nanoparticle-bound substrates allows the amplification of molecular vibrational spectra up to  $10^5$ -fold [69]. Although the technique has not been widely applied for detecting

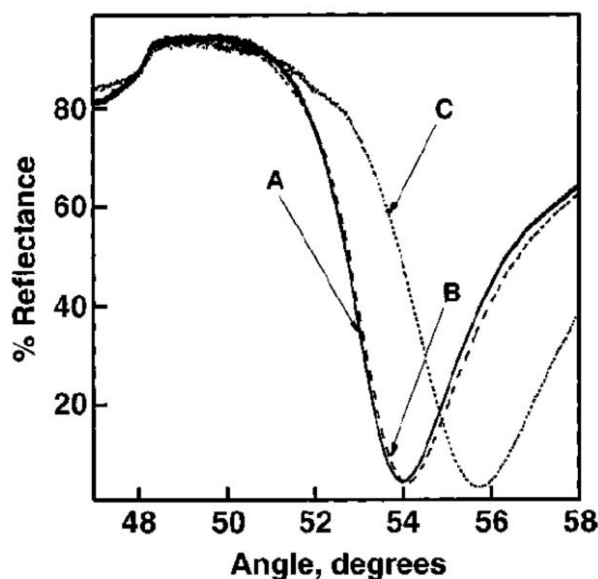


**Fig. 6-23** Surface plasmon resonance (SPR) spectroscopy use for DNA analysis enhanced by Au nanoparticles: **A** SPR spectrum of the DNA-primer-functionalized surface, **B** SPR spectrum after hybridization with the DNA-

analyte molecules, and **C** SPR spectrum after hybridization with the DNA-analyte molecules conjugated with Au nanoparticles. (Adopted from [167], Figure 1, with permission.)

biorecognition events on surfaces, it was demonstrated that a cytochrome c-Au nanoparticle conjugate associated with an Ag surface revealed an SERS spectrum [168, 169]. Semiconductive nanoparticles (e.g., CdS, CdSe) can be used as fluorescent labels for immunosensing and DNA sensing, providing tunable wavelength, narrow emission peaks, and 100-fold higher stability than molecular fluorescent dyes [69].

#### 6.6.2

#### **Electronic Transduction of Biosensing Events by Nanoparticle-Biomaterial-Functionalized Arrays**

Redox-enzymes can be contacted with electrodes by the tethering of redox units to the proteins [170–173] or by the surface reconstitution of apo-proteins on electron-relay cofactor units [174–178]. Recently, the electrical contacting of redox-enzymes was accomplished by the reconstitution of the apo-flavoenzyme apo-glucose oxidase (apo-GOx) with a 1.4 nm Au<sub>55</sub>-nanoparticle functionalized with *N*<sup>6</sup>-(2-aminoethyl)-flavin adenine dinucleotide (FAD cofactor amino-derivative, 45). The conjugate produced was assembled on a thiolated monolayer using various dithiols (46–48) as linkers (Figure 6-24A) [179]. Alternatively, the FAD-functionalized Au nanoparticle could be assembled on a thiolated monolayer associated with an electrode, with apo-GOx subsequently reconstituted on the functional nanoparticles (Figure 6-24B). The enzyme-electrodes prepared by these two routes reveal similar protein surface coverages of ca.  $1 \times 10^{-12}$  mole·cm<sup>-2</sup>. The nanoparticle-reconstituted glucose oxidase layer is electrically contacted with the electrode without any additional mediators, and it stimulates the bioelectrocatalyzed oxidation of glucose (Figure 6-24C). The resulting nanoparticle-reconstituted enzyme electrodes reveal unprecedentedly efficient electrical communication with the electrode (electron transfer turnover rate ca. 5000 s<sup>-1</sup>). This electrical contacting makes the enzyme-electrode insensitive to oxygen or to common oxidizable interferants such as ascorbic acid.

A related electrochemical method was employed for the Au nanoparticle-based quantitative detection of the 406-base human cytomegalovirus DNA sequence (HCMV DNA) [180]. The HCMV DNA was immobilized on a microwell surface and hybridized with an oligonucleotide-modified Au nanoparticle. The resulting surface-immobilized Au nanoparticle double-stranded assembly was treated with HBr/Br<sub>2</sub>, resulting in the oxidative dissolution of the gold particles. The solubilized Au<sup>3+</sup> ions were electrochemically reduced and accumulated, and then determined by anodic stripping voltammetry using a sandwich-type screen-printed microband electrode (SPMBE). The combination of the sensitive detection of Au<sup>3+</sup> ions at the SPMBE by non-linear mass transfer of the ions and the release of a large number of Au<sup>3+</sup> ions upon the dissolution of the particle associated with a single recognition event provides an amplification path that enables the detection of the HCMV DNA at a concentration of  $5 \times 10^{-12}$  M.

The conductivity stimulated by patterned nanoparticle bridges provides an alternative route for designing miniaturized biosensors. This was exemplified by the





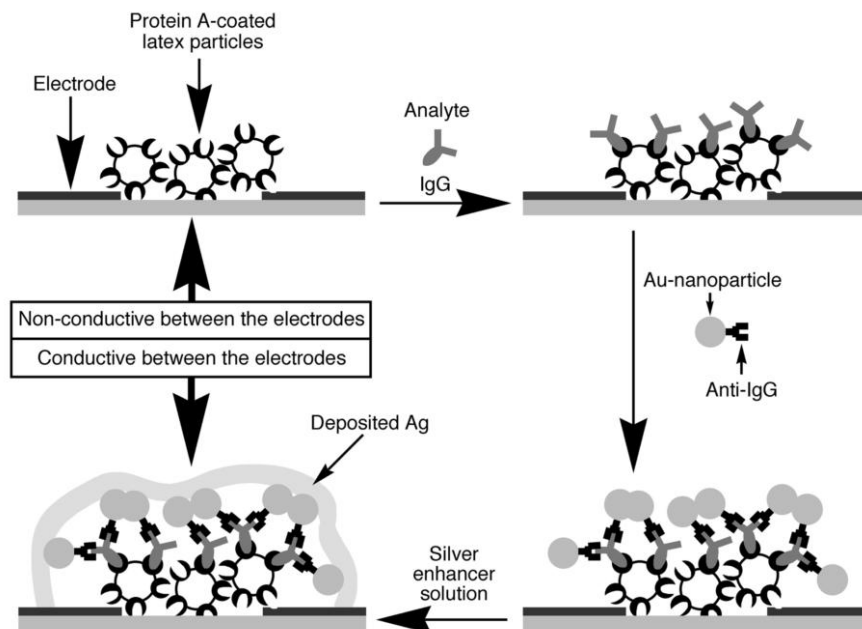


**Fig. 6-25** Immunosensing at micro-sized Au electrodes based on the change of conductivity between the Au strips upon binding of Au nanoparticles followed by silver deposition.

oppositely charged polyelectrolyte results in the aggregation of the latex particles and their fixation in the gap. Adsorption of protein A on the latex surface yields a sensing interface for the human immunoglobulin (IgG) antigen. The association of human immunoglobulin on the surface is probed by the association of the secondary Au-labeled anti-human IgG antibodies to the surface, followed by the catalytic deposition of a silver layer on the Au particles. The silver layer bridges the gap between two microelectrodes, resulting in a conductive “wire”. Typical resistances between the microelectrodes were 50–70  $\Omega$ , whereas control experiments generated resistances  $>10^3 \Omega$ . The method enabled the analysis of human IgG with a detection limit of ca.  $2 \times 10^{-13}$  M.

DNA detection has also been performed using microelectrodes fabricated on a silicon chip (Figure 6-26) [182]. A probe nucleic acid (49) was immobilized on the  $\text{SiO}_2$  interface in the gap separating the microelectrodes. The target 27-mer nucleotide (50) was then hybridized with the probe interface, and subsequently a nucleic acid (51)-functionalized Au nanoparticle was hybridized with the free 3'-end of the target DNA. The Au nanoparticle catalyzed hydroquinone-mediated reduction of  $\text{Ag}^+$  ions, resulting in the deposition of silver on the particles, lowering the resistance between the electrodes. Single-base mutants of the analyte oligonucleotide (50) were washed off from the capture-nucleic acid (49) by the application of a buffer of an appropriate ionic strength, so were not detected. A difference of  $10^6$  in the gap resistance was found between the analyte and the

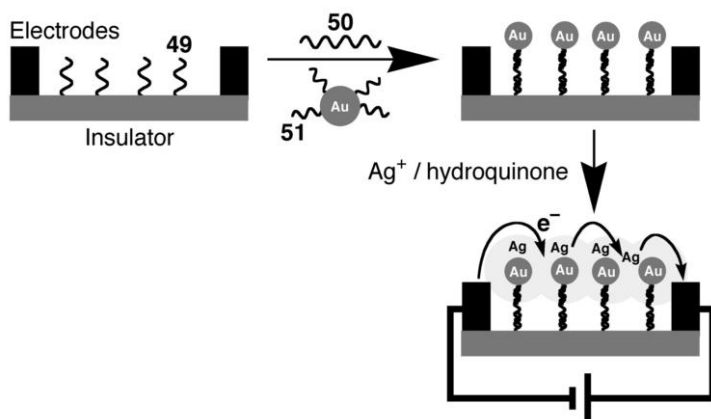


**Fig. 6-26** The use of a DNA-nanoparticle conjugate and subsequent silver deposition to connect two microelectrodes, as a means to sense a DNA analyte.

mutants. The low resistances between the microelectrodes were found to be controlled by the concentration of the target DNA, and the detection limit for analysis is in the region of  $5 \times 10^{-13}$  M. This sensitivity translates to ca.  $1 \mu\text{g} \cdot \mu\text{L}^{-1}$  of human genomic DNA or ca.  $0.3 \text{ ng} \cdot \mu\text{L}^{-1}$  of DNA from a small bacterium. These concentrations suggest that the DNA may be analyzed with no pre-PCR amplification.

Photoelectrochemical transduction of DNA recognition processes has been shown by use of semiconductor (CdS) nanoparticles modified with nucleic acids [183]. Semiconductor CdS nanoparticles ( $2.6 \pm 0.4$  nm) were functionalized with the two thiolated nucleic acids 52 and 53 that are complementary to the 5' and 3' ends of a target DNA (54). An array of CdS nanoparticle layers was constructed on an Au electrode by a layer-by-layer hybridization process (Figure 6-27). Illumination of the array resulted in the generation of a photocurrent. The photocurrent increases with the number of CdS nanoparticle layers, and the photocurrent action spectra follow the absorbance features of the CdS nanoparticles, implying that the photocurrents originate from the photoexcitation of the CdS nanoparticles. That is, photoexcitation of the semiconductor causes the formation of an electron-hole pair. Transfer of conduction band electrons, and the concomitant transfer of electrons from a sacrificial electron donor to the valence band holes, yields a steady-state photocurrent in the system. The ejection of the conduction-band electrons into the electrode occurred from nanoparticles in intimate contact with the electrode support. This is supported by the fact that  $\text{Ru}(\text{NH}_3)_3^{6+}$  units ( $E^0 = -0.16$  V vs SCE) that are electrostatically bound to the DNA enhance the photocurrent from the DNA-CdS array. That is, the  $\text{Ru}(\text{NH}_3)_6^{3+}$  units act as an electron wiring element that facilitates electron hopping to the electrode through the DNA tether from CdS particles that lack contact with the electrode. The system is important not only as it demonstrates the use of photoelectrochemistry as a transduction method for DNA sensing, but also since the system reveals the nano-engineering of organized DNA-

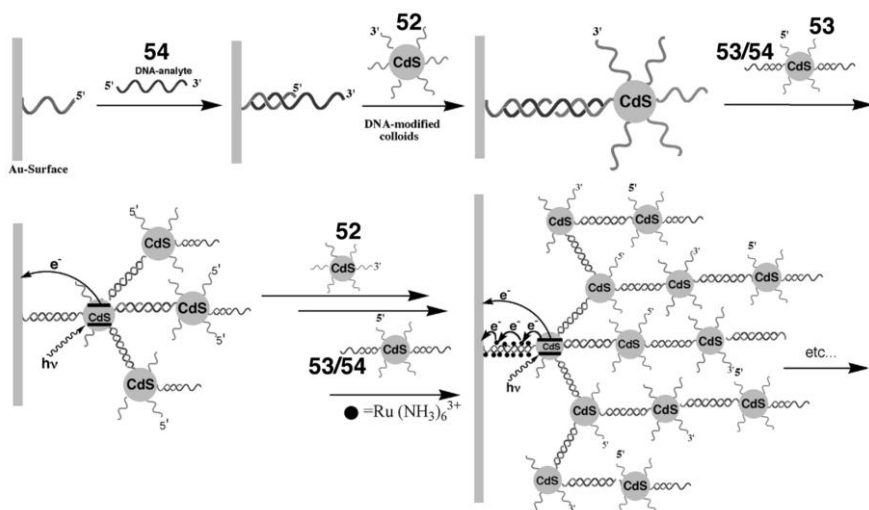


**Fig. 6-27** The construction of CdS-nanoparticle/DNA superstructures and their use for the generation of photocurrents.

tethered semiconductor nanoparticles on conductive supports. These latter nano-engineered structures are the first step toward electronic nano-circuitry (see discussion in Section 6.6.3).

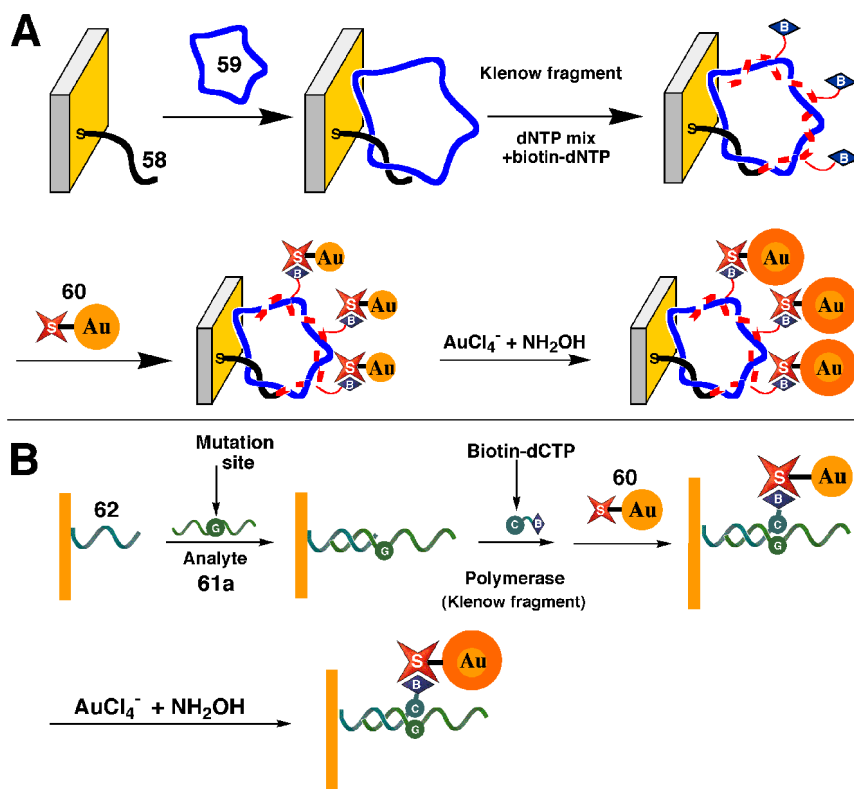
Nanoparticles provide a high-mass method of labeling nucleic acid-DNA, making microgravimetric sensing methods (e.g., QCM) ideal for the detection of recognition events. Furthermore, as nanoparticles act as catalysts for the deposition of metals, even higher mass changes may be stimulated. For a quartz piezoelectric crystal (AT-cut), the crystal resonance frequency changes by  $\Delta f$  when a mass change  $\Delta m$  occurs on the crystal according to Eq. (1) (the Sauerbrey equation), where  $f_0$  is the fundamental frequency of the quartz crystal,  $\Delta m$  is the mass change,  $A$  is the piezoelectrically active area,  $\rho_q$  is the density of quartz ( $2.648 \text{ g}\cdot\text{cm}^{-3}$ ), and  $\mu_q$  is the shear modulus ( $2.947 \times 10^{11} \text{ dyn}\cdot\text{cm}^{-2}$  for AT-cut quartz).

$$\Delta f = -2 \cdot f_0^2 \frac{\Delta m}{A \cdot (\mu_q \cdot \rho_q)^{1/2}} \quad (1)$$

Microgravimetric DNA detection using nucleic acid-functionalized Au nanoparticles as “nano-weights” was accomplished by the hybridization of a target DNA (55) (5'-AGCGTAGGATAGATATACGGTTCGCGC-3') to an Au-quartz crystal modified with a probe oligonucleotide, followed by the hybridization of the interface with an Au nanoparticle functionalized with a nucleic acid (56) (5'-HS-(CH<sub>2</sub>)<sub>6</sub>-GCGGAACCGTATA-3' complementary to the free 3'-segment of the target DNA (55) [184, 185]. Further amplification of the response was reported by the use of a secondary Au nanoparticle that is functionalized with the nucleic acid (57) (5'-TCTATCCTACGCT-(CH<sub>2</sub>)-SH-3') that is complementary to the 5'-segment of the

target DNA (55). Hybridization of the secondary nucleic acid-labeled Au nanoparticle with 55 followed by hybridization to the primary nanoparticle layer, yields a “second generation” of Au nanoparticles reminiscent of the growth of dendrimers [185, 186]. Concentrations as low as  $1 \times 10^{-10}$  M of DNA could be sensed by the amplification of the target DNA by the nucleic acid-functionalized Au nanoparticle labels.

A different approach to the amplified quartz-crystal-microbalance analysis of DNA utilizes the catalytic metal deposition on the nanoparticle labels [187]. Figure 6-28A depicts the amplified detection of the 7229-base M13 $\phi$  DNA using the catalytic deposition of gold on an Au nanoparticle conjugate [188]. The primer (58) is assembled on an Au/quartz crystal. After hybridization with M13 $\phi$  DNA (59), the



(61) 5'-AGCGTAGGATAGATATACGGTTCGCGC-3'

(61a) 5'-AGCGCTCCAGTGATATACGGTTCGCGC-3'

(62) 5'-TCTATCCTACGCT-(CH<sub>2</sub>)-SH-3'

**Fig. 6-28** **A** Amplified detection of the 7229-base M13 $\phi$  DNA using the catalytic deposition of gold on an Au nanoparticle conjugate. **B** Analysis of a single base mismatch in DNA using the catalytic deposition of gold on an Au nanoparticle conjugate.

double-stranded assembly is replicated in the presence of dATP, dGTP, dUTP and biotinylated-dCTP (B-dCT). The resulting biotin-labeled replica is then reacted with a streptavidin-Au nanoparticle conjugate (60), and the resulting Au-labeled replica is subjected to the Au nanoparticle-catalyzed deposition of gold by the  $\text{NH}_2\text{OH}$ -stimulated reduction of  $\text{AuCl}_4^-$ . The replication process represents the primary amplification, since it increases the mass associated with the crystal and simultaneously generates a high number of biotin labels for the association of the streptavidin-Au nanoparticle conjugate. The binding of the nanoparticle conjugate represents the secondary amplification step for the analysis of the M13 $\phi$  DNA. The third step, catalyzed precipitation of the metal, gives the highest amplification. The M13 $\phi$  DNA could be sensed by this method with a lower detection limit of ca.  $1 \times 10^{-15}$  M. This amplification route was also applied for the analysis of a single base mismatch in DNA, exemplified by the analysis of the mutant (61a) that includes the single base substitution of the A-base in the normal gene (61) with a G-base (Figure 6-28B). The analysis of the mutant is performed by the immobilization of probe DNA (62) that is complementary to the normal gene (61) as well as to the mutant (61a) up to one base prior to the mutation site, on the Au-quartz crystal. Hybridization of the normal gene or the mutant with this probe interface, followed by the reaction of the hybridized surfaces with biotinylated dCTP, B-dCTP, in the presence of Klenow fragments, incorporates the biotin-labeled base only into the assembly that includes the mutant. The subsequent association of the streptavidin-Au conjugate (60), followed by the catalyzed deposition of gold on the Au nanoparticles, amplifies the analysis of the single base mismatch in 61a. Figure 6-29, curve (a), shows the microgravimetric detection of the mutant 61a by this method, where the normal gene (61) does not alter the frequency of the crystal

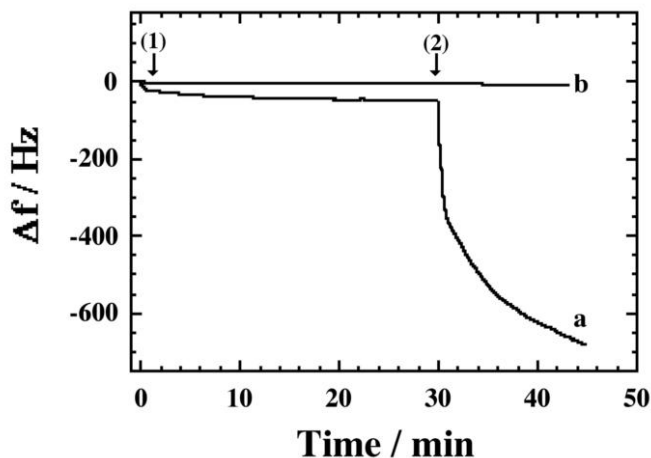


**Fig. 6-29** Microgravimetric detection of a single-base mutant enhanced by the catalytic deposition of gold on an Au nanoparticle conjugate. A frequency change is observed with a mutant (a) and with a normal DNA

sequence (b). Arrow (1) shows the attachment of the Sav-Au conjugate. Arrow (2) shows catalytic deposition of gold on the Au nanoparticles. (Adopted from [188], Scheme 1 and Figure 1(B), with permission.)

(Figure 6-29, curve (b)). Using this method, the mutant could be detected with a detection limit of  $5 \times 10^{-13}$  M.

The immobilization of nanoparticles on surfaces may also be used to yield high surface area electrodes [189]. Enhanced electrochemical detection of nucleic acids was reported by the roughening of flat gold electrodes with an Au nanoparticle monolayer [190]. The roughening of an Au-quartz crystal with a monolayer consisting of Au nanoparticles has also been employed for the enhanced microgravimetric analysis of DNA [191].

### 6.6.3

#### **Biomaterial-Nanoparticle Arrays for Electronic Circuitry**

As discussed above (cf. Chapter 6.5.2), DNA molecules can be loaded with metallic or semiconductive nanoparticles, which form wires or networks upon their deposition onto a solid. In order to use these nanowires for electronic circuitry, they should be electrically connected to the external world, and they need to be conductive. Since nanoparticles are loaded onto the DNA template with gaps between them, the issue of electrical conductivity is important. Electron transport through DNA has been one of the most intensively debated subjects in chemistry over the past ten years [192, 193], and it is still under extensive theoretical and experimental investigation. In order to examine the electrical conductivity of ds-DNA spacers connecting Au nanoparticles, thiol-derivatized oligonucleotides were adsorbed on Au nanoparticles, and then the DNA-functionalized Au nanoparticles were bridged with DNA chains composed of double-stranded helices of various lengths (24, 48 or 72 bases). These helices were terminated on both sides with single-stranded domains complementary to the oligonucleotides bound to the Au nanoparticles [194]. The resulting Au nanoparticle aggregates linked with ds-DNA spacers were deposited on an electrically non-conductive solid support, and their conductivity was measured by the four-probe method. Surprisingly, the conductivities of the aggregates formed from all three linkers ranged from  $10^{-5}$  to  $10^{-4}$  S cm<sup>-1</sup> at room temperature, and they showed similar temperature-dependent behavior. The similarity of the electrical properties of the aggregates originates from the fact that the DNA spacers are compressed, thus providing small and similar distances between the Au nanoparticles. Accordingly, the measured conductivity parameters reflect the electrical properties of the metallic nanoparticles separated by short gaps. The conductivity of metallic nanoparticle aggregates can be enhanced upon the chemical deposition of another metal (e.g., Ag deposition on Au aggregates). DNA-functionalized Au nanoparticles were placed between microelectrodes by hybridization with complementary DNA molecules immobilized in the non-conductive gap between two electrodes [195]. Then the nanoparticles were subjected to the reductive deposition of Ag to enlarge the metallic species and bridge the gaps between them with deposited Ag. The subsequent value of conductivity was found to be dependent on the original loading of the gap with Au nanoparticles, thus allowing the quantitative measurements of the DNA-functionalized Au nanoparticles bound to the surface.

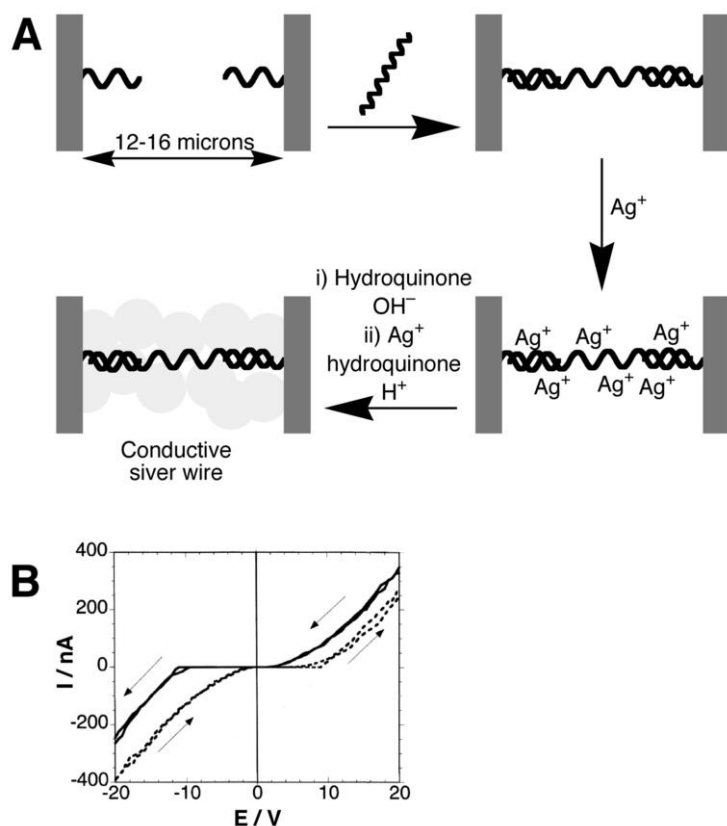


**Fig. 6-30** **A** The construction of a wire bridging two microelectrodes by the deposition of nanoparticles on a bridging DNA strand, followed by silver deposition. **B** I–V curves obtained from the structures produced. (Part B adopted from [196], Figure 6-4(a), with permission.)

A single nanowire produced on a DNA template bridging two micro-size electrodes was constructed [196, 197]. Two micro-electrodes facing each other (12–16  $\mu\text{m}$  separation) were functionalized with 12-base oligonucleotides that were then bridged with a 16  $\mu\text{m}$  long  $\lambda$ -DNA (Figure 6-30A). The resulting phosphate units of the DNA bridge were loaded with  $\text{Ag}^+$  ions by ion-exchange, which were then reduced to Ag metal by hydroquinone. The small Ag aggregates produced along the DNA backbone were then used as catalysts for further reductive deposition of silver, eventually leading to the formation of an Ag nanowire. This micrometer-sized element had a typical width of 100 nm and a granular morphology (as determined by AFM). Electrical measurements revealed non-linear I–V curves (Figure 6-30B). A similar approach was used to generate highly conductive nanowires bridging macroscopic Au electrodes [198]. The DNA molecules were positioned between macroscopic Au electrodes and loaded with  $\text{Pd}^{2+}$  ions. The ions were then chemi-

cally reduced to continuous metallic wires, providing specific conductivity only one order of magnitude below than of bulk palladium.

## 6.7

### Biomaterial-Functionalized Magnetic Particles

Magnetic particles (microspheres, nanospheres, and ferrofluids) are widely studied and applied in various fields of biology and medicine such as magnetic targeting (drugs, genes, radiopharmaceuticals), magnetic resonance imaging, diagnostics, immunoassays, RNA and DNA purification, and cell separation and purification [199]. These magnetic particles are generally of the “core-shell” type: biological species (cells, nucleic acids, proteins) are connected to the magnetic “core” through organic linkers, often organized as a polymeric “shell” around the core. The magnetic core is usually composed of  $\text{Fe}_3\text{O}_4$ , and its primary modification with an organic “shell” can include the adsorption of an organic polymer or the covalent attachment of organosilane molecules. Organic functional groups introduced by these techniques allow the coupling of biomolecules to the organic “shell”. Several synthetic approaches have been applied to couple artificial magnetic particles to biomolecules, which were then used for various bioanalytical applications. For example, antibody molecules were adsorbed on synthetic  $\text{Fe}_3\text{O}_4$  magnetic particles and were then used for specific binding to cells and the separation of the cells in an external magnetic field [200, 201]. DNA molecules were reacted with a mixture of  $\text{Fe}^{2+}$  and  $\text{Fe}^{3+}$  ions that were electrostatically associated with DNA chains [202]. These iron ions were then chemically reacted to give  $\text{Fe}_3\text{O}_4$  magnetic particles associated with the DNA molecules. The labeled DNA could hybridize with complementary oligonucleotides, and the magnetic particles linked to the DNA molecules allowed the separation of the labeled from the non-labeled DNA strands.

The natural protein ferritin can be used to generate precisely sized and shaped magnetic particles in a protein cavity [203]. For this purpose, the non-magnetic natural core composed of  $5 \text{ Fe}_2\text{O}_3 \cdot 9 \text{ H}_2\text{O}$  was chemically removed from the protein cavity, and an artificial magnetic core composed of magnetite ( $\text{Fe}_3\text{O}_4$ ) [104] or magnetite/maghemite ( $\text{Fe}_3\text{O}_4/\gamma\text{-Fe}_2\text{O}_3$ ) [204] was generated inside it. The natural protein shell remains, providing binding groups for the covalent attachment of biomolecules. Some bacteria (e.g., *Magnetospirillum magnetotacticum* MS-1 [205], *Magnetospirillum* sp. MGT-1 [206], *Magnetospirillum* sp. AMB-1 [207], and *Magnetospirillum gryphiswaldense* [208]) produce natural magnetic particles ( $\text{Fe}_3\text{O}_4$ , 50–100  $\mu\text{m}$  in size) aligned in chains and enveloped by a lipid membrane [209, 210]. These naturally produced lipid-covered magnetic particles can be isolated from the parent bacteria [211] and modified with biomolecules using bifunctional coupling reagents (e.g., glutaric dialdehyde). They have been applied for fluoroimmunoassay [212–214], chemiluminescence immunoassay [215], mRNA recovery [216], and as DNA carriers [216, 217]. Most of these techniques are based on the magnetic separation of the magnetic nanoparticle-linked biomolecules from the non-labeled biomolecules.



The immobilization of enzymes on magnetic particles yields biocatalytically active particles. In one example, alcohol dehydrogenase was covalently bound to  $\text{Fe}_3\text{O}_4$  magnetic particles, and the immobilized enzyme continued to demonstrate high biocatalytic activity [218, 219].

Most of the applications of biomaterial-magnetic particle hybrid conjugates involve the concentration, separation, regeneration, mechanical translocation, and targeting of biomaterials. As these subjects do not deal directly with nanoparticle-biomaterial conjugates, we will not cover them here. Some recent research, however, has been directed to the coupling of functional magnetic particles with biomaterial to yield magnetically-controlled functions. Magnetic particles were modified with redox-relay groups such as ferrocene or bipyridinium units and applied for the magneto-switched activation or deactivation of the bioelectrocatalytic functions of redox-enzymes (Figure 6-31A) [220]. Ferrocene (**63**)-functionalized magnetite particles were used for the magnetic switching of the bioelectrocatalyzed oxidation of glucose in the presence of glucose oxidase (GOx) (Figure 6-31B). Magnetic attraction of the particles to the electrode enabled the oxidation of the ferrocene-linked redox units that mediated the GOx-biocatalyzed oxidation of glucose. Positioning of an external magnet above the electrochemical cells lifts the magnetic particles from the electrode, and the bioelectrocatalyzed oxidation of glucose is switched off. Figure 6-31C shows the magneto-switched bioelectrocatalyzed oxidation of glucose by positioning the external magnet below and above the electrode. Similar magnetic switching of the bioelectrocatalyzed reduction of nitrate in the presence of nitrate reductase (NR) was accomplished by the application of  $N,N'$ -bipyridinium (**64**)-functionalized magnetic particles. Similarly, magnetic nanoparticles linked to nicotinamide adenine dinucleotide through PQQ were used for the magnetic switching of the bioelectrocatalyzed oxidation of lactate to pyruvate using lactate dehydrogenase (LDH) [221]. These particles were employed for the dual selective sensing of lactate and glucose in the presence of LDH and GOx [222] (Figure 6-32). An Au electrode was functionalized with a ferrocene-labeled monolayer, and PQQ- $\text{NAD}^+$ -modified particles were suspended in electrolyte solution. Removal of the magnetic particles from the electrode by means of the external magnet enables the electrochemical detection of glucose at potentials more positive than 0.32 V (vs SCE) by the ferrocene-mediated bioelectrocatalyzed oxidation of glucose in the presence of GOx (Figure 6-33A). Attraction of the functional magnetite particles to the electrodes by the external magnet enables the amperometric analysis of lactate in the potential range  $-0.13 \text{ V} < E < 0.32 \text{ V}$  (Figure 6-33B).

A novel approach to DNA analysis [223] (Figure 6-34) involved the use of magnetic particles modified by a nucleic acid (**65**) that hybridizes with a biotinylated target DNA (**66**). The resulting hybridized complex was then reacted with a streptavidin-Au nanoparticle conjugate (**67**). A silver shell was catalytically generated on the Au nanoparticles linked to the DNA molecules, and then the magnetically labeled assembly was moved to an electrode by means of an external magnet, where electrochemical stripping of the Ag layer provided an amperometric signal for the quantitative determination of the analyte DNA.

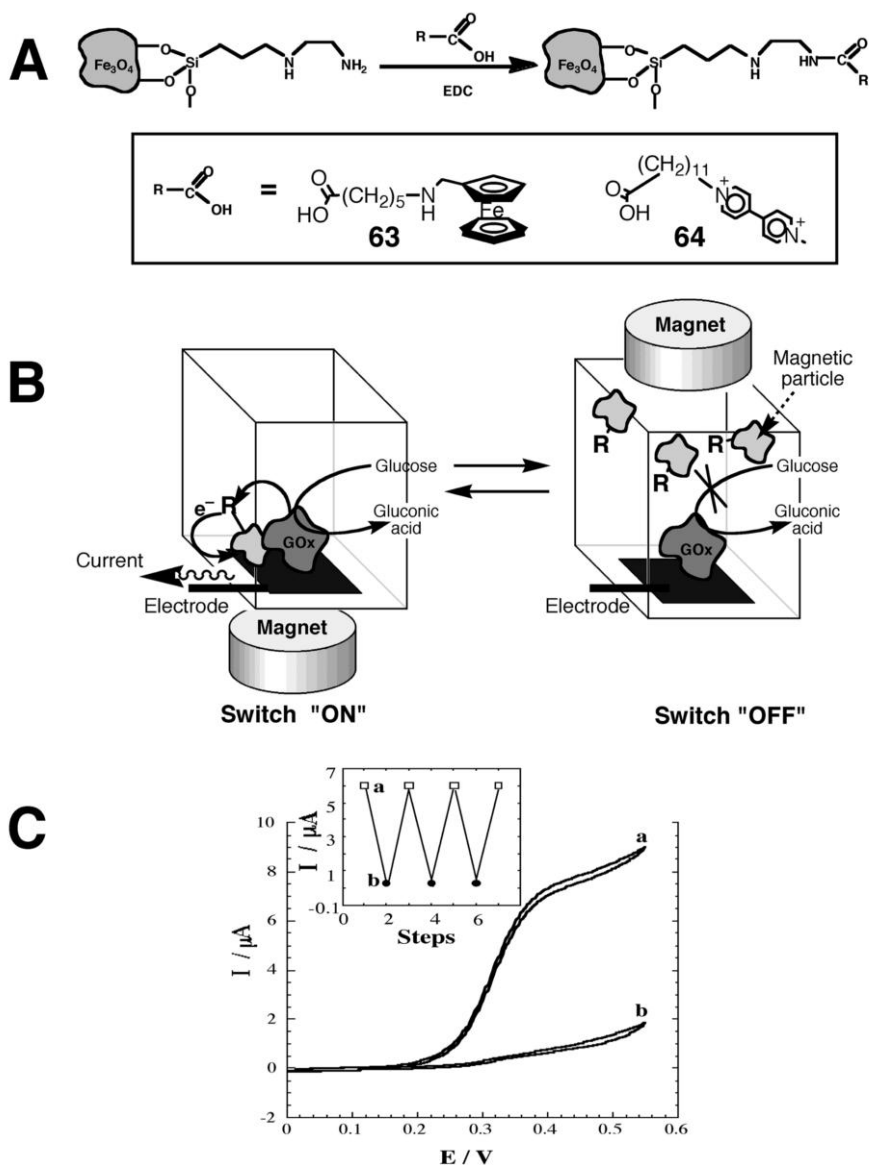


**Fig. 6-31** **A** Synthesis of redox-relay functionalized magnetic particles. **B** Magneto-switched bioelectrocatalyzed oxidation of glucose in the presence of glucose oxidase and ferrocene-functionalized magnetic particles. **C** Cyclic voltammograms corresponding to the magneto-switched bioelectrocatalyzed oxidation of glucose: (a) Ferrocene-functionalized magnetic particles are attracted to the electrode by means of an external magnet.

(b) Ferrocene-functionalized magnetic particles are retracted from the electrode by means of an external magnet. Inset: Cyclic switching "ON" and "OFF" the bioelectrocatalyzed oxidation of glucose by the reversible attraction and retraction of the functionalized-magnetic particles to and from the electrode, respectively. (Adopted from [220], Schemes 1 and 2, Figure 1(B), with permission.)

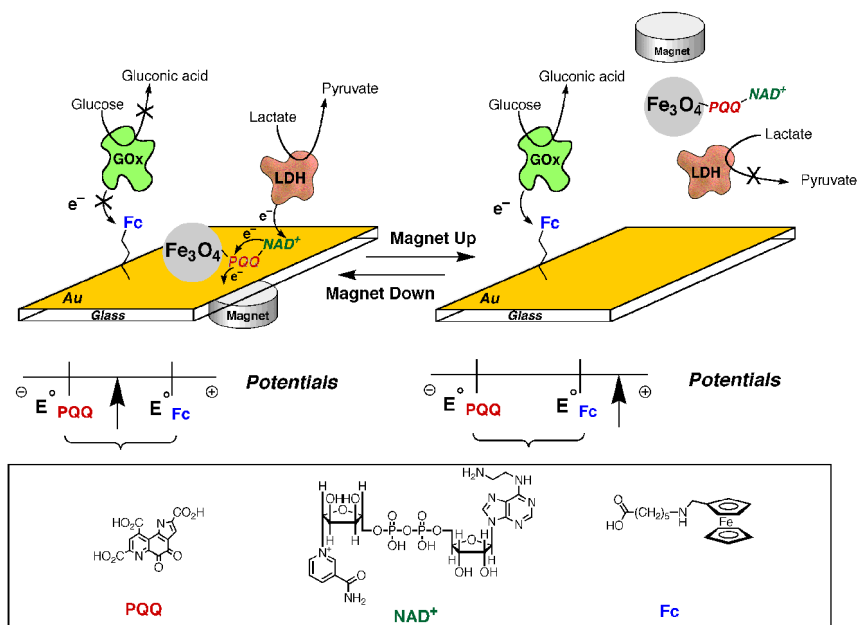


**Fig. 6-32** Magneto-switched dual biosensing of glucose and lactate. (Adopted from [222], Figure 1, with permission.)

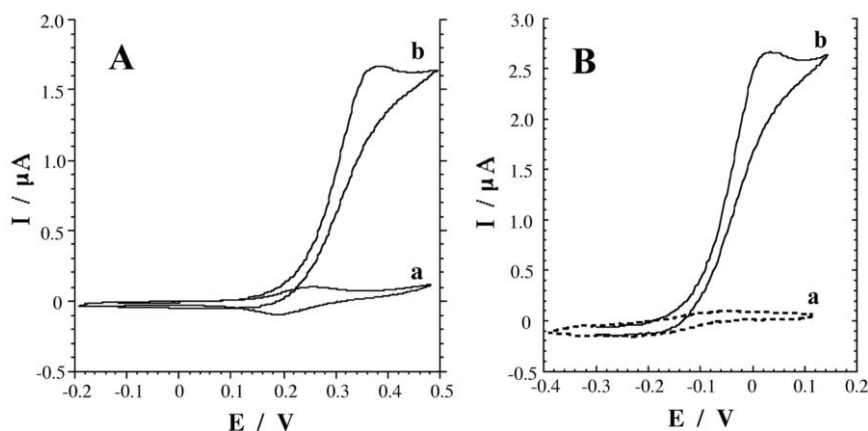


**Fig. 6-33** **A** Cyclic voltammograms of the ferrocene-monolayer-functionalized Au electrode when the  $\text{NAD}^+$ /PQQ-functionalized magnetic particles are retracted from the electrode by the external magnet: (a) in the presence of GOx, 1  $\text{mg mL}^{-1}$ ; LDH, 2  $\text{mg mL}^{-1}$ ; (b) in the presence of GOx, 1  $\text{mg mL}^{-1}$ ; LDH, 2  $\text{mg mL}^{-1}$ ; glucose, 50 mM; lactate, 20 mM. **B** Cyclic voltammograms of the ferrocene-

monolayer-functionalized Au electrode in the presence of  $\text{NAD}^+$ /PQQ-functionalized magnetic particles attracted to the electrode by the magnet: (a) in the presence of GOx, 1  $\text{mg mL}^{-1}$ ; LDH, 2  $\text{mg mL}^{-1}$ ; (b) in the presence of GOx, 1  $\text{mg mL}^{-1}$ ; LDH, 2  $\text{mg mL}^{-1}$ ; glucose, 50 mM; lactate, 20 mM. (Adopted from ref. 222, Figure 6-3, with the permission.)

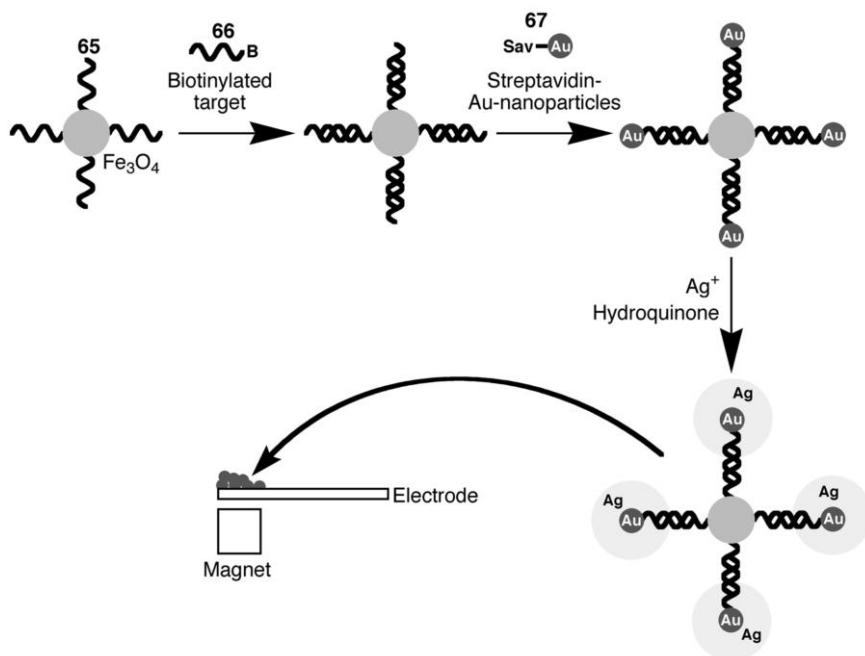


**Fig. 6-34** Assembly of DNA molecules at magnetic particles followed by their association with Au nanoparticles and further silver deposition, and the DNA analysis by electrochemical Ag stripping.

The mechanical rotation of magnetic particles using an external rotating magnet has also been used as an amplification method for electrochemical sensing [224]. In these systems, chemical transformations are controlled by convection of the solution and its constituents rather than by diffusion. As a result, mass transport to the magnetic particles is controlled by the rotational speed of the particles around the electrode axis. Pyrroloquinoline quinone (68)-functionalized magnetic particles were employed for the electrocatalyzed oxidation of NADH under rotation (Figure 6-35A). The electrocatalytic anodic currents are controlled by the circular rotation speed of the particles (Figure 6-35B). Similarly, the ferrocene (69)-functionalized particles were used to control the bioelectrocatalyzed oxidation of glucose in the presence of GOx by means of the circular rotation of the particles produced by the external magnetic rotor (Figure 6-36A). The bioelectrocatalytic current provided by the soluble GOx and ferrocene mediator linked to the rotating magnetic particles were dependent on the particle rotation speed (Figure 6-36B). The calibration plots derived from the cyclic voltammograms show a dramatic influence of the particle rotation speed on the sensitivity of the bioelectrocatalytic system to glucose (Figure 6-36C). This method represents a novel route to the

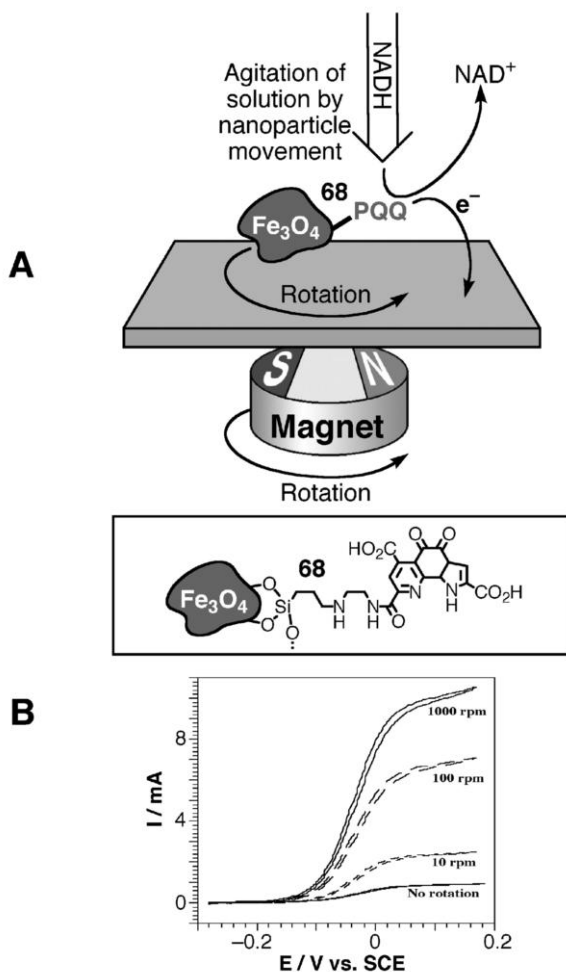


**Fig. 6-35** **A** Electrocatalytic oxidation of NADH enhanced by circular rotation of the PQQ-functionalized magnetic particles induced by the rotation of an external magnet. **B** Cyclic voltammograms corresponding to the electrocatalytic oxidation of NADH upon different rotation speeds of the PQQ-functionalized magnetic particles.

amplification of bioelectronic detection schemes or the enhancement of biological recognition processes. The labeling of biological components by magnetic particles (e.g., antibodies or nucleic acids), and their external rotation by means of the magnetic rotor, may enhance the formation of antigen-antibody complexes or hybridization, respectively, by the agitation of the solution. Similarly, biorecognition events transduced by means of bioelectrocatalytic labels may be amplified by coupling the bioelectrocatalytic label to magnetic labels and rotating the conjugated biorecognition complexes with an external magnetic rotor.

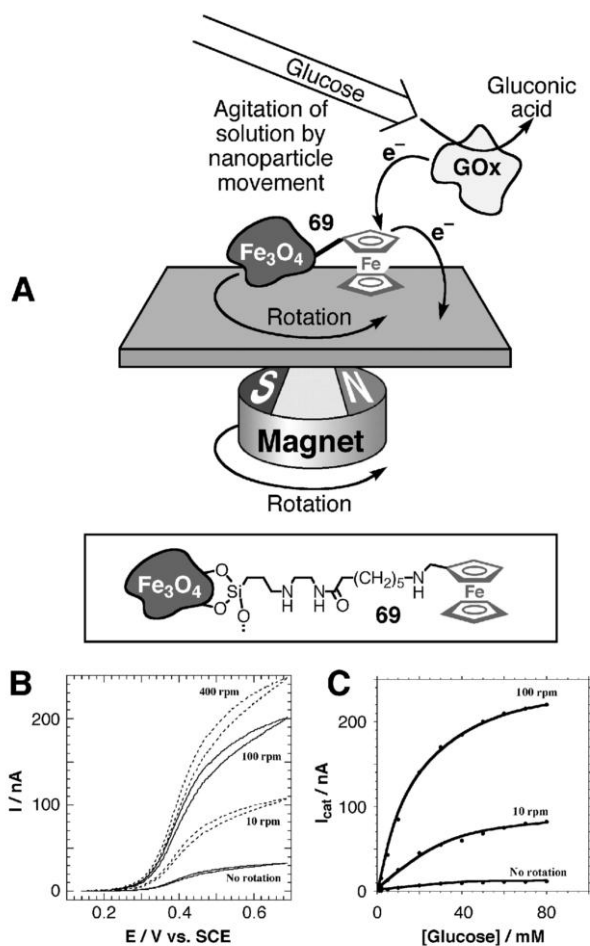


**Fig. 6-36** **A** Electrocatalytic oxidation of glucose in the presence of glucose oxidase enhanced by circular rotation of the ferrocene-functionalized magnetic particles induced by the rotation of an external magnet. **B** Cyclic

voltammograms corresponding to the electrocatalytic oxidation of glucose upon different rotation speeds of the ferrocene-functionalized magnetic particles. **C** Calibration plots obtained with different rotation speeds.

### Acknowledgment

Our research on biomaterial-nanoparticle hybrid systems is supported by the German-Israeli Foundation (GIF).

### References

- 1 R. FEYNMAN, "There is Plenty of Room at the Bottom", in: *The Pleasure of*

*Finding Things Out*, J. ROBBINS (Ed.), Perseus Books, 1999.

- 2 D. QIN, Y. N. XIA, J. A. ROGERS, R. J. JACKMAN, X. M. ZHAO, G. M. WHITESIDES, *Top. Curr. Chem.* **1998**, *194*, 1–20.
- 3 D. M. TENNANT, K. FEDER, K. F. DREYER, R. P. GNALL, T. L. KOCH, U. KOREN, B. I. MILLER, M. G. YOUNG, *Microelectron. Eng.* **1995**, *27*, 427–437.
- 4 *Metal Nanoparticles. Synthesis, Characterization and Application*. D. L. FELDHEIM, C. A. FOSS, JR. (Eds.), Marcel Dekker, New York, **2002**.
- 5 F. C. MELDRUM, J. FLATH, W. KNOLL, *Langmuir* **1997**, *13*, 2033–2049.
- 6 L. SPANHEL, H. WELLER, A. FOJTIK, A. HENGLEIN, *Ber. Bunsen-Ges. Phys. Chem.* **1987**, *91*, 88–94.
- 7 E. STATHATOS, P. LIANOS, F. DEL MONTE, D. LEVY, D. TSIUVAS, *Langmuir* **1997**, *13*, 4295–4300.
- 8 R. RIZZA, D. FITZMAURICE, S. HEARNE, G. HUGHES, G. SPOTO, E. CILIBERTO, H. KERP, R. SCHROPP, *Chem. Mater.* **1997**, *9*, 2969–2982.
- 9 D. L. KLEIN, R. ROTH, A. K. L. KIM, A. P. ALIVISATOS, P. L. McEUEEN, *Nature* **1997**, *389*, 699–701.
- 10 D. L. FELDHEIM, C. D. KEATING, *Chem. Soc. Rev.* **1998**, *27*, 1–12.
- 11 A. N. SHIPWAY, E. KATZ, I. WILLNER, *Chem. Phys. Chem.* **2000**, *1*, 18–52.
- 12 A. BADIA, S. SINGH, L. DEMERS, L. CUCCIA, G. R. BROWN, R. B. LENNOX, *Chem. Eur. J.* **1996**, *2*, 359–363.
- 13 H. YAO, O. MOMOZAWA, T. HAMATANI, K. KIMURA, *Chem. Mater.* **2001**, *13*, 4692–4697.
- 14 A. MIYAZAKI, Y. NAKANO, *Langmuir* **2000**, *16*, 7109–7111.
- 15 M. VALINA-SABA, G. BAUER, N. STICH, F. PITTNER, T. SCHALKHAMMER, *Mater. Sci. Eng.* **1999**, *8–9*, 205–209.
- 16 M. LAHAV, A. N. SHIPWAY, I. WILLNER, *J. Chem. Soc. Perkin Trans. 2* **1999**, 1925–1931.
- 17 W. CHEN, D. GROUQUIST, J. ROARK, *J. Nanosci. Nanotechnol.* **2002**, *2*, 47–53.
- 18 A. N. SHIPWAY, I. WILLNER, *Chem. Comm.* **2001**, 2035–2045.
- 19 T. W. KIM, D. C. CHOO, J. H. SHIM, S. O. KANG, *Appl. Phys. Lett.* **2002**, *80*, 2168–2170.
- 20 J. LIU, M. GOMEZ-KAIFER, A. E. KAIFER, In: *Structure and Bonding*, J.-P. SAUVAGE (Ed.), New York, Springer, **2001**, *99*, 141–162.
- 21 D. L. FELDHEIM, K. C. GRABAR, M. J. NATAN, T. E. MALLOUK, *J. Am. Chem. Soc.* **1996**, *118*, 7640–7641.
- 22 T. TRINDADE, P. O'BRIEN, N. L. PICKETT, *Chem. Mater.* **2001**, *13*, 3843–3858.
- 23 J. T. LUE, *J. Phys. Chem. Solids* **2001**, *62*, 1599–1612.
- 24 K. GRIEVE, P. MULVANEY, F. GRIESER, *Cur. Opin. Colloid Interface Sci.* **2000**, *5*, 168–172.
- 25 M. BRUST, C. J. KIELY, *Colloid Surf. A* **2002**, *202*, 175–186.
- 26 W. P. MCCONNELL, J. P. NOVAK, L. C. BROUSSEAU, R. R. FUERER, R. C. TENENT, D. L. FELDHEIM, *J. Phys. Chem. B* **2000**, *104*, 8925–8930.
- 27 R. GANGOPADHYAY, A. DE, *Chem. Mater.* **2000**, *12*, 608–622.
- 28 G. T. HERMANSON, A. K. MALLIA, P. K. SMITH, *Immobilized Affinity Ligand Techniques*, Academic, London, **1992**.
- 29 R. F. TAYLOR, *Protein Immobilization*, Marcel Dekker, New York, **1990**.
- 30 A. F. COLLINGS, F. CARUSO, *Rep. Prog. Phys.* **1997**, *60*, 1397–145.
- 31 S. V. RAO, K. W. ANDERSON, L. G. BACHAS, *Mikrochim. Acta* **1998**, *128*, 127–143.
- 32 W. H. SCOUTEN, J. H. LUONG, R. S. BROWN, *Trends Biotechnol.* **1995**, *13*, 178–185.
- 33 T. RAJH, J. M. NEDELJKOVIC, L. X. CHEN, O. POLUEKTOV, M. C. THURNAUER, *J. Phys. Chem. B* **1999**, *103*, 3515–3519.
- 34 J. B. BRODERICK, M. J. NATAN, T. V. O'HALLORAN, R. P. VAN DUYN, *Biochemistry* **1993**, *32*, 13771–13776.
- 35 C. YONGLI, Z. XIUFANG, G. YANDAO, Z. NANMING, Z. TINGYING, S. XINQI, *J. Colloid Int. Sci.* **1999**, *214*, 38–45.
- 36 J. DE GROOT, R. E. HESTER, *J. Phys. Chem.* **1988**, *92*, 2044–2048.
- 37 J. E. GESTWICKI, L. E. STRONG, L. L. KISSELING, *Angew. Chem. Int. Ed.* **2000**, *39*, 4567–4570.
- 38 W. SHENTON, S. A. DAVIS, S. MANN, *Adv. Mater.* **1999**, *11*, 449–452.
- 39 I. D. G. MACDONALD, W. E. SMITH, *Langmuir* **1996**, *12*, 706–713.

- 40 B. N. ROSPENDOWSKI, K. KELLY, C. R. WOLF, W. E. SMITH, *J. Am. Chem. Soc.* **1991**, *113*, 1217–1225.
- 41 H. MATTOUSSI, J. M. MAURO, E. R. GOLDMAN, G. P. ANDERSON, V. C. SUNDAR, F. V. MIKULEC, M. G. BAWENDI, *J. Am. Chem. Soc.* **2000**, *122*, 12142–12150.
- 42 H. LARSERICSDOTTER, S. OSCARSSON, J. BUIJS, *J. Colloid Inter. Sci.* **2001**, *237*, 98–103.
- 43 F. CARUSO, *Adv. Mater.* **2001**, *13*, 11–22.
- 44 F. CARUSO, H. MÖHWALD, *J. Am. Chem. Soc.* **1999**, *121*, 6039–6046.
- 45 F. CARUSO, H. FIEDLER, K. HAAGE, *Colloids Surf. A* **2000**, *169*, 287–293.
- 46 C. SCHÜLER, F. CARUSO, *Macromol. Rapid Commun.* **2000**, *21*, 750–753.
- 47 F. CARUSO, C. SCHÜLER, *Langmuir* **2000**, *16*, 9595–9603.
- 48 Y. LVOV, F. CARUSO, *Anal. Chem.* **2001**, *73*, 4212–4217.
- 49 R. MAHTAB, J. P. ROGERS, C. J. MURPHY, *J. Am. Chem. Soc.* **1995**, *117*, 9099–9100.
- 50 R. MAHTAB, J. P. ROGERS, C. P. SINGLETON, C. J. MURPHY, *J. Am. Chem. Soc.* **1996**, *118*, 7028–7032.
- 51 R. MAHTAB, H. H. HARDEN, C. J. MURPHY, *J. Am. Chem. Soc.* **2000**, *122*, 14–17.
- 52 J. R. LAKOWICZ, I. GRZYCZYNSKI, Z. GRZYCZYNSKI, K. NOWACZYK, C. J. MURPHY, *Anal. Biochem.* **2000**, *280*, 128–136.
- 53 S. R. BIGHAM, J. L. COFFER, *J. Cluster Sci.* **2000**, *11*, 359–372.
- 54 W. YANG, D. TRAU, R. RENNEBERG, N. T. YU, F. CARUSO, *J. Colloid Inter. Sci.* **2001**, *234*, 356–362.
- 55 M. A. HAYAT, *Colloidal Gold: Principles, Methods, and Applications*, Academic Press, New York, **1989**.
- 56 S. S. GHOSH, P. M. KAO, A. W. MCCUE, H. L. CHAPPELLE, *Bioconjugate Chem.* **1990**, *1*, 71–76.
- 57 C. A. MIRKIN, R. L. LETSINGER, R. C. MUCIC, J. J. STORHOFF, *Nature* **1996**, *382*, 607–609.
- 58 S.-J. PARK, A. A. LAZARIDES, C. A. MIRKIN, P. W. BRAZIS, C. R. KANNEWURF, R. L. LETSINGER, *Angew. Chem. Int. Ed.* **2000**, *39*, 3845–3848.
- 59 G. P. MITCHELL, C. A. MIRKIN, R. L. LETSINGER, *J. Am. Chem. Soc.* **1999**, *121*, 8122–8123.
- 60 F. PATOLSKY, R. GILL, Y. WEIZMANN, T. MOKARI, U. BANIN, I. WILLNER, *J. Am. Chem. Soc.*, in press (2003).
- 61 R. L. LETSINGER, R. ELGHANIAN, G. VISWANADHAM, C. A. MIRKIN, *Bioconjugate Chem.* **2000**, *11*, 289–291.
- 62 A. BARDEA, A. DAGAN, I. BEN-DOV, B. AMIT, I. WILLNER, *Chem. Commun.* **1998**, 839–840.
- 63 K. C. GRABAR, J. E. DEUTSCH, M. J. NATAN, *J. Polym. Prepr.* **1995**, 69–70.
- 64 X. YANG, L. A. WENZLER, J. QI, X. LI, N. C. SEEMAN, *J. Am. Chem. Soc.* **1998**, *120*, 9779–9786.
- 65 W.-L. SHAIU, D. D. LARSON, J. VESENKA, E. HENDERSON, *Nucleic Acids Res.* **1993**, *21*, 99–103.
- 66 M. BRUCHEZ, JR., M. MORONNE, P. GIN, S. WEISS, A. P. ALIVISATOS, *Science* **1998**, *281*, 1013–1015.
- 67 K. OKANO, S. TAKAHASHI, K. YASUDA, D. TOKINAGA, K. IMAI, M. KOGA, *Anal. Biochem.* **1992**, *202*, 120–125.
- 68 T. SOUKKA, H. HÄRMÄ, J. PAUKKUNEN, T. LÖVGREN, *Anal. Chem.* **2001**, *73*, 2254–2260.
- 69 C. M. NIEMEYER, *Angew. Chem. Int. Ed.* **2001**, *40*, 4128–4158.
- 70 H. JEON, G. G. SHIPLEY, *J. Biol. Chem.* **2000**, *275*, 30465–30470.
- 71 M. MALECKI, A. HSU, L. TRUONG, S. SANCHEZ, *Proc. Natl. Acad. Sci. USA* **2002**, *99*, 213–218.
- 72 O. MEDALIA, M. HEIM, R. GUCKENBERGER, R. SPERLING, J. SPERLING, *J. Struct. Biol.* **1999**, *127*, 113–119.
- 73 A. C. TEMPLETON, S. CHEN, S. M. GROSS, R. W. MURRAY, *Langmuir* **1999**, *15*, 66–76.
- 74 A. K. BOAL, V. M. ROTELLO, *J. Am. Chem. Soc.* **1999**, *121*, 4914–4915.
- 75 M. J. HANNON, V. MORENO, M. J. PRIETO, E. MOLDRHEIM, E. STETTEN, I. MEISTERMANN, C. J. ISAAC, K. J. SANDERS, A. RODGER, *Angew. Chem. Int. Ed.* **2001**, *40*, 880–884.
- 76 A. U. BIELINSKA, C. CHEN, J. JOHNSON, J. R. BAKER, JR., *Bioconjugate Chem.* **1999**, *10*, 843–850.
- 77 K. IJIMA, M. YOSHIZUMI, M. HASHIMOTO, S. KIM, M. ETO, J. AKO,



- Y. Q. KIANG, N. SUDOH, K. HOSODA, K. NAKAHARA, K. TODA, Y. OUCHI, *Circulation* **2000**, 101, 805–811.
- 78 M. J. HOSTETTLER, A. C. TEMPLETON, R. W. MURRAY, *Langmuir* **1999**, 15, 3782–3789.
- 79 A. K. BOAL, V. M. ROTELLO, *J. Am. Chem. Soc.* **2000**, 122, 734–735.
- 80 C. M. MCINTOSH, E. A. ESPOSITO III, A. K. BOAL, J. M. SIMARD, C. T. MARTIN, V. M. ROTELLO, *J. Am. Chem. Soc.* **2001**, 123, 7626–7629.
- 81 B. DUBERTRET, M. CALAME, A. J. LIBCHABER, *Nature Biotech.* **2001**, 19, 365–370.
- 82 C. PETIT, A. TALEB, M.-P. PILENI, *Adv. Mater.* **1998**, 10, 259–261.
- 83 C. B. MURRAY, C. R. KAGAN, M. G. BAWENDI, *Science* **1995**, 270, 1335–1338.
- 84 T. VOSSMEYER, G. RECK, L. KATSIKAS, E. T. K. HAUPT, B. SCHULZ, H. WELLER, *Science* **1995**, 267, 1476–1479.
- 85 A. SASHCHUK, E. LIFSHITZ, R. REISFELD, T. SARADAROV, M. ZELNER, A. WILLENZ, *J. Sol-Gel Sci. Technol.* **2002**, 24, 31–38.
- 86 S. A. DAVIS, M. BREULMANN, K. H. RHODES, B. ZHANG, S. MANN, *Chem. Mater.* **2001**, 13, 3218–3226.
- 87 W. SHENTON, D. PUM, U. B. SLEYTR, S. MANN, *Nature* **1997**, 389, 585–587.
- 88 S. DIELUWEIT, D. PUM, U. B. SLEYTR, *Supramol. Sci.* **1998**, 5, 15–19.
- 89 S. A. DAVIS, H. M. PATEL, E. L. MAYERS, N. H. MENDELSON, G. FRANCO, S. MANN, *Chem. Mater.* **1998**, 10, 2516–2524.
- 90 B. A. KORGEL, D. FITZMAURICE, *Adv. Mater.* **1998**, 10, 661–665.
- 91 R. P. ANDRES, J. D. BIELEFELD, J. I. HENDERSON, D. B. JANES, V. R. KOLAGUNTA, C. P. KUBIAK, W. J. MAHONEY, R. G. OSIFCHIN, *Science* **1996**, 273, 1690–1693.
- 92 M. BRUST, D. BETHELL, D. J. SCHIFFRIN, C. J. KIELY, *Adv. Mater.* **1995**, 7, 795–797.
- 93 S. MANN, W. SHENTON, M. LI, S. CONNOLY, D. FITZMAURICE, *Adv. Mater.* **2000**, 12, 147–150.
- 94 R. BASHIR, *Superlattices Microstr.* **2001**, 29, 1–16.
- 95 C. M. NIEMEYER, *Appl. Phys. A* **1999**, 68, 119–124.
- 96 P. C. WEBER, D. H. OHLENDORF, J. J. WENDOLOSKI, F. R. SALEMME, *Science* **1989**, 243, 85–88.
- 97 B. K. SINHA, C. F. CHINGELL, *Methods Enzymol.* **1979**, 62, 295–308.
- 98 U. PIRAN, W. J. RIORDAN, *J. Immunol. Methods* **1990**, 133, 141–143.
- 99 T. SANO, M. W. PANDORI, X. M. CHEN, C. L. SMITH, C. R. CANTOR, *J. Biol. Chem.* **1995**, 270, 28204–28209.
- 100 T. SANO, C. R. CANTOR, *Proc. Natl. Acad. Sci. USA* **1995**, 92, 3180–3184.
- 101 S. CONNOLY, D. FITZMAURICE, *Adv. Mater.* **1999**, 11, 1202–1205.
- 102 S. CONNOLY, S. COBBE, D. FITZMAURICE, *J. Phys. Chem. B* **2001**, 105, 2222–2226.
- 103 P. M. HARRISON, P. AROSIO, *Biochim. Biophys. Acta* **1996**, 1275, 161–203.
- 104 F. C. MELDRUM, B. R. HEYWOOD, S. MANN, *Science* **1992**, 257, 522–523.
- 105 T. DOUGLAS, D. P. E. DICKSON, S. BETTERIDGE, J. CHARNOCK, C. D. GARNER, S. MANN, *Science* **1995**, 269, 54–57.
- 106 F. C. MELDRUM, T. DOUGLAS, S. LEVI, P. AROSIO, S. MANN, *J. Inorg. Biochem.* **1995**, 8, 59–68.
- 107 K. K. W. WONG, S. MANN, *Adv. Mater.* **1996**, 8, 928–931.
- 108 M. LI, K. W. WONG, S. MANN, *Chem. Mater.* **1999**, 11, 23–26.
- 109 W. SHENTON, S. A. DAVIS, S. MANN, *Adv. Mater.* **1999**, 11, 449–452.
- 110 S. R. WHALEY, D. S. ENGLISH, E. L. HU, P. F. BARBARA, A. M. BELCHER, *Nature* **2000**, 405, 665–666.
- 111 C. A. MIRKIN, *Inorg. Chem.* **2000**, 39, 2258–2272.
- 112 J. J. STORHOFF, C. A. MIRKIN, *Chem. Rev.* **1999**, 99, 1849–1862.
- 113 C. A. MIRKIN, R. L. LETSINGER, R. C. MUCIC, J. J. STORHOFF, *Nature* **1996**, 382, 607–609.
- 114 R. C. MUCIC, J. J. STORHOFF, C. A. MIRKIN, R. L. LETSINGER, *J. Am. Chem. Soc.* **1998**, 120, 12674–12675.
- 115 J. J. STORHOFF, A. A. LAZARIDES, R. C. MUCIC, C. A. MIRKIN, R. L. LETSINGER, G. C. SCHATZ, *J. Am. Chem. Soc.* **2000**, 122, 4640–4650.
- 116 R. ELGHANIAN, J. J. STORHOFF, R. C.

- MUCIC, R. L. LETSINGER, C. A. MIRKIN, *Science* **1997**, 277, 1078–1081.
- 117 J. J. STORHOFF, R. ELGHANIAN, R. C. MUCIC, C. A. MIRKIN, R. L. LETSINGER, *J. Am. Chem. Soc.* **1998**, 120, 1959–1964.
- 118 R. A. REYNOLDS, III, C. A. MIRKIN, R. L. LETSINGER, *J. Am. Chem. Soc.* **2000**, 122, 3795–3796.
- 119 G. R. SOUZA, J. H. MILLER, *J. Am. Chem. Soc.* **2001**, 123, 6734–6735.
- 120 E. DUJARDIN, L.-B. HSIN, C. R. C. WANG, S. MANN, *Chem. Commun.* **2001**, 1264–1265.
- 121 A. P. ALIVISATOS, K. P. JOHNSON, X. PENG, T. E. WILSON, C. J. LOWETH, M. P. BRUCHEZ JR., P. G. SCHULTZ, *Nature* **1996**, 382, 609–611.
- 122 C. J. LOWETH, W. B. CALDWELL, X. PENG, A. P. ALIVISATOS, P. G. SCHULTZ, *Angew. Chem. Int. Ed.* **1999**, 38, 1808–1812.
- 123 C. M. NIEMEYER, B. CEYHAN, *Angew. Chem. Int. Ed.* **2001**, 40, 3685–3688.
- 124 S.-J. PARK, A. A. LAZARIDES, C. A. MIRKIN, R. L. LETSINGER, *Angew. Chem. Int. Ed.* **2001**, 40, 2909–2912.
- 125 C. M. NIEMEYER, W. BÜRGER, J. PEPLIES, *Angew. Chem. Int. Ed.* **1998**, 37, 2265–2268.
- 126 S. R. NICEWARNER-PENA, R. G. FREEMAN, B. D. REISS, L. HE, D. J. PENNA, I. D. WALTON, R. CROMER, C. D. KEATING, M. J. NATAN, *Science* **2001**, 294, 137–141.
- 127 F. A. ARMSTRONG, G. S. WILSON, *Electrochim. Acta* **2000**, 45, 2623–2645.
- 128 A. HELLER, *Acc. Chem. Res.* **1990**, 23, 128–134.
- 129 A. HELLER, *J. Phys. Chem.* **1992**, 96, 3579–3587.
- 130 I. WILLNER, E. KATZ, *Angew. Chem. Int. Ed.* **2000**, 39, 1180–1218.
- 131 J. WANG, *J. Pharm. Biomed. Anal.* **1999**, 19, 47–53.
- 132 H.-L. SCHMIDT, W. SCHUHMAN, *Biosens. Bioelectron.* **1996**, 11, 127–135.
- 133 I. WILLNER, E. KATZ, B. WILLNER, *Electroanalysis* **1997**, 13, 965–977.
- 134 I. WILLNER, G. ARAD, E. KATZ, *Bioelectrochem. Bioenerg.* **1998**, 44, 209–214.
- 135 I. WILLNER, E. KATZ, F. PATOLSKY, A. F. BÜCKMANN, *J. Chem. Soc. Perkin. Trans. 2* **1998**, 1817–1822.
- 136 E. KATZ, B. FILANOVSKY, I. WILLNER, *New J. Chem.* **1999**, 23, 481–487.
- 137 E. KATZ, I. WILLNER, A. B. KOTLYAR, *J. Electroanal. Chem.* **1999**, 479, 64–68.
- 138 S. C. BARTON, H.-H. KIM, G. BINYAMIN, Y. ZHANG, A. HELLER, *J. Am. Chem. Soc.* **2001**, 123, 5802–5803.
- 139 T. CHEN, S. C. BARTON, G. BINYAMIN, Z. GAO, Y. ZHANG, H.-H. KIM, A. HELLER, *J. Am. Chem. Soc.* **2001**, 123, 8630–8631.
- 140 I. WILLNER, A. DORON, E. KATZ, *J. Phys. Org. Chem.* **1998**, 11, 546–560.
- 141 R. BLONDER, E. KATZ, I. WILLNER, V. WRAY, A. F. BÜCKMANN, *J. Am. Chem. Soc.* **1997**, 119, 11747–11757.
- 142 G. SUNDARABABU, H. GAO, H. SIGRIST, *Photochem. Photobiol.* **1995**, 61, 540–544.
- 143 S. K. BHATIA, J. L. TEIXEIRA, M. ANDERSON, L. SHRIVER-LAKE, J. M. CALVERT, J. H. GEORGER, J. J. HICKMAN, C. S. DUCEY, P. E. SCHOEN, F. S. LIGLER, *Anal. Biochem.* **1993**, 208, 197–205.
- 144 N. KIMIZUKA, M. TANAKA, T. KUNITAKE, *Chem. Lett.* **1999**, 1333–1334.
- 145 S. DEKI, Y. AOI, O. HIROI, A. KAJINAMI, *Chem. Lett.* **1996**, 433–434.
- 146 Y. MAEDA, T. NAKAMURA, K. UCHIMURA, T. MATSUMOTO, H. TABATA, T. KAWAI, *J. Vac. Sci. Technol. B* **1999**, 17, 494–496.
- 147 T. TORIMOTO, M. YAMASHITA, S. KUWABATA, T. SAKATA, H. MORI, H. YONEYAMA, *J. Phys. Chem. B* **1999**, 103, 8799–8803.
- 148 J. L. COFFER, S. R. BIGHAM, X. LI, R. F. PINIZZOTTO, Y. G. RHO, R. M. PIRTLE, I. L. PIRTLE, *Appl. Phys. Lett.* **1996**, 69, 3851–3853.
- 149 M. SASTRY, A. KUMAR, S. DATAR, C. V. DHARMADHIKARI, K. N. GANESH, *Appl. Phys. Lett.* **2001**, 78, 2943–2945.
- 150 A. KUMAR, M. PATTARKINE, M. BHADHADE, A. B. MANDALE, K. N. GANESH, S. S. DATAR, C. V. DHARMADHIKARI, M. SASTRY, *Adv. Mater.* **2001**, 13, 341–344.
- 151 S. HAN, J. LIN, F. ZHOU, R. L. VELLANOWETH, *Biochem. Biophys. Res. Commun.* **2000**, 279, 265–269.

- 152 E. HUANG, M. SATJAPIPAT, S. HAN, F. ZHOU, *Langmuir* **2001**, 17, 1215–1224.
- 153 J. RICHTER, R. SEIDEL, R. KIRSCH, M. MERTIG, W. POMPE, J. PLASCHKE, H. K. SCHACKERT, *Adv. Mater.* **2000**, 12, 507–510.
- 154 Y. MAEDA, H. TABATA, T. KAWAI, *Appl. Phys. Lett.* **2001**, 79, 1181–1183.
- 155 J. K. N. MBINDYO, B. D. REISS, B. R. MARTIN, C. D. KEATING, M. J. NATAN, T. E. MALLOUK, *Adv. Mater.* **2001**, 13, 249–254.
- 156 C. M. NIEMEYER, B. CEYHAN, S. GAO, L. CHI, S. PESCHEL, U. SIMON, *Colloid Polym. Sci.* **2001**, 122, 6305–6306.
- 157 L. M. DEMERS, S.-J. PARK, T. A. TATON, Z. LI, C. A. MIRKIN, *Angew. Chem. Int. Ed.* **2001**, 40, 3071–3073.
- 158 T. A. TATON, R. C. MUCIC, C. A. MIRKIN, R. L. LETSINGER, *J. Am. Chem. Soc.* **2000**, 122, 6305–6306.
- 159 T. A. TATON, C. A. MIRKIN, R. L. LETSINGER, *Science* **2000**, 289, 1757–1760.
- 160 J. REICHERT, A. CSÁKI, J. M. KÖHLER, W. FRITZSCHE, *Anal. Chem.* **2000**, 72, 6025–6029.
- 161 T. A. TATON, G. L. LU, C. A. MIRKIN, *J. Am. Chem. Soc.* **2001**, 123, 5164–5165.
- 162 S. SCHULTZ, D. R. SMITH, J. J. MOCK, D. A. SCHULTZ, *Proc. Natl. Acad. Sci. USA* **2000**, 97, 996–1001.
- 163 G. BAUER, F. PITTNER, T. SCHALKHAMMER, *Mikrochim. Acta* **1999**, 131, 107–114.
- 164 S. KUBITSCHKO, J. SPINKE, T. BRÜCKNER, S. POHL, N. ORANTH, *Anal. Biochem.* **1997**, 253, 112–122.
- 165 L. A. LYON, M. D. MUSICK, M. J. NATAN, *Anal. Chem.* **1998**, 70, 5177–5183.
- 166 P. ENGLEBIENNE, A. V. HOONACKER, M. VERHAS, *Analyst* **2001**, 126, 1645–1651.
- 167 L. HE, M. D. MUSICK, S. R. NICE-WARNER, F. G. SALINAS, S. J. BENKOVIC, M. J. NATAN, C. D. KEATING, *J. Am. Chem. Soc.* **2000**, 122, 9071–9077.
- 168 C. D. KEATING, K. M. KOVALESKI, M. J. NATAN, *J. Phys. Chem. B* **1998**, 102, 9404–9413.
- 169 C. D. KEATING, K. M. KOVALESKI, M. J. NATAN, *J. Phys. Chem. B* **1998**, 102, 9414–9425.
- 170 Y. DEGANI, A. HELLER, *J. Phys. Chem.* **1987**, 91, 1285–1289.
- 171 W. SCHUHMANN, T. J. OHARA, H.-L. SCHMIDT, A. HELLER, *J. Am. Chem. Soc.* **1991**, 113, 1394–1397.
- 172 I. WILLNER, A. RIKLIN, B. SHOHAM, D. RIVENZON, E. KATZ, *Adv. Mater.* **1993**, 5, 912–915.
- 173 A. BADIA, R. CARLINI, A. FERNANDEZ, F. BATTAGLINI, S. R. MIKKELSEN, A. M. ENGLISH, *J. Am. Chem. Soc.* **1993**, 115, 7053–7060.
- 174 A. RIKLIN, E. KATZ, I. WILLNER, A. STOKER, A. F. BÜCKMANN, *Nature* **1995**, 376, 672–675.
- 175 I. WILLNER, V. HELEG-SHABTAI, R. BLONDER, E. KATZ, G. TAO, A. F. BÜCKMANN, A. HELLER, *J. Am. Chem. Soc.* **1996**, 118, 10321–10322.
- 176 E. KATZ, A. RIKLIN, V. HELEG-SHABTAI, I. WILLNER, A. F. BÜCKMANN, *Anal. Chim. Acta* **1999**, 385, 45–58.
- 177 L.-H. GUO, G. MCLENDON, H. RAZA-FITRIMO, Y. GAO, *J. Mater. Chem.* **1996**, 6, 369–374.
- 178 H. ZIMMERMANN, A. LINDGREN, W. SCHUHMANN, L. GORTON, *Chem. Eur. J.* **2000**, 6, 592–599.
- 179 Y. XIAO, F. PATOLSKY, E. KATZ, J. F. HAINFELD, I. WILLNER, *Science* **2003**, 299, 1877–1881.
- 180 L. AUTHIER, C. GROSSIROT, P. BROSSIER, B. LIMOGES, *Anal. Chem.* **2001**, 73, 4450–4456.
- 181 O. D. VELEV, E. W. KALER, *Langmuir* **1999**, 15, 3693–3698.
- 182 S.-J. PARK, T. A. TATON, C. A. MIRKIN, *Science* **2002**, 295, 1503–1506.
- 183 I. WILLNER, F. PATOLSKY, J. WASSERMAN, *Angew. Chem. Int. Ed.* **2001**, 40, 1861–1864.
- 184 X. C. ZHOU, S. J. O'SHEA, S. F. Y. LI, *Chem. Commun.* **2000**, 953–954.
- 185 F. PATOLSKY, K. T. RANJIT, A. LICHTENSTEIN, I. WILLNER, *Chem. Commun.* **2000**, 1025–1026.
- 186 S. HAN, J. LIN, M. SATJAPIPAT, A. J. BECA, F. ZHOU, *Chem. Commun.* **2001**, 609–610.
- 187 I. WILLNER, F. PATOLSKY, Y. WEIZMANN, B. WILLNER, *Talanta* **2002**, 56, 847–856.

- 188 Y. WEIZMANN, F. PATOLSKY, I. WILLNER, *Analyst* **2001**, 126, 1502–1504.
- 189 A. DORON, E. KATZ, I. WILLNER, *Langmuir* **1995**, 11, 1313–1317.
- 190 H. CAI, C. XU, P. HE, Y. FANG, J. *Electroanal. Chem.* **2001**, 510, 78–85.
- 191 H. LIN, H. ZHAO, J. LI, J. TANG, M. DUAN, L. JIANG, *Biochem. Biophys. Res. Comm.* **2000**, 274, 817–820.
- 192 S. O. KELLEY, J. K. BARTON, *Science* **1999**, 283, 375–381.
- 193 M. RATNER, *Nature* **1999**, 397, 480–481.
- 194 S.-J. PARK, A. A. LAZARIDES, C. A. MIRKIN, P. W. BRAZIS, C. R. KANNEWURF, R. L. LETSINGER, *Angew. Chem. Int. Ed.* **2000**, 39, 3845–3848.
- 195 R. MÖLLER, A. CSÁKI, J. M. KÖHLER, W. FRITZSCHE, *Langmuir* **2001**, 17, 5426–5430.
- 196 E. BRAUN, Y. EICHEN, U. SIVAN, G. BEN-YOSEPH, *Nature* **1998**, 391, 775–778.
- 197 Y. EICHEN, E. BRAUN, U. SIVAN, G. BEN-YOSEPH, *Acta Polymerica* **1998**, 49, 663–670.
- 198 J. RICHTER, M. MERTIG, W. POMPE, I. MÖNCH, H. K. SCHACKERT, *Appl. Phys. Lett.* **2001**, 78, 536–538.
- 199 *Scientific and Clinical Applications of Magnetic Carriers*, U. HÄFELI, W. SCHÜTT, J. TELLER, M. ZBOROWSKI (Eds.), Plenum Press, New York, **1997**.
- 200 S. V. SONTI, A. BOSE, J. *Colloid Inter. Sci.* **1995**, 170, 575–585.
- 201 J. ROGER, J. N. PONS, R. MASSART, A. HALBREICH, J. C. BACRI, *Eur. Phys. J.* **1999**, 5, 321–325.
- 202 S. MORNET, A. VEKRIS, J. BONNET, E. DUGUET, F. GRASSET, J.-H. CHOY, J. PORTIER, *Mater. Lett.* **2000**, 42, 183–188.
- 203 D. P. E. DICKSON, S. A. WALTON, S. MANN, K. WONG, *NanoStructured Mater.* **1997**, 9, 595–598.
- 204 K. K. W. WONG, T. DOUGLAS, S. GIDER, D. D. AWSCHALOM, S. MANN, *Chem. Mater.* **1998**, 10, 279–285.
- 205 R. P. BLAKEMORE, D. MARATEA, R. S. WOLFE, *J. Bacteriol.* **1979**, 140, 720–729.
- 206 T. MATSUNAGA, F. TADOKORO, N. NAKAMURA, *IEEE Trans. Magnetism* **1990**, 26, 1557–1559.
- 207 T. MATSUNAGA, T. SAKAGUCHI, F. TADOKORO, *Appl. Microbiol. Biotechnol.* **1991**, 35, 651–655.
- 208 K. H. SCHEIFER, D. SCHULER, S. SPRING, M. WEIZENEGGER, R. AMANN, W. LUDWIG, M. KOHLER, *Syst. Appl. Microbiol.* **1991**, 14, 379–385.
- 209 Y. A. GORBY, T. J. BEVERIDGE, R. P. BLAKEMORE, *J. Bacteriol.* **1988**, 170, 834–841.
- 210 T. MATSUNAGA, *Trend. Biotech.* **1991**, 9, 91–95.
- 211 T. MATSUNAGA, H. TAKEYAMA, *Supramol. Sci.* **1998**, 5, 391–394.
- 212 N. NAKAMURA, K. HASHIMOTO, T. MATSUNAGA, *Anal. Chem.* **1991**, 63, 268–272.
- 213 N. NAKAMURA, J. G. BURGESS, K. YAGIUDA, S. KUDO, T. SAKAGUCHI, T. MATSUNAGA, *Anal. Chem.* **1993**, 65, 2036–2039.
- 214 N. NAKAMURA, T. MATSUNAGA, *Anal. Chim. Acta* **1993**, 281, 585–589.
- 215 T. MATSUNAGA, M. KAWASAKI, X. YU, N. TSUJIMURA, N. NAKAMURA, *Anal. Chem.* **1996**, 68, 3551–3554.
- 216 K. SODE, S. KUDO, T. SAKAGUCHI, N. NAKAMURA, T. MATSUNAGA, *Biotechnol. Tech.* **1993**, 7, 688–694.
- 217 H. TAKEYAMA, A. YAMAZAWA, N. NAKAMURA, T. MATSUNAGA, *Biotechnol. Tech.* **1995**, 9, 355–360.
- 218 M. SHINKAI, H. HONDA, T. KOBAYASHI, *Biocatalysis* **1991**, 5, 61–69.
- 219 M.-H. LIAO, D.-H. CHEN, *Biotech. Lett.* **2001**, 23, 1723–1727.
- 220 R. HIRSH, E. KATZ, I. WILLNER, *J. Am. Chem. Soc.* **2000**, 122, 12053–12054.
- 221 E. KATZ, L. SHEENEY-HAJ-ICHIA, I. WILLNER, *Chem. Eur. J.* in press.
- 222 E. KATZ, L. SHEENEY-HAJ-ICHIA, A. F. BÜCKMANN, I. WILLNER, *Angew. Chem. Int. Ed.* **2002**, 41, 1343–1346.
- 223 J. WANG, D. XU, R. POLSKY, *J. Am. Chem. Soc.* **2002**, 124, 4208–4209.
- 224 E. KATZ, I. WILLNER, *Angew. Chem. Int. Ed.* **2003**, in press.

## 7

**Conclusions and Perspectives***All Authors*

Nanoparticles, whether they originate from semiconductors or from metals, are generally associated with the appearance of novel properties. The most far-reaching consequence of their small size is without doubt the change in their electronic properties. Next in importance are changes in other properties, both physical and chemical. These changes are what ultimately constitute the value of nanosciences and nanotechnology. Novel properties become available without making new materials!

If particles are small enough, they become electronically comparable to atoms and molecules, following quantum mechanical rules instead of the laws of classical physics. That is why nanoparticles are called “quantum dots” or sometimes “artificial atoms”. The reason for this behavior is the disappearance of band structures and the formation of discrete energy levels, these being linked to an increase in the already existing band gaps in the case of semiconductor particles and the formation of quantized states in the case of metal nanoparticles. Two-dimensional arrays of quantum dots as well as one-dimensional arrangements (quantum wires) therefore reach a new dimension of quality with respect to possible future applications. The synthesis of all types of quantum dots is therefore a challenge for both chemists and physicists. Their easy availability is of decisive importance if nanoparticles are to play an industrial role, and in fact II-VI, III-V as well as Ib-VI semiconductor nanoparticles are routinely accessible by various wet-chemical methods in gram amounts.

Even the most difficult step in all synthetic procedures, the achievement of monodispersity of the particles, can be controlled satisfactorily. This is true of both semiconductor and metal nanoparticles. Because of the long history of metal nanoparticles, there has been plenty of time to develop perfect syntheses. One decisive finding opened up completely novel strategies for both semiconductor and metal nanoparticles: the use of protecting ligand shells, usually consisting of organic molecules. Amines, phosphines, phosphine oxides, thiols, and numerous other classes of compounds have been used. Such coordinating molecules not only support the synthesis of monodisperse nanoparticles by their kinetic and size-

limiting functions; they also make the particles soluble in solvents, depending on the chemical nature of the ligand molecules. Here, traditional chemical procedures such as chromatography, crystallization, etc. can be used for purification. Semiconductor nanoparticles include the II–VI type, e.g., CdS, CdSe and CdTe, the III–V type, mainly represented by GaN, GaP, GaAs or InP and InAs, and the Ib–VI type, available as copper selenide and telluride nanoclusters and as silver and gold selenide and telluride species. However, metal nanoparticles have also had a remarkable renaissance after a hundred years' sleep. This is especially true of magnetic nanoparticles. Apart from leading to a general increase in our knowledge of magnetism, these offer unimagined application possibilities.

Although magnetic nanoparticles are currently being used in several industrial and medical applications, systematic research into the magnetic properties of nanoscale particles is still lacking. The reason for this is clearly linked to a lack of high-quality samples. Against this background, exciting fundamental studies on the size dependence of the magnetic properties in dilute systems can be expected. Questions concerning magnetic phase transitions such as the transition from the ferromagnetic to the superparamagnetic state will attract considerable attention. Going a step further, one may expect fundamentally new results for highly ordered dense magnetic systems. The alignment of the spins of neighboring particles relative to each other will be especially interesting for magnetic transport properties such as giant magnetic resistance. The possibility of preparing perfectly ordered domains of almost single-sized and well-defined particles extending over wide areas will lead to a major step forward in the exciting field of spintronics. Exciting developments in the use of magnetic nanoparticles in biology and medicine are also expected. Smart magnetic nanoparticles used in an improved hyperthermal therapy in which tumor cells are recognized and well-defined and controllable magnetic labels for the investigation of the nanostructure and dynamics of cells are two goals for the future.

The fascinating electronic “inner life” of nanoparticles is only of academic relevance if we fail to use them in nanoelectronics, optoelectronics, and other sophisticated techniques. One precondition for such use is that we must learn how to organize nanoparticles in three dimensions, but even more importantly in one and two dimensions. Developments during the last decade have resulted in impressive progress. Self-assembly techniques in particular have been so much improved that nowadays semiconductor as well as metal nanoparticles can be arranged in perfectly ordered assemblies of remarkable extensions. Our first ideas about interparticle relationships became known from these 2D arrangements. As it turned out, this kind of “chemistry” between the particles, among other things, determines the nature of their collective behavior.

It is rather more difficult to routinely organize nanoparticles in one direction. To do this, appropriate templates are indispensable. Several approaches using polymer molecules or DNA look interesting, but still do not give results that could be regarded as a breakthrough.

On the other hand, techniques have been developed that even allow writing with

nanoparticles. Dip-pen lithography is one of these methods, accompanied by “nano-electrochemical” modifications of surfaces, enabling the nanoparticles to be fixed in a final step.

Much progress has been achieved in understanding charge transport phenomena through nanostructured materials. The electrical properties of nanoparticles are mainly determined by the Coulomb charging energy, and the phenomena can, in principle, be understood in terms of single electron tunneling (SET) within the framework of the “orthodox theory of SET”. Furthermore, in the smallest particles, like Au<sub>55</sub>, additional effects due to the discrete nature of the energy states occur, and need to be taken into account in the discussion of the electrical transport phenomena and the characteristic excitation energies. This makes the physics of these structures much more complicated. At least, the “orthodox theory” has to be extended for this size regime, and since the electron distribution is then no longer a pure Fermi distribution, electrical capacitances cannot be discussed classically, and even the tunneling time for electrons can be affected.

These effects have not been studied experimentally or theoretically in much detail. Thus, most of the presently applied models are at least incomplete with respect to the huge variety of different control parameters in the chemical design of molecularly organized nanoparticles. Nevertheless, applying chemically tailored metal nanoparticles in SET might be an alternative approach to the main-stream developments, like CMOS technologies, in the future. But it remains an open question whether these nanoparticles or other molecular objects, like nanotubes or organic/organometallic molecules, remain stable under the operating conditions of a high-performance electrical circuits. With respect to circuit design, precise control over size and topology is needed. At the same time, one needs to keep in mind the fact that a 10 nm CMOS device, the technological fabrication of which is one of the great challenges of the next decade, consists of a few thousand atoms and consequently contains only 5–10 doping atoms in the relevant volume fraction of the respective semiconductor. It will be an extraordinarily difficult task to find methods which allow precise control over the distribution of the doping sites over the respective device elements. In contrast, a chemically designed molecule is precise on the atomic level and available on a molar scale. Furthermore, SET devices, as they can be built up with chemically tailored building blocks, control the motion of just a few electrons instead of several hundreds or thousands of them. Since power consumption is roughly proportional to the number of electrons transferred from a voltage source to the ground in logic operations, SET devices could reduce the power consumption drastically.

It is evident, for any kind of chemical approach, that reliance on the present-day paradigm of information exchange in logic elements or memory devices will require defect-tolerant computer architectures with suitable, intelligent software. On the other hand, it may be possible to develop alternative routes which require more complex architectures and different principles of information exchange where the problems associated with redundancy, current density, performance speed, and especially contact resistance and charge redistribution at the lead-to-molecule in-

interface are less relevant. Solving these problems will be one of the great challenges in chemistry.

The fact that nanoparticles and biomaterials (such as enzymes, antibodies, and nucleic acids) are of similar dimensions turns hybrid systems, consisting of both, into attractive nanoelements or building blocks of nanostructures and devices. Several functions and applications of biomaterial-nanoparticle hybrid systems, including analytical applications, signal-triggered electronic functions, nanostructures for circuitry, and the assembly of devices, are of importance. Some of these functions represent viable technologies, whereas others are still in an embryonic phase that requires additional fundamental research. The analytical applications of nanoparticle-biomaterial systems have advanced tremendously in the last decade. The understanding of the unique optical properties of nanoparticles and the photophysics of coupled interparticle interactions has enabled these particles to be used as optical labels for recognition events. Similarly, the catalytic properties of biomaterials have enabled biorecognition events to be amplified. If nanoparticle-biomaterial hybrid systems are assembled on surfaces, the electronic detection of biorecognition events can become feasible by means of electrical conductivity or piezoelectric or photoelectrochemical transduction.

Novel techniques, such as electronic sensing amplified by the movement of magnetic particles by an external magnetic motor, represent a new analytical concept. Many future applications of rotating magnetic particles are envisaged in the detection of antigen-antibody, nucleic acid-DNA, protein-DNA, or receptor-cell interactions. Also, enhanced reactivity at rotating magnetic particles (e.g., accelerated hybridization or polymerization) may facilitate analytical processes. Future analytical perspectives of nanoparticle-hybrid systems may involve the mechanical actuation of microelements. The detection of biomaterials by the mechanical movement of microlevers due to surface stress interactions is well established. The integration of charged nanoparticles as labels for such biorecognition events may enhance the surface stress and provide mechanical activation of micro-objects.

The electronic triggering of redox-proteins by the incorporation of nanoparticles represents a novel strategy for the electrical contacting of redox-enzymes with their macroscopic environment. The use of other nano-objects to facilitate electrical contacting, such as the application of metallic nano-rods or carbon nanotubes, is a future challenge. The magnetic triggering of redox-proteins will certainly find applications in the tailoring of complex sensor systems and the development of new surface-patterning methods.

The biggest challenges are ahead of us, however, and exciting systems are envisaged for the future. Besides the interesting nano-architectures that may be generated, fundamental problems, such as probing charge transport phenomena in nanoparticle-biomaterial systems, may be highlighted. Nonetheless, the organization of nanoparticle architectures on biomaterial templates involves relatively simple motifs that do not make full use of the biomaterial's catalytic functions. The replication of nanoparticle-labeled DNA, and specifically the tailoring of PCR for the formation of nanoparticle wires, represents a novel approach to the design of



biological machines for the synthesis of nanoparticle wires and circuitry. Finally, the use of nanoparticle-biomaterial composite systems for the fabrication of nano-devices is at a very early stage. Nevertheless, it is already clear that fascinating new phenomena may be discovered.

Combining the unique properties of nanoparticles and biomaterials provides a unique opportunity for physicists, chemists, biologists, and material scientists to mold the new area of nanobiotechnology.

## Index

### **a**

*ab initio* of clusters 115  
 absorption spectroscopy 242, 244, 384  
 A-DNA 283f  
 AFM 285, 394f  
 AFM analyses 296  
 AFM height determination 296  
 AFM tip 277, 295  
 Ag nanoparticles 355  
 alcohol reduction process 192  
 alkylselenolate ligands 163  
 alloy-like 262  
 amphiphilic 191  
 analysis of DNA 407  
 analyte DNA 388  
 anisotropic agglomeration 290  
 anti-ferromagnetic cobalt oxide 207, 229  
 antigen-antibody 369  
 arc discharge 201  
 Arrhenius equation 134, 359  
 artificial atoms 249, 305f, 330  
 artificial molecules 249, 355  
 artificial opals 243  
 artificial solids 355  
 atomic-force microscopy (AFM) 244  
 Au nanoparticle-functionalized DNA 389, 399  
 Au nanoparticles 269, 347, 372, 375, 381, 383, 386, 393, 397ff, 405ff  
 Au nanorods 384  
 Au<sub>55</sub> building blocks 254  
 Au<sub>55</sub> clusters 270, 287, 351  
 Aufbau principle 310  
 Auger decay processes 320  
 Auger photoionization 32

### **b**

band 10  
 band edge luminescence 307

band gap 27, 55, 63, 80, 95, 102, 305, 313  
 band gap energy 22  
 B-DNA 283  
 bidentate phosphine ligands 162, 178  
 bimetallic colloids of copper and palladium 197  
 bimetallic metal carbonyl clusters 197  
 bimetallic nanoparticles 192, 197  
 binary alloy nanocrystals 218, 220  
 biofuel cells 371  
 biological fluorescence marking 305  
 biomaterial-functionalized nanoparticles 375  
 biomaterial-magnetic particle hybrid conjugates 410  
 biomaterial-nanoparticle conjugates 370  
 biomaterial-nanoparticle hybrid systems 370  
 biomaterials 378f, 390  
 biomolecules 373ff  
 biopromotor/bioinhibitor 376  
 bioreactors 371  
 biorecognition 414  
 biosensors 371, 390, 398  
 biotin-functionalized nanoparticles 381  
 biotin-functionalized proteins 381  
 bleaching 66, 68  
 Bloch wall 222  
 block-copolymers 56, 272  
 blocking temperature 227  
 Bragg diffraction 270  
 Brewster angle microscopy 246  
 building blocks 251f, 256, 378

### **c**

carbon nanotubes 7, 19  
 catalysts 200  
 catalytic properties of nanoparticles 390  
 CdS colloids 34, 53  
 CdS nanoparticles 51, 56, 59, 60, 244, 246, 248, 313, 392f, 403

- CdS quantum dots 56
  - CdS/HgS QDQWs 68
  - CdSe 313
  - CdSe colloidal quantum dots 34, 249
  - CdSe films 55, 62, 64, 81ff, 98, 242, 246, 256, 320
  - CdSe nanoparticles 55, 62ff, 64, 81ff, 98, 242, 246, 248f, 320, 347
  - CdSe particles 242f
  - CdSe quantum dots 10, 32, 320
  - CdSe quantum rods 319f
  - CdSe/ZnS core-shell nanocrystals 56
  - CdSe/ZnS quantum rods 320
  - CdTe nanocrystals 61, 247
  - CdTe QDs 61
  - chalcogen-bridged molecular clusters 107
  - chalcogen-bridged silver clusters 158
  - charge quantization 34
  - charge transfer bands 326
  - chemical reduction 191
  - chemical self-assembly 270
  - chemical solution deposition (CD) 246
  - chemical vapor deposition (CVD) 201, 244
  - circular dichroism (CD) 373
  - citrate 193
  - close packing 243
  - clusters 118, 240, 296, 297
  - CMOS (complementary metal-oxide-semiconductor) 43
  - Co nanodisks 229
  - Co nanoparticles 13, 204ff, 216, 227, 259, 267
  - Co nanorods 229
  - coagulation 274
  - coalescence 252
  - cobalt 256
  - cobalt modifications 206
  - cobalt nanoparticles 200, 203, 207, 228f, 291
  - cobalt nanorods 265
  - co-deposition of biomaterial 391
  - coercivity 225ff
  - coinage metal elements 107
  - colloid preparation 191
  - colloidal CdS 54
  - colloidal crystals 242, 256
  - colloidal gold particles 189
  - colloidal nanocrystals 308, 320
  - colloidal organometallic syntheses 202
  - colloidal platinum 192
  - colloidal quantum dots 28f, 31, 34
  - colloidal rhodium 196
  - colloidal semiconductor nanocrystals 33
  - colloidal semiconductor quantum dots 32
  - colloidal silver 196
  - colloids of gold 196
  - complementary metal-oxide-semiconductor (CMOS) 43
  - complementary oligonucleotides 379
  - conductive atomic force microscopy (AFM) 308
  - coordination numbers 143, 147
  - copper 192
  - copper chalcogenide clusters 109, 123, 139, 143, 158, 175
  - copper selenide clusters 132, 322f
  - copper sulfide clusters 109, 113f, 133, 147, 176, 323
  - copper telluride clusters 145, 147, 153, 157, 326f
  - copper-telluride-telluroate clusters 155, 177
  - CoPt<sub>3</sub> nanocrystals 209ff, 216, 256, 259, 258, 262ff
  - CoPt<sub>3</sub> nanoparticles 208, 211, 258
  - CoPt<sub>3</sub> nanowires 229
  - core-shell nanocrystals 63, 71, 102
  - II–VI core-shell nanocrystals 92
  - core-shell nanoparticles 55, 63, 71, 102
  - core-shell-type magnetic nanoparticles 220
  - Coulomb attraction 23
  - Coulomb blockade (CB) 35ff, 41, 44, 333, 336f, 343, 347, 351, 353, 359
  - Coulomb blockade island 37
  - Coulomb blockade regime 42
  - Coulomb blocking of tunneling events 330
  - Coulomb charging 359
  - Coulomb effects 328
  - Coulomb energy 332f
  - Coulomb gap 36, 39, 348f, 361f
  - Coulomb interaction 23, 310, 329
  - Coulomb island 333, 337
  - Coulomb staircase 336, 339
  - Coulombic repulsion 189
  - crystal growth 253
  - crystalline phase of nanoparticles 206
  - crystallized nanoparticles 241
  - Cu<sub>2</sub>Se clusters 127, 161
  - Cut-Off Wavelength (COW) 330
  - cyclic voltammograms 412f
  - cytochrome 400
  - cytochrome c 391f
- d**
- 1D 251f, 280
  - 1D-nanoparticle aggregates 291
  - 2D 251f, 260, 262, 267, 280
  - 2D electron gases (2DEGs) 25
  - 3D 251f, 255, 260ff, 267, 270
  - 3D organization 251
  - 3D superlattice formation 243

- data storage devices 199
- de Broglie 7
- de Broglie wavelength 14, 20, 330
- 2 DEG 26
- demagnetization 221
- dendrimer 253
- density of states 13f
- diblock copolymer 274f
- dielectrophoresis 401
- differential scanning calorimetry (DSC) 371
- diop-pen technique 278
- dipole-dipole interacting 291
- dip-pen nanolithography 277, 295
- DNA 56, 250, 281, 285, 369, 372f, 375, 377, 382f, 387, 398, 405
- DNA analysis 410
- DNA biosensors 384
- DNA chips 390
- DNA detection 402
- DNA film 393
- DNA-functionalized Au nanoparticles 384f, 394, 396, 407
- DNA-functionalized nanoparticles 384f, 392
- DNA-functionalized surface 398
- DNA reactivity 376
- DNA recognition 403
- DNA sensing 399f
- DNA spacers 407
- DNA template 386, 393
- DNA template molecule 386
- DNA/oligonucleotides 371
- $\gamma$ -DNA 282f
- DOS (density of states) 308, 318
- double barrier junction 339
- double barrier tunnel junction (DBTJ) 308, 313
- double-barrier SET junction 341
- double-quantum-well nanocrystals 71
- DSC 373
- dynamic light scattering 380
- e**
- electron microscopy 64
- electrodeposition (ED) 201, 246
- electroluminescence 247
- electron beam lithography 27
- electron beam lithographic process 340
- electron diffraction 87, 242
- electron emitters 19
- electron hole pair 30
- electron scattering 64
- electron transport through DNA 407
- electrospray organometallic chemical vapor deposition 248
- electrostatic stabilization 189
- electrostatic trapping 349
- emission spectra 94
- emission spectroscopy 242
- energy quantization 339
- enzyme electrodes 400
- enzymes 379
- EXAFS (extended X-ray absorption fine structure) 59
- exchange anisotropy 229
- excitation spectrum 309
- excitons 30f
- excitonic band gap 310
- exclusion chromatography 52
- f**
- Fast Fourier Transform (FFT) 58
- Fe nanoparticles 217
- Fe nanorods 229
- $\gamma$ -Fe<sub>2</sub>O<sub>3</sub> nanocrystals 218
- FePd 220
- FePt colloidal crystal 258
- FePt nanoparticles 218, 220, 256, 271
- Fermi energy 13
- Fermi function 42
- Fermi level 10, 36
- Fermi wavenumber 13
- ferrofluids 200, 259f
- ferromagnetic 227, 291
- ferromagnetic materials 222
- film formation 274
- fluorescence 90, 94f, 30f, 306, 319f, 384
- fluorescence quantum yield 89
- fluorescence spectra 93
- fluorescence spectroscopy 373
- fluorescent colloidal quantum dots 34
- fluorescent dyes 76, 377, 400
- Fractional Quantum Hall Effect 18
- Frank-Kasper polyhedra 150, 166
- free-electron model 11
- frequency-controlled single-electron tunneling 338
- full-shell clusters 194f
- g**
- GaAs nanocrystals 80, 81, 93
- GaN nanocrystals 81
- gold 192
- gold nanoparticles 252, 261f, 272, 275ff, 278, 281, 285, 293, 371, 373
- Gold Number of Zsigmondy 191
- gold-selenide cluster 182
- Green's function theory 341

guest-functionalized nanoparticles 379  
 guided self-assembly 268

## **h**

Hatree-Fock 8  
 hcp-Co nanodisks 291  
 hcp-Co nanorods 214  
 HgE (E = S, Se, Te) nanoparticles 56  
 HgS quantum well 68  
 HgTe nanoparticles 58  
 high-resolution electrospray ionization mass spectrometry 183  
 HOPG (Highly oriented pyrolytic graphite) 313  
 hormone-receptor 369  
 HRSEM 258, 259  
 HRTEM 54f, 58, 67, 97, 204, 212  
 human immunoglobulin 402  
 hybrid biomaterial-nanoparticle 390  
 hydrophobic colloids 377

## **i**

icosahedral gold particles 205  
 immunoglobulin 371ff  
 InAs core/shell nanocrystals 92  
 InAs nanoparticles 63, 80ff, 86f, 89, 307, 310, 313  
 InAs QDs 312, 315  
 inert gas condensation 201  
 InP nanoparticles 80f, 86f, 95, 249  
 intermetallic compounds 207  
 inverse opals 244, 270  
 IR-emitting nanocrystals 65  
 IR-emitting quantum dots of HgTe 247  
 Ir nanoclusters 195  
 iron nanoparticles 218

## **k**

Kondo effect 26

## **l**

labeled DNA 409  
 Langmuir-Blodgett (LB) 239, 244, 269, 343  
 Langmuir-Blodgett technique 392  
 laser pyrolysis 201  
 lattice mismatch 91  
 lattice-matched superstructures 265  
 layer-by-layer 239  
 layer-by-layer assembly 247  
 layer-by-layer deposition 372, 397  
 layer-type clusters 132  
 LB 246  
 LB films 270  
 LED 90, 96

ligand-stabilized Au nanoparticles 353  
 ligand-stabilized nanoparticles 329  
 ligation of DNA 379  
 light-emitting diode 62  
 lithographic techniques 27  
 luminescence 68  
 luminescence excitation 68  
 luminescence quantum yield 62, 64f  
 luminescence semiconductor nanocrystals 64

## **m**

magnetic metal nanocrystals 203  
 magnetic anisotropy 222, 227, 266  
 magnetic colloidal crystals 259  
 magnetic metal nanoparticles 200  
 magnetic nanocrystals 206, 210, 259  
 magnetic nanoparticles 217f, 226, 289, 291  
 magnetic particles 199, 409f, 413  
 magnetic properties 220  
 magnetic properties of the cobalt 207  
 magnetic resonance 68  
 magnetic susceptibility ( $\chi$ ) 222  
 magnetite nanoparticles 256  
 magnetization 221, 225, 227f  
 magnetocrystalline and shape anisotropies 227  
 magneto-electronic 381  
 mass spectroscopy 252  
 MBE 27  
 metal colloids 187  
 metallic nanowires 19  
 metal nanoparticles 187, 256  
 metal-nonmetal transition 330  
 metal-organic chemical vapor deposition (MOCVD) 244  
 metal-oxide-semiconductor field effect transistors (MOSFETs) 25  
 metal-telluride clusters 175  
 metal vapor synthesis 191  
 micellar film formation 272  
 micellar films 275  
 micelles 56, 272  
 microgravimetric DNA detection 404  
 mineralization 274  
 mismatch in DNA 406  
 mixed-valence clusters 141  
 mixed-valence copper telluride clusters 327  
 MnPt 220  
 MOCVD 27  
 modified Anderson-Hubbard Hamiltonian 362  
 molecular beam epitaxy (MBE) 80, 201  
 molecular crystals 242  
 monoclonal antibodies 379

- monolayers 246, 269
- Moore's Law 328
- multidomain structure 225
- multilayer films 244, 372
- multilayer systems 391
- multilayers of nanoparticles 397
- multiple quantum well 25
  
- n**
- naked clusters 115
- nanobiotechnology 369f
- II–VI nanocrystallites 55
- nanocrystal quantum dots 318
- nanocrystal superlattices 242
- nanocrystals 19, 201
- nanoelectronic devices 292
- nanoeptaxy 68
- nanogravimetry 244
- nanoparticle biomaterial conjugates 397f
- nanoparticle biomaterial hybrid systems 390
- nanoparticle crosslinking 382
- nanoparticle fluorescence 398
- nanoparticle linked biomolecules 409
- nanoparticle protein conjugates 371
- nanoparticles 369, 373ff, 377f, 380f, 389, 404
- nanoparticles as building blocks 280
- nanoparticles for the recognition 376
- nanoparticles functionalized 379
- nanoparticles of gold 193
- nanoparticles of iron and iron carbides 201
- nanoporous alumina 280
- nanoscience 5f
- nanosized HgTe 58
- nanosurfaced surfaces 275
- nanosurfaces 378
- nanotechnology 5
- nanotectonic 244
- nano-transistors 5
- nanowires 214
- Ni nanorods 218
- nickel nanoparticles 218
- NMR 60
- NMR spectroscopy 61
- nano-onions 66
- normal incident pulsed laser deposition 201
  
- o**
- oligonucleotides 279, 397
- oligonucleotide sequences 278
- oligonucleotide-modified Au nanoparticle 400
- oligonucleotides 385f, 394
- one-dimensional (1D) arrays 356
- one-dimensional organization 280
- one-dimensional Schrödinger equation 15
- one-dimensional wires 297
- one-dimensional self-assembly 289
- optical absorption spectra 33
- optical spectroscopy 305f, 315, 319
- optically detected magnetic resonance (ODMR) 58
- opto-electronic devices 305
- organic fluorophores 30, 32
- organometallic cluster 187
- organometallic precursor molecules 199
- orthogonal assembly process 279
- Ostwald ripening 82
  
- p**
- palladium-platinum alloy 192
- particle-in-a-box 15, 330
- particle-in-a-box potential 19
- Pd clusters 394
- Pd nanoclusters 194, 349
- phosphine ligands 125, 155, 157, 163, 175, 325
- phosphorus 182
- photobleaching 64
- photochemical deposition 248
- photoconductivity 249
- photocorrosion 55
- photodegradation 83
- photo-egadation 89
- photoetching 60
- photo-functional protein 392
- photoluminescence 28, 55, 58, 83, 89, 241
- photoluminescence excitation 241
- photolysis 198
- photonic bandgap 270
- photonic crystals 59, 270
- photonic states 270
- photooxidation 64
- plasmon resonance 399
- PLE (photoluminescence excitation) 306, 310f, 315, 319
- PLE spectra 307, 316, 319
- poly(methylmethacrylate) (PMMA) 268
- poly(*p*-phenyleneethynylene) (PPE) 268
- poly(vinyl alcohol) 191f
- poly(vinylpyrrolidone) (PVP) 191f, 268
- polyelectrolyte 372
- polymers 191
- powder diffraction 325
- powder X-ray diffraction 61
- powder XRD 87
- PPh<sub>3</sub> 253
- PPh<sub>3</sub> ligands 268, 270

proteins 379  
 Pt nanoparticles 281  
 PtFe nanocrystals 267  
 optoelectronic devices 381  
 PVP 285

**q**

QD band gap 310  
 QD level 313  
 QDQWs 69  
 Qds 319  
 QRs 319  
 quantum chemical investigations 111  
 quantum computers 44  
 quantum-confined 22  
 quantum-confined systems 8  
 quantum confinement 6, 10, 41, 89, 306  
 quantum confinement effects 307, 310  
 quantum dot cellular automata 43  
 quantum dot laser 4  
 quantum dot quantum wells 66  
 quantum dots 6, 8f, 20ff, 30f, 33, 35, 37, 39ff, 249, 287, 297, 305f, 339  
 quantum effects 328  
 quantum Hall edge states 43  
 quantum mechanical aspects 33  
 quantum mechanical tunneling 331  
 quantum mechanics 6f  
 quantum metrology 338  
 quantum rods (QRs) 305f  
 quantum size CdS membranes 54  
 quantum sized 280  
 quantum size effects 27, 305, 308, 310, 329, 342, 358  
 quantum size particles 55  
 quantum structures 305  
 quantum well 6, 66, 91  
 quantum well laser 33  
 quantum-well nanocrystals 71  
 quantum wires 6, 18, 306  
 quantum yield 53, 314  
 qubits (quantum bits) 44

**r**

radiolysis 198  
 radiolytic and photochemical reduction 191  
 Raman scattering 398  
 receptor proteins 386  
 resistance quantum 332  
 Resonance Raman spectra 51  
 resonance-enhanced absorption 398  
 reverse micelles 201  
 reverse micelles 359  
 reverse micelles 56

RNA and DNA purification 409  
 rules of quantum mechanics 332

**s**

salt reduction 192  
 SAXS 211f  
 scanning tunneling microscopy (STM) 244, 306, 308, 340f  
 scanning tunneling spectroscopy (STS) 343  
 Scherrer equation 58  
 Schrödinger equation 7f, 12, 14, 22  
 SE 337  
 IV–VI semiconductor nanocrystals 61  
 II–IV semiconductor 241, 244  
 II–V semiconductor 80  
 II–VI semiconductor 93, 96  
 II–VI semiconductor nanoparticles 50, 55, 57, 81  
 III–V semiconductor 93  
 III–V semiconductor nanocrystals 61, 79ff, 84, 249  
 III–V semiconductor QDs 80  
 SE structures 340  
 SE transistor 336, 340  
 Se<sup>2-</sup>/SePh<sup>-</sup>-bridged copper clusters 136  
 Se<sup>2-</sup>/SeR<sup>-</sup>-bridged copper clusters 135  
 secondary ion mass spectrometric (SIMS) 253  
 selenide clusters 147, 323  
 selenide ligands 166, 182  
 selenide/selenolate clusters 136, 142  
 selenido/selenolato-bridged clusters 118  
 selenido/selenolato-bridged copper clusters 135  
 selenium ligands 116, 120, 124, 127, 137, 182  
 selenium-bridged copper clusters 116, 134f  
 selenium-bridged gold clusters 181  
 self-assembled magnetic nanocrystals 267  
 self-assembled monolayers (SAMs) 261, 295, 341, 376  
 self-assembled quantum dots 28, 32f  
 self-assembling 272  
 self-assembling of metal nanoparticles 272  
 self-assembly 277  
 self-assembly from solution 261  
 self-assembly of monodisperse nanoparticles 255  
 self-assembly of nanoparticles 261  
 self-organization 242, 259f, 269, 275, 280  
 SEM 256, 258, 271  
 semiconductive nanoparticles 400  
 semiconductor 7, 19  
 semiconductor crystal 7

- semiconductor diode laser 320
- semiconductor nanoparticles 7, 241, 244, 249f, 250, 256, 305ff, 314, 320
- semiconductor quantum dots 6
- serum albumin 372f
- SET 331, 338f, 345, 353
- SET transistor 345, 347f
- shape anisotropy 229
- silver nanoparticles 262, 371
- silver selenide/selenolate clusters 139
- silver-selenium clusters 158
- silver-tellurium clusters 169
- single electronics (SE) 329
- single-crystal X-ray diffraction 147, 239
- single-domain magnet 226
- single-domain particles 222, 224f, 227
- single-electron charging 351
- single-electron devices 329, 345, 352
- single-electron logic (SEL) 329
- single-electron switches 251
- single-electron transistor 29, 37, 39, 43, 308, 329, 333, 337, 349
- single-electron transition 333
- single-electron tunneling (SET) 35, 41f, 305, 308, 329, 331, 338
- singlet excitation energies 322
- size quantization 29
- size-dependent magnetic behavior 220
- Size-Induced Metal-Insulator Transition (SIMIT) 330
- size-quantization 330
- S-layers 275
- small-angle X-ray diffraction (SAXRD) 254
- small-angle X-ray scattering (SAXS) 64, 211, 380
- small-angle XRD 57
- Smoluchowski model 380
- solid-state absorption spectra 324
- solid-state SET devices 353
- solid-state UV-VIS spectroscopy 323
- sonochemical synthesis 202
- spherical quantum dot 23
- spin-coating 249
- spontaneous self-assembly 263
- SPR spectrum 399
- sputtering 201
- Stark effect 313
- steric stabilization 189
- STM (scanning tunneling microscope) 312, 316, 340f, 394
- Stokes shift 30
- Stranski-Krastanov 27
- streptavidin-functionalized Au nanoparticles 373
- STS 345, 352
- sulfur ligands 113
- sulfur-bridged copper clusters 109, 118, 134
- superconductive quantum interference device (SQUID) 221
- superlattice formation 242
- superlattices 242, 252, 255
- superparamagnetic 225ff, 258, 290
- superstructures 239, 241f
- surface plasmon resonance 398
- surface plasmons 33
- surface-enhanced fluorescence 390
- surface-enhanced Raman scattering (SERS) 399
- surface-enhanced Raman spectroscopy (SERS) 390
- surface-enhanced resonance Raman (SERR) 373
- surfactants 28f
- synchrotron radiation 71
- t**
- telluride ligands 147, 155, 157, 177
- tellurium-bridged copper clusters 147
- tellurolate ligands 170
- TEM (HRTEM) 53, 55ff, 69, 88f, 187, 208ff, 213, 244, 252, 254, 256, 263, 268, 272, 281f, 287, 291
- thermogravimetric analyses 325
- thiolated DNA 395
- TiO<sub>2</sub> nanoparticles 374, 391f
- tip-induced nanoelectrical reaction 295
- Tollman cone angle 160
- TOPO 80, 82, 86, 92f, 213
- TOPO method 62
- TOP-TOPO 93, 95
- transistors 251, 292
- transmission electron microscopy (TEM) 32, 51, 87, 97, 242, 310, 320, 380,
- tunnel junction 35f, 339f
- tunneling 305f
- tunneling conductance spectra 310, 315
- tunneling DOS 310
- tunneling electron transport 200
- tunneling resistance  $R_T$  339
- tunneling spectra 316
- tunneling spectroscopy 308, 319
- tunneling spectroscopy on Au<sub>55</sub> monolayers 343
- tunneling transport 308
- TURBOMOLE 111, 115, 133
- two-dimensional 243
- two-dimensional assembly 358



**u**

UV lithography 338  
UV-VIS absorption spectroscopy 61, 241  
UV-VIS solid-state absorption spectra  
327  
UV-VIS spectroscopy 92, 326

**v**

vacuum induction 281

**w**

wide-angle X-ray diffraction (WAXRD) 254  
wide-angle X-ray scattering 64  
wide-angle XRD 57

**x**

XPS (X-ray photoelectron spectroscopy) 71,  
275, 324  
X-ray analysis 169  
X-ray diffraction (SARXD) 54f, 58, 99, 242,  
244, 252  
X-ray photoelectron spectroscopy (XPS) 64,  
87, 96  
X-ray spectroscopy 64  
XRD 55f, 57, 93, 99, 101, 204, 208

**z**

ZnS nanocrystals 93, 101  
ZnSe core-shell nanocrystals 56  
ZnSe nanocrystals 62